Engineering Intravenous Therapies for Trauma

Trey Joseph Pichon

A dissertation

submitted in partial fulfillment of the

requirements for the degree of

Doctor of Philosophy

University of Washington

2023

Reading Committee:

Suzie H. Pun, Chair

Nathan J. White

Drew L. Sellers

Program Authorized to Offer Degree:

Bioengineering

University of Washington

Abstract

Engineering Intravenous Therapies for Trauma

Trey Joseph Pichon

Chair of the Supervisory Committee:
Suzie H. Pun
Department of Bioengineering

Trauma leading to severe hemorrhage and shock on average kills patients within 3 to 6 hours after injury. With average prehospital transport times reaching 1-6 hours in low- to middle-income countries, stopping the bleeding and reversing hemorrhagic shock is vital. This thesis aims to develop a "Bridge to Blood" that combines PolySTAT, an intravenous hemostat that crosslinks fibrin at the wound site, with a Low Volume Resuscitant (LVR) designed to refill the vascular space after severe hemorrhage. For PolySTAT, the main goals of this work have been to continue its translation through the optimization of its water solubility and synthesis method (**Chapter 2**), to determine its safety and efficacy in large animal models (**Chapter 3**), and to understand mechanistically how PolySTAT affects coagulation (**Chapter 4**). All of these chapters support the clinical translation of PolySTAT and gather the data necessary for an Investigational New Drug Application with the FDA. For the LVR, the goal of this work was to show proof of concept of how to engineer polymer chemistry, structure, and architecture to provide the desired oncotic effect *in vivo* and to avoid disruption of coagulation in *in vitro* assays (**Chapter 5**). This chapter has set the foundation for the lab to engineer new LVRs and complete the "Bridge to Blood". **Chapter 6** demonstrates how to leverage the flexible nature of the PolySTAT platform, and its ability to target fibrin networks in vivo, to target to and activate CAR T Cells in solid tumors as a potential treatment for cancer. The final chapter, **Chapter 7**, outlines future work to build on the PolySTAT and LVR platforms in hopes of overcoming challenges identified from the work completed in the previous chapters.

Dedication

This is dedicated to four individuals:

To my mom, thank you for teaching me to never see barriers in my life, and that it is never too late to follow a new passion. Whenever I need guidance in life, I turn to you. Thank you.

To my dad, thank you for always reminding me “Don’t be a one bun” (which means don’t do things half-a**ed) and for spending countless hours taking me to baseball practices and games. Those are some of the happiest memories of my life.

To my lovely daughter Elodie, you fill my day with toothless smiles, dancing, funny faces, and laughter. Thank you for bringing pure joy to my life.

To my beautiful wife Leighton, we moved across the country, we got married, survived a pandemic, bought a fixer upper, and had a daughter, what will the next five years bring? I am so happy and thankful to share this life with you.

I love y’all.

Acknowledgements

I received so much support from the community around me, and I wish I was a better writer to express how thankful I am:

Suzie, who truly puts her students first, thank you!
Nathan, who makes being an ER doctor look so cool (he jumps out of helicopters) and unknowingly, almost made me want to go to medical school too.
Drew, who is NOT the curmudgeon of the lab, but is an endless source of new ideas.
To the rest of my committee members, Cole DeForest, Nate Sniadecki, and Hongxia Fu, thank you for the support, guidance, and for challenging my ideas.

Bob, who is described by everyone "Ah I love Bob".
Alex, whose genuine curiosity and excitement about the world made him the best desk mate.
Xu, who, if I ever need a major surgery, I want him to do the surgery.
Dan, who taught me how to be a chemist and to always strive to be a better scientist.
Clinton, whose adventurous spirit inside and outside the lab made him a joy to work with.
Lucy, who introduced me to the world of bubble tea, and now I am officially addicted.
Ben, who is the king of memes, trying new reactions, and telling me about the best places to eat.
Ethan, whose creativity is going to take the trauma work to new heights and who reminded me that all those hours struggling in the lab builds character.
To the rest of the Punions (Nataly, Shixian, Albert, Meilyn, Ian, Gary, Emmeline, Audrey, Kairui, Kefan, Melissa, Abe, Mishti, Sydney, Joey, Tran, Omeed, Ben M, Jai, Yunshi) and to the rest of the EM Lab (Kristyn, Sue, Alex, Chang Yeop, Sarah) – All of y'all made the lab feel like a family, thank you for making it such a joy to come to lab every day!

Quirk, who I call whenever I need to laugh.
The Brew Crew (Eric, Seth, David), here's to a future of many more winning brews together.
To the rest of all my friends in Seattle, the Northeast, and Georgia, thank you for all the good times we have shared together. Looking forward to many more!

To all the Gore associates who mentored me and helped me get to this point, thank you!

Finally, to my family in Georgia, Nashville, and Seattle, thank y’all for supporting both Leighton and me through this endeavor. Love y’all!

TABLE OF CONTENTS

Chapter 1. ENGINEERED INTRAVENOUS THERAPIES FOR TRAUMA

Trey J. Pichon, Nathan J. White, Suzie H. Pun

Abstract: Trauma leading to severe hemorrhage and shock on average kills patients within 3 to 6 hours after injury. With average prehospital transport times reaching 1-6 hours in low- to middle-income countries, stopping the bleeding and reversing hemorrhagic shock is vital. First-generation intravenous hemostats rely on traditional drug delivery platforms, such as self-assembling systems, fabricated nanoparticles, and soluble polymers due to their active targeting, biodistribution, and safety. We discuss some challenges translating these therapies to patients, as very few have successfully made it through preclinical evaluation in large-animals, and none have translated to the clinic. Finally, we discuss the physiology of hemorrhagic shock, highlight a new low volume resuscitant (LVR) PEG-20k, and end with considerations for the rational design of LVRs.

This work has resulted in a publication: Pichon *et al. Current Opinion in Biomedical Engineering.* (2023) **27:**100456.

1.1 INTRODUCTION

Trauma was responsible for more than 4 million deaths worldwide in 2019, a total greater than tuberculosis, HIV, and malaria combined, with road injuries being the leading cause of death for people aged 5 to 49.[1] The WHO estimates that 90% of trauma-related deaths occur in low- and middle-income countries, where average prehospital transport times can range from 1-6 hours.[2,3]

During trauma-related severe hemorrhage (>30% total blood loss), hypovolemia and hypoperfusion of organs can lead to hemorrhagic shock.[4] The reduced oxygen supply leads to anaerobic respiration, and results in lactate and acidosis. The severe blood loss and shock result in trauma-induced coagulopathy (TIC) impairing the body's ability to clot, and perpetuating the vicious cycle (Fig 1 below).[5] Multiple randomized control trials (RCTs) indicate the vast majority of hemorrhage-related fatalities occur within 3 to 6 hours after injury.[6,7] Damage control resuscitation prioritizes surgical control to stop the bleeding, while simultaneously resuscitating to restore the intravascular space to reverse hemorrhagic shock in hopes of preventing TIC.[8]

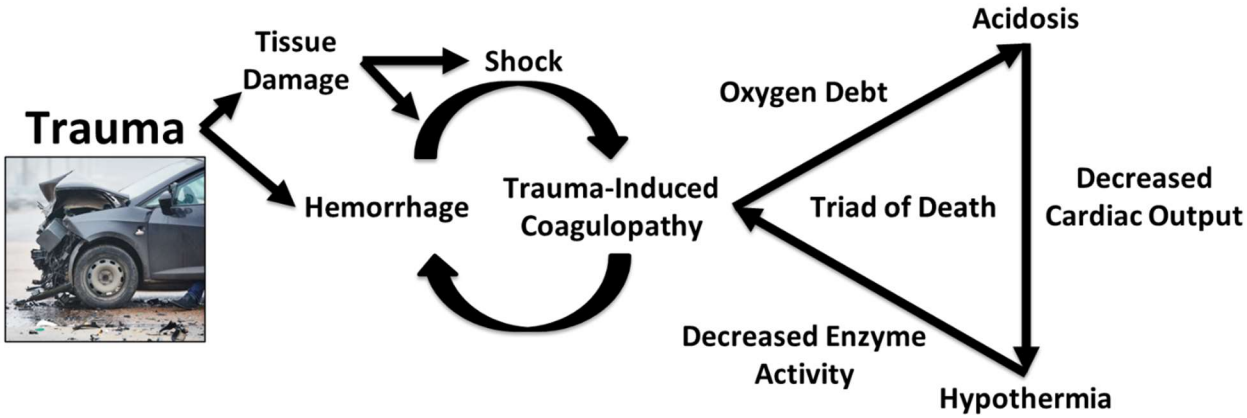

Figure 1. Vicious cycle of severe hemorrhage from trauma. Tissue damage and severe hemorrhage from trauma lead to hemorrhagic shock. All three of these result in trauma-induced coagulopathy (TIC) which leads to more hemorrhage. TIC is part of the triad of death where it is compounded by acidosis and hypothermia.

This review focuses on synthetic intravenous hemostats and fluid resuscitants (as opposed to purified or isolated natural products), that leverage polymer chemistry, bioengineering, and drug delivery principles to treat hemorrhage and hemorrhagic shock in the prehospital setting.

1.2 Intravenous Hemostats

Hemostasis is driven by a quiescent circulating system of fully soluble proteins (vWf, fibrinogen) and colloidal particles (platelets, erythrocytes) that can be rapidly activated by blood factors (FII, FX, etc.) to self-assemble into an insoluble heterogenous hemostatic plug to halt bleeding.[9]

Furthermore, this system undergoes platelet-driven mechanical contraction and compaction of the fibrin network to stabilize the plug and fully close the wound. In primary hemostasis, platelets form an initial plug at the wound site. The activated platelets release coagulation factors and provide a surface to initiate secondary hemostasis that results in the formation of a fibrin network that reinforces the clot on the backside of the vessel.

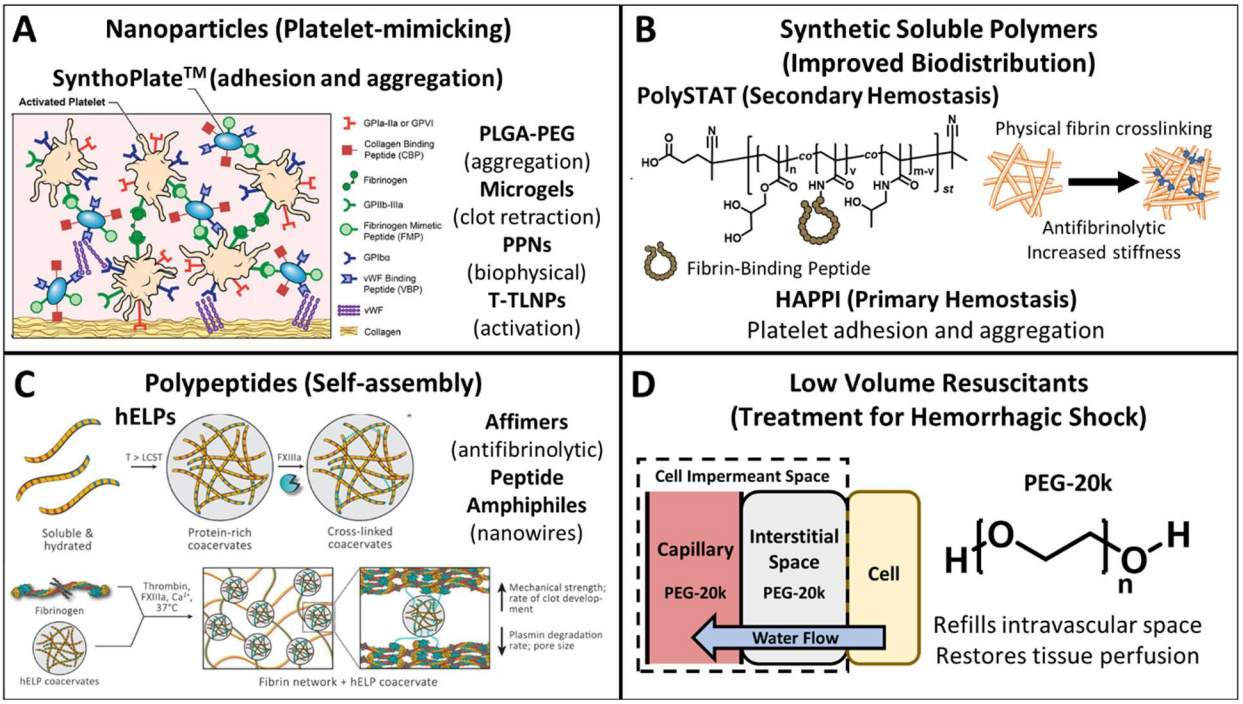

Figure 2. Synthetic intravenous hemostats and low volume resuscitants. A) Nanoparticle systems recapitulate one or multiple characteristics of platelets - adhesion, aggregation, clot retraction, activation, and biophysical. B) Synthetic soluble polymer systems improve biodistribution (compared to nanoparticles), and target both primary and secondary hemostasis. C) Polypeptides self-assemble at the wound site to increase the mechanical strength of clots or disrupt native enzymatic activity. D) Low volume resuscitants consisting of PEG-20k act as both a cell impermeant and a traditional colloid which drives water from the intracellular space and interstitial space to the intravascular space. Figure 2A was modified from [24] by under the Creative Commons Attribution 4.0 International license. Figure 2C was modified from [33] under the Creative Commons CC BY-NC-ND 4.0 International License.

Traditional drug delivery platforms, such as self-assembling systems (e.g., liposomes, peptide amphiphiles), fabricated nanoparticles (e.g. polymer micelles), and soluble polymers (e.g. polymer-peptide conjugates) were used as the basis of most first-generation intravenous hemostats. The active targeting and pharmacokinetic properties of these systems promoted accumulation at the active site of bleeding. More recent intravenous hemostats capitalize on the modularity of the parent platforms to recapitulate biophysical aspects of hemostasis and deliver payloads that augment the hemostatic plug.

1.2.1 *Fabricated Nanoparticles (Polymer Micelles)*

Nanoparticle hemostats target primary hemostasis and mimic one or more properties of platelets – biophysical, aggregation, adhesion, clot retraction, and activation.[10,11] The Lavik group reported 400-500 nm particles consist of a degradable polyester core of poly(lactic-co-glycolic acid) (PLGA) or poly(lactic acid) (PLA) with poly(ethylene glycol) (PEG) arms functionalized with GRGDS peptides that bind to activated platelets and increase platelet aggregation. These particles increase survival in a lethal, non-coagulopathic rat blast trauma model (single bolus injection immediately after injury, dose = 5 mg/kg) and doses of 0.8 mg/kg, 2 mg/kg, and 3.3 mg/kg halt bleeding in a lethal, non-coagulopathic porcine grade III liver injury model (single bolus injection 5 minutes after injury), while 6.6 mg/kg led to rapid exsanguination.[12,13] The platform is flexible; the polyester core has been replaced with chitosan succinate[14] or polyurethane nanocapusles that can be used for drug delivery.[15] Additionally, Gkikas et al. attached the fluorescent dye DiD and gold particles to hemostatic PLGA-PEG nanoparticles to image internal bleeding with near-infrared imaging, and X-ray computed tomography.[16] Hong et al. evaluated PLGA-PEG-GRGDS particles of various sizes and reported that particle size affected targeting of platelets, lung accumulation, platelet adhesion, and survivability in a lethal, non-coagulopathic rat inferior vena cava puncture model (single bolus injection immediately after injury, dose = ~67 - 89 mg/kg).[17]

The Barker group developed poly(N-isopropylacrylamide-co-acrylic acid) microgels decorated with fibrin-specific variable domain-like recognition motifs (sdFvs). Due to interactions between the soft microgels and polymerized fibrin network, the particles recapitulated platelet clot retraction by collapsing fibrin networks and increasing clot stiffness, which decreased bleeding

times in a lethal, non-coagulopathic rat femoral bleed model (single bolus injection 5 min prior to injury, dose = 40 - 50 mg/kg).[18,19] To decrease cost, the Brown group replaced the antibody fragments with peptides that mimic fibrin knob 'B' and targets fibrin hole 'b'. These new "Fibrin-Affine Microgels with Clotting Yield" showed similar activity to the 1st generation antibody particles and decreased bleeding in a non-coagulopathic mouse liver laceration model (single bolus injection 5 minutes prior to injury, dose = 5 - 50 mg/kg).[20] Fibrin-targeted poly(N-isopropylacrylamide) nanogels have been loaded with tissue-type plasminogen activator (tPA), for delivery of targeted therapeutics.[21]

The Sen Gupta Group incorporates multiple peptide functionalities in their platelet-mimicking nanoparticles. SynthoPlate™ consists of 200 nm lipid vesicles with a PEG outer shell, decorated with three different peptides, vWF- and collagen-binding, and a fibrinogen mimic that binds active platelet integrin GPIIb-IIIa. SynthoPlate™ recapitulates both platelet adhesion and aggregation, improving "golden hour" survival in a lethal, non-coagulopathic porcine femoral artery traumatic bleed model (single bolus injection 1 minute after injury, dose = 1.7×10^{11} particles/kg).[22–24] Their next-generation platelet-mimicking procoagulant nanoparticles (PPNs) recreate the procoagulant function of the platelet surface through diastearyol phosphatidylserine that is masked by plasmin-cleavable PEG. The anionic phospholipid is cloaked in circulation but unmasked at the site of injury, creating a surface to bind blood factors and results in the upregulation of thrombin generation. The PPNs decrease bleeding in a lethal, thrombocytopenic mouse liver transection model (single bolus injection 20 minutes before injury, dose = 2 mg/kg) and decreased bleeding in a lethal rat liver transection model (single bolus injection immediately after injury, dose = 2 mg/kg).[25] Because the PPNs rely on thrombin generation that can be impaired in TIC, thrombin-loaded injury-site-targeted lipid nanoparticles (t-TLNPs) that release thrombin at the wound site were also recently reported. The t-TLNPs decrease bleeding and reverse severe coagulopathy in both a mouse tail-clip model (thrombocytopenia and heparin, single bolus injection 15 minutes before injury, targeted thrombin dose = 0.031 mg/kg) and a mouse liver transection (heparin, single bolus injection immediately after injection, targeted thrombin dose = 0.031 mg/kg). [26]

1.2.2 *Synthetic Soluble Polymers*

In contrast to the nanoparticle systems discussed previously, unimeric peptide-polymer conjugates do not form supramolecular structures in solution. Unlike nanoparticles which are recognized and rapidly cleared by the reticuloendothelial system, soluble polymers offer a more desirable biodistribution for intravenous hemostat applications. We have previously reported PolySTAT, a soluble polymer displaying multiple fibrin-binding peptides, that physically crosslinks and reinforces the fibrin network that forms during secondary hemostasis. PolySTAT reduces bleeding and improves survival in a lethal, non-coagulopathic rat femoral bleed model (single bolus injection immediately after injury, dose = 15 mg/kg).[27–29] Recently, using a similar concept, the Mitragotri group developed HAPPI (hemostatic agent via polymer peptide infusion), hyaluronic acid polymer with grafted collagen-binding and von Willebrand factor-binding peptides. Their system exhibited selective binding to activated platelets, promoted platelet accumulation in vitro, and improved survival time in a lethal, non-coagulopathic rat inferior vena cava traumatic puncture model (single bolus injection immediately after injury, dose = 12 mg/kg).[30]

1.2.3 *Polypeptides*

Lastly, polypeptides have been developed to target and bind hemostatic factors, with some designed to self-assemble into hierarchical structures. Kearney et al. screened libraries of scaffold proteins to identify fibrinogen-binding proteins, and further showed that the proteins delay plasmin-mediated breakdown of clots by interfering with plasminogen-fibrin binding.[31]

Elastin-like polypeptides (ELPs) use a repeat pentapeptide (VPGXG) based off human tropoelastin that enables stimuli-responsive (pH, temp., light, salt) hydrophobic-driven collapse and aggregation in solution.[32] Urosev et al. developed a recombinantly-produced 69 kDa hemostatic elastin-like polypeptide (hELP), that included an interspersed glutamine-based recognition sequence optimized for FXIIIa activity, and a lysine-donor block that enables hELPs to be covalently crosslinked into fibrin gels by FXIIIa. At physiologic temperature of 37 C, above the lower critical solution temperature of the ELP, the hydrophobic phase separation mechanically stiffened fibrin clots, and decreased clot porosity, which improved clotting kinetics and decreased fibrinolysis.[33] The in vivo hemostatic efficacy of hELPs has not yet been reported.

Klein et al. developed a panel of tissue factor-targeting peptides attached to a generic peptide amphiphile (PA) sequence. When near each other, these 14-28 amino acids long (1.6-3.1 kDa) PAs self-assemble to form nanofibers of ~10-20 nm in diameter with lengths in the micrometer range. The best performing tissue factor-targeted PAs decreased blood loss by 35% - 59% compared to controls in a non-coagulopathic rat liver punch injury model (single bolus injection before injury, dose = ~5.6 – 7.1 mg/kg).[34,35]

1.2.4 *A Key Challenge to clinical translation.*

Pre-clinical synthetic injectable hemostatic agents have shown great promise in preclinical rodent models. However, significant challenges arise when moving to large animal models mainly due to a lack of models accurately reproducing human traumatic coagulopathy.[36,37] Porcine models are a popular choice for trauma and resuscitation research and development given their larger size, blood volume, and similar cardiovascular system to humans. However, swine have distinct differences compared to humans when considering their blood coagulation and pulmonary systems. Pigs are hypercoagulable compared to humans and create very strong, robust blood clots with dense fibrin networks, that unlike humans, do not undergo significant fibrinolysis.[38] Hemodilution can be used to create a dilutional coagulopathy; however, significant dilution is needed to make the clots hypocoagulable. Therefore, complex polytrauma with hemorrhagic shock alone is often insufficient to induce coagulopathy and hyperfibrinolysis like that seen with human traumatic coagulopathy.

Pigs are also distinct from humans in that their lungs that are laden with pulmonary macrophages. When exposed to therapies in the form of nanoparticles and polymers, pigs tend to exhibit complement activation-related pseudoallergy (CARPA) that mimics anaphylaxis. CARPA is mediated by massive release of vasoactive substances by pulmonary macrophages, leading to leading to significant pulmonary vasoconstriction. The Lavik group has mitigated CARPA response to their synthetic platelets through optimization of infusion rate, concentration, charge, PEG molecular weight (MW) and density, and have also developed in vitro screening tools to predict a therapy's likelihood of triggering CARPA.[12,13,15,39] Formulations that did not activate complement in vitro also avoided complement activation in vivo. However, unexpectedly, hard

thrombi were observed in uninjured tissues of animals treated with both control and hemostatic nanoparticles, but not with saline, emphasizing the need for further safety studies with injected nanoparticles.[40] To date, CARPA reactions to SynthoPlate™ have not been reported. In addition to reducing blood loss and prolonging acute survival in a lethal, non-coagulopathic porcine femoral artery traumatic bleed model, SynthoPlate™ has also been shown to be well-tolerated without clinically-relevant thromboembolic events after repeated dosing in healthy dogs where thrombocytopenia is common.[24,41,42] However, due to the ethical constraints around clinical trials, the standard for demonstrating efficacy in preclinical trauma testing is high. The reader is encouraged to review a recent recommendation on end points for conducting trauma-related clinical trials.[6,7]

1.3 RESUSCITATION FLUIDS

1.3.1 *Principles of Fluid Resuscitation*

Severe hemorrhage (>30% total blood loss or >1.5 L of blood) results in hemorrhagic shock that requires fluid resuscitation to reduce mortality. The body replaces this lost volume through transcapillary refill, an auto-resuscitative process whereby 500 to 1500 mL of fluid are transferred from the interstitial and intracellular spaces to refill the intravascular space (Figure 3A below shows a breakdown of water in the human body). The fluid is believed to mainly come from skeletal muscle, which accounts for ~40% of total body mass and contains ~5 L and ~15 L of interstitial and intracellular fluid, respectively.[43]

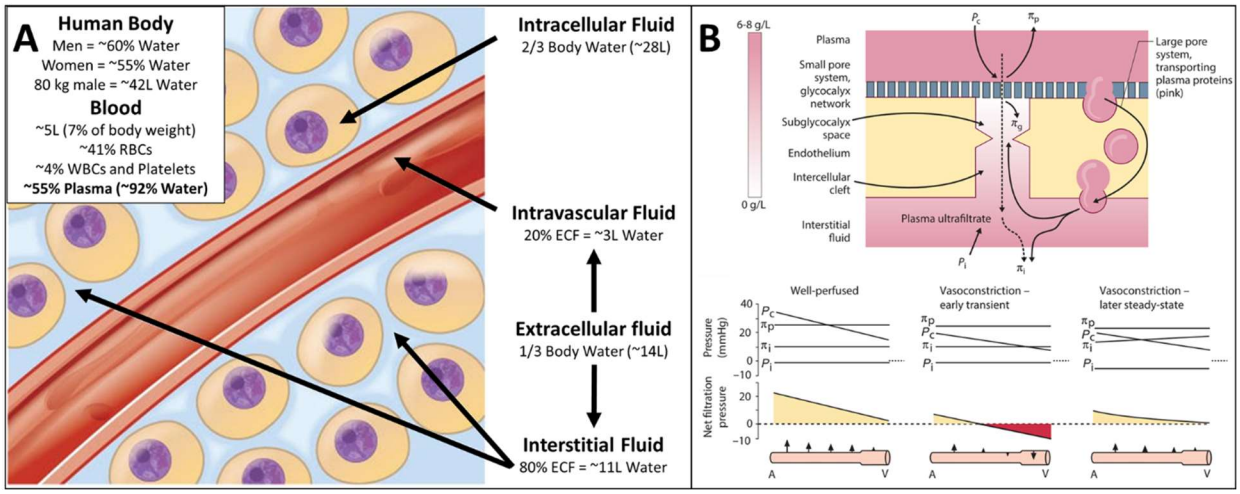

Figure 3. Principles of fluid resuscitation. A) Distribution of water between different compartments in the human body. B) Schematic of the Revised Starling principle that leads to fluid filtration across the capillary wall and three scenarios of filtration pressures (normal, transient capillary refill during severe hemorrhage, and reduced fluid filtration during shock). Figure 3A was modified from [78] by Lindsay M. Bigaet al. under the Creative Commons CC BY-SA 4.0 International License. Figure 3B was modified from [46] by Neil Herring and David J. Paterson, Copyright 2018 and reproduced by permission of Taylor and Francis Group, LLC, a division of Informa plc.

Water in the body is moved from compartment to compartment through the tight control of capillary walls and cell membranes. Since fluid resuscitants provide water, salts, and sometimes macromolecules, it is important to understand how the water and other constituents move across compartments. Volume kinetics applies pharmacokinetics fundamentals to analyze and simulate how the volume of intravenously administered fluids are distributed and eliminated in the body. The reader is directed to two excellent reviews that cover the application, math, and clinical implications.[44,45]

In the body, fluid flows out of the capillary beds into the interstitial space, which then drains into the lymphatic system and is returned to the intravascular space. The inside of blood vessels (intraluminal) is composed of endothelial cells connected by tight junctions and adherens that prevent plasma proteins from passing between cells. The intraluminal surface of endothelial cells is covered in a negatively charged layer of glycoproteins known as the endothelial glycocalyx (GCX), a structure that is crucial to modulating immune recognition, coagulation, and inflammation at the surface of endothelial cells. The GCX also serves as a semipermeable, filtration barrier for plasma proteins that creates a near protein-free ultrafiltrate of fluid that passes between endothelial cells from vasculature to interstitium (Figure 3B above).

The transport of fluid across the vessel wall was classically described by the Starling Equation which was updated after the development of the Michel-Weinbaum GCX model to the following:

$$J_V = L_P S[(\Delta P_{c-i}) - \sigma_d(COP)] = L_P S[(P_c - P_i) - \sigma_d(\pi_P - \pi_G)]$$

The fluid flux, J_V, is dictated by two opposing forces, i) the difference between the intravascular pressure in the capillary bed (P_c) and the interstitial space (P_i), which pushes fluid out of the

capillary, and ii) the colloid osmotic pressure (COP), which is the difference between the plasma (π_P) and the subglycocalyx space (π_G) osmotic pressures, and drives water into the capillary. S is the capillary surface area, L_P is the hydraulic conductance, or physically, the permeability of the vascular wall to water, and σ_d is the osmotic reflection coefficient, or physically, the permeability of the vascular wall to solutes.[46–48]

During normal steady state, pressure drops along the length of the capillary bed and plasma-free fluid is constantly flowing across the capillaries into the interstitial space, with fluid flux decreasing from the arterial to the venous side due to reduced intravascular pressure.

When severe hemorrhage occurs, blood pressure is reduced, coupled with arteriolar vasoconstriction and a decrease in precapillary resistance. Therefore, P_c is sharply decreased on the arterial side of capillaries. As a result, P_c is reduced below COP, leading to transient transcapillary refill that causes fluid to be reabsorbed into the intravascular space. Eventually, the revised Starling equation factors adjust and a steady state fluid flow outwards from the intravascular space to the interstitial returns (albeit at a much lower J_V). Severe trauma is associated with sympathoadrenal activation, inflammation, and shedding of the endothelial glycocalyx and leaky capillary barriers, which significantly disrupts these finely tuned Starling forces.[49]

1.3.2 *Clinical Use of Resuscitation Fluids*

There have been many attempts to use non sanguineous resuscitation fluids, including crystalloids (normal saline, lactated ringers, hyperoncotic saline) or colloids (albumin, starches, dextrans, gelatin) for resuscitation of critical illness and injury. While these fluids can provide temporary intravascular volume expansion during resuscitation of shock, they have largely been replaced by blood products for use during hemorrhage due to their negative effects on blood coagulation and association with increased organ failure and mortality in trauma patients.[50–53] However, new engineered colloids are in development that may provide new and interesting capabilities.

1.3.3 *PEG-20k as a Novel Low Volume Resuscitant*

A single low volume infusion (10% of estimated blood volume) of a concentrated, 10% w/v, 20 kDa PEG (PEG 20k) solution has shown remarkable potential as a new fluid resuscitant.[54] The

PEG-20k (also called a "low volume resuscitant" or LVR) acts both as a cell impermeant, drawing fluid out of the intracellular space and shrinking parenchymal and endothelial cells to alleviate compression of capillaries, and a traditional colloid increasing intravascular volume to reperfuse tisses.[55] The LVR increases the tolerance of a patient's organs to the low volume state of hemorrhagic shock, similar to organ preservation, improving a patient's ability to cope with low blood pressure or the hypotensive state. To quantify the effect of a resuscitation fluid on the metabolic tolerance of animals to the low volume state, a metric known as "LVR time" is used. The LVR time reflects the duration of reduced lactate levels that is achieved after LVR administration.

In a lethal, severe hemorrhagic shock rat model, where ~50 - 60% of total blood volume was removed, PEG-20k registered the maximum possible LVR time of 240 minutes, and fully rescued MAP back to baseline levels (single bolus infusion of 10% of estimated blood volume of 10% w/v PEG-20k, dose = ~625 mg/kg).[56] In a preclinical porcine model of lethal hemorrhagic shock, PEG-20k had superior survival rates (100%, n=6) at 24 hours compared to whole blood (16.7%, n=6) and Hextend (0%, n=5), all treatments were given via a single bolus infusion of 10% of estimated total blood volume.[57] In a lethal, non-coagulopathic hybrid-model of controlled (tail bleed) and uncontrolled (splenic bleed) hemorrhage in rats, PEG-20k had an LVR time of 240 minutes (100% survival), and PEG-20k-treated rats did not show any signs of clot rupturing, even though their average MAP nearly returned to baseline after infusion.[54] Additional mechanistic studies revealed that PEG-20k did not affect the extrinsic or intrinsic coagulation pathways, but did disrupt platelet-fibrin(ogen) interactions leading to a mild thrombocytopenia.[58–61] Measurements of capillary blood flow in rats during resuscitation showed PEG-20k increased blood flow from baseline much more than normal saline.[55] To better understand the ratio of PEG-20k in the intravascular space versus the interstitial space, the osmotic reflection coefficient (σ_d) was measured in rats and found to be 0.65, which means ~65% of the PEG molecules stay in the intravascular space while ~35% migrate to the interstitial space.[62] This ratio may be key to the favorable action of PEG-20k by enabling an oncotic gradient moving fluid from cellular to interstitial and intravascular spaces, thus preventing cytotoxic cellular edema. Additional in vivo studies exploring the effect of MW demonstrated PEG-20k and PEG-40k had nearly identical efficacy in a lethal hemorrhagic shock rat model, whereas PEG-8k and PEG-100k, while still increasing the LVR time compared to the

saline control, did not perform as well.[54] In a mouse biodistribution study, it was reported only ~4% of radiolabeled PEG-20k remained in the mouse at 72 hours post injection.[63]

1.3.4 *Considerations for future polymer-based LVRs*

PEG-based LVRs have highlighted the potential of polymer engineering to open the door to new rationally designed low volume resuscitants. Reversible addition-fragmentation chain-transfer (RAFT) (Figure 4A), atom transfer radical polymerization (ATRP), and ring-opening metathesis polymerization (ROMP) are all controlled polymerization techniques frequently used in drug delivery.[64,65] RAFT, ATRP, and ROMP allow the precise control of length (degree of polymerization and MW), composition (statistical or block copolymers, single-unit insertion), dispersity, architecture (linear, comb, radiant star, hyperbranched), degradability (enzymatic, hydrolytic, thermal), stimuli-responsive linkers, and end-group functionalization across a wide-range of monomers (neutral, anionic, cationic, zwitterionic, peptides, DNA, sugars).[66–72] The field of drug delivery has leveraged these techniques to create polymer vehicles (peptide conjugates, micelles) that can target, circulate, and release therapies to control biodistribution, pharmacokinetics, and degradation in the body (Figure 4B and 4C below).[73,74]

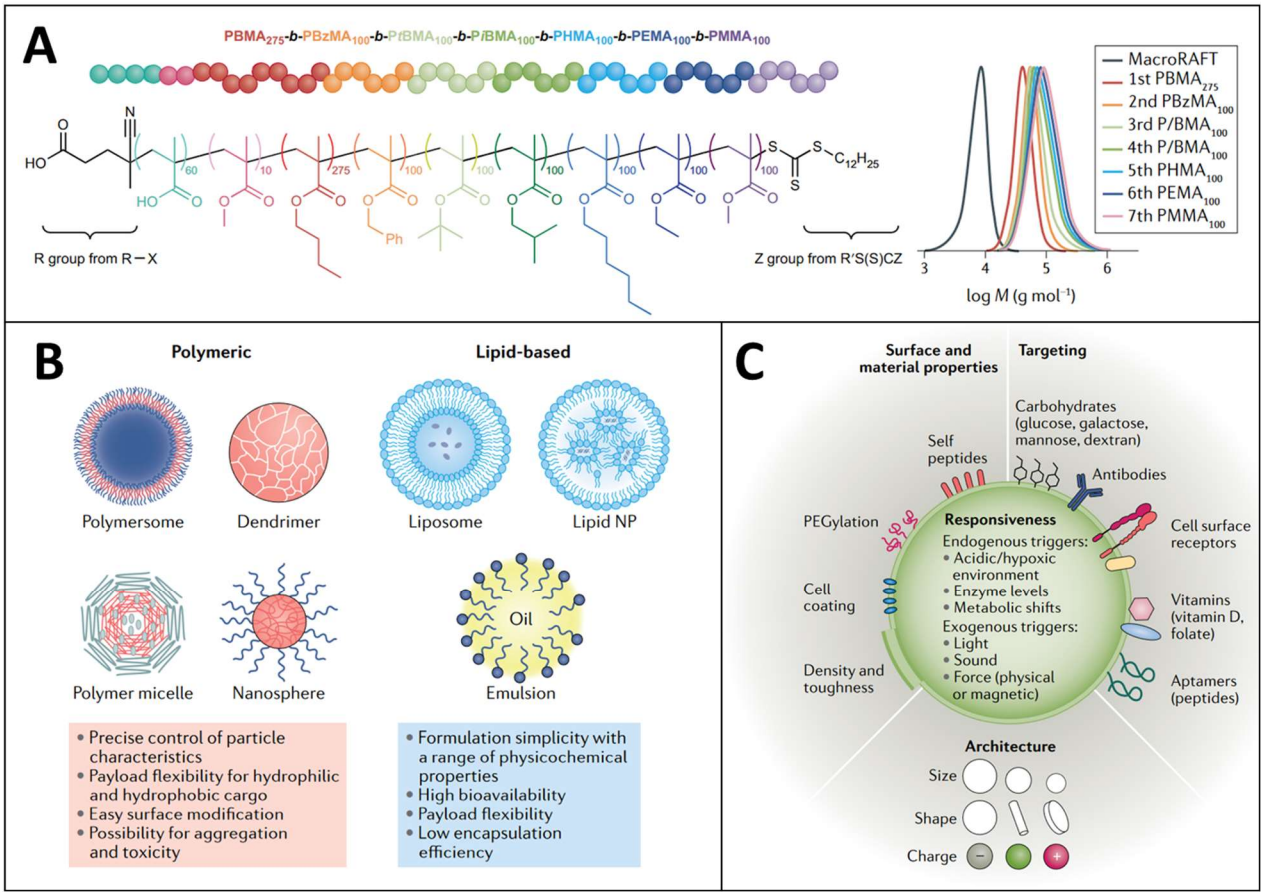

Figure 4. Overview of the flexibility of common drug delivery vehicles. A) RAFT allows for the precise control of MW even with complex block copolymers with multiple monomer types. B) Pros and cons of polymeric and lipid nanoparticle systems. C) Different targeting, biophysical, and architecture characteristics used in drug delivery systems. Figure 2A was reprinted from [63] by Nghia P. Truong et al., Copyright 2021 with permission from Copyright Clearance Center: Spring Nature. Figures 2B and 2C was reprinted from [73] by Michael J. Mitchell et al., Copyright 2020 with permission from Copyright Clearance Center: Spring Nature.

Appropriate tailoring of MW of polymers is crucial to balancing half-life, distribution to peripheral tissues, and excretion to control COP while minimizing tissue accumulation which could lead to unintended toxicity and/or tissue edema.[75] A distribution study in mice with radio-labeled PEGs of MWs from 3k to 190k indicates circulation half-life increases an order of magnitude from PEG-6k to PEG-20k, and another order of magnitude moving to PEG ≥ 50k, with clearance closely following an inverse relationship to half-life. The urinary clearance of PEG abruptly decreases

around ~30k, and liver accumulation increases with MW above a MW of 50k driven by Kupffer cell uptake. The authors concluded PEG-50k exhibited the longest half-life with low organ accumulation.[63]

Although PEG-based LVRs have shown promise in preclinical testing, there have been recent instances of anaphylaxis from COVID-19 vaccines with PEG as the suspected culprit. Since osmotic pressure is a colligative property (proportional to the number of moles), other neutral, water-soluble polymers will all have similar osmolarities in solution. Poly(vinyl alcohol) for instance has similar biodistribution to PEG, and could potentially be used as an alternative.[76] Additionally, the clinical use of fluid resuscitation has revealed that the amount of administered water is important to avoiding tissue edema. Two ways to limit the amount of water administered, are i) to increase the concentration of LVR or ii) increase the osmotic potential of the polymer. Moving away from linear polymers to new architectures can help reduce solution viscosity and increase water holding capacity, which has been shown recently with hyperbranched polyglycerols (HPGs). HPGs have also shown increased biodistribution and improved blood compatibility compared to their linear counterparts of similar MWs.[77,78]

To increase the osmotic potential, charged polymers (anionic, cationic, zwitterionic) can attract counter ions in solution through the Gibbs-Donan effect, resulting in a non-linear osmotic effect. This is displayed by albumin which has 17 negative charges at physiologic conditions.[46] However, cationic polymers are known to bind to negatively charged surfaces (e.g. GCX) and show higher rates of hemolysis. Anionic polymers will be repelled by the GCX, unless appropriately sized, but show rapid kidney accumulation, and can act as a surface to activate FXII in the blood. Zwitterionic polymers display high blood compatibility, without any effect on blood coagulation, and can coordinate higher amounts of water compared to the glycerol units of PEG.[77,79] Recently, Kumar et al. functionalized 6 kDa dextran with amine (N)-oxide-based zwitterionic groups (100DS1NOx). The incorporation of zwitterionic groups, doubled the osmolarity of dextran, and created a low-fouling colloid that decreased cell accumulation, showed no adverse effect on coagulation in vitro, and was rapidly cleared via renal filtration and hepatic circulation showing very little organ accumulation. In a lethal, severe hemorrhagic shock rat model 100DS1NOx increases survival time compared to commercial 6% hydroxyethyl starch (HES 130/0.4) and

performs similar to plasma (five bolus injections given five minutes apart, dose = 64 mg/kg per bolus [320 mg/kg total]).[80]

1.4 Conclusions

Prehospital care is vital to ensuring the patient makes it to the ER. In preclinical animal models, fully synthetic intravenous hemostats and LVRs directly treat TIC to stop bleeding and refill the vascular space to reverse hemorrhagic shock, respectively. First-generation therapies continue to highlight design constraints and needs, refine animal models, and elucidate biophysical aspects of clotting. We believe drug delivery platforms provide the design flexibility necessary to continue to innovate in the field of trauma care.

1.5 References

1. Vos, T. *et al.* Global burden of 369 diseases and injuries in 204 countries and territories, 1990–2019: a systematic analysis for the Global Burden of Disease Study 2019. *The Lancet* **396**, 1204–1222 (2020).
2. World health statistics 2022: monitoring health for the SDGs, sustainable development goals. https://www.who.int/publications-detail-redirect/9789240051157.
3. Kironji, A. G. *et al.* Identifying barriers for out of hospital emergency care in low and low-middle income countries: a systematic review. *BMC Health Serv Res* **18**, 291 (2018).
4. Cannon, J. W. Hemorrhagic Shock. *N Engl J Med* **378**, 370–379 (2018).
5. Moore, E. E. *et al.* Trauma-induced coagulopathy. *Nat Rev Dis Primers* **7**, 1–23 (2021).
6. Mayer, S. A. *et al.* Recommended Primary Outcomes for Clinical Trials Evaluating Hemostatic Agents in Patients With Intracranial Hemorrhage: A Consensus Statement. *JAMA Network Open* **4**, e2123629 (2021).
7. Spinella, P. C. *et al.* Recommended primary outcomes for clinical trials evaluating hemostatic blood products and agents in patients with bleeding: Proceedings of a National Heart Lung and Blood Institute and US Department of Defense Consensus Conference. *Journal of Trauma and Acute Care Surgery* **91**, S19 (2021).
8. Leibner, E., Andreae, M., Galvagno, S. M. & Scalea, T. Damage control resuscitation. *Clin Exp Emerg Med* **7**, 5–13 (2020).

9. Risser, F., Urosev, I., López-Morales, J., Sun, Y. & Nash, M. A. Engineered Molecular Therapeutics Targeting Fibrin and the Coagulation System: a Biophysical Perspective. *Biophys Rev* **14**, 427–461 (2022).
10. Luc, N. F. *et al.* Bioinspired artificial platelets: past, present and future. *Platelets* **33**, 35–47 (2022).
11. Raghunathan, S., Rayes, J. & Sen Gupta, A. Platelet-inspired nanomedicine in hemostasis thrombosis and thromboinflammation. *J of Thrombosis Haemost* **20**, 1535–1549 (2022).
12. Onwukwe, C. *et al.* Engineering Intravenously Administered Nanoparticles to Reduce Infusion Reaction and Stop Bleeding in a Large Animal Model of Trauma. *Bioconjugate Chem.* **29**, 2436–2447 (2018).
13. Hubbard, W. B. *et al.* Hemostatic nanoparticles increase survival, mitigate neuropathology and alleviate anxiety in a rodent blast trauma model. *Sci Rep* **8**, 10622 (2018).
14. Zhang, P. *et al.* GRGDS-functionalized chitosan nanoparticles as a potential intravenous hemostat for traumatic hemorrhage control in an animal model. *Nanomedicine: Nanotechnology, Biology and Medicine* **14**, 2531–2540 (2018).
15. Maisha, N., Rubenstein, M., Bieberich, C. J. & Lavik, E. Getting to the Core of It All: Nanocapsules to Mitigate Infusion Reactions Can Promote Hemostasis and Be a Platform for Intravenous Therapies. *Nano Lett.* **21**, 9069–9076 (2021).
16. Gkikas, M. *et al.* Systemically Administered Hemostatic Nanoparticles for Identification and Treatment of Internal Bleeding. *ACS Biomater. Sci. Eng.* **5**, 2563–2576 (2019).
17. Hong, C. *et al.* Modulating Nanoparticle Size to Understand Factors Affecting Hemostatic Efficacy and Maximize Survival in a Lethal Inferior Vena Cava Injury Model. *ACS Nano* **16**, 2494–2510 (2022).
18. Brown, A. C. *et al.* Ultrasoft microgels displaying emergent platelet-like behaviours. *Nature Mater* **13**, 1108–1114 (2014).
19. Welsch, N., Brown, A. C., Barker, T. H. & Lyon, L. A. Enhancing clot properties through fibrin-specific self-cross-linked PEG side-chain microgels. *Colloids and Surfaces B: Biointerfaces* **166**, 89–97 (2018).
20. Nandi, S. *et al.* Synthetic Platelet Microgels Containing Fibrin Knob B Mimetic Motifs Enhance Clotting Responses. *Advanced Therapeutics* **4**, 2100010 (2021).

21. Mihalko, E. P. *et al.* Fibrin-specific poly(N-isopropylacrylamide) nanogels for targeted delivery of tissue-type plasminogen activator to treat thrombotic complications are well tolerated in vivo. *Bioengineering & Translational Medicine* **7**, e10277 (2022).
22. Modery-Pawlowski, C. L., Tian, L. L., Ravikumar, M., Wong, T. L. & Gupta, A. S. In vitro and in vivo hemostatic capabilities of a functionally integrated platelet-mimetic liposomal nanoconstruct. *Biomaterials* **34**, 3031–3041 (2013).
23. Dyer, M. R. *et al.* Intravenous administration of synthetic platelets (SynthoPlate) in a mouse liver injury model of uncontrolled hemorrhage improves hemostasis: *Journal of Trauma and Acute Care Surgery* **84**, 917–923 (2018).
24. Hickman, D. A. *et al.* Intravenous synthetic platelet (SynthoPlate) nanoconstructs reduce bleeding and improve 'golden hour' survival in a porcine model of traumatic arterial hemorrhage. *Sci Rep* **8**, 3118 (2018).
25. Sekhon, U. D. S. *et al.* Platelet-mimicking procoagulant nanoparticles augment hemostasis in animal models of bleeding. *Science Translational Medicine* **14**, eabb8975 (2022).
26. Girish, A. *et al.* Platelet-Inspired Intravenous Nanomedicine for Injury-Targeted Direct Delivery of Thrombin to Augment Hemostasis in Coagulopathies. *ACS Nano* (2022) doi:10.1021/acsnano.2c05306.
27. Chan, L. W. *et al.* A synthetic fibrin cross-linking polymer for modulating clot properties and inducing hemostasis. *Science translational medicine* **7**, (2015).
28. Lamm, R. J. *et al.* Peptide valency plays an important role in the activity of a synthetic fibrin-crosslinking polymer. *Biomaterials* **132**, 96–104 (2017).
29. Lamm, R. J. *et al.* Optimizing the Polymer Chemistry and Synthesis Method of PolySTAT, an Injectable Hemostat. *ACS Biomater. Sci. Eng.* **6**, 7011–7020 (2020).
30. Gao, Y. *et al.* A polymer-based systemic hemostatic agent. *Science Advances* **6**, eaba0588 (2020).
31. Kearney, K. J. *et al.* Affimer proteins as a tool to modulate fibrinolysis, stabilize the blood clot, and reduce bleeding complications. *Blood* **133**, 1233–1244 (2019).
32. Nash, M. A. Elastin-like polypeptides: protein-based polymers for biopharmaceutical development: Medicinal Chemistry and Chemical Biology Highlights. *CHIMIA* **76**, 478–478 (2022).

33. Urosev, I., Morales, J. L. & Nash, M. A. Phase Separation of Intrinsically Disordered Protein Polymers Mechanically Stiffens Fibrin Clots. *Advanced Functional Materials* **30**, 2005245 (2020).
34. Morgan, C. E. *et al.* Tissue-Factor Targeted Peptide Amphiphile Nanofibers as an Injectable Therapy To Control Hemorrhage. *ACS Nano* **10**, 899–909 (2016).
35. Klein, M. K. *et al.* Development of Optimized Tissue-Factor-Targeted Peptide Amphiphile Nanofibers to Slow Noncompressible Torso Hemorrhage. *ACS Nano* **14**, 6649–6662 (2020).
36. Ask, A. *et al.* Spotlight on animal models of acute traumatic coagulopathy: an update. *Transfusion and Apheresis Science* **61**, 103412 (2022).
37. Parr, M. J. *et al.* Traumatic Coagulopathy: Where are the Good Experimental Models? *Journal of Trauma and Acute Care Surgery* **65**, 766–771 (2008).
38. Velik-Salchner, C. *et al.* Normal values for thrombelastography (ROTEM®) and selected coagulation parameters in porcine blood. *Thrombosis Research* **117**, 597–602 (2006).
39. Maisha, N. *et al.* Engineering PEGylated Polyester Nanoparticles to Reduce Complement-Mediated Infusion Reaction. *Bioconjugate Chem.* **32**, 2154–2166 (2021).
40. Maisha, N. *et al.* PEGylated Polyester Nanoparticles Trigger Adverse Events in a Large Animal Model of Trauma and in Naïve Animals: Understanding Cytokine and Cellular Correlations with These Events. *ACS Nano* **16**, 10566–10580 (2022).
41. Insight, N. Haima Therapeutics Receives Phase II TVSF Award from the State of Ohio to Develop its SynthoPlate Product for Veterinary Use. https://www.pharmasalmanac.com/articles/haima-therapeutics-receives-phase-ii-tvsf-award-from-the-state-of-ohio-to-develop-its-synthoplate-product-for-veterinary-use.
42. Guillaumin, J., Satchell, P. W., Yaxley, P. E., Bruckman, M. A. & Gupta, A. S. Safety profile of repeated infusion of platelet-like nanoparticles in healthy dogs. *American Journal of Veterinary Research* **83**, (2022).
43. Dull, R. O. & Hahn, R. G. Transcapillary refill: The physiology underlying fluid reabsorption. *Journal of Trauma and Acute Care Surgery* **90**, e31 (2021).
44. Hahn, R. G. & Warner, D. S. Volume Kinetics for Infusion Fluids. *Anesthesiology* **113**, 470–481 (2010).

45. Hahn, R. G. Understanding volume kinetics. *Acta Anaesthesiologica Scandinavica* **64**, 570–578 (2020).
46. Herring, N. & Paterson, D. J. *Levick's Introduction to Cardiovascular Physiology*. (CRC Press, 2018). doi:10.1201/9781351107754.
47. Woodcock, T. E. & Woodcock, T. M. Revised Starling equation and the glycocalyx model of transvascular fluid exchange: an improved paradigm for prescribing intravenous fluid therapy. *BJA: British Journal of Anaesthesia* **108**, 384–394 (2012).
48. Woodcock, T. E. & Michel, C. C. Advances in the Starling Principle and Microvascular Fluid Exchange; Consequences and Implications for Fluid Therapy. *Frontiers in Veterinary Science* **8**, (2021).
49. Johansson, P., Stensballe, J. & Ostrowski, S. Shock induced endotheliopathy (SHINE) in acute critical illness - a unifying pathophysiologic mechanism. *Critical Care* **21**, 25 (2017).
50. Harada, M. Y. *et al.* 10-Year trend in crystalloid resuscitation: Reduced volume and lower mortality. *International Journal of Surgery* **38**, 78–82 (2017).
51. Jones, D. G. *et al.* Crystalloid resuscitation in trauma patients: deleterious effect of 5L or more in the first 24h. *BMC Surgery* **18**, 93 (2018).
52. Zarychanski, R. *et al.* Association of Hydroxyethyl Starch Administration With Mortality and Acute Kidney Injury in Critically Ill Patients Requiring Volume Resuscitation: A Systematic Review and Meta-analysis. *JAMA* **309**, 678–688 (2013).
53. Kashy, B. K. *et al.* Effect of hydroxyethyl starch on postoperative kidney function in patients having noncardiac surgery. *Anesthesiology* **121**, 730–739 (2014).
54. Mangino, M. J. *Polyethylene Glycol Polymers in Low Volume Resuscitation*. https://apps.dtic.mil/sti/citations/AD1105416 (2020).
55. Plant, V. *et al.* Low-Volume Resuscitation for Hemorrhagic Shock: Understanding the Mechanism of PEG-20k. *J Pharmacol Exp Ther* **361**, 334–340 (2017).
56. Parrish, D., Lindell, S. L., Reichstetter, H., Aboutanos, M. & Mangino, M. J. Cell impermeant based low volume resuscitation in hemorrhagic shock: A biological basis for injury involving cell swelling. *Ann Surg* **263**, 565–572 (2016).

57. Khoraki, J. *et al.* Superior Survival Outcomes of a Polyethylene Glycol-20k Based Resuscitation Solution in a Preclinical Porcine Model of Lethal Hemorrhagic Shock. *Annals of Surgery* **275**, e716–e724 (2022).
58. Liebrecht, L. K. *et al.* Thromboelastographic analysis of novel polyethylene glycol based low volume resuscitation solutions. *PLOS ONE* **13**, e0207147 (2018).
59. Liebrecht, L. K. *et al.* Effects of a novel low volume resuscitation solutions on coagulation and platelet function. *PLOS ONE* **14**, e0215386 (2019).
60. Wickramaratne, N. *et al.* Acute resuscitation with polyethylene glycol-20k: A thromboelastographic analysis. *Journal of Trauma and Acute Care Surgery* **87**, 322–330 (2019).
61. Bakaltcheva, I., Ganong, J. P., Holtz, B. L., Peat, R. A. & Reid, T. Effects of high-molecular-weight cryoprotectants on platelets and the coagulation system. *Cryobiology* **40**, 283–293 (2000).
62. Parrish, D. *et al.* New Low Volume Resuscitation Solutions Containing PEG-20k. *J Trauma Acute Care Surg* **79**, 22–29 (2015).
63. Yamaoka, T., Tabata, Y. & Ikada, Y. Distribution and Tissue Uptake of Poly(ethylene glycol) with Different Molecular Weights after Intravenous Administration to Mice. *Journal of Pharmaceutical Sciences* **83**, 601–606 (1994).
64. Truong, N. P., Jones, G. R., Bradford, K. G. E., Konkolewicz, D. & Anastasaki, A. A comparison of RAFT and ATRP methods for controlled radical polymerization. *Nat Rev Chem* **5**, 859–869 (2021).
65. Sutthasupa, S., Shiotsuki, M. & Sanda, F. Recent advances in ring-opening metathesis polymerization, and application to synthesis of functional materials. *Polym J* **42**, 905–915 (2010).
66. University, C. M. Preparation of Functional Materials - Matyjaszewski Polymer Group - Carnegie Mellon University. http://www.cmu.edu/maty/materials/index.html.
67. Moad, C. L. & Moad, G. Fundamentals of reversible addition–fragmentation chain transfer (RAFT). *Chemistry Teacher International* **3**, 3–17 (2021).

68. Blosch, S. E., Scannelli, S. J., Alaboalirat, M. & Matson, J. B. Complex Polymer Architectures Using Ring-Opening Metathesis Polymerization: Synthesis, Applications, and Practical Considerations. *Macromolecules* **55**, 4200–4227 (2022).
69. Kammeyer, J. K., Blum, A. P., Adamiak, L., Hahn, M. E. & Gianneschi, N. C. Polymerization of protecting-group-free peptides via ROMP. *Polym. Chem.* **4**, 3929–3933 (2013).
70. Elling, B. R., Su, J. K., Feist, J. D. & Xia, Y. Precise Placement of Single Monomer Units in Living Ring-Opening Metathesis Polymerization. *Chem* **5**, 2691–2701 (2019).
71. Tanaka, J., Archer, N. E., Grant, M. J. & You, W. Reversible-Addition Fragmentation Chain Transfer Step-Growth Polymerization. *J. Am. Chem. Soc.* **143**, 15918–15923 (2021).
72. Hakobyan, K., McErlean, C. S. P. & Müllner, M. Activating ATRP Initiators to Incorporate End-Group Modularity into Photo-RAFT Polymerization. *Macromolecules* **53**, 10357–10365 (2020).
73. Ekladious, I., Colson, Y. L. & Grinstaff, M. W. Polymer–drug conjugate therapeutics: advances, insights and prospects. *Nat Rev Drug Discov* **18**, 273–294 (2019).
74. Mitchell, M. J. *et al.* Engineering precision nanoparticles for drug delivery. *Nat Rev Drug Discov* **20**, 101–124 (2021).
75. Adamik, K.-N. & Yozova, I. D. Colloids Yes or No? - a “Gretchen Question” Answered. *Frontiers in Veterinary Science* **8**, (2021).
76. Yamaoka, T., Tabata, Y. & Ikada, Y. Comparison of Body Distribution of Poly(vinyl alcohol) with Other Water-soluble Polymers after Intravenous Administration. *Journal of Pharmacy and Pharmacology* **47**, 479–486 (1995).
77. Jawanda, M., Lai, B. F. L., Kizhakkedathu, J. N., Ishihara, K. & Narain, R. Linear and hyperbranched phosphorylcholine based homopolymers for blood biocompatibility. *Polym. Chem.* **4**, 3140–3146 (2013).
78. Imran ul-haq, M., Lai, B. F. L., Chapanian, R. & Kizhakkedathu, J. N. Influence of architecture of high molecular weight linear and branched polyglycerols on their biocompatibility and biodistribution. *Biomaterials* **33**, 9135–9147 (2012).

79. Wen, J., Weinhart, M., Lai, B., Kizhakkedathu, J. & Brooks, D. E. Reversible hemostatic properties of sulfabetaine/quaternary ammonium modified hyperbranched polyglycerol. *Biomaterials* **86**, 42–55 (2016).
80. Kumar, R. *et al.* Low-Fouling Zwitterionic Polymeric Colloids as Resuscitation Fluids for Hemorrhagic Shock. *Advanced Materials* **34**, 2207376 (2022).

Chapter 2. OPTIMIZING THE POLYMER CHEMISTRY AND SYNTHESIS METHOD OF POLYSTAT, AN INJECTABLE HEMOSTAT

Robert J. Lamm[†], Trey J. Pichon[†], Frederick Huyan, Xu Wang, Alexander N. Prossnitz, Karl T. Manner, Nathan J. White, Suzie H. Pun

[†]Authors contributed equally to this work.

Abstract: There is a lack of prehospital hemostatic agents, especially for noncompressible hemorrhage. We previously reported PolySTAT, a unimeric, injectable hemostatic agent, that physically crosslinks fibrin to strengthen clots. In this work we sought to improve the water-solubility and synthesis yield of PolySTAT to increase the likelihood of clinical translation, reduce cost, and facilitate future mass production. First, we focused on side-chain engineering of the carrier polymer backbone to improve water-solubilty. We found that substitution of the 2-hydroxyethyl methacrylate (HEMA) monomer with glycerol monomethacrylate (GmMA) significantly improved the water-solubility of PolySTAT without compromising efficacy. Both materials, increased clot firmness and decreased lysis as measured by rotational thromboelastometry (ROTEM). Additionally, we confirmed the in vivo activity of GmMA-based PolySTAT by improving rat survival in a femoral artery bleed model. Second, to reduce waste, we evaluated PolySTAT synthesis via direct polymerization of peptide monomers. Methacrylamide and methacrylate peptide-monomers were synthesized and polymerized via reversible addition-fragmentation chain transfer (RAFT) polymerization. This approach markedly improved the yield of PolySTAT synthesis, while maintaining its biological activity in ROTEM. This work demonstrates the flexibility of PolySTAT to a variety of comonomers and synthetic routes and establishes direct RAFT polymerization of peptide monomers as a potential route of mass production.

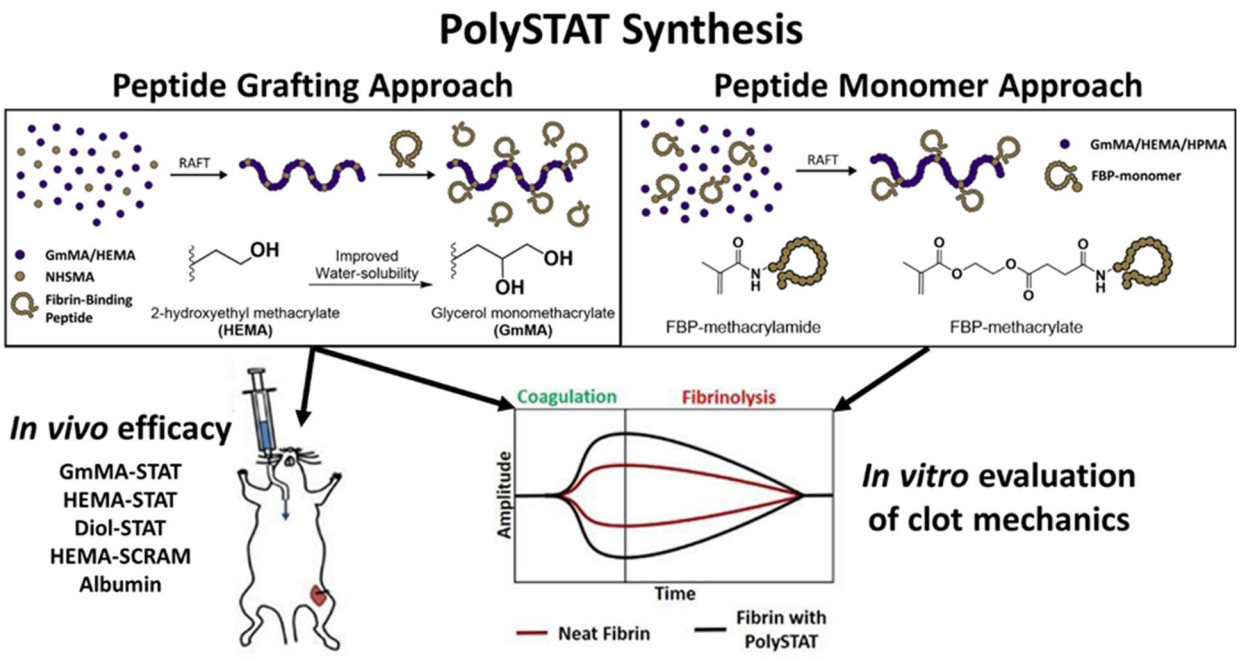

This work has resulted in a publication: *Lamm et al. ACS Biomaterials Science & Engineering.* (2020) **6.12:** 7011-7020

2.1 INTRODUCTION

When considering manufacturing of PolySTAT, FBP is the most expensive component of PolySTAT accounting for 90% of the cost. We previously reported that a minimum of 4 FBPs per polymer is required for *in vitro* and *in vivo* PolySTAT activity.[20] In this work, we continue PolySTAT optimization to improve water-solubility and synthesis yield to increase the likelihood of clinical translation and future mass production. First, increased water-solubility is desirable for improved storage stability in liquid form and for achieving higher solution concentrations. The

latter might be needed for alternative administration routes where bioavailability is lower than intravenous administration for water-soluble polymers of similar molecular weight to PolySTAT.[24] Either for use in the austere environments of a battlefield or for overcoming implementation barriers in Global Health applications, both storage stability and ease of administration are key needs. FBP has extremely limited aqueous solubility due to its large number of hydrophobic amino acids and requires a polymer carrier backbone to impart water-solubility to the system. HEMA is a material commonly used for its biocompatible nature. However, its solubility in water is low, reflected by the fact that it forms hydrogels with minimal cross-linking in water.[25,26] To increase water-solubility, a side-chain engineering approach was used to explore alternative monomers to HEMA. Second, to address synthesis yield, our reported method of PolySTAT synthesis involves FBP peptide grafting to polymers containing activated esters, a process which requires anhydrous solvents for high yield. An alternative approach to generation of peptide polymers that we and others have published is direct copolymerization of peptide monomers.[27,28] We sought to maintain the current structure of PolySTAT, while increasing water-solubility and FBP incorporation efficiency. If high conversion can be achieved, high peptide-loading efficiency can be obtained using the peptide monomer approach. The overall goal of this work is to evaluate the effect of the hydrophilicity of the polymer carrier backbone and peptide incorporation method on peptide conjugation efficiency, water-solubility, and *in vitro* and *in vivo* polymer activity.

2.2 Materials and Methods

Materials

2,2′-Azobis(2-methylpropionitrile) (AIBN), 4-cyanopentanoic acid dithiobenzoate (CTP), 2-hydroxyethyl methacrylate (HEMA), glycidyl methacrylate (GMA) and all other reagents were purchased from Sigma-Aldrich (Saint Louis, MO) unless noted otherwise. 4-Cyano-4-(ethylsulfanylthiocarbonyl) sulfanyl pentanoic acid (ECT) was a gift from Profs. Anthony Convertine and Patrick Stayton (University of Washington, Bioengineering), N-hydroxysuccinimide methacrylate (NHSMA) was purchased from TCI America (Portland, OR). The fibrin binding peptide (FBP; Sequence: Ac-Y(DGl)C(HPr)YGLCYIQGK),[29] developed by the Caravan group, as well as the scrambled peptide (Ac-YICGQ(DGl)AC(HPr)LYGK) were both purchased from two suppliers, GL Biochem (Shanghai, China) and Elim Biopharm (Hayward,

California), as custom orders. Human fibrinogen, thrombin, and plasmin were purchased from Enzyme Research Laboratories (South Bend, IN).

Hydrolysis of glycidyl methacrylate to glycerol monomethacrylate

Glycerol monomethacrylate (GmMA) was synthesized via hydrolysis of glycidyl methacrylate (GMA) as described previously for poly(GMA).[30] GMA (11.4 mL) was added to DI water (68.6 mL) at a mass ratio of 15% in a two-necked round bottom flask with one neck sealed and a vigreux column in the other. The mixture was sparged with air and stirred at 80 °C for 16 h. The solution was subsequently cooled, and sodium chloride added to a final concentration of 300 mg/mL. GmMA was extracted into an organic phase via 3x washes with 30 mL ethyl acetate. GmMA was isolated by removal of ethyl acetate via rotavap and stored at -20 °C.

Synthesis of pHEMA and pGmMA

pHEMA and pGmMA were synthesized via reversible addition-fragmentation chain transfer (RAFT) polymerization as described previously.[19] Briefly, monomer (HEMA or GmMA) was combined with CTP and AIBN at 200:1:0.333 ratio in dimethylacetamide at a monomer concentration of 0.6 M. This mixture reacted for 24 h at 70 °C. pHEMA polymers were precipitated in diethyl ether, redissolved in dimethylacetamide, and precipitated again in diethyl ether. Precipitated polymer was collected by centrifugation at 7197 x g. pGmMA polymers were precipitated in diethyl ether followed by dissolution in dimethylsulfoxide and a second precipitation in acetone. pGmMA polymers were collected by the same method as the pHEMA polymers. Dithiobenzoate groups were removed via an end-capping reaction with 20x molar excess AIBN at 70 °C for 24 hours.

Polymer characterization

Polymers were characterized via gel permeation chromatography (GPC) in dimethylformamide with static light scattering and refractive index detectors (MiniDawn Treos and OptilabTRex, respectively, both from Wyatt Technology, Santa Barbara, CA) to determine molecular weight and dispersity index (PDI). ^{1}H nuclear magnetic resonance (NMR) spectroscopy on a Bruker AV 300 was utilized to determine conversion of the polymer prior to purification, and composition after purification.

Polymerization kinetics of p(HEMA-co-NHSMA) and p(GmMA-co-NHSMA)

Backbone polymers were synthesized as described previously,[19,20] with a 40:160:1:0.333 NHSMA:comonomer:CTP:AIBN ratio. A large scale reaction was split into multiple reaction vessels and reactions were stopped at 2 h, 4 h, 8 h, 12 h, and 24 h. Samples (10 μL) of each reaction was combined with 700 μL of deuterated DMSO, and subsequently analyzed via NMR. Percent conversion was determined with NMR spectroscopy.

Synthesis of PolySTAT via conjugation

PolySTAT was synthesized as described previously.[19,20] Backbones containing HEMA or GmMA copolymerized with NHSMA were synthesized as described above with a 40:160:1:0.333 NHSMA:comonomer:CTP:AIBN ratio. Polymers were precipitated, end-capped, and characterized as described above. Polymers were conjugated to FBP via reaction of the C-terminal lysine in the peptide under organic basic conditions in DMSO at a varying ratios of peptide:NHS with N.N-diisopropylethylamine added at a 5:1 ratio base:peptide[31] for 24 h at 50 °C, after which unreacted NHSMA groups were capped with 10x molar ratio of 1-amino-2-propanol. Peptide-polymer conjugates were purified by extensive dialysis as follows. First, the product was dialyzed against phosphate-buffered saline (PBS) for 24 h (3 buffer changes, 4 L of buffer) during which a precipitate formed. Contents of the dialysis bag were collected and centrifuged at 4500 x g for 8 min to remove insoluble material; the supernatant was collected and moved to a fresh dialysis bag. Dialysis continued for 24 h (3 buffer changes), followed by water for 48 h (6 dialysate changes) to remove PBS salts. Peptide content of materials was determined using the extinction coefficient of FBP and the materials' absorbance at a wavelength of 280 nm using a NanoDrop 2000 UV-Vis spectrophotometer (Thermo Fisher Scientific, Waltham, MA). For the alternative formulation "Diol-STAT", a backbone containing HEMA copolymerized with NHSMA was synthesized with double the typical amount of NHSMA for an 80:120:1:0.333 NHSMA:comonomer:CTP:AIBN ratio. All the normal synthesis steps above were followed, except unreacted NHSMA groups were endcapped with 3-amino-1,2-propanediol. Normal purification and characterization as outlined above were followed.

Solubility testing

Solubility of polymers was determined by the absorbance at a wavelength of 650 nm. Polymers were weighed out into a 96 well plate and water or PBS added at a final concentration of 100 mg/mL. Immediately after addition of solvent, the plate was analyzed using a Tecan Infinite M1000 plate reader (Tecan, Männedorf, Switzerland) and measurements were taken every minute over 2 h.

ROTEM Characterization of PolySTATs from various synthesis strategies

ROTEM experiments consisted of 300 µL of clotting solution in a standard ROTEM cup placed in a ROTEM whole blood hemostasis analyzer (ROTEM, Instrumentation Laboratory, Bedford, MA, USA). The clotting solution consisted of human fibrinogen, thrombin, and plasmin that were purified from human plasma. All clotting factors were purchased from Enzyme Research Laboratories (South Bend, IN). Final concentrations in the ROTEM were 1.5-2 mg/mL fibrinogen, 0.5-1 IU/mL thrombin, 2-4 µg/mL plasmin, 0.1 mmol/L CaCl2, and 5 µmol/L PolySTAT at pH 7.4. Measured parameters in ROTEM included: (i) the clotting time (CT), measured as the time between reagent addition to clot formation; (ii) α-angle, which reflects the rate of clot formation, (iii) the maximum clot firmness (MCF), the highest strength observed for the clot, (iv) the lysis index-30 minutes (LI-30), the percentage of MCF retained 30 minutes after initiation of clot formation, and (v) maximum lysis (ML), the percentage of clot strength lost compared to the MCF at the end of analysis.

PolySTAT evaluation in a rat femoral artery injury and fluid resuscitation model

The rat femoral artery injury and fluid resuscitation model was performed as described previously.[19,20] Using this model, active PolySTAT had demonstrated a proportional survival benefit of at least 0.6 when compared to an albumin oncotic control (80% survival vs. 20% survival respectively). This survival effect size was adequate to ensure 87% power to detect the difference in proportional survival with n = 5 in each experimental group, assuming a 0.15 null difference and with alpha = 0.05. We expected a similar effect size in the current study, so the same number of rats (n = 5) per experimental group was used as in previous studies. Power analysis calculations were completed using the Sample Size and Power Analysis tool in JMP statistical software, version 15.1.0. Animal experiments were carried out in accordance with protocols approved by the University of Washington Institutional Care and Use Committee. Briefly, male Sprague Dawley

rats (270g-370g) were randomized into one of four treatment groups (albumin, GmMA-STAT, HEMA-STAT, and HEMA-SCRAM). Rats were anesthetized by isoflurane then a ketamine-xylazine cocktail injection in the hindlimb, followed by a tracheotomy for ventilation and isoflurane anesthesia. Both the jugular vein and carotid artery were cannulated. The carotid artery was used to monitor vitals (blood pressure and heart rate), perform a controlled catheter hemorrhage, and collect blood samples for blood gas measurements. The jugular vein was used for administration of resuscitation fluids and intravascular administration of the treatment groups. The femoral artery of the left hind limb was isolated and a proximal branch off the artery was ligated with a suture to prevent backflow of blood following injury. Surgical microclamps were placed both proximally (distal of the ligated branch) and distally along the artery. Baseline blood gas and metabolites were evaluated to ensure healthy baseline respiration and lactate levels ($pCO_2 \leq 55$ mmHg, $sO_2\% \geq 95\%$, cLac ≤ 1.0 mmol/L) prior to hemorrhage. After baselines were confirmed appropriate, a 3mm longitudinal incision was made with micro scissors in between the surgical clamps. The rat was then catheter hemorrhaged down to a mean arterial pressure (MAP) between 40-50 mmHg. Once achieved, the clamps were pulled, and free bleed (t = 0min) was initiated. Immediately, a blinded treatment was administered by the surgeon (dose = 15 mg/kg). All PolySTAT formulations were dissolved in PBS, then lyophilized. The treatment was reconstituted by the addition of water for injection to the lyophilized sample prior to administration. At regular intervals, blood was collected at the edges of the surgical site by pre-weighed gauze. The surgeon was careful not to disturb the clot nor the femoral artery. After 15 min of free bleeding (t = 15 min), fluid resuscitation was started at a rate of 3 mL/min per kg for a total volume up to 60 mL/kg. Resuscitation was stopped and restarted as needed to reach and maintain a blood pressure target of MAP = 60 mmHg. Protocol ended when official death was declared by the blinded surgeon or at t = 75 min, which was deemed survival. After the end of the protocol, final clot mass was added to the hemorrhage volumes of each rat.

Synthesis of FBP-containing methacrylamide monomer, FBP-methacrylamide

FBP-methacrylamide was synthesized via reaction of the C-terminal lysine in FBP with NHSMA under basic conditions in DMSO at a 1:2 ratio with N,N-diisopropylethylamine added at a 5:1 ratio base:peptide.[31] This was reacted for 24 h at 50° C and subsequently precipitated in diethyl ether to remove unreacted NHSMA. Ninhydrin assay confirmed that amines were consumed. Molecular

weight was confirmed via MALDI-ToF (Bruker Autoflex Max, Billerica, Massachusetts). After a proof of concept synthesis, FBP-methacrylamide was subsequently ordered from GL Biochem (Shanghai, China) as a custom order.

Synthesis of PolySTAT via FBP-methacrylamide

To first determine optimum chain transfer agent (CTA) and CTA:intitiator ratio, a degree of polymerization of 200 was targeted by combining 2-hydroypropyl methacrylate (HPMA) and CTA, either ECT or CTP, at a 200:1 ratio in dimethyl sulfoxide (DMSO) and adding AIBN at varying amounts. These mixtures were allowed to react under argon for 24 h at 70 °C. The desired product was purified from unreacted monomer by 2x precipitation in acetone, with DMSO as the intermediate solvent. Precipitated polymer was collected by centrifugation at 4500 x g. Dithiobenzoate and trithiocarbonate groups were removed via an end capping reaction with 20x molar excess AIBN at 70 °C for 24 hours. Polymers were characterized as described above. FBPMA-containing copolymers were synthesized as above, but with a target composition of 8% FBPMA by combining FBPMA and HPMA at a ratio of 16:184:1:0.333 FBPMA:HPMA:CTP:AIBN.

Synthesis of FBP-containing methacrylate monomer, FBP-methacrylate

NHS-activated mono-2-(methacryloyloxy)ethyl succinate (NHS-SMA) as described previously.[32] FBP-methacrylate was synthesized via reaction of the C-terminal lysine in FBP with NHS-SMA under organic basic conditions in DMSO at a 1:2 ratio with base added at a 5:1 ratio base:peptide.[31] A common reaction contained 176 mg FBP (100 mg/mL) dissolved in DMSO, 67 mg NHS-SMA, 94 µL N,N-diisopropylethylamine. This was reacted for 24 h at 50° C and subsequently precipitated in diethyl ether to remove unreacted NHS-SMA. Reaction progress was monitored by the ninhydrin test[33] for unreacted amines.

Synthesis of PolySTAT via FBP-methacrylate

Copolymers containing FBP-methacrylate were synthesized similarly to pHEMA and pGmMA. A composition of 5% FBP-methacrylate was targeted by combining FBP-methacrylate and HEMA or GmMA at a ratio of 10:190:1:0.333 FBP-methacrylate:comonomer:CTP:AIBN. Polymers were precipitated, end-capped, and characterized as above.

2.3 Results and Discussion

A. Comonomer Evaluation: HEMA vs. GmMA

We first explored alternative comonomers to HEMA that might increase PolySTAT solubility without compromising efficacy or safety. We decided to focus on uncharged monomers to decrease the likelihood of non-specific binding and thromboembolic complications. Cationic polymers not only bind to anionic proteins in the ECM and the negatively charged cell surfaces of erythrocytes through electrostatic interactions but are cleared quickly and can be toxic.[34–36] Anionic polymers are recognized by scavenger receptors of the innate immune system and are also retained in the kidney.[37,38] Additionally, we focused on side-chain engineering instead of the incorporation of a hydrophilic polymer block to prevent unintentional macromolecular assembly or water-shielding.[39] Glycerol monomethacrylate (GmMA) has been used in drug delivery systems and has the same methacrylate backbone as HEMA, but has a 1,2 vicinal diol instead of a single hydroxyl group and is therefore more hydrophilic.[30,40,41] The synthetic strategy for preparing GmMA and HEMA-based PolySTAT is shown in Figure 1.

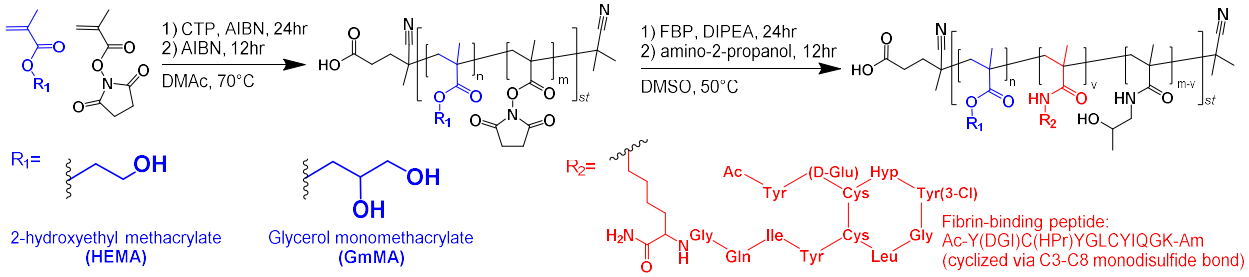

Figure 1. Overview of strategy for peptide-grafted polymers. Reversible addition-fragmentation chain-transfer polymerization (RAFT) was used to prepare copolymers p(HEMA-co-NHSMA) and p(GmMA-co-NHSMA); n = ~160-190, m = ~30-40. PolySTAT was obtained from these polymer precursors by reacting the primary amine of the terminal lysine of a fibrin-binding peptide (FBP) with the activated ester of NHSMA.

Polymerization kinetics of p(HEMA-co-NHSMA) and p(GmMA-co-NHSMA) for peptide-grafted polymers

The kinetics for copolymerization of HEMA or GmMA with NHSMA were determined by ^{1}H NMR (Figures S1-S4). Copolymers containing NHSMA and either HEMA or GmMA were polymerized to > 80% conversion, using a CTA:I ratio of 3:1, by 24 hours. For both copolymers, degrees of polymerization of 200 were targeted, along with 20% NHSMA content. p(GmMA-co-NHSMA) and p(HEMA-co-NHSMA) displayed similar conversions over the course of the 24 hour copolymerization when percent conversion was averaged between NHSMA and the respective comonomer (Figure 2A). The ratio of NHMSA to comonomer incorporation in the polymer was determined by ^{1}H NMR (Figure 2B). In general, NHSMA polymerizes faster compared to the comonomer (GmMA or HEMA). The higher rate of NHSMA incorporation results in a gradient copolymer, where NHSMA content is higher at the beginning of the copolymer chain, then decreases along the length as NHSMA is consumed.

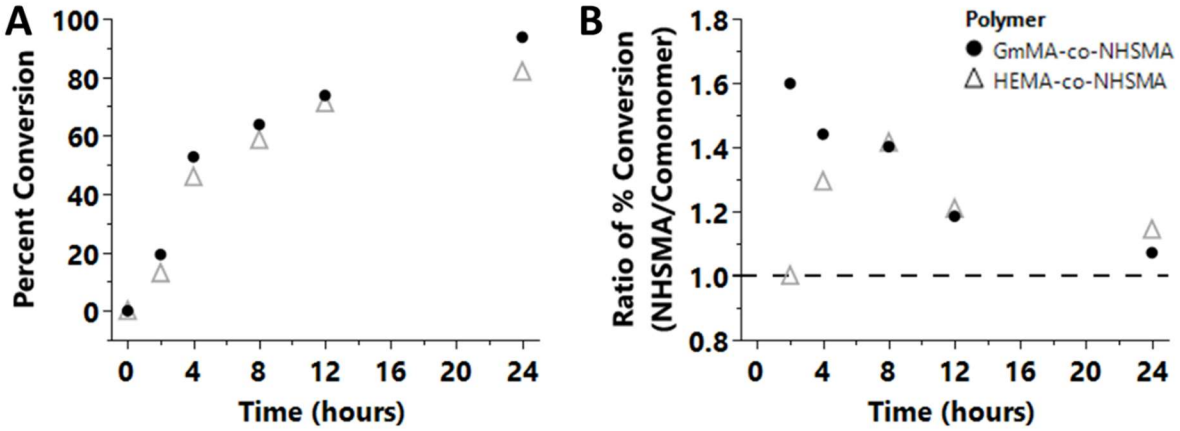

Figure 2. Polymerization kinetics of p(GmMA-co-NHSMA) and p(HEMA-co-NHSMA). A) Percent conversion over time of p(GmMA-co-NHSMA) (black circles) and p(HEMA-co-NHSMA) (grey, hollow triangles). B) Ratio of the percent conversion of NHSMA to the percent conversion of the comonomer (GmMA or HEMA). The dotted line indicates when the ratio is 1, or the percent conversions for NHSMA and the comonomer are equal.

Although the polymerization kinetics are similar, it was observed that p(GmMA-co-NHSMA) crosslinks in the solid-state at room temperature. After 24hrs, an increase in high molecular weight species can be observed by GPC (Figure S5). Additionally, after an extended period (> 1 month) the material will form a swollen, insoluble hydrogel. Thus, the peptide conjugation step is time-sensitive. There is no evidence of solid-state, room temperature crosslinking with p(HEMA-co-NHSMA) when evaluated by GPC.

Conjugation of FBP to p(GmMA-co-NHSMA) is a highly efficient reaction with nearly 100% conjugation in some cases. Similar conjugation efficiencies for both HEMA- and GmMA-based polymers were observed (Figure S6A). Additionally, the ability to control valency with molar feed of FBP in the conjugation step was observed for GmMA-STAT, which was previously observed[20] for HEMA-STAT (Figure S6B). By varying the FBP to p(GmMA-co-NHSMA) ratio during peptide grafting, GmMA-based PolySTAT with valencies from 5-15 FBP per backbone were prepared for this study, while a minimum of 1 and up to a maximum of 36 FBP per backbone for GmMA-STAT have been achieved.

Solubility of pHEMA, pGmMA, p(HEMA-co-FBP) and p(GmMA-co-FBP)

Turbidity, assessed by absorbance at 650 nm, was used to quantify the solubility of homopolymers in phosphate buffered saline (PBS) and water.[42] Homopolymers of HEMA and GmMA showed a large difference in solubility; after 40 minutes absorbance was greater than 0.4 arbitrary units for HEMA polymers in both aqueous solvents, whereas pGmMA absorbance was less than 0.2 arbitrary units by 20 minutes in both solvents (Figures 3A, 3B). This difference was decreased for peptide-conjugated polymers (Figure 3C). However, there was a statistically significant difference in absorbance between HEMA-based PolySTAT and GmMA-based PolySTAT ($p < 0.001$), with valencies of 6 and 8 FBP/backbone, respectively. The difference between GmMA-based PolySTAT and pure PBS was also significant ($p < 0.01$).

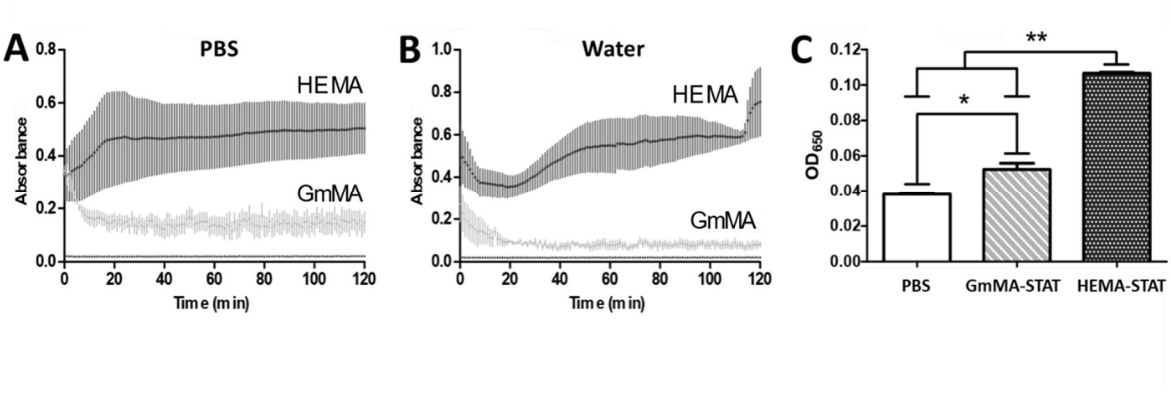

Figure 3. Solubility of HEMA and GmMA polymers. Absorbance measurements at a wavelength of 650 nm were taken to quantify polymer-solubility in water and pH 7.4 PBS. A) Solubility kinetics of pHEMA and pGmMA homopolymers over 2 hours in PBS. The solvent only baseline measurement points are below the GmMA points. B) Solubility kinetics of pHEMA and pGmMA homopolymers over 2 hours in DI water. C) Absorbance at 650 nm for GmMA-STAT

(valency = 6 pep/backbone) and HEMA-STAT (valency = 8 pep/backbone) after 1 h in water. The background control consisted of a volume control of PBS in water. Differences determined by one-way ANOVA with Tukey Post-Hoc (*, $p < 0.01$; **, $p < 0.001$). The solubility studies were performed in triplicate with the samples taken from a single batch of homopolymers and PolySTAT for each respective backbone. Table S1 provides overview of materials.

ROTEM Characterization of GmMA-based PolySTAT synthesized via FBP conjugation

ROTEM was used to compare the effect of GmMA-STAT and HEMA-STAT on clot mechanics. GmMA-STAT with valencies of 10 and 15 FBP/backbone and HEMA-STAT with valencies of 7 and 10 FBP/backbone were evaluated. Previously, we reported that a minimum FBP valency of 4 is needed to confer activity to PolySTAT.[20] Figure 4A shows typical ROTEM traces across the PBS volume control and all valencies for PolySTAT with both backbones. GmMA-based PolySTAT increased clot firmness and decreased clot lysis (Figure 4B-E) similarly to HEMA-based PolySTAT.

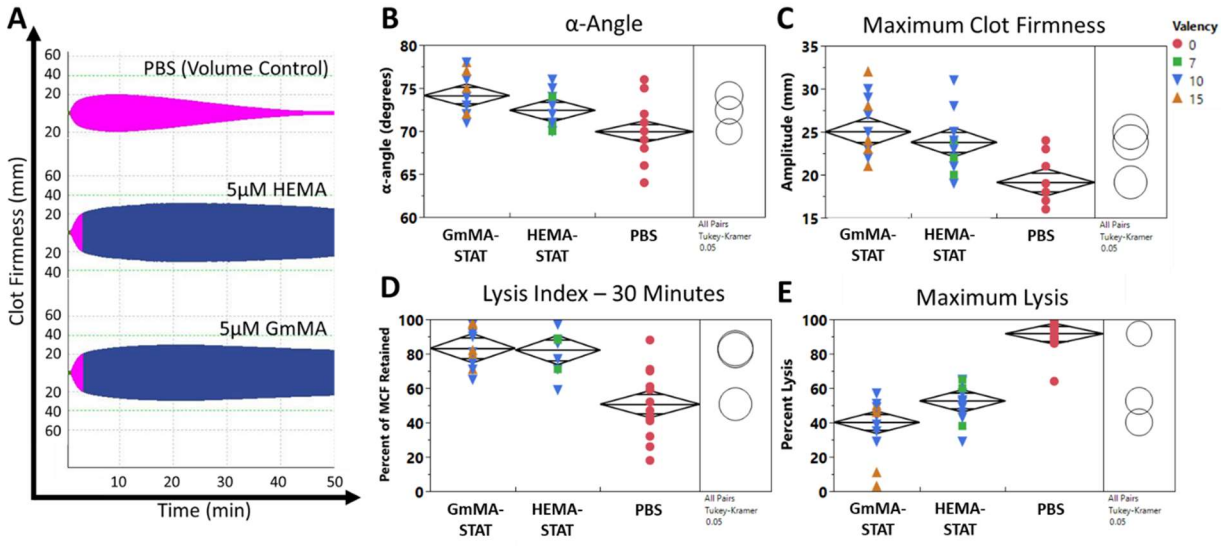

Figure 4. ROTEM characterization of GmMA-based PolySTAT synthesized via FBP conjugation. Across all ROTEM data GmMA-STAT with valencies of 10 (n = 9) and 15 (n = 5) FBP/backbone and HEMA-STAT with valencies of 7 (n = 3) and 10 (n = 11) FBP/backbone were evaluated. A) Typical ROTEM traces for PBS volume control, GmMA-STAT, and HEMA-STAT at a final concentration of 5μM, regardless of PolySTAT valency. B-E) A comparison of the following ROTEM parameters: α-angle, maximum clot firmness, lysis index at 30 minutes, and

maximum lysis for a PBS volume control (n = 16), GmMA-STAT (n = 14), and HEMA-STAT (n = 14). For each plot, the mean diamonds display the 95% confidence interval. A one-way ANOVA was used to compare the treatments with comparisons for all pairs using Tukey-Kramer HSD with $\alpha = 0.05$. The Tukey HSD comparison circles are shown to display differences between the treatment groups. The clotting solution only consisted of the following factors purified from human plasma - fibrinogen, thrombin, and plasmin.

For all ROTEM parameters, GmMA-STAT displayed statistically significant ($p < 0.0001$) differences compared to the PBS volume control. Similarly, HEMA-STAT showed statistically significant differences across all ROTEM parameters (α-angle $p = 0.0456$, MCF $p = 0.0012$, LI-30 $p < 0.0001$, ML $p < 0.0001$). Across all ROTEM parameters there was no statistically significant difference between GmMA-STAT and HEMA-STAT. Therefore, HEMA-STAT and GmMA-STAT displayed similar activity in ROTEM across a range of FBP valencies.

In vivo performance of PolySTATs in femoral artery injury and fluid resuscitation model

We evaluated GmMA-based PolySTAT in a rat femoral artery injury model (Figure 5A) to confirm that the activity in ROTEM translated to *in vivo* efficacy. We have found this controlled model serves as a reliable test method for quality control. We use it to confirm activity and to compare formulations of PolySTAT. The rats' bleed profiles, response to resuscitation, and survival rates were used to compare GmMA-STAT to HEMA-STAT. Previous work demonstrated adequate power to reliably detect differences in proportional survival with n = 5 per group. Rats underwent a controlled catheter hemorrhage to normalize the initial blood pressure, followed by removal of the microclamps to initiate free bleeding and administration of the blinded treatment. After 15 minutes of free bleeding, fluid resuscitation was initiated with a 0.9% saline infusion.

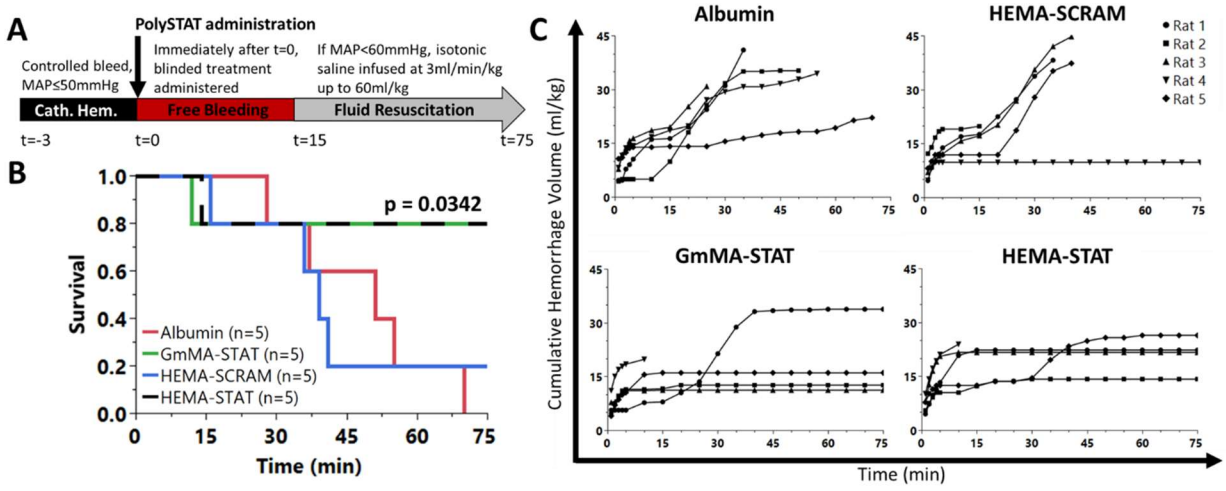

Figure 5. *In vivo* evaluation of PolySTAT with different backbones in a rat traumatic injury model. A) Timeline of rat femoral artery injury and fluid resuscitation model. B) Kaplan-Meier survival curve over the 75-min experiment (n = 5 per condition) for HEMA-STAT, HEMA-SCRAM, GmMA-STAT, and the oncotic control albumin. Both GmMA-STAT (green line) and HEMA-STAT (black line) showed the same statistically significant increase in survival (p = 0.0342) compared to albumin. P-values were determined by log-rank Mantel-Cox test with comparisons against the albumin control. C) Cumulative hemorrhage volumes for individual rats for each treatment condition. Table S1 provides overview of materials.

PolySTATs with average valencies of 8 FBP for both GmMA and HEMA backbones, were found to have similar efficacy *in vivo* (Figure 5B). Both PolySTAT formulations displayed significantly improved survival (p = 0.0342) over the oncotic control (albumin). In addition, both formulations trend towards improved survival (p = 0.1268) compared to the scrambled peptide control (valency = 11) with the HEMA backbone (HEMA-SCRAM), which has been observed previously.[19] The hemorrhage volumes for rats administered GmMA-STAT and HEMA-STAT displayed similar trends as well (Figure 5C), showing similar plateaus in hemorrhage volumes as in previous studies.[19,20] The plateaus are indicative of a decreased likelihood of rebleeding to occur during resuscitation. It should be noted that both PolySTAT formulations had a death prior to resuscitation. When the distribution of bleed intensities is evaluated for all the rats in this study, a normal distribution is observed (Figure S7). The rats for these respective deaths displayed the highest bleed intensities (upper 95%) for the entire study, suggesting that early deaths can sporadically occur at these abnormally high bleed intensities irrespective of the treatment. This

and our previous studies have shown strong indication that ROTEM characterization of clot strength is predictive of outcome in our rat model of traumatic injury and fluid resuscitation.[19,20] Additionally, a third backbone was evaluated *in vitro* and *in vivo* (Figure S8 and S9). This formulation referred to as Diol-STAT, used a HEMA-NHSMA backbone but with double the amount of NHS (~40%). After conjugation of FBP, remaining NHS groups were endcapped with 3-amino-1,2-propanediol to increase hydrophilicity by adding an extra hydroxyl group. This backbone had similar performance to HEMA and GmMA, further supporting the robust nature of PolySTAT's activity against changes in backbone solubility. Lai et al., has shown that modulating the hydrophobicity and lower critical solution temperature of polyacrylates and polyacrylamides directly affected the lateral aggregation rate of fibrin protofibrils during clot formation which ultimately led in some cases to significantly weaker clots, increased lysis, and disrupted platelet binding.[43,44] Similarly, it is hypothesized that FBP interacts with staggered fibrin monomers in protofibrils similar to αC interactions that stabilize lateral aggregations in fibrin polymerization.[20] Although the move from HEMA-STAT to GmMA-STAT did result in increased water-solubility imparted by a more hydrophilic backbone, the *in vitro* and *in vivo* results do not indicate a difference in PolySTAT activity. GmMA-STAT, synthesized with post conjugation of the FBP peptide, displayed improved survival *in vivo* compared to controls with similar hemorrhage volumes and efficacy to the original formulation of PolySTAT with the HEMA backbone.

B. Peptide Monomer Copolymerization Synthesis

Our group was one of the first to show that RAFT polymerization could be used to polymerize peptide monomers with well-defined composition and molecular weight.[27,28] We sought to maintain the current structure of PolySTAT (distribution of FBP, DP = 200, low-dispersity) from the conjugation method, while increasing water-solubility and FBP incorporation efficiency. If high conversion can be achieved, high peptide-loading efficiency can be obtained using the peptide monomer approach.

We considered several factors in peptide monomer copolymerization: (i) monomer type, (ii) solvent, and (iii) chain transfer agent. Methacrylamides and methacrylates have different polymerization kinetics. Copolymers comprising methacrylamides and methacrylates are difficult to control during polymerization; the monomers prefer to homopolymerize, so copolymers between the two monomer types are difficult to obtain without significant gradients.[45] Another

challenge in direct peptide monomer copolymerization is the restricted solubility of FBP monomers. FBP is converted to a peptide monomer by reaction of the free amine of the terminal lysine in FBP, which increases the hydrophobicity of FBP. For chain transfer agent choice, we evaluated trithiocarbonate (ECT) in comparison to the dithiobenzoate (CTP) typically used in PolySTAT synthesis. From previous experience, these CTAs work well with both methacrylates and methacrylamides. ECT has a lower transfer constant compared to CTP, and the use of both would allow us to tune our polymerizations.[46] Altogether, we optimized direct peptide monomer copolymerization around the following parameters: comonomer (methacrylate vs. methacrylamide), chain transfer agent (dithiobenzoate vs. trithiocarbonate), solvent, and CTA:I ratio in the two synthetic strategies shown in Figure 6.

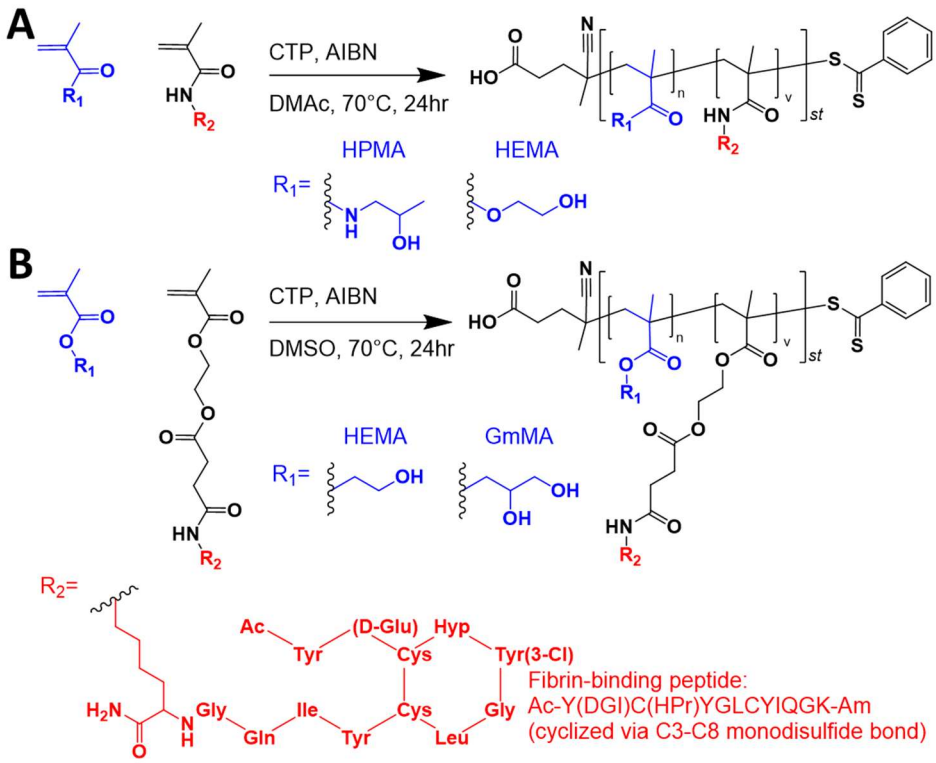

Figure 6. Overview of synthetic strategy for peptide-monomer copolymerization. A) . FBP-methacrylamide synthesized by reacting the primary amine of the terminal lysine of FBP with N-hydroxysuccinimide methacrylate (NHSMA), was copolymerized via RAFT with HPMA and HEMA. **B)** FBP-methacrylate synthesized by reacting the primary amine of the terminal lysine of FBP with NHS-activated mono-2-(methacryloyloxy)ethyl succinate (NHS-SMA) was copolymerized via RAFT with HEMA and GmMA.

FBP-methacrylamide Polymer Synthesis

The methacrylamide monomer HPMA was selected as the comonomer for polymerization with FBP-methacrylamide. Similar to GmMA, HPMA is a biocompatible, neutrally-charged, and water-soluble polymer used in drug delivery systems.[28,47,48] FBP-methacrylamide monomers were synthesized by reacting the C-terminal lysine of FBP with N-hydroxysuccinimide methacrylate, with HPLC purification and characterization by MALDI-ToF (Figure S10). HPMA homopolymers showed greatest conversion with ECT as the chain transfer agent (CTA); however, low CTA:initiator ratios were necessary to achieve > 80% conversion. Conversion using CTP as the CTA could be increased with 48 hour polymerizations, but there are concerns of control due to increased opportunities for termination events.

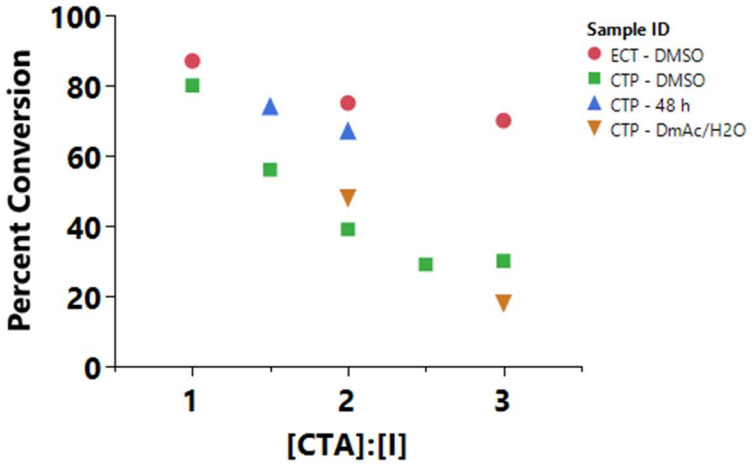

Figure 7. Polymer conversion at different CTA:initiator ratios of FBP-methacrylamide in organic solvents. Kinetics measurement were taken by proton NMR spectroscopy for FBP-methacrylamide polymerizations with HPMA p(HPMA-co-FBPMA). Polymerizations were performed in DMSO for optimal FBP solubility.

In addition to this, poor control of homopolymers at the necessary CTA:I ratios suggest this is not the ideal synthesis route (Table S2). Even with the poor control, the HPMA-co-FBPMA was still active by ROTEM (Figure S11).

FBP-methacrylate Polymer Synthesis

FBP-methacrylate was synthesized by reacting the C-terminal lysine of FBP with NHS-activated mono-2-(methacryloyloxy)ethyl succinate (NHS-SMA) with characterization by MALDI-ToF (Figure S12) and NMR (Figure S13) to confirm presence of vinyl peaks. Copolymers of HEMA and FBP-methacrylate resulted in polymers poorly soluble in DMSO. Copolymers of GmMA and FBP-methacrylate were synthesized successfully. These reactions achieved > 90% conversion by NMR with 4.6 peptides per polymer achieved from a target of 5 determined by UV-Vis. MW by MALDI-ToF shows a median m/z of 43,821 (Figure S14). Thus, copolymerization of GmMA with FBP-methacrylate is a promising approach for large-scale synthesis of PolySTAT. However, under our current conditions, recovery of the peptide monomer is only 60% after purification. Further optimization of this copolymerization strategy, especially in the peptide monomer purification step, may make this the best option in the future. This strategy removes the need for anhydrous solvents, simplifies purification post-polymerization, and does not have the transesterification/cross-linking issue of p(GmMA-co-NHSMA).

2.4 CONCLUSIONS

We demonstrate in this work that PolySTAT activity is robust to varied comonomers and synthesis strategies. This allows us to focus on synthetic efficiency and ease. GmMA maintains peptide conjugation efficiency compared to HEMA while improving the solubility of PolySTAT. There is no difference in performance when evaluated by ROTEM nor *in vivo*. Peptide monomers can be copolymerized with high conversion by RAFT polymerization but due to the need for monomer purification, there is no improvement of peptide incorporation efficiency. However, this method remains a viable route of mass production by avoiding anhydrous solvents during the polymerization and the crosslinking issue with p(GmMA-NHSMA), along with simplifying purification post-polymerization. Future work will continue to support the translation of the GmMA-formulation of PolySTAT and continue to evaluate it against the user needs for a prehospital systemic hemostatic agent. Future studies powered to hemorrhage volume or survival are required to demonstrate significant differences between GmMA-STAT and other bleeding therapies. GmMA-STAT will need to be evaluated in a trauma-induced coagulopathic bleed model that recapitulates the fibrin dysfunction observed in the clinic. Additionally, the ease of filtration for sterilization and the maximum-achievable concentration in solution will be benchmarked for GmMA-STAT to understand the benefit of the increased water-solubility.

2.5 Acknowledgements and Funding Sources

We thank Dr. James Carothers for use of his Nanodrop 2000. We thank Dr. Selvi Srinivasan for guidance on NHS-SMA synthesis. We thank Dr. Kristyn Ringgold of the Emergency Medicine Research Laboratory for her technical assistance.

This work was supported by NIH 1R01HL139007. RJL was supported by an NSF Graduate Fellowship (2013163249) and NIH Training Grant NIBIB T32EB1650. TJP was supported by an NSF Graduate Fellowship (DGE-1762114). ANP was supported by an NSF Graduate Fellowship (DGE-1762114).

2.6 Abbreviations

HEMA, 2-hydroxyethyl methacrylate; GmMA, glycerol monomethacrylate; ROTEM, rotational thromboelastometry; RAFT, reversible addition-fragmentation chain transfer; YLL, years of life lost; LMICs, low- and middle- income countries; TCCC, Tactical Combat Casualty Care; TXA, Tranexamic acid; pHEMA, poly(hydroxyethyl methacrylate); FBP, fibrin-binding peptide; rVIIa, recombinant factor VIIa; AIBN, 2,2′-azobis(2-methylpropionitrile); CTP, 4-cyanopentanoic acid dithiobenzoate; GMA, glycidyl methacrylate; ECT, 4-cyano-4-(ethylsulfanylthiocarbonyl) sulfanyl pentanoic acid; NHSMA, N-hydroxysuccinimide methacrylate; GPC, gel permeation chromatography; PDI, polydispersity index; NMR, nuclear magnetic resonance; PBS, phosphate-buffered saline; CTA, chain transfer agent; DMSO, dimethyl sulfoxide; NHS-SMA, NHS-activated mono-2-(methacryloyloxy)ethyl succinate; CT, clotting time; MCF, maximum clot firmness; LI-30, lysis index-30 minutes; ML, maximum lysis; GmMA-STAT, PolySTAT with GmMA backbone; HEMA-STAT, PolySTAT with HEMA backbone; HEMA-SCRAM, PolySTAT with scrambled peptide and HEMA backbone; MAP, mean arterial pressure; p(HPMA-co-FBPMA), PolySTAT with HPMA backbone synthesized with FBP-methacrylamide peptide monomer.

2.7 References

(1) James, S. L. et al., Global, Regional, and National Incidence, Prevalence, and Years Lived with Disability for 354 Diseases and Injuries for 195 Countries and Territories, 1990–2017:

A Systematic Analysis for the Global Burden of Disease Study 2017. *The Lancet* **2018**, *392* (10159), 1789–1858. https://doi.org/10.1016/S0140-6736(18)32279-7.

(2) Cannon, J. W. Hemorrhagic Shock. *N Engl J Med* **2018**, *378* (4), 370–379. https://doi.org/10.1056/NEJMra1705649.

(3) Nielsen, K.; Mock, C.; Joshipura, M.; Rubiano, A. M.; Zakariah, A.; Rivara, F. Assessment of the Status of Prehospital Care in 13 Low- and Middle-Income Countries. *Prehospital Emergency Care* **2012**, *16* (3), 381–389. https://doi.org/10.3109/10903127.2012.664245.

(4) Kironji, A. G.; Hodkinson, P.; de Ramirez, S. S.; Anest, T.; Wallis, L.; Razzak, J.; Jenson, A.; Hansoti, B. Identifying Barriers for out of Hospital Emergency Care in Low and Low-Middle Income Countries: A Systematic Review. *BMC Health Serv Res* **2018**, *18* (1), 291. https://doi.org/10.1186/s12913-018-3091-0.

(5) Tisherman, S. A.; Schmicker, R. H.; Brasel, K. J.; Bulger, E. M.; Kerby, J. D.; Minei, J. P.; Powell, J. L.; Reiff, D. A.; Rizoli, S. B.; Schreiber, M. A. Detailed Description of All Deaths in Both the Shock and Traumatic Brain Injury Hypertonic Saline Trials of the Resuscitation Outcomes Consortium: *Annals of Surgery* **2015**, *261* (3), 586–590. https://doi.org/10.1097/SLA.0000000000000837.

(6) Butler, F. K.; Holcomb, J. B.; Schreiber, M. A.; Kotwal, R. S.; Jenkins, D. A.; Champion, H. R.; Bowling, F.; Cap, A. P.; Dubose, J. J.; Dorlac, W. C.; Dorlac, G. R.; McSwain, N. E.; Timby, J. W.; Blackbourne, L. H.; Stockinger, Z. T.; Strandenes, G.; Weiskopf, R. B.; Gross, K. R.; Bailey, J. A. Fluid Resuscitation for Hemorrhagic Shock in Tactical Combat Casualty Care: TCCC Guidelines Change 14-01--2 June 2014. *J Spec Oper Med* **2014**, *14* (3), 13–38.

(7) Eastridge, B. J.; Mabry, R. L.; Seguin, P.; Cantrell, J.; Tops, T.; Uribe, P.; Mallett, O.; Zubko, T.; Oetjen-Gerdes, L.; Rasmussen, T. E.; Butler, F. K.; Kotwal, R. S.; Holcomb, J. B.; Wade, C.; Champion, H.; Lawnick, M.; Moores, L.; Blackbourne, L. H. Death on the Battlefield (2001-2011): Implications for the Future of Combat Casualty Care. *Journal of Trauma and Acute Care Surgery* **2012**, *73* (6). https://doi.org/10.1097/TA.0b013e3182755dcc.

(8) Peng, H. T. Hemostatic Agents for Prehospital Hemorrhage Control: A Narrative Review. *Military Med Res* **2020**, *7* (1), 13. https://doi.org/10.1186/s40779-020-00241-z.

(9) Wu, X.; Benov, A.; Darlington, D. N.; Keesee, J. D.; Liu, B.; Cap, A. P. Effect of Tranexamic Acid Administration on Acute Traumatic Coagulopathy in Rats with Polytrauma and Hemorrhage. *PLoS ONE* **2019**, *14* (10), e0223406. https://doi.org/10.1371/journal.pone.0223406.

(10) Wright, C. Battlefield Administration of Tranexamic Acid by Combat Troops: A Feasibility Analysis. *BMJ Military Health* **2014**, *160* (4), 271–272. https://doi.org/10.1136/jramc-2013-000152.

(11) Culligan, W. B.; Tien, H. C. Tranexamic Acid Autoinjector for Prehospital Care of Noncompressible Hemorrhage. *Journal of Trauma and Acute Care Surgery* **2011**, *71* (5), S501. https://doi.org/10.1097/TA.0b013e318232ea1e.

(12) Hubbard, W. B.; Lashof-Sullivan, M.; Greenberg, S.; Norris, C.; Eck, J.; Lavik, E.; VandeVord, P. Hemostatic Nanoparticles Increase Survival, Mitigate Neuropathology and Alleviate Anxiety in a Rodent Blast Trauma Model. *Sci Rep* **2018**, *8* (1), 10622. https://doi.org/10.1038/s41598-018-28848-2.

(13) Onwukwe, C.; Maisha, N.; Holland, M.; Varley, M.; Groynom, R.; Hickman, D.; Uppal, N.; Shoffstall, A.; Ustin, J.; Lavik, E. Engineering Intravenously Administered Nanoparticles to Reduce Infusion Reaction and Stop Bleeding in a Large Animal Model of Trauma. *Bioconjugate Chem.* **2018**, *29* (7), 2436–2447. https://doi.org/10.1021/acs.bioconjchem.8b00335.

(14) Modery-Pawlowski, C. L.; Tian, L. L.; Ravikumar, M.; Wong, T. L.; Gupta, A. S. In Vitro and in Vivo Hemostatic Capabilities of a Functionally Integrated Platelet-Mimetic Liposomal Nanoconstruct. *Biomaterials* **2013**, *34* (12), 3031–3041. https://doi.org/10.1016/j.biomaterials.2012.12.045.

(15) Dyer, M. R.; Hickman, D.; Luc, N.; Haldeman, S.; Loughran, P.; Pawlowski, C.; Sen Gupta, A.; Neal, M. D. Intravenous Administration of Synthetic Platelets (SynthoPlate) in a Mouse Liver Injury Model of Uncontrolled Hemorrhage Improves Hemostasis: *Journal of Trauma and Acute Care Surgery* **2018**, *84* (6), 917–923. https://doi.org/10.1097/TA.0000000000001893.

(16) Hickman, D. A.; Pawlowski, C. L.; Shevitz, A.; Luc, N. F.; Kim, A.; Girish, A.; Marks, J.; Ganjoo, S.; Huang, S.; Niedoba, E.; Sekhon, U. D. S.; Sun, M.; Dyer, M.; Neal, M. D.; Kashyap, V. S.; Sen Gupta, A. Intravenous Synthetic Platelet (SynthoPlate) Nanoconstructs

Reduce Bleeding and Improve 'Golden Hour' Survival in a Porcine Model of Traumatic Arterial Hemorrhage. *Sci Rep* **2018**, *8* (1), 3118. https://doi.org/10.1038/s41598-018-21384-z.

(17) Brown, A. C.; Stabenfeldt, S. E.; Ahn, B.; Hannan, R. T.; Dhada, K. S.; Herman, E. S.; Stefanelli, V.; Guzzetta, N.; Alexeev, A.; Lam, W. A.; Lyon, L. A.; Barker, T. H. Ultrasoft Microgels Displaying Emergent Platelet-like Behaviours. *Nature Mater* **2014**, *13* (12), 1108–1114. https://doi.org/10.1038/nmat4066.

(18) Welsch, N.; Brown, A. C.; Barker, T. H.; Lyon, L. A. Enhancing Clot Properties through Fibrin-Specific Self-Cross-Linked PEG Side-Chain Microgels. *Colloids and Surfaces B: Biointerfaces* **2018**, *166*, 89–97. https://doi.org/10.1016/j.colsurfb.2018.03.003.

(19) Chan, L. W.; Wang, X.; Wei, H.; Pozzo, L. D.; White, N. J.; Pun, S. H. A Synthetic Fibrin Cross-Linking Polymer for Modulating Clot Properties and Inducing Hemostasis. *Science translational medicine* **2015**, *7* (277).

(20) Lamm, R. J.; Lim, E. B.; Weigandt, K. M.; Pozzo, L. D.; White, N. J.; Pun, S. H. Peptide Valency Plays an Important Role in the Activity of a Synthetic Fibrin-Crosslinking Polymer. *Biomaterials* **2017**, *132*, 96–104. https://doi.org/10.1016/j.biomaterials.2017.04.002.

(21) Kanaide, H.; Shainoff, J. R. Cross-Linking of Fibrinogen and Fibrin by Fibrin-Stabilizing Factor (Factor XIIIa). *Translational Research* **1975**, *85* (4), 574–597.

(22) Chan, L. W.; White, N. J.; Pun, S. H. A Fibrin Cross-Linking Polymer Enhances Clot Formation Similar to Factor Concentrates and Tranexamic Acid in an *in Vitro* Model of Coagulopathy. *ACS Biomater. Sci. Eng.* **2016**, *2* (3), 403–408. https://doi.org/10.1021/acsbiomaterials.5b00536.

(23) Gao, Y.; Sarode, A.; Kokoroskos, N.; Ukidve, A.; Zhao, Z.; Guo, S.; Flaumenhaft, R.; Gupta, A. S.; Saillant, N.; Mitragotri, S. A Polymer-Based Systemic Hemostatic Agent. *Science Advances* **2020**, *6* (31), eaba0588. https://doi.org/10.1126/sciadv.aba0588.

(24) Yamaoka, T.; Tabata, Y.; Ikada, Y. Fate of Water-Soluble Polymers Administered via Different Routes. *J Pharm Sci* **1995**, *84* (3), 349–354. https://doi.org/10.1002/jps.2600840316.

(25) Duvall, C. L.; Convertine, A. J.; Benoit, D. S. W.; Hoffman, A. S.; Stayton, P. S. Intracellular Delivery of a Proapoptotic Peptide via Conjugation to a RAFT Synthesized

Endosomolytic Polymer. *Mol. Pharmaceutics* **2010**, *7* (2), 468–476. https://doi.org/10.1021/mp9002267.

(26) Chu, D. S.; Sellers, D. L.; Bocek, M. J.; Fischedick, A. E.; Horner, P. J.; Pun, S. H. MMP9-Sensitive Polymers Mediate Environmentally-Responsive Bivalirudin Release and Thrombin Inhibition. *Biomater. Sci.* **2014**, *3* (1), 41–45. https://doi.org/10.1039/C4BM00259H.

(27) Apostolovic, B.; Deacon, S. P. E.; Duncan, R.; Klok, H.-A. Hybrid Polymer Therapeutics Incorporating Bioresponsive, Coiled Coil Peptide Linkers. *Biomacromolecules* **2010**, *11* (5), 1187–1195. https://doi.org/10.1021/bm901313c.

(28) Johnson, R. N.; Burke, R. S.; Convertine, A. J.; Hoffman, A. S.; Stayton, P. S.; Pun, S. H. Synthesis of Statistical Copolymers Containing Multiple Functional Peptides for Nucleic Acid Delivery. *Biomacromolecules* **2010**, *11* (11), 3007–3013. https://doi.org/10.1021/bm100806h.

(29) Kolodziej, A. F.; Nair, S. A.; Graham, P.; Mcmurry, T. J.; Ladner, R. C.; Wescott, C.; Sexton, D. J.; Caravan, P. Fibrin Specific Peptides Derived by Phage Display: Characterization of Peptides and Conjugates for Imaging. *Bioconjugate Chemistry* **2012**, *23*, 548–556.

(30) Cunningham, V. J.; Alswieleh, A. M.; Thompson, K. L.; Williams, M.; Leggett, G. J.; Armes, S. P.; Hill, B.; S, S. Y.; Musa, O. M. Poly(Glycerol Monomethacrylate) − Poly(Benzyl Methacrylate) Diblock Copolymer Nanoparticles via RAFT Emulsion Polymerization: Synthesis, Characterization, and Interfacial Activity. **2014**. https://doi.org/10.1021/ma501140h.

(31) Yanjarappa, M. J.; Gujraty, K. V; Joshi, A.; Saraph, A.; Kane, R. S. Synthesis of Copolymers Containing an Active Ester of Methacrylic Acid by RAFT : Controlled Molecular Weight Scaffolds for Biofunctionalization. *Biomacromolecules* **2006**, *7*, 1665–1670.

(32) Das, D.; Srinivasan, S.; Kelly, A. M.; Chiu, D. Y.; Daughtery, B. K.; Ratner, D. M.; Stayton, P. S.; Convertine, A. J. RAFT Polymerization of Ciprofloxacin Prodrug Monomers for the Controlled Intracellular Delivery of Antibiotics. *Polym. Chem* **2016**, *7*, 826–837. https://doi.org/10.1039/c5py01704a.

(33) Sun, S.-W.; Lin, Y.-C.; Weng, Y.-M.; Chen, M.-J. Efficiency Improvements on Ninhydrin Method for Amino Acid Quantification. *Journal of Food Composition and Analysis* **2006**, *19* (2–3), 112–117. https://doi.org/10.1016/j.jfca.2005.04.006.

(34) Burke, R. S.; Pun, S. H. Extracellular Barriers to in Vivo PEI and PEGylated PEI Polyplex-Mediated Gene Delivery to the Liver. *Bioconjugate Chem.* **2008**, *19* (3), 693–704. https://doi.org/10.1021/bc700388u.

(35) Samal, S. K.; Dash, M.; Vlierberghe, S. V.; Kaplan, D. L.; Chiellini, E.; Blitterswijk, C. van; Moroni, L.; Dubruel, P. Cationic Polymers and Their Therapeutic Potential. *Chem. Soc. Rev.* **2012**, *41* (21), 7147–7194. https://doi.org/10.1039/C2CS35094G.

(36) Novo, L.; Rizzo, L. Y.; Golombek, S. K.; Dakwar, G. R.; Lou, B.; Remaut, K.; Mastrobattista, E.; van Nostrum, C. F.; Jahnen-Dechent, W.; Kiessling, F.; Braeckmans, K.; Lammers, T.; Hennink, W. E. Decationized Polyplexes as Stable and Safe Carrier Systems for Improved Biodistribution in Systemic Gene Therapy. *J Control Release* **2014**, *195*, 162–175. https://doi.org/10.1016/j.jconrel.2014.08.028.

(37) Yu, Q.; Wei, Z.; Shi, J.; Guan, S.; Du, N.; Shen, T.; Tang, H.; Jia, B.; Wang, F.; Gan, Z. Polymer–Doxorubicin Conjugate Micelles Based on Poly(Ethylene Glycol) and Poly(N-(2-Hydroxypropyl) Methacrylamide): Effect of Negative Charge and Molecular Weight on Biodistribution and Blood Clearance. *Biomacromolecules* **2015**, *16* (9), 2645–2655. https://doi.org/10.1021/acs.biomac.5b00460.

(38) Liu, G. W.; Prossnitz, A. N.; Eng, D. G.; Cheng, Y.; Subrahmanyam, N.; Pippin, J. W.; Lamm, R. J.; Ngambenjawong, C.; Ghandehari, H.; Shankland, S. J.; Pun, S. H. Glomerular Disease Augments Kidney Accumulation of Synthetic Anionic Polymers. *Biomaterials* **2018**, *178*, 317–325. https://doi.org/10.1016/j.biomaterials.2018.06.001.

(39) Mu, Q.; Hu, T.; Yu, J. Molecular Insight into the Steric Shielding Effect of PEG on the Conjugated Staphylokinase: Biochemical Characterization and Molecular Dynamics Simulation. *PLoS One* **2013**, *8* (7). https://doi.org/10.1371/journal.pone.0068559.

(40) Kopeček, J.; Kopečková, P.; Minko, T.; Lu, Z.-R.; Peterson, C. M. Water Soluble Polymers in Tumor Targeted Delivery. *Journal of Controlled Release* **2001**, *74* (1), 147–158. https://doi.org/10.1016/S0168-3659(01)00330-3.

(41) Save, M.; Weaver, J. V. M.; Armes, S. P.; McKenna, P. Atom Transfer Radical Polymerization of Hydroxy-Functional Methacrylates at Ambient Temperature:

Comparison of Glycerol Monomethacrylate with 2-Hydroxypropyl Methacrylate. *Macromolecules* **2002**, *35* (4), 1152–1159. https://doi.org/10.1021/ma011541r.

(42) Shin, H. C.; Alani, A. W. G.; Rao, D. A.; Rockich, N. C.; Kwon, G. S. Multi-Drug Loaded Polymeric Micelles for Simultaneous Delivery of Poorly Soluble Anticancer Drugs. *Journal of Controlled Release* **2009**, *140* (3), 294–300. https://doi.org/10.1016/j.jconrel.2009.04.024.

(43) Lai, B. F. L.; Zou, Y.; Brooks, D. E.; Kizhakkedathu, J. N. The Influence of Poly-N-[(2,2-Dimethyl-1,3-Dioxolane)Methyl]Acrylamide on Fibrin Polymerization, Cross-Linking and Clot Structure. *Biomaterials* **2010**, *31* (22), 5749–5758. https://doi.org/10.1016/j.biomaterials.2010.03.076.

(44) Lai, B. F. L.; Zou, Y.; Yang, X.; Yu, X.; Kizhakkedathu, J. N. Abnormal Blood Clot Formation Induced by Temperature Responsive Polymers by Altered Fibrin Polymerization and Platelet Binding. *Biomaterials* **2014**, *35* (8), 2518–2528. https://doi.org/10.1016/j.biomaterials.2013.12.003.

(45) Perrier, S. *50th Anniversary Perspective* : RAFT Polymerization—A User Guide. *Macromolecules* **2017**, *50* (19), 7433–7447. https://doi.org/10.1021/acs.macromol.7b00767.

(46) Moad, G.; Rizzardo, E.; Thang, S. H. Living Radical Polymerization by the RAFT Process – A Third Update. *Aust. J. Chem.* **2012**, *65* (8), 985–1076. https://doi.org/10.1071/CH12295.

(47) Chu, D. S. H.; Schellinger, J. G.; Bocek, M. J.; Johnson, R. N.; Pun, S. H. Optimization of Tet1 Ligand Density in HPMA-Co-Oligolysine Copolymers for Targeted Neuronal Gene Delivery. *Biomaterials* **2013**, *34* (37), 9632–9637. https://doi.org/10.1016/j.biomaterials.2013.08.045.

(48) Schellinger, J. G.; Pahang, J. A.; Johnson, R. N.; Chu, D. S. H.; Sellers, D. L.; Maris, D. O.; Convertine, A. J.; Stayton, P. S.; Horner, P. J.; Pun, S. H. Melittin-Grafted HPMA-Oligolysine Based Copolymers for Gene Delivery. *Biomaterials* **2013**, *34* (9), 2318–2326. https://doi.org/10.1016/j.biomaterials.2012.09.072.

2.8 SUPPORTING INFORMATION

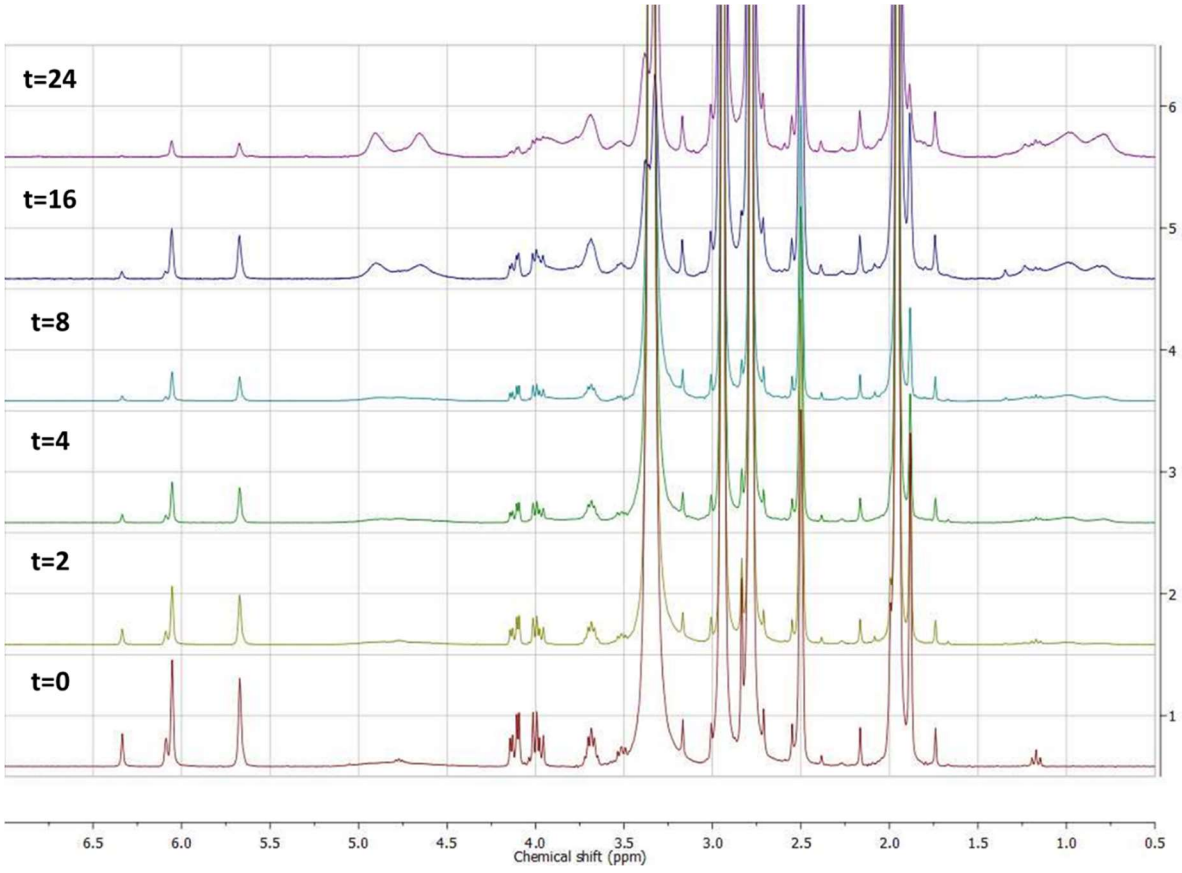

Figure S1. Proton NMR spectroscopy of p(GmMA-co-NHSMA) in DMSO-d_6 used to determine polymerization kinetics.

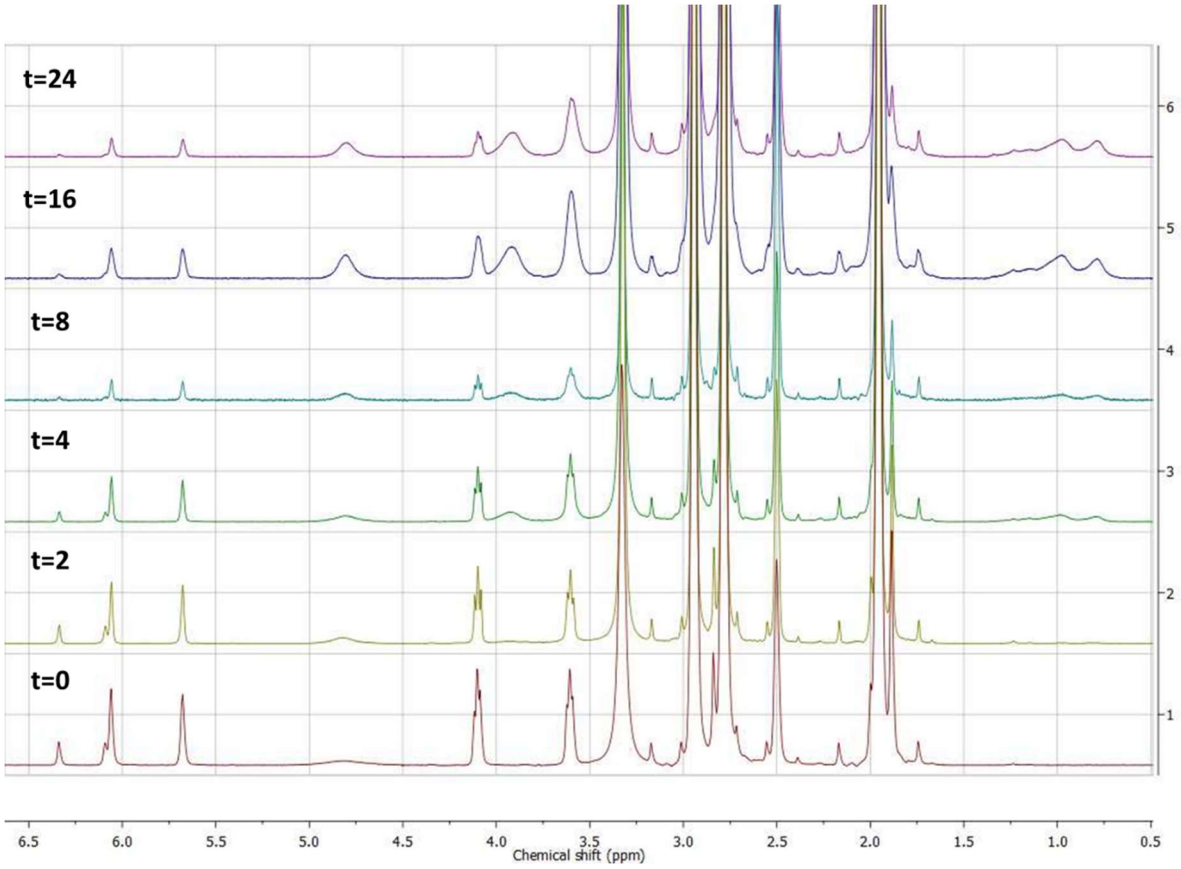

Figure S2. Proton NMR spectroscopy of p(HEMA-co-NHSMA) in DMSO-d6 used to determine polymerization kinetics.

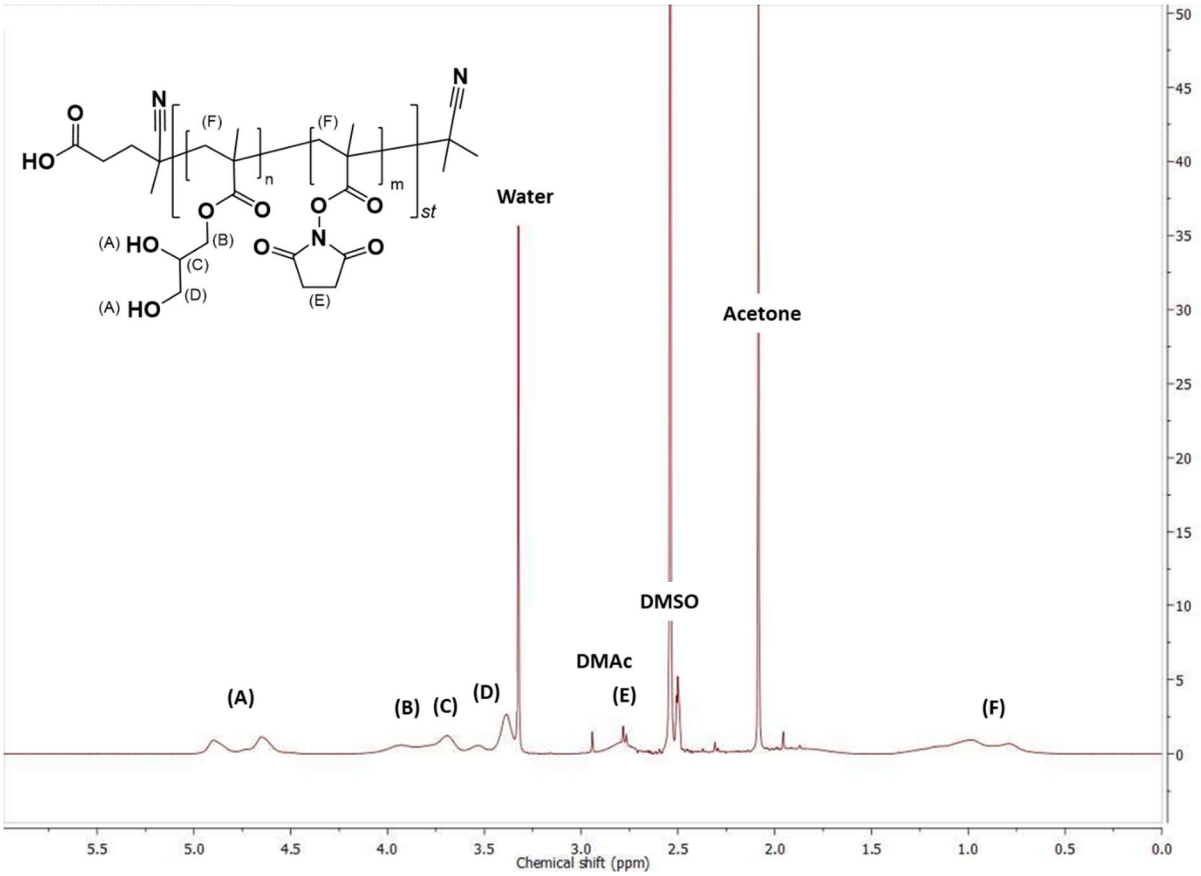

Figure S3. Proton NMR spectroscopy of p(GmMA-co-NHSMA) in DMSO-d6. NMR taken after precipitation in acetone from DMSO.

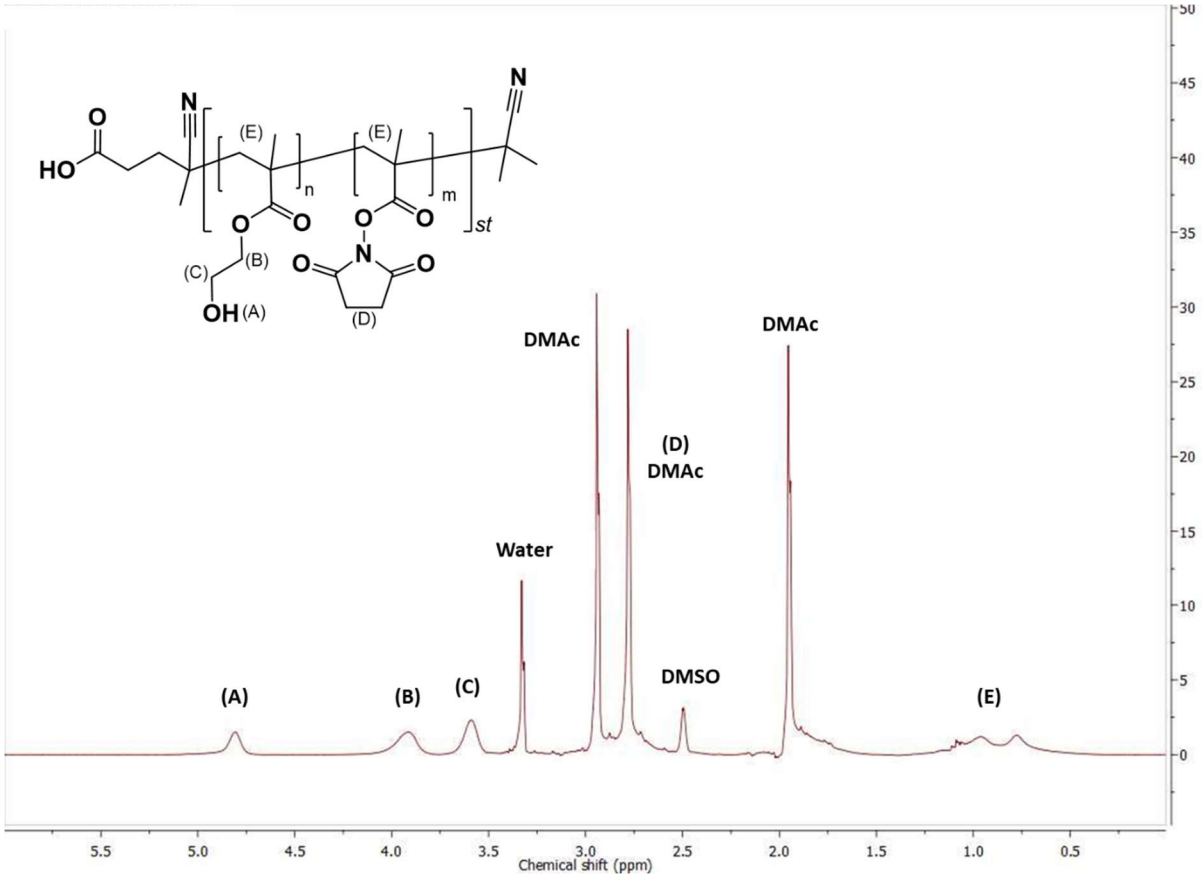

Figure S4. Proton NMR spectroscopy of p(HEMA-co-NHSMA) in DMSO-d$_6$. NMR taken after precipitation in diethyl ether from DMAc.

Table S1. Overview of polymer characterization for materials used in Figures 3 and 5.

Sample	Backbone	Dispersity	NHSMA Content (%)	Pep/backbone	Backbone Theoretical MW (g/mol)	Theoretical MW with peptide (g/mol)	Backbone MW (g/mol)	Theoretical MW with peptide (g/mol)
Source	-	GPC	NMR	UV-Vis	NMR	NMR + UV-Vis	GPC	GPC + UV-Vis
p(HEMA)	N/A	1.265	N/A	N/A	26,030	N/A	28,630	N/A
p(GmMA)	N/A	1.062	N/A	N/A	32,030	N/A	29,100	N/A
GmMA-STAT	p(GmMA-co-NHSMA)	1.158	18.4	8	29,660	42,680	25,870	38,890
HEMA-STAT	p(HEMA-co-NHSMA)	1.151	18	8	25,070	38,090	25,490	38,510
HEMA-SCRAM	p(HEMA-co-NHSMA)	1.151	18	11	25,070	41,570	25,490	41,990

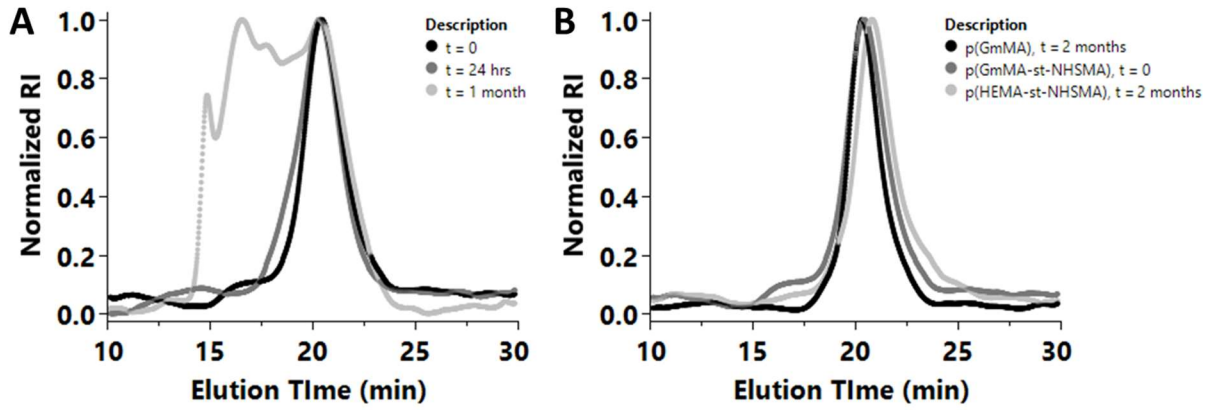

Figure S5. GPC traces showing crosslinking of p(GmMA-NHSMA) over time. A) Batch of p(GmMA-NHSMA) stored at RT under vacuum for different time points. B) Comparison of two-month-old p(GmMA) (DP = 200) and two-month-old p(HEMA-co-NHSMA) with t = 0 p(GmMA-NHSMA).

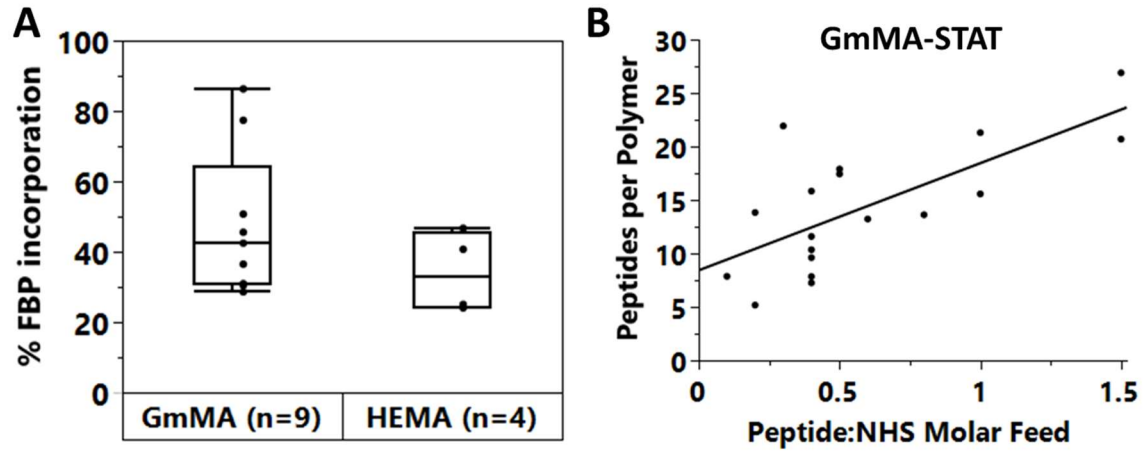

Figure S6. Comparison of synthetic efficiency. A) Percent of the FBP incorporated in polymers, determined after purification and lyophilization of GmMA-STAT and HEMA-STAT. B) The linear relationship between valency or FBP per polymer as a function of the molar feed of FBP.

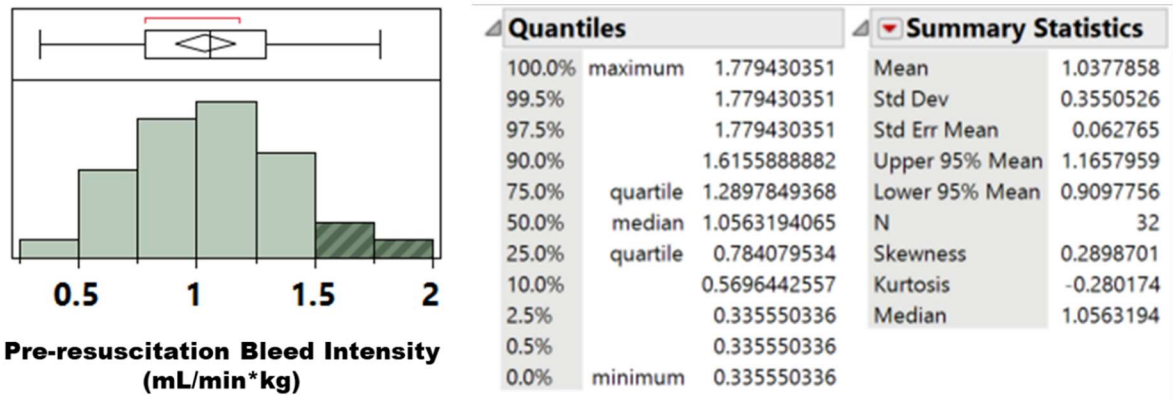

Figure S7. Distribution of the pre-resuscitation bleed intensities for the animal study. All early deaths occurred in the > 95% quantiles. The bleed intensities are normally distributed as indicated by the skewness, kurtosis, and agreement between the mean and median.

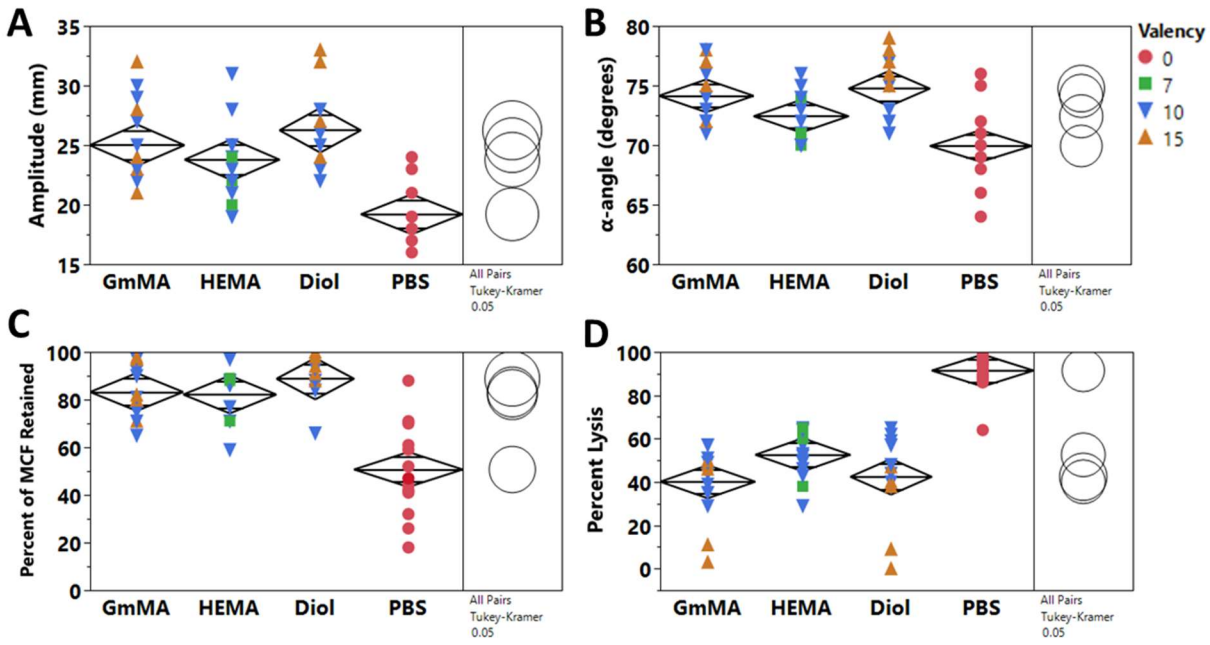

Figure S8. ROTEM characterization of Diol-based PolySTAT synthesized via FBP conjugation. Diol-STAT with valencies of 10 (n = 7) and 15 (n = 5) FBP/backbone were evaluated across all ROTEM data. These were evaluated in the same experiments as shown in the main text. For all ROTEM parameters, Diol-STAT displayed statistically significant ($p < 0.0001$) differences compared to the PBS volume control. There was no statistically significant difference between Diol-STAT (n = 12) and the other PolySTAT formulations. For each plot, the mean diamonds

display the 95% confidence interval. A one-way ANOVA was used to compare the treatments with comparisons for all pairs using Tukey-Kramer HSD with $\alpha = 0.05$. The Tukey HSD comparison circles are shown to display differences between the treatment groups.

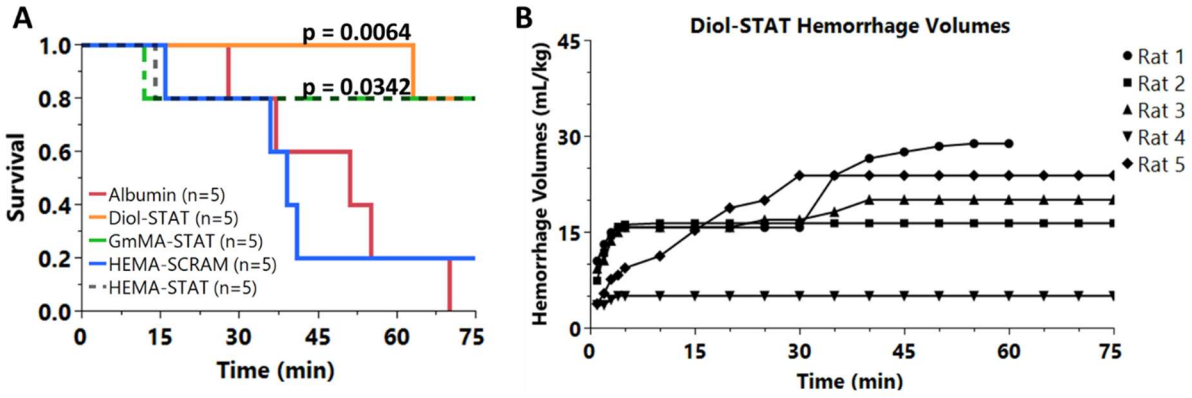

Figure S9. In vivo evaluation of PolySTAT in a rat traumatic injury model. Diol-STAT was evaluated in the same experiments as shown in the main text. A) Kaplan-Meier survival curve over the 75-min experiment (n = 5 per condition) for Diol-STAT, HEMA-STAT, HEMA-SCRAM, GmMA-STAT, and the oncotic control albumin. All three PolySTAT formulations showed statistically significant increase in survival (Diol-STAT p = 0.0064, GmMA-STAT and HEMA-STAT p = 0.0342) compared to albumin. P-values were determined by log-rank Mantel-Cox test with comparisons against the albumin control. B) Cumulative hemorrhage volumes for individual rats for the Diol-STAT treatment condition.

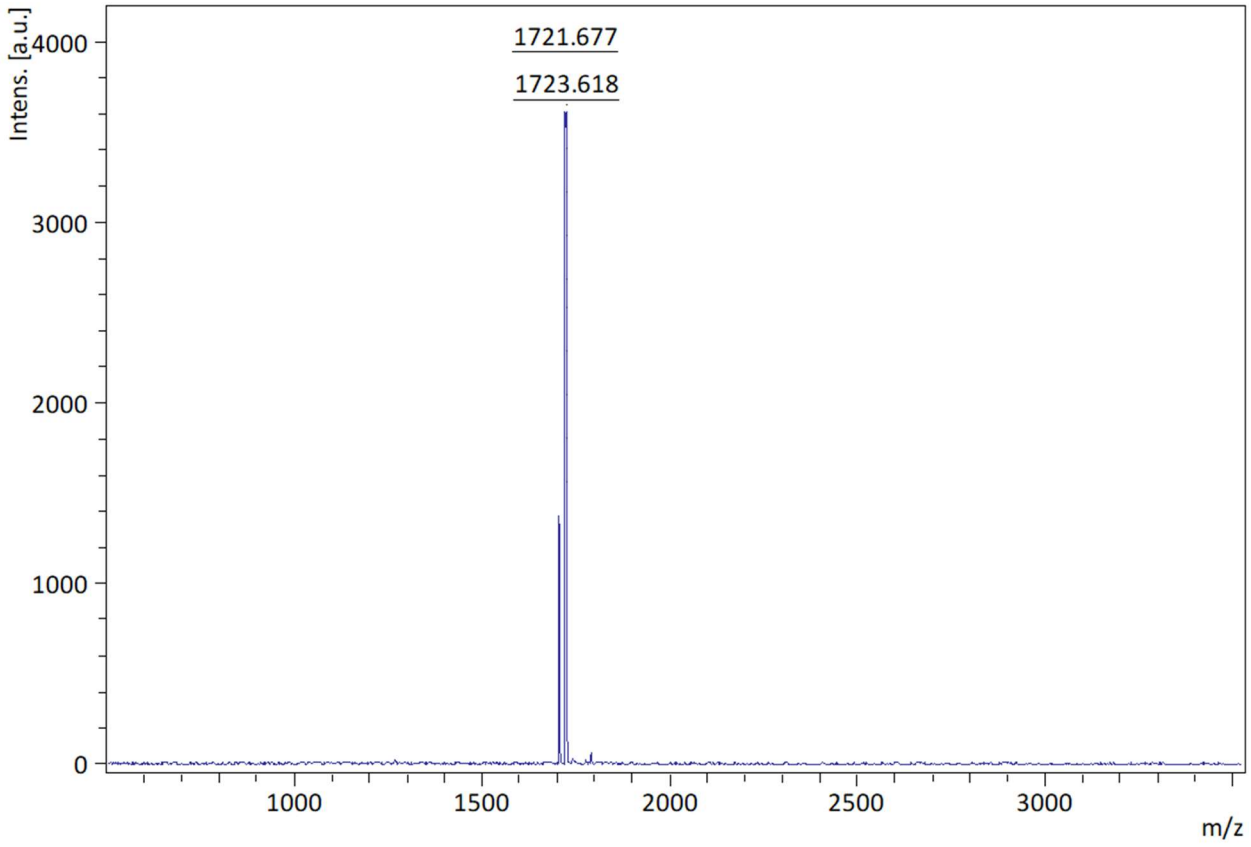

Figure S10. MALDI-ToF of FBP-methacrylamide with a sodium counterion.

Table S2. Reaction conditions for FBP-methacrylamide synthesis.

Monomer	CTA	Initiator	Solvent	Conc. (M)	CTA:I	Time (h)	Conversion (%)	Control	FBP/Polymer
HPMA	CTP	AIBN	DMSO	2	1	24	80	Poor	-
HPMA	CTP	AIBN	DMSO	2	1.5	24	56	-	-
HPMA	CTP	AIBN	DMSO	2	1.5	48	74	-	-
HPMA	CTP	AIBN	DMSO	2	2	24	39	-	-
HPMA	CTP	AIBN	DMSO	2	2	48	67	-	-
HPMA	CTP	AIBN	DMSO	2	2.5	24	29	-	-
HPMA	CTP	AIBN	DMSO	2	3	24	30	-	-
HPMA	CTP	AIBN	DmAc/H2O	2	2	24	48	-	-
HPMA	CTP	AIBN	DmAc/H2O	2	3	24	18	-	-
HPMA	ECT	AIBN	DMSO	2	1	24	87	Okay	-
HPMA	ECT	AIBN	DMSO	2	2	24	75	Good	-
HPMA	ECT	AIBN	DMSO	2	3	24	70	Good	-
HPMA-st-FBPMA	CTP	AIBN	DMSO	2	1	24	80	Poor	13

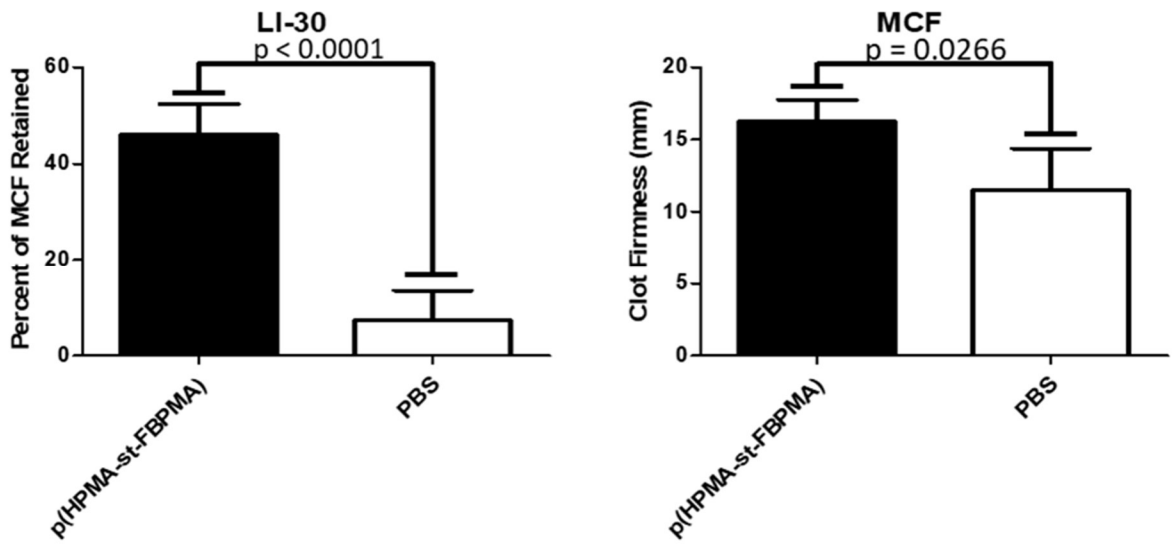

Figure S11. ROTEM characterization of PolySTAT synthesized via FBP-methacrylamide. ROTEM shows decreased lysis (A), and increased clot strength (B) of clots formed under hyperfibrinolytic conditions.

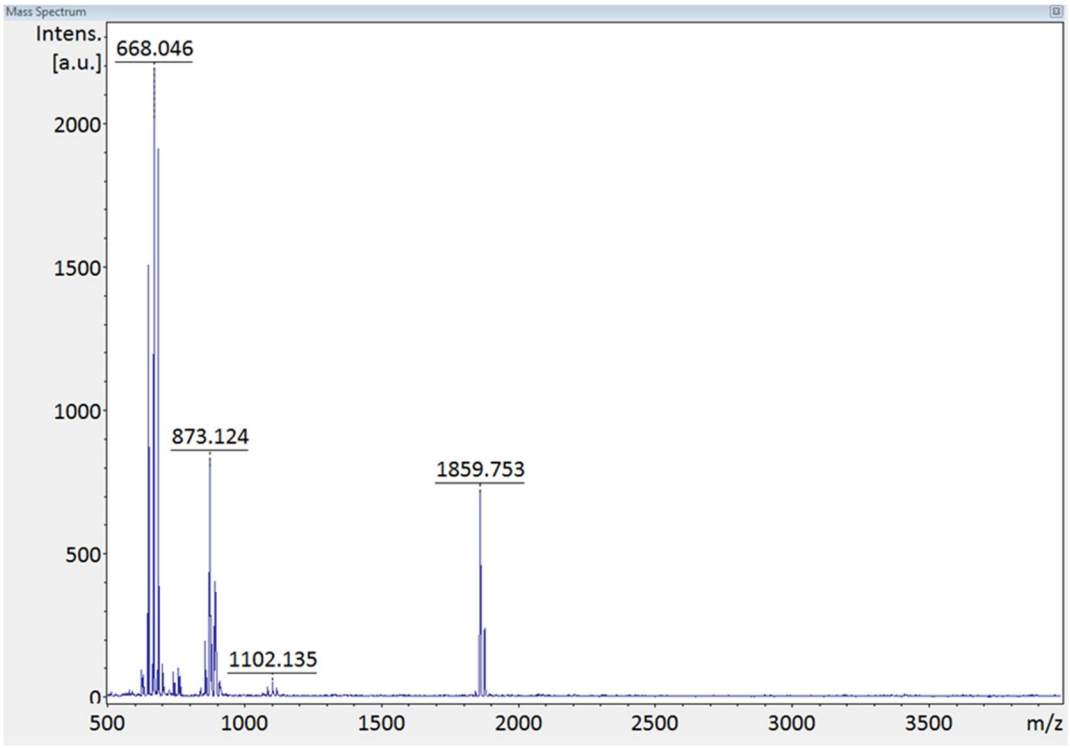

Figure S12. MALDI-ToF of FBP-methacrylate. The correct molecular weight (1859 g/mol) for FBP-SMA with a sodium counterion was observed.

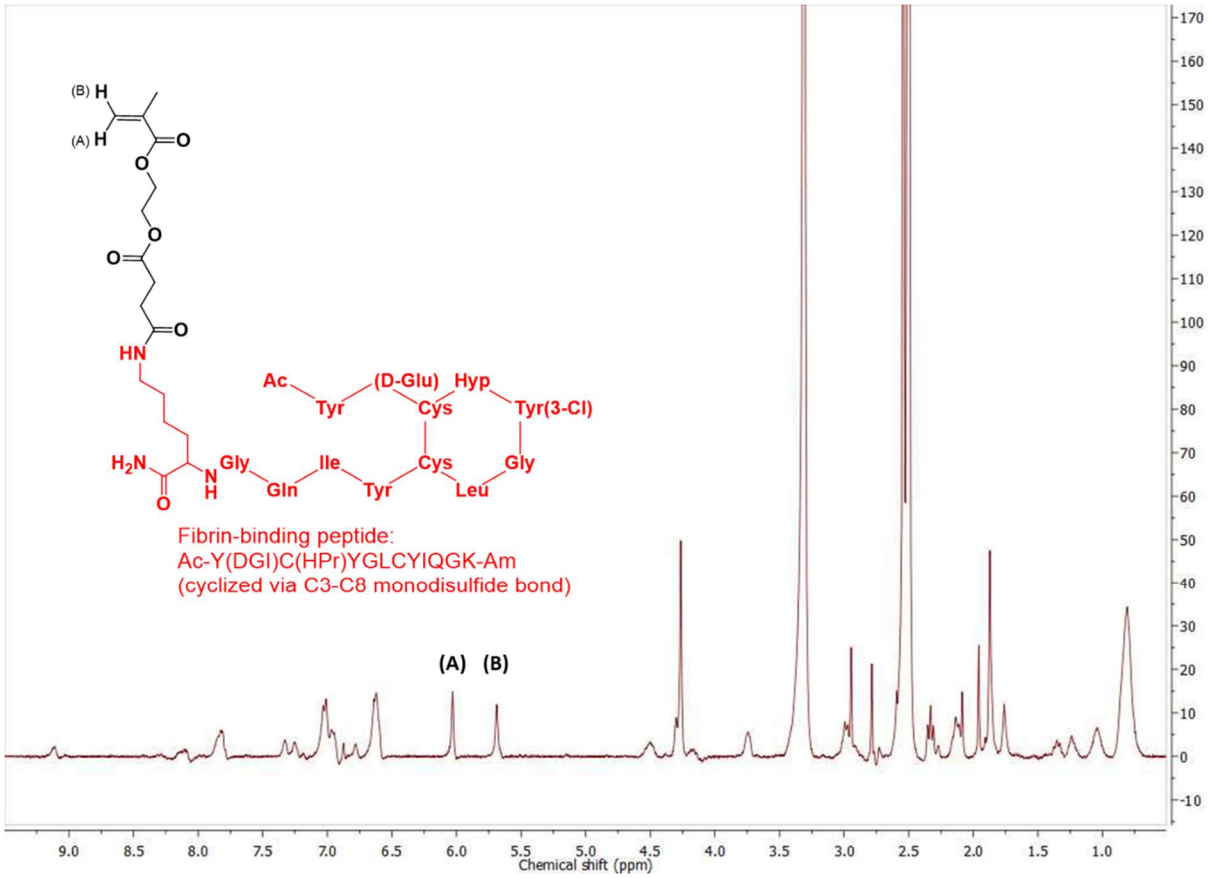

Figure S13. Proton NMR spectroscopy of FBP-methacrylate in DMSO-d_6.

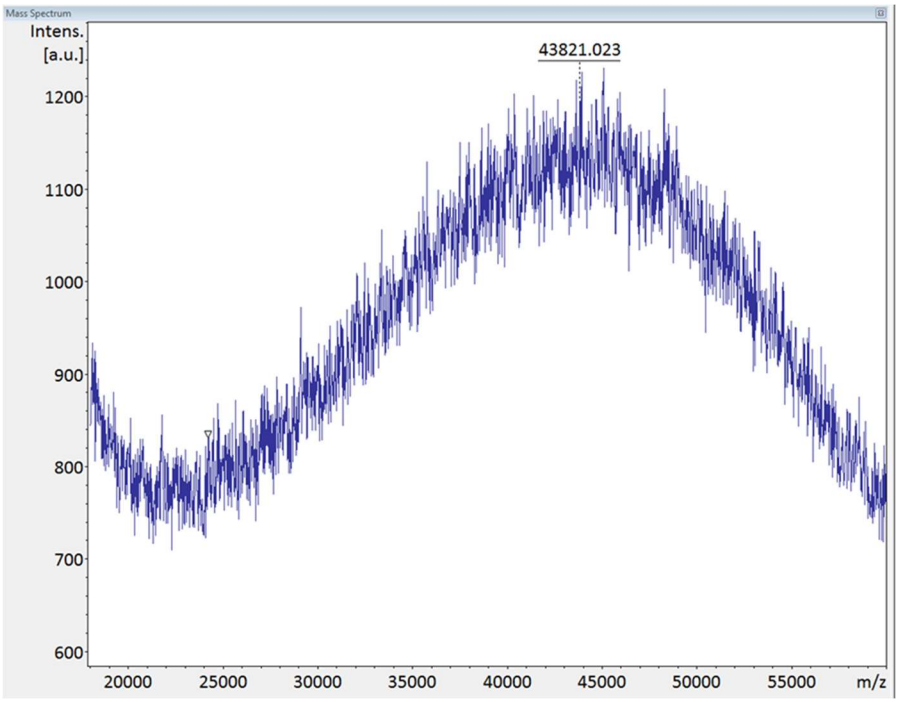

Figure S14. MALDI-ToF of PolySTAT via FBP-methacrylate. A molecular weight of 40,528.46 g/mol was targeted with a measured median m/z of 43,821.023 g/mol by MALDI-ToF. A high power was used to overcome the difficulty of getting the entire polymer to ionize and fly.

Chapter 3. EVALUTATION OF POLYSTAT IN ANIMAL MODELS OF SEVERE TRAUMA

Trey J. Pichon, Xu Wang, Kristyn M. Ringgold, Patrick Fillingham, Clarissa Bargellini, Jessica M. Snyder, Nathan J. White, Suzie H. Pun

3.1 INTRODUCTION

The goal of this work is to continue the translation of PolySTAT and provide the data necessary for an Investigational New Drug (IND) application with the FDA. As such, the FDA requires efficacy data in two animal species[1]. We have been successful in rats with the femoral bleed model.[2–5] However, the rat femoral bleed model does not simulate any of the coagulopathies present in trauma patients. Given PolySTAT is an anti-fibrinolytic, the ultimate goal is to create hyperfibrinolysis in rats, therefore, the first portion of this chapter overviews attempts to create this. The second portion of this chapter details work in Swine. Due to the similar cardiovascular systems and blood volumes to humans, swine make an ideal large-animal model.[6] In addition, the Emergency Medicine group has nearly 30 years of experience developing hemorrhage models in swine. Even so, swine present a challenge due to the lack of fibrinolysis and extremely dense and robust clots. This puts PolySTAT at an immediate disadvantage since its primary effect is as a antifibrinolytic, and without fibrinolysis present, we are relying on its ability to increase clot firmness. To start, a deadly hemodilution aorta bleed model was developed based off the work of Mitterlechner et al.[7] and combined with the EM group's aorta tear model which is a high-pressure, arterial bleed.[8] The hemodilution leads to a dilutional coagulopathy and substantially decreases clot firmness. We present data on PolySTAT's safety and efficacy in this model. Then, we detail efforts to create an alternative hemodilution model of a deadly liver transection model, and the ultimate liver laceration model to evaluate PolySTAT. Finally, we end with recent efforts to model wound mechanics of the aorta tear to aid in future developments of intravenous therapies for trauma.

3.2 MATERIALS AND METHODS

3.2.1 *Materials*

2,2′-Azobis(2-methylpropionitrile) (AIBN), 4-cyanopentanoic acid dithiobenzoate (CTP), glycidyl methacrylate (GMA) and all other reagents were purchased from Sigma-Aldrich (Saint Louis, MO) unless noted otherwise. N-hydroxysuccinimide methacrylate (NHSMA) was purchased from TCI America (Portland, OR). The fibrin binding peptide (FBP; Sequence: Ac-Y(DGl)C(HPr)YGLCYIQGK),[9] developed by the Caravan group, as well as the scrambled peptide

(Ac-YICGQ(DGl)AC(HPr)LYGK) were purchased from Elim Biopharm (Hayward, California), as custom orders. Human fibrinogen, thrombin, and plasmin were purchased from Enzyme Research Laboratories (South Bend, IN).

3.2.2 *Hydrolysis of glycidyl methacrylate to glycerol monomethacrylate*

Glycerol monomethacrylate (GmMA) was synthesized via hydrolysis of glycidyl methacrylate (GMA) as described previously for poly(GMA).[10] GMA (11.4 mL) was added to DI water (68.6 mL) at a mass ratio of 15% in a two-necked round bottom flask with one neck sealed and a vigreux column in the other. The mixture was sparged with air and stirred at 80 °C for 16 h. The solution was subsequently cooled, and sodium chloride added to a final concentration of 300 mg/mL. GmMA was extracted into an organic phase via 3x washes with 30 mL ethyl acetate. GmMA was isolated by removal of ethyl acetate via rotavap and stored at -20 °C.

3.2.3 *Synthesis of pGmMA-co-NHSMA*

pGmMA-co-NHSMA was synthesized via reversible addition-fragmentation chain transfer (RAFT) polymerization as described previously.[2,5,11] Briefly, GmMA and NHSMA were combined with CTP and AIBN at 180:20:1:0.333 ratio in dimethylacetamide at a monomer concentration of 0.6 M. This mixture reacted for 24 h at 70 °C. Polymers were precipitated in diethyl ether followed by dissolution in dimethylsulfoxide and a second precipitation in 50-50 acetone/ether. Precipitated polymer was collected by centrifugation at 7197 x g. Dithiobenzoate groups were removed via an end-capping reaction with 20x molar excess AIBN at 70 °C for 24 hours.

3.2.4 *Synthesis of 2-Propenoic acid, 2-methyl-, 2-[[[(3',6'-dihydroxy-3-oxospiro [isobenzofuran-1(3H),9'-[9H]xanthen]-5-yl)amino]thioxomethyl]amino]ethyl ester (AEMA-FITC)*

Fluorescein 5(6)-isothiocyanate (1 g/2.58 mmol) and 1.1 equivalents of 2-Aminoethyl methacrylate hydrochloride (470 mgs/2.84 mmol) were added to a round bottom flask with a stir bar. DMSO (25.8 mL/0.1 M) was added. Once the constituents were dissolved (pale yellow solution), 2.6 equivalents of DIPEA (1.29 mL) were added dropwise (turned to deep orange color). The mixture was stirred at RT overnight. The solution was precipitated one time in cold 6% HCl

solution (10x volume of reaction) constantly swirled over ice. The orange precipitate was filtered off with a glass frit. The precipitate was collected into a glass vial then lyophilized overnight. The solid, orange monomer was stored at -20 °C. Yield was > 90%. The monomer was pure by 1H nuclear magnetic resonance (NMR) spectroscopy on a Bruker AV 300 and TLC (not shown).

3.2.5 *Synthesis of FITC-labeled PolySTAT backbone (pGmMA-co-AEMA-FITC-co-NHSMA)*

pGmMA-co-AEMA-FITC-co-NHSMA was synthesized via reversible addition-fragmentation chain transfer (RAFT) polymerization as described previously.[2,5,11] Briefly, comonomers GmMA, AEMA-FITC, and NHSMA were combined with CCC and AIBN at 170:10:20:1:0.333 ratio in dimethylacetamide at a monomer concentration of 0.6 M. This mixture reacted for 20 h at 70 °C. Copolymers were precipitated in diethyl ether followed by dissolution in dimethylsulfoxide and a second precipitation in 50-50 acetone/diethyl ether. Precipitated polymer was collected by centrifugation at 7197 x g. Trithiocarbonate groups were removed via an end-capping reaction with 20x molar excess AIBN at 70 °C for 12 hours.

3.2.6 *Polymer characterization*

Polymers were characterized via gel permeation chromatography (GPC) in dimethylformamide with static light scattering and refractive index detectors (MiniDawn Treos and OptilabTRex, respectively, both from Wyatt Technology, Santa Barbara, CA) to determine molecular weight and dispersity index (PDI). ^{1}H nuclear magnetic resonance (NMR) spectroscopy on a Bruker AV 300 was utilized to determine conversion of the polymer prior to purification, and composition after purification.

3.2.7 *Synthesis of PolySTAT via conjugation*

PolySTAT was synthesized as described previously.[2,5] Copolymers synthesized above were conjugated to FBP via reaction of the C-terminal lysine in the peptide under organic basic conditions in DMSO at a varying ratios of peptide:NHS with N.N-diisopropylethylamine added at a 5:1 ratio base:peptide[12] for 24 h at 50 °C, after which unreacted NHSMA groups were capped with 10x molar ratio of 1-amino-2-propanol. Peptide-polymer conjugates were purified by extensive dialysis as follows. First, the product was dialyzed against phosphate-buffered saline (PBS) for 24 h (3 buffer changes, 4 L of buffer) during which a precipitate formed. Contents of

the dialysis bag were collected and centrifuged at 4500 x g for 8 min to remove insoluble material; the supernatant was collected and moved to a fresh dialysis bag. Dialysis continued for 24 h (3 buffer changes), followed by water for 48 h (6 dialysate changes) to remove PBS salts. Peptide content of materials was determined using the extinction coefficient of FBP and the materials' absorbance at a wavelength of 280 nm using a NanoDrop 2000 UV-Vis spectrophotometer (Thermo Fisher Scientific, Waltham, MA).

3.2.8 *ROTEM Characterization of PolySTAT*

ROTEM experiments consisted of 300 µL of clotting solution in a standard ROTEM cup placed in a ROTEM whole blood hemostasis analyzer (ROTEM, Instrumentation Laboratory, Bedford, MA, USA). The clotting solution consisted of human fibrinogen, thrombin, and plasmin that were purified from human plasma. All clotting factors were purchased from Enzyme Research Laboratories (South Bend, IN). Final concentrations in the ROTEM were 1.5-2 mg/mL fibrinogen, 0.5-1 IU/mL thrombin, 2-4 µg/mL plasmin, 0.1 mmol/L CaCl2, and 5 µmol/L PolySTAT at pH 7.4. Measured parameters in ROTEM included: (i) the clotting time (CT), measured as the time between reagent addition to clot formation; (ii) α-angle, which reflects the rate of clot formation, (iii) the maximum clot firmness (MCF), the highest strength observed for the clot, (iv) the lysis index-30 minutes (LI-30), the percentage of MCF retained 30 minutes after initiation of clot formation, and (v) maximum lysis (ML), the percentage of clot strength lost compared to the MCF at the end of analysis.

3.2.9 *Development of rat coagulopathic models*

Polytrauma Model

Animal experiments were carried out in accordance with protocols approved by the University of Washington Institutional Care and Use Committee. This protocol was adapted from the ACOT model developed by Darlington *et al.*[13] Male Sprague Dawley rats (270g-370g) were anesthetized by isoflurane then a ketamine-xylazine cocktail injection in the hindlimb, followed by a tracheotomy for ventilation and isoflurane anesthesia. Both the jugular vein and carotid artery were cannulated. The carotid artery was used to monitor vitals (blood pressure and heart rate), perform a controlled catheter hemorrhage, and collect blood samples for blood gas measurements. The jugular vein was used for administration of resuscitation fluids and intravascular administration of

the treatments. Baseline ROTEM (EXTEM and FIBTEM), blood gas, and metabolites were evaluated to ensure healthy baseline coagulation, respiration, and lactate levels ($pCO2 \leq 55$ mmHg, $sO2\% \geq 95\%$, $cLac \leq 1.0$ mmol/L) prior to initiating polytrauma. For the polytrauma, a midline incision was made, the surgeon performed a liver crush, 10 cm of intestines crush, fractured both hind femurs, and muscle crush of both hind limbs. After polytrauma, the rat was then catheter hemorrhaged down to a mean arterial pressure (MAP) below 40 mmHg over 5 minutes then maintained below 40 mmHg with intermittent blood draws over 60 minutes. After controlled hemorrhage, the shock period is initiated and the rat was allowed to autoresuscitate for 30 minutes. At the end of the 30 minute shock period (t90), the protocol was ended and the rat's blood was evaluated in ROTEM (EXTEM and FIBTEM). Throughout the study, if blood pressure falls below 15 mmHg, the rat will be euthanized humanely while under anesthesia using barbiturate overdose.

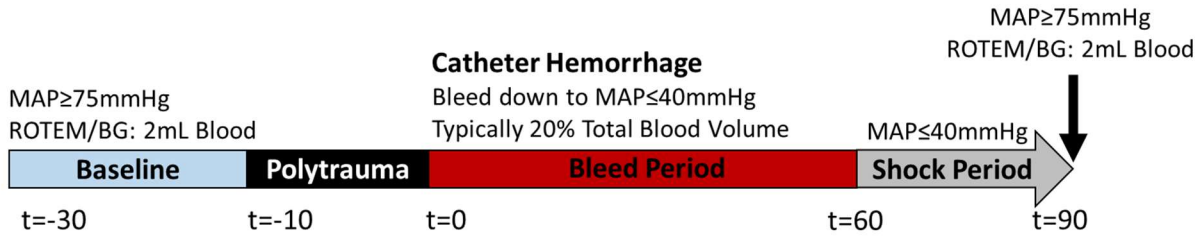

Shock-only Model

Animal experiments were carried out in accordance with protocols approved by the University of Washington Institutional Care and Use Committee. This procedure was adapted from Moore *et al.*[14] The same instrumentation and baseline procedure was followed as outlined above in the Polytrauma model. After baseline, a controlled hemorrhage over 5 minutes down to a MAP of $\leq$ 20 mmHg was performed. The rat was maintained in shock by drawing blood as needed to keep the rat below a MAP $\leq$ 25 mmHg. After 30 minutes, the rat's blood was evaluated in ROTEM (EXTEM and FIBTEM). Throughout the study, if blood pressure falls below 15 mmHg, the rat will be euthanized humanely while under anesthesia using barbiturate overdose.

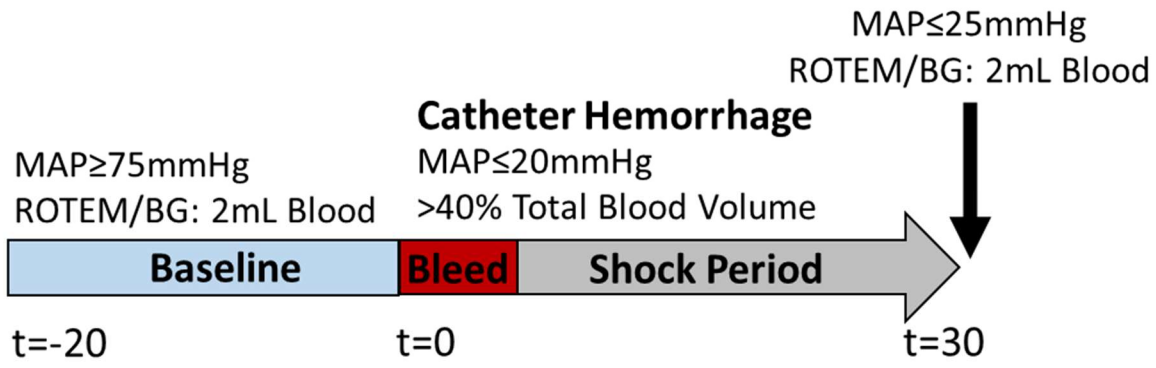

Lipopolysaccharides (LPS) Infusion Model

Animal experiments were carried out in accordance with protocols approved by the University of Washington Institutional Care and Use Committee. The same instrumentation and baseline procedure was followed as outlined above in the Polytrauma model. After baseline, rats were intravenously injected a single bolus of LPS (1.5 mg/kg, 111:B4, Sigma). ROTEM (EXTEM and FIBTEM) was evaluated at 60, 120, and 180 minutes after LPS administration. Throughout the study, if blood pressure falls below 15 mmHg, the rat will be euthanized humanely while under anesthesia using barbiturate overdose.

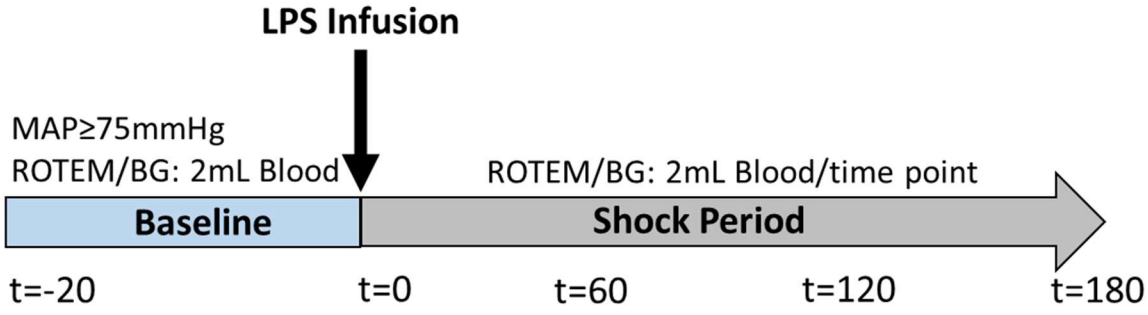

Hemodilution

Animal experiments were carried out in accordance with protocols approved by the University of Washington Institutional Care and Use Committee. This procedure was adapted from Moore *et al*.[14] The same instrumentation, baseline, catheter hemorrhage, and shock procedure were followed as outlined above in the shock-only model. At the end of the 30 minute shock period, a hemodilution was performed with isotonic saline (20 mL/kg, infused at 3 mL/[min*kg]) over 10 minutes. During the hemodilution, the femoral artery of the left hind limb was isolated and a proximal branch off the artery was ligated with a suture to prevent backflow of blood following injury. Surgical microclamps were placed both proximally (distal of the ligated branch) and

distally along the artery. A 3mm longitudinal incision was made with micro scissors in between the surgical clamps. Once hemodilution was complete, the clamps were pulled, and free bleed (t = 0min) was initiated. Immediately, a blinded treatment was administered by the surgeon (dose = 15 mg/kg). After 3 min of free bleeding (t = 43 min), fluid resuscitation was started at a rate of 3 mL/min per kg for a total volume up to 40 mL/kg. Resuscitation was stopped and restarted as needed to reach and maintain a blood pressure target of MAP = 60 mmHg. At regular intervals, blood was collected at the edges of the surgical site by pre-weighed gauze. The surgeon was careful not to disturb the clot nor the femoral artery. After the end of the protocol, final clot mass was added to the hemorrhage volumes of each rat. Protocol ended when official death was declared by the blinded surgeon or at t = 120 min, which was deemed survival. Throughout the study, if blood pressure falls below 15 mmHg, the rat will be euthanized humanely while under anesthesia using barbiturate overdose.

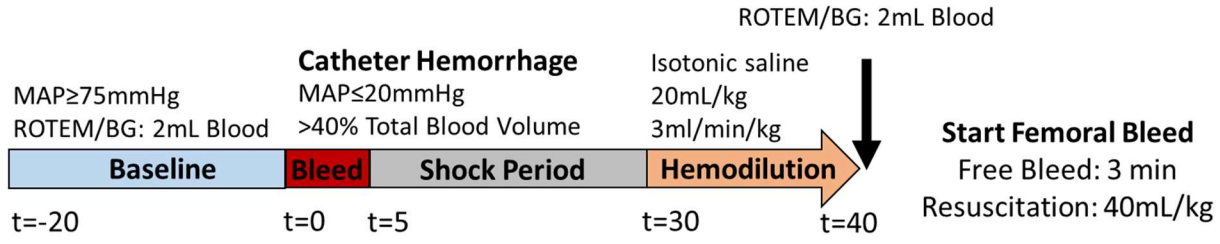

Resuscitation

Animal experiments were carried out in accordance with protocols approved by the University of Washington Institutional Care and Use Committee. This procedure was adapted from Moore *et al*.[14] The same instrumentation, baseline, catheter hemorrhage, and shock procedure were followed as outlined above in the shock-only model. During the shock period, the femoral artery of the left hind limb was isolated and a proximal branch off the artery was ligated with a suture to prevent backflow of blood following injury. Surgical microclamps were placed both proximally (distal of the ligated branch) and distally along the artery. A 3mm longitudinal incision was made with micro scissors in between the surgical clamps. At the end of the 30 minute, the clamps were pulled, and free bleed (t = 0min) was initiated. Immediately, a blinded treatment was administered by the surgeon (dose = 15 mg/kg) and fluid resuscitation was started at a rate of 3 mL/min per kg for a total volume up to 60 mL/kg. Resuscitation was stopped and restarted as needed to reach and

maintain a blood pressure target of MAP = 60 mmHg. At regular intervals, blood was collected at the edges of the surgical site by pre-weighed gauze. The surgeon was careful not to disturb the clot nor the femoral artery. After the end of the protocol, final clot mass was added to the hemorrhage volumes of each rat. Protocol ended when official death was declared by the blinded surgeon or at t = 120 min, which was deemed survival. Throughout the study, if blood pressure falls below 15 mmHg, the rat will be euthanized humanely while under anesthesia using barbiturate overdose.

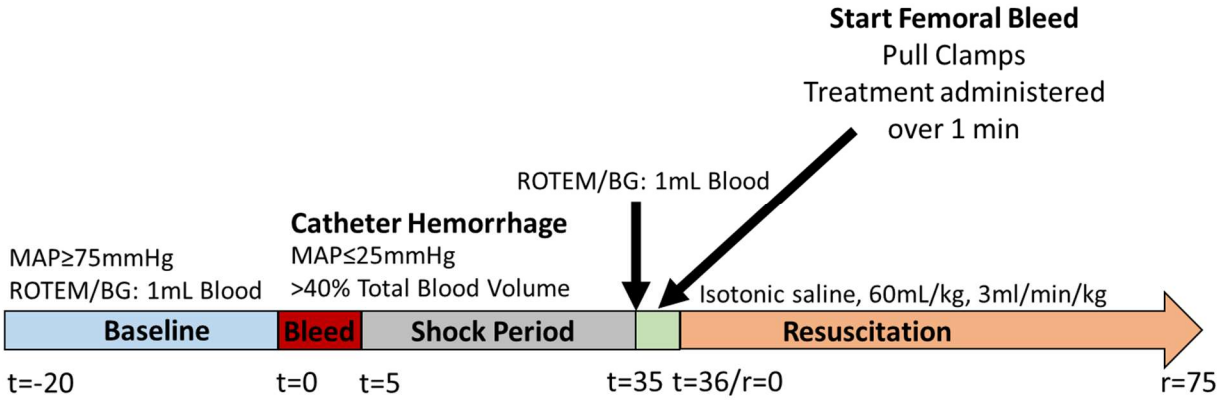

3.2.10 *PolySTAT evaluation in a swine hemodilution aortic tear and fluid resuscitation model*

Animal experiments were carried out in accordance with protocols approved by the University of Washington Institutional Care and Use Committee. Domestic swine (female, adolescent, ~19-25 kg) were randomized into one of three treatment groups (TXA, PolySCRAM, and PolySTAT). A total of 10 pigs were evaluated in each arm. Swine were sedated via intramuscular injection of Ketamine followed by a subcutaneous buprenorphine injection. Anesthesia was maintained by continuous isoflurane via an endotracheal tube. After anesthesia, swine were catheterized via (i) the jugular vein with a Swan-Ganz catheter to measure CVP, PAP, and cardiac output, (ii) the left and right femoral artery for catheter hemorrhage, blood draws, and monitoring MAP, (iii) the right femoral vein for resuscitation and substance administration. ECG contacts were attached to the chest and front limb to monitor heart rhythm. Treatments were infused via the jugular vein. A splenectomy was performed to prevent auto-resuscitation. The bladder was catheterized to measure urine output to monitor kidney function. The aorta was isolated at midline near the kidney. Two dots, placed 3 mm longitudinally apart are marked, then a curved needle is used to place the suture through the aorta wall (enters one dot, then exits the other). Pressure was maintained until

bleeding from the suture stops. The two ends of the suture were twisted together, and the suture was exteriorized through the midline incision and secured in place. The swine midsection was closed. Next, coagulopathy was induced through a normovolemic 1:1 hemodilutionas described by Mitterlechner et al.[7], ~42% total blood volume was removed and replaced with 6% hydroxyethyl starch in electrolyte solution (Hextend). Fifteen minutes after hemodilution, the bleed period was started by a catheter hemorrhage at a rate of 35 cc/kg over 30 min. After MAP ≤ 50 mmHg (typically 2 min), the suture was pulled to tear the aorta. Catheter hemorrhage continued until MAP ≤ 30 mmHg (typically 2 additional minutes). Five minutes after the aorta tear, the blinded treatment was administered over 10 minutes. At the end of catheter hemorrhage, the shock period was started. Shock was continued until lactate ≥ 2 mmol/L and a decreased cardiac output and end-tidal carbon dioxide (ETCO2) are observed (typically 10-30 minutes). After the shock period, the prehospital phase was initiated (T0) with an aggressive resuscitation (3 cc/kg/min) with Lactated Ringer's solution. This was started and stopped as needed to maintain MAP ≥ 60 mmHg or until a maximum resuscitation volume of 60 cc/kg was reached. If the MAP dropped below 10 mmHg for at least 1 min, and the MAP waveform was lost (indicating cardia arrest), then the pig was deemed a clinical death and euthanized by pentobarbital overdose. The prehospital phase was ended at 120 minutes (T120) and the ER phase began with a blood transfusion of blood collected during the hemodilution. The pig was monitored for 60 minutes (T180), after which the study ended, and the pig deemed survived. The pig was then euthanized by pentobarbital overdose. At the pig was deemed dead by the clinician, the midsection was reopened, and pre-weighed gauze were used to measure the amount of intraperitoneal hemorrhage. A segment of the aorta encompassing the wound site was harvested along with biopsies of the ileum, pancreas, kidney, liver, heart, and lung. All tissue samples were fixed in 10% buffered formalin solution.

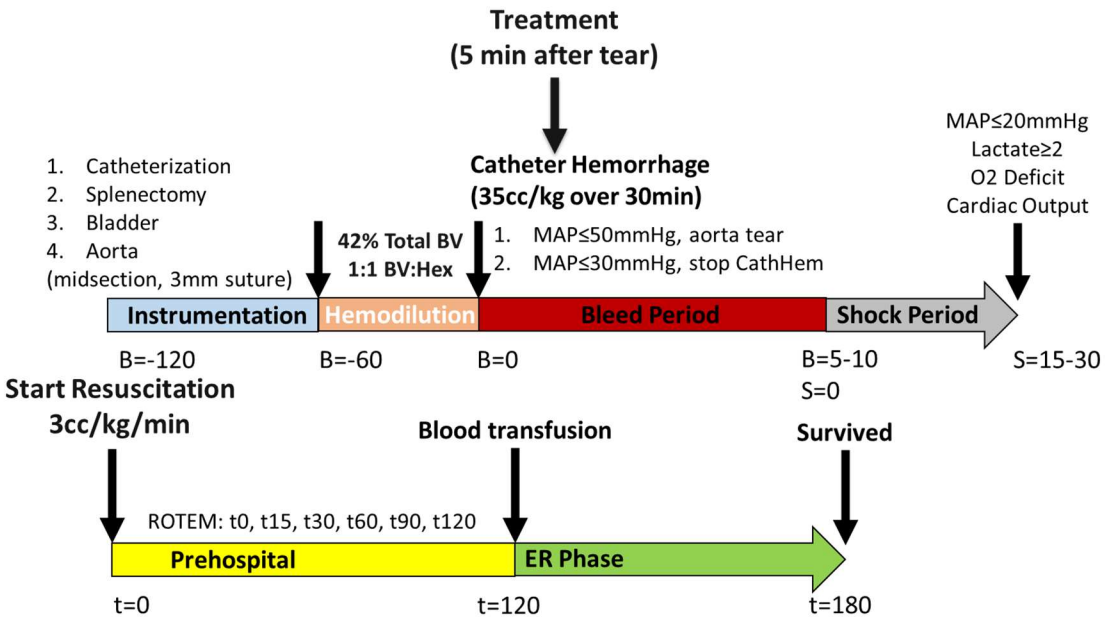

Figure 1. Experimental protocol used for the swine hemodilution aortic tear and resuscitation model.

3.2.11 *PolySTAT evaluation in a swine hemodilution liver transection and fluid resuscitation model*

Animal experiments were carried out in accordance with protocols approved by the University of Washington Institutional Care and Use Committee. This procedure was adapted from Massimo *et al.*[15,16] Domestic swine (female, adolescent, ~19-25 kg) were randomized into one of three treatment groups (TXA, PolySCRAM, and PolySTAT). A total of 10 pigs were evaluated in each arm. Swine were sedated via intramuscular injection of Ketamine followed by a subcutaneous buprenorphine injection. Anesthesia was maintained by continuous isoflurane via an endotracheal tube. After anesthesia, swine were catheterized via (i) the jugular vein with a Swan-Ganz catheter to measure CVP, PAP, and cardiac output, (ii) the left and right femoral artery for catheter hemorrhage, blood draws, and monitoring MAP, (iii) the right femoral vein for resuscitation and substance administration. ECG contacts were attached to the chest and front limb to monitor heart rhythm. Treatments were infused via the jugular vein. A splenectomy was performed to prevent auto-resuscitation. The bladder was catheterized to measure urine output to monitor kidney function. Next, coagulopathy was induced through a hemodilution, ~42% total blood volume was removed and replaced with Lactated Ringer's (LR) solution over 30 minutes. Fifteen minutes after

hemodilution, the left lobe of the liver was isolated by gently pulling it out of the cavity with forceps so the posterior side was visible. For the liver transection model, a premeasured stencil of different widths 3-6 cm was used to measure from the base of the hilum and draw a line perpendicular to the main white ligament on the underside (posterior) of the liver. Once the line was made, the surgeon started a timer and using large surgical scissors, fulling transected the lobe from marked line (distal from the hilum). The transected piece was fully removed, and the midsection was quickly closed with stables over two minutes. At the end of two minutes (T2), the treatment was administered over 10 minutes. At T15, the shock period ended regardless of lactate, cardiac output, and end tidal levels, and resuscitation was initiated (1 cc/kg*min) with LR solution. This was started and stopped as needed to maintain MAP ≥ 60 mmHg or until a maximum resuscitation volume of 60 cc/kg was reached. If the MAP dropped below 10 mmHg for at least 1 min, and the MAP waveform was lost (indicating cardia arrest), then the pig was deemed a clinical death and euthanized by pentobarbital overdose. The pig was monitored for 180 minutes (T180), after which the study ended, and the pig deemed survived. The pig was then euthanized by pentobarbital overdose. After the pig was deemed dead by the clinician, the midsection was reopened, and pre-weighed gauze were used to measure the amount of intraperitoneal hemorrhage. Biopsies of the ileum, pancreas, kidney, liver, heart, and lung were all harvested. All tissue samples were fixed in 10% buffered formalin solution. The weight of the transected left lobe was weighed, and the largest vessels imaged with a camera and measured for later analysis.

For the liver laceation model, the same exact procedure was followed, however instead of scurgical scissors, the surgeon used a scalpel blade with a preset depth of 1 cm. A deep laceration was made by cutting along the line drawn by the stencil on the posterior side of liver. At the end of the study, the laceration was fully cut (transected from the body) so it could be weighed, vessels imaged, and measured similar to the transection model.

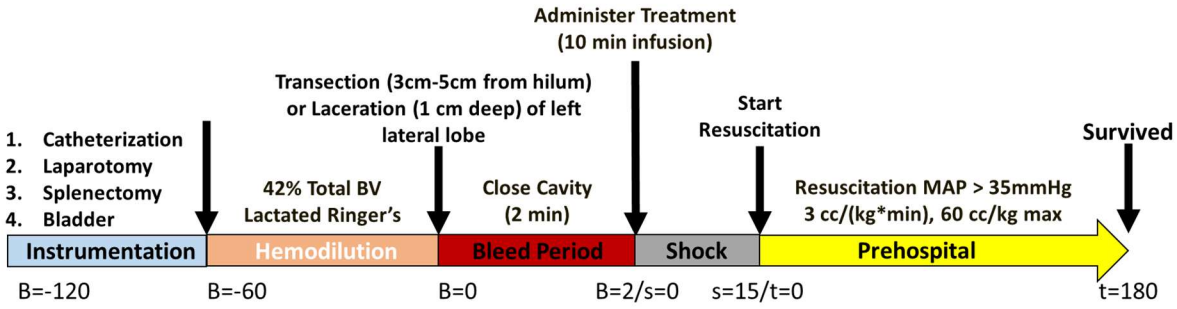

3.2.12 *ROTEM monitoring of swine hemostasis*

Whole blood was drawn into sodium citrate tubes at different timepoints, and hemostatic capacity was measured via EXTEM in ROTEM. The whole blood was then spun down at 5,000g for fifteen minutes to obtain platelet poor plasma. This was then evaluated in EXTEM as well. Tissue factor, phospholipids, and CaCl2 are used to activate coagulation through the extrinsic pathway.

3.2.13 *Estimation of PolySTAT concentration in swine blood*

The exact same animal protocol was followed as outlined above except FITC-PolySTAT (10% FITC) was infused as the treatment. Blood samples were collected in citrated tubes at normal time points used in the study. PPP was prepared from the samples as outlined above. A stock of FITC-PolySTAT was made in PBS, then serially diluted and 100 µL were aliquoted into a 96 well plate. A standard curve was generated based on measured emission at 525 with excitation at 490. A serial dilution was made of the PPP in PBS at timepoints baseline, post dilution, T0, and T15. Emission was measured, and the concentration of PolySTAT was estimated based on a linear fit to the standard curve.

3.2.14 *Confocal Microscopy of FITC-labeled PolySTAT Clots*

The exact same animal protocol was followed as outlined above. Whole blood clots were harvested from the peritoneal cavity of swine infused with FITC-PolySTAT (10% FITC). The clots were randomly sectioned by the surgeon and immediately submerged in 10% buffered formalin solution for 8 hours. The clots were rinsed with normal saline multiple times, then stored in 70% ethanol/saline solution overnight at 4C. The fixed clots were sectioned with a fresh disposable razor blade. For fibrin clots, blood samples were taken at baseline, post dilution, T0, and T15 from FITC-PolySTAT infused pigs. The blood was spun down as outlined above. The PPP was clotted in a 96 well plate with the EXTEM assay reagents. The clots sat covered and undisturbed on a hot plate maintained at 37C for 1 hour. The well plate was then submerged in 10% buffered formalin solution for 8 hours. The clots were rinsed with saline, and then the 96 well plate was submerged in 70% ethanol/saline solution overnight at 4C. The clots were removed from the well plate then submerged in liquid nitrogen in a shallow dish. Once frozen, the clots were shattered in the liquid nitrogen then quickly transferred while frozen to an 8 well confocal glass bottom coverslip. All

clots were imaged on a Leica SP8X Confocal Microscope with an 20X air lens, and 40X water immersion lens.

3.2.15 *Overview of PolySTAT used in swine study*

PolySTAT: Twenty batches of PolySTAT (total = 5.9 grams) were synthesized and combined for an average FBP/backbone of 12. The batches used FBP peptide from 3 different batches supplied by Elim, and two batches of GmMA and NHSMA monomers. The PolySTAT was synthesized over a period of three months. Each individual batch was characterized and QC'd as outlined above. The combined PolySTAT was dissolved in DI H2O at 10 mg/ml followed by sterile filtering with 0.45 µm hydrophilic PVDF filters. The filters had been pre-fouled with a 1% BSA solution, then rinsed with DI H2O multiple times. Falcon tubes were filled with 37.5 mL of filtered PolySTAT solution and were frozen then lyophilized.

3.3 Rat Coagulopathic Model Development Results and Discussion

3.3.1 *Polytrauma to Create Acute Coagulopathy of Trauma Model*

The goal of this work was to create a coagulopathic rat model that recapitulated clinically relevant fibrinolysis. As a starting point, an acute coagulopathy of trauma (aCOT) model developed by Darlington et al. Figure 2 below shows the model overview.

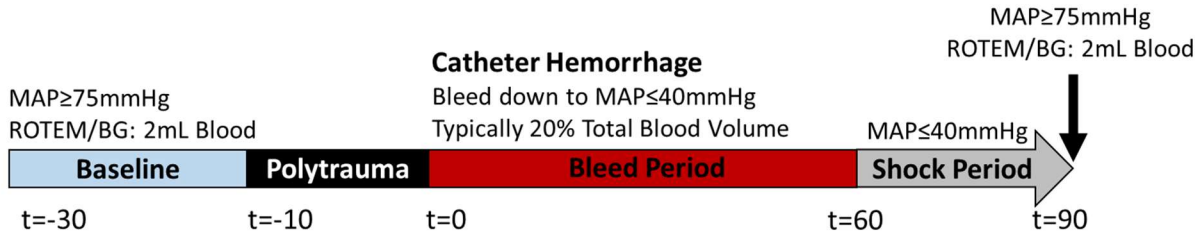

Figure 2. Model overview for an aggressive polytrauma coagulopathic bleed model in rats.

To evaluate the severity of the coagulopathy, a ROTEM sample was taken at the end of t=90 minutes. However, the model was never evaluated for survival by adding in the femoral artery bleed model of uncontrolled hemorrhage.

The aCOT model developed by Darlington was a 4 hour protocol,[13] however we started with a 90 minute protocol to see if we could reach significant levels of fibrinolysis in a shorter amount of time. The same polytrauma protocol was followed. Figure 3 below shows the EXTEM results.

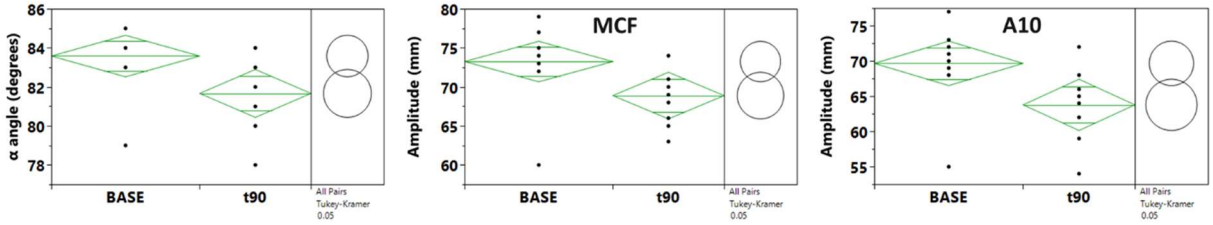

Figure 3. Whole Blood EXTEM comparison of Base and T90 timepoints for the polytrauma model in rats. Left: Alpha angle, center: maximum clot firmness, and right: A10. Although there was a statistically significant drop in all firmness parameters, no lysis was observed in any of the rats evaluated.

There was a significant drop in the rate of clot formation (alpha angle), and clot firmness (A10 and MCF) indicating the development of a trauma-induced coagulopathy. However, no lysis was observed (Figure 4 below).

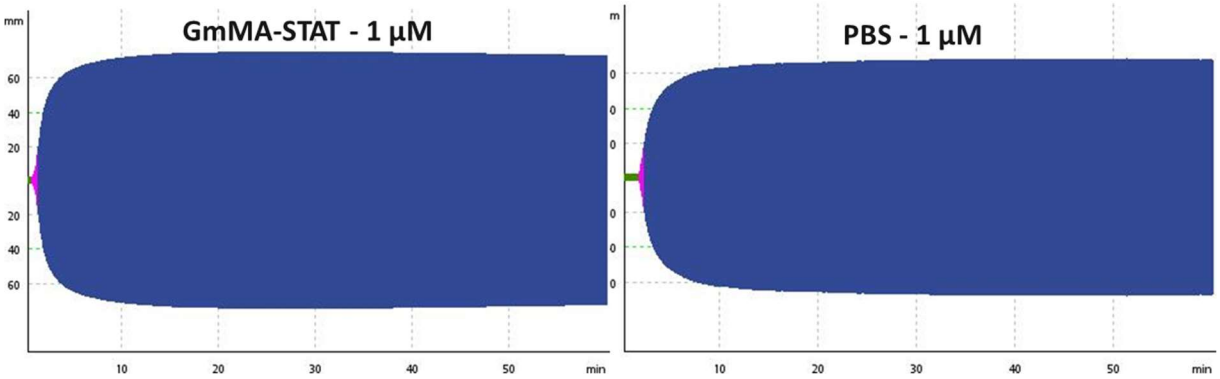

Figure 4. Whole Blood EXTEM T90 samples spiked with PolySTAT (left) and PBS volume control (right). The final concentration in the blood was 1 µM, and no difference was observed visually in the temomograms.

No effect from PolySTAT was observed when spiked into the blood at a final concentration of 1 µM. Figure 5 below shows a FIBTEM comparison of base and T90.

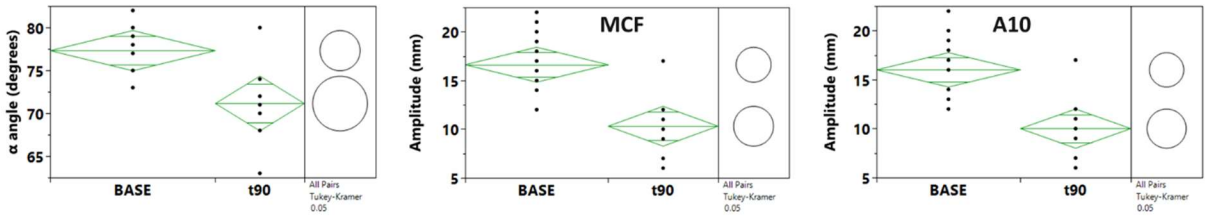

Figure 5. FIBTEM comparison of Base and T90 timepoints for the polytrauma model in rats. Left: Alpha angle, center: maximum clot firmness, and right: A10. Although there was a statistically significant drop in all firmness parameters, no lysis was observed in any of the rats evaluated.

FIBTEM shows a much greater decrease from baseline in clot firmness and alpha angle. It should be noted that alpha angle is not reliably determined in FIBTEM or when plasma is evaluated in EXTEM. Similar to EXTEM, there was no lysis observed in FIBTEM (Figure 6 below) and a direct comparison of EXTEM and FIBTEM at T90 is shown (Figure 7 below).

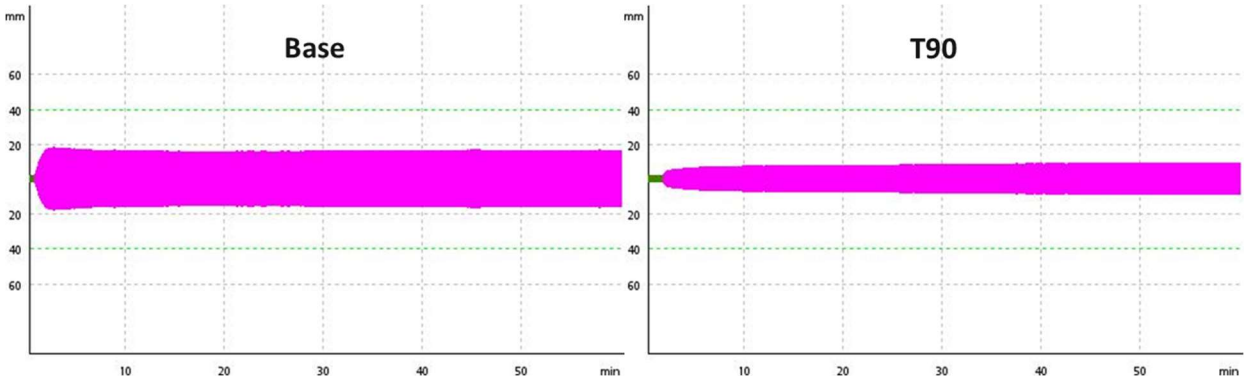

Figure 6. FIBTEM comparison of Base (left) and T90 (right) timepoints for the polytrauma model in rats. No fibrinolysis was observed, although there was a significant drop in all other clotting parameters indicating a significant drop in fibrinogen concentration.

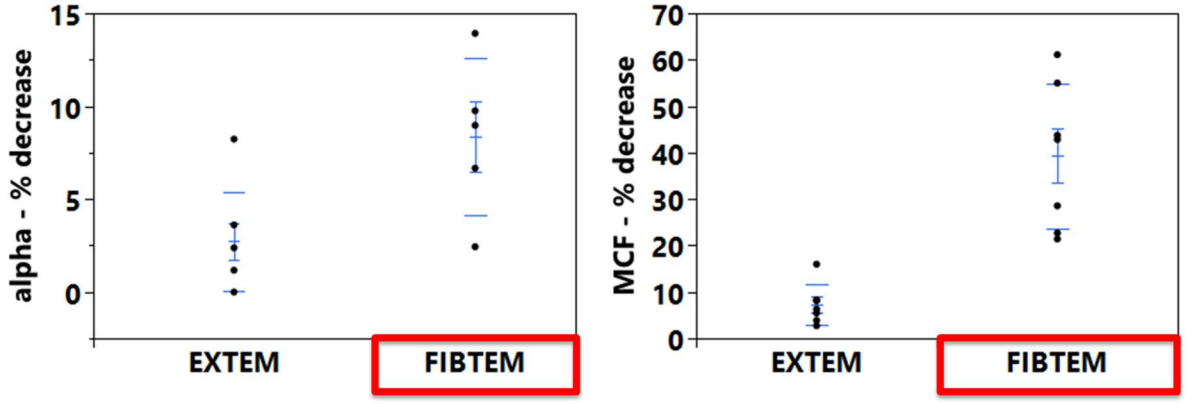

Figure 7. Comparison of the % decrease from baseline to T90 for both EXTEM and FIBTEM for both alpha angle (left) and maximum clot firmness (right). There is a much greater decrease in FIBTEM, indicating a larger effect on fibrinogen in the polytrauma model.

PolySTAT was spiked into T90 blood samples from the polytrauma model to see if it was able to rescue clot firmness even without fibrinolysis present. Two concentrations of PolySTAT (1 µM and 5 µM) were evaluated (Figure 8 Below).

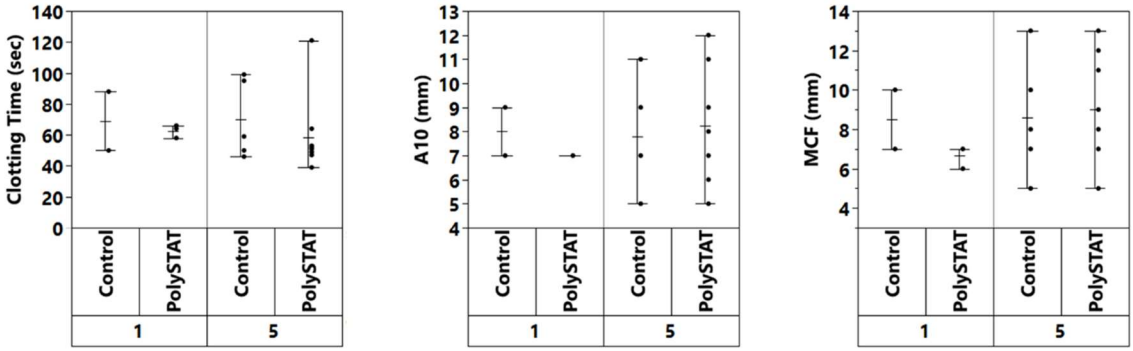

Figure 8. Comparison of PolySTAT and volume control spiked into T90 FIBTEM samples at two different concentrations (1 µM and 5 µM). There was no significant increase in clotting parameters due to PolySTAT compared to the volume control at either concentration (left: clotting time, middle: A10, and right: MCF).

PolySTAT was unable to rescue clot firmness in the polytrauma model.

3.3.2 *Severe Hemorrhagic Shock ("Shock-Only") Model*

Next, we moved to a "Shock-Only" model based off the work of Moore et al. which reported a severe hemorrhagic shock model that was able to recapitulate fibrinolysis (Figure 9 below).[14]

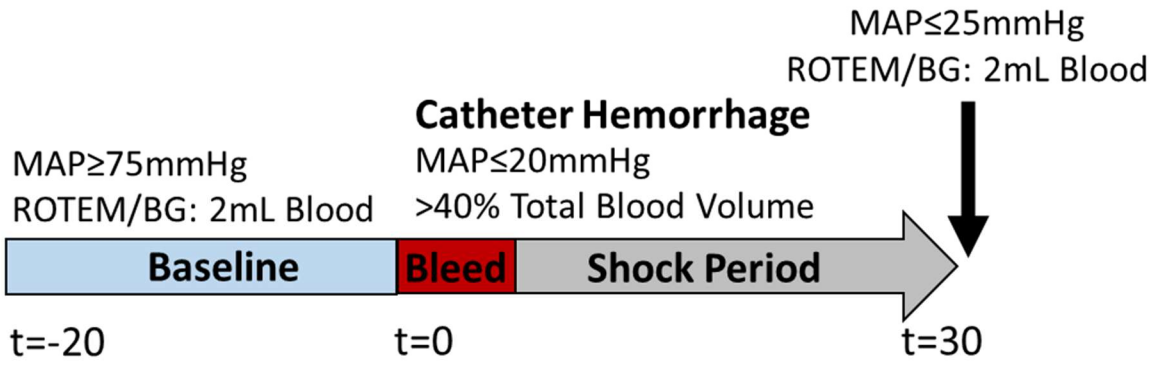

Figure 9. Model overview for a "shock-only" coagulopathic bleed model in rats. To evaluate the severity of the coagulopathy, a ROTEM sample was taken at the end of t=30 minutes. However, the model was never evaluated for survival by adding in the femoral artery bleed model of uncontrolled hemorrhage.

This model created a coagulopathy that reduced clot firmness and decreased alpha angle, however similar to the polytrauma model, no fibrinolysis was observed in ROTEM (Figure 10 and Figure 11).

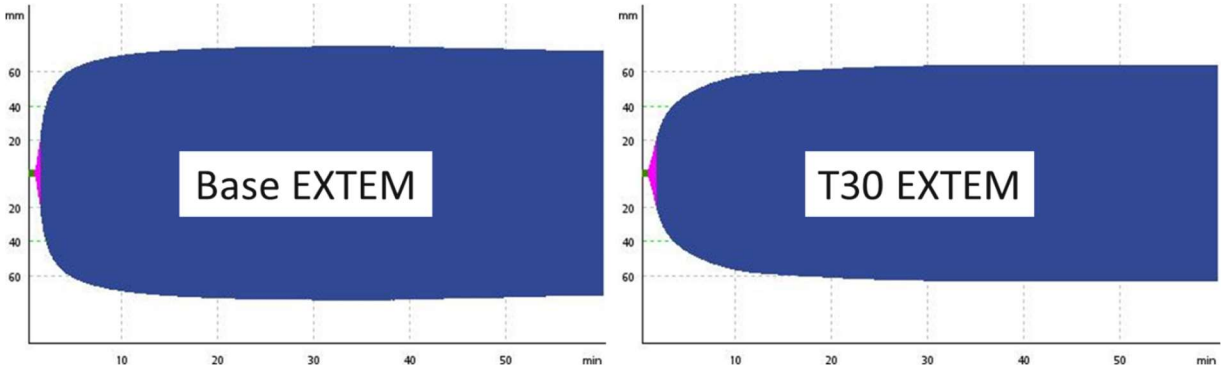

Figure 10. EXTEM comparison of Base (left) and T30 (right) timepoints for the shock-only model in rats. No fibrinolysis was observed, although there was a significant drop in all clot firmness parameters.

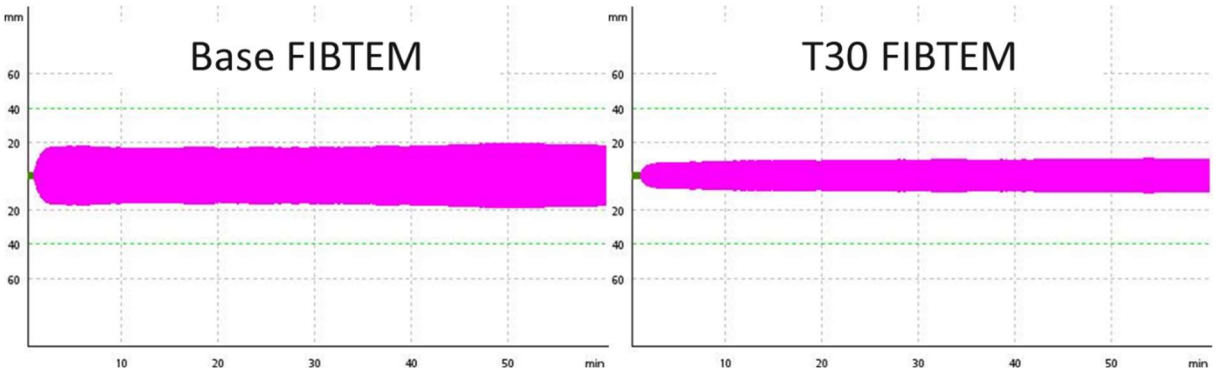

Figure 11. FIBTEM comparison of Base (left) and T30 (right) timepoints for the polytrauma model in rats. No fibrinolysis was observed, although there was a significant drop in all other clotting parameters indicating a significant drop in fibrinogen concentration.

The shock-only model consumed fibrinogen and greatly increased lactate levels of the rats, and created similar alpha angles, A5, A10, and MCF levels to the polytrauma model (Figure 12).

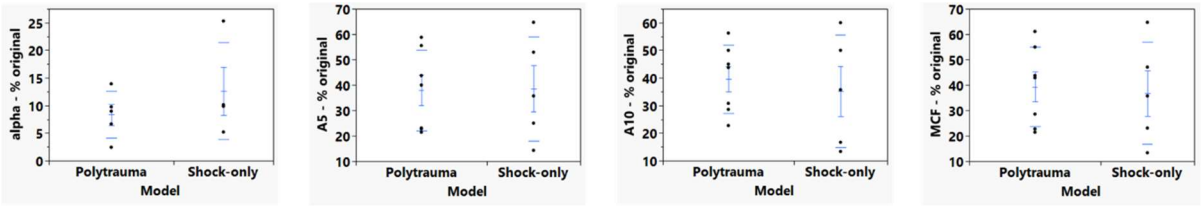

Figure 12. Comparison of the % decrease from baseline to the final timepoints (polytrauma = T90 and shock-only = T30) for FIBTEM for the polytrauma and shock-only models. Left: alpha angle, second from left: A5, second from right: A10, right: MCF. Similar changes in coagulation are observed in FIBTEM when comparing the two models.

Moore et al. also reported the ability of the bile salt taurocholic acid, TUCA, (Figure 13) to "unmask" fibrinolytic shutdown in rats and increase fibrinolysis by stabilizing tPA against PAI-1.[17] They report a TUCA-TEG assay where TUCA is spiked into blood to show the fibrinolysis potential of rat blood that would otherwise be masked. We observed that blood spiked with TUCA led to a brightly red-colored plasma (Figure 13). This was assumed to be hemolysis occurring due to the bile salt disrupting the cell membrane of red blood cells. Due to this observation, we believed

it was not possible to intravenously infuse TUCA and we only evaluated it spiked into blood (Figure 14).

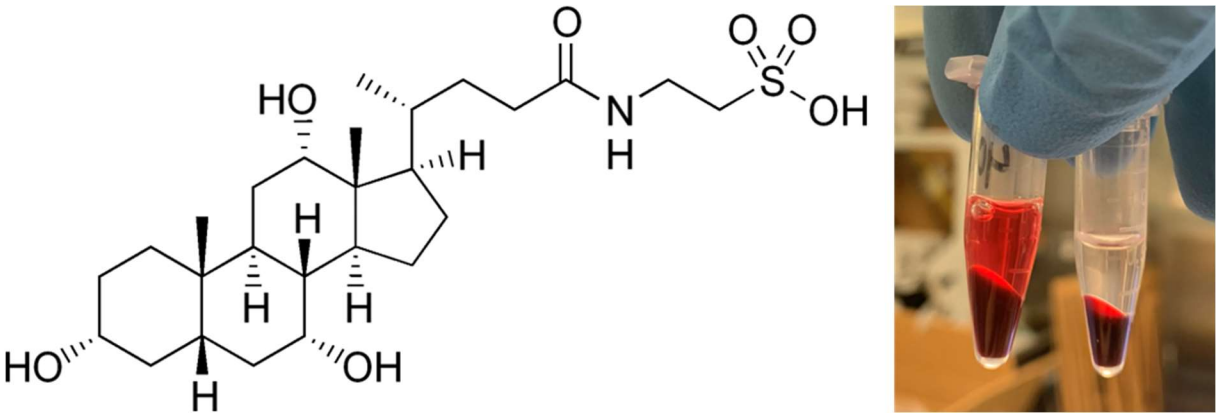

Figure 13. Taurocholic Acid (TUCA) is a bile acid that is found in mammals. It has been used to prevent fibrinolysis shutdown in rat blood by spiking it into blood samples for TEG.[17] It is believed to complex with tPA to prevent deactivation by PAI-1. Left: TUCA molecule, right: blood spiked with TUCA when spun down showed plasma with bright red color probably indicating hemolysis, whereas the same blood (right Eppendorf in picture) when spun down did not show any red color in the plasma.

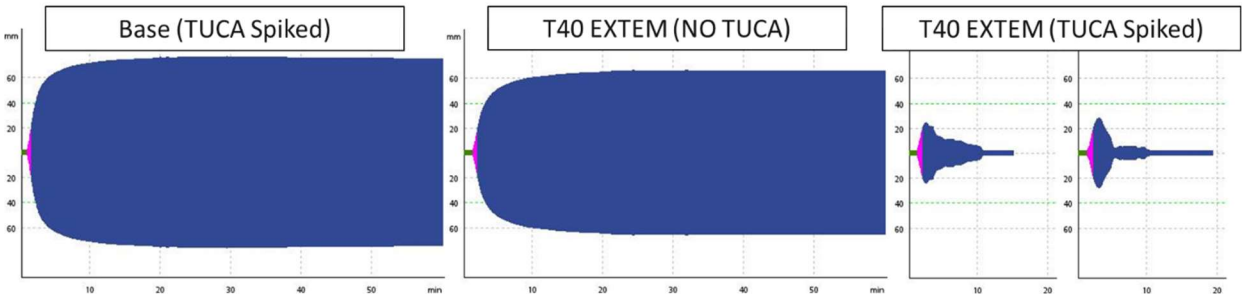

Figure 14. EXTEM from shock-only rat model. Left: TUCA-spiked baseline blood showed no signs of fibrinolysis. Center: T40 EXTEM showed no signs of fibrinolysis. Right: T40 blood samples spiked with TUCA showed rapid clot breakdown.

Whole blood spiked with TUCA showed what appeared to be rapid clot lysis in EXTEM. Interestingly, base blood spiked with TUCA showed no effect, while the lysis only occurred in T40 blood after severe hemorrhagic shock. Unfortunately, when TUCA spiked T40 blood was evaluated in both FIBTEM and by evaluating the plasma in EXTEM, there was no evidence of fibrinolysis (Figure 15 below).

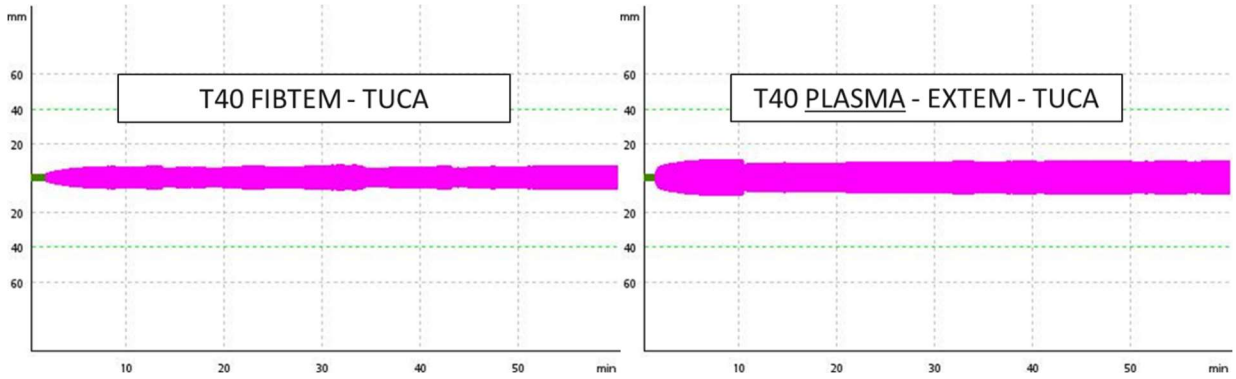

Figure 15. T40 FIBTEM (left) and Plasma EXTEM (right) samples from shock-only rat model with TUCA-spiked into the blood or plasma. There was no evidence of fibrinolysis.

Since TUCA did not lead to fibrinolysis in plasma and was assumed to not be possible to intravenously administered, we moved to evaluating rat plasmin. Previous work and literature have shown that both human tPA and plasmin can be used to lyse rat clots, however it must be used at very high concentrations (100x) compared to native rat enzymes, and the activity is very short-lived in the blood so continuous infusions must be done.[18] This would be cost prohibitive, even in small animals such as rats. Figure 16 below shows TEMs for baseline rat blood spiked with native rat plasmin.

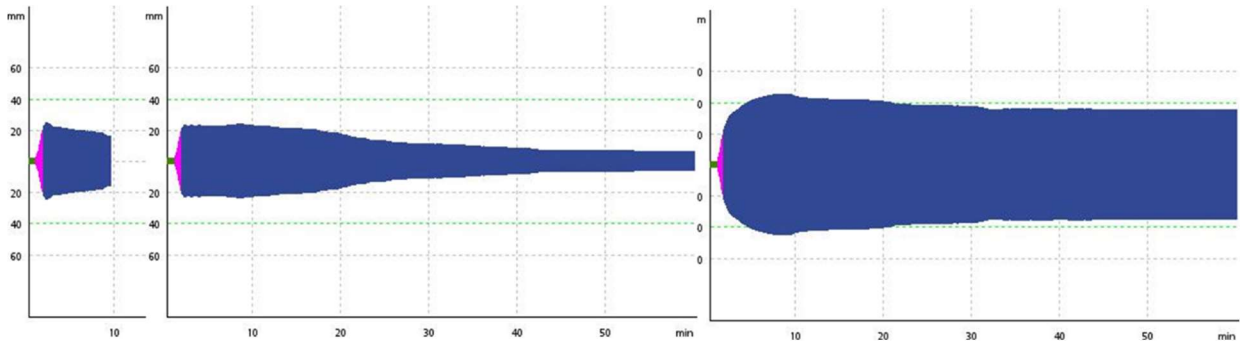

Figure 16. Rat baseline EXTEM samples spiked with rat plasmin purchased from abcam. All three TEMs are from the same rat blood, indicating the plasmin-spiking was inconsistent in creating lysis. No effect was observed when infused intravenously (image not shown).

Although clot lysis was observed, the activity of the rat plasmin was inconsistent when spiked into the blood. Next, FIBTEM was run on the whole blood spiked with plasmin (Figure 17 below).

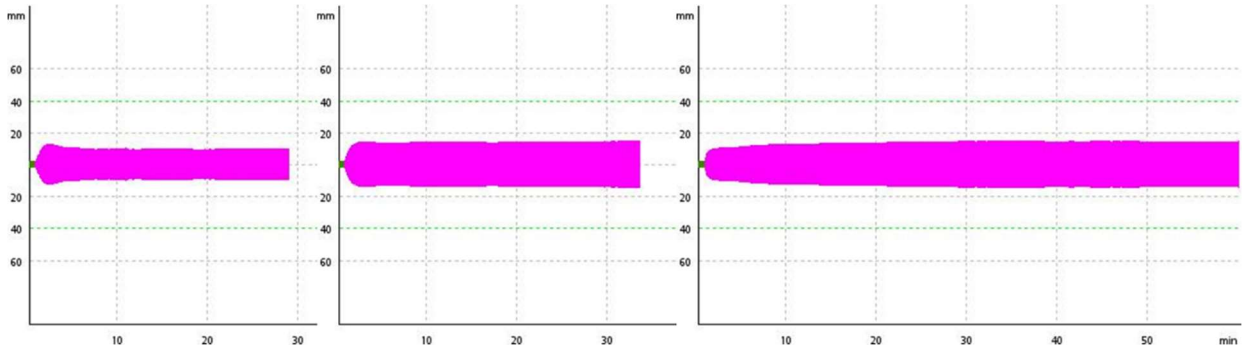

Figure 17. Rat baseline FIBTEM samples spiked with rat plasmin purchased from abcam. No evidence of fibrinolysis was found. The same plasmin concentrations that showed lysis in EXTEM were used.

Unfortunately, no fibrinolysis was observed with FIBTEM. It is surprising that with both TUCA and rat plasmin no fibrinolysis was observed even though there was significant clot lysis observed in EXTEM. Potentially, the TUCA is disrupting platelet surface receptors due to its ability to disrupt cell membranes. In the case of plasmin, it could be cleaving platelet surface receptors. This would result in clot lysis without affecting the fibrin network.

3.3.3 *LPS-induced Disseminated Intravascular Coagulation (DIC) Model*

From literature, LPS leads to high levels of TNF-α, which result in the secretion of alpha-granules from platelets.[19,20] These granules contain large amounts of tPA. Therefore, we attempted a single, large bolus infusion of LPS to induce fibrinolysis. Figure 18 (below) gives a model overview.

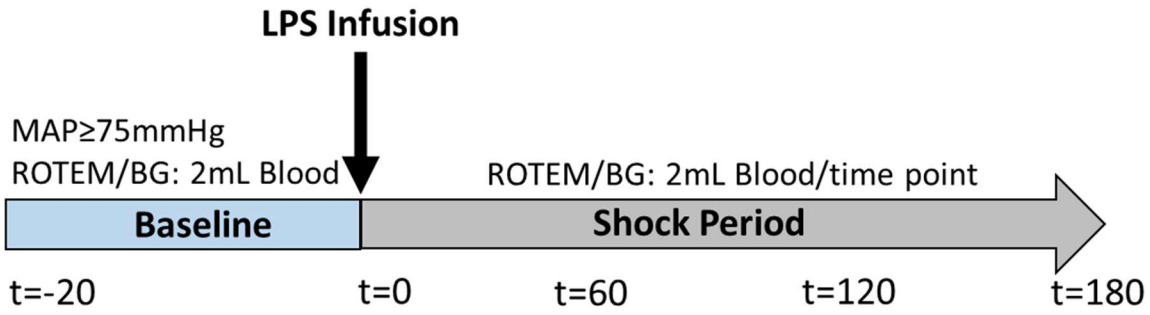

Figure 18. LPS-infusion model of disseminated intravascular coagulation (DIC). A large single bolus infusion of LPS (1.5 mg/kg) was given, after which the rat was monitored over 180 minutes.

The LPS created an extremely hypercoagulable state, which was qualitatively observed by issues of rat blood clotting during blood draws and clogging the ROTEM pipette during testing. LPS is often used in sepsis and DIC models.[21,22] These hypercoagulable states consume clotting factors, especially fibrinogen over time. Additionally, the high levels of TNF-α activates leukocytes, which secrete ROS species that oxidize fibrinogen and prime it for degradation. This both consumes, compromises, and introduces defects into the fibrin network. At 180 minutes, fibrinogen oxidation affects Aα and Bβ subdomains, resulting in extremely impaired or no clotting observed in FIBTEM (Figures 19 and 20 below). Although extremely coagulopathic, no fibrinolysis was observed in EXTEM.

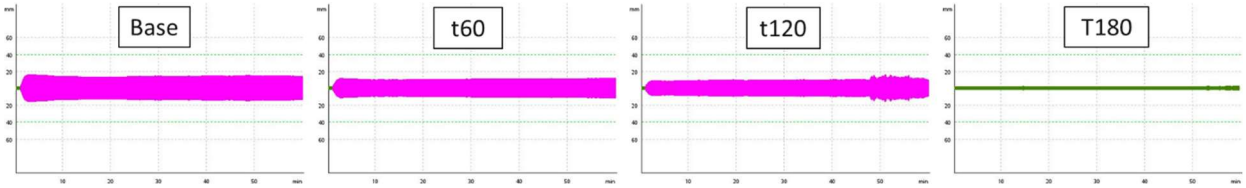

Figure 19. FIBTEM at baseline, 60, 120, and 180 minutes. At T180 minutes, the fibrinogen levels are so low that no coagulation is observed in FIBTEM.

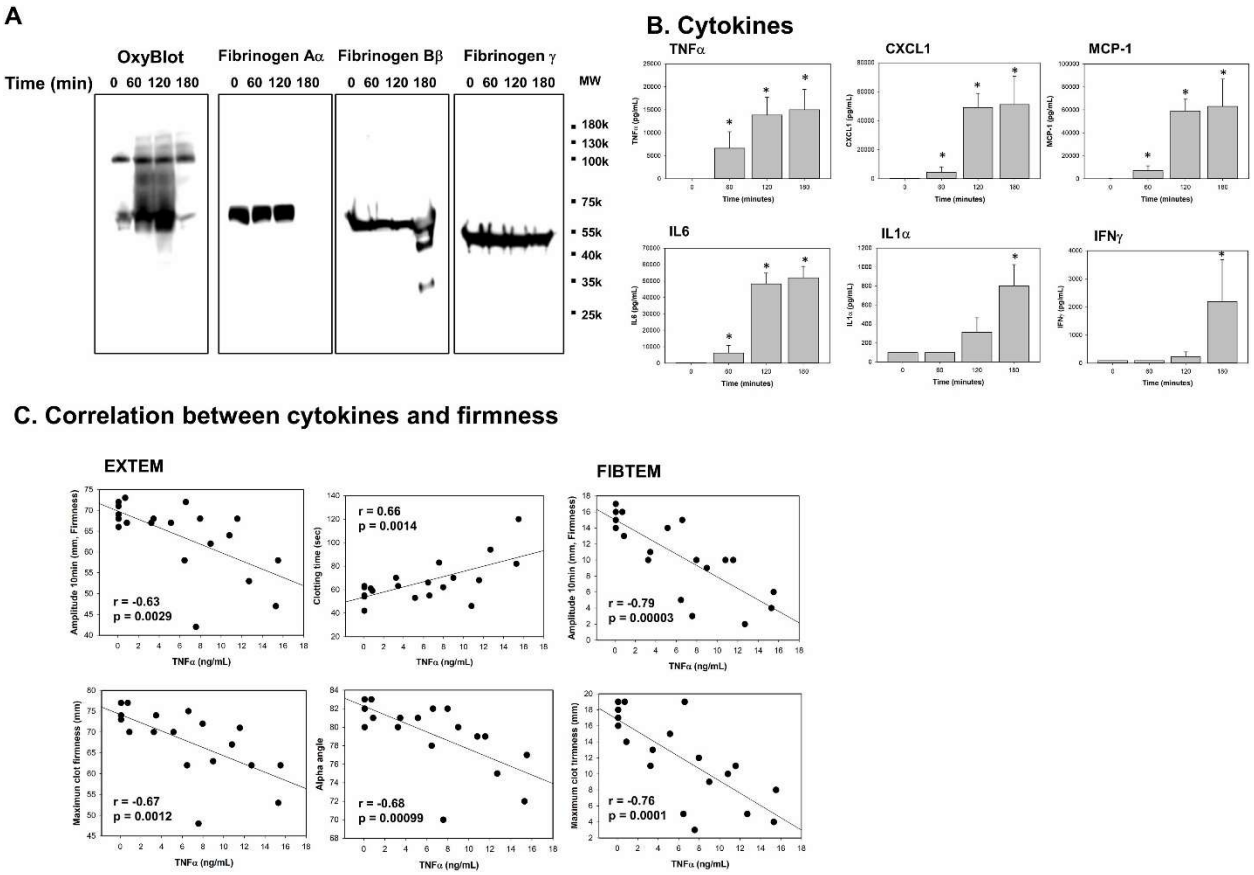

Figure 20. Fibrinogen is oxidized and degraded in endotoxin-induced inflammation, causing coagulopathy in rats. Whole blood and plasma were collected at the indicated time points from LPS-injected male rats (n = 5). (A) Plasma was analyzed by OxyBlot and immunoblotting using fibrinogen Aα, Bβ and γ – specific antibodies. Data are representative of 3 independent experiments. (B) Cytokines were measured from plasma at the indicated time points by multiplex cytokine analysis kit (n = 5, mean ± standard error of the mean (SEM)). *$p < 0.05$ vs. control. ANOVA and Bonferroni post-hoc test. (C) Amplitude, clotting time, α-angle, and MCF were measured in FIBTEM and EXTEM. Relationships between TNFα and amplitude, clotting time, α-angle, or MCF, were determined by linear regression analysis using Pearson correlation coefficient.

The critically low level of fibrinogen at T180 results in clot contraction artifacts observed in EXTEM (Figure 21 below).

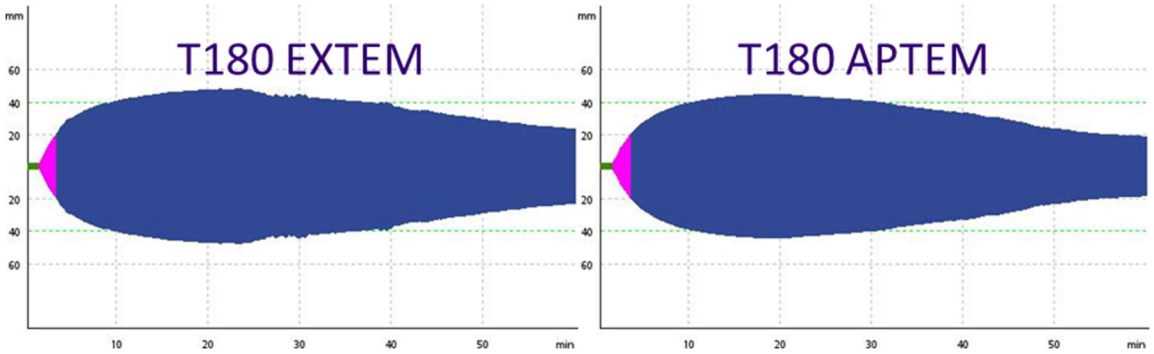

Figure 21. EXTEM (left) and APTEM (right) samples at T180 timepoint. The fibrinogen levels are so low that clot contraction artifacts can be seen in ROTEM. APTEM inhibits fibrinolysis through aprotinin indicating that the artifact is due to clot contraction.

Even though fibrinolysis was not observed with this model, we did attempt to combine it with the femoral artery bleed due to the extreme coagulopathic nature of the model. However, rats did not bleed when the femoral cut was introduced, and they quickly and robustly clotted. This LPS, sterile inflammation model was ultimately used for an investigation in the oxidation of fibrinogen.[23]

3.3.4 *Lethal coagulopathic femoral artery bleed model*

Although no fibrinolysis was observed, we were interested in seeing if PolySTAT would have any benefit in the extreme coagulopathies created by these different rat models. The shock model was identified as the easiest model to combine with the rat femoral bleed model. Due to the severe hypotension created by the shock-only model, the blood pressure needed to be increased prior or during the release of the clamps for the femoral bleed to create significant hemorrhage. Two different approaches were attempted, first to hemodilute the blood with normal saline prior to the clamps being pulled (Figure 22), and second to pull the clamps then quickly increase blood pressure with an aggressive resuscitation with normal saline (Figure 23).

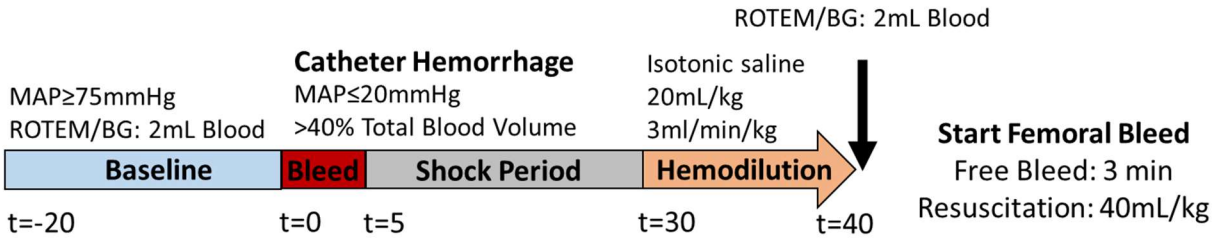

Figure 22. Combination of the shock-only model with subsequent hemodilution and femoral bleed model. Two rats were evaluated with this model, and the hemorrhage was too aggressive with no clotting observed.

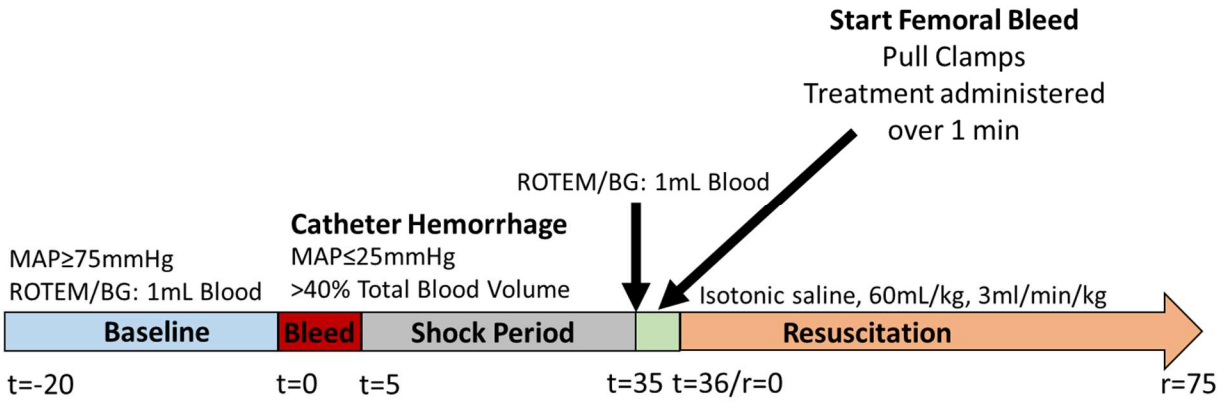

Figure 23. Model overview for an aggressive coagulopathic femoral bleed model of uncontrolled hemorrhage in rats.

The aggressive resuscitation (Figure 23) was chosen to move forward due to no clots forming in the hemodilution model, and the rats rapidly bleeding out. Figure 24 below shows images from the small study (n=5 TXA and n=5 PolySTAT).

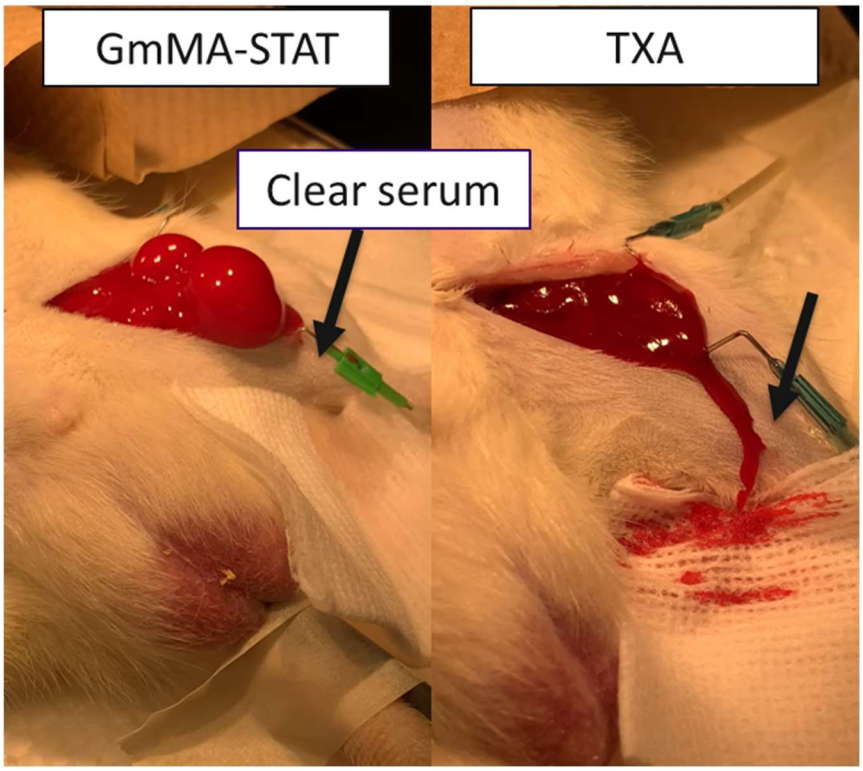

Figure 24. Images of PolySTAT (15 mg/kg) and TXA (15 mg/kg) treated rats in coagulopathic femoral artery bleed model. N = 5 for both treatements were evaluated. All five TXA rats died, while n = 2 PolySTAT treated rats survived. Interestingly, the two PolySTAT that survived were FITC-labeled PolySTAT, and the n=3 that were died were normal unlabeled GmMA-STAT.

For the PolySTAT treated rats, large firm hematomas were observed, although only 2 out of 5 rats survived, whereas the TXA treated rats showed fragile hematomas prone to rupture. The two rats that survived were infused with FITC-labeled PolySTAT, that then allowed the clots to be harvested, fixed, and imaged on confocal microscopy. Figure 25 below shows the confocal images.

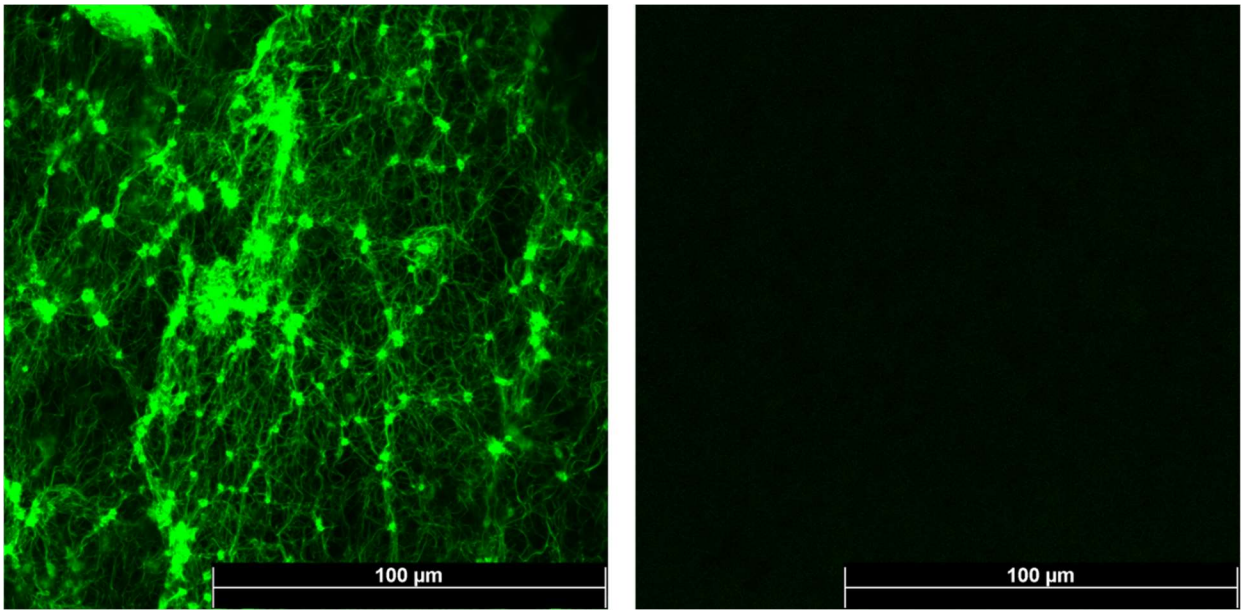

Figure 25. Confocal image of clots harvested from coagulopathic shock rat model (from Figures 17 and 18). Left: Clot harvested from rat infused with FITC-labeled GmMA-STAT, rat survived in aggressive coagulopathic model. The fibrin network can be observed due to the bound FITC-labeled PolySTAT. Right: Clot harvested from rat infused TXA standard of care, rat died, and no FITC was detected in the clot under confocal.

The clots harvested from the rats that survived showed large amounts of FITC-labeled PolySTAT throughout the clots. The TXA control clots showed no evidence of FITC. There were bright punctates of FITC-PolySTAT, and these were hypothesized to be clumps of platelets that had contracted FITC-PolySTAT covered fibrin fibrils. No additional staining was performed to investigate this further. Overall, PolySTAT showed good targeting to the clot, however it was not able to fully compensate for the aggressive coagulopathic femoral bleed model. It should be noted that the hemorrhagic shock model used in this work was different than the model ultimately used for the low volume resuscitant (LVR) work in Chapter 5 of this thesis. For the LVR work, we had to move away from giving the Ketamine/Xylazine injection and just use isofluorane with the nose cone (Figure 26 below).

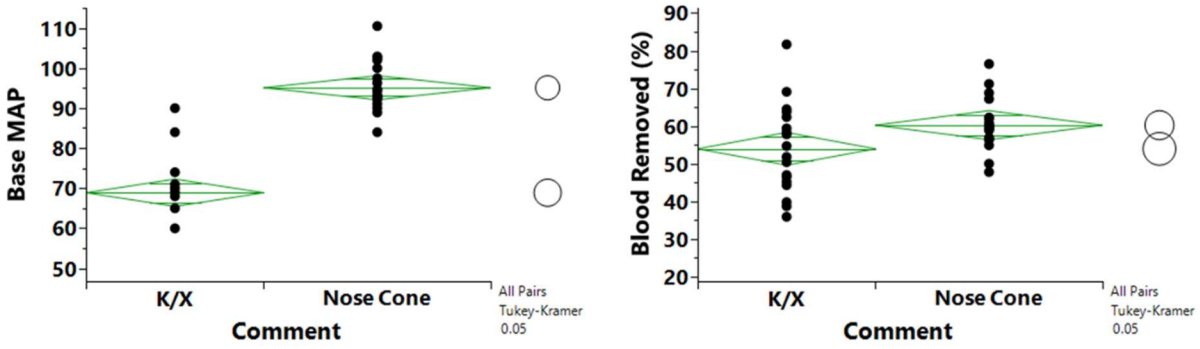

Figure 26. Comparison of ketamine-xylazine injection vs. isofluorane only via nose cone for rats in severe hemorrhagic shock model used in the low volume resuscitant work. Moving from K/X injection to nosecone with iso-fluorane-only resulted in a higher base blood pressure and more consistent and higher hemorrhage volumes to reach necessary shock levels in rats.

It was found that the K/X injection suppressed blood pressure, and slowly wore off over 1-2 hours. This made the shock model more variable with regards to the amount of blood that needed to be removed to get the rats into shock. This time variable is also important with regards to the speed to instrument the rat, which can range from 20 minutes to 1 hour depending on complications. Therefore, if this coagulopathic femoral artery bleed is revisited, it is advised to modify the model to eliminate the K/X injection.

3.4 Hemodilution Swine Aorta Tear Model Results and Discussion

3.4.1 *Overview of changes in blood counts, blood gas, and ROTEM due to dilutional coagulopathy*

Blood factors were measured at baseline, post hemodilution, and T0. Figure 27 below outlines the change in blood factors and lactate at each time point across all treatments.

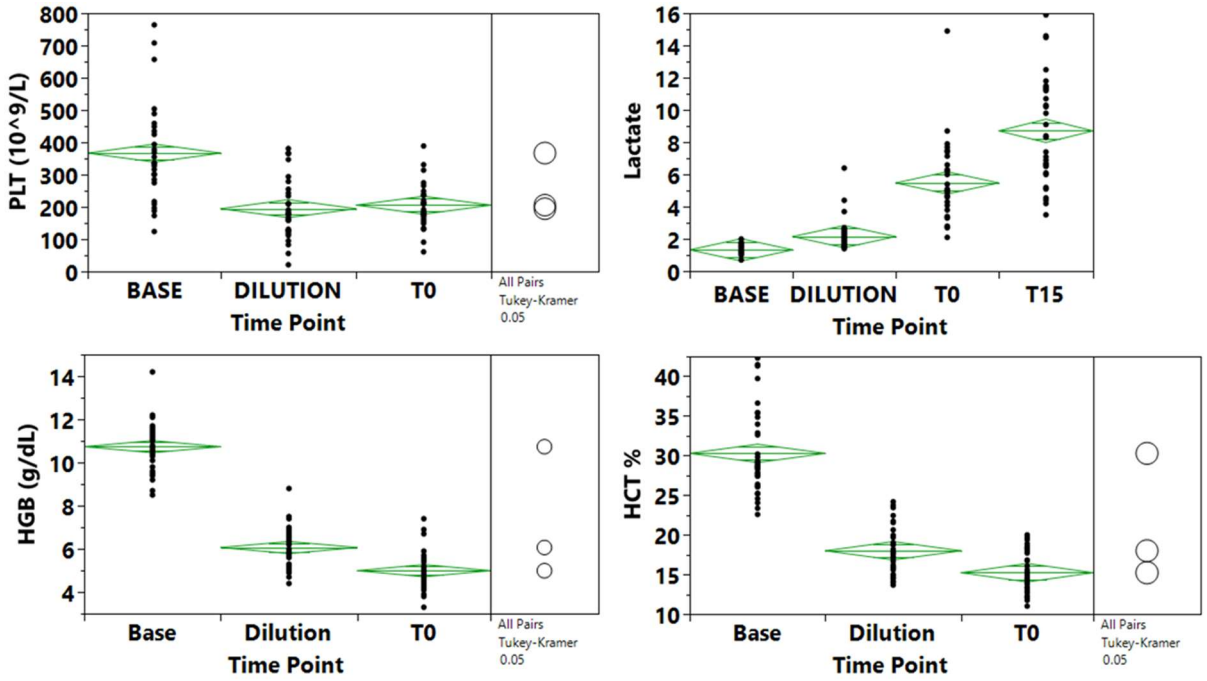

Figure 27. Changes in average platelet count in g/L (top left), lactate in mmol/L (top right), hemoglobin in g/dL (bottom left), and hematocrit in % (bottom right) across all of the experimental groups.

The hemodilution (Base → Dilution) leads to a large decrease in platelet count, hemoglobin, and hematocrit. The platelet count stays constant through shock (Dilution → T0), however hemoglobin and hematocrit continue to decrease due to the free bleeding from the aortic tear. Lactate on average increases across all the initial time points. Figure 28 below displays typical whole blood EXTEM temograms measured at baseline, post dilution, and T0.

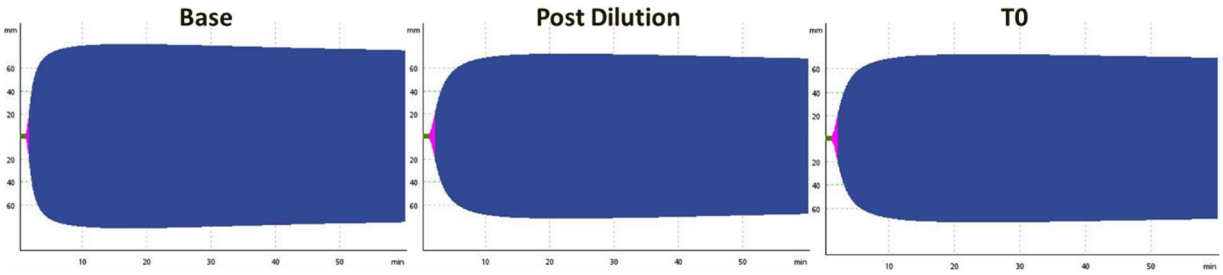

Figure 28. Typical ROTEM temograms measured with EXTEM for whole blood. Base (far left) was measured with baseline blood without any dilution, post dilution (middle) was measured after the hemodilution was complete, and T0 (right) was measured after the aorta tear, shock period was complete, and full administration of the treatment.

Figure 29 below displays the main EXTEM parameters measured with whole blood across all groups in the study.

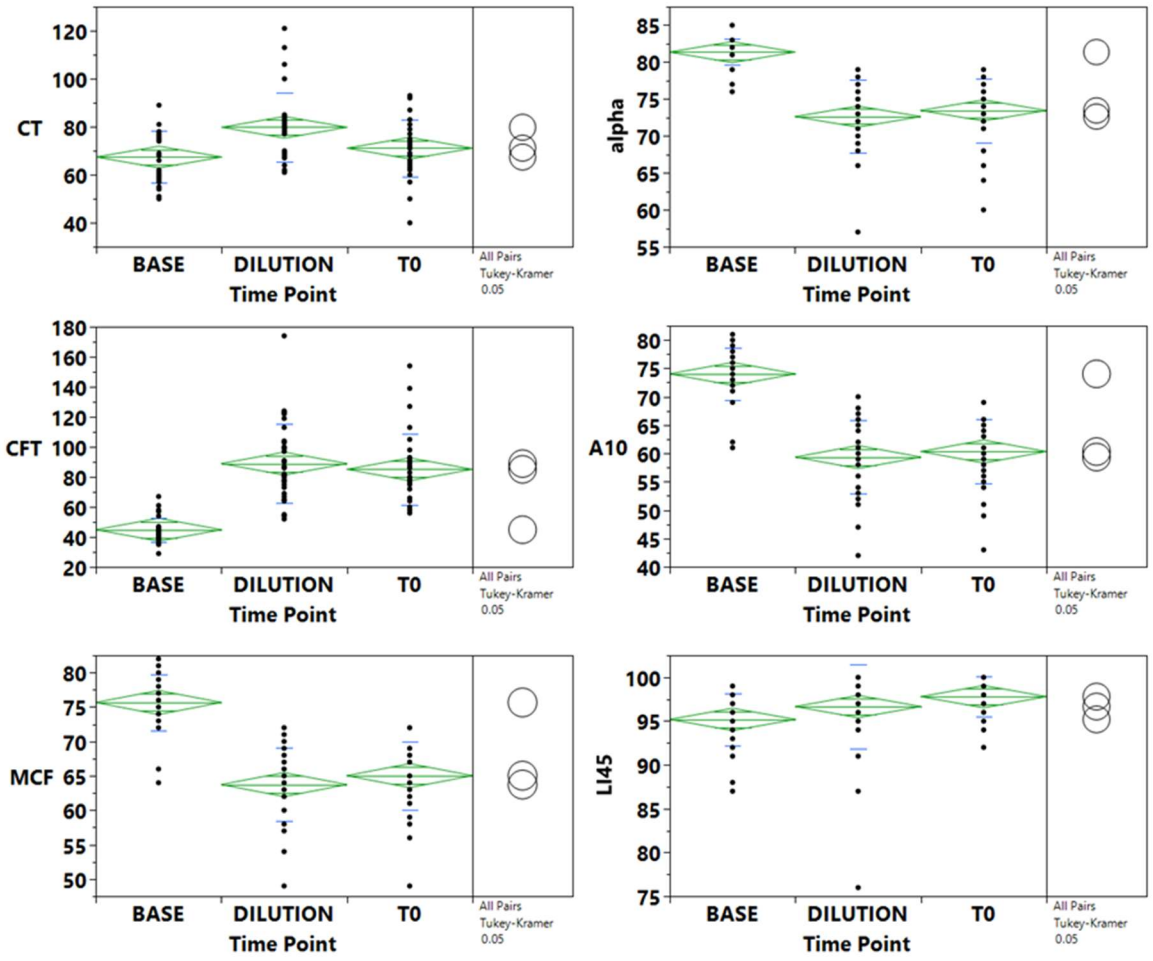

Figure 29. Average measured ROTEM parameters with EXTEM in whole blood across all groups in the study. Clotting time in seconds (top left), alpha angle in degrees (top right), clot firmness time in seconds (middle left), amplitude at 10 min in mm (middle right), maximum clot firmness in mm (bottom left), and lysis index at 45 min in % (bottom right).

The hemodilution increases clotting time and clot firmness time, while it decreases alpha angle, A10, and MCF. As clotting factors are diluted it leads to both a decrease in clotting kinetics and overall firmness. The LI45 do seem to indicate lysis occurring however upon further investigation this is an artifact of clot contraction (Figure S3). Figure 30 below displays typical plasma EXTEM temograms measured at baseline, post dilution, and T0.

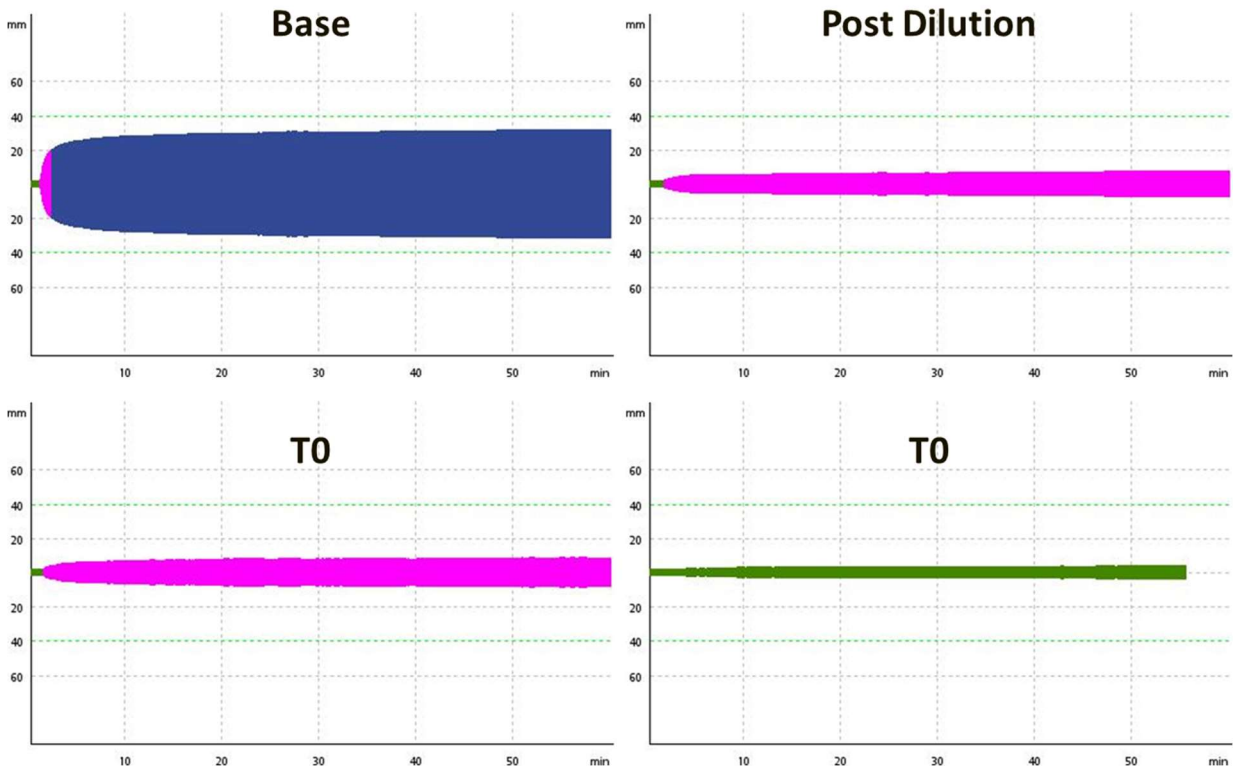

Figure 30. Typical ROTEM temograms measured with EXTEM for platelet poor plasma. Base (top left) was measured with baseline plasma without any dilution, post dilution (top right) was measured after the hemodilution was complete, and T0 was measured after the aorta tear, shock period was complete, and full administration of the treatment. The bottom left T0 displays a typical firmer clot while the bottom right T0 displays a weaker clot where no clotting time was registered due to it being the lower detection limit of the ROTEM. Transition from green to pink indicates a clot has been detected.

The hemodilution successfully depleted fibrinogen as indicated by the large drop in clot firmness from baseline to post dilution. Figure 31 below displays the main EXTEM parameters measured with plasma across all groups in the study.

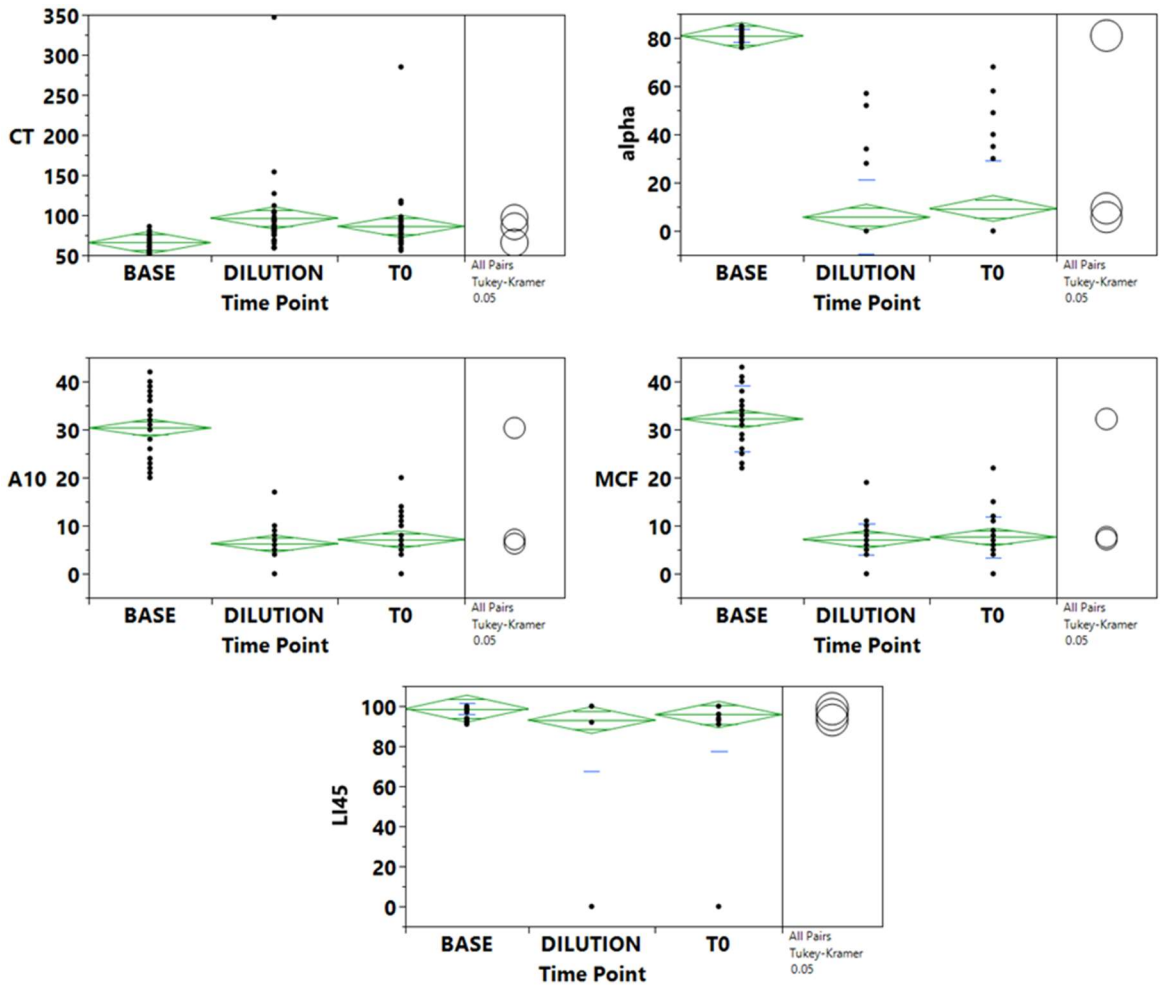

Figure 31. Average measured ROTEM parameters with EXTEM in plasma across all groups in the study. Clotting time in seconds (top left), alpha angle in degrees (top right), amplitude at 10 min in mm (middle left), maximum clot firmness in mm (middle right), and lysis index at 45 min in % (bottom).

Similar to whole blood, there is a decrease in both clotting kinetics and firmness. However, whereas whole blood only sees a drop of ~13% in MCF, plasma sees ~79% drop in MCF. This indicates there is a larger drop in fibrinogen versus platelets, resulting in a more drastic effect in plasma versus whole blood.

3.4.2 *Survival, hemorrhage volumes, and MAP/PAP*

Figure 32 below displays the Kaplan-Meier survival curve and hemorrhage rates for each treatment.

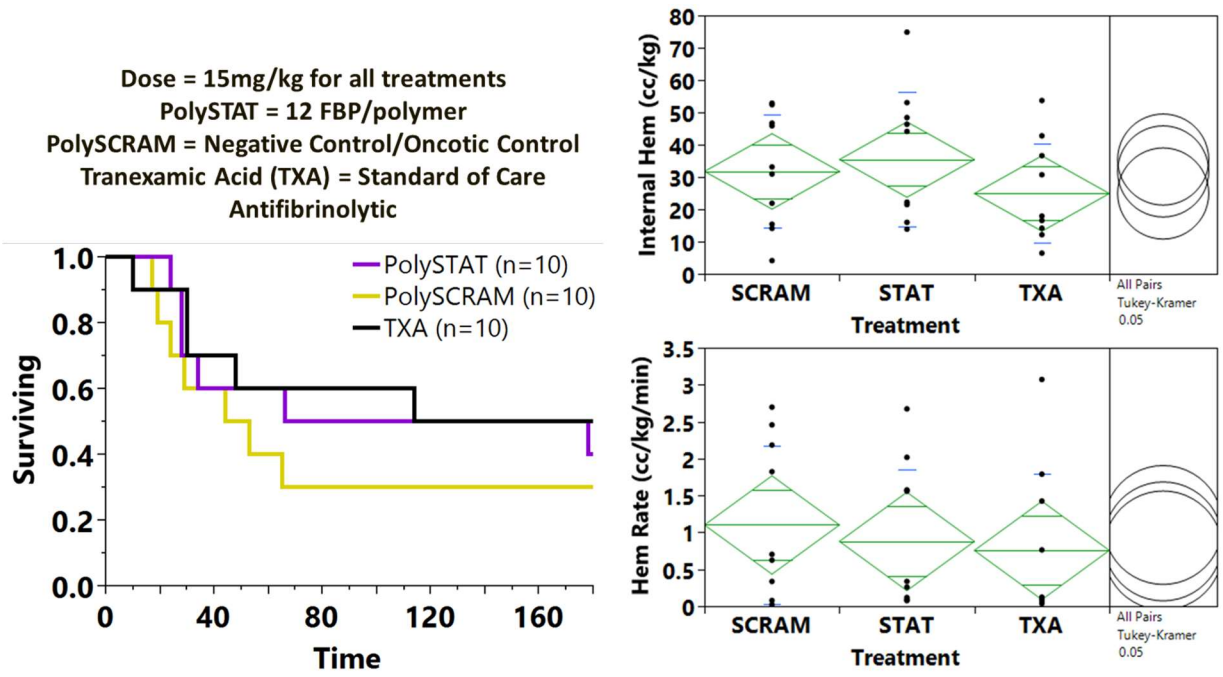

Figure 32. Kaplan-Meier survival curve (left) showing survival for PolySTAT (purple) = 40%, TXA (black) = 50%, and PolySCRAM (gold) = 30%. There was no statistically significant difference between the three treatments, although there was a trend towards PolySCRAM decreasing survival. Internal hemorrhage by treatment (top right) and internal hemorrhage over survival time or hemorrhage rate (bottom right), both showed no statistically significant difference between treatments.

There was no statistically significant difference between the three treatments in survival, internal hemorrhage, or internal hemorrhage rate. In survival there appears to be a slight trend towards a decrease in survival with PolySCRAM. Figure 33 below displays the mean arterial pressure (MAP) and Pulmonary Arterial Pressure (PAP) from the aorta tear until the end of the treatment infusion.

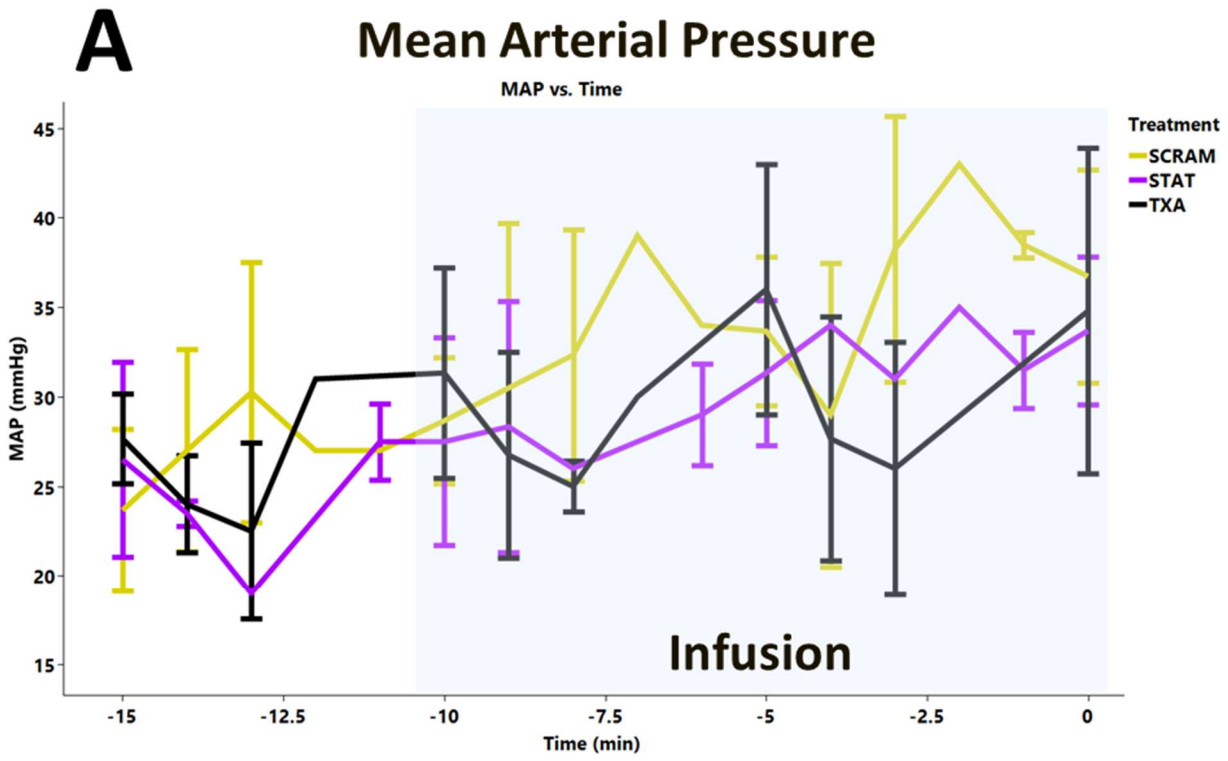
A
Mean Arterial Pressure
MAP vs. Time
MAP (mmHg)
45
40
35
30
25
20
15
-15
-12.5
-10
-7.5
-5
-2.5
0
Time (min)
Infusion
Treatment
SCRAM
STAT
TXA

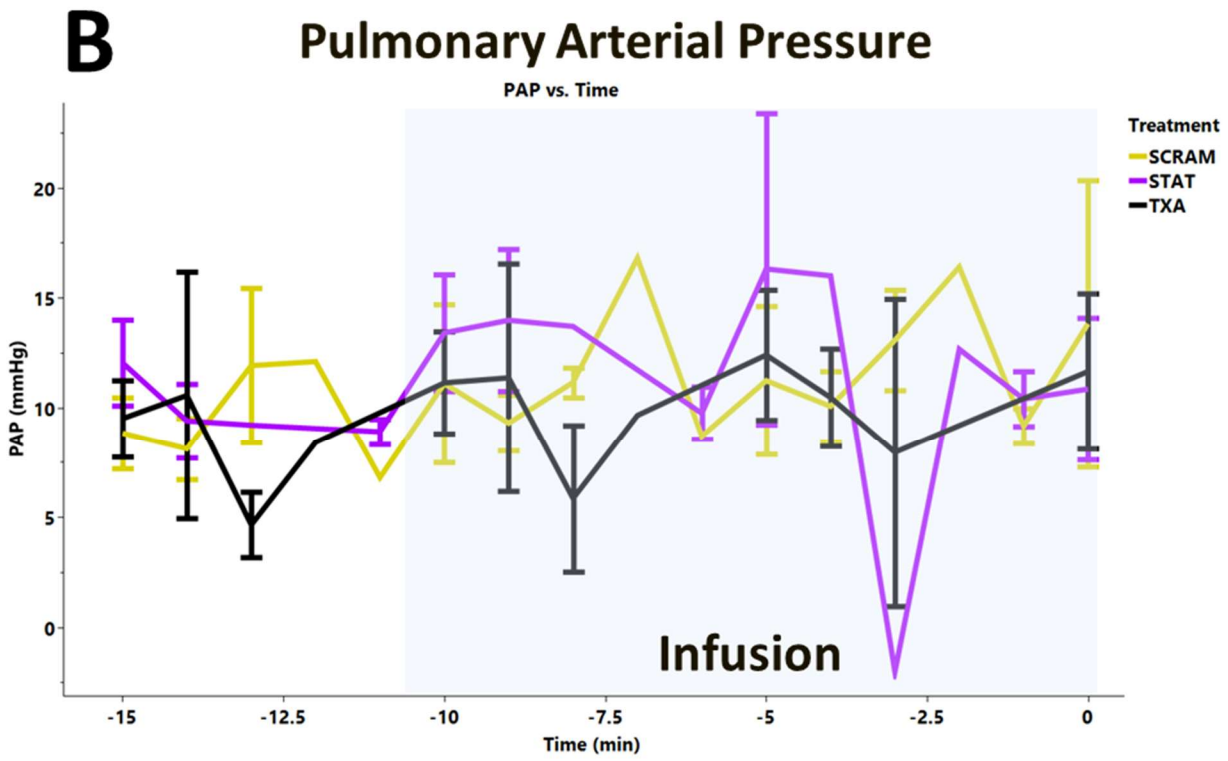
B
Pulmonary Arterial Pressure
PAP vs. Time
PAP (mmHg)
20
15
10
5
0
-15
-12.5
-10
-7.5
-5
-2.5
0
Time (min)
Infusion
Treatment
SCRAM
STAT
TXA

Figure 33. A) Mean Arterial Pressure (MAP) and B) Pulmonary Arterial Pressure (PAP) from the aorta tear (-15 min) until the end of the treatment infusion (0 min). The treatment is administered over 10 minutes and starts 5 minutes after the aorta tear.

No difference in the treatments is observed in MAP or PAP. Complement Activation-Related Pseudoallergy (CARPA) was not observed with any of the treatments.

3.4.3 *Pretreatment Effects*

Multiple parameters measured prior to the treatment administration (Baseline and Post Dilution) were screened for an effect on survival outcome. Figure 34 below shows the ROTEM parameters for both whole blood and plasma that showed the largest effect.

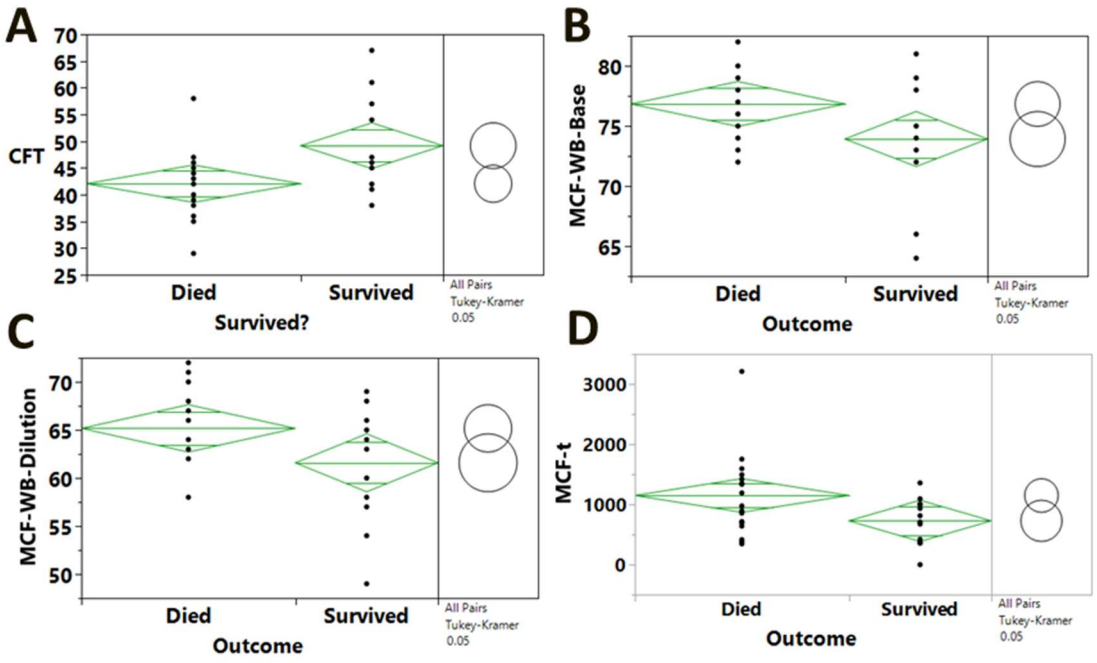

Figure 34. ROTEM parameters of both whole blood and plasma at baseline and post dilution that showed the largest effect on survival. Clot Firmness Time (CFT) of whole blood at baseline (A) was statistically significant ($p = 0.0134$, two-sided t-test), Maximum Clot Firmness (MCF) of whole blood at baseline (B) was borderline statistically significant ($p = 0.0528$, two-sided t-test), MCF of whole blood at dilution (C) was borderline statistically significant ($p = 0.0696$,

two-sided t-test), Time to MCF of plasma at dilution (D) was borderline statistically significant (p = 0.0607, two-sided t-test).

CFT of whole blood at baseline had the largest effect, followed by MCF of whole blood at baseline and dilution, and MCF-t of plasma at dilution. Figure S1 shows CFT and MCF of plasma at the same timepoints. There is no effect seen in plasma. This seems to indicate that platelets are playing the main role in driving this effect in whole blood. However, the MCF-t does indicate that the plasma does play a role in how long it takes to form the clot, which has implications for the level of dilution either in how much it is knocking down overall fibrinogen, or prothrombin concentration. Figure 35 below shows the effect of platelet count on survival at baseline and post dilution.

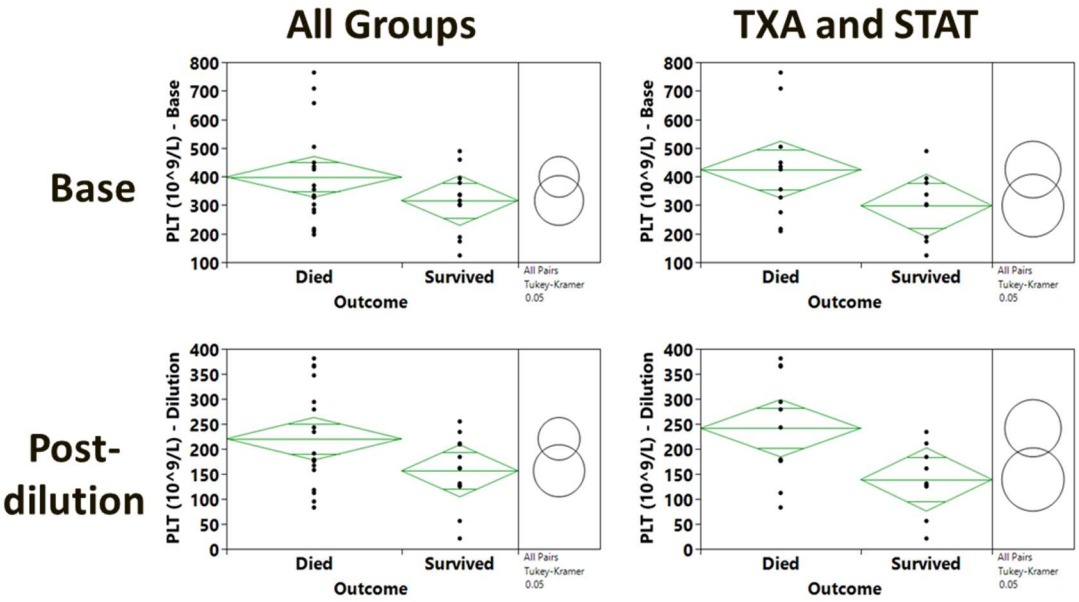

Figure 35. The average platelet counts across all groups (left column) against survival outcome, at baseline (top) not statistically significant, at post dilution (bottom) borderline statistically significant (p = 0.0612, two-sided t-test). TXA and PolySTAT treatments only (right column), at baseline (top) not statistically significant, at post dilution (bottom) statistically significant (p = 0.0211, two-sided t-test).

There seems to be a slight stratification of survival outcome by platelet count at post dilution, with the stratification becoming statistically significant for the TXA and PolySTAT groups. Interestingly higher platelet count trends towards a decrease in survival.

3.4.4 *Post-treatment Effects*

Multiple parameters measured after treatment administration (T0 and T15) were screened for an effect on survival outcome. Figure 36 below displays the two most significant effects.

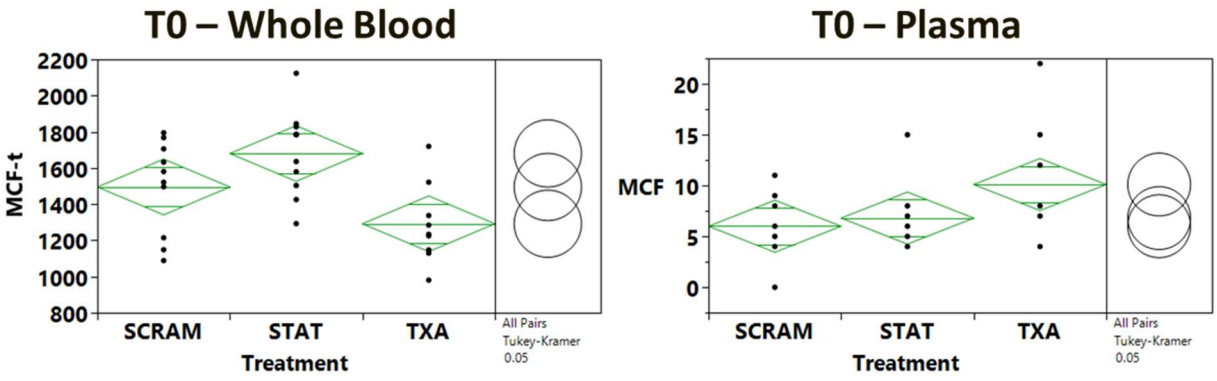

Figure 36. ROTEM parameters at T0 across treatments. At this time, the treatments were fully administered. Time to Maximum Clot Firmness (MCF-t) in whole blood (left), there was a statistically significant difference between PolySTAT and TXA ($p = 0.003$, Oneway Anova). Maximum Clot Firmness (MCF) in plasma (right), there was a borderline statistically significant difference between TXA and PolySCRAM ($p = 0.0695$, Oneway Anova).

The MCF-t (seconds) in whole blood at T0 was increased with PolySTAT compared to TXA by ~400 seconds on average. This indicates a decrease in clotting kinetics with the PolySTAT treatment. Also, at T0, the MCF was borderline higher for TXA in plasma compared to PolySCRAM. This is proportional to the amount of fibrinogen left in circulation and would indicate that TXA treated pigs might have higher amounts of fibrinogen on average in circulation. TXA only inhibits fibrin degradation, not fibrinogen degradation. Figure 37 below shows the other largest effect at T0, platelet count.

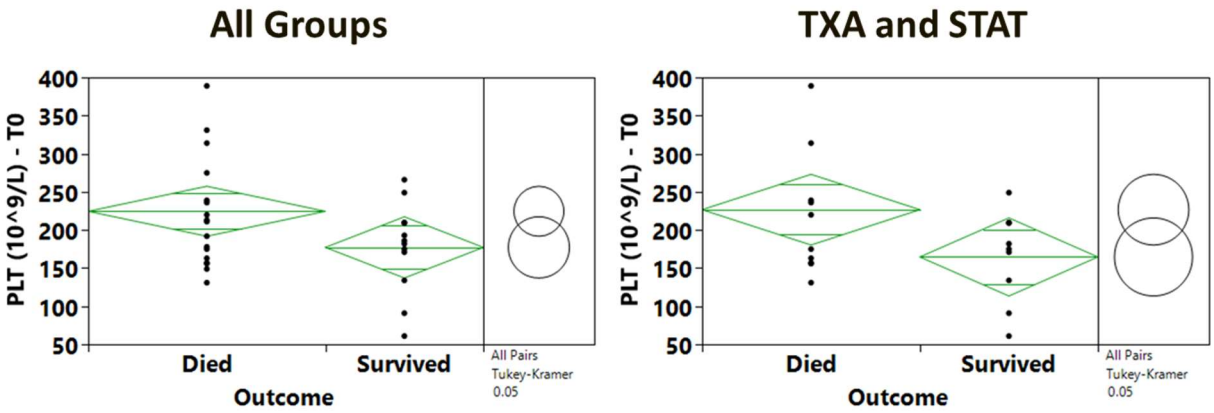

Figure 37. Platelet counts compared at T0 across survival outcome across all groups (left) and just the antifibrinolytics PolySTAT and TXA (right), both were borderline statistically significant ($p = 0.0718$ and $p = 0.0753$, two-sided t-test), respectively.

Platelet count was borderline statistically significant at T0 with regards to survival outcome. As observed at earlier time points, a higher platelet count had a negative impact on survival. There was no statistical difference when looking at all treatment groups versus just TXA and PolySTAT.

3.4.5 *Parametric Survival Fit*

To estimate the effect of different parameters identified above, a parametric survival fit model was run. Figure 38 below displays the results.

Parametric Survival Fit

Effect Summary

Source	LogWorth	PValue
Internal Hem Rate (cc/kg/min)	7.070	0.00000
CFT-WB-Base	1.211	0.06145
Group Treatment	0.688	0.20506
PLT (10^9/L) - Dilution	0.571	0.26865
Total Cath. Hemorrhage Volume at T0 (mL/kg)	0.327	0.47123
MCF-t-WB-T0	0.154	0.70180

Remove Add Edit Undo ☐ FDR

Time to event: Time	AICc	185.8370	Observation Used	30
Distribution: Weibull	BIC	190.1894	Uncensored Values	18
Censored By: Censor	-2*LogLikelihood	162.9798	Right Censored Values	12

Whole Model Test

ChiSquare	DF	Prob>Chisq
56.1997	6	<.0001*

Parameter Estimates

Term	Estimate	Std Error	Lower 95%	Upper 95%
Intercept	2.46363828	1.4423204	-0.363258	5.2905343
Group Treatment[SCRAM]	-0.1170371	0.0891241	-0.291717	0.057643
Internal Hem Rate (cc/kg/min)	-0.9987601	0.1279809	-1.249598	-0.747922
Total Cath. Hemorrhage Volume at T0 (mL/kg)	0.0281037	0.0407327	-0.051731	0.1079383
PLT (10^9/L) - Dilution	0.00165559	0.0014851	-0.001255	0.0045663
CFT-WB-Base	0.04364446	0.0265949	-0.008481	0.0957695
MCF-t-WB-T0	0.00018877	0.0004858	-0.000763	0.0011409
δ	0.34351047	0.0668996	0.2123896	0.4746313

Confidence Intervals are Wald

Figure 38. Parametric survival fit model evaluating the most significant factors observed at different time points. Overall, the most significant factor was the internal hemorrhage rate (p = 0.00000, parameter estimate = -0.998) which had an inverse relationship with survival (higher hemorrhage resulted in decreased survival).

As expected, the internal hemorrhage rate was the most significant factor (-0.998), and had a negative impact on survival time, meaning increased hemorrhage rate decreased survival. The model was run again without hemorrhage rate as an effect to evaluate the other parameters. Figure 39 below displays the results.

Parametric Survival Fit

Effect Summary

Source	LogWorth	PValue
Total Cath. Hemorrhage Volume at T0 (mL/kg)	3.825	0.00015
CFT-WB-Base	2.809	0.00155
MCF-t-WB-T0	2.468	0.00340
Group Treatment	1.182	0.06570
PLT (10^9/L) - Dilution	0.384	0.41290

Remove Add Edit Undo ☐ FDR

Time to event: Time	AICc	210.7578	Observation Used	30
Distribution: Weibull	BIC	215.4753	Uncensored Values	18
Censored By: Censor	-2*LogLikelihood	191.6669	Right Censored Values	12

Whole Model Test

ChiSquare	DF	Prob>Chisq
27.5126	5	<.0001*

Parameter Estimates

Term	Estimate	Std Error	Lower 95%	Upper 95%
Intercept	-2.6096398	3.5004289	-9.470354	4.2510747
Group Treatment[SCRAM]	-0.362165	0.1848199	-0.724405	7.5251e-5
Total Cath. Hemorrhage Volume at T0 (mL/kg)	0.3118615	0.0857122	0.1438687	0.4798543
PLT (10^9/L) - Dilution	-0.0025667	0.0030888	-0.008621	0.0034871
CFT-WB-Base	0.14594804	0.0507943	0.046393	0.2455031
MCF-t-WB-T0	-0.0023218	0.0006978	-0.003689	-0.000954
δ	0.70136829	0.1424362	0.4221984	0.9805381

Confidence Intervals are Wald

Figure 39. Parametric survival fit model evaluating the most significant factors observed at different time points with the internal hemorrhage rate removed. The effects (top) are listed in decreasing effect size (total catheter hemorrhage > CFT in whole blood at baseline > MCF-t in whole blood at T0 > PolySCRAM treatment > Platelet count at dilution).

The effects from most significant to least are as follows: total catheter hemorrhage (0.311) > CFT in whole blood at baseline (0.146) > MCF-t in whole blood at T0 (-0.002) > PolySCRAM treatment (-0.362) > Platelet count at dilution (-0.003). Catheter hemorrhage, platelet count, and CFT were all controlled for by randomization of the treatments, Figure 40 below displays the average of each of these across the treatments.

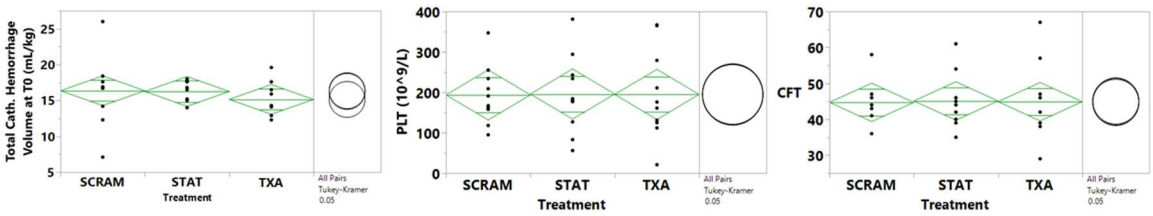

Figure 40. Total catheter hemorrhage volume at T0 (left), Platelet count at dilution (center), and CFT in whole blood at baseline (right) across all treatments. Across all three, there was no statistically significant difference between treatments.

3.4.6 *Low-dose of PolySTAT and Co-administration with Fibrinogen Concentrate*

Based on the parameter estimations (excluding internal hemorrhage rate), PolySCRAM treatment, catheter hemorrhage, platelet count at dilution, CFT in whole blood at baseline, and MCF-t in whole blood at T0 had the largest effects on survival. The catheter hemorrhage, platelet count, and CFT effects are controlled for by randomization of the treatments (Figure 15 above). During the study, the catheter hemorrhage is initiated before the aorta tear, but then the aorta tear is done typically halfway through the catheter hemorrhage (4 min CATHHEM, aorta tear at 2min). This relationship could suggest that a less severe uncontrolled bleeding through the aorta would result in needing to draw more blood from the CATHHEM to compensate and get the pig into shock. Additionally, it is interesting that platelet count was a factor and it showed increased importance with the two antifibrinolytic treatments (TXA and PolySTAT). This could be explained by the clot contraction artifacts observed (Figure S3). This artifact was augmented when evaluated under APTEM, suggesting that inhibition of fibrinolysis could exasperate the contraction artifacts. Also, considering this is a high-pressure wound, there would be a greater concentration of platelets at the wound site due to upregulation of VWF from the high shear.[24] The ROTEM temograms do not fully represent the wound site where there would be a higher concentration of platelets compared to systemic circulation. The PolySCRAM estimate seems to indicate there is a small effect from PolySTAT that compensates for the negative oncotic effect from the polymer backbone. Finally, MCF-t could indicate that PolySTAT is adversely affecting clotting kinetics. Lamm et al observed a decrease in alpha angle and an increase in clotting time when PolySTAT was dosed at a high concentration of 20 μM instead of the typical dose of 5 μM.[2] Additionally, the FDA advises that when scaling up therapies from animals to humans, that dosing should be based off of surface area

not body weight.[25] Converting the typical PolySTAT dose of 15 mg/kg to the advised surface area dose for swine would decrease the dose to 3.3 mg/kg. In ROTEM and rats a final blood concentration of 5 μM is targeted as the optimal PolySTAT dose. Figure S3 outlines an estimated blood concentration in two pigs of ~8 μM at T0 based on measured hematocrit levels and the catheter hemorrhage. To measure the concentration of PolySTAT in the bloodstream of the pigs at different time points, a FITC-labeled PolySTAT was infused. Based off a standard curve for the FITC-PolySTAT, measured blood concentrations in the blood of two pigs were ~8.7 μM and 5.5 μM at T0 and ~2.9 μM and ~2.3 μM at T15 (SI Figure S4). These results seem to support that we are potentially dosing at too high of a concentration. Another possibility for the lack of PolySTAT efficacy could be a decreased affinity of FBP for pig fibrin. To evaluate this, clots were randomly harvested from different areas of the peritoneal cavity of the pigs infused with FITC-PolySTAT, fixed, and them imaged on a confocal microscope. Figure 41 below shows images of two of the clots.

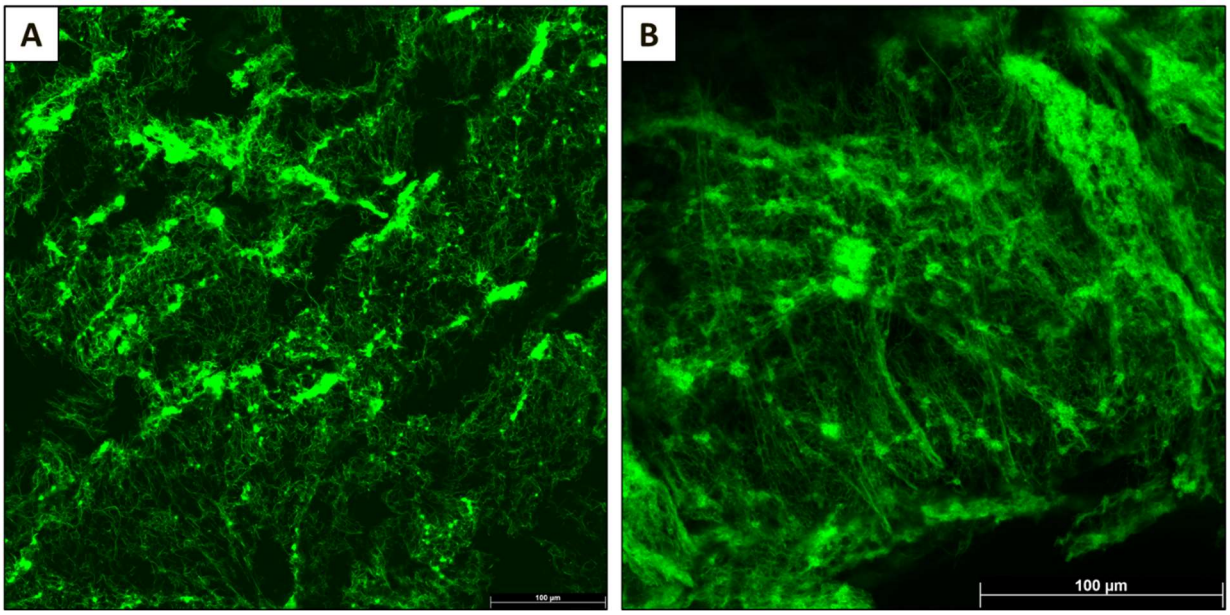

Figure 41. Confocal microscopy of blood clots harvested from the peritoneal cavity of pigs infused with FITC-labeled PolySTAT.

From the clots harvested, ~50% of the clots had signs of FITC-labeled PolySTAT. There were areas of bright punctate that seem to indicate clustering of fibrin by platelets, large thick strands of fibrin, and more diffuse networks of thin fibrin. This all reflected the three different fibrin networks observed by Chernysh et al.[24] It is well known that platelets locally release fibrinogen

from alpha granules upon activation. Therefore, to get an idea of the fibrinogen remaining in circulation at baseline, post dilution, T0, and T15, the plasma samples from the FITC-infused pigs were clotted with EXTEM, fixed, cryofractured, then imaged on the confocal microscope. For timepoints baseline and post dilution, 5 µM FITC-PolySTAT was added. Figure 42 below shows the resulting confocal images.

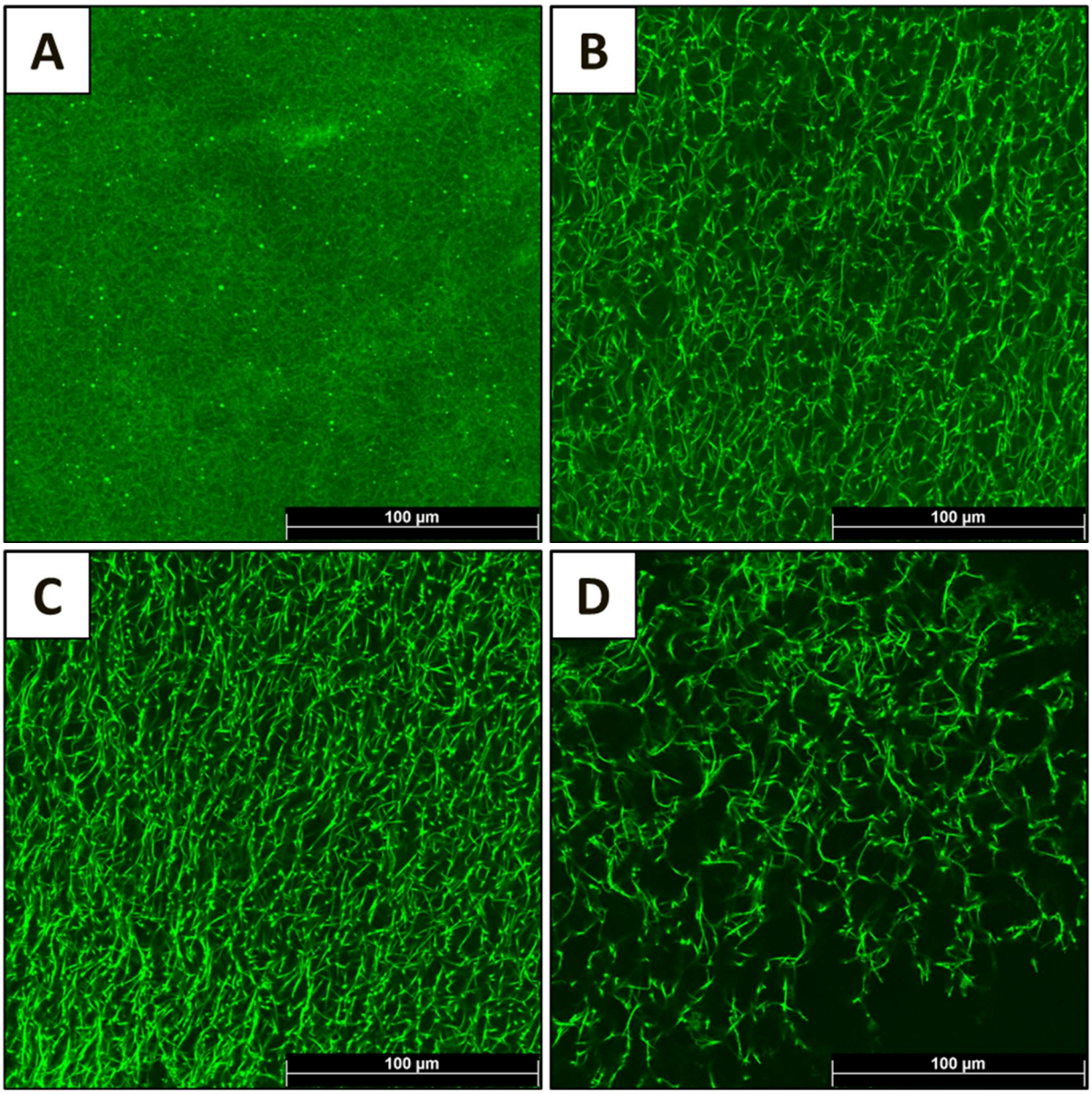

Figure 42. Confocal microscopy of plasma samples from FITC-labeled PolySTAT infused pigs at baseline (A), post dilution (B), T0 (C), and T15 (D). The plasma samples were clotted with EXTEM, fixed in 10% formalin, then cryofractured.

An extremely dense fibrin network was observed at baseline which is typical of pigs.[26] The confocal images appear to reflect their respective ROTEM curves (Figure 43 below) indicating that even when the clot strength is below the detection limit, there are still clots forming. This confirmed FBP binding to pig fibrinogen as well.

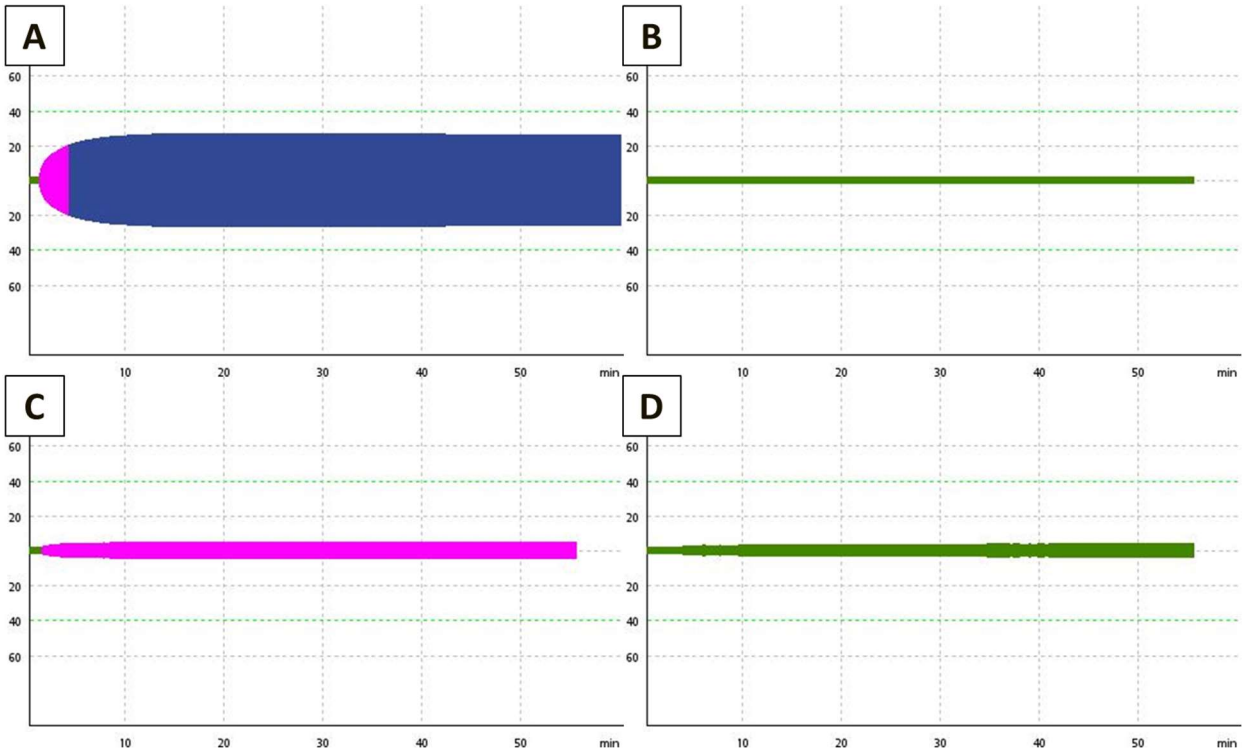

Figure 43. ROTEM temograms measured with EXTEM of platelet poor plasma samples from FITC-labeled PolySTAT infused pigs at baseline (A), post dilution (B), T0 (C), and T15 (D).

It is remarkable how dense the fibrin network is at baseline, at higher magnification the high degree of branching and compaction of the fibrin network can be seen (Figure 44 below).

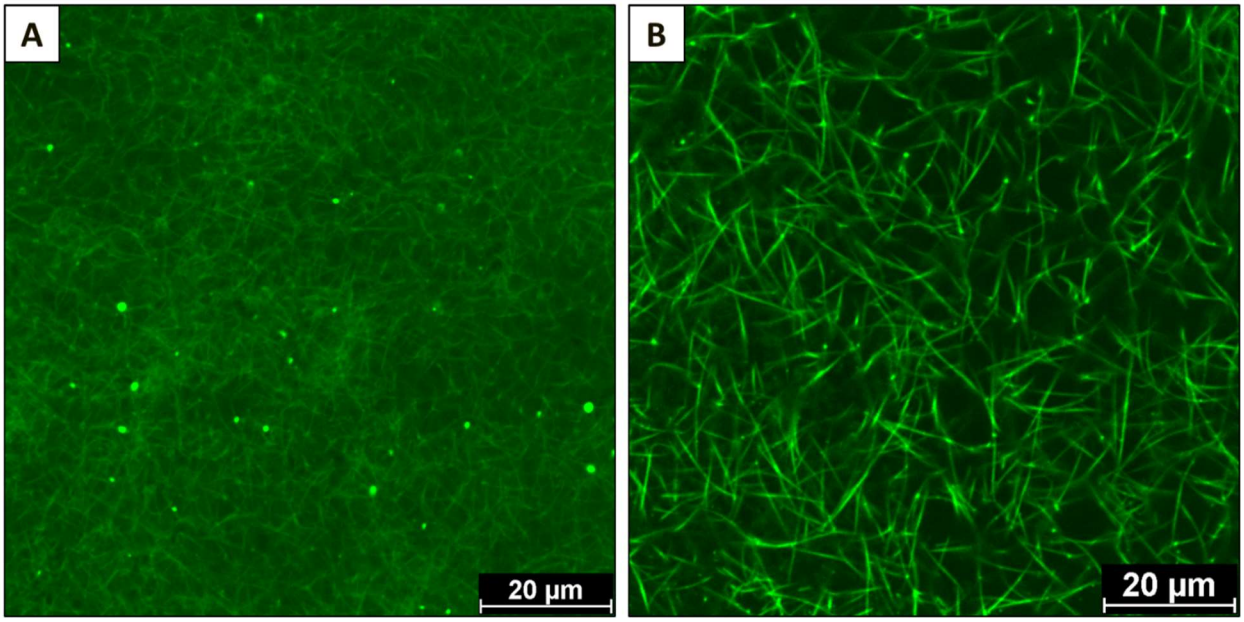

Figure 44. Confocal images at high magnification of baseline (A) and post dilution (B) plasma clots from FITC-infused pigs.

This seems to highlight the importance of the hemodilution to knockdown clotting strength in swine. Lamm et al. observed no efficacy of PolySTAT in their study of swine without hemodilution.[3] Based on the results above, estimates put the range of PolySTAT concentration in the blood at ~5 µM - 8 µM. While the FDA recommends dosing based off surface area not body weight when moving to large animals and humans, which would decrease the dose from 15 mg/kg to 3.3 mg/kg (Figure 45 below) .[25]

Figure 45. Calculation of the low dose of PolySTAT based on FDA Guidance for Industry.

Based off the calculations made in Figure S4, the 3.3 mg/kg dose would put the blood concentration at ~1.8 µM. To provide some margin in error due to the lower blood concentration than expected, we used a dose of 5 mg/kg which was estimated to be ~2.75 µM. Figure 46 below shows the measured PolySTAT concentration for all the swine evaluated with the low dose of 5 mg/kg.

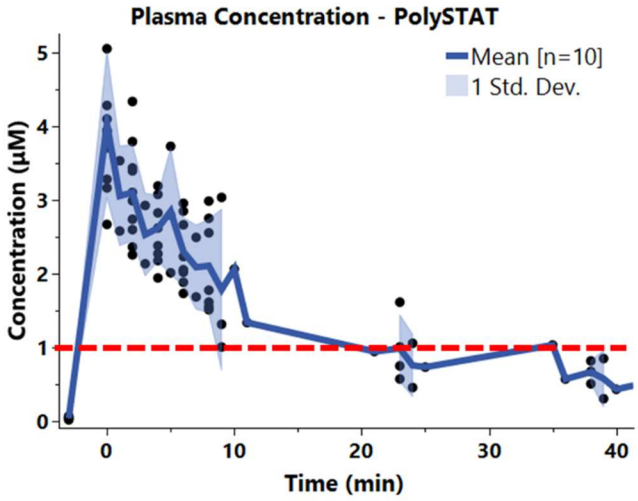

Figure 46. Measured PolySTAT concentration in swine plasma (n=10) during aorta tear model with low dose (5 mg/kg). The initial peak in the plasma was ~3-5 µM. A red line at 1 µM is the minimum concentration where PolySTAT has shown activity in *in vitro* assays.

The low dose of PolySTAT was still slightly below the 5 μM target concentration, and it was rapidly diluted due to blood loss, and the aggressive resuscitation used in the model.

Previous work by Chan et al. highlighted that too low of a fibrinogen concentration decreases the efficacy of PolySTAT (Figure 47 below).[5,27] In addition, it is now standard of care in the EU to treat severe trauma patients with an initial dose of 3-4g of fibrinogen concentrate.[28,29] The hemodilution is aggressively knocking down fibrinogen in the pigs. Hydroxyethyl starch solutions are also known to decrease FVIII, von Willebrand Factor, and increase partial thromboplastin time.[30,31]

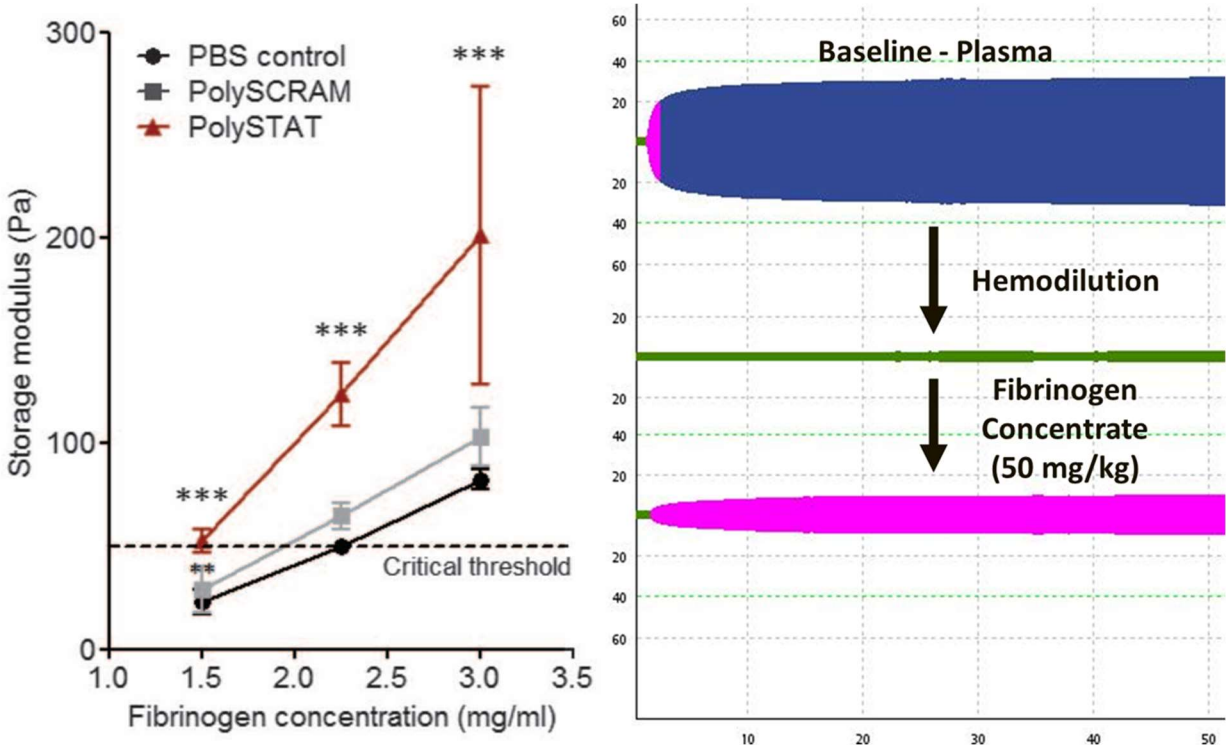

Figure 47. Storage modulus as a function of fibrinogen concentration for PolySTAT, PolySCRAM, and PBS control (left) and EXTEM TEMs of swine plasma (right) at baseline, after hemodilution with Hextend, and after administration with 50 mg/kg fibrinogen concentrate.

From the work of Martini et al. a fibrinogen concentrate dose of > 37.5 mg/kg was targeted. In their model (60% hemodilution), this resulted in a blood concentration of ~1.5 mg/ml.[32] We decided to move forward with 50 mg/kg, but we wanted to use the minimal amount of fibrinogen

for two reasons: (i) fibrinogen concentrate is ~1.2k per gram and (ii) a high dose (200 mg/kg) has shown to combat hemodilution and improve survival, which could hide PolySTAT's effect.

Figure 48 below shows the results of the additional arms (5mg/kg PolySTAT and 5mg/kg PolySTAT + 50 mg/kg Fibrinogen Concentrate) evaluated in the aorta tear hemodilution model.

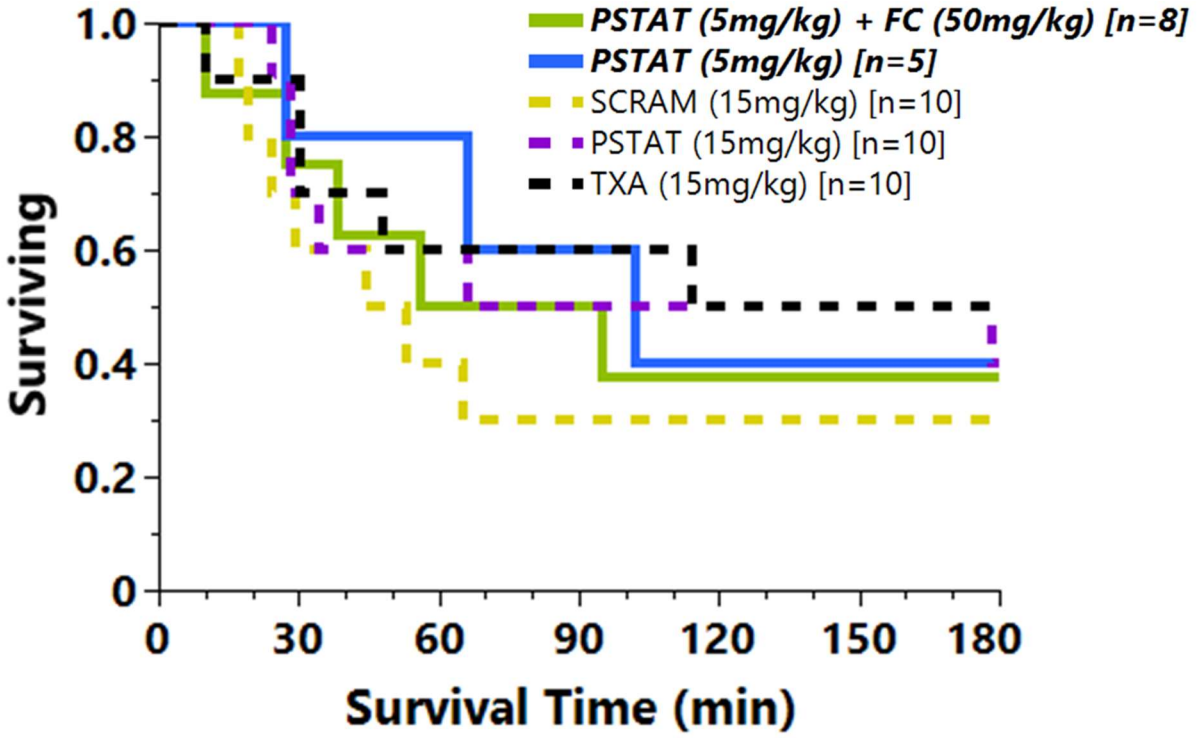

Figure 48. Kaplan-Meier Survival Curve for Swine Hemodilution Aorta Tear Model. Two additional arms were evaluated, Blue line: 5mg/kg PolySTAT (low dose) and Green Line: PolySTAT (5mg/kg) co-administered with Fibrinogen Concentrate (50mg/kg). No improvement in survival was observed.

Unfortunately, the low dose of PolySTAT and the con-administration with fibrinogen concentrate did not improve survival outcomes. Additional reasons for the lack of efficacy are explored in the next section.

3.5 Estimation and Modeling of Aorta Tear Wound Forces

Due to the lack of efficacy of PolySTAT in the hemodilution aorta tear swine model, but the impressive efficacy in rats, a comparison was made between the wounds for each species to see if there were any potential differences to explore further. To get a rough estimate of the vessel forces that need to be overcome, some basic calculations were made using the Law of Laplace, which is a common equation used to understand trends in vessel wall tension as intraluminal vessel pressure and vessel internal radius scale (Figure 49 below).

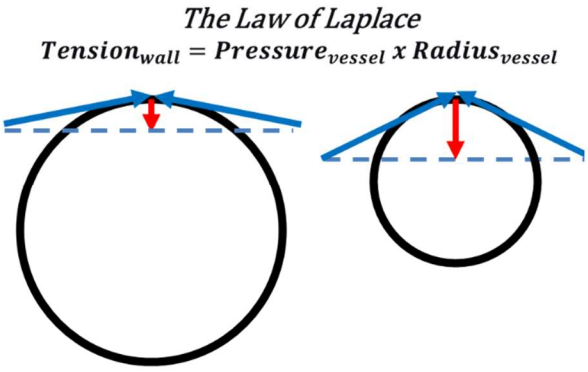

Table 1. Application of the pressure-curvature-tension relation to the blood vessels (T = P × R)

Type of vessel	Mean pressure within		Radius R	Tension T in wall	Amount of elastic tissue
	mm. Hg	*dynes/cm.²*		*dynes/cm.*	
Aorta and large arteries	100	1.3×10^5	1.3 cm. down	170,000	Very elastic, two coats
Small distributary arteries	90	1.2×10^5	0.5 cm.	60,000	Much elastic tissue but more muscular
Arterioles	60	8×10^4	0.15 mm. – 62 μ	1,200–500	Thin elastica intima only
Capillaries	30	4×10^4	4 μ	16	None
Venules	20	2.6×10^4	10 μ	26	None except in largest
Veins	15	2×10^4	200 μ up	400	Elastic fibers reappear
Vena cava	10	1.3×10^4	1.6 cm.	21,000	Very elastic increasing with size.

Figure 49. Overview of the Law of Laplace. Left: If you draw vectors that are tangent to the walls of vessels, for larger vessels it takes a larger vector to create the normal force necessary to match the intraluminal pressure. This means larger vessels have higher wall tension compared to smaller vessels. Right: Table shows mean vessel pressure, radius, and wall tension for different size arteries, veins, and capillaries in the body. Table used without permission from [33] by Alan C. Burton.

The Law of Laplace was used to get rough estimates of the wall tension and stress along the length of the wound (calculated by dividing the wall tension by the wound length) for both the swine and rats. Figure 50 below shows the vessel geometries, wound size, and calculations for species.

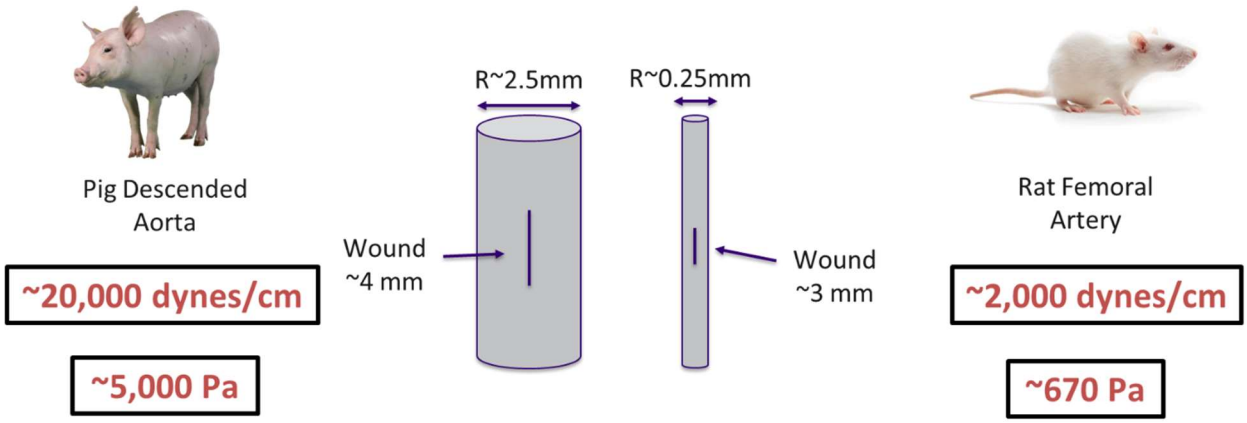

Figure 50. Wound geometries, estimated wall tension, and wound stress for swine (left) and rats (right). The descended aorta vessel in swine is estimated to have a wall tension of ~20,000 dynes/cm, with an average wound stress along the tear of ~5,000 Pa. The femoral artery of the rat is estimated to have a wall tension of ~2,000 dynes/cm, with an average wound stress along the tear of ~670 Pa.

Interestingly, due to the larger size of the descended aorta in swine, there is ~10x the wall tension compared to the femoral artery in rats. This results in a much greater force that the clot must overcome to effectively close the tear. Similarly, when adding in the length of the wound, there is ~7.5x greater stress along the wound in the swine compared to rats. Next, we were interested in evaluating the impact the clot's weight could have on hemostasis. Qualitatively, it has been observed that the clots in the swine aorta tear model are often found away from the tear site, and large clots are removed throughout the peritoneum. External pressure applied to the wound site plays an important role in stopping bleeding, and the Law of Laplace has been applied to calculating sub-bandage pressures needed to be supplied by bandages.[34] In the rat model, a nice deep pocket is made during the isolation of the femoral artery, and this allows a large hematoma to form directly on top of the wound site (Figure 51 below).

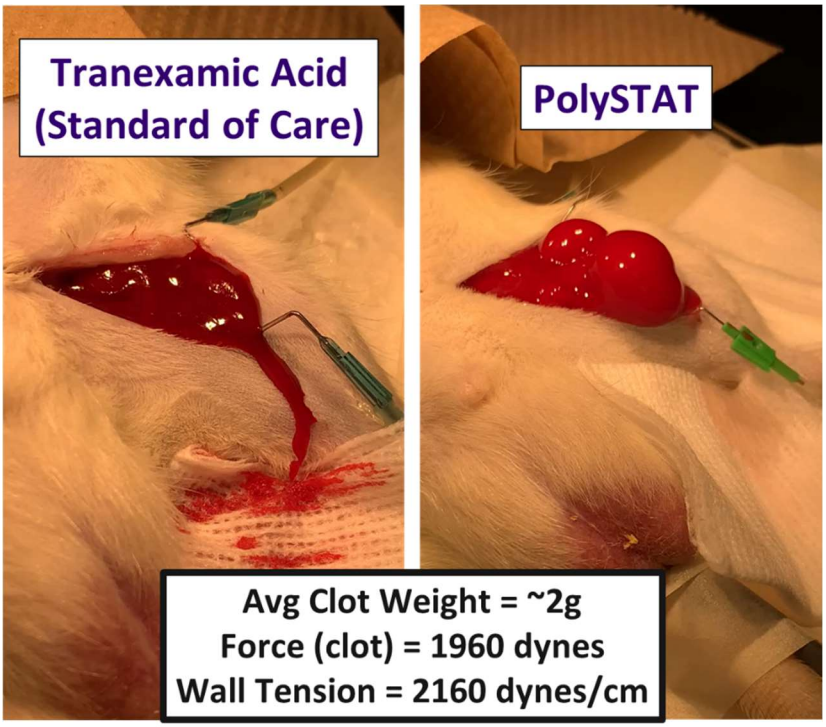

Figure 51. Estimation of the average force due to the clot that forms during the femoral artery bleed in rats. Left: TXA control clot, Right: PolySTAT clot showing a large hematoma. The average clot weight from the GmMA-STAT study (Chapter 2) was ~2 grams for PolySTAT treated rats. The force due to the weight of this clot would be ~1960 dynes, which is on order of the vessel wall tension.

It is estimated that the force from just the average weight of PolySTAT clots is ~1960 dynes, which is on the same order of magnitude as the wall tension of the femoral artery. This is just considering the mass of the clot, not any internal pressure that would form due to clot contraction forces pulling down on the clot. The femoral artery wound also provides a lot of exposed muscle and fat surface area for the hematoma to adhere to. This adhesion of the hematoma is extremely important to hemostasis. KYT Chan et al. showed that a topical administration of FXIIIa increased wound adhesion, which led to increased survival in the same rat femoral bleed model.[35]

To evaluate the relationship between survival, hemorrhage, wound geometries, and wound mechanics, the aorta tears for most of the pigs were measured (Figure 52 below) and split out by outcome.

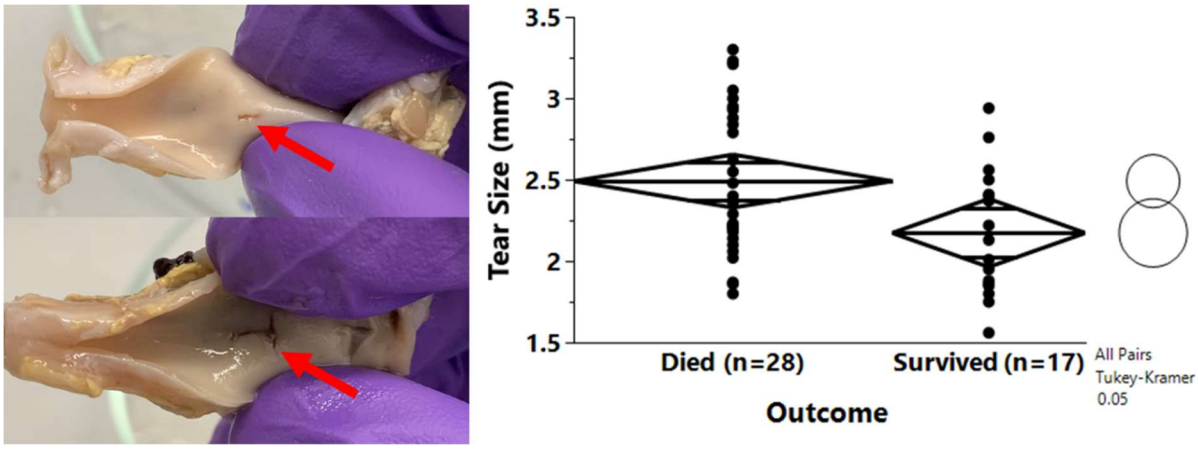

Figure 52. Harvested aorta tear length vs. survival outcome. Left: Aorta tears were transected at the end of the model, then kept in buffered formaldehyde solution. The aortas were measured with calipers for the tear length and the inner circumference (luminal surface). Right: Tear size vs. survival outcome showed that there was a statistically significant increase in tear length in the swine that died compared to the swine the survived ($p = 0.02$, two-sided t-test).

There is a statistically significant difference in tear size for pigs that died versus survived. However, it should be noted that the aortas are under tension when inside the body, and when they are harvested, they shrink back, which decreases the length of the tear. Therefore, this measurement most likely is confounded with tension/elastic recovery of the vessel. In addition to measuring tear length, we also measured the inner circumference of the vessel from which we calculated the inner vessel radius. To get an estimate of the final parameter, intraluminal pressure, we used the highest achieved mean arterial pressure for the swine during resuscitation. This allowed us to calculate the vessel wall tension and the average stress across the tear. Table 1 below shows the results for swine that survived versus died. A standard two-side t-test was used to check for significance.

Table 1. Compiled wound geometries and mechanics, along with survival, hemorrhage, and bleed intensity.

Column	Survivors					Nonsurvivors					P Value
	N	Mean	Std. Error	Lower 95% CI	Upper 95% CI	N	Mean	Std. Error	Lower 95% CI	Upper 95% CI	
Tear Size (mm)	17	**2.17**	0.10	1.96	2.38	28	**2.49**	0.08	2.33	2.66	**0.02**
Aorta ID Circumference (cm)	16	**1.42**	0.03	1.36	1.47	28	**1.37**	0.02	1.33	1.41	**0.17**
Aorta Internal Radius (mm)	16	**2.24**	0.04	2.16	2.32	28	**2.18**	0.03	2.12	2.24	**0.26**
Maximum Achieved MAP (mmHg)	16	**59.31**	2.30	54.67	63.95	27	**45.67**	1.77	42.09	49.24	**<0.0001**
Max Wound Tension (Dynes/cm)	15	**17663.80**	738.33	16171.59	19156.01	27	**13247.48**	550.32	12135.25	14359.71	**<0.0001**
Max Wound Stress (Pa)	15	**8389.47**	521.35	7335.77	9443.16	27	**5571.15**	388.59	4785.77	6356.52	**<0.0001**
Hemorrhage (mL/kg)	17	**13.84**	2.89	8.02	19.66	29	**41.82**	2.21	37.36	46.28	**<0.0001**
Survival Time (min)	17	**180.00**	7.10	165.68	194.32	29	**46.03**	5.44	35.07	57.00	**<0.0001**
Hemorrhage Rate (mL/[kg*min])	17	**0.08**	0.17	-0.27	0.42	29	**1.45**	0.13	1.18	1.71	**<0.0001**

Other than internal vessel radius, everything else showed statistically significant differences between pigs that died versus survived. SI Figures 13-15 show the bivariate correlations between all the parameters in Table 1. From these, a strong correlation between wound mechanics, survival, and hemorrhage can be observed. As to be expected, swine that bleed more, are more likely to die, and swine with lower maximum resuscitation mean arterial pressures, don't survive as long. Also, average stress across the wound trended with hemorrhage rate (Figure 53 below).

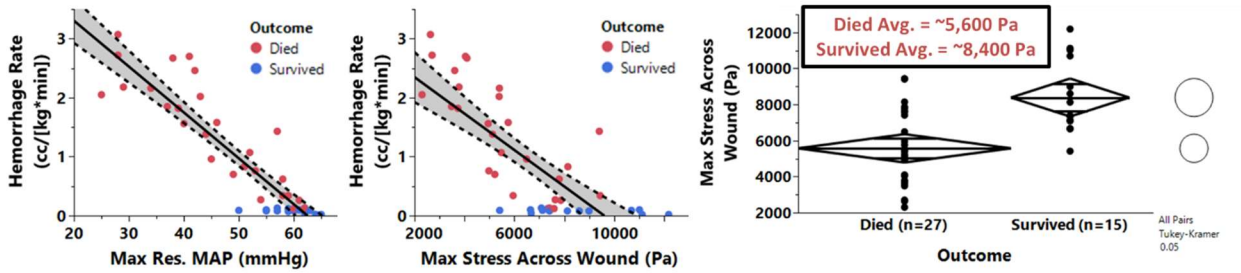

Figure 53. Relationship between hemorrhage rate, survival, blood pressure and stress across the wound. Left: Simple linear fit (shaded = 95% confidence interval) of Hemorrhage Rate (cc/[kg*min]) as a function of Max Resuscitation MAP (mmHg) - R^2 = 0.82, p = <0.0001, slope = -0.089/-0.066 (lower 95%/upper 95%); Middle: Simple linear fit (shaded = 95% confidence interval) of Hemorrhage Rate (cc/[kg*min]) as a function of Max Stress Across Wound (Pa) - R^2 = 0.59, p = <0.0001, slope = -0.000391/-0.000226 (lower 95%/upper 95%); Right: Max Stress Across Wound (Pa) across survival outcome, swine that survived showed higher stress across the wound compared to those that died (p = <0.001, two-sided t-test).

Based on the average wound stress for survived versus died, a difference of ~2800 Pa was found, which is an order of magnitude higher than the elastic modulus increase by PolySTAT in the rheometer and indicates that PolySTAT has to greatly increase the stiffness of clots to stop the bleeding. Since the Law of Laplace is an extremely simplified model of vessel mechanics. We pursued a simple pipe flow model leveraging direct pressure measurements made in the pigs. We placed two catheters, one above the tear (via carotid artery) and one below the tear (via femoral artery) in order to measure the pressure drop due to the aorta tear. Using a simple pipe flow model, the hemorrhage rate, shear rate, wall shear stress, and dynamic pressure across a cardiac cycle can be estimated (Figures 54 and 55).

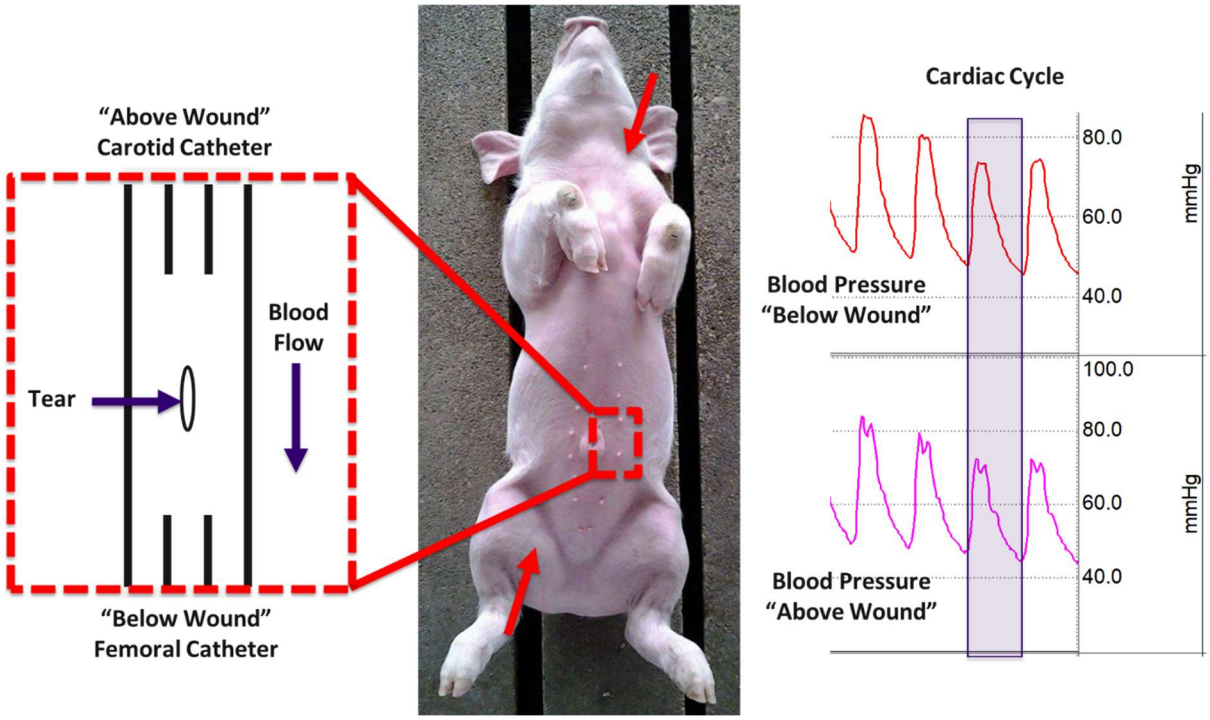

Figure 54. Overview of catheter setup to measure the pressure drop across the aorta tear. One catheter is fed through the carotid artery down to measure the blood pressure above the wound, while the second catheter is fed through the femoral artery up to measure pressure below the wound.

Figure 55. Simple pipe flow simulation of hemorrhage through a tear.

From the simple pipe flow model, a very high shear rate was found that supports that this high shear wound will have a high platelet content. However, it should be noted that this model probably overestimates shear rate due to the assumption that it is rigid pipe flow, whereas the actual vessel wall is flexible. A similar study in mice showed that as the relative aspect ratio of the wound area to the vessel radius increases, the wound shear rates decrease. This further supports that rat model has a lower shear rate compared to the descended aorta. Additionally, the average dynamic pressure, or the pressure the clot must overcome to stop bleeding, was on the order of magnitude as the average stress across the wound. This simple pipe flow model further supports the swine tear model being too aggressive for PolySTAT to show efficacy.

3.6 DEVELOPMENT OF A LIVER BLEED MODEL IN SWINE

Since modeling of the swine aorta tear model indicated that the vessel size and wound were too aggressive, we attempted to develop a new severe hemorrhage model that would target vessels with lower wall tensions and provide a better clotting surface. The liver was chosen due to its large venous blood supply, high level of vascularization, large surface area, and clinical relevance. Table

2 gives an overview of the estimated wall tension for liver vessels. Due to the lower pressure of veins, the wall tension of the vessels is greatly reduced and more similar to the rat femoral artery.

Table 2. Diameter, pressure, and tall tension for various vessels in the liver.

Vessel	Diameter (mm)	Pressure (mmHg)	Wall Tension (dynes/cm)
Rat Femoral Artery	0.5	60	2,000
Descending Aorta (abdominal region)	20	60	20,000
Hepatic Artery at origin	5	60	5,000
Main Portal Vein [Branches]	10 - 20 [4]	5 - 10	300 - 3,000
Main Hepatic Vein	15	10	2,500
Portal Triad Vessels/Hepatic Vein	0.05 - 0.1	5-10	17 - 67

After a literature review, a deadly liver transection (Grade IV injury) model was chosen as a starting point. In this model, the left lobe is isolated and the lobe is fully transected 3 cm from the hilum of the liver. Figure 56 below shows a quick overview with a 4 cm transection.

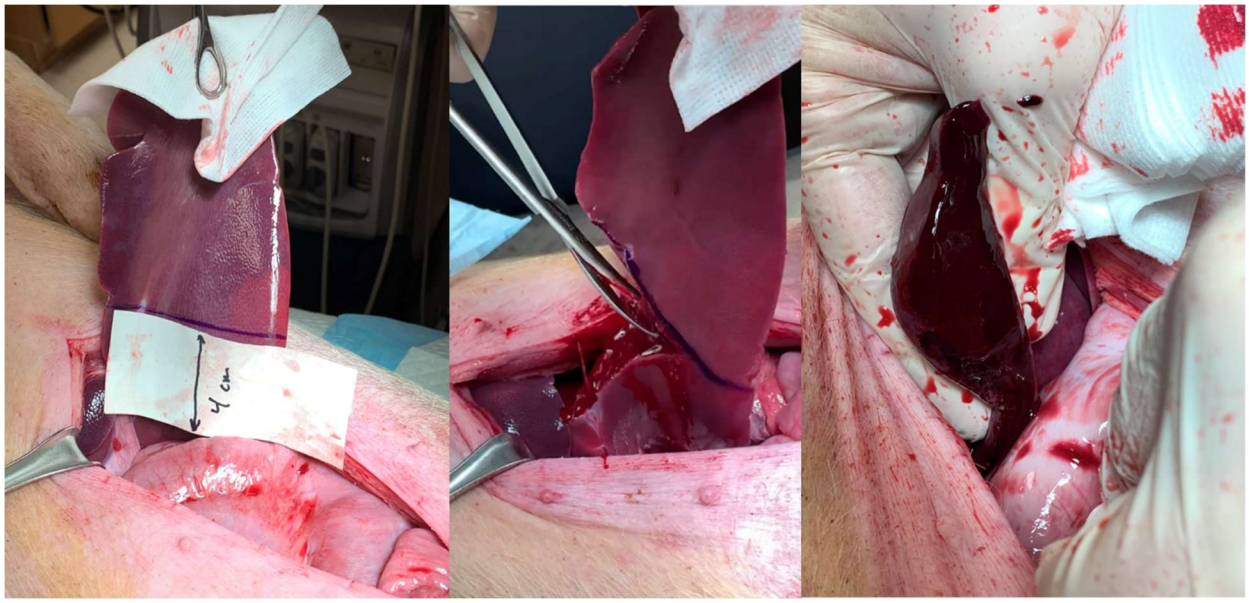

Figure 56. Images of the liver transection model. Left: The left lobe of the pig's liver is isolated and pulled out of the abdomen. A stencil with a set distance is laid at the base of the hilum, and the stencil is perpendicular to white ligament on the underside of the lobe. Next a mark is made. Middle: Using surgical scissors, the left lobe is fully transected and removed from the abdomen. The abdomen is rapidly stapled shut over two minutes. Right: Image of the clot formed on the end of the transection inside the peritoneum.

The original model called for a 3 cm transection however, this study was evaluating a pressurized external hemostat, and it was found that the 3 cm transection was too aggressive and resulted in rapid deaths. Therefore, a 4 cm transection was evaluated. With this wound, the cut surface of the liver provided a large surface area to form a clot, and there was typically one or two small arteries that provided higher pressure bleeds in combination with the low pressure bleed of the veins. Figure 58 below shows the cut surface from the transected side of the left lobe. The large vessels are either hepatic or portal vein branches, while the white encased smaller vessels are from the hepatic artery. It was observed that these solid organ wounds create large vessel cross-sections that remain open.

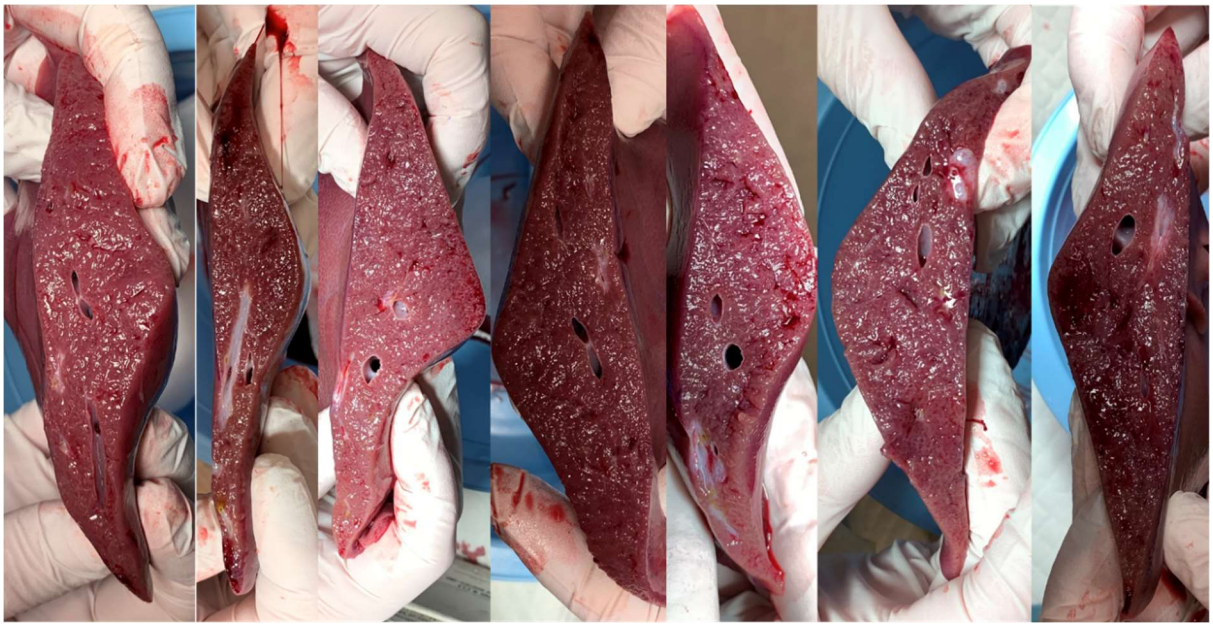

Figure 57. Images of the cut surfaces of the transected left lobes. There are a few larger branches of the hepatic vein and portal vein present, while the hepatic artery branches are smaller.

Even with the less aggressive 4 cm transection, there was still 100% mortality. Additionally, there was a cluster of rapid deaths (Figure 57 below).

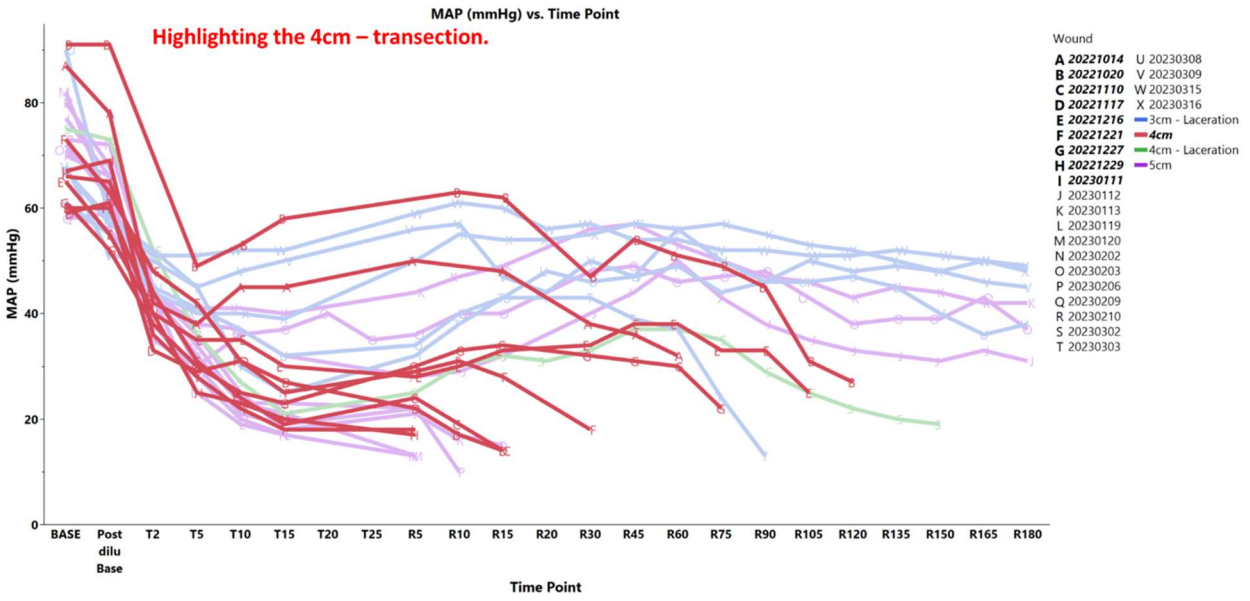

Figure 58. Mean arterial pressure (MAP) in mmHg versus time points in the liver transection and liver laceration models. The 4 cm transection (red) data is highlighted.

The 4 cm liver transection resulted in a rapid drop in MAP over ten minutes with some instances rebleeding events. The resuscitation rate of 1 cc/(kg*min) was 3x slower than the resuscitation rate in the aorta tear model 3 cc/(kg*min). Even with this less aggressive resuscitation rate, there was significant bleeding and rebleeding. It should be noted, that due to the liver transection being venous bleed, it is unknown how much resuscitation rate would affect the hemorrhage rates and stress on the clots. The aorta tear is a major artery, and as a result the MAP increases due to the aggressive resuscitation directly translate to an increased stress on the clot at the tear. The uncertainty around switching from a major arterial bleed to a major venous bleed, also called into question about the concentration of PolySTAT reaching the liver wound. Therefore, we used the same FITC-labeled PolySTAT from the aorta tear, and dosed it at 10 mg.kg. Blood samples were taken from the femoral artery (arterial blood), jugular vein (mixed blood), and the portal vein (venous blood). The plasma concentration of FITC-PolySTAT was measured and is shown in Figure 59 below.

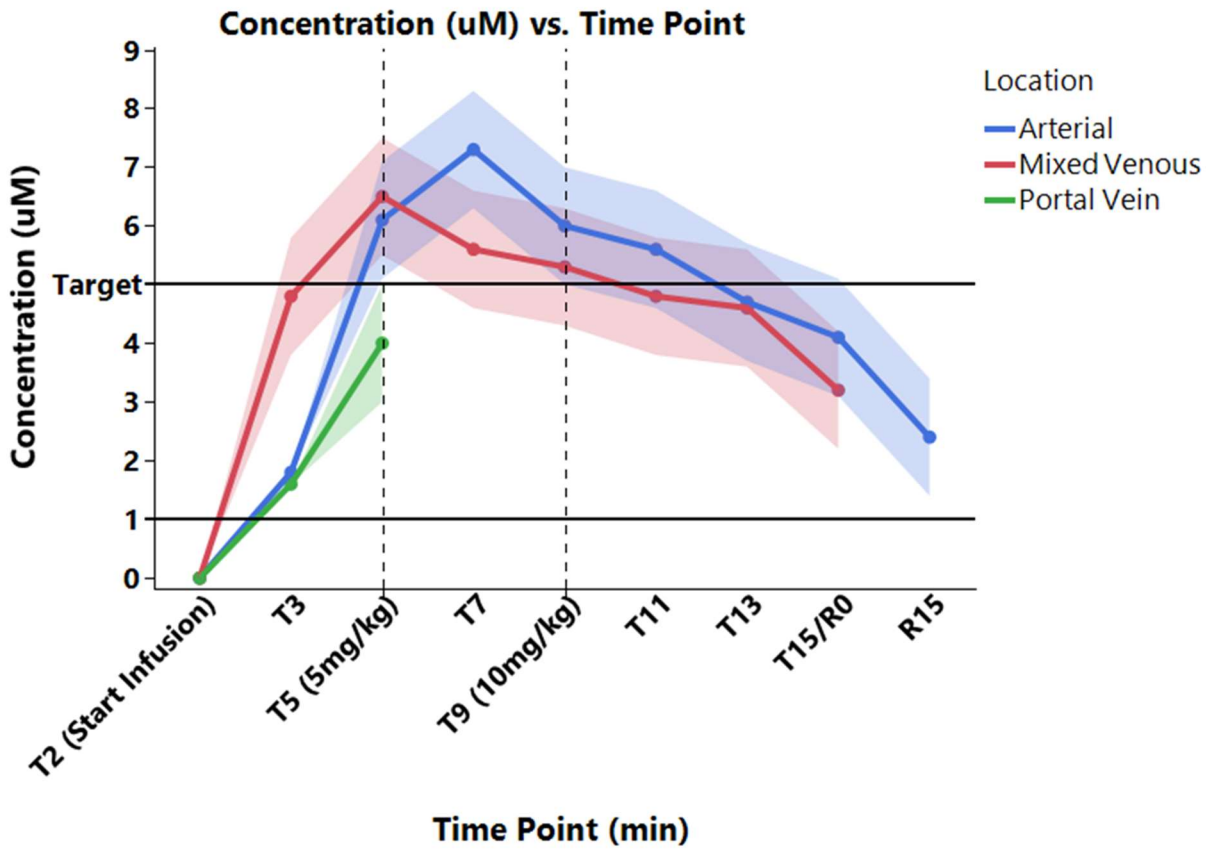

Figure 59. FITC-PolySTAT (dose 10 mg/kg) concentration measured at the femoral artery (arterial blood), jugular vein (mixed venous), and the portal vein (venous blood) over time in a sham pig with similar blood loss to the 4 cm transection. Concentration was measured in n=1 pig, and the standard deviation from the plasma measurements in the aorta bleed were added to show an estimation of the range of blood concentration. The portal vein collapsed T5 due to low blood pressure and blood was unable to be drawn from it. The pig died at R15.

The PolySTAT appears first in the mixed venous, followed by the aterial blood, and finally the portal vein. The 10 mg/kg dose appears to provide a good level of PolySTAT in the blood and better hits the target concentration of 5 µM. Unfortunately, the portal vein collapsed and further measurements were not able to be made. It is unknown if this collapse would occur without the catheter and during the liver transection. However, overall these results gave us more confidence we were hitting the desired PolySTAT concentration at the liver.

Next, we wanted to get an estimate of the decrease in blood loss needed to enable the pig to survive. For this we evaluated a series of sham pigs (Figure 60 below).

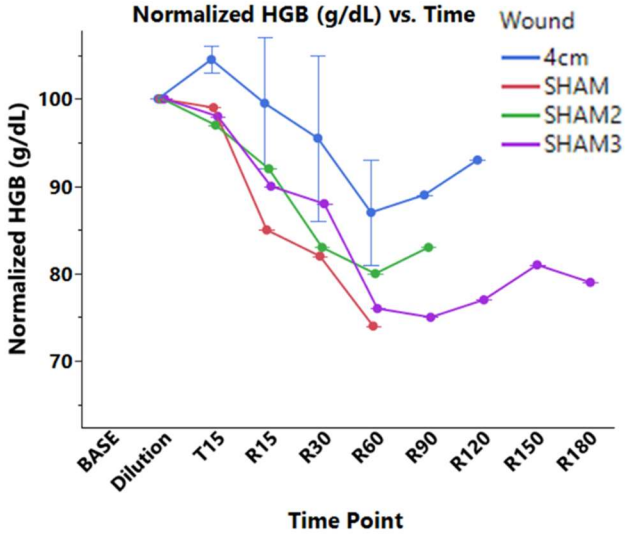

Type	Hem. Vol.	Hem. Rate
Injury (4 cm)	23 cc/kg	N/A
Sham 1	23 cc/kg	Constant
Sham 2	19 cc/kg	Venous
Sham 3	15 cc/kg	Venous

Figure 60. Overview of sham pigs evaluated to find hemorrhage level necessary for survival in the liver model. No injurty was made, and the hemorrhage was done with a controlled bleed using programed rates with a peristaltic pump. Normalized hemoglobin was used to compare blood loss to the 4 cm liver transection. Sham 1 (red) used a constant hemorrhage rate that matched the overall average hemorrhage volume measured in the 4 cm transection which was too aggressive compared to the slower venous bleeds, and led to a fast death. Sham 2 decreased the overall hemorrhage volume to 19 cc/kg, and used a controlled bleed program based on a slower venous bleed. This once again led to death. Sham 3 used the same venous bleed profile but decreased the overall hemorrhage to 15 cc.kg, and this led to survival.

From the sham pigs, it is estimated that hemorrhage needs to be decreased from ~23 cc/kg to ~15 cc/kg (Sham 3) for the pigs to survive. Although this was a reasonable amount of blood loss to decrease, the 4 cm transection seemed to lead to too quick of deaths to provide time for PolySTAT to be efficacious. Therefore, we decided to evaluate a 5 cm transection to see if we could increase the average survival time. Figure 61 below shows the mean arterial pressure versus time for the 5 cm transection pigs.

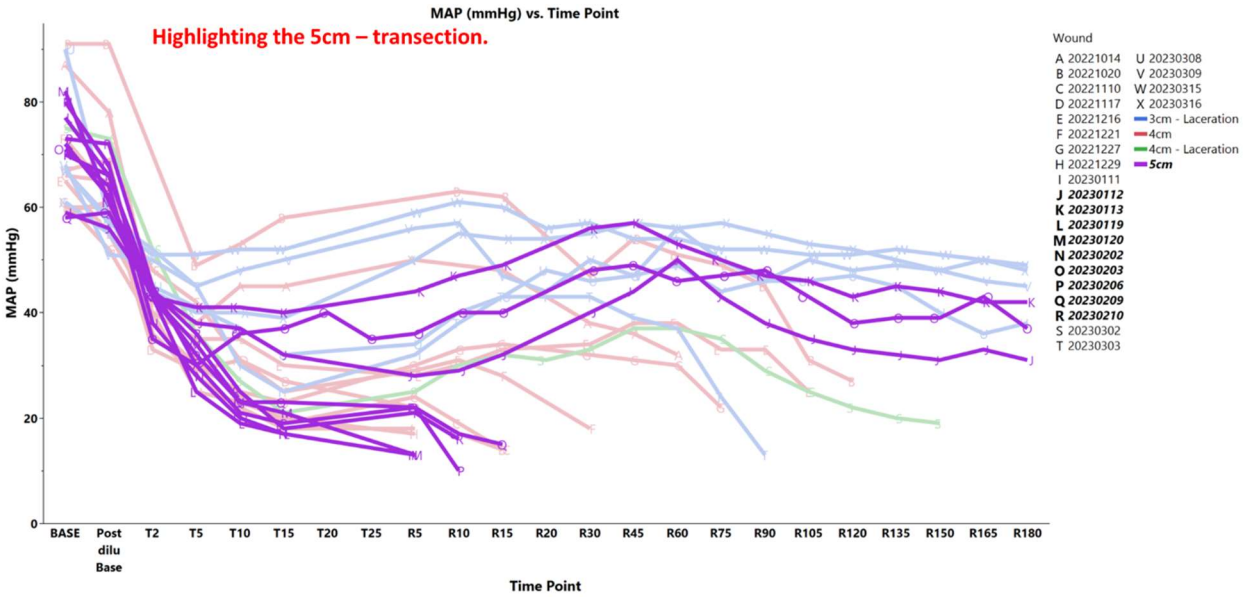

Figure 61. Mean arterial pressure (MAP) in mmHg versus time points in the liver transection and liver laceration models. The 5 cm transection (purple) data is highlighted.

Although, the 5 cm transection did result in n = 3 survivors, which were the first survivals we had with a liver transection, there was an even tighter cluster of rapid deaths. Pictures of the transected livers are shown in Figure 62 below.

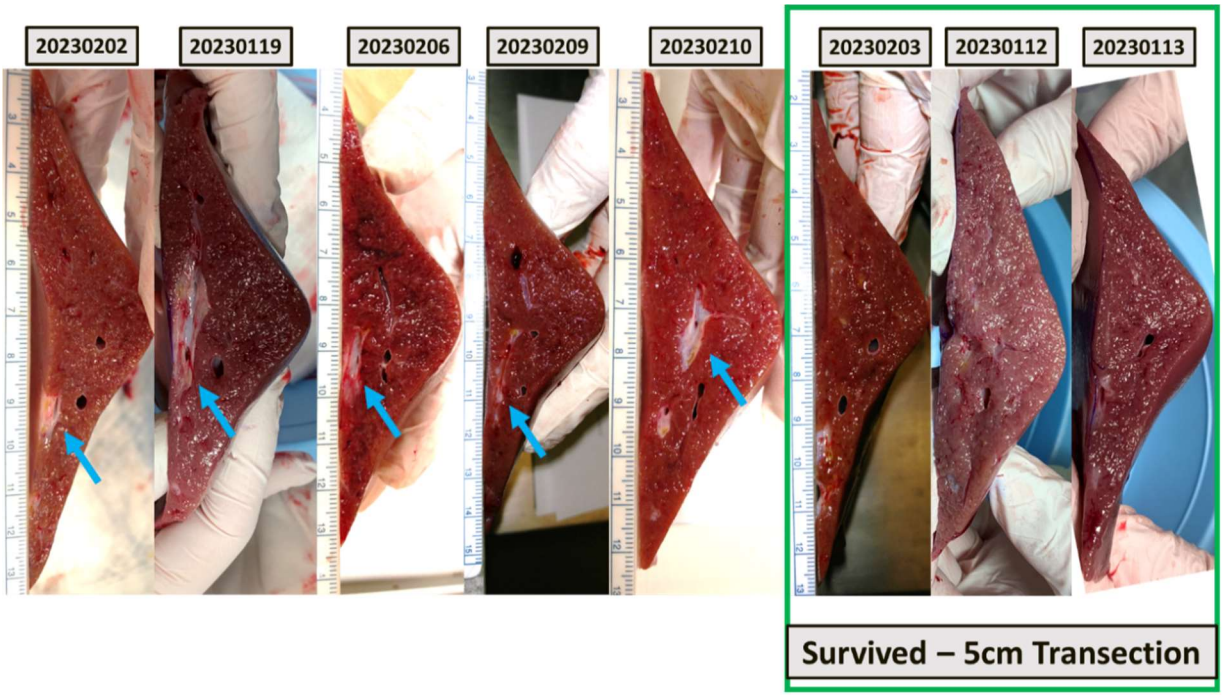

Figure 62. Images of the transected left lobes from the 5 cm liver transection model. The n = 5 rapid hemorrhage deaths indicated that a major artery branch was cut, leading to vessel cuts along the lengths of the vessels. Whereas the n = 3 pigs that survived (green box) did not have a similar vessel cut.

Unfortunately, the distance of the 5 cm transection appeared to coincide with a branching of the hepatic artery and led to lengthwise cuts of these vessels that resulted in rapid bleed outs. Due to the aggressiveness of the transection model, we decided to explore a deep laceration cut that did not fully transect the left lobe, but left it barely attached. We hypothesized that leaving the other side of the liver in the cavity would slow down the bleed due to the opposite side trying to close down on the wound (Figure 63 below).

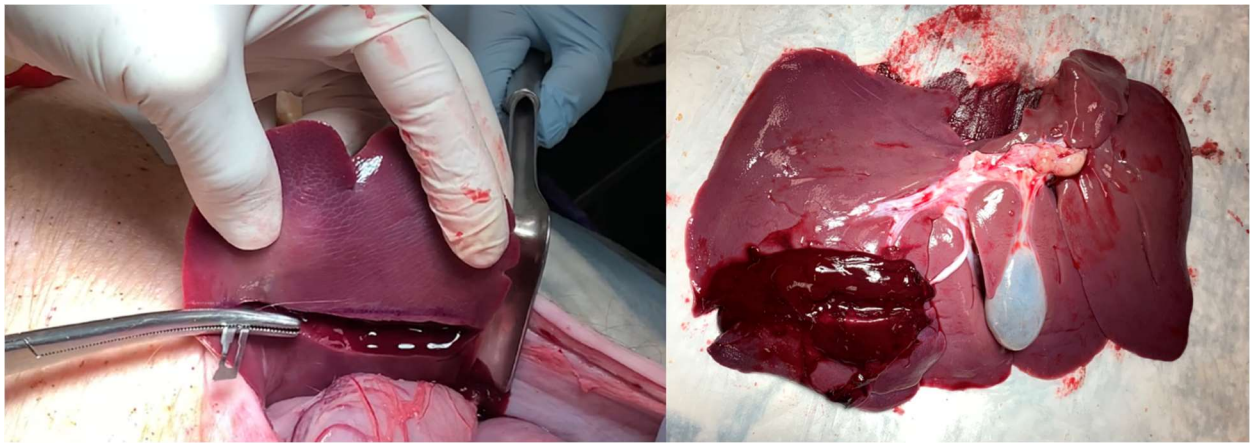

Figure 63. Images from the 1 cm deep liver laceration model. Left: Similar to the transection model, a template is placed then a line drawn on the liver. A scalpel blade set with a depth of 1 cm is used to cut along the line. The left lobe is then laid back into the peritoneum and stapled shut. Right: A harvested liver showing the large clot that forms in the laceration model. The clot can hold the two sides of the wound together.

The liver laceration model created a nice large, localized clot that bridged and held together the two sides of the left lobe on either side of the laceration. It should be noted that the stencil/measuring system was changed for the 3 cm liver laceration model. Instead of the distance indicating the distance away from the hilum, for the 3 cm liver laceration we moved to measuring from the distance at the end of the ligament left lobe ligament that ran on the underside of the liver. Therefore, for the liver transection in order of distance away from the hilum 5 cm (furthest) > 4 cm > 3 cm (closest), while for the laceration 3 cm (further from the hilum) > 4 cm, while the 4 cm distance corresponds to the same distance from the hilum as the 4 cm liver transection model. The 3 cm liver laceration distance would be ~ 6 cm in the liver transection model. Figure 64 below shows the MAP versus time point for the 3 cm liver laceration model.

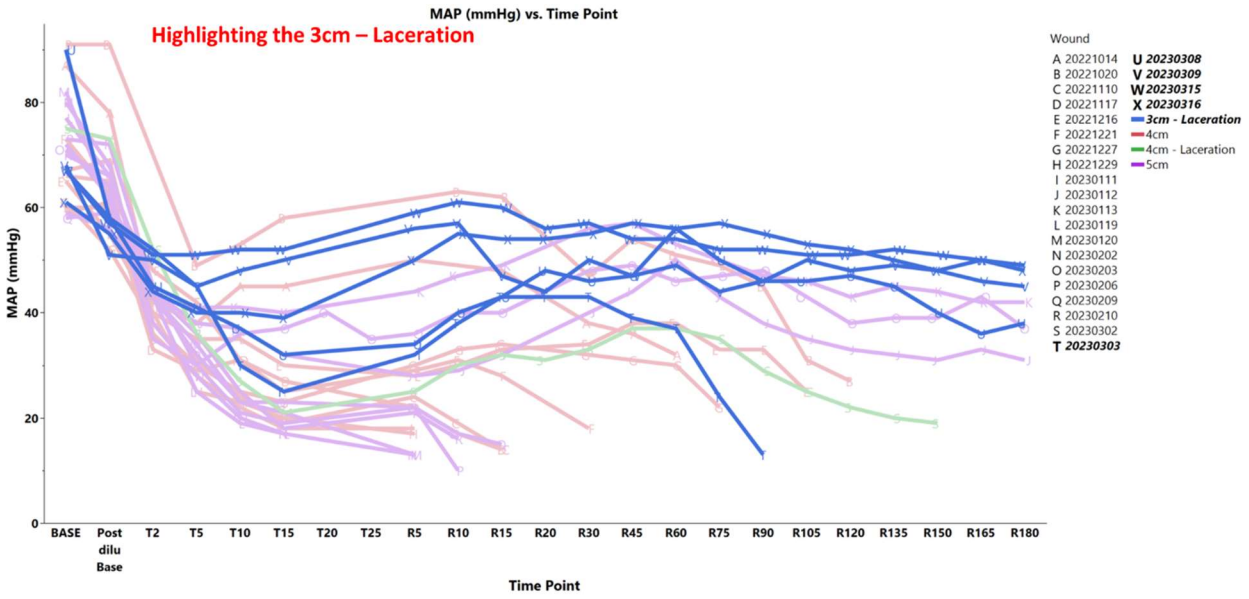

Figure 64. Mean arterial pressure (MAP) in mmHg versus time points in the liver transection and liver laceration models. The 3 cm laceration (blue) data is highlighted.

Moving to the 3 cm laceration (corresponding to a distance or 6 cm from the hilum) model greatly increase survival and slowed down hemorrhage. We evaluated n = 1 pig with a 4 cm laceration (corresponding to the same distance as 4 cm transection). This pig had a similar bleed profile to the 4 cm transection (Figure 65 below).

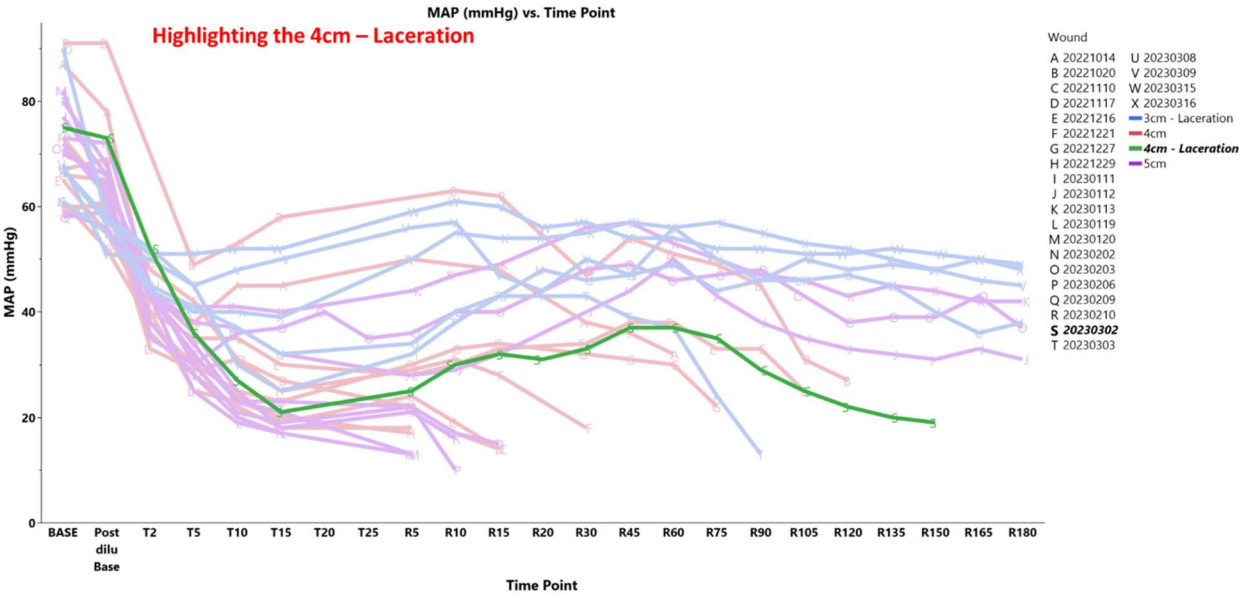

Figure 65. Mean arterial pressure (MAP) in mmHg versus time points in the liver transection and liver laceration models. The 4 cm laceration (green) data is highlighted.

The lactate levels (mmol/L) versus time point are shown in Figure 66 below.

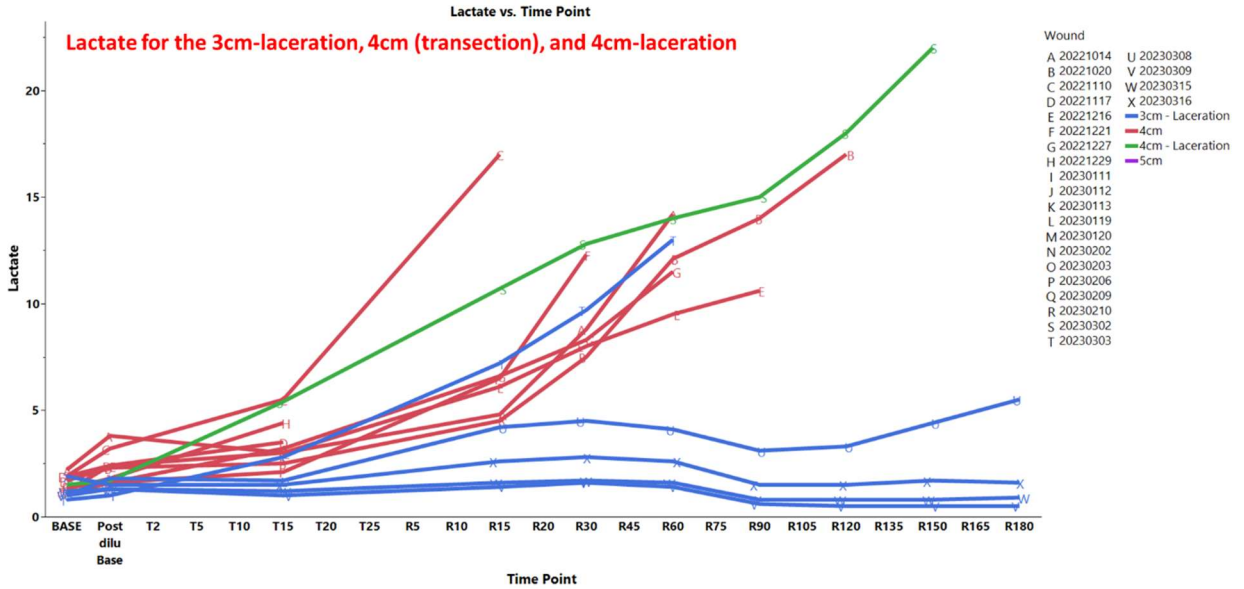

Figure 66. Lactate in mmol/L versus time point for the different liver bleed models.

From the lactate levels, the 3 cm laceration pigs were not getting as sick as the transection models. Figure 68 below shows the survival curve and internal hemorrhage volumes for the different wounds evaluated (excluding the n = 1, 4 cm laceration).

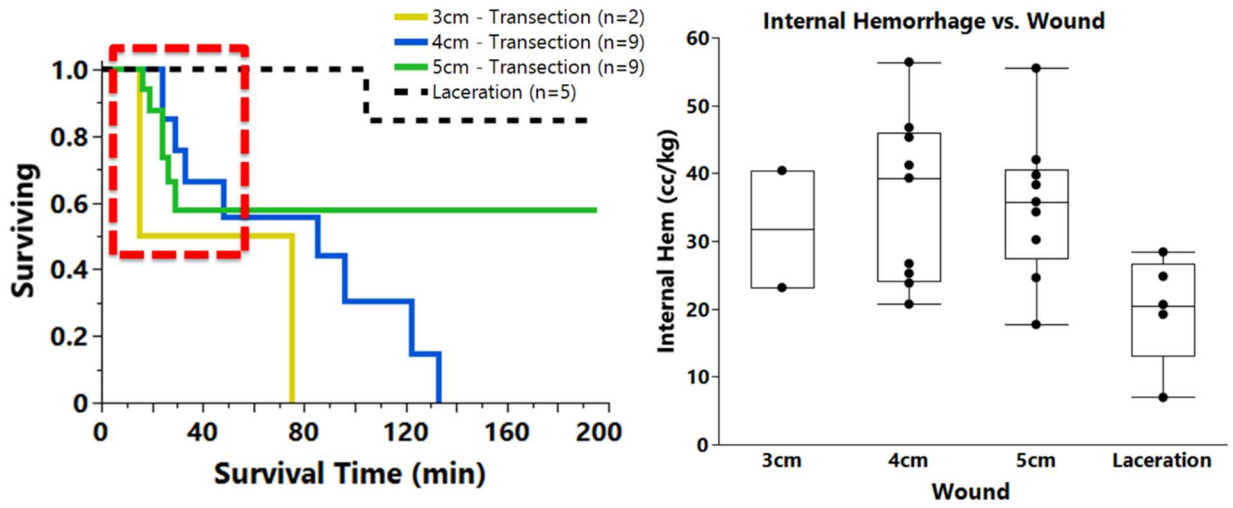

Figure 67. Kaplan-Meier survival curve (left) for the liver transection and laceration model in swine and average internal hemorrhage (right) measured for each wound. Left: There was a statistically significant increase in survival when comparing Laceration vs. 5cm – Transection ($p < .0001$), Laceration vs. 4 cm – Transection ($p < .0001$), and 5cm – Transection vs. 4 cm – Transection ($p < .0001$). P-values were determined by log-rank Mantel-Cox test. Right: There was a statistically significant decrease in hemorrhage moving from the 4 cm – transection to the laceration model ($p = 0.043$). A fit model for a repeated measure, one-way anova with tukey post-hoc analysis ($\alpha = 0.050$) was used for statistical analysis.

Unfortunately, due to the grant expiring that supported this model development work, we were unable to evaluate additional pigs in the 4 cm laceration. Therefore, we decided to move forward with the least aggressive model, the 3 cm liver laceration, and complete a small pilot study comparing PolySTAT (10 mg/kg), PolySTAT (10 mg/kg) + TXA (15 mg/kg), Saline Volume Control, and TXA (15 mg/kg). All treatments were given at the same volume in a single bolus infusion over 10 minutes.

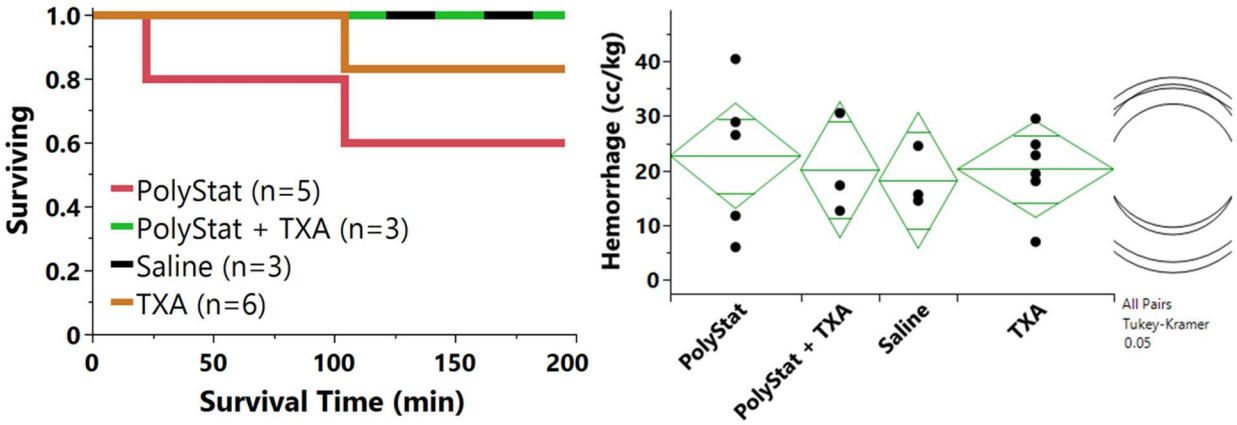

Figure 68. Survival curves and hemorrhage volumes for 3 cm liver laceration pilot study. No statistically significant differences in survival (left) nor hemorrhage volumes (right) were observed.

Unfortunately, the model did not show any difference in treatment. Future work will evaluate the images of vessels and measurements to see if similar to the aorta bleed, wound mechanics are playing a role, and we can see any effect when controlling for vessel size.

3.7 CONCLUSIONS

Overall, these swine studies were exciting for many reasons. These were the first major swine studies evaluating PolySTAT. The slight improvement in survival compared to PolySCRAM was important to see due to the negative impact of the resuscitative nature of PolySTAT's polymer. [3] In all the swine experiments there were no signs of CARPA, or any other signs of distress due to the PolySTAT infusion. Histology of major organs showed no evidence of systemic thrombosis, even in swine that were co-administered fibrinogen concentrate and PolySTAT. We successfully imaged intravenously administered FITC-labeled PolySTAT in clots harvested from both rats and swine, which confirmed PolySTAT's ability to target the wound site. The FITC-PolySTAT also enabled us to do some simple biodistribution studies that decreased the dose of PolySTAT in swine from 15 mg/kg to 10 mg/kg. Finally, the modeling of wound mechanics and hemorrhage has set the foundation for additional work to understand the mechanical limits of intravenous hemostats, which is key to pushing this field forward.

3.8 Acknowledgements and Funding Sources

We would like to thank the UW Keck Center and Dr. Nathaniel Peters for lending their equipment and expertise in completing the confocal microscopy imaging. This work was supported by NIH 1R01HL139007. TJP was supported by an NSF Graduate Fellowship (DGE-1762114)

3.9 References

(1) Research, C. for D. E. and. *Investigational New Drug (IND) Application*. FDA. https://www.fda.gov/drugs/types-applications/investigational-new-drug-ind-application (accessed 2022-01-14).

(2) Lamm, R. J.; Lim, E. B.; Weigandt, K. M.; Pozzo, L. D.; White, N. J.; Pun, S. H. Peptide Valency Plays an Important Role in the Activity of a Synthetic Fibrin-Crosslinking Polymer. *Biomaterials* **2017**, *132*, 96–104. https://doi.org/10.1016/j.biomaterials.2017.04.002.

(3) Lamm, R. J. Engineering and Evaluating Fibrin-Targeted Biomaterials for Hemostasis. Thesis, 2018. https://digital.lib.washington.edu:443/researchworks/handle/1773/43296 (accessed 2022-01-13).

(4) *Optimizing the Polymer Chemistry and Synthesis Method of PolySTAT, an Injectable Hemostat | ACS Biomaterials Science & Engineering*. https://pubs.acs.org/doi/abs/10.1021/acsbiomaterials.0c01189 (accessed 2022-01-14).

(5) Chan, L. W.; Wang, X.; Wei, H.; Pozzo, L. D.; White, N. J.; Pun, S. H. A Synthetic Fibrin Cross-Linking Polymer for Modulating Clot Properties and Inducing Hemostasis. *Science translational medicine* **2015**, *7* (277).

(6) Hildebrand, F.; Andruszkow, H.; Huber-Lang, M.; Pape, H.-C.; van Griensven, M. Combined Hemorrhage/Trauma Models in Pigs—Current State and Future Perspectives. *Shock* **2013**, *40* (4), 247–273. https://doi.org/10.1097/SHK.0b013e3182a3cd74.

(7) Mitterlechner, T.; Innerhofer, P.; Streif, W.; Lödl, M.; Danninger, T.; Klima, G.; Hansson, K.; Fries, D. Prothrombin Complex Concentrate and Recombinant Prothrombin Alone or in Combination with Recombinant Factor X and FVIIa in Dilutional Coagulopathy: A Porcine Model. *Journal of Thrombosis and Haemostasis* **2011**, *9* (4), 729–737. https://doi.org/10.1111/j.1538-7836.2011.04211.x.

(8) White, N. J.; Wang, X.; Liles, W. C.; Stern, S. Fibrinogen Concentrate Improves Survival During Limited Resuscitation of Uncontrolled Hemorrhagic Shock in a Swine Model. *Shock* **2014**, *42* (5), 456–463. https://doi.org/10.1097/SHK.0000000000000238.

(9) Kolodziej, A. F.; Nair, S. A.; Graham, P.; Mcmurry, T. J.; Ladner, R. C.; Wescott, C.; Sexton, D. J.; Caravan, P. Fibrin Specific Peptides Derived by Phage Display: Characterization of Peptides and Conjugates for Imaging. *Bioconjugate Chemistry* **2012**, *23*, 548–556.

(10) Cunningham, V. J.; Alswieleh, A. M.; Thompson, K. L.; Williams, M.; Leggett, G. J.; Armes, S. P.; Hill, B.; S, S. Y.; Musa, O. M. Poly(Glycerol Monomethacrylate) − Poly(Benzyl Methacrylate) Diblock Copolymer Nanoparticles via RAFT Emulsion Polymerization: Synthesis, Characterization, and Interfacial Activity. **2014**. https://doi.org/10.1021/ma501140h.

(11) Chan, L. W.; White, N. J.; Pun, S. H. A Fibrin Cross-Linking Polymer Enhances Clot Formation Similar to Factor Concentrates and Tranexamic Acid in an *in Vitro* Model of Coagulopathy. *ACS Biomater. Sci. Eng.* **2016**, *2* (3), 403–408. https://doi.org/10.1021/acsbiomaterials.5b00536.

(12) Yanjarappa, M. J.; Gujraty, K. V; Joshi, A.; Saraph, A.; Kane, R. S. Synthesis of Copolymers Containing an Active Ester of Methacrylic Acid by RAFT : Controlled Molecular Weight Scaffolds for Biofunctionalization. *Biomacromolecules* **2006**, *7*, 1665–1670.

(13) Darlington, D. N.; Craig, T.; Gonzales, M. D.; Schwacha, M. G.; Cap, A. P.; Dubick, M. A. Acute Coagulopathy of Trauma in the Rat. *Shock* **2013**, *39* (5), 440–446. https://doi.org/10.1097/SHK.0b013e31829040e3.

(14) Moore, H. B.; Moore, E. E.; Morton, A. P.; Gonzalez, E.; Fragoso, M.; Chapman, M. P.; Dzieciatkowska, M.; Hansen, K. C.; Banerjee, A.; Sauaia, A.; Silliman, C. C. Shock-Induced Systemic Hyperfibrinolysis Is Attenuated by Plasma-First Resuscitation: *Journal of Trauma and Acute Care Surgery* **2015**, *79* (6), 897–904. https://doi.org/10.1097/TA.0000000000000792.

(15) Cau, M. F.; Ali-Mohamad, N.; Yeh, H.; Baylis, J. R.; Peng, H.; Gao, H. Z.; Rezende-Neto, J.; Grecov, D.; White, N. J.; Tenn, C.; Semple, H. A.; Beckett, A.; Kastrup, C. J. Percutaneous Delivery of Self-Propelling Thrombin-Containing Powder Increases Survival

from Noncompressible Truncal Hemorrhage in a Swine Model of Coagulopathy and Hypothermia. *Journal of Trauma and Acute Care Surgery* **2022**, *93* (2S), S86. https://doi.org/10.1097/TA.0000000000003670.

(16) Cau, M. F.; Ali-Mohamad, N.; Baylis, J. R.; Zenova, V.; Khavari, A.; Peng, N.; McFadden, A.; Donnellan, F.; Owen, D. R.; Schaeffer, D. F.; Nagaswami, C.; Litvinov, R. I.; Weisel, J. W.; Rezende-Neto, J.; Semple, H. A.; Beckett, A.; Kastrup, C. J. Percutaneous Delivery of Self-Propelling Hemostatic Powder for Managing Non-Compressible Abdominal Hemorrhage: A Proof-of-Concept Study in Swine. *Injury* **2022**, *53* (5), 1603–1609. https://doi.org/10.1016/j.injury.2022.01.024.

(17) Moore, H. B.; Moore, E. E.; Lawson, P. J.; Gonzalez, E.; Fragoso, M.; Morton, A. P.; Gamboni, F.; Chapman, M. P.; Sauaia, A.; Banerjee, A.; Silliman, C. C. Fibrinolysis Shutdown Phenotype Masks Changes in Rodent Coagulation in Tissue Injury versus Hemorrhagic Shock. *Surgery* **2015**, *158* (2), 386–392. https://doi.org/10.1016/j.surg.2015.04.008.

(18) Bird, E.; Tamura, J.; Bostwick, J. S.; Steinbacher, T. E.; Stewart, A.; Liu, Y.; Baumann, J.; Feyen, J.; Tamasi, J.; Schumacher, W. A. Is Exogenous Tissue Plasminogen Activator Necessary for Antithrombotic Efficacy of an Inhibitor of Thrombin Activatable Fibrinolysis Inhibitor (TAFI) in Rats? *Thrombosis Research* **2007**, *120* (4), 549–558. https://doi.org/10.1016/j.thromres.2006.11.010.

(19) Poll, T. van der; Jonge, E. de; An, H. ten C. *Cytokines as Regulators of Coagulation*; Landes Bioscience, 2013.

(20) Held, F.; Hoppe, E.; Cvijovic, M.; Jirstrand, M.; Gabrielsson, J. Challenge Model of TNFα Turnover at Varying LPS and Drug Provocations. *J Pharmacokinet Pharmacodyn* **2019**, *46* (3), 223–240. https://doi.org/10.1007/s10928-019-09622-x.

(21) *LPS-Induced Rodent Sepsis Model - Creative Biolabs*. https://www.creative-biolabs.com/drug-discovery/therapeutics/lps-induced-rodent-sepsis-model.htm (accessed 2023-08-16).

(22) Wang, B.; Wu, S.; Ma, Z.; Wang, T.; Yang, C. BMSCs Pre-Treatment Ameliorates Inflammation-Related Tissue Destruction in LPS-Induced Rat DIC Model. *Cell Death Dis* **2018**, *9* (10), 1–12. https://doi.org/10.1038/s41419-018-1060-5.

(23) Han, C. Y.; Pichon, T. J.; Wang, X.; Ringgold, K. M.; St John, A. E.; Stern, S. A.; White, N. J. Leukocyte Activation Primes Fibrinogen for Proteolysis by Mitochondrial Oxidative Stress. *Redox Biology* **2022**, *51*, 102263. https://doi.org/10.1016/j.redox.2022.102263.

(24) Chernysh, I. N.; Nagaswami, C.; Kosolapova, S.; Peshkova, A. D.; Cuker, A.; Cines, D. B.; Cambor, C. L.; Litvinov, R. I.; Weisel, J. W. The Distinctive Structure and Composition of Arterial and Venous Thrombi and Pulmonary Emboli. *Sci Rep* **2020**, *10* (1), 5112. https://doi.org/10.1038/s41598-020-59526-x.

(25) Research, C. for D. E. and. *Estimating the Maximum Safe Starting Dose in Initial Clinical Trials for Therapeutics in Adult Healthy Volunteers*. U.S. Food and Drug Administration. https://www.fda.gov/regulatory-information/search-fda-guidance-documents/estimating-maximum-safe-starting-dose-initial-clinical-trials-therapeutics-adult-healthy-volunteers (accessed 2022-01-10).

(26) Landskroner, K.; Olson, N.; Jesmok, G. Cross-Species Pharmacologic Evaluation of Plasmin as a Direct-Acting Thrombolytic Agent: Ex Vivo Evaluation for Large Animal Model Development. *Journal of Vascular and Interventional Radiology* **2005**, *16* (3), 369–377. https://doi.org/10.1097/01.RVI.0000148828.40438.D3.

(27) Chan, L. W.-G. Peptide-Functionalized Biomaterials for Hemostasis and Cancer Imaging. 189.

(28) Spahn, D. R.; Bouillon, B.; Cerny, V.; Duranteau, J.; Filipescu, D.; Hunt, B. J.; Komadina, R.; Maegele, M.; Nardi, G.; Riddez, L.; Samama, C.-M.; Vincent, J.-L.; Rossaint, R. The European Guideline on Management of Major Bleeding and Coagulopathy Following Trauma: Fifth Edition. *Critical Care* **2019**, *23* (1), 98. https://doi.org/10.1186/s13054-019-2347-3.

(29) Innerhofer, N.; Treichl, B.; Rugg, C.; Fries, D.; Mittermayr, M.; Hell, T.; Oswald, E.; Innerhofer, P. First-Line Administration of Fibrinogen Concentrate in the Bleeding Trauma Patient: Searching for Effective Dosages and Optimal Post-Treatment Levels Limiting Massive Transfusion—Further Results of the RETIC Study. *J Clin Med* **2021**, *10* (17), 3930. https://doi.org/10.3390/jcm10173930.

(30) Kozek-Langenecker, S. A. Effects of Hydroxyethyl Starch Solutions on Hemostasis. *Anesthesiology* **2005**, *103* (3), 654–660. https://doi.org/10.1097/00000542-200509000-00031.

(31) Türkan, H.; Ural, A. U.; Beyan, C.; Yalçin, A. Effects of Hydroxyethyl Starch on Blood Coagulation Profile. *European Journal of Anaesthesiology | EJA* **1999**, *16* (3), 156–159.

(32) Martini, J.; Maisch, S.; Pilshofer, L.; Streif, W.; Martini, W.; Fries, D. Fibrinogen Concentrate in Dilutional Coagulopathy: A Dose Study in Pigs. *Transfusion* **2014**, *54* (1), 149–157. https://doi.org/10.1111/trf.12241.

(33) Burton, A. C. On the Physical Equilibrium of Small Blood Vessels. *American Journal of Physiology-Legacy Content* **1951**, *164* (2), 319–329. https://doi.org/10.1152/ajplegacy.1951.164.2.319.

(34) Thomas, S. The Production and Measurement of Sub-Bandage Pressure: Laplace's Law Revisited. *J Wound Care* **2014**, *23* (5), 234–246. https://doi.org/10.12968/jowc.2014.23.5.234.

(35) Chan, K. Y. T.; Yong, A. S. M.; Wang, X.; Ringgold, K. M.; John, A. E. S.; Baylis, J. R.; White, N. J.; Kastrup, C. J. The Adhesion of Clots in Wounds Contributes to Hemostasis and Can Be Enhanced by Coagulation Factor XIII. *Scientific Reports* **2020**, *10* (1), 20116. https://doi.org/10.1038/s41598-020-76782-z.

3.10 SUPPORTING INFORMATION

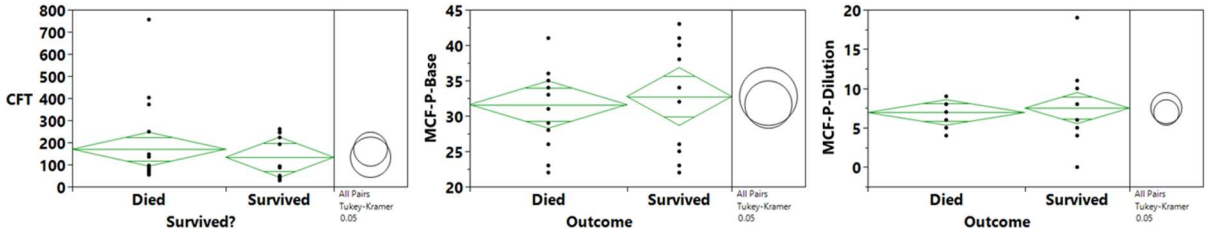

Figure S 1. CFT of plasma at baseline (left) and MCF of plasma at baseline (center) and dilution (right).

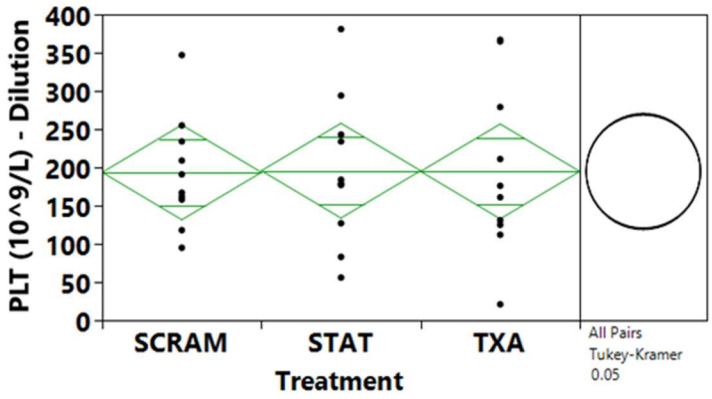

Figure S 2. Platelet count at dilution for each treatment.

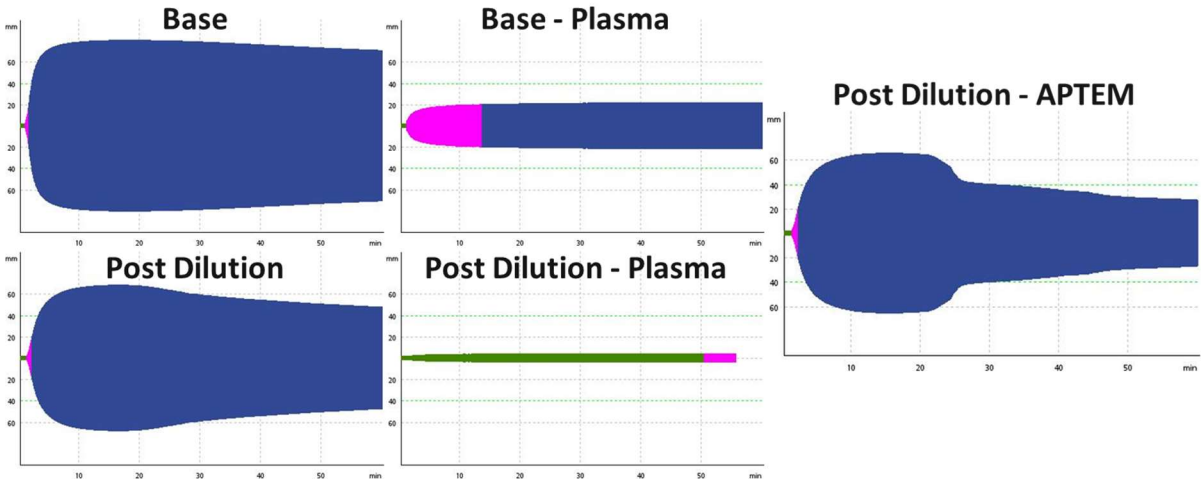

Figure S 3. Contraction artifacts seen in ROTEM. Visual contraction can be observed, and elimination of the artifacts with plasma (no platelets) but not in APTEM implies either contraction or adhesion.

Measured

Pig ID	Time Point	Measured Conc. (uM)
20211028	T0	8.7
20211028	T15	2.9
20211029	T0	5.5
20211029	T15	2.3

Estimated

Pig ID	20211028			Pig ID	20211029	
Blood/Vol.	60	ml/kg		Blood/Vol.	60	ml/kg
Weight	19.2	kg		Weight	19.2	kg
Tot. Blood Vol.	1152	ml		Tot. Blood Vol.	1152	ml
CATHHEM	309	ml		CATHHEM	271	ml
Blood Remaining	843	ml		Blood Remaining	881	ml
Dose	15	mg/kg		Dose	15	mg/kg
PSTAT	288	mg		PSTAT	288	mg
Infusion Vol.	28.8	mL		Infusion Vol.	28.8	mL
Hematocrit	15.58	%		Hematocrit	19.4	%
Plasma Volume	740	ml		Plasma Volume	739	ml
Conc. PSTAT	0.39	mg/ml		Conc. PSTAT	0.39	mg/ml
Conc. PSTAT	8.01	uM		Conc. PSTAT	8.02	uM

Figure S 4. Estimated FITC-PolySTAT concentrations, (left) measured after infusion with FITC-PolySTAT followed by measurement via fluorescence, and (right) estimation based on the administered dose, blood volumes, and hematocrit levels of the pigs. The estimated dose is for T0, and shows good agreement with the measured concentrations.

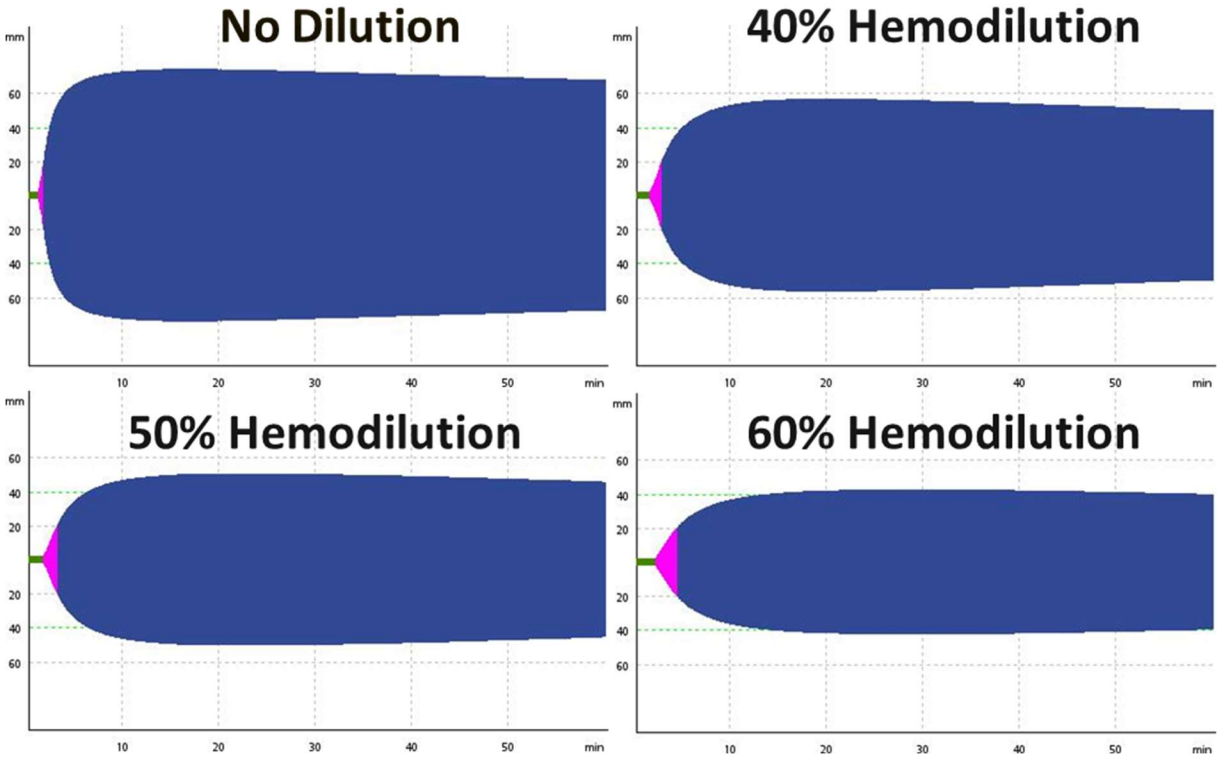

Figure S 5. Simulated hemodilutions of 40%-60% with pig whole blood. Baseline blood without dilution (top left), 40% hemodilution (top right), 50% hemodilution (bottom left), 60% hemodilution (bottom right).

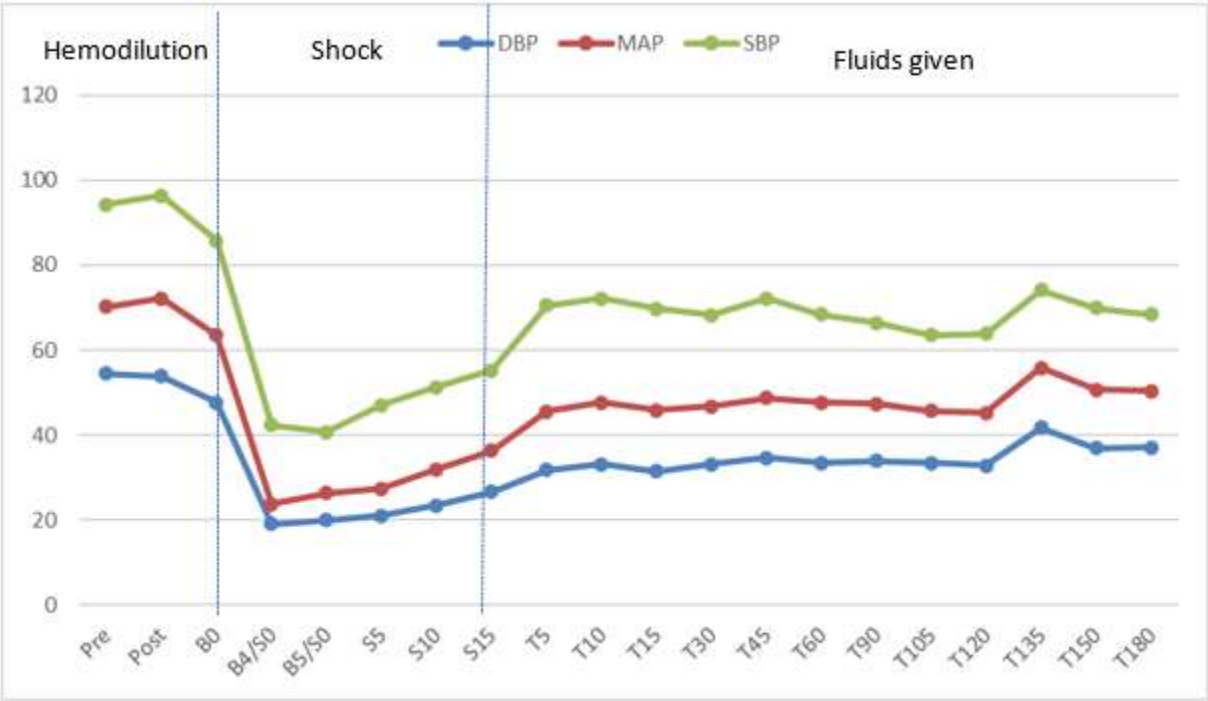

Figure S 6. Aortic blood pressure for all animals measured during hemodilution, hemorrhage (shock), and during fluid resuscitation (fluids given). SBP= systolic blood pressure, DBP = diastolic blood pressure, MAP=mean arterial blood pressure, in mmHg.

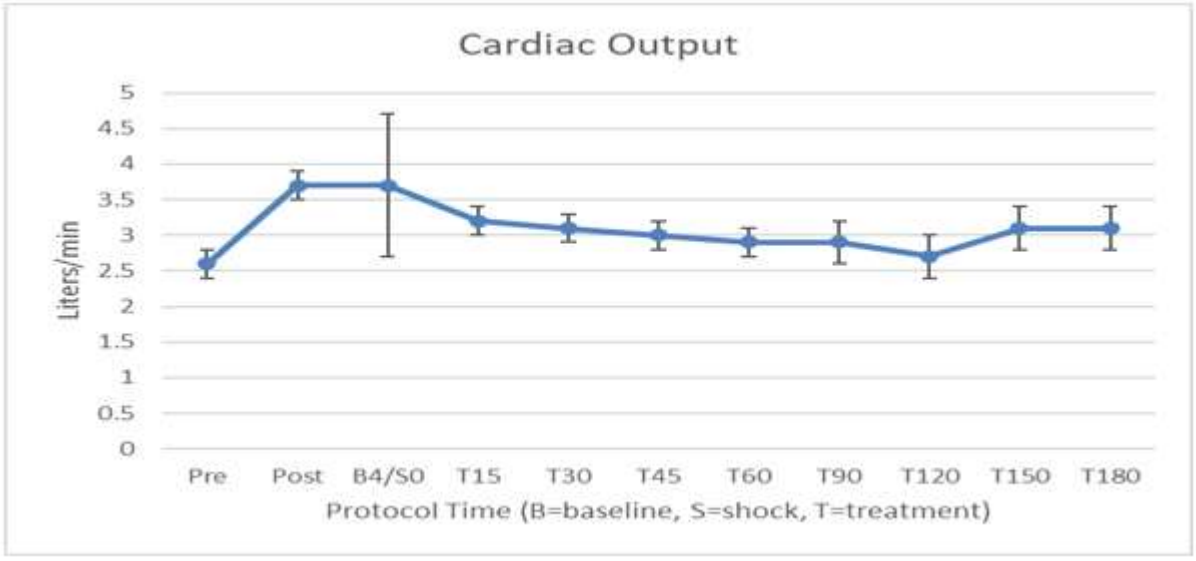

Figure S 7. Cardiac output for all animals measured in L/min during hemodilution, at baseline, during hemorrhagic shock, and during fluid resuscitation.

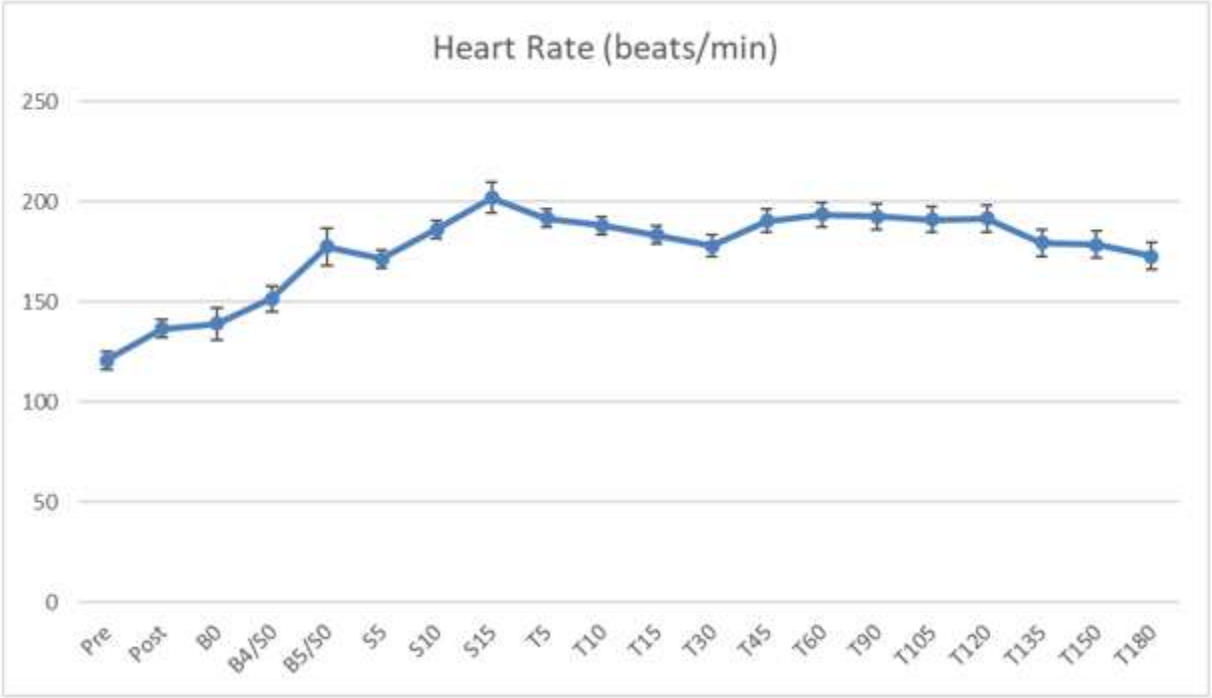

Figure S 8. Heart rate for all animals measured in beats/min during hemodilution, at baseline, during hemorrhagic shock, and during fluid resuscitation.

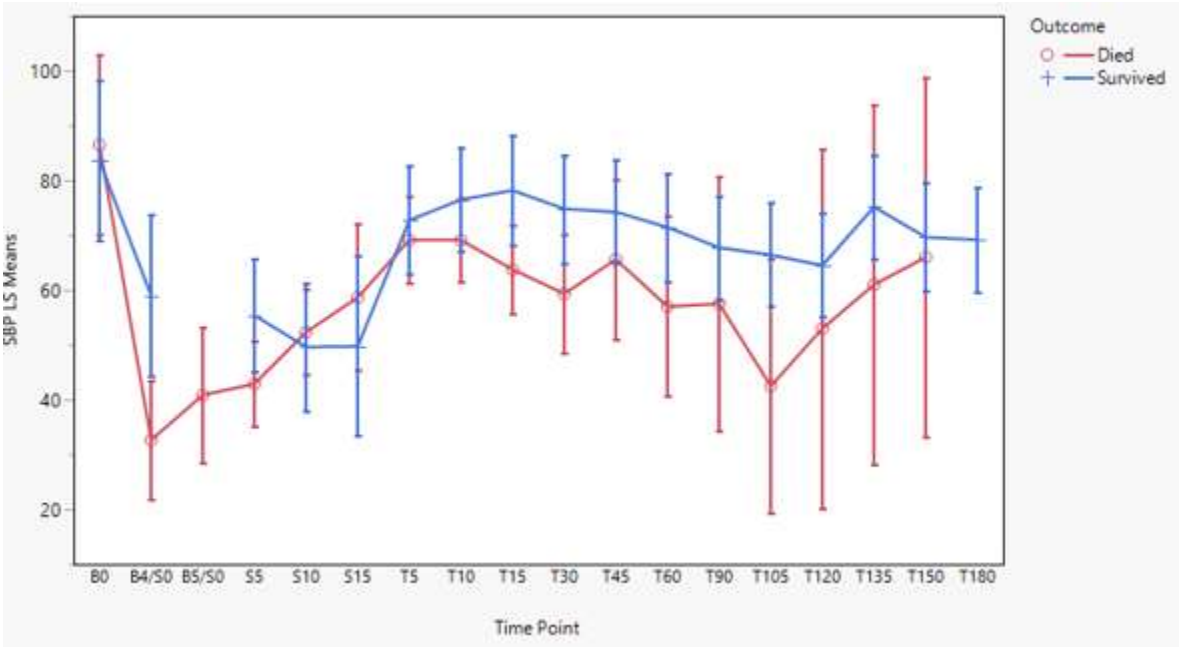

Figure S 9. Summary SBP=systolic blood pressure, in mmHg, compared by survivorship.

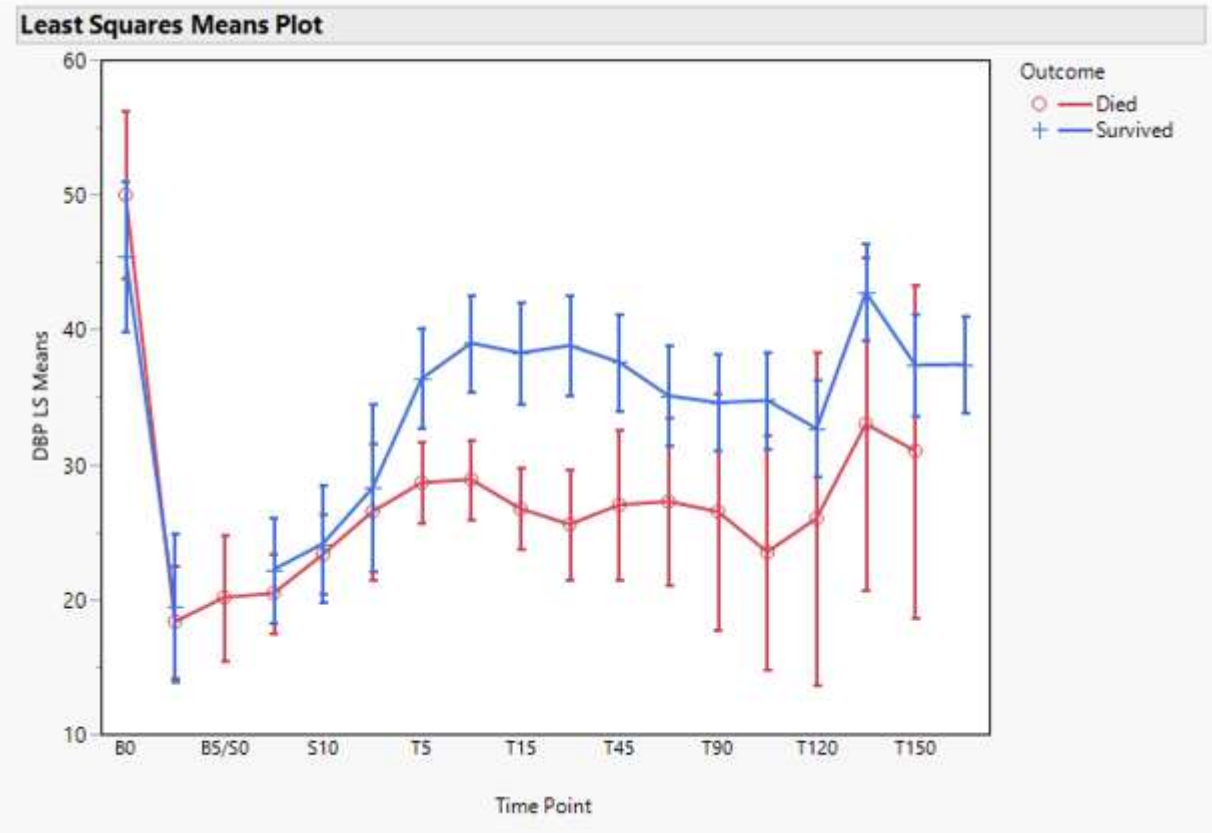

Figure S 10. Summary DBP=diastolic blood pressure, in mmHg, compared by survivorship.

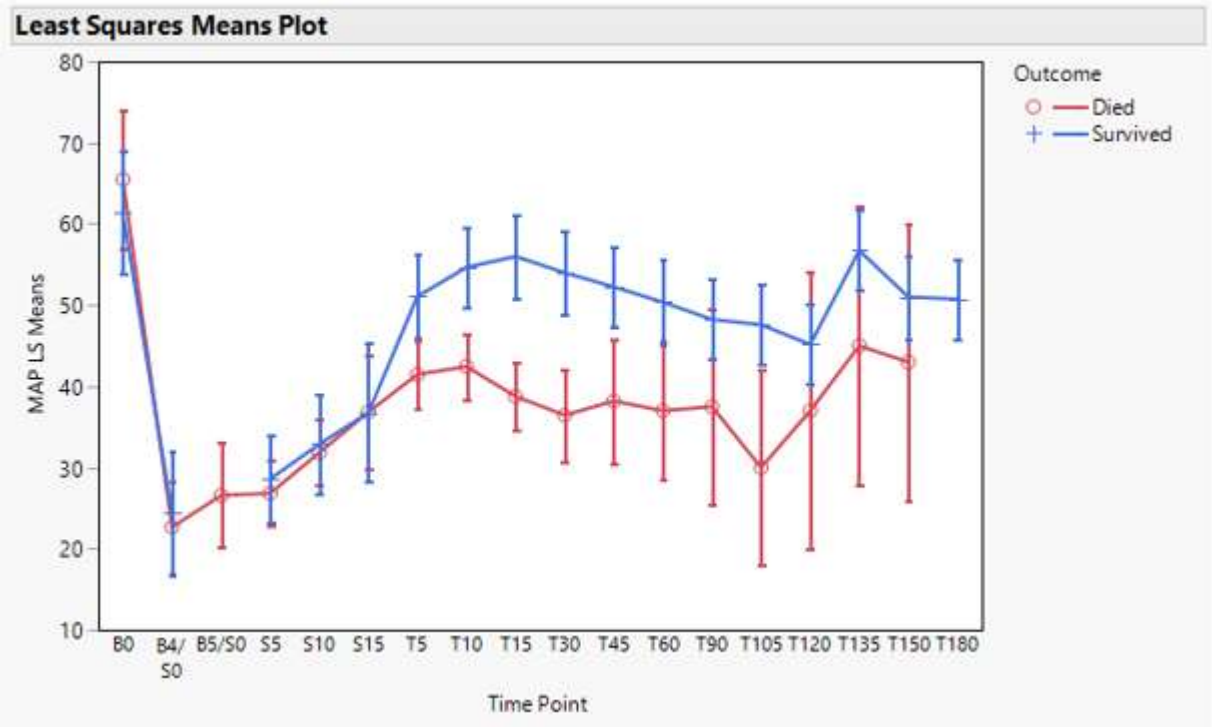

Figure S 11. Summary MAP = mean arterial pressure, in mmHg compared by survivorship.

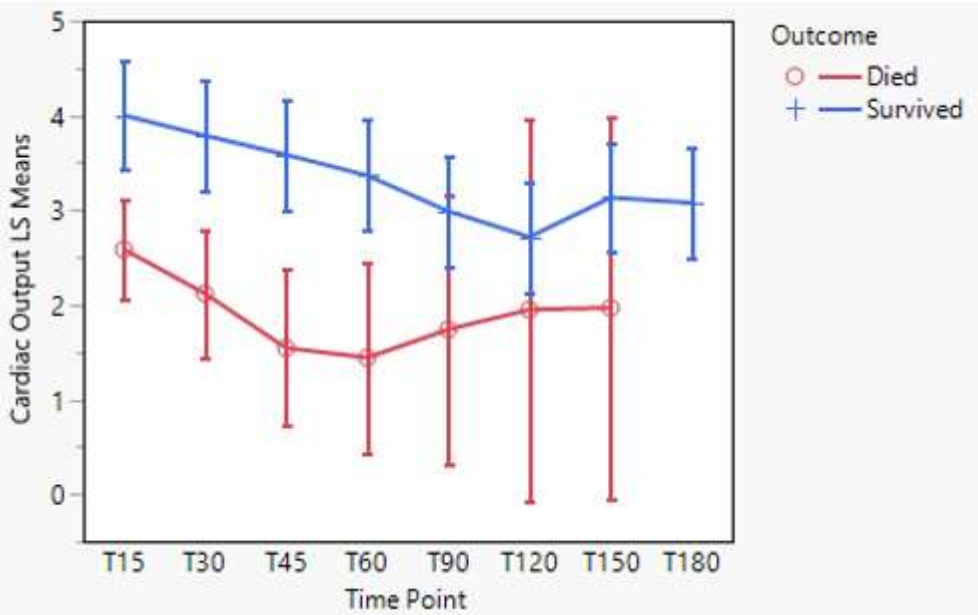

Figure S 12. Summary cardiac output in liters/min compared by survivorship.

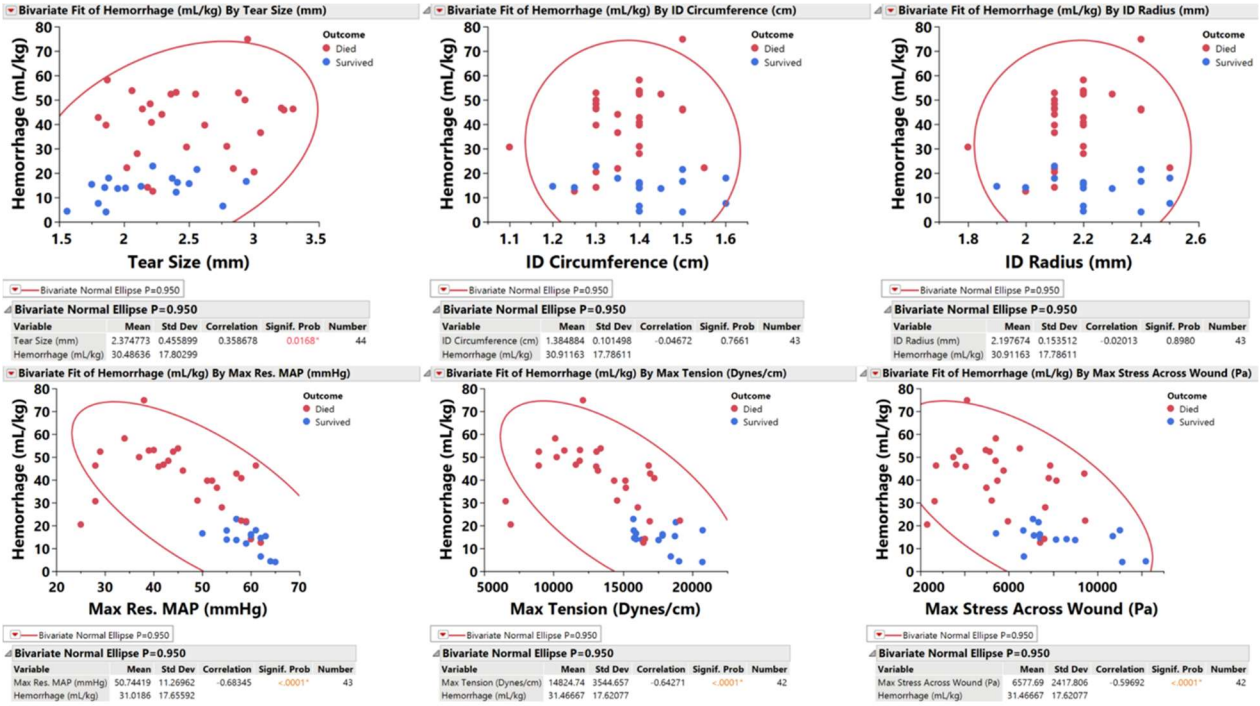

Figure S 13. Bivariate correlations between blood loss and wound geometry and mechanics. Bivariate correlations with 95% CI ellipses.

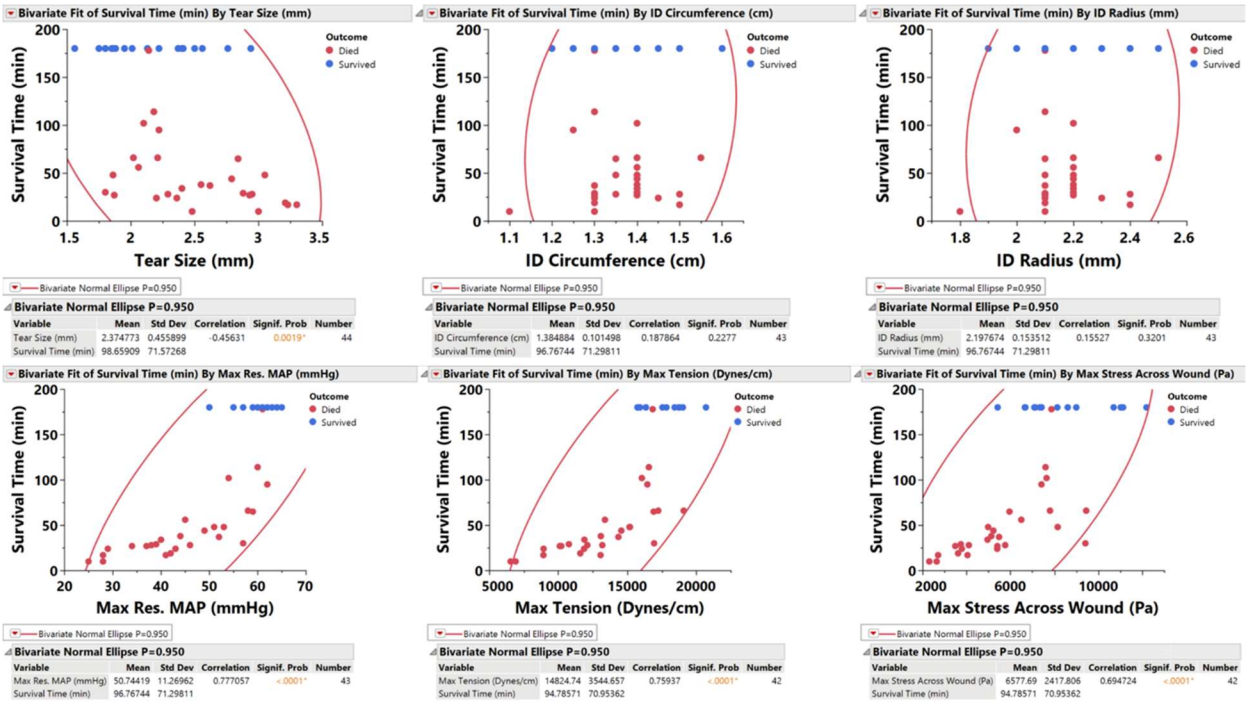

Figure S 14. Bivariate correlations between survival and wound geometry and mechanics. Bivariate correlations with 95% CI ellipses.

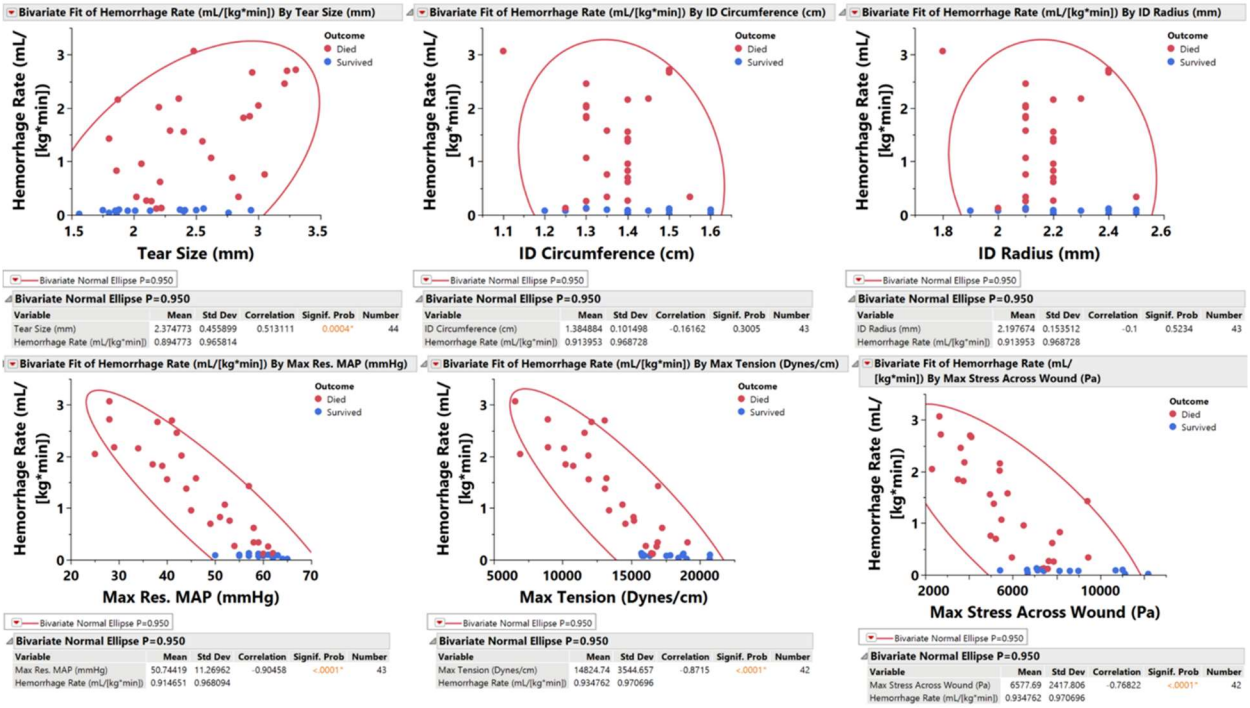

Figure S 15. Bivariate correlations between bleed intensity and wound geometry and mechanics. Bivariate correlations with 95% CI ellipses.

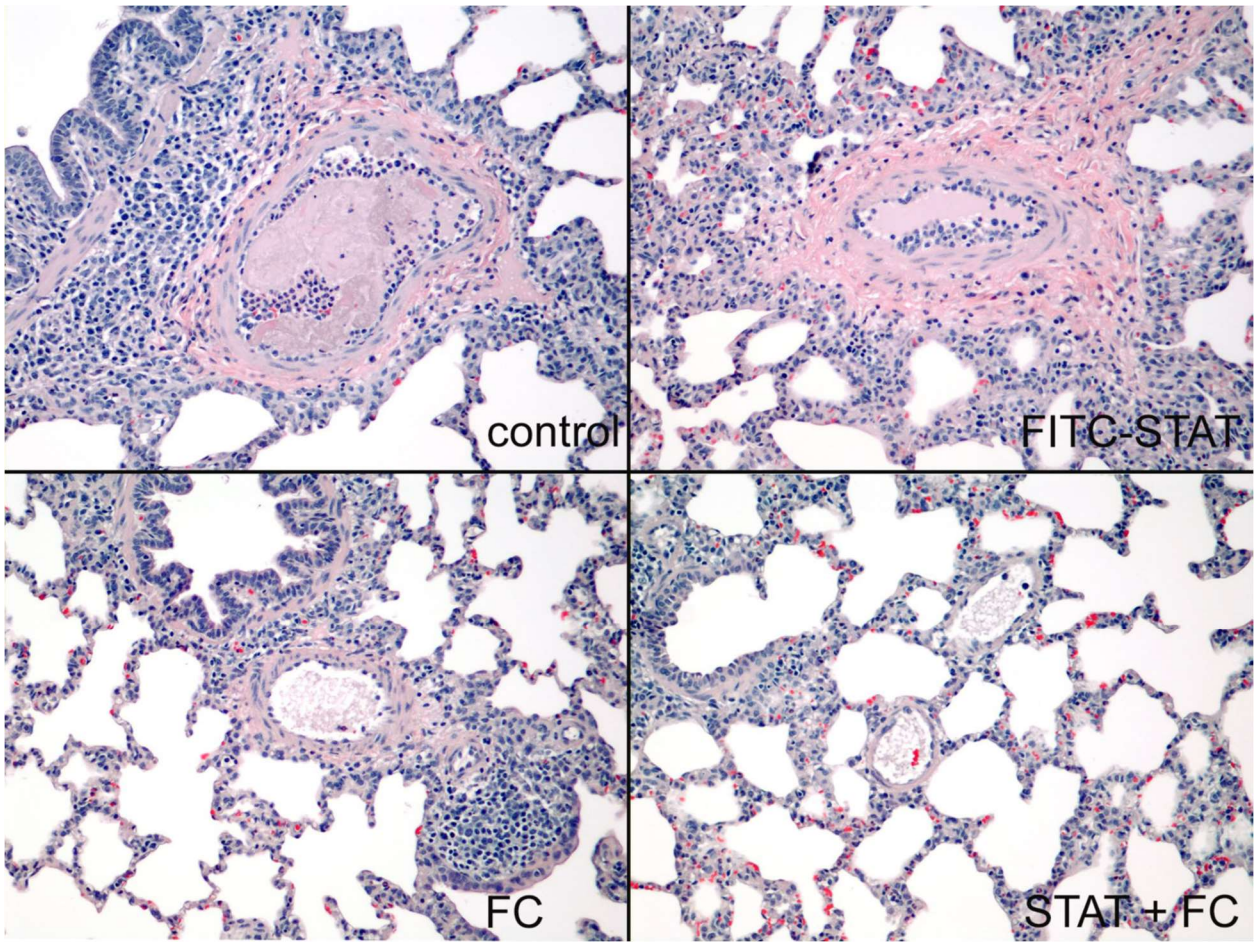

Figure S 16. Representative histology images from lung biopsies taken during aorta tear study.

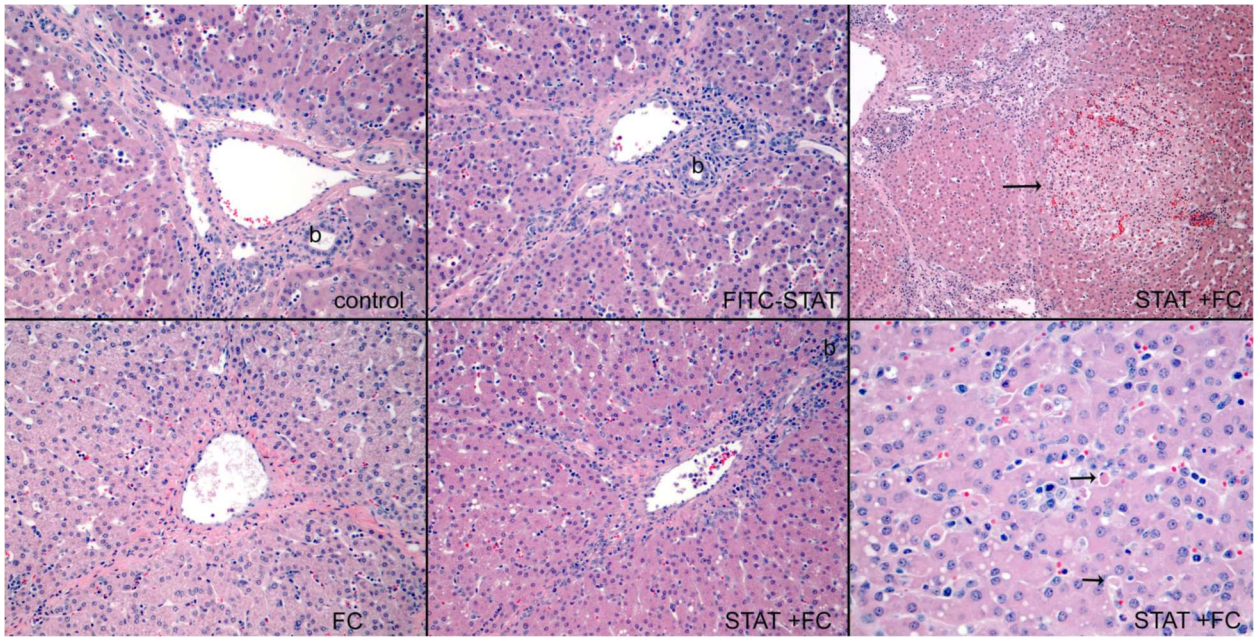

Figure S 17. Representative histology images from liver biopsies taken during aorta tear study.

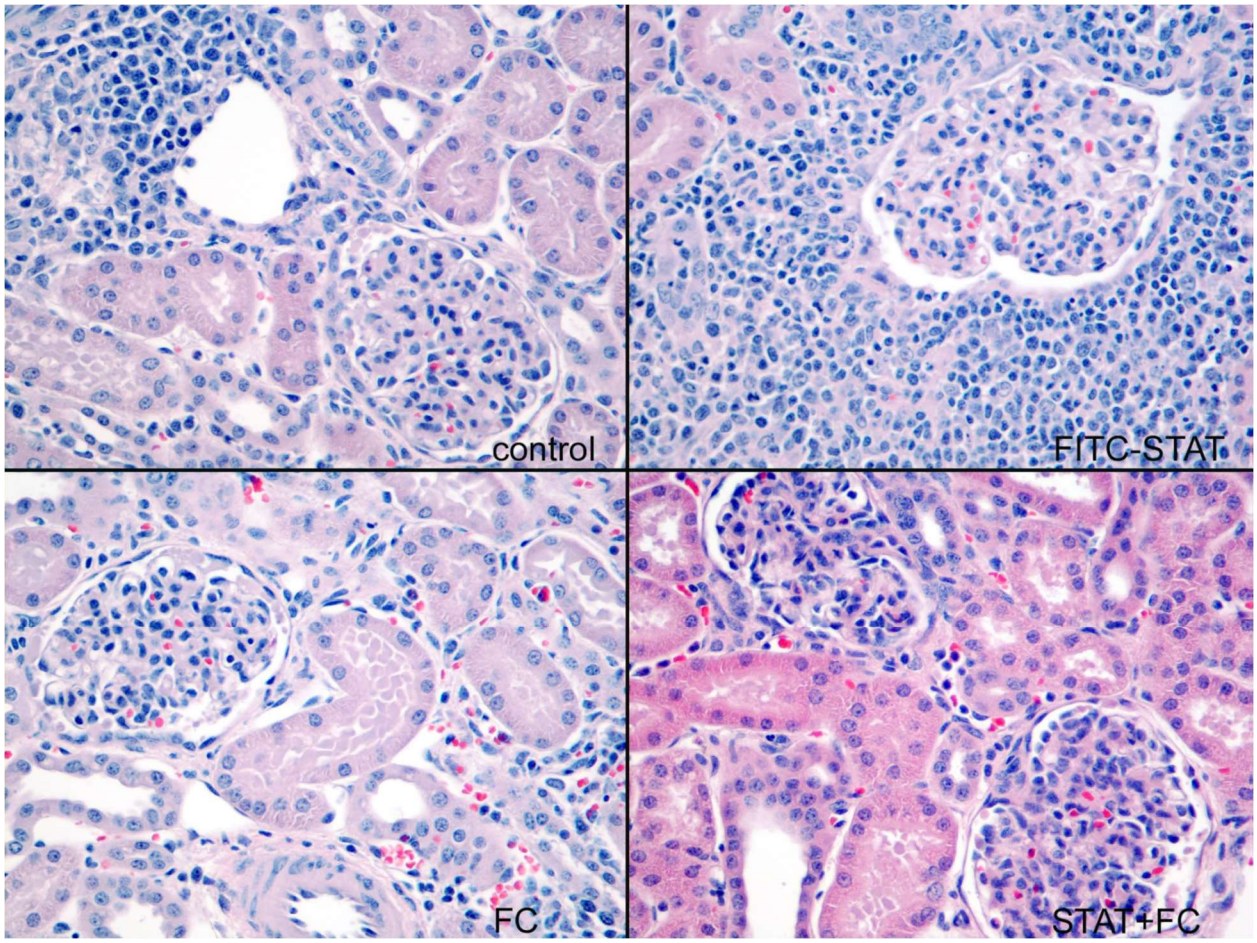

Figure S 18. Representative histology images from kidney biopsies taken during aorta tear study.

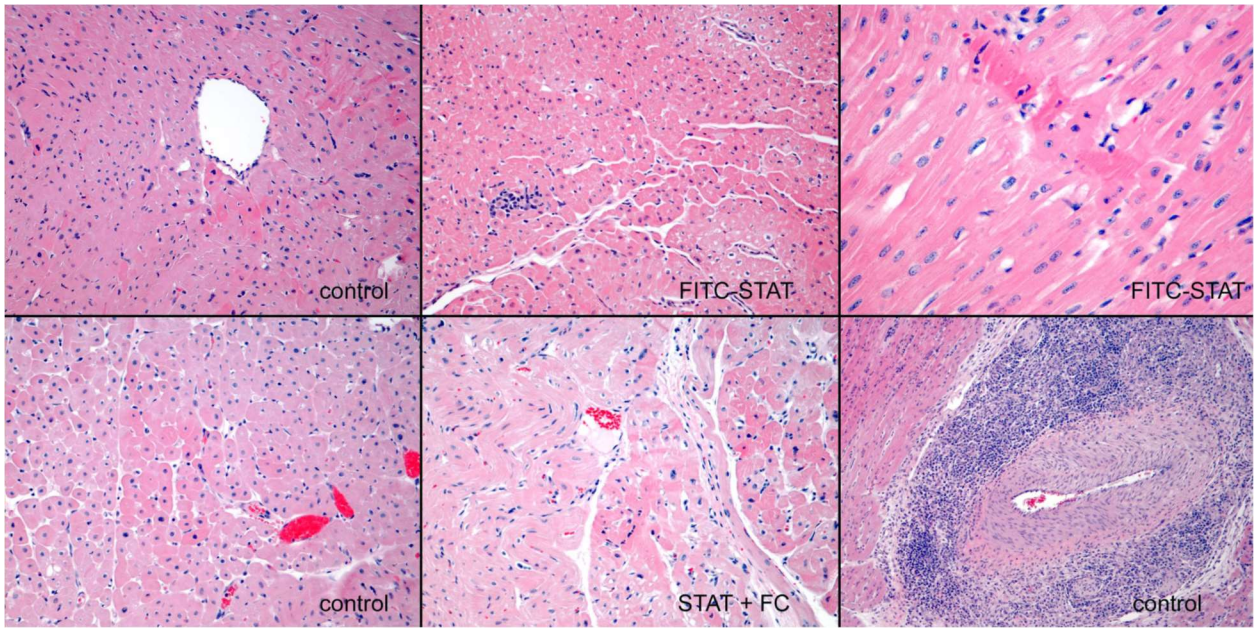

Figure S 19. Representative histology images from heart biopsies taken during aorta tear study.

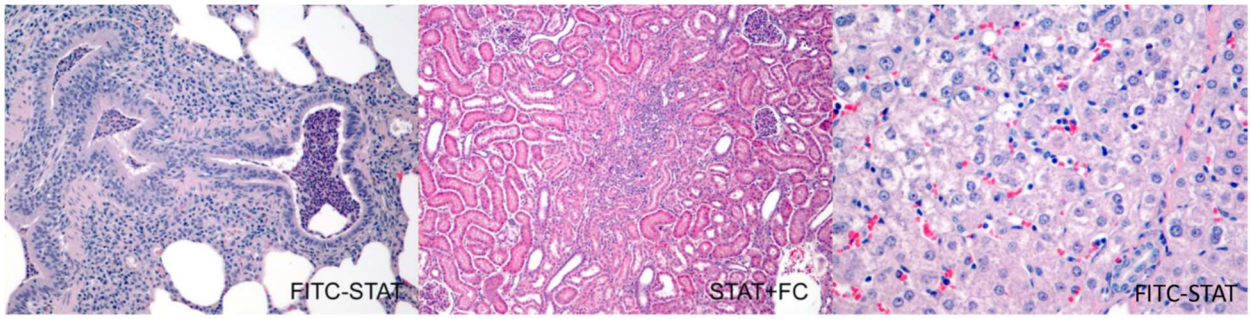

Figure S 20. Incidental lesions identified during evaluation of histology images by a blinded pathologist (left: lung, middle: kidney, right: liver).

Chapter 4. MECHANISTIC UNDERSTANDING OF POLYSTAT – CLOT CONTRACTION AND ANTIFIBRINOLYTIC

Trey J. Pichon, Melissa Ling, Mishti Dhawan, Dang Truong, Sophie Baggett, Ava Obenaus, Chang Yeop Han, Nathan J. Sniadecki, Suzie H. Pun, Nathan J. White

4.1 INTRODUCTION

The overall goal of this chapter is to analyze the mechanism by which PolySTAT affects clots. We started our inquiry from two observations from our prior studies: first, polySTAT-treated clots have higher contraction in whole blood compared to control blood and second, polySTAT-treated clots have reduced fibrinolysis compared to control clots.

Clot Contraction: We observed during both rat and swine studies that PolySTAT-spiked (5 µM) blood samples have increased clot contraction compared to the saline control (Fig 1, left). In addition, we observed in some ROTEM studies that the addition of PolySTAT led to traces that reflect clot lysis (Fig 1, center and right). The first part of this chapter investigates what could be leading to these observations.

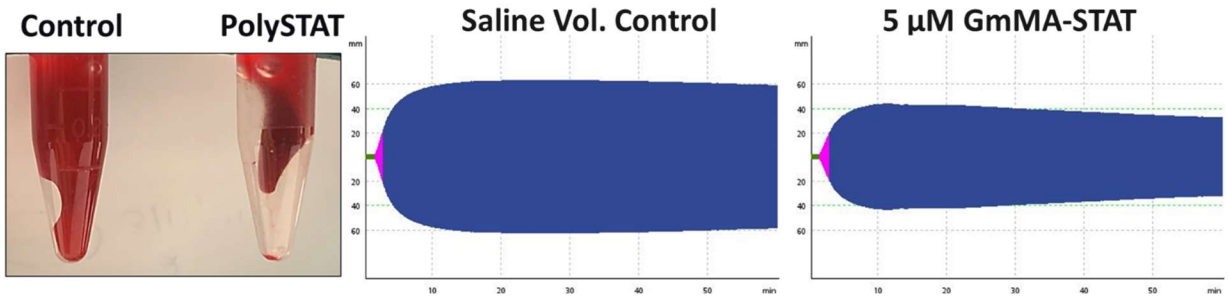

Figure 1. Overview of clot contraction artifacts seen when PolySTAT is spiked into the blood at 5 µM concentration. Left: Image visually showing the increased contraction due to PolySTAT. Center and Right: EXTEM of baseline swine blood that shows the clot lysis artifact observed with PolySTAT.

Anti-fibrinolysis: The second part of this chapter investigates the anti-fibrinolytic action of PolySTAT. Our previous work showed that PolySTAT's physical crosslinks decrease the pore size of fibrin networks, while increasing fibril density and thickness. These physical changes are thought to slow plasmin's diffusion through the clot, and increase the number of fibrils that need to be lysed to decrease clot strength. Our ROTEM studies in both purified protein systems and simulated trauma-induced coagulopathy plasma reveal that PolySTAT increases both clot firmness and lysis time. PolySTAT's may delay lysis through physical impacts on clot structure (fiber density/size, mechanical stiffness) or by impacting enzymes/zymogens of the fibrinolysis pathway (tPA, plasmin(ogen), uPA) (Figure 2 below).

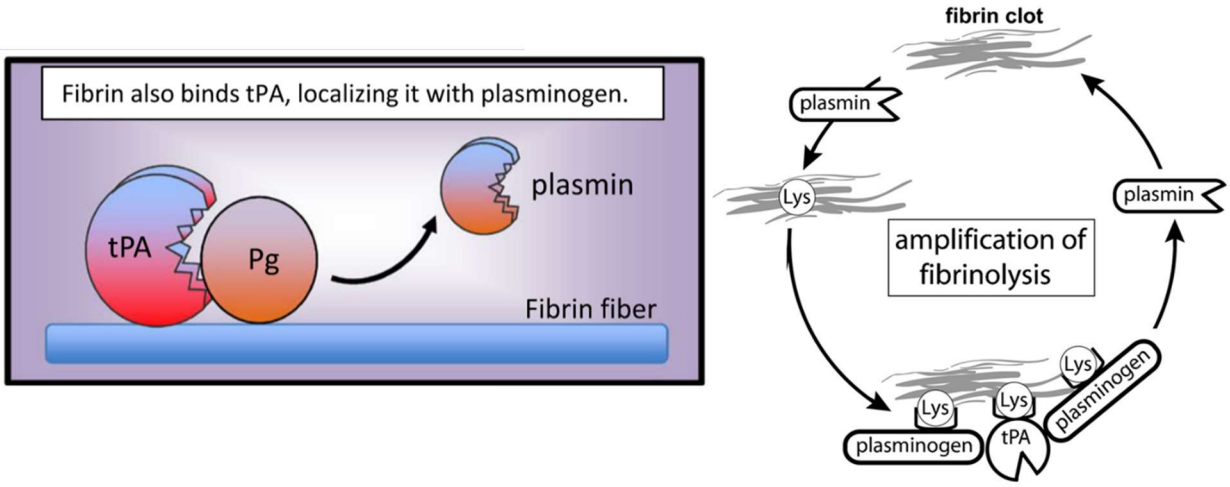

Figure 2. Fibrin catalyzes its own destruction. Left: Upon conversion of fibrinogen to fibrin, cryptic binding sites for both tPA and plasminogen are revealed, which enables the creation of plasmin. Figure was reused with permission from [1] by Marlien Pieters and Alisa S. Wolberg under the Creative Commons Attribution-NonCommercial-No Derivatives License (CC BY NC ND). Right: Plasmin degrades fibrin and leads to the creation of new binding sites for tPA and plasminogen, which further increases the concentration of plasmin. Figure was reused with permission from Taylor & Francis Online for [2] by Bonno N. Bouma and Laurent O. Mosnier.

Fibrin is known to catalyze its own destruction by two mechanisms. First, upon conversion from fibrinogen to fibrin, cryptic binding sites for tPA and plasminogen are revealed that enable the production of plasmin; bound tPA has ~100-1000 greater activity than in solution. Second, the digestion of fibrin gels into fibrin degradation products exposes C-terminal lysines that provide more binding sites for tPA and plasminogen. Additionally, the fibrin-binding peptide (FBP) used in PolySTAT is based on the Tn6 peptide XArXCPY(G/D)LCArIX (Ar = aromatic) developed by the Caravan group.[3,4] Tn6, in addition to binding fibrin (K_d = 2.9 μM), binds with high affinity to a mix of fibrin degradation products DD(E) comprised of both D-Dimers and two E fragments (K_d = 0.85 μM). While the exact binding sites for Tn6 are unknown, the number of equivalent binding sites N_{bd} were similar for both fibrin (N_{bd} = 2.4) and DD(E) (N_{bd} = 2.0). Considering that Tn6 binds DD(E), FBP is expected to bind other fibrin(ogen) degradation products such as Fragment X, Y, D, and a range of D-Dimers.

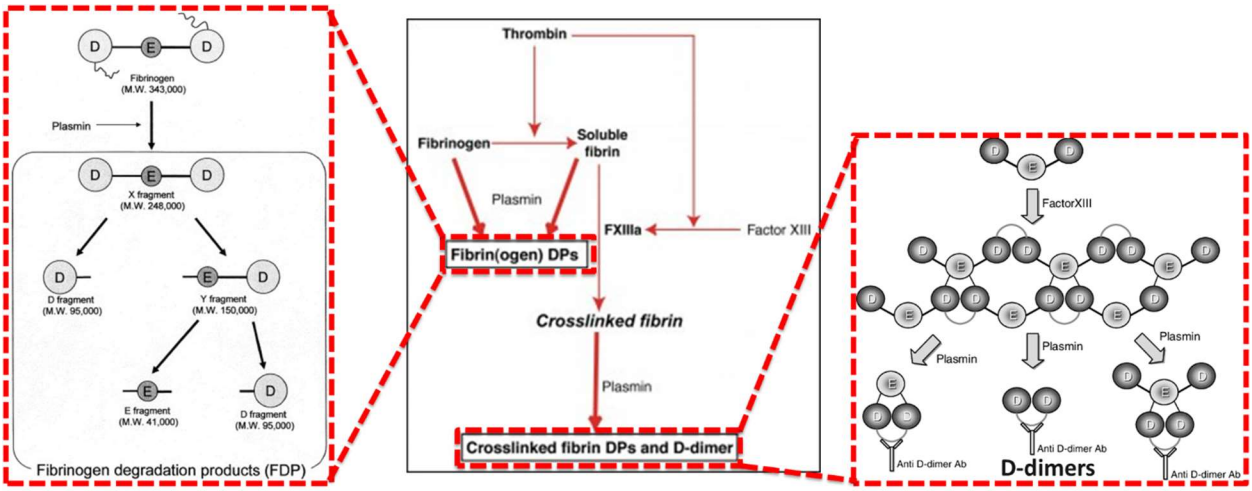

Figure 3. Plasmin can act on both fibrinogen and fibrin. Left: Overview of different fibrinogen degradation products after plasmin degradation. Figure was reused with permission from [5] by Hidenobu Aziawa *et al.* license no. 5611030702578 by Elsevier. Middle: Figure was reused with permission from eClinPath.com (Action of plasmin on fibrinogen or fibrin) [6] by Tracy Stokol under the Creative Commons Attribution-NonCommercial-ShareAlike 4.0 International License. Right: Overview of different fibrin degradation products due to FXIIIa crosslinking and plasmin degradation. Figure was reused without permission from [7] by Giuseppe Lippi *et al*.

These fibrinogen degradation products (FDPs) are elevated in the bloodstream in trauma, with increased D-Dimer concentration correlating with poorer outcomes.[8,9] Additionally, DD(E) has been shown to increase plasmin generation by tPA, while tPA and plasminogen both bind to D-Dimers.[10,11]

Due to the elevation of FDPs in the blood of trauma patients, we are interested in:

1) Is PolySTAT able to interfere with tPA-plasminogen binding/complexation on fibrin?
2) Do FDPs competitively inhibit PolySTAT's ability to bind fibrin?
3) Does PolySTAT localize FDPs to clots *in vivo* and increase fibrinolysis?

Given the difficulty of showing efficacy in swine, this mechanistic understanding is critical gap we need to fill for continued clinical translation of PolySTAT,

4.2 MATERIALS AND METHODS

4.2.1 *Materials*

Thrombin and FXIIIa, were purchased from Enzyme Research Laboratories (South Bend, Indiana) unless otherwise noted. Chromogenix Substrates S-2251 (Plasmin) and S-2288 (tPA) were purchased from DiaPharma Group, Inc. (West Chester, OH). Human whole blood was purchased from Bloodworks Northwest (Seattle, WA).

4.2.2 *Rheometer Clot contraction*

A method based on Tutwiler *et al.* was used.[12] Healthy donor whole blood (n=7) was collected in standard 3.2% sodium citrate tubes. The blood was evaluated within 4 hours of the blood draw. Blood samples were incubated with the treatment for 5 minutes prior to evaluation. A TA Instruments Discovery Series Hybrid Rheometer (DHR-3) equipped with a solvent trap was used. All experiments were conducted at 37 °C, 3% strain, 5 rad/sec with a 20 mm stainless steel cone and plate (1 degree). A rheometer gap of 313 μM with 131 μL of blood was used. Samples were reconstituted with thrombin/Ca and immediately pipetted onto the peltier plate.

4.2.3 *Platelet Plug Micropost Microfluidic Assay*

The microfluidic devices were manufactured out of polydimethylsiloxane (PDMS) using a soft lithography technique. Prior to the experiment, the channels were incubated with Alexa-647 labeled Bovine Serum Albumin (BSA-647) for 1 hour, rinsed with Tyrode's buffer, incubated with rat tail collagen I for an hour, and rinsed with Tyrode's buffer. Each sample was prepared with 960 μL of sodium citrated whole blood, 40 μL of p-selectin antibody (BioLegend concentration), and 53 μL of saline, polySTAT, or polySCRAM (5 μM). The blood was perfused through each microfluidic channel at a shear rate of 40,000 s^{-1} (volumetric flow rate of 120 μL/min) for the first 15-20 seconds, then reduced to a shear rate of 640 s^{-1} (volumetric flow rate of 3.2 μL/min) for the remaining time to avoid clogging the channel. Phase and fluorescent time-lapse images were taken every 2-3 seconds (control was every 2 secs, polySTAT and SCRAM were every 3 secs). The projected area of the plug and post deflection overtime were measured using custom MATLAB scripts. Platelet-plug contractile force (F) was determined from the deflection of the post (δ) using

Hooke's Law ($F = k\delta$) where the spring constant $k = (3\pi Ed^4)/(64L^3)$ and E is the modulus of elasticity of PDMS, d is the diameter of the post, and L is the length of the post. To obtain confocal images of the FITC-labeled polySTAT and polySCRAM the channels were flushed with a 0.9% saline to remove the remaining blood in the channel and fixed with paraformaldehyde.

4.2.4 *Platelet activation assay with polySTAT*

Aliquots of 450 µL of whole blood were incubated for 5 min at room temperature with 50 µL of 50 µM polySTAT or polySCRAM, DPBS 2% fetal bovine serum (FBS, Gibco), or adenosine diphosphate (ADP, Bio/Data) for positive activation control. Aliquots of 5 µL were then incubated with antibody solutions of FITC antihuman PAC-1 (1:10, BD Biosciences), APC antihuman CD62P (1:10, BD Biosciences), and/or PE antihuman CD61 (1:10, BD Biosciences) for 20 min at room temperature. Cells were fixed in DPBS 1% PFA and analyzed on an Attune NxT (Invitrogen) flow cytometer.

4.2.5 *PolySTAT binding assay with polySTAT*

Isolation of platelets from whole blood

Whole blood (Bloodworks) was centrifuged at 200g for 20 min at room temperature. Platelet-rich plasma from the top layer was diluted at 1:1 v/v ratio with Dulbecco's phosphate-buffered saline (DPBS, Gibco) supplemented with 2 mM ethylenediaminetetraacetic acid (EDTA, Invitrogen) and centrifuged at 100g for 20 min at room temperature. The supernatant was separated and centrifuged at 800g for 20 min at room temperature to pellet platelets. Platelets were rinsed with DPBS 2 mM EDTA and resuspended in DPBS.

Platelet-binding assay

Aliquots of 10^6 platelets were pelleted at 800g for 5 min at room temperature and incubated for 20 min at room temperature with 20, 5, 1, or 0 µM of FITC-labelled polySTAT or polySCRAM in DPBS supplemented with 1% bovine serum albumin (Miltenyi). Platelets were fixed in 200 µL of DPBS 1% BSA 0.1% paraformaldehyde (Alfa Aesar) and analyzed on an Attune NxT (Invitrogen) flow cytometer.

4.2.6 *Chromogenic assay with polySTAT and fibrin gels*

PolySTAT, polySCRAM, TXA, or HEPES buffer treatments were added to a 96-well plate (Corning) with final concentrations of 0.2 to 20 μM for polySTAT, 5 μM for polySCRAM, and 15 μg/mL for TXA. Plasminogen, thrombin, calcium chloride, tissue plasminogen activator (tPA), and Chromogenix Substrate 2251 (Diapharma) were added in final concentrations of 8.46 μg/mL, 0.5 NIH U/mL, 10 mM, 25 ng/mL, and 0.8 mM, respectively. Fibrinogen was added last to form gels in final concentrations of 0.5, 1.5, and 4.5 mg/mL. Absorbance measurements were taken at 405 nm on a Tecan plate-reader every 5 min for 120 min at 37°C.

4.2.7 *Turbidity assay and lysis times with polySTAT and fibrin-degradation products (FDPs)*

Titrations of fragment E, fragment D, D-dimer, and BSA negative control were added to a 96-well plate with final concentrations of 0.039 μg/mL to 10 μ/mL. Treatments of polySTAT and polySCRAM were added to each titration with final concentrations of 5 μM. Plasminogen, thrombin, calcium chloride, and tPA were added in final concentrations of of 8.46 μg/mL, 0.5 NIH U/mL, 10 mM, and 25 ng/mL, respectively. Fibrinogen was added last to form gels in a final concentration of 0.5 mg/mL. Absorbance measurements were taken at 340 nm on a Tecan plate-reader every 5 min for 120 min at 37°C. Lysis times were calculated as the time taken to reach half of the maximum absorbance in Graphpad Prism.

4.3 Clot Contraction: Results and Discussion

<u>PolySTAT creates clot contraction artifacts in ROTEM of rat and swine whole blood.</u>

During rat studies, artifacts in ROTEM were observed that resembled clot lysis when PolySTAT was spiked into the blood samples at a final concentration of 5 μM (Figure 4).

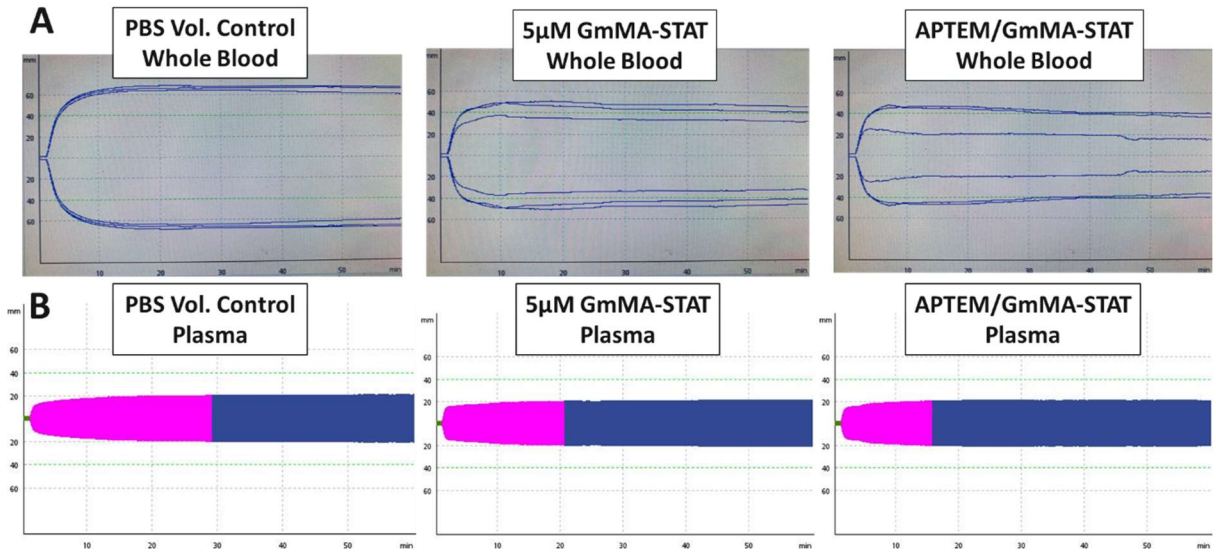

Figure 4. PolySTAT creates clot contraction artifacts in ROTEM with rat blood from an LPS model of sepsis. A) No lysis artifacts were observed with blood spiked with PBS as a volume control. APTEMs were run to see if the reduction in clot firmness was due to lysis, and aprotnin was unable to rescue clot firmness. B) Blood samples were spun down to remove platelets, and plasma was evaluated in EXTEM. No lysis was observed indicating that platelets were responsible for the ROTEM artifacts.

The artifacts were not observed in rat blood without PolySTAT. Samples were run with Aprotinin (APTEM), which inhibits lysis, however the artifacts were still observed. Next, the blood was spun down to remove platelets, and run again. No artifacts were observed supporting hypothesis that the artifact was due to platelet-induced clot contraction. Similar artifacts were once again observed during swine studies for the aorta tear hemodilution model (Figure 5 below).

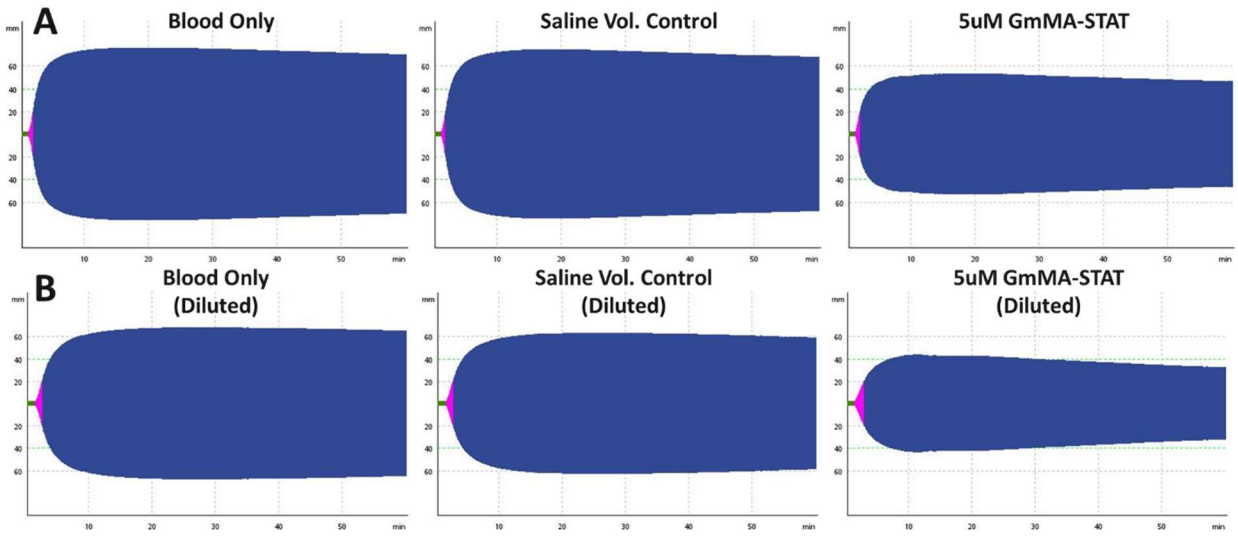

Figure 5. PolySTAT creates clot contraction artifacts in ROTEM with both normal and hemodiluted pig blood. Similar clot contraction artifacts to rats were observed in swine blood. A) Normal baseline blood. B) Hemodiluted swine blood.

The contraction artifacts were observed in both baseline blood and hemodiluted blood when PolySTAT was spiked in at 5 µM. Again, APTEM analysis confirmed the artifact was not due to lysis but rather platelet-induced contraction. To observe this contraction visually, samples of blood were mixed with PolySTAT following the same protocol as for ROTEM analysis except pipetting the mixtures into a clear Eppendorf tube instead of a ROTEM cup for easy visualization (Figure 6). We could clearly observe more rapid clot contraction in all PolySTAT-treated blood compared to blood mixed with saline.

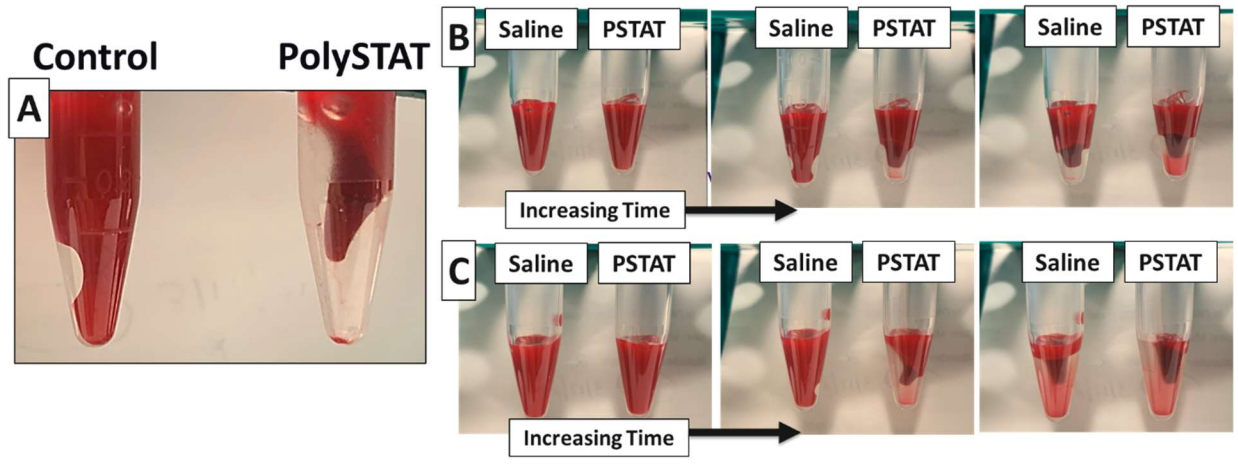

Figure 6. PolySTAT visually increases clot contraction in both normal and hemodiluted pig blood. A) Representative image of swine whole blood with and without PolySTAT. PolySTAT increases overall clot retraction of the clot. B) Normal baseline swine blood treated with PolySTAT showed faster clot retraction. C) Similar results were observed with hemodiluted swine blood.

Next, a rheometer was used to measure platelet contraction forces (Figure 7 below).

Figure 7. Contraction forces of undiluted whole human blood was measured in n=7 donors using a rheometer. Platelet function diminishes after four hours, and each rheometer run takes 30 minutes to complete. It was also found that best practice requires n=3 runs (repeats) need to be run per treatment and averaged together for each donor. Therefore, only two treatments can be compared due to time constraints.

A small amount of blood ~131 µL treated with either PolySTAT or PolySCRAM (final concentration = 5 µM) is sandwiched between a cone and plate after being activated by thrombin. A small oscillation is applied to measure the storage and loss modulus over time as the blood clots. The gap on the rheometer is fixed and the rheometer applies an upward force to maintain the gap as the blood contracts, pulling down on the plate. The force required by the rheometer to counter the platelet contraction force is reported as a negative value due to the direction it is applied on the rheometer (up = negative, down = positive). Figure 8 below shows the full curves for each donor.

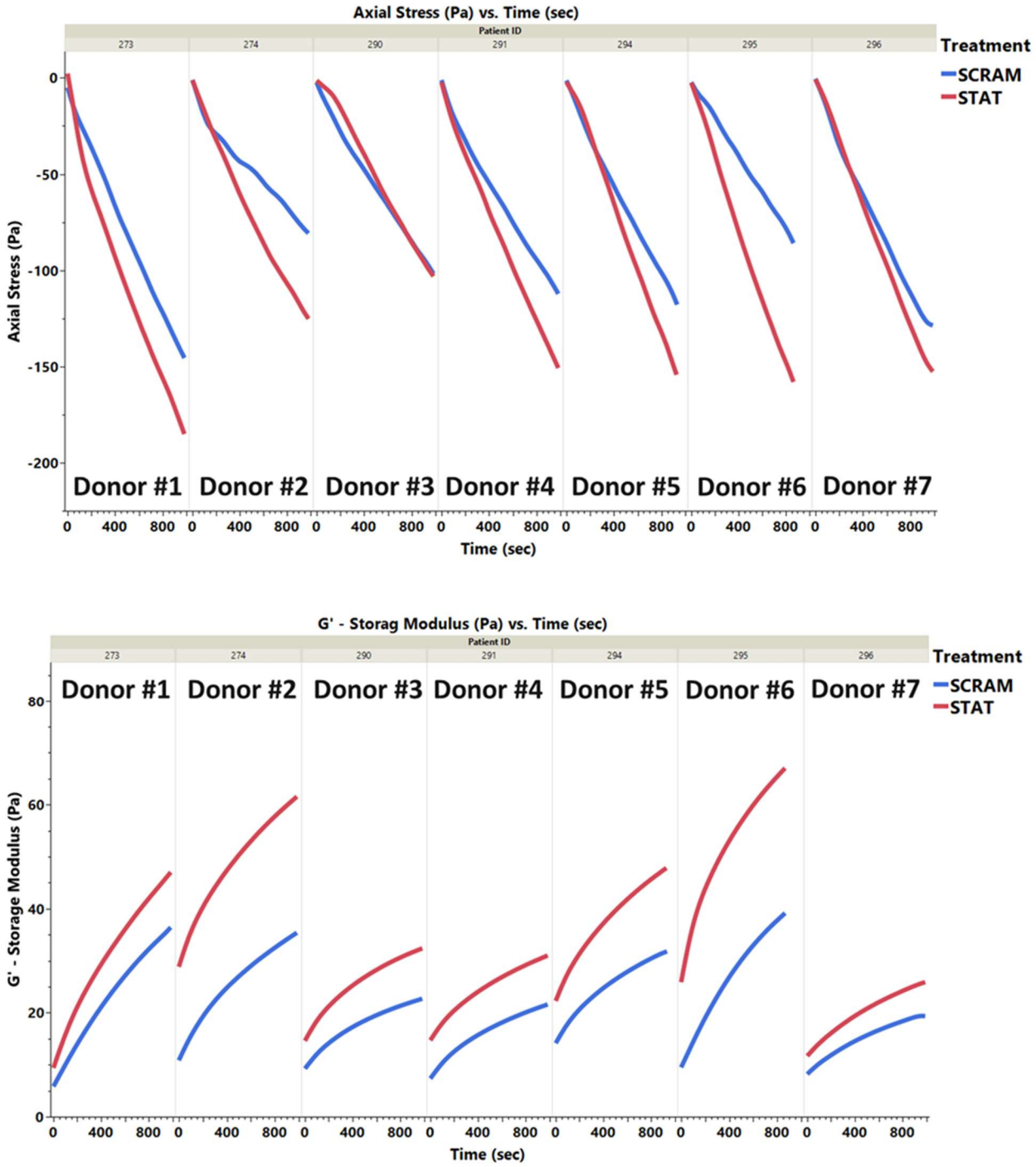

Figure 8. Rheometer measurements of clot contraction forces (top) and clot storage modulus (bottom) of undiluted whole human blood (n=7 donors). The lines, red = PolySTAT (5μM) and blue PolySCRAM control (5 μM), show the average of n=3 repeats per donor.

PolySTAT increased both clot elastic modulus and clot contraction forces compared to the PolySCRAM control. Figure 9 displays the compiled parameters from the rheometer analysis.

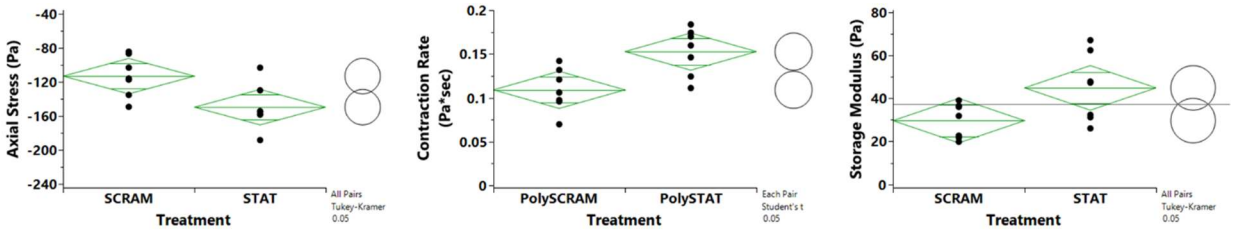

Figure 9. Compiled axial stress, contraction rate, and storage modulus for rheomoeter measurements of human whole blood (n=7). Left: Overall contraction forces or axial stress were higher for PolySTAT treated blood compared to PolySCRAM controls. The negative value is due to the direction of the force on the rheometer. Results were statistically significant, two-sided t-test = 0.0194, SCRAM = -113 Pa, and STAT = -150 Pa. Middle: The rate of force generation was higher for PolySTAT treated clots compared to PolySCRAM controls. A linear fit was done to the linear portions of the axial stress vs time data and the slope was taken as the rate of force generation. Results were statistically significant, two-sided t-test = 0.0080, SCRAM = 0.109 Pa/sec and STAT = 0.153 Pa/sec. Right: PolySTAT treated clots had a higher storage modulus compared to the PolySCRAM treated controls. Results were statistically significant two-sided t-test = 0.0430, SCRAM = 29.7 Pa, STAT = 44.9 Pa. A fit model for a repeated measure, one-way anova with tukey post-hoc analysis ($\alpha = 0.050$) with donor as a random source effect was used.

PolySTAT increases clot contraction forces, contraction rate, and storage modulus of clots in human blood. Now that we confirmed the increase in clot contraction, we were interested to see if this occurred in primary hemostasis or only during secondary hemostasis. Therefore, we used a microfluidic platelet plug assay developed by the Sniadecki group to evaluate PolySTAT's effect on primary hemostasis (Figure 10 below).

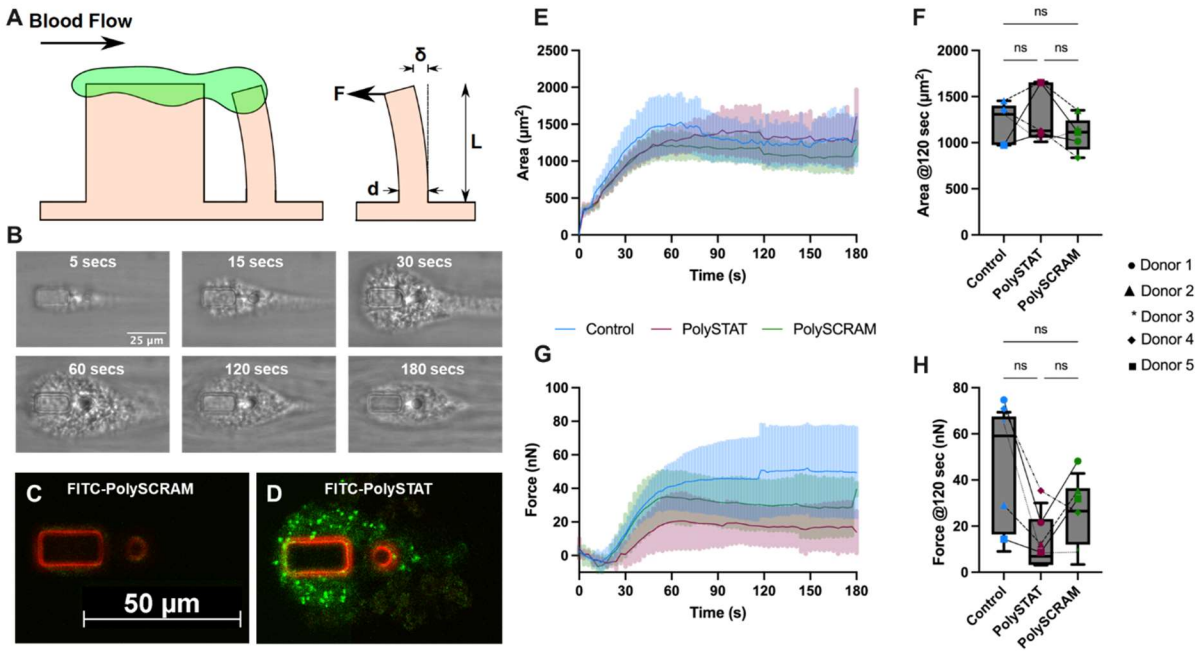

Figure 10. PolySTAT has no effect on platelet-plug area or contractile force. (A) A PDMS microfluidic channel was comprised of eight discrete force sensors comprised of a rigid block and flexible post. As blood was perfused through the channel, the block created a high shear gradient to activate platelets and the platelets aggregated (green) around the force sensor, encapsulating the post. As the platelets contracted, they deflected the post. Post deflection (δ) was measured to calculate platelet-plug contractile force (F) using Hooke's Law ($F = k\delta$) where $k = (3\pi Ed4)/(64L3)$ and E is the modulus of elasticity, d is the diameter of the post, and L is the length of the post. (B) A top-down view of phase images showing platelet-plug growth overtime. (C) FITC-labeled PolySCRAM did not bind to the platelet plug, while (D) FITC-labeled PolySTAT did. (E) Average platelet-plug area over time. (F) Average platelet-plug area 120 seconds after blood entered the channel. (G) Average platelet-plug contractile force over time. (H) Average platelet-plug contractile force 120 seconds after blood entered the channel. Statistics are a one-way ANOVA with a Turkey's multiple comparisons test (ns is $p>0.05$).

We confirmed using FITC-labeled PolySTAT that PolySTAT was incorporated into the platelet plugs, whereas FITC-labeled PolySCRAM was not seen colocalized with platelet plugs. In n = 5 human blood donors, PolySTAT did not statistically lead to a change in either platelet plug area nor platelet plug forces. It should be noted that in platelet plug forces there was a trend towards PolySTAT decreasing forces compared to controls. Overall, while PolySTAT did localize to the

platelet plugs, PolySTAT did not inhibit platelet plug formation nor did it affect primary hemostasis. We were interested to evaluate how much of the localization is due to fibrin in the platelet plugs or due to non-specific binding with platelets. We attached FITC to the same fibrin-binding peptide (FBP) that is conjugated to PolySTAT. This FITC-labeled FBP has been used by other groups to image fibrin networks in confocal microscopy.[13] Figure 11 below shows that the FITC-labeled FBP binds to the platelet plug similar to PolySTAT, thus confirming that fibrin is present in the platelet plug.

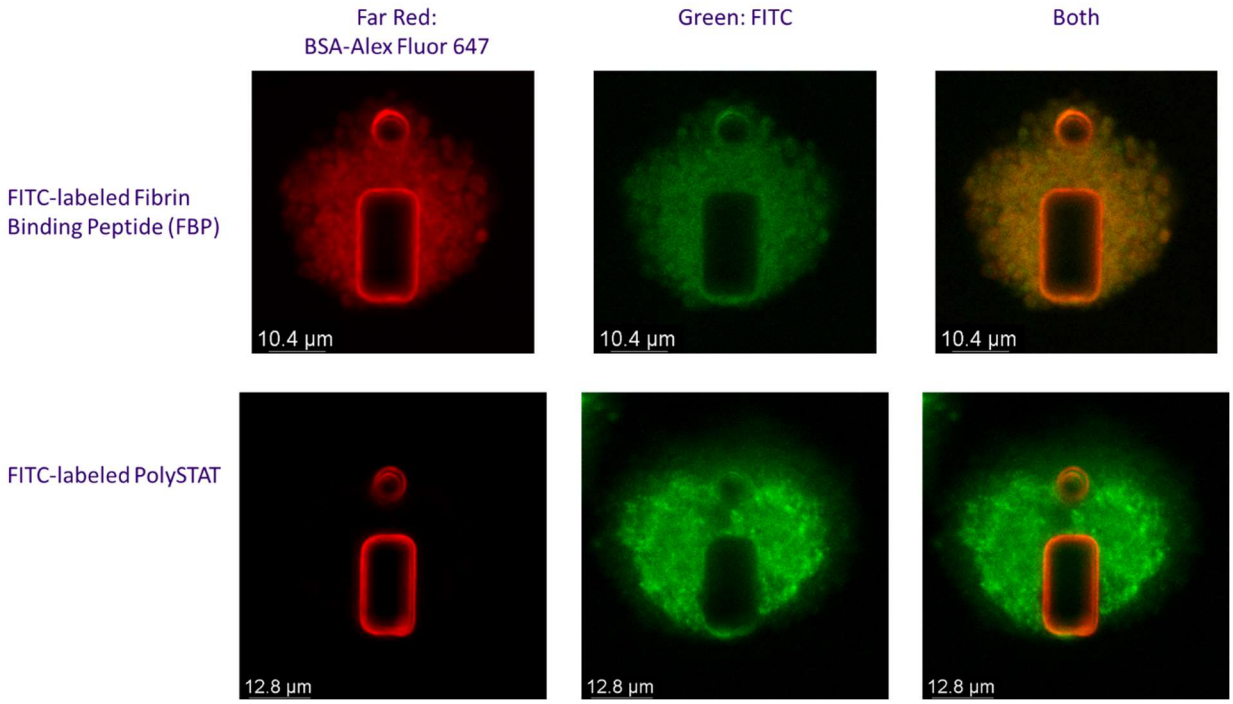

Figure 11. Confocal microscopy of fixed platelet plugs from microfluidic assay. Top: FITC-labeled FBP binds to platelet plugs. Bottom: FITC-labeled PolySTAT binds to platelet plugs.

During platelet plug formation, platelets bind fibrinogen via integrin αIIbβ3, and fibrinogen bridges neighboring platelets. During activation, platelets secrete α-granules containing thrombin, which converts the bound fibrinogen into fibrin.[14] Additionally, platelet plugs exhibit a core-shell morphology, where there is a tight platelet core that is difficult to be penetrated by 70 kDa dextran (PolySTAT ~50kDa).[15] However, the shell has ~2x the porosity compared to the core, contains fewer p-selectin positive platelets, and a higher concentration of fibrin. The Sniadecki group have confirmed that their *in vitro* platelet plugs exhibit a core-shell morphology that can be seen via a

p-selectin binding fluorescent antibody. Therefore, the PolySTAT is most likely binding to the shell of the plugs and not the core. Next, flow cytometry was used to investigate non-specific binding of PolySTAT to platelets (Figure 12 below).

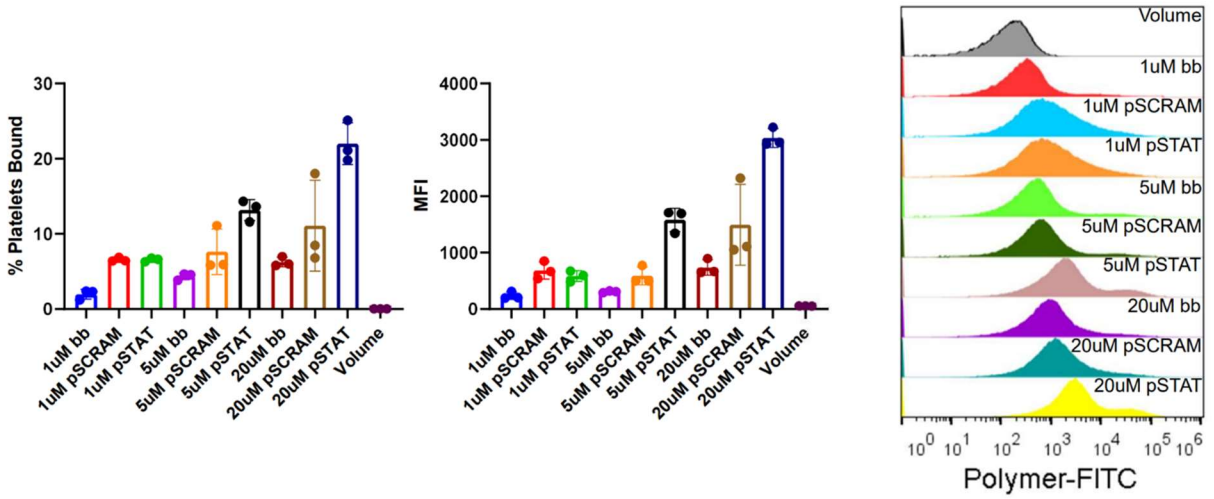

Figure 12. PolySTAT nonspecifically binds to platelets at 5 µM and 20 µM concentrations. FITC-labeled PolySTAT, PolySCRAM, and polymer backbone "bb" were incubated with washed platelets at 5 µM and 20 µM concentrations.

Flow cytometry confirmed that PolySTAT does nonspecifically bind to platelets more than both the PolySCRAM control and the backbone polymer. There are several possible explanations for the higher binding of PolySTAT vs PolySCRAM to platelets. First, the FBP in PolySTAT includes a chloro-tyrosine which was altered to an alanine in scrambled FBP to ensure lack of binding to fibrin. Second, the two peptides have different distributions of hydrophobic amino acids in the sequence which may lead to differences in non-specific hydrophobic interaction to platelets. Finally, there could be differences in absolute number of peptides attached to PolySTAT versus PolySCRAM. Unfortunately, due to the FITC-labeling of the backbone, we are unable to run UV-Vis to measure the number of peptides attached to both PolySTAT and PolySCRAM. Due to the nonspecific binding of PolySTAT to platelets, we were interested to see if the binding leads to platelet activation, which would be concerning for systemic thrombosis. Figure 13 below shows the evaluation of platelet activation via flow cytometry.

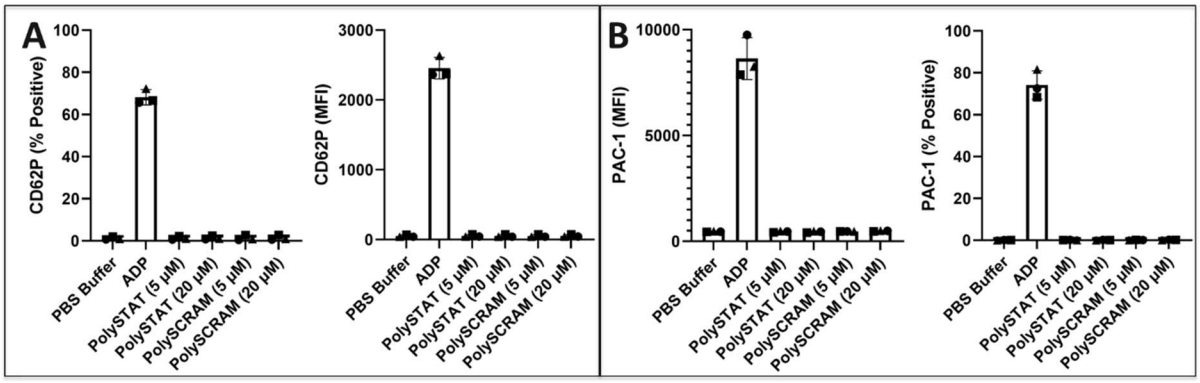

Figure 13. PolySTAT does not activate platelets via flow cytometry. Washed platelets from n=3 human donors were evaluated for platelet activation after being incubated with PBS, PolySTAT, and PolySCRAM at 5uM and 20uM concentrations. ADP was used as a positive control and showed platelet activation via PAC-1 and CD62P (P-selectin).

PolySTAT and PolySCRAM do not activate washed platelets (both PAC-1 and P-selectin negative) from human donors (evaluated within 30 minutes of collection), whereas the ADP positive control showed strong activation. SI Figure 1 shows the raw flow plot. Although we did not see any impact to platelet plug formation in the microfluidic assay, we wanted to make sure that the nonspecific absorption of PolySTAT did not interfere with the platelets' ability to aggregate. We used the traditional platelet aggregometry assay (Figure 14 below).

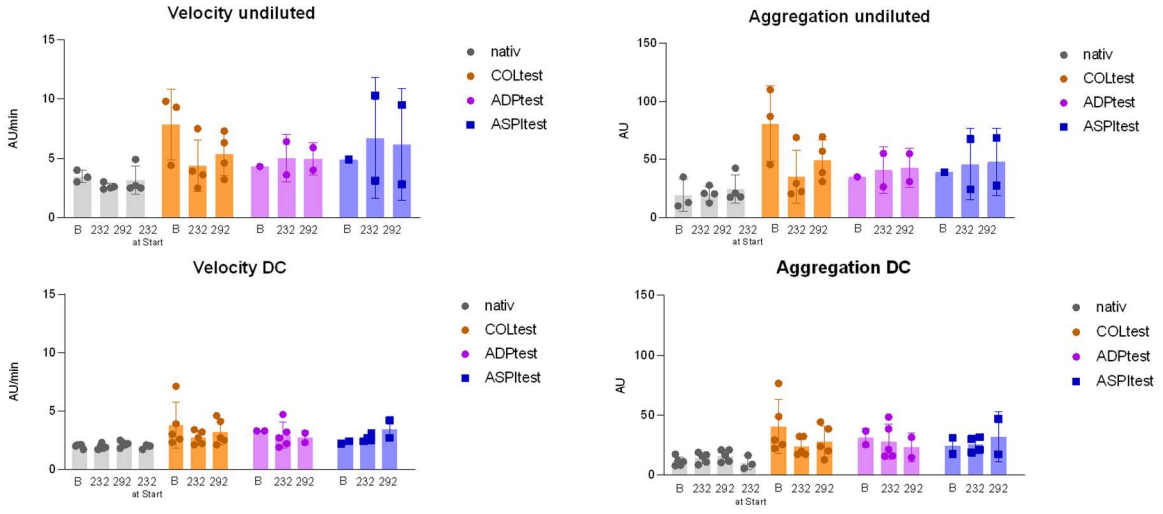

Figure 14. PolySTAT does not activate platelets via multiplate analysis. PolySTAT does not activate platelets in multiplate aggregometry in both diluted and undiluted blood at 5uM concentration. Key: B = Saline control, 232 = PolySTAT, and 292 = PolySCRAM.

We did not see any difference in platelet aggregation for the PolySTAT or PolySCRAM compared to the volume control. From the microfluidic, flow cytometry, and platelet aggregation data we see no signs that PolySTAT directly acts on platelets to increase platelet forces, nor does it affect primary hemostasis. Therefore, we hypothesize that PolySTAT's ability to increase clot contraction and platelet contraction forces is a result of the PolySTAT-driven changes to the fibrin network. For example, PolySTAT may improve the ability of the fibrin network to mechanotransduce platelet forces, making the fibrin less likely to rupture due to platelet forces, or the stiffening of the fibrin network may induce the platelets to pull harder, as it is well known that platelets are mechano-sensitive.[16,17]

We next evaluated whether a large dose of FXIIIa would replicate the effect caused by PolySTAT. Tutwiler et al. found that clot retraction can be broken down into three phases – 1) initiation, 2) linear, and 3) clot stabilization. When FXIIIa is inhibited, clot contraction stalls and is not able to undergo phase 3, which is the phase when the most contraction occurs.[12] We hypothesized that PolySTAT's faster stabilization of clots compared to FXIIIa is key to the contraction artifacts. FXIIIa is produced early on in clotting, when ~1% to 2% of fibrinogen has been converted to fibrin (20% is needed to make a visible thrombus), meaning FXIIIa is working on soluble fibrin fibrils. However, the plasma concentration of fibrinogen and FXIII are 9 μM and 0.07 μM, respectively, while PolySTAT reaches 5 μM in plasma in our dosing regimen. Therefore, PolySTAT can start binding and physically crosslinking fibrin much earlier in hemostasis compared to FXIIIa. It is estimated that FXIIIa begins crosslinking γ-chains between neighboring fibrin molecules within 5 to 10 minutes, however α-chain crosslinking occurs more slowly. The α-chain crosslinks increase tensile strength of fibers by increasing protofibril density, and the α-chain crosslinks prevent fibrinolysis by impeding the ability of plasmin to cleave fibrin.[18]

We hypothesized a high dose of FXIIIa spiked into the blood would similarly increase clot contraction and platelet contraction forces. Figures 15 and 16 below show rheometer measurements of platelet contraction forces for 0.1 µM addition of FXIIIa to human blood.

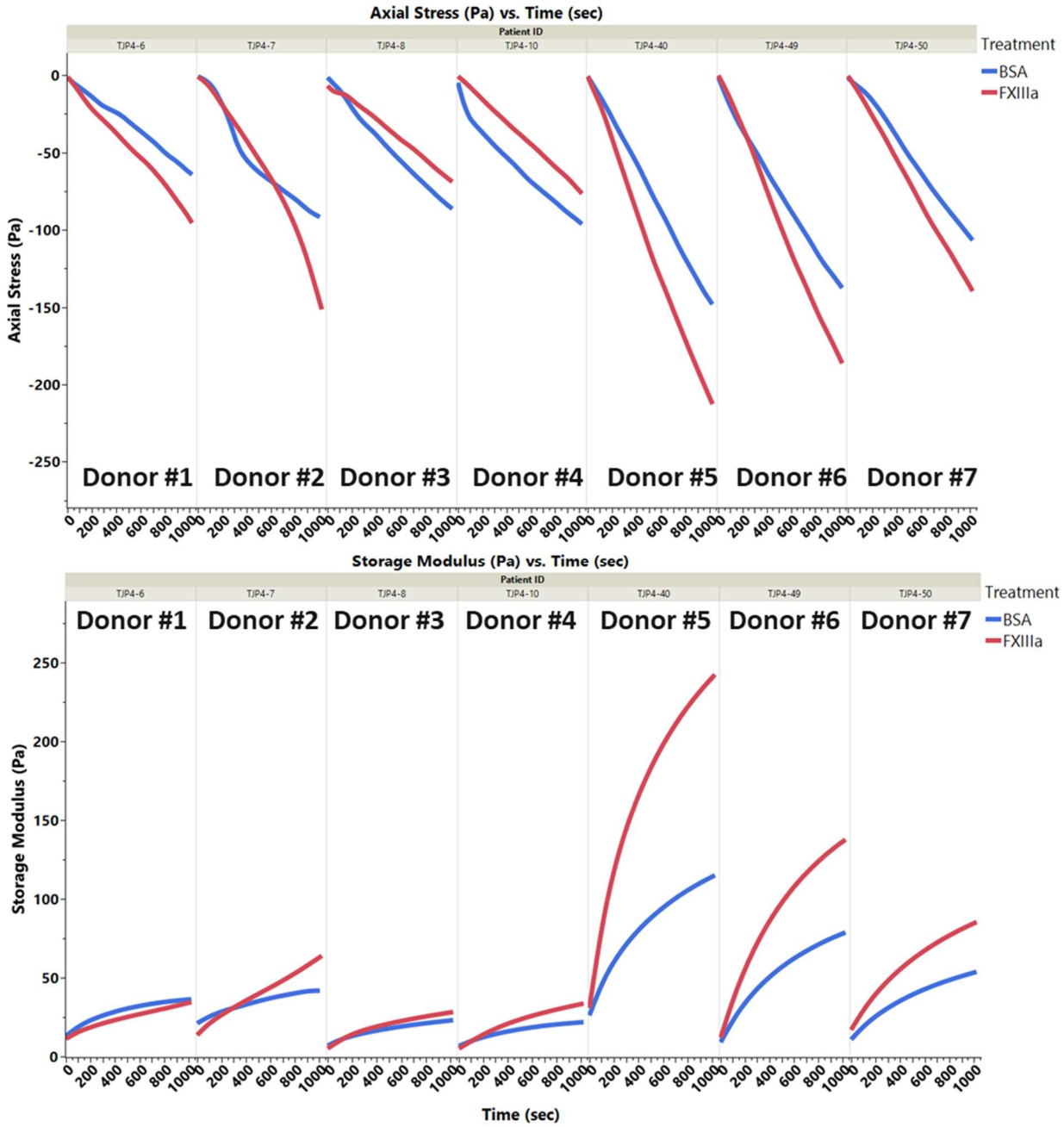

Figure 15. Rheometer measurements of clot contraction forces (top) and clot storage modulus (bottom) of undiluted whole human blood (n=7 donors). The lines, red = FXIIIa (0.1µM) and blue BSA control (0.45µM), show the average of n=3 repeats per donor.

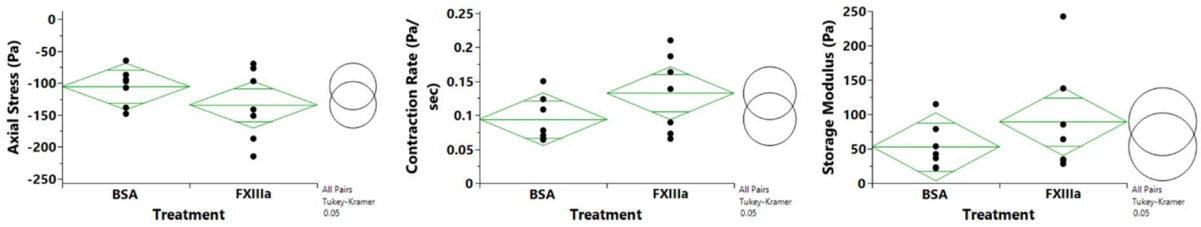

Figure 16. Comparison of axial Stress (left), contraction Rate (middle), and storage modulus (right) measured for 0.1µM FXIIIa spiked into human blood (n=7 donors). Left: There was no statistically significant increase in axial stress when comparing FXIIIa to BSA ($p = 0.071$). Middle: There was a statistically significant increase in contraction rate of FXIIIa spiked blood compared to BSA (0.0379). Left: There was no statistically significant change in storage modulus when comparing FXIIIa to BSA ($p = 0.075$). A fit model for a repeated measure, one-way anova with tukey post-hoc analysis ($\alpha = 0.050$) with donor as a random source effect was used.

The 0.1µM dose of FXIIIa did increase the contraction rate of platelets compared to BSA. While there was no statistically significant increase in axial stress and storage modulus, there was a trend similar to PolySTAT. The clot contraction still needs to be confirmed visually using Eppendorf tubes as was done in Figure 16 above.

4.4 Clot Contraction: Conclusions

We confirmed that the ROTEM artifacts due to PolySTAT in both swine and rat blood were due to an increased amount of clot contraction. The contraction forces were quantified with a rheometer and showed in normal human blood that PolySTAT increases the rate of platelet contraction forces, increases the overall clot contraction forces, and increases the elastic modulus of whole blood clots. Further investigation showed PolySTAT does not act directly on platelets and does not affect primary hemostasis. Therefore, the increase in clot contraction is a result of changes in the fibrin network due to PolySTAT. Our lead hypotheses are that PolySTAT is either increasing the mechanotransduction efficiency of the fibrin network early on in clotting, enabling clot contraction to occur faster OR that the increase stiffness of the fibrin network due to PolySTAT is causing platelets to pull harder on the network due to their mechanosensitive nature. In all likelihood it is a combination of the two, and trying to decouple them to measure the relevant contribution of each

would be difficult to do. We showed a high dose of FXIIIa shows similar results as PolySTAT although not statistically significant in overall axial stress, and clot modulus. Visual clot contraction with FXIIIa still needs to be evaluated visually, and it would be interesting to evaluate even higher doses of FXIIIa.

Overall, the current body of work has important implications for the translation of PolySTAT:

1. We showed for the first time that PolySTAT does not affect primary hemostasis, which further supports the safety of PolySTAT.
2. It is unknown if the increased clot contraction due to PolySTAT is beneficial or detrimental to clotting. Typically, the contraction of clots is essential and beneficial to hemostasis, however too much contraction could stress a clot and cause it to pull away from the ECM on the backside of vessels.

4.5 Anti-fibrinolytic Mechanism: Results and Discussion

4.5.1 *Evaluation of PolySTAT's effect on tPA and Plasminogen in solution (no fibrin gel)*

We first evaluated tPA's activity by a commercial tPA chromogenic assay. As tPA cleaves a substrate, a para-nitroaniline chromophore is released and absorbance is read at 405 nm. This was used to quantify enzymatic activity. The activity of tPA was measured in the presence of PolySTAT, PolySCRAM, and a HEPES volume control (Figure 17 below).

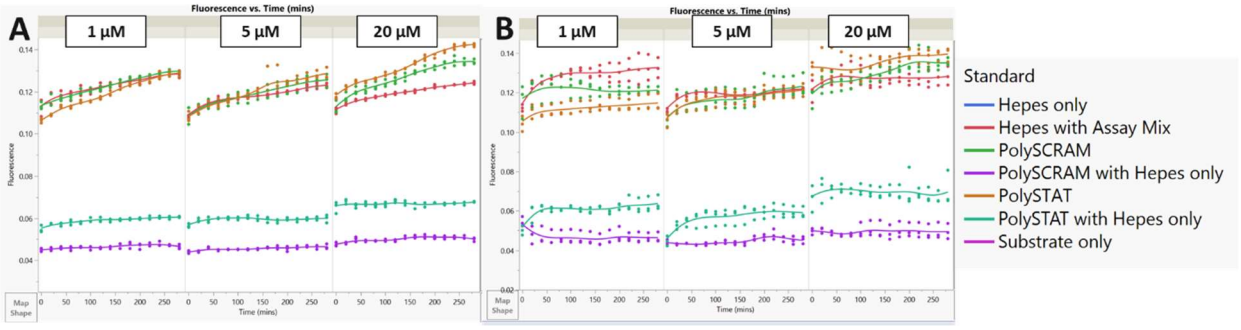

Figure 17. tPA chromogenic assay absorbance measurements over five hours (n=2). A) First replicate of purified system and B) second replicate. There was no difference in tPA activity at 1

µM, 5 µM, and 20 µM concentration of PolySTAT and PolySCRAM compared to the HEPES volume control.

There was no difference between tPA activity towards the chromogenic substrate in the presence of PolySTAT versus PolySCRAM and the volume control. Overall, tPA activity was very low free in solution. It is well-known that tPA activity increases 2-3 orders of magnitude in the presence of fibrin.[11] Next, we evaluated plasmin generation from plasminogen by tPA in another commercial chromogenic assay. This used a substrate that was plasmin cleavable, and the para-nitroaniline chromophore absorbance at 405 nm was used to monitor the production of plasmin. Figure 18 below shows the raw curves of the tPA-Plasminogen chromogenic assay.

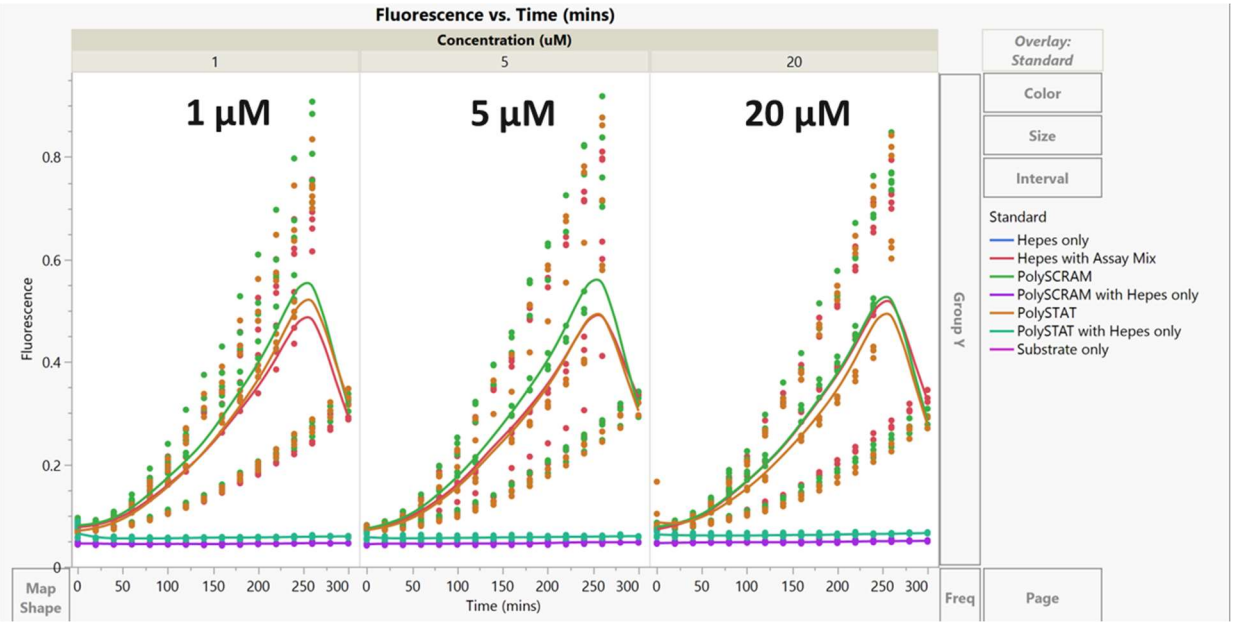

Figure 18. tPA-Plasminogen chromogenic assay absorbance measurements over five hours (n=2). Overlay of triplicate analysis. There was no difference in plasmin generation at 1 µM, 5 µM, and 20 µM concentration of PolySTAT and PolySCRAM compared to the HEPES volume control.

Similar to the tPA chromogenic assay, when plasminogen is free in solution (no fibrin present), PolySTAT does not affect the generation of plasmin by tPA. Figure 19 shows the change in absorbance over time (slope of the linear portions of the raw curves).

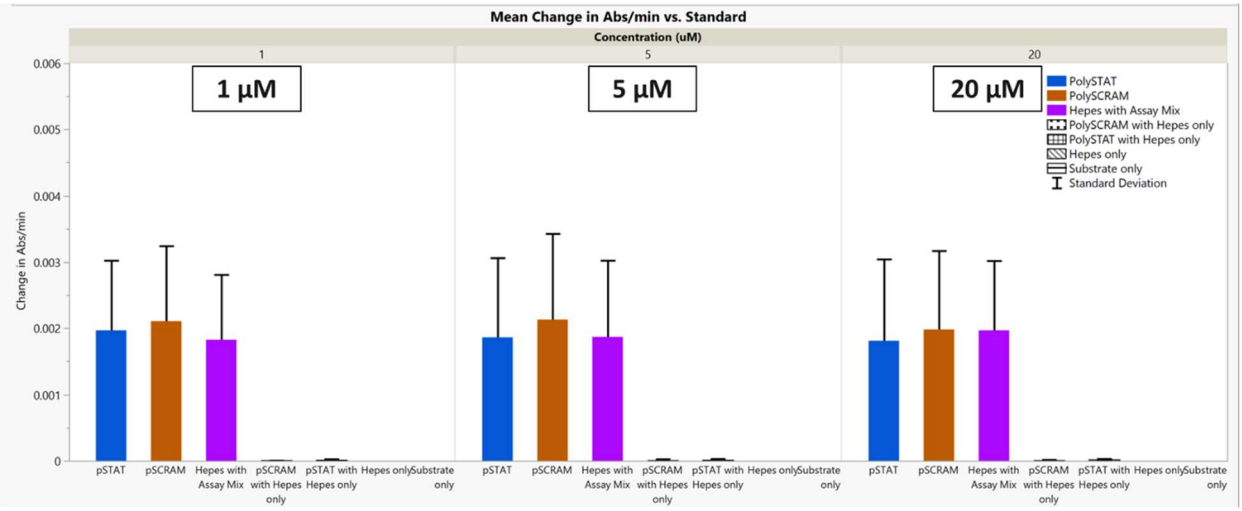

Figure 19. Change in absorbance over time for tPA-Plasminogen chromogenic assay. There was no difference between PolySTAT, PolySCRAM, and the HEPES volume control at any of the concentrations evaluated 1 µM, 5 µM, and 20 µM. PolySTAT does not affect the conversion of plasminogen to plasmin by tPA.

There was no difference in the rate of plasmin generation across treatments without fibrin present. Next, the same tPA-Plasminogen chromogenic assay was repeated in the presence of 0.5 mg/mL, and 1.5 mg/mL fibrin gels (Figure 20 below)

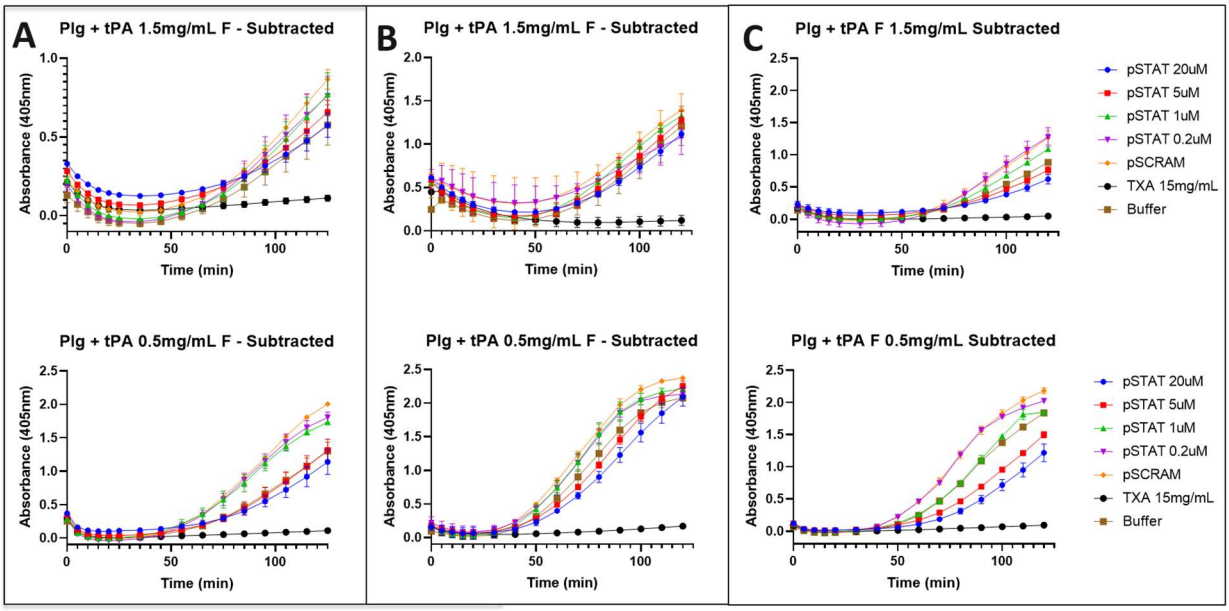

Figure 20. tPA-Plasminogen chromogenic assay with fibrin gels (n = 3 replicates). Two fibrinogen concentrations were evaluated - 1.5 mg/mL (top) and 0.5 mg/mL (bottom). Overall, the 0.5 mg/mL concentration provided better separation between the treatments. Each column represents the raw data for abosorbance monitored at 405 nm for a replicate.

Interestingly, there did appear to be some increase in plasmin generation for both PolySTAT and PolySCRAM compared to the buffer control. Figure 21 below shows the slope of the raw absorbance curves to look at plasmin generation rate.

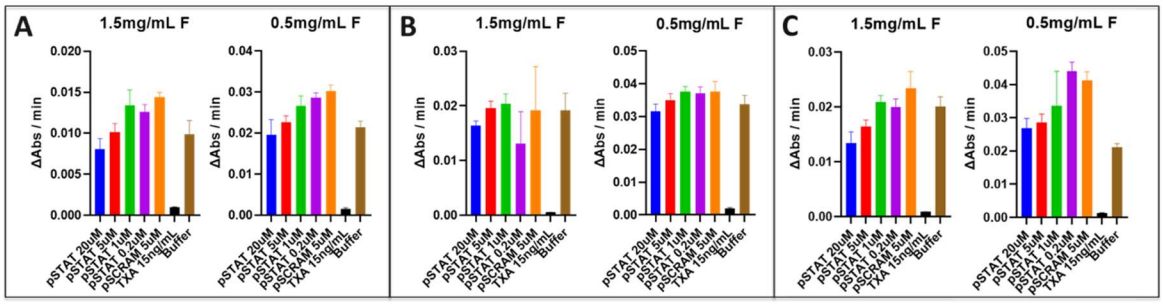

Figure 21. Rate of plasmin generation from tPA-Plasminogen chromogenic assays with fibrin gels (n = 3).

There appears to be a dose response with PolySTAT for plasmin generation. With increasing polySTAT concentration, there is a decrease in plasmin generation; however, at the maximum dose of 20 µM PolySTAT, the plasmin generation rate matches the buffer control. Interestingly, the presence of PolySCRAM and 0.2 µM PolySTAT similarly increases the rate of plasmin generation. However, all the effects from PolySTAT and PolySCRAM are extremely small compared to the current standard of care anti-fibrinolytic TXA, which is a lysine analogue that competitively inhibits plasminogen binding to prevent the generation of plasmin. Overall, PolySTAT does not interfere with tPA and plasminogen binding. Next, we investigated the interaction between FDPs and PolySTAT in a turbidity assay. As clots form, the fibrin gel becomes insoluble and leads to an increase in turbidity (opaqueness of the well), which then decreases as the clot breaksdown during lysis. From the change in turbidity, the lysis time was calculated, which is the time it takes for the turbidity to decrease by 50% from its maximum turbidity value (Figure 22 below).

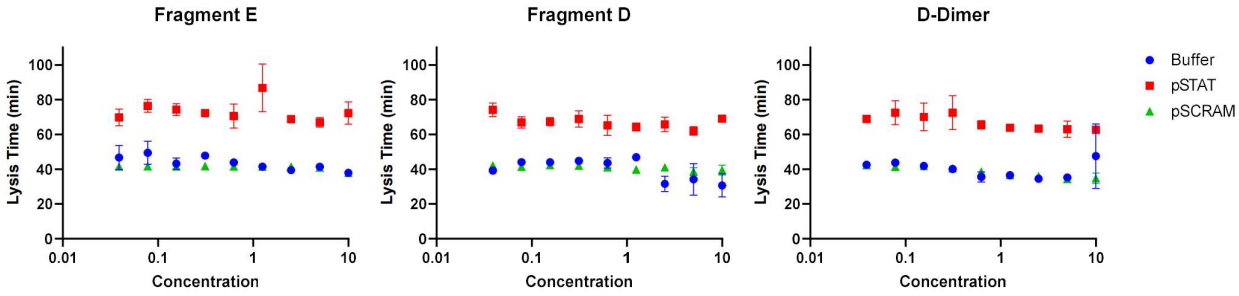

Figure 22. Lysis time from fibrin turbidity assays in the presence of either fibrinogen degradation products (Fragments E and D) or D-dimers.

Various FDPs were evaluated (Fragment E, D, and D-Dimers) across a serial dilution. Across all FDPs and concentrations, 5 µM PolySTAT showed increased lysis time (decreased fibrinolysis) compared to both PolySCRAM and the buffer control. Additionally, there were similar lysis times seen across FDP concentrations, which indicates that the FDPs evaluated do not affect lysis time by themselves, and they do not competitively inhibit PolySTAT.

4.6 Anti-fibrinolytic Mechanism: Conclusions

First, PolySTAT showed little to no effect on plasmin generation in tPA-Plasminogen chromogenic assays both free in solution and in the presence of fibrin gels. This supports PolySTAT's primary anti-fibrinolytic action is due to the physical changes it makes to the fibrin network. Second, in a turbidity assay evaluating lysis time with three FDPs (Fragment E, Fragment D, and D-Dimers), there was no effect on lysis time from the presence of the FDPs. Additionally, PolySTAT was not competitively inhibited by the presence of the FDPs and showed increased lysis time (decreased fibrinolysis) compared to the PolySCRAM and buffer controls.

4.7 References

1. Pieters, M. & Wolberg, A. S. Fibrinogen and fibrin: An illustrated review. *Research and Practice in Thrombosis and Haemostasis* **3**, 161–172 (2019).
2. Bouma, B. N. & Mosnier, L. O. Thrombin activatable fibrinolysis inhibitor (TAFI)—How does thrombin regulate fibrinolysis? *Annals of Medicine* **38**, 378–388 (2006).
3. Kolodziej, A. F. *et al.* Fibrin Specific Peptides Derived by Phage Display: Characterization of Peptides and Conjugates for Imaging. *Bioconjugate Chem.* **23**, 548–556 (2012).
4. Oliveira, B. L. & Caravan, P. Peptide-based fibrin-targeting probes for thrombus imaging. *Dalton Trans.* **46**, 14488–14508 (2017).
5. Aizawa, H. *et al.* Conventional detection method of fibrinogen and fibrin degradation products using latex piezoelectric immunoassay. *Biosensors and Bioelectronics* **18**, 765–771 (2003).
6. Stokol, T. Action of plasmin on fibrinogen or fibrin. *eClinpath* https://eclinpath.com/dd_fdps/.
7. Lippi, G. *et al.* D-dimer testing for suspected venous thromboembolism in the emergency department. Consensus document of AcEMC, CISMEL, SIBioC, and SIMeL. *Clinical Chemistry and Laboratory Medicine* **52**, 621–628 (2014).
8. Jiang, R. M., Pourzanjani, A. A., Cohen, M. J. & Petzold, L. Associations of longitudinal D-Dimer and Factor II on early trauma survival risk. *BMC Bioinformatics* **22**, 122 (2021).

9. An, Z.-P., Huang, H.-B. & Wang, Z.-G. Correlation between Plasma D-Dimer Level and Severity and Prognosis in Patients Admitted at Emergency Department with Trauma. *Clin Lab* **66**, (2020).
10. Kearney, K. J. *et al.* Affimer proteins as a tool to modulate fibrinolysis, stabilize the blood clot, and reduce bleeding complications. *Blood* **133**, 1233–1244 (2019).
11. Hudson, N. E. Biophysical Mechanisms Mediating Fibrin Fiber Lysis. *Biomed Res Int* **2017**, (2017).
12. Tutwiler, V. *et al.* Kinetics and mechanics of clot contraction are governed by the molecular and cellular composition of the blood. *Blood* **127**, 149–159 (2016).
13. Weiss, N. *et al.* FITC-linked Fibrin-Binding Peptide and real-time live confocal microscopy as a novel tool to visualize fibrin(ogen) in coagulation. *J Clin Transl Res* **3**, 276–282 (2017).
14. Litvinov, R. I., Farrell, D. H., Weisel, J. W. & Bennett, J. S. The Platelet Integrin αIIbβ3 Differentially Interacts with Fibrin Versus Fibrinogen *. *Journal of Biological Chemistry* **291**, 7858–7867 (2016).
15. Stalker, T. J. *et al.* Hierarchical organization in the hemostatic response and its relationship to the platelet-signaling network. *Blood* **121**, 1875–1885 (2013).
16. Lam, W. A. *et al.* Mechanics and contraction dynamics of single platelets and implications for clot stiffening. *Nature Materials* **10**, 61–66 (2011).
17. Hansen, C. E., Qiu, Y., McCarty, O. J. T. & Lam, W. A. Platelet Mechanotransduction. *Annual Review of Biomedical Engineering* **20**, 253–275 (2018).
18. Ariëns, R. A. S., Lai, T.-S., Weisel, J. W., Greenberg, C. S. & Grant, P. J. Role of factor XIII in fibrin clot formation and effects of genetic polymorphisms. *Blood* **100**, 743–754 (2002).

4.8 SUPPLEMENTAL

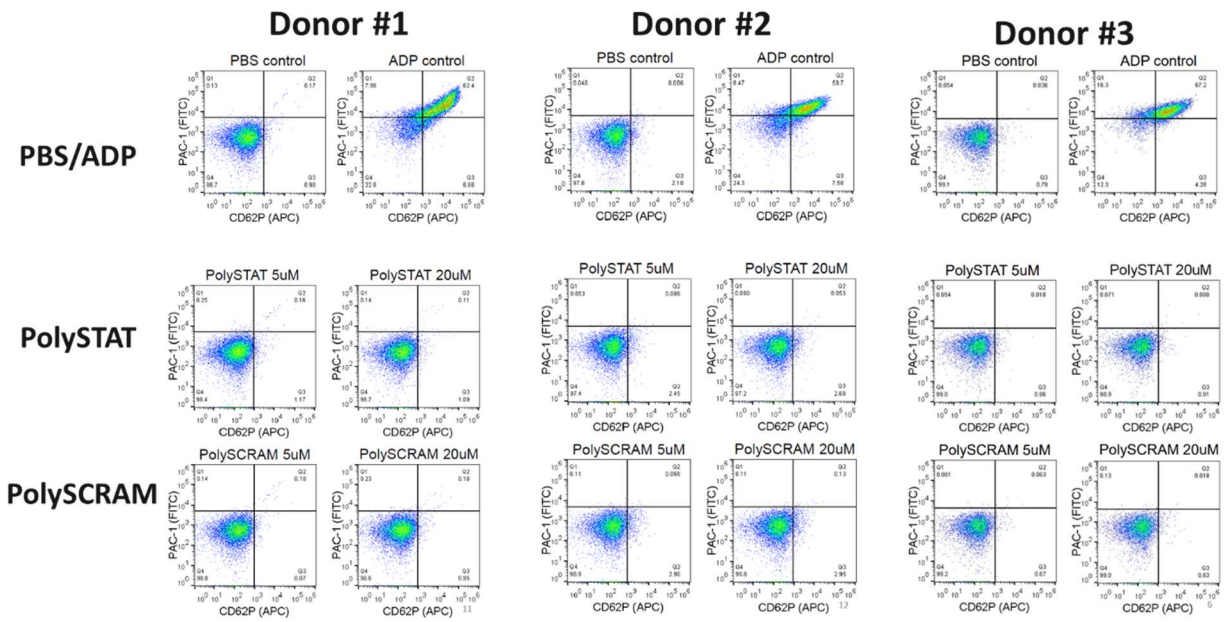

Figure S 1. Flow cytometry plots for platelet activation using PAC-1 and P-selectin (CD62).

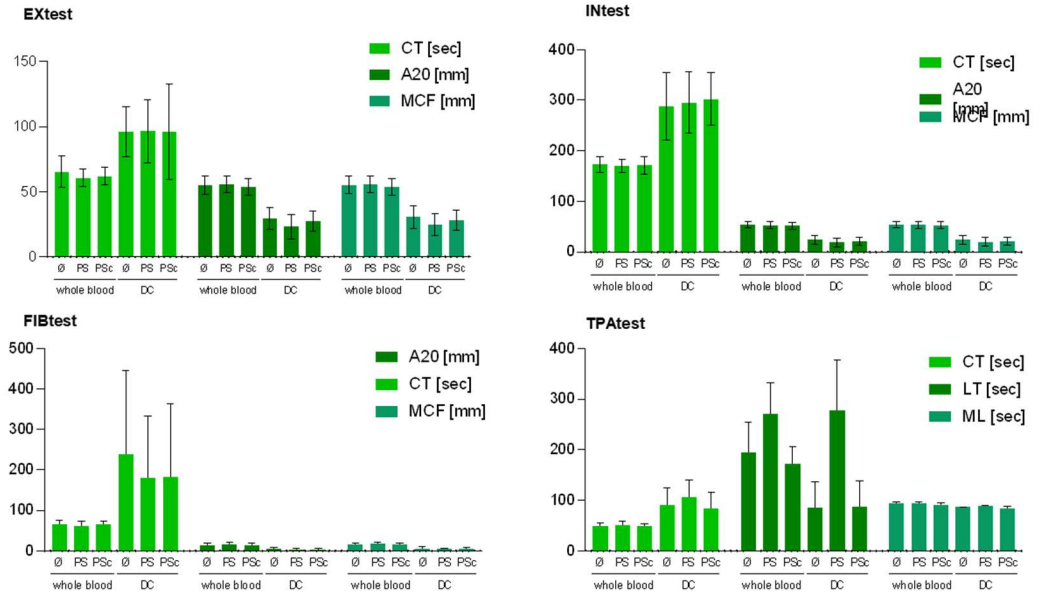

Figure S 2. Clot Pro tPA assay with hemodiluted patient samples.

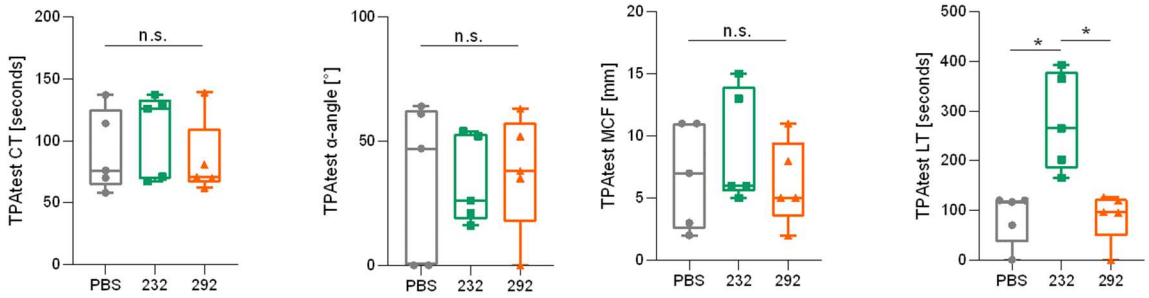

Figure S 3. TPA test from hemodiluted patient blood samples.

Chapter 5. ENGINEERING LOW VOLUME RESUSCITANTS FOR THE PREHOSPITAL CARE OF SEVERE HEMORRHAGIC SHOCK

Trey J. Pichon, Xu Wang, Kristyn M. Ringgold, Ethan E. Mickelson, Sarah Stucky, Alexander E. St. John, Shayna L. Hilburg, Wen-Chia Huang, Maggie Lu, Lilo D. Pozzo, Nathan J. White, Suzie H. Pun

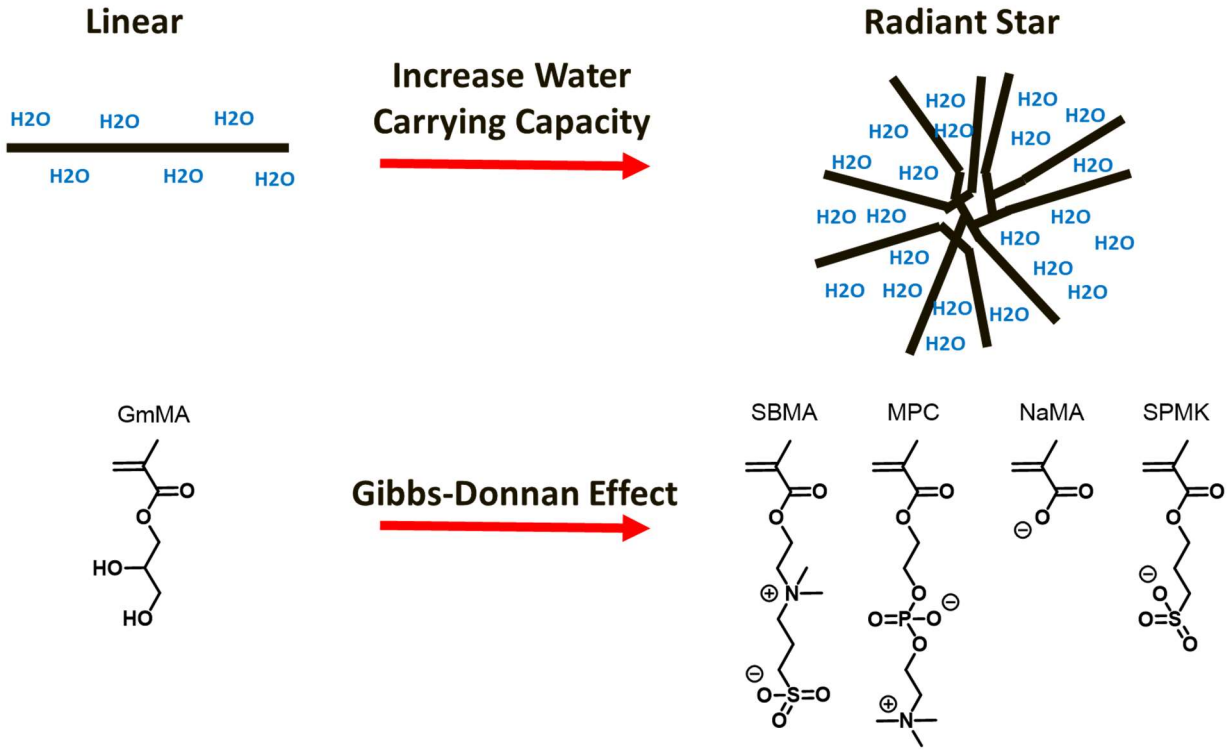

5.1 INTRODUCTION

During trauma-related severe hemorrhage, hypovolemia and hypoperfusion of organs can lead to hemorrhagic shock.[1] Shock is triggered by insufficient blood flow to the organs which leads to anaerobic respiration, lactate build-up, ATP depletion[2] and shutdown of cellular sodium pumps.[3] The inactivation of sodium pumps leads to a rapid flow of sodium ions and chloride counter ions into cells with which water follows. Water flows from the intravascular system into the interstitial space. Restoring the lost intravascular volume is the main goal of resuscitation, which can reperfuse organs through capillary refill and improvement of cardiac output. Although resuscitation with plasma, platelets, red blood cells, and whole blood are the ideal approaches to restore hemostasis, pay back oxygen debt, and restore the intravascular volume, these biologic treatments are not always readily available[4,5]. Treatment with large volumes of crystalloids (fluids containing electrolytes) can exasperate acidosis and lead to hypothermia if not adequately warmed[6]. In addition, the crystalloids only stay in the vascular space temporarily and will flow into the interstitial space[7]. Hexyl starches (Hextend), which have been used to keep water in the intravascular space, can lead to dilutional coagulopathy. Recently, the Mangino group demonstrated the promise of PEG 20k as a Low-Volume Resuscitant (LVR).[8–11] A large, single-dose (10% of blood volume), of a highly concentrated solution (10%-20% w/v) of PEG 20k was given to rats in hemorrhagic shock. The PEG 20k LVR restored blood pressure back to baseline values within 15 minutes and decreased lactate levels from > 9mmol/L to within baseline levels. The PEG 20k is sufficiently sized to prevent extravasation from the intravascular space even with the hyperpermeability observed with the severe endothelial dysfunction (endotheliopathy of trauma). The osmolarity of PEG acts as a powerful oncotic that causes water to rush back into the intravascular space.

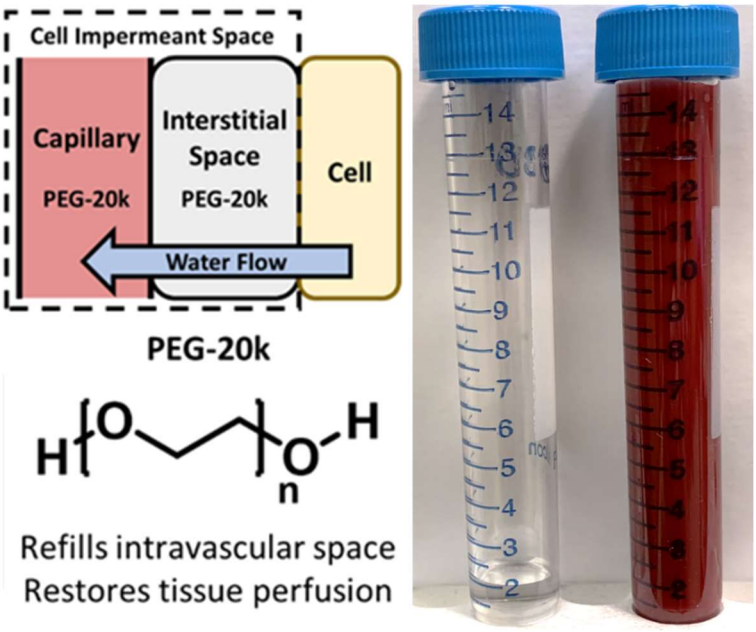

Figure 1. Overview of Low Volume Resuscitants using 20 kDa Polyethylene glycol (PEG20K). Left: PEG20K partitions between the capillary and interstitial space but is unable to enter cells. The osmotic pressure of PEG20K drives water out of swollen parenchymal cells and into the capillaries, refilling the vascular space. Right: A single bolus infusion of 10% TBV of LVRs (clear solution) can refill the lost volume of a severe hemorrhage of 60-75% total blood volume.

Our goal is to advance LVR technology by using new polymer architectures to increase circulation time and by employing different polymer compositionsto avoid the risk of PEG allergy, which is becoming more prevalent due to the widespread use of PEG. Ultimately, this LVR could be paired with PolySTAT and a synthetic oxygen carrier which will provide hemostasis and repay oxygen debt, respectively. This all-in-one resuscitative therapy would be extremely shelf-stable and enable better prehospital care in austere environments.

5.2 MATERIALS AND METHODS

5.2.1 *Materials*

2,2′-Azobis(2-methylpropionitrile) (AIBN), 4-((((2-carboxyethyl)thio)carbonothioyl)thio)-4-cyanopentanoic acid (CCC), Dimethyl sulfoxide (DMSO), Dimethylformamide (DMF), N-(3-Dimethylaminopropyl)-N′-ethylcarbodiimide hydrochloride (EDC), 4-(Dimethylamino)pyridine (DMAP), Dichloromethane (DCM), N,N-Dimethylacetamide (DMAc), and all other reagents were purchased from Sigma-Aldrich (Saint Louis, MO) unless noted otherwise. 4-Cyano-4-(ethylsulfanylthiocarbonyl)sulfanylpentanoic acid (ECT) was purchased from AmBeed (Arlington Hts, IL), 3-[[2-(Methacryloyloxy)ethyl]dimethylammonio]propane-1-sulfonate (SBMA), 2-Methacryloyloxyethyl phosphorylcholine (MPC), and 3-Sulfopropyl methacrylate potassium salt (SPMK) were purchased from TCI America (Portland, OR). Glycerol monomethacrylate (GmMA) was purchased from Polysciences, Inc. (Warrington, PA). 2,2'-Azobis[2-(2-imidazolin-2-yl)propane]dihydrochloride (VA-044) was purchased from FUJIFILM Wako Chemicals U.S.A (Richmond, VA).

5.2.2 *Synthesis of linear LVRs*

Neutral Homopolymers: pGmMA was synthesized via reversible addition-fragmentation chain transfer (RAFT) polymerization as described previously.[12] Briefly, GmMA monomer was combined with CCC and AIBN at the following ratios - 110:1:0.2 (DP 100), 220:1:0.2 (DP200), 330:1:0.2 (DP300) in dimethylacetamide at a monomer concentration of 0.6 M. A small amount of DMF was spiked in as an internal standard for NMR. The mixture was purged with argon for at least 15 min. This mixture reacted for 18 h at 70 °C. pGmMA polymers were precipitated 2x in diethyl ether. Precipitated polymer was collected by centrifugation at 7197 x g. Trithiocarbonate groups were removed via an end-capping reaction with 20x molar excess AIBN at 70 °C for 24 hours. The pGmMA polymers were then dialyzed against DI water for 2 days, with a minimum of six bath changes, followed by lyophilization.

Zwitterionic Homopolymers: SBMA monomer was combined with CCC and VA-044 at the following ratios – 100:1:0.2 (DP100), 200:1:0.2 (DP200), and 300:1:0.2 (DP300) in normal saline (0.9% w/v, NaCl) at a monomer concentration of 0.6 M. A small amount of DMF was spiked in

as an internal standard for NMR. The mixture was purged with argon for at least 15 min. This mixture was reacted for 12 h at 44 °C. The solution was then open to atmosphere and diluted to a final polymer concentration of 2 mM. Then, trithiocarbonate groups were removed via an end-capping reaction with 20x molar excess VA-044 at 44 °C for 24 hours. The pSBMA polymers were dialyzed against 0.9% w/v saline (NaCl) for 1 day, with a minimum of three bath changes, and were then dialyzed against DI water for 2 days, with a minimum of six bath changes, which would result in the polymer crashing out of solution. The contents of the dialysis bag were vigorously mixed to suspend the polymer, and then the polymer was precipitated by mixing 5 mL of the suspension, with 40 mL of methanol in a 50 mL conical tube. Methanol was used to remove as many NaCl counterions as possible. Precipitated polymer was collected by centrifugation at 7197 x g, followed by removal of residual methanol overnight under high vac. The same steps were followed for MPC and SPMK.

5.2.3 *Polymer characterization*

Polymers were characterized via gel permeation chromatography (GPC) in phosphate buffered saline with multi angle light scattering and refractive index detectors (MiniDawn Treos and OptilabTRex, respectively, both from Wyatt Technology, Santa Barbara, CA) to determine molecular weight from 100% mass recovery and dispersity index (PDI). ^{1}H nuclear magnetic resonance (NMR) spectroscopy on a Bruker AV 300 was utilized to determine conversion of the polymer prior to purification. Vapor pressure osmometry (Vapro 5600) was used to measure osmolarity as a function of molar concentration for the different polymers. Each polymer was dissolved in 0.9% normal saline (NaCl) and was run in triplicate.

5.2.4 *Synthesis of HEMA-ECT (hECT) CTA monomer*

4-Cyano-4-((ethylsulfanylthiocarbonyl)sulfanyl)pentanoic acid (ECT) (1 g, 3.8 mmol), hydroxyethyl methacrylate (HEMA) (1.2 g, 9.1 mmol), and 4-dimethylaminopyridine (DMAP) (1.5 g, 12.2 mmol) were dissolved in DCM (38 mL, 0.1 M reaction concentration) in a round bottom flask (RBF) with a stir bar. The RBF was capped, and the solution was cooled over ice for 15 minutes, then N-(3-Dimethylaminopropyl)-N′-ethylcarbodiimide hydrochloride (EDC • HCl) (874 mgs, 4.6 mmol). Pyridine (353 µL, 4.36 mmol) was added to the mixture. The reaction was stirred over ice and allowed to warm to room temperature while stirring overnight. The mixture

was washed 3x with a 1:1 volume with a cold saturated brine solution, followed by a 3x wash with cold 0.1M HCl solution, a 3x wash with cold saturated sodium bicarbonate solution, and a final wash with cold saturated brine solution. The collected DCM was dried over sodium sulfate. The solvent was rotovapped off to obtain a deep orange oil. Purity was confirmed by proton NMR and TLC. The CTA monomer was stored at -20C.

5.2.5 *Synthesis of poly(GmMA-co-hECT) and poly(SBMA-co-hECT) Radiant Stars*

The synthesis of radiant stars was adapted from the work of Das et al.[13]

Synthesis of p(GmMA-co-hECT) macroCTA core

GmMA monomer was combined with hECT and AIBN at the following molar ratio 2.333:1:0.1 (GmMA:hECT:AIBN) in dimethylacetamide at a monomer concentration of 0.6 M. A small amount of DMF was spiked in as an internal standard for NMR. The mixture was purged with argon for at least 15 min. This mixture reacted for 18 h at 70 °C. p(GmMA-co-hECT) polymers were precipitated 5x in diethyl ether. Precipitated polymer was collected by centrifugation at 7197 x g.

Chain Extension of p(GmMA-co-hECT) macroCTA core

For a DP400, GmMA monomer was combined with p(GmMA-co-hECT) macroCTA and AIBN at the following molar ratio 600:1:0.00752 (GmMA:MacroCTA:AIBN) in dimethylacetamide at a monomer concentration of 0.6 M. A small amount of DMF was spiked in as an internal standard for NMR. The mixture was purged with argon for at least 15 min. This mixture reacted for 12 h at 70 °C (targeting 67% conversion to hit DP400). p(GmMA-co-hECT) polymers were precipitated 5x in diethyl ether. Precipitated polymer was collected by centrifugation at 7197 x g. Trithiocarbonate groups were removed via an end-capping reaction with 20x molar excess AIBN to the concentration of trithiocarbonate groups at 70 °C for 24 hours. The RS-GmMA polymers were then dialyzed against DI water for 2 days, with a minimum of six bath changes, followed by lyophilization.

Synthesis of p(SBMA-co-hECT) macroCTA core

SBMA monomer was combined with hECT and AIBN at the following molar ratio 2.333:1:0.1 (GmMA:hECT:AIBN) in a mixed solvent of 75% DMSO/25% 0.9% normal (NaCl) saline at a monomer concentration of 0.6 M. A small amount of DMF was spiked in as an internal standard for NMR. The mixture was purged with argon for at least 15 min. This mixture reacted for 12 h at 70 °C. p(SBMA-co-hECT) polymers were precipitated 5x in 50:50 diethyl ether/acetone. Precipitated polymer was collected by centrifugation at 7197 x g.

Chain Extension of p(SBMA-co-hECT) macroCTA core

SBMA monomer was combined with p(SBMA-co-hECT) macroCTA and AIBN at the following molar ratios (SBMA:MacroCTA:VA-044) – 100:1:0.00752 (DP100), 200: 1:0.00752 (DP200), and 400: 1:0.00752 (DP400) in normal saline (0.9% w/v, NaCl) at a monomer concentration of 0.6 M. A small amount of DMF was spiked in as an internal standard for NMR. The mixture was purged with argon for at least 15 min. This mixture reacted for 12 h at 44 °C. The solution was then open to atmosphere and diluted to a final polymer concentration of 2 mM. Then, trithiocarbonate groups were removed via an end-capping reaction with 20x molar excess VA-044 to the concentration of trithiocarbonate end groups at 44 °C for 24 hours. The pSBMA polymers were dialyzed against 0.9% w/v saline (NaCl) for 1 day, with a minimum of three bath changes, and were then dialyzed against DI water for 2 days, with a minimum of six bath changes, which would result in the polymer crashing out of solution. The contents of the dialysis bag were vigorously mixed to suspend the polymer, and then the polymer was precipitated by mixing 5 mL of the suspension, with 40 mL of methanol in a 50 mL conical tube. Methanol was used to remove as many NaCl counterions as possible. Precipitated polymer was collected by centrifugation at 7197 x g, followed by removal of residual methanol overnight under high vac.

5.2.6 *Rat severe hemorrhagic shock model*

Animal experiments were carried out in accordance with protocols approved by the University of Washington Institutional Care and Use Committee. Model was slightly modified from Plant et al.[8] Male Sprague Dawley rats (270g-370g) were anesthetized by isoflurane via nosecone. During baseline, two femoral artery catheter lines were placed in the hind limbs, one to perform a controlled catheter bleed, and the second to constantly monitor vitals (blood pressure and heart rate) and collect blood samples for blood gas measurements. A venous line is placed in the left

hind limb for intravascular administration of the low-volume resuscitants. After catheterization, baseline blood gas and metabolites were evaluated to ensure healthy baseline respiration and lactate levels ($pCO2 \leq 55$ mmHg, $sO2\% \geq 95\%$, $cLac \leq 1.0$ mmol/L) prior to hemorrhage. After the rat is baselined, a single bolus of 500 mg/kg of heparin is given to prevent clogging of the catheter lines during hemorrhage. Next, the rat was catheter hemorrhaged down to a mean arterial pressure (MAP) ≤ 25 mmHg over five minutes (typically 7-10 cc of blood). After a MAP ≤ 25 mmHg was reached, a timer was started for the shock period. Blood was withdrawn as needed up to a maximum of 60% total blood volume to maintain MAP ≤ 25 mmHg (shock period) for at least 30 minutes until a lactate ≥ 8 mmol/L is achieved. The total blood volume (TBV) of the rat was estimated as previously described by Arora et al.[14]

$$Total\ Blood\ Volume\ (mL) = Weight\ of\ Rat\ (g) * 0.06 + 0.77$$

After 30 minutes, blood gas was checked every 15 minutes until the goal lactate was achieved. At the end of the shock period (lac ≥ 8 mmol/L), the low volume resuscitant will be infused intravenously over 10 minutes (10% TBV). Blood gas and MAP will be recorded over 90 minutes, at the end of which the rat will be humanely euthanized via barbiturate overdose.

5.2.7 *ROTEM Evaluation*

Whole human blood was purchased from Bloodworks Northwest (50 mL total blood in 3.2% sodium citrate). Half of the human blood was centrifuged down to make platelet-poor plasma (PPP). Two ROTEM deltas (Werfen, Bedford, MA/Serial #s 3733 and 4515) were used using the standard manufacturer's protocol for EXTEM ($CaCl_2$ + recombinant tissue factor + polybrene) for both whole blood and PPP. For each test, 40 µL of treatment was mixed with 360 µL of whole blood or plasma (10% TBV) in an Eppendorf tube then immediately evaluated on the ROTEM to prevent any separation of the blood. EXTEM of PPP was used as a surrogate for the standard FIBTEM test to measure the fibrinogen contribution to coagulation.

5.2.8 *Platelet Aggregometry*

Healthy donor whole blood (n=4) in 3.2% sodium citrate was incubated with either a saline control or a low volume resuscitant (LVR) for 5 min. LVRs tested were polyethylene glycol (PEG) and synthesized polymers LVR102 and LVR113. Samples were then activated with either 10 mM adenosine diphosphate or 2 mg/mL collagen (Chrono-Log, Havertown, PA). The platelet

aggregation response was then measured by impedance aggregometry using a Chrono-Log Model 700 according to manufacturer specifications. Each condition was run simultaneously. The raw curves were collected along with the metrics reported by the Chrono-Log (Amplitude, Slope, area under the curve (AUC)).

5.2.9 *Small-angle X-ray Scattering*

X-Ray scattering was measured using a Xenocs Xeuss 3.0 (Grenoble, France) SAXS instrument with a copper radiation source. Samples were analyzed in a 1.2 mm diameter quartz capillary and measured at four detector distances (266, 370, 900, and 1800 mm sample-to-detector distances with counting times of 300, 900, 1380, and 1800 seconds, respectively) to cover a q-range of approximately 5x10-3 to 4x10-1 Å-1. Polymer samples were run at 15 mg/mL and 5 mg/mL in phosphate buffered saline (PBS). Scattering contribution from PBS and the capillary have been subtracted from polymer solution scattering data. Data reduction and processing were completed using XSACT software (Xenocs, Grenoble, France). Data fitting to monodisperse gaussian coil or star polymer models was completed on 15 mg/mL sample data using SASView 5.0.5.[15–19] Fits were qualitatively assessed on 5mg/mL sample data and confirmed there was no concentration-dependent structure factor leading to correlations between polymers.

5.3 Results and Discussion

5.3.1 *Synthesis and Characterization of Linear LVRs of various Sizes and Chemistries*

From literature, PEG with molecular weights of 20-40 kDa were active as LVRs. Leveraging RAFT, we were able to easily explore different size ranges of methacrylates. However, compared to PEG, methacrylates are very different chemically which leads to a different size in solution (Figure 2 below).

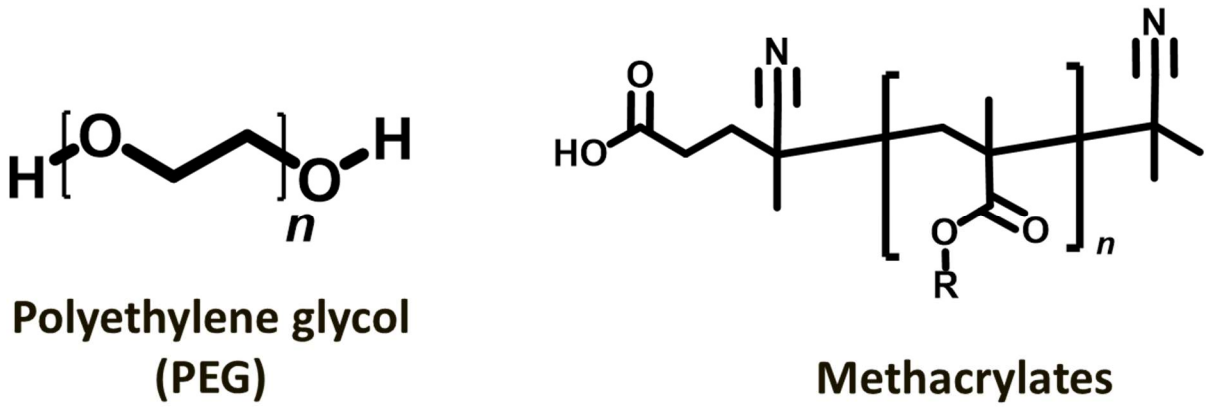

Figure 2. Chemical structure of PEG (left) and methacrylates (right).

PEG has a very low molecular weight repeat unit at 44 g/mol, whereas the methacrylate with the smallest side chain polymethacrylic acid (PMMA), has a repeat unit of 88 g/mol. Additionally, PEG has a backbone of alternating C-O and C-C σ-bonds, while methacrylates instead have a purely carbon-carbon backbone. Therefore, we could not simply synthesize 20-40 kDa methacrylates, and needed to explore a different molecular weight range compared to PEG. Additionally, one benefit of methacrylates is the chemical flexibility and tailorability of the sidechain, which we were interested in leveraging. Due to the different sidechains we explored in this work, we found it easier to fix degree of polymerization (DP) across different side chains, instead of fixing molecular weight.

To start, we estimated the size of methacrylates compared to PEG to see what ranges of DP we should explore. There are many ways to characterize the size of polymers (Figure 3 below).

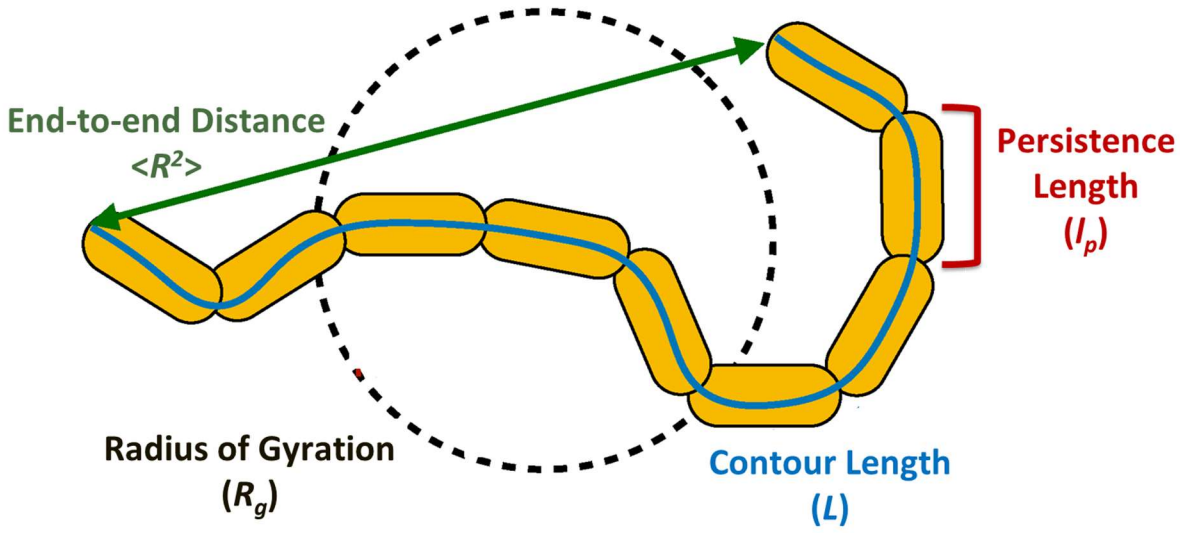

Figure 3. Cartoon depicting some of the different ways to characterize the size of a polymer.

The contour length of polymers just considers the bond length of the repeat unit and the DP, and assumes the polymer is fully stretched out:

$$Contour\ Length\ (L) = nl$$

Where L is the contour length, n is the number of repeats, and l is the bond length. However, polymer chains are coiled up in solution, so to consider chain rigidity the average squared end-to-end distance of the polymer $< R^2 >$ is used:

$$< R^2 > = C_\infty nl^2$$

Where (C_∞) is the characteristic ratio, or a dimensionless factor for chain rigidity, n is the number of repeats, and l is the bond length. The end-to-end distance is a simple descriptor that is easy to calculate and only describes the distance between the two ends of the polymer coil. To get a real sense of the size of a polymer, radius of gyration (R_g) is the average squared distance of a point on the polymer coil from its center of mass (moment of inertia) is a better descriptor that can be measured using small-angle x-ray scattering. For a freely jointed chain the mean average of R_g^2 can be estimated by dividing the mean end-to-end distance squared by 6:[20–22]

$$< R_g^2 > = \frac{< R^2 >}{6}$$

Table 1 below shows repeat unit bond lengths and characteristic ratios (C_∞) from literature.[23]

Table 1. Comparison of bond length for each monomer repeat unit and characteristic ratio.

Polymer	Repeat Unit Bond Length (nm)	Characteristic Ratio (C∞)
Polyethylene glycol	0.438	6.9
Polymethyl methacrylate	0.308	8.1
Polyhexyl methacrylate		12.2
Polyoctadecyl methacrylate		20.6

As can be seen in Table 1, although PEG has a longer bond length, it has a much more flexible backbone (lower C_∞) compared to methacrylates. It is well documented that PEG graft density on the surfaces dictates whether the polymer forms a mushroom-shape (bending back on itself) or an extended (more rigid) conformation. Interestingly for methacrylates, the side chain can be used as a tool to tailor the rigidity of the backbone. As the side chain of the methacrylate increases in length, C_∞ increases as a result, and the backbone of the methacrylate is more rigid and extended in solution. Given the values from Table 1, the following estimates for the size of PEG compared to polyglycerol monomethacrylate (pGmMA) of 20 kDa are given in Table 2 below. Since there is not a reported C_∞ for pGmMA, the value for polyhexyl methacrylate was used.

Table 2. Theoretical contour length, root mean squared end to end distance, and the radius of gyration for PEG 20k and pGmMA 20k.

Polymer	MW (kDa)	DP (units)	Contour Length (nm)	$\sqrt{< R^2 >}$ (nm)	$\sqrt{< R_g^2 >}$ (nm)
PEG 20k	20	454	199	78	32
pGmMA 20k	20	125	38	38	16

There is a large difference in the contour length, root mean square of the end-to-end-distance, and the radius of gyration for PEG, indicating that the polymer bends back on itself, and is more compact in solution due to the flexibility of its backbone. Methacrylates on the other hand can achieve a relatively high radius of gyration at a lower degree of polymerization of PEG. Following these calculations, we decided to synthesize a panel of DP100, 200, and 300 pGmMA polymers.

Although methacrylates, from a theoretical standpoint, could match the range of R_g for PEG, we were concerned about the larger molecular weight of the higher DP pGmMAs (DP200 = 32 kDa and DP300 = 48 kDa). The osmotic pressure (Π) of a polymer is proportional to the number of moles of solute (n_{solute}), where V = volume, R = molar gas constant, and T = temperature.

$$\Pi = \frac{n_{solute} RT}{V}$$

Since the oncotic potential of these LVRs is dictated by their osmotic pressure, the molar concentration in the blood is critical. Therefore, due to the 2-3x higher molecular weight of the methacrylate-based LVRs, a greater mass concentration of methacrylate-based LVR is needed for the same molar concentration of PEG-based LVRs. We were concerned if we would run into issues reaching these high concentrations in the blood, and if this would impact performance. Therefore, we sought out additional methacrylate side chains that may be able to increase the water-carrying capacity of the methacrylate compared to pGmMA. The hydration number (n_H) for a polymer is the number of water molecules coordinated per repeat unit, and this is typically understood to be the amount of non-freezing water coordinated (strongly bound) with the polymer measured by dynamic scanning calorimetry. In general, it is known for methacrylates that the following trend is seen for water-coordinating strength of the oxygens on their sidechains $O_{hydroxyl} > O_{carbonyl} > O_{alkoxy}$. The hydroxyl group can hydrogen-bond via both the oxygen and the hydrogen, while the carbonyl is highly electronegative, and a water molecule is bridged between two monomers, and the alkoxy group typically presents more steric hinderance. Unfortunately, pGmMA has not been measured in literature so we estimated it from data for pHEMA and assumed that the extra hydroxyl group would coordinate one additional water (very conservative estimate). From our lab's previous experience, moving from pHEMA to pGmMA resulted in a large increase in water-solubility for PolySTAT. Table 3 below shows estimates for PEG and various methacrylates from literature.[24–27]

Table 3. Hydration numbers from literature measured by DSC for various polymers.

Polymer	Type	Hydration Number (n_H)
PEG	Neutral	3.2
pHEMA		3.2
pGmMA		4.2 (estimated)
pSPMK	Anionic	4
pMPC	Zwitterionic	9
pSBMA		0-14

Based on literature, we decided to move forward with the commercial zwitterionic monomers 2-methacryloyloxyethyl phosphorylcholine (MPC) and N-(3-sulfopropyl)-N-methacroyloxyethyl-N,N-dimethylammonium betaine (SBMA), which showed ~2x the water-carrying capacity compared to pGmMA. Additionally, it is known that the negative charge of albumin leads to a larger than expected osomotic pressure due to the Gibbs-Donan effect. We hypothesized that moving to zwitterionic methacrylates would have the same effect and as a result be more potent oncotically *in vivo*. It should be noted that we did synthesize and evaluate SPMK, however this polymer resulted in toxicity concerns and acted as a synthetic heparin by completely inhibiting coagulation in rats (SI Figures S2 and S3).

Based on the theory outlined above, we synthesized a panel of pGmMA, pMPC, and pSBMA linear polymers of DP100, 200, and 300 via RAFT (Figure 4 below).

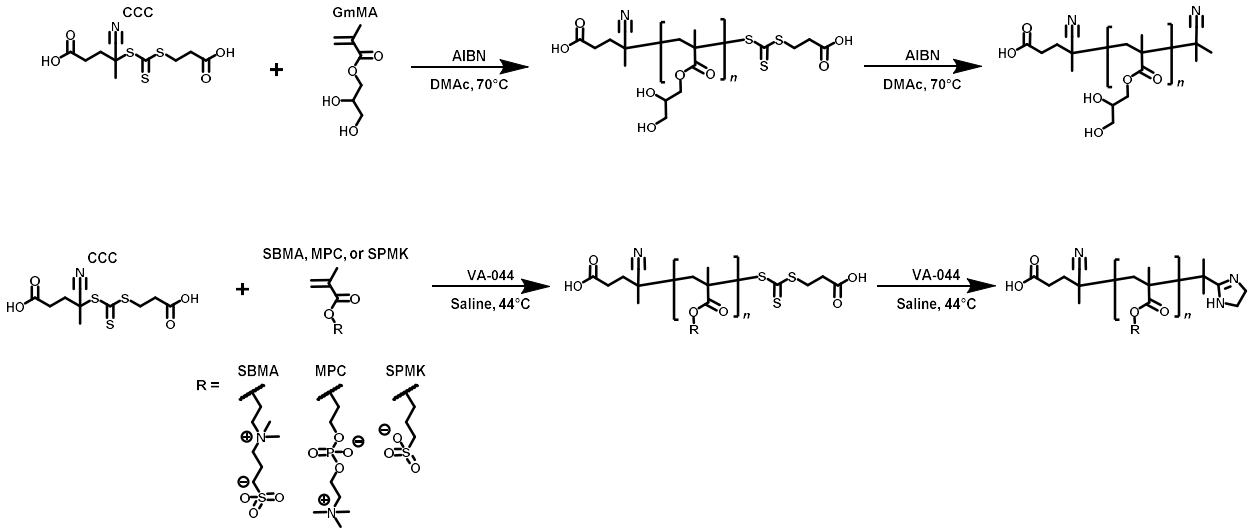

Figure 4. Reaction scheme for the synthesis of linear neutral and zwitterionic polymers.

Conversion of all polymers were characterized by ^{1}H NMR. Conversion was then used to calculate theoretical molecular weights (Mn). The molecular weight (Mn) and dispersity were determined using 100% mass recovery (RI Detector, Wyatt Optilab T-rex) and multiangle light scattering (MALS, Wyatt miniDAWN Treos) gel permeation chromatography (GPC). The running solvent was phosphate buffered saline (PBS) (flow rate: 0.5 mL/min) at room temperature and samples were prepared at 10 mg/mL. Figure 5 shows the GPC traces of each of the synthesized polymers, and Table 4 below summarizes the molecular weights calculated from NMR conversion and the molecular weights and dispersity indices measured from GPC.

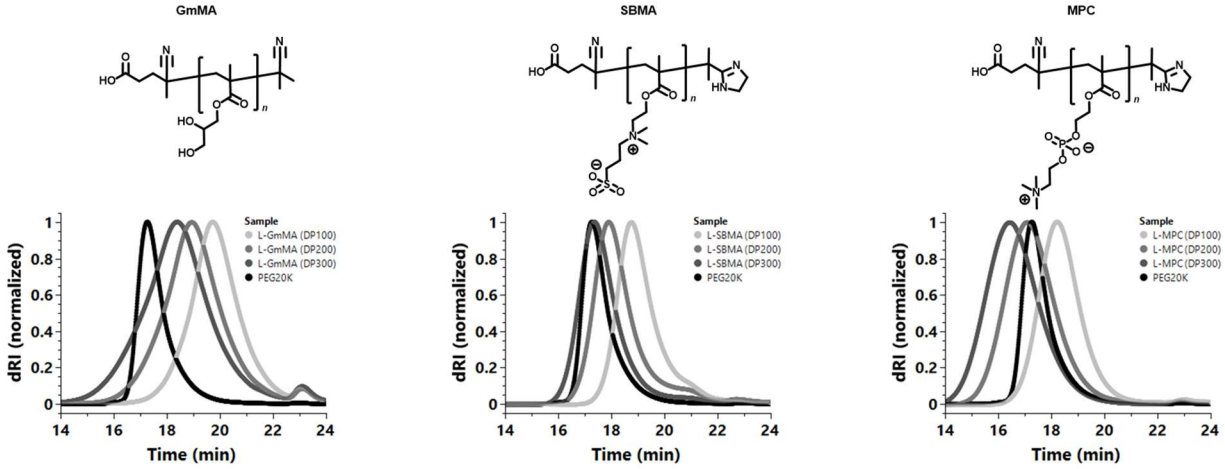

Figure 5. Gel Permeation Chromatograms of DP100, 200, and 300 linear LVRs. Left: GmMA homopolymers, Middle: SBMA zwitterionic homopolymer, and Right: MPC zwitterionic homopolymer. Each trace is overlaid with PEG 20K as a comparison. All polymers were run at 10 mg/mL concentration in PBS.

Table 4. Overview of Linear LVRs Synthesized.

Sample ID	Monomer	Target DP	NMR Analysis			GPC Analysis	
			Conversion (%)	DP	MW (kDa)	PDI	MW (kDa)
L-GmMA (DP100)	GmMA	100	93	102	16	1.06	18
L-GmMA (DP200)		200	90	198	32	1.09	40
L-GmMA (DP300)		300	90	297	48	1.08	58
L-MPC (DP100)	MPC	100	100	100	30	1.08	24
L-MPC (DP200)		200	100	200	59	1.18	66
L-MPC (DP300)		300	100	300	89	1.06	91
L-SBMA (DP100)	SBMA	100	100	100	28	1.16	13
L-SBMA (DP200)		200	100	200	56	1.25	28
L-SBMA (DP300)		300	100	300	84	1.02	61

We successively synthesized a range of neutral and zwitterionic methacrylates with a range of PDIs 1.02-1.25 and molecular weights ~ 18 kDa to 90 kDa. There was good agreement between the theoretical MW from ^{1}H NMR conversion and GPC 100% mass recovery measurements for GmMA and MPC, however SBMA showed a larger discrepancy. This could be due to interactions with the column. The panel of linear methacrylates were then characterized using small-angle x-ray scattering (SAXS) to directly measure their R_gs, the results are shown in Figure 6 below.

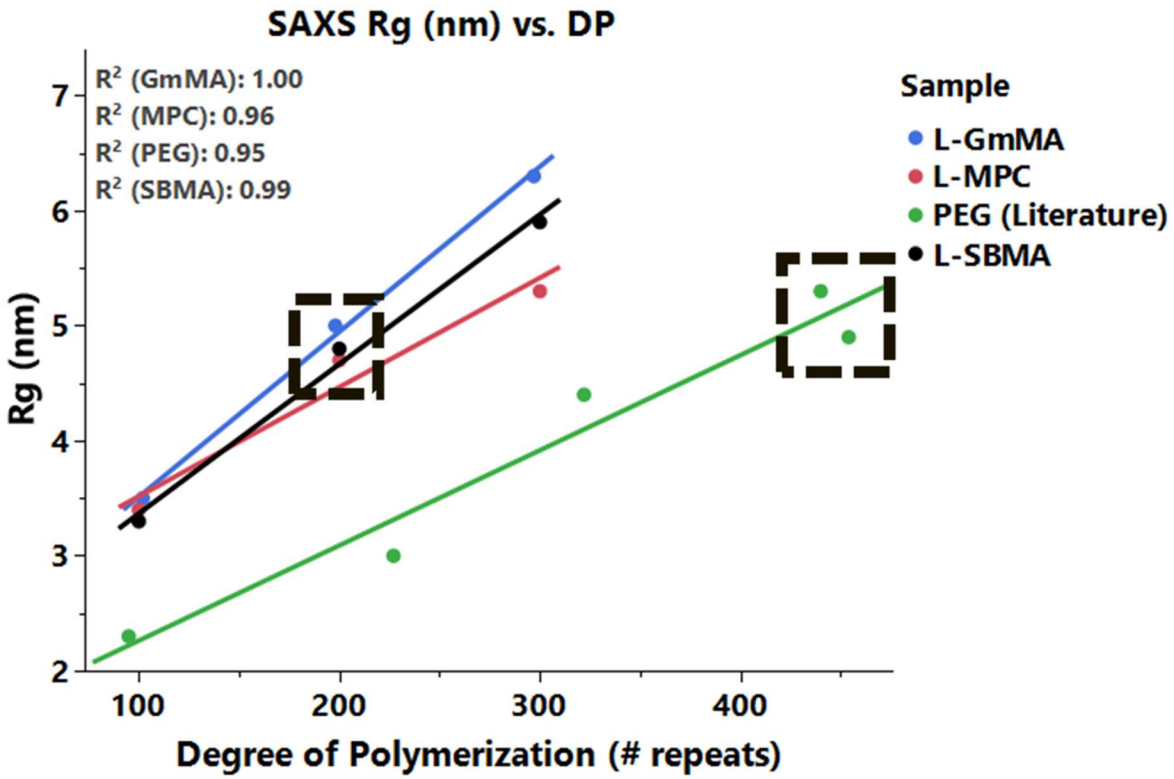

Figure 6. SAXS radius of gyration measurements as a function of degree of polymerization. As expected, we observe a good linear relationship between degrees of polymerization and Rg.

The black boxes show that the DP200 pGmMA (MW = 32 kDa), pMPC (MW = 59 kDa, and pSBMA (MW = 56 kDa) all have similar Rgs compared to PEG 20k. Next, the osmolarity of the linear methacrylates in 0.9% normal saline (NaCl) was measured by vapor pressure osmometry (Figure 7 below).

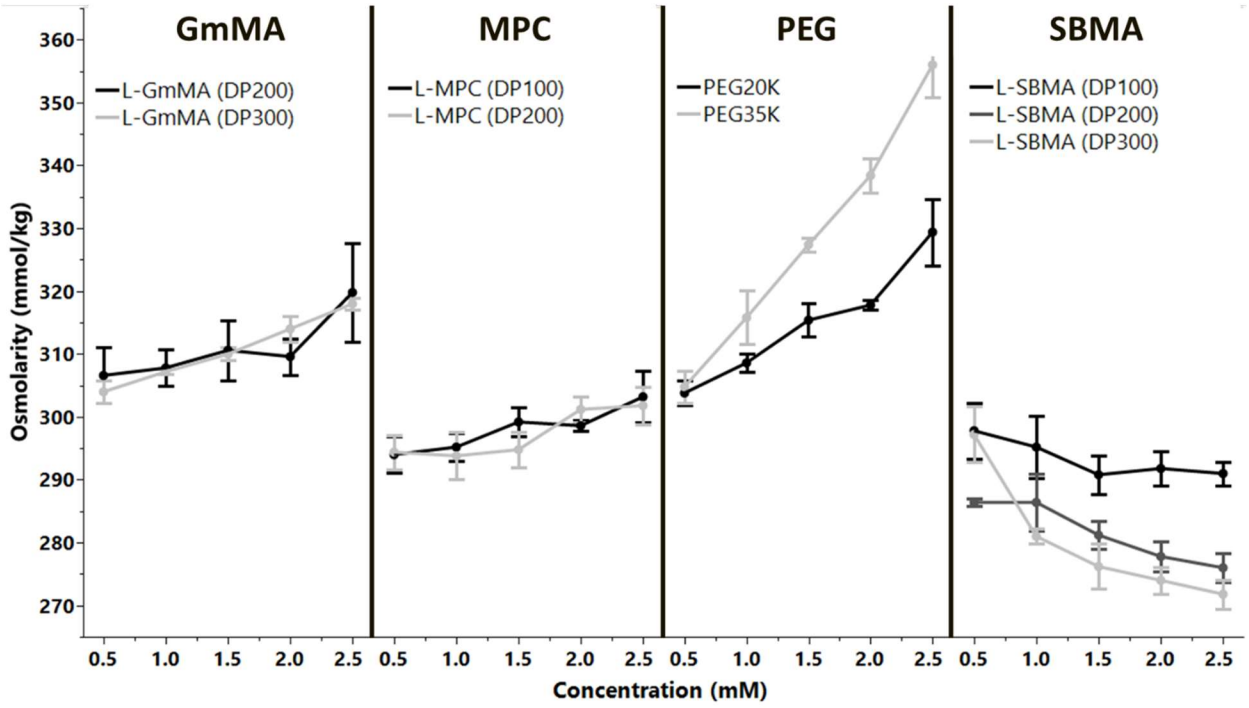

Figure 7. Vapor pressure osmometry measurements of pGmMA (left), pMPC (middle left), PEG (middle right), and pSBMA (right). All measurements were done using a Vapro 5600 in triplicate. Error bars are 1 standard deviation from the mean.

Interestingly, pGmMA (DP 200 and 300) showed similar osmolarity to PEG 20K. However, both pMPC and pSBMA showed lower osmolarity, and in the case of pSBMA, there was a decrease in osmolarity as molar concentration increased. There are probably two factors contributing to this phenomenon. First, this decrease is likely partly due to self-assembly of the pSBMA in solution leading to larger macromolecules that decrease the overall number of moles of solute. For 0.9% w/v NaCl solution, the concentration of Na^+ and Cl^- ions are both 0.15 M. Although the overall concentration of pSBMA in solution is much smaller at 0.5 - 2.5 mM, the concentration of 3-sulfopropyl and dimethyl ammonium groups for the DP100, DP200, and DP300 are both 0.05 - 0.25 M, 0.1 - 0.5 M, and 0.15 - 0.75 M, respectively. Therefore, the concentration of salt ions are lower than the concentration of charged groups in the zwitterionic polymer, so they are able to self-assemble. Second, the baseline osmolarity of the 0.9% NaCl solution was measured at 281 ± 1.22 mmol/kg (data not shown). So at the high polymer concentrations, the osmolarity is dropping below the salt solution by itself, which seems to indicate that the salt ions are being coordinated by the polymer. This is decreasing the overall solute concentration of ions in solution and causing

the osmolarity to drop below the value of just the 0.9% NaCl solution by itself. Overall, the zwitterionic methacrylates show lower osmolarity compared to both pGmMA and PEG. Vapor pressure osmometry does not measure the Gibbs-Donan effect, which is extremely difficult to measure and is typically theoretically calculated. Future work will be done to use DSC to directly measure nonfreezing bound water, and to measure the hydrodynamic radius of the polymers either through Dynamic Light Scattering or ^{1}H NMR.

5.3.2 *Initial Screening of LVRs with Rotational Thromboelastography Evaluation and a Severe Hemorrhagic Shock Model in Rats*

We next used ROTEM to evaluate the effect of all the synthesized linear polymers on coagulation using human plasma. The kept molar concentrations of polymers constant so that solutions of 10%, 20%, and 30% w/v were made for DP 100, 200, and 300, respectively, and all were evaluated at 10% total blood volume in ROTEM which is what was done in previous studies for PEG20K.[28,29] All the ROTEM runs included a saline volume control and Figure 8 shows the difference from the saline control for linear pGmMA of DP 100, 200, and 300.

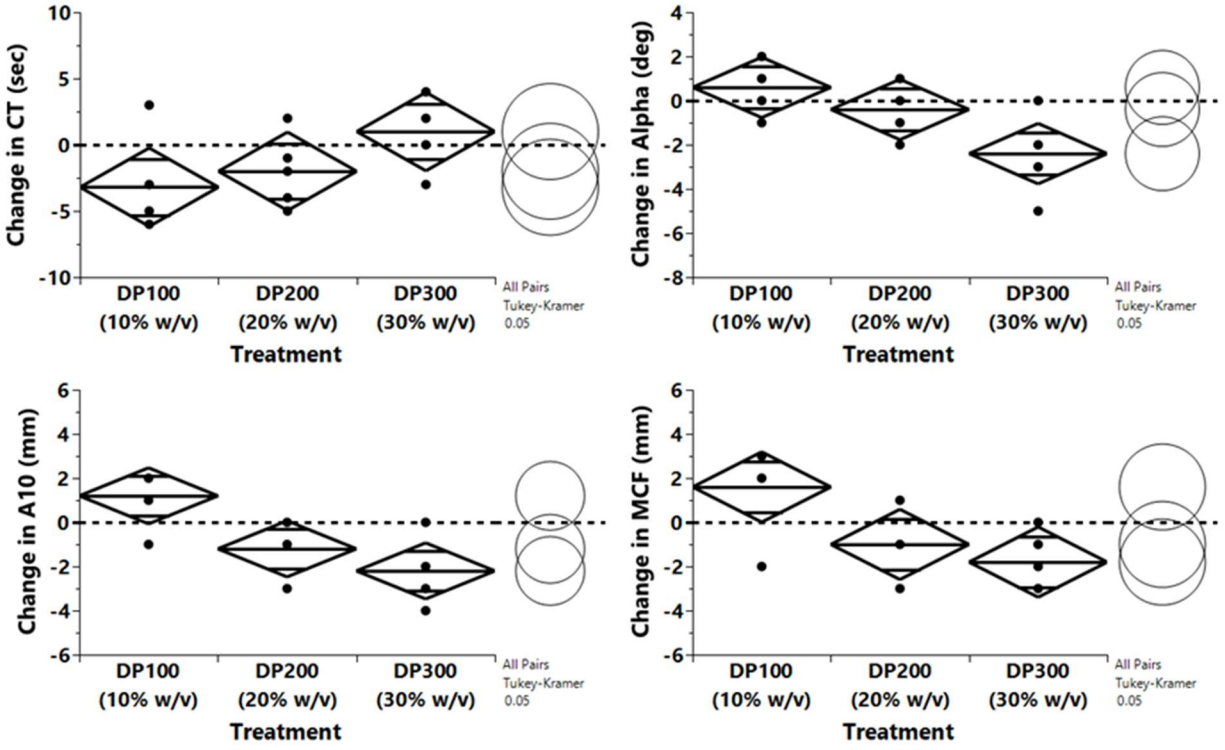

Figure 8. Linear GmMA ROTEM in human donor plasma (n=5). The data displayed is the difference from a saline volume control run at the same time for each donor. A dotted line is placed

at zero to represent no change from the saline control. Top left: Change in clotting time measured in seconds, there was no significant change from the saline control, however there was a significant difference between DP100 and DP300 ($p = 0.0235$). Top right: Change in alpha angle measured in degrees, DP300 was the only treatment significantly different from saline ($p = 0.0058$). While DP300 was significantly different from both DP100 and DP200 ($p = 0.0012$ and $p = 0.0158$, respectively). Bottom left: Change in A10 measured in mm, DP300 was the only treatment significantly different from saline ($p = 0.0059$). While DP300 was significantly different from DP100 and DP200 ($p = 0.0002$ and $p = 0.0093$, respectively). Bottom right: Change in maximum clot firmness measured in mm, there was no significant change from the saline control, however DP300 was significantly different from both DP100 and DP200 ($p = 0.0017$ and $p = 0.0199$, respectively). A fit model for a repeated measure, one-way anova with tukey post-hoc analysis ($\alpha = 0.050$) with donor as a random source effect was used.

Overall, only linear DP300 GmMA showed a significant change in the alpha angle (lower CL = -0.6 degrees, upper CL = -3.8 degrees) and A10 (lower CL = -0.6, upper CL = -3.6). Interestingly, there was a trend towards the DP100 slightly increasing alpha angle, A10, and MCF compared to saline, however it was not significant. Next, we evaluated the linear zwitterions MPC (Figure 9) and SBMA (Figure 10) below.

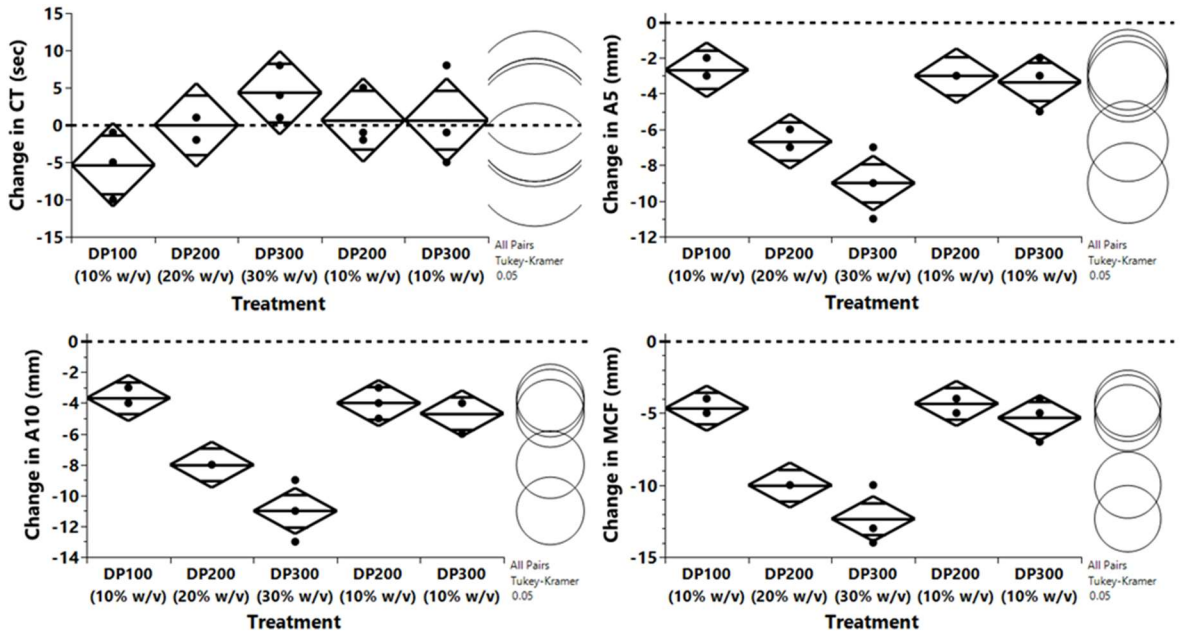

Figure 9. Linear MPC ROTEM in human donor plasma (n=3). The data displayed is the difference from a saline volume control run at the same time for each donor. A dotted line is placed at zero to represent no change from the saline control. Top left: Change in clotting time measured in seconds, there was no significant change from the saline control, however there was a significant difference between DP100 and DP300 ($p = 0.0174$). Top right: Change in A5 measured in mm. Instead of alpha angle, A5 was reported instead due to alpha angle sometimes being not being measured with plasma samples. DP100, DP200 (20% w/v), and DP300 (30% w/v) were all significantly different from saline ($p = 0.0285$, $p = <0.0001$, and $p = <0.0001$, respectively). DP200 (20% w/v) and DP300 (30% w/v) were significantly different from the same treatments dosed at the lower concentration of 10% w/v ($p = 0.0035$ and $p = 0.0001$, respectively). However, the 10% w/v concentration of DP200 and DP300 were still significantly different from the saline control ($p = 0.0139$ and $p = 0.0069$, respectively). Bottom left: Change in A10 measured in mm. DP100, DP200 (20% w/v), and DP300 (30% w/v) were all significantly different from saline ($p = 0.0104$, $p = <0.0001$, and $p = <0.0001$, respectively). DP200 (20% w/v) and DP300 (30% w/v) were significantly different from the same treatments dosed at the lower concentration of 10% w/v ($p = 0.0058$ and $p = 0.0002$, respectively). However, the 10% w/v concentration of DP200 and DP300 were still significantly different from the saline control ($p = 0.0058$ and $p = 0.0019$, respectively). Bottom right: Change in MCF measured in mm. DP100, DP200 (20% w/v), and DP300 (30% w/v) were all significantly different from saline ($p = 0.0024$, $p = <0.0001$, and $p = <0.0001$,

respectively). DP200 (20% w/v) and DP300 (30% w/v) were significantly different from the same treatments dosed at the lower concentration of 10% w/v ($p = 0.0005$ and $p = >0.0001$, respectively). However, the 10% w/v concentration of DP200 and DP300 were still significantly different from the saline control ($p = 0.0041$ and $p = 0.0008$, respectively). A fit model for a repeated measure, one-way anova with tukey post-hoc analysis ($\alpha = 0.050$) with donor as a random source effect was used.

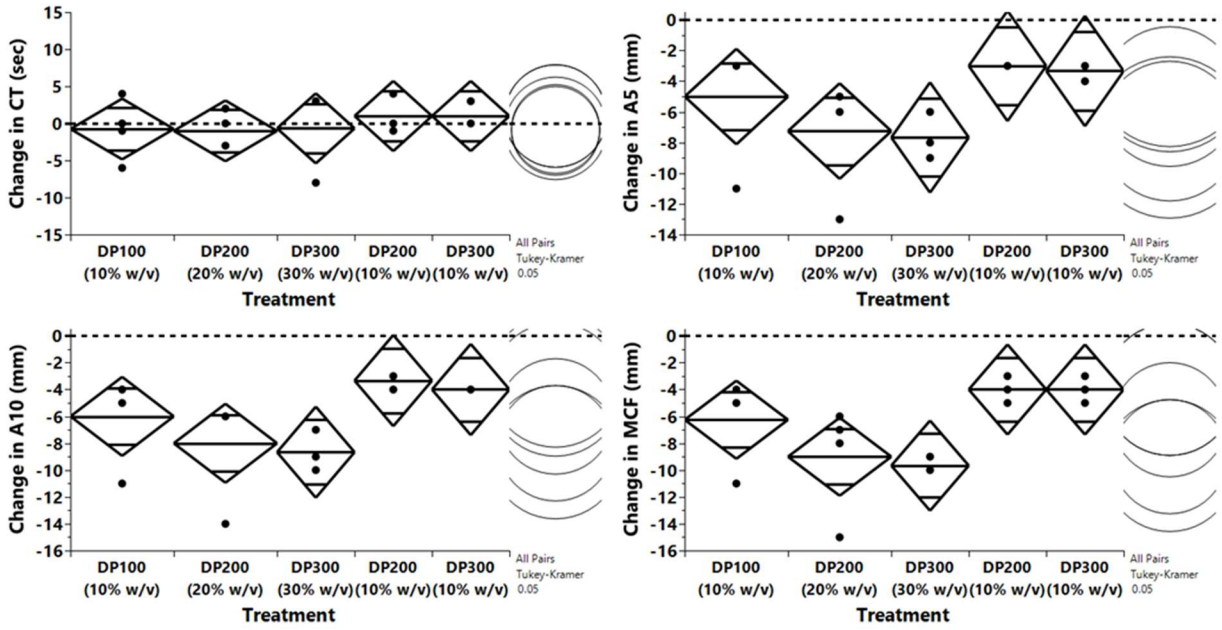

Figure 10. Linear SBMA ROTEM in human donor plasma (n=3). The data displayed is the difference from a saline volume control run at the same time for each donor. A dotted line is placed at zero to represent no change from the saline control. Top left: Change in clotting time measured in seconds, there was no significant change from the saline control. Top right Change in A5 measured in mm. Instead of alpha angle, A5 was reported instead due to alpha angle sometimes being not being measured with plasma samples. There was no significant change from the saline control. Bottom left: Change in A10 measured in mm. There was no significant change from the saline control. Bottom right: Change in MCF measured in mm. There was no significant change from the saline control. A fit model for a repeated measure, one-way anova with tukey post-hoc analysis ($\alpha = 0.050$) with donor as a random source effect was used.

MPC significantly affected coagulation compared to the saline control and led to softer clots. We evaluated lower %w/v concentrations of the DP200 and DP300 polymers, which reduced the impact on coagulation but was still significant. SBMA showed similar trends to MPC, but with more variation that resulted in n=3 donors being too small a sample size to see significance statistically. Since, A10 levels correlate highly with plasma fibrinogen levels, the decrease in clot firmness could suggest either the zwitterions are somehow binding fibrinogen (possibly through electrostatic charge) and decreasing the concentration of it, or that it is disrupting fibrin polymerization, and changing clot structure, resulting in softer clots.[30] Follow-up turbidity and SEM analysis could be run to investigate this further.

Next, we completed some initial in vivo experiments using a severe hemorrhagic shock model (Figure 11 below).

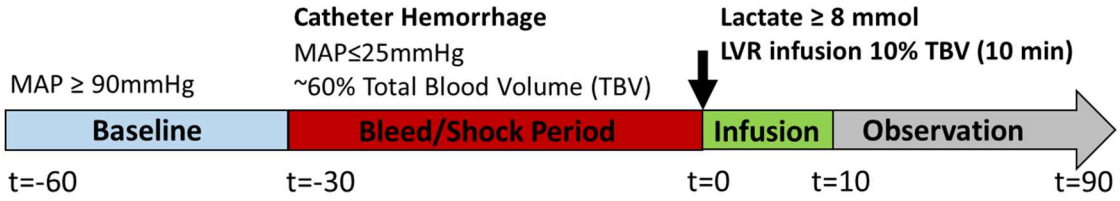

Figure 11. Overview of the severe hemorrhagic shock model.

Blood pressure versus time during the study are shown below for the DP200 and 300 for pGmMA (Figure 12) and the DP100, 200, and 300 for pSBMA (Figure 13).

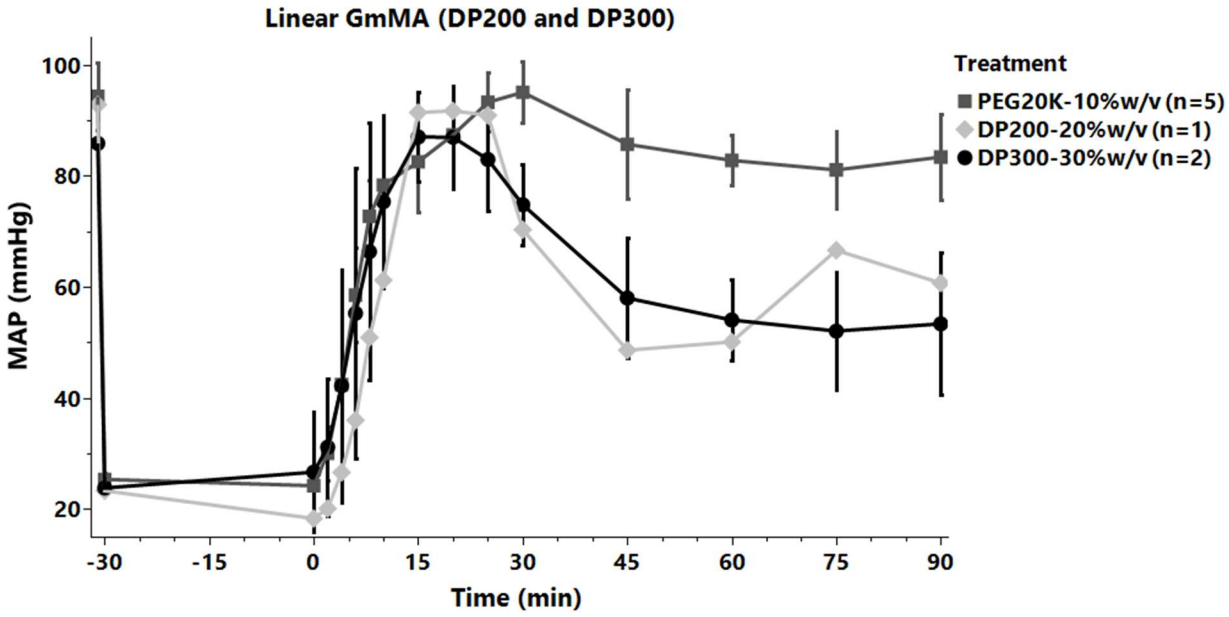

Figure 12. Blood pressure comparison of different linear GmMA LVRs during the severe hemorrhagic shock rat model. Both the DP200 (20% w/v) and the DP300 (30% w/v) were unable to rescue MAP as well as PEG20K.

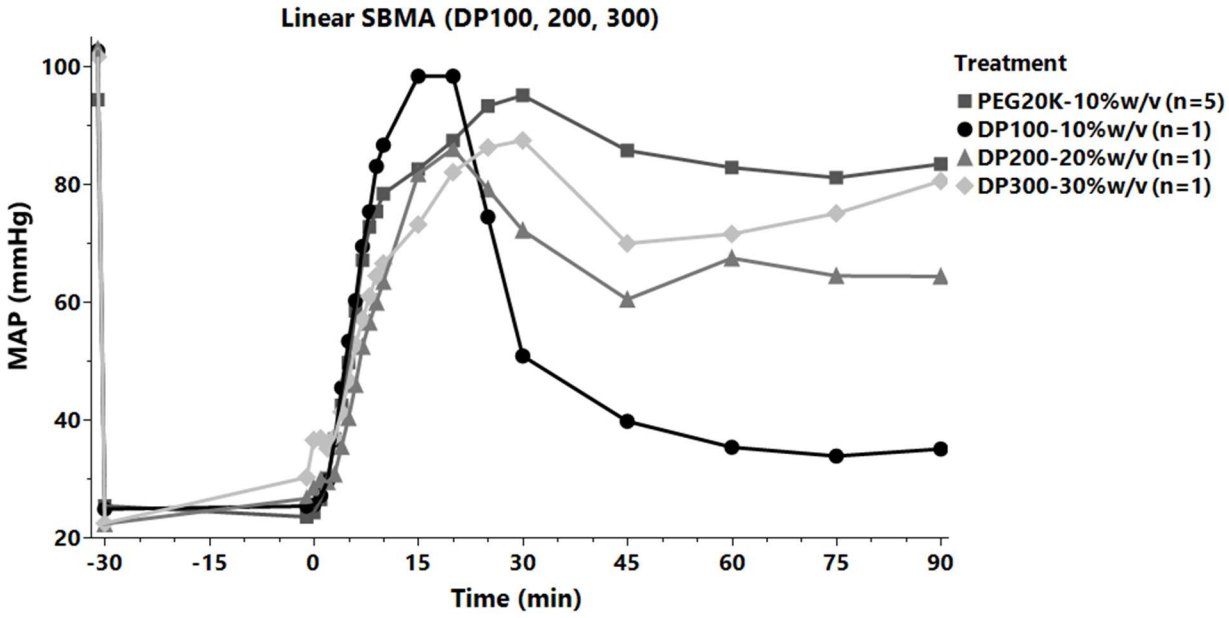

Figure 13. Blood pressure comparison of different linear SBMA LVRs during the severe hemorrhagic shock rat model. The DP100 (10% w/v) was rapidly cleared from the bloodstream due to its small size, while the DP200 (20% w/v) showed a sustained higher MAP, and the DP300 (30% w/v) was able to rescue MAP similar to PEG20K.

From the initial *in vivo* screening experiment, pGmMA couldn't match the performance of PEG 20k, while pSBMA of DP300 increased MAP to a similar level as PEG 20k at 90 minutes. However, from the ROTEM studies pSBMA performed poorly while pGmMA displayed very little effect on coagulation. These initial studies indicated that for pGmMA we needed to increase size to improve biodistribution, and find some way to increase its oncotic potency, while for pSBMA, we needed to find a way to decrease the concentration in the blood to try and prevent coagulopathies. We hypothesized that moving away from a linear architecture and to a radiant star might help improve the drawbacks of both pGmMA and pSBMA. Previous work in literature has shown that the water-carrying capacity of PEG can be improved by moving from linear PEG to hyper-branched PEG (HPG). HPG also showed better blood compatibility compared to its linear counterparts of similar molecular weights.[31–33]

5.3.3 *Synthesis and Characterization of Radiant Star LVRs of various Sizes and Chemistries*

Figure 14 below shows the reaction scheme outlining the synthesis of radiant stars using RAFT adapted from Das *et al*.[13]

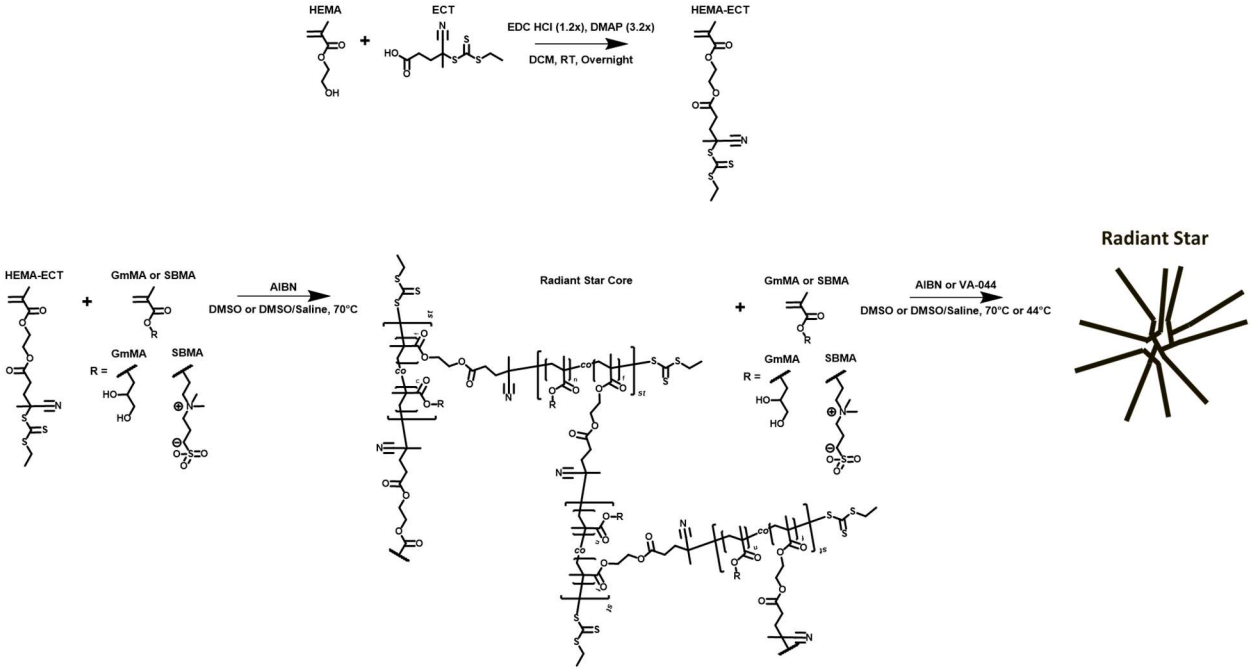

Figure 14. Reaction scheme for synthesis of HEMA-ECT (hECT) and the radiant stars.

From the screening experiments, we decided to synthesize DP100 and DP200 radiant stars of pSBMA to directly compare to the linear counterparts in ROTEM, while we synthesized DP400 of both pSBMA and pGmMA to try and improve *in vivo* performance. Conversion of all polymers were characterized by ^{1}H NMR. Conversion was then used to calculate theoretical molecular weights (Mn). The molecular weight (Mn) and dispersity were determined using 100% mass recovery (RI Detector, Wyatt Optilab T-rex) and multiangle light scattering (MALS, Wyatt miniDAWN Treos) gel permeation chromatography (GPC). The running solvent was phosphate buffered saline (PBS) (flow rate: 0.5 mL/min) at room temperature and samples were prepared at 10 mg/mL. Figure 15 shows the GPC traces of each of the synthesized polymers, and Table 5 below summarizes the molecular weights calculated from NMR conversion and the molecular weights and dispersity indices measured from GPC.

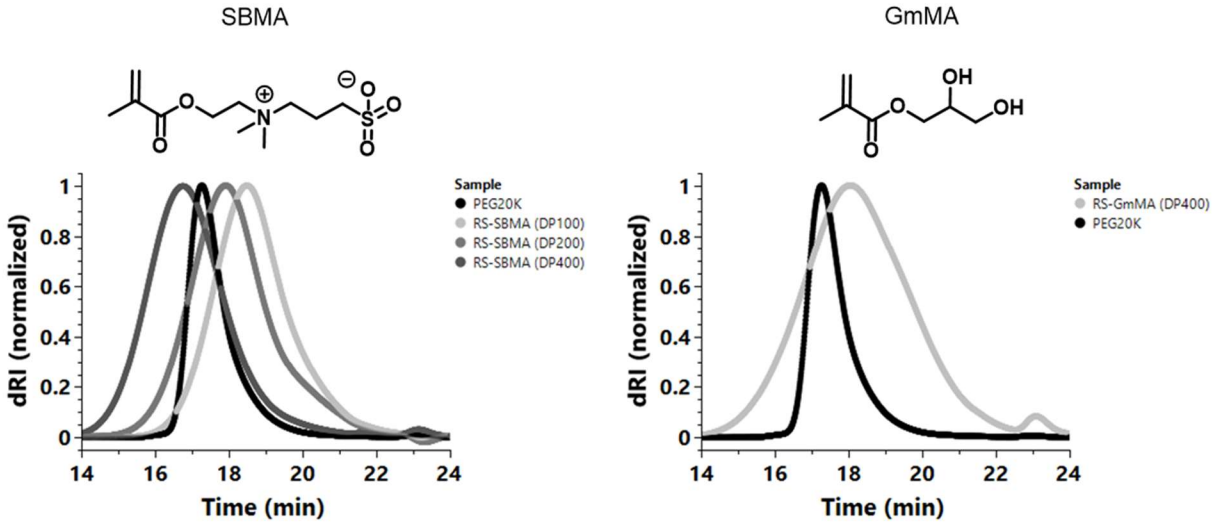

Figure 15. Gel Permeation Chromatograms of radiant star LVRs. Left: SBMA zwitterionic radiant stars that were chain extended by DP100, 200, and 400 repeat units, and Right: GmMA radiant star chain extended by DP400. All polymers were run at 10 mg/mL concentration in PBS.

Table 5. Overview of Radiant Star LVRs Synthesized.

Sample ID	Monomer	NMR Analysis				GPC Analysis	
		Conversion (%)	Total DP	Per Arm DP	MW (kDa)	PDI	MW (kDa)
RS-SBMA (DP100)	SBMA	96	96	13	35	1.02	33
RS-SBMA (DP200)		96	192	27	62	1.09	42
RS-SBMA (DP400)		98	392	54	118	1.12	93
RS-GmMA (DP400)	GmMA	67	402	56	70	1.01	78

We successively synthesized a range of pSBMA zwitterionic methacrylates and a radiant star pGmMA with a comparable range of PDIs 1.02-1.12 and molecular weights ~ 35 kDa to 118 kDa to the linear couterparts. There was good agreement between the theoretical MW from ^{1}H NMR conversion and GPC 100% mass recovery measurement for GmMA, however SBMA showed a larger discrepancy. This could be due to interactions with the column. From ^{1}H NMR analysis we estimated that each radiant star has ~7 arms. However, SAXS analysis found that 3 arms provided the best fit of the data (data not shown). Figure 16 below shows the SAXS analysis of each of the radiant stars synthesized along with the previous linear LVRs for comparison.

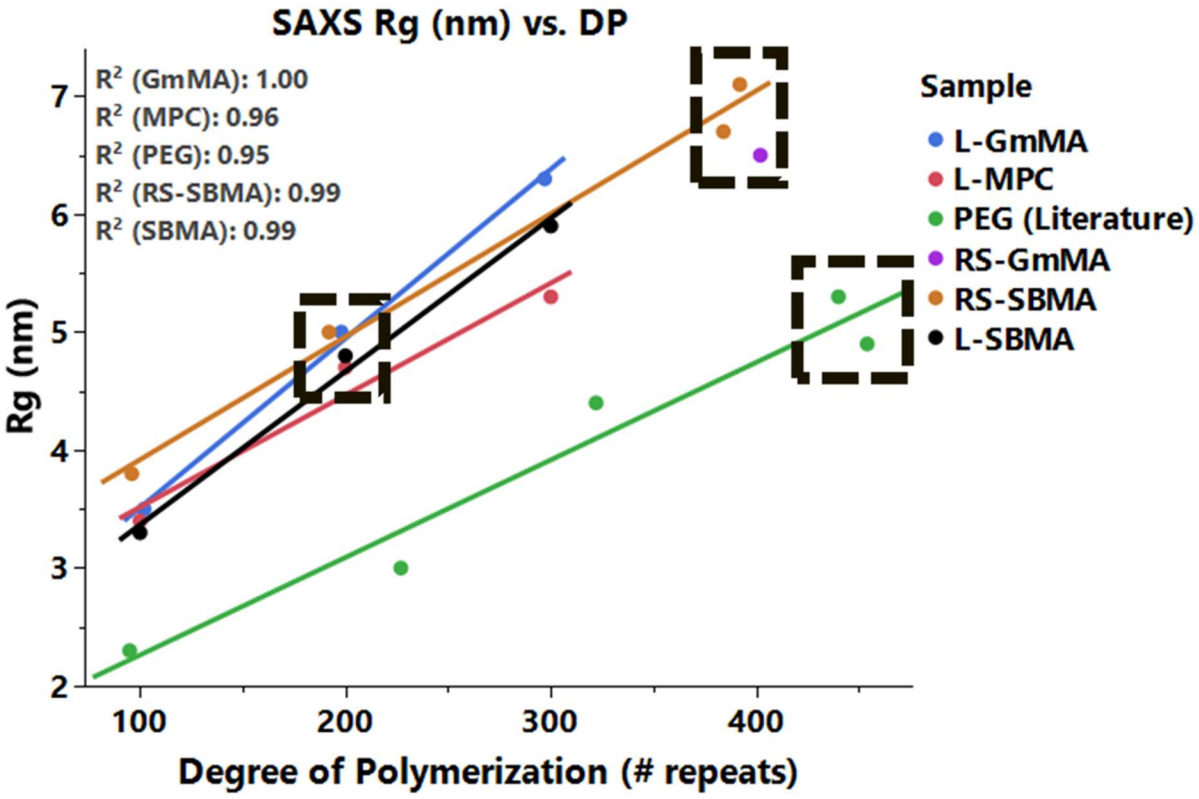

Figure 16. SAXS radius of gyration measurements as a function of degree of polymerization.

As expected, we observe a good linear relationship between degrees of polymerization and Rg. A similar trend in Rg versus degree of polymerization were measured for the pSBMA radiant stars. The DP400 pSBMA and pGmMA radiant stars showed larger Rgs compared to the DP300 linear counterparts, and the PEG 20k. The radiant stars were then evaluated in vapor pressure osmometry and compared to their linear counterparts (Figure 17 below).

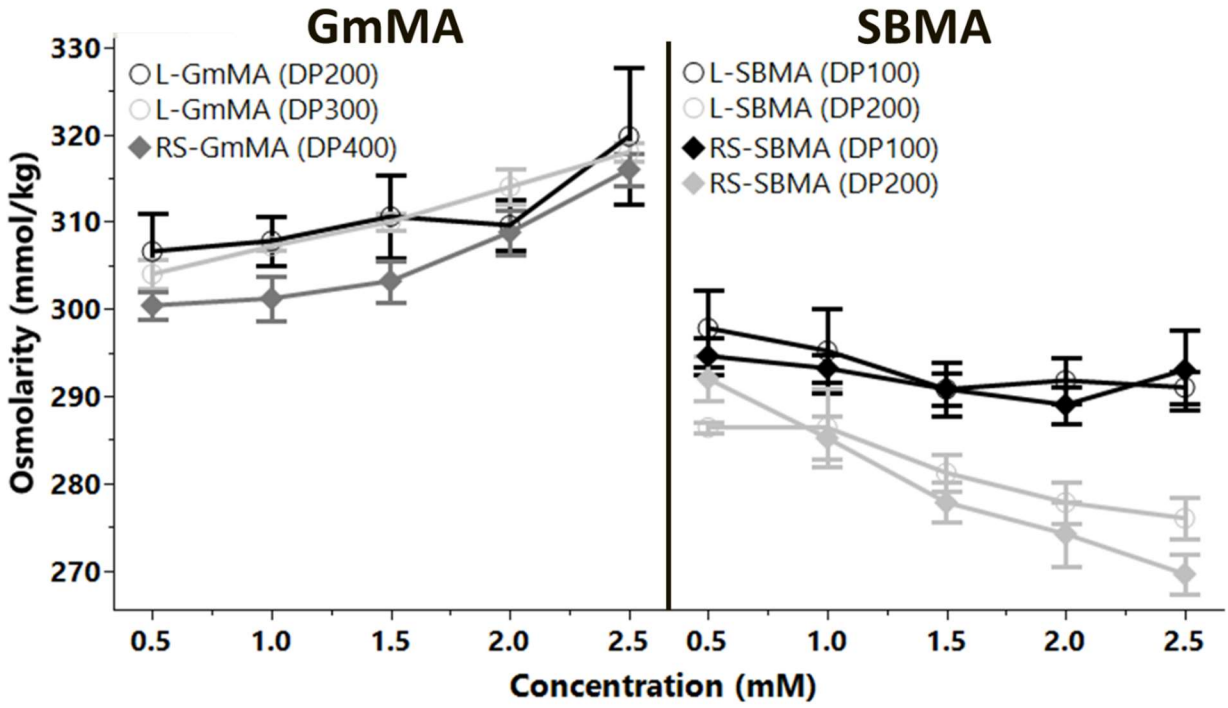

Figure 17. Vapor pressure osmometry measurements of pGmMA (left) and pSBMA (right). All measurements were done using a Vapro 5600 in triplicate. Error bars are 1 standard deviation from the mean.

Interestingly, the radiant stars followed similar osmolarity trends as the linear counterparts. The pSBMA radiant stars showed the same decrease in osmolarity with molar concentration indicating they most likely self-assembled as well. Similar to the linear polymers, future work will be done to use DSC to directly measure nonfreezing bound water, and to measure the hydrodynamic radius of the polymers either through Dynamic Light Scattering or NMR.

5.3.4 *Characterization of radiant stars on their impact on coagulation*

Next, we were curious if the radiant star forms of SBMA would show any improvement over linear counterparts. We compared both in ROTEM analysis of coagulation in human plasma (Figure 18 below).

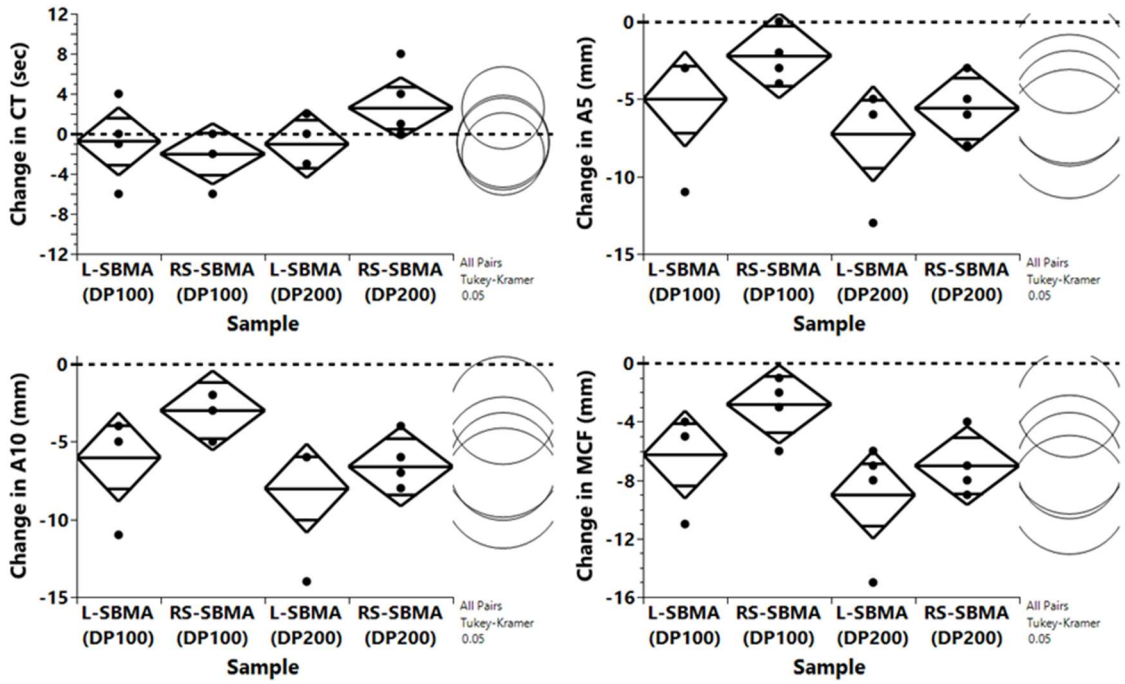

Figure 18. ROTEM Comparison of Linear (n=3) and Radiant Star SBMA (n=4) in human donor plasma. The data displayed is the difference from a saline volume control run at the same time for each donor. A dotted line is placed at zero to represent no change from the saline control. Top left: Change in clotting time measured in seconds, there was no significant change from the saline control. Top right Change in A5 measured in mm. Instead of alpha angle, A5 was reported instead due to alpha angle sometimes being not being measured with plasma samples. There was no significant change from the saline control. Bottom left: Change in A10 measured in mm. There was no significant change from the saline control. Bottom right: Change in MCF measured in mm. There was no significant change from the saline control. A fit model for a repeated measure, one-way anova with tukey post-hoc analysis ($\alpha = 0.050$) with donor as a random source effect was used.

Although not significant, we did observe a slight trend towards a smaller effect in coagulation. From the linear zwitterions we know that decreasing the number of moles of polymer in the blood decreases the impact on coagulation. The radiant stars are designed to be the same size but increase the water-carrying capacity of the LVR. This would enable us to use a lower molar concentration in the blood, and hopefully further mitigate the effects on coagulation. Therefore, we moved

forward with the radiant star formulations at the largest DP for both SBMA and GmMA for further coagulation characterization and evaluation in vivo.

We proceeded to evaluate the following final material set – Hextend (commercial colloid), PEG20K, RS-SBMA (DP400), and RS-GmMA (DP400) *in vivo*. Figure 19 below shows ROTEM evaluation of human whole blood.

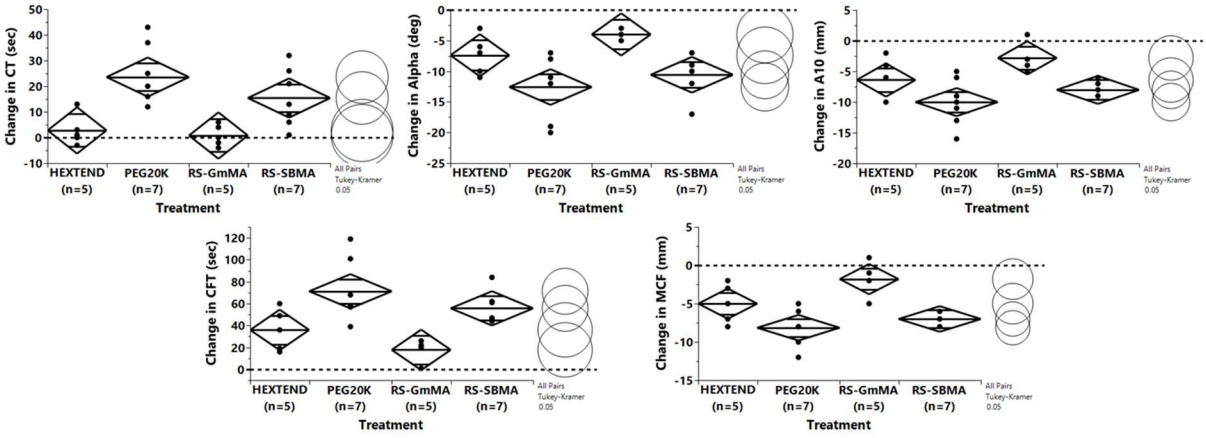

Figure 19. ROTEM evaluation of final LVRs in human whole blood (n=5-7). The data displayed is the difference from a saline volume control run at the same time for each donor. A dotted line is placed at zero to represent no change from the saline control. Top left: Change in clotting time measured in seconds, both PEG20K and RS-SBMA were statistically different from the saline control ($p = 0.0003$ and $p = 0.0178$, respectively). Top middle: Change in alpha angle measured in degrees, Hextend, PEG20K, and RS-SBMA were all statistically different from the saline control ($p = 0.0153$, $p = <0.0001$, and $p = <0.0001$, respectively). Top right: Change in A10 measured in mm, Hextend, PEG20K, and RS-SBMA were all statistically different from the saline control ($p = 0.0010$, $p = <0.0001$, and $p = <0.0001$, respectively). Bottom left: Change in clot firmness time measured in sec, Hextend, PEG20K, and RS-SBMA were all statistically different from the saline control ($p = 0.0144$, $p = <0.0001$, and $p = <0.0001$, respectively). Bottom right: Change in maximum clot firmness measured in mm, Hextend, PEG20K, and RS-SBMA were all statistically different from the saline control ($p = 0.0004$, $p = <0.0001$, and $p = <0.0001$, respectively). A fit model for a repeated measure, one-way anova with tukey post-hoc analysis ($\alpha = 0.050$) with donor as a random source effect was used.

In whole blood, PEG20K and the radiant star SBMA both increased clotting time compared to saline. Hextend, PEG20K, and the radiant star SBMA all decrease the rate of clot firmness, and lead to overall softer clots. The PEG20K and RS-SBMA were not statistically different from each other, and both impacted clotting similarly leading to a hypocoagulable state with decreased clot firmness. The radiant star GmMA did not show a statistical difference from saline across the typical ROTEM parameters reported. Next, we evaluated the same treatments in human plasma to remove platelets and see the effect on fibrinogen (Figure 20 below).

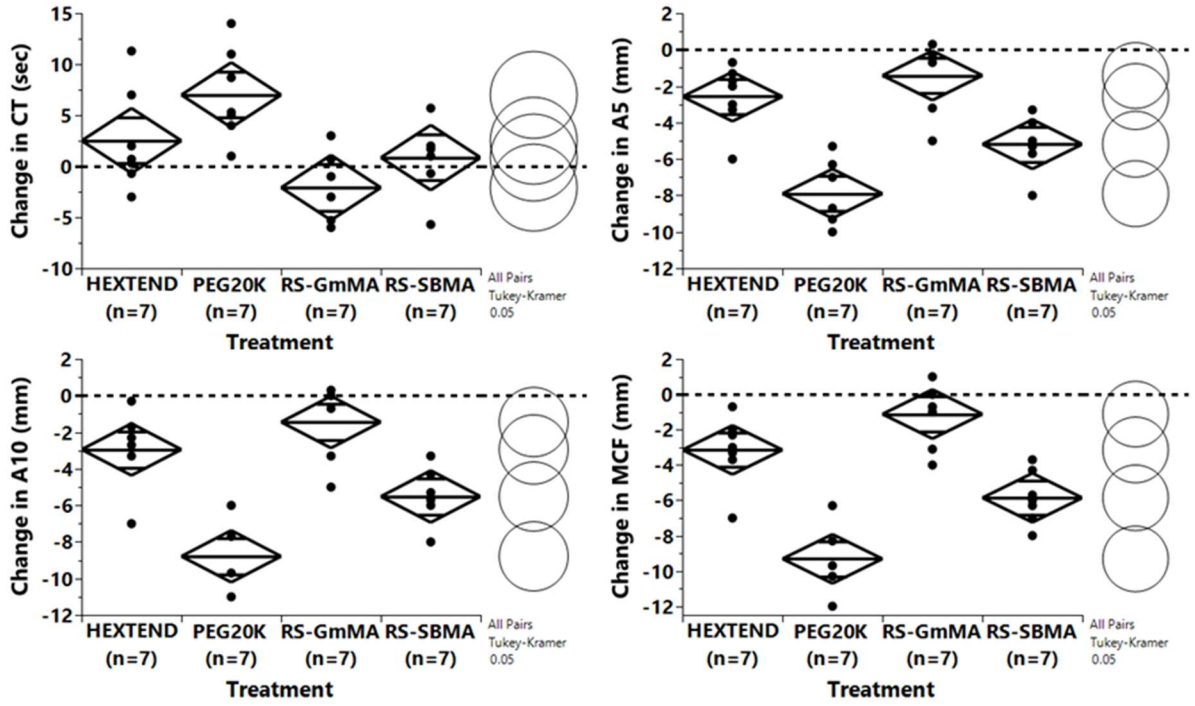

Figure 20. ROTEM evaluation of final LVRs in human plasma (n=7). The data displayed is the difference from a saline volume control run at the same time for each donor. A dotted line is placed at zero to represent no change from the saline control. Top left: Change in clotting time measured in seconds, PEG20K was statistically different from the saline control ($p = 0.0040$). Top right: Change in A5 measured in mm. Instead of alpha angle, A5 was reported instead due to alpha angle sometimes being not being measured with plasma samples. Hextend, PEG20K, and RS-SBMA were all statistically different from the saline control ($p = 0.0004$, $p = <0.0001$, and $p = <0.0001$, respectively). Bottom left: Change in A10 measured in mm, Hextend, PEG20K, and RS-SBMA were all statistically different from the saline control ($p = 0.0001$, $p = <0.0001$, and $p = <0.0001$, respectively). Bottom right: Change in maximum clot firmness measured in mm,

Hextend, PEG20K, and RS-SBMA were all statistically different from the saline control ($p = <0.0001$, $p = <0.0001$, and $p = <0.0001$, respectively). A fit model for a repeated measure, one-way anova with tukey post-hoc analysis ($\alpha = 0.050$) with donor as a random source effect was used.

Similar to whole blood, PEG20K increased clotting time. Hextend, PEG20K, and RS-SBMA all led to a significant decrease in clot firmness and led to a hypocoagulable state similar to whole blood. To evaluate whether or not Hextend, PEG20K, and RS-SBMA are only disrupting fibrin/fibrinogen or if they are disrupting thrombin activity, we investigated the effect of the treatments on thrombin generation in human plasma. Figure 21 below shows the raw curves quantifying the concentration of thrombin generated when clotting was activated by tissue factor.

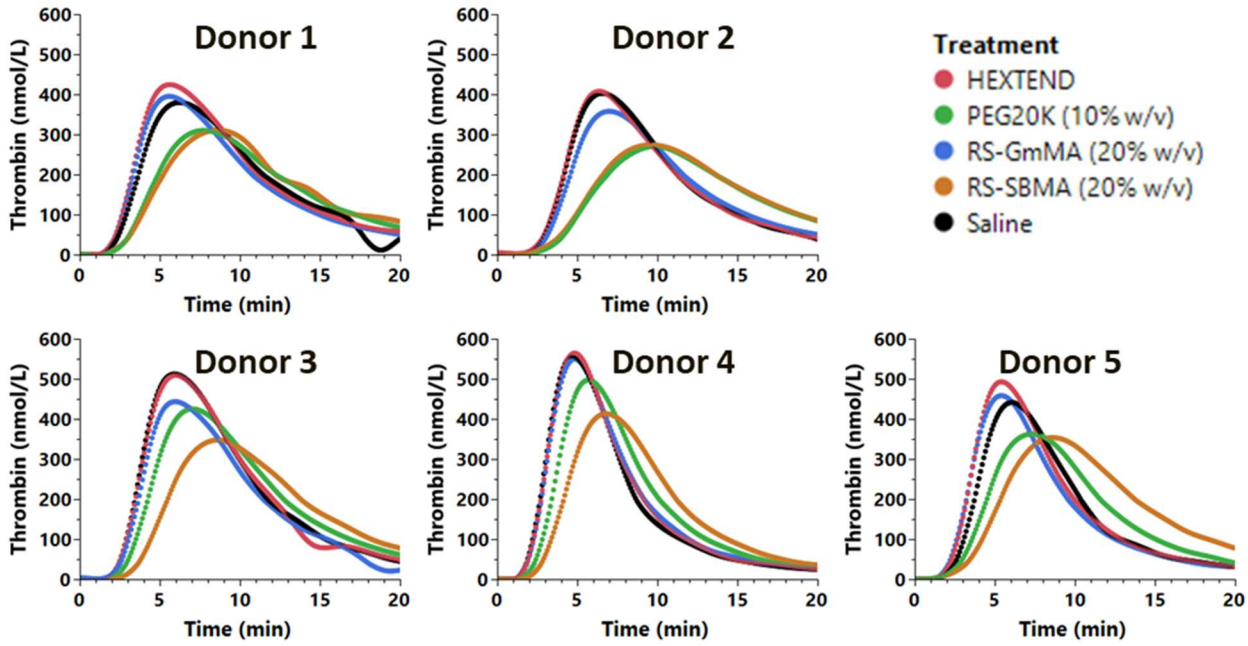

Figure 21. Raw Curves for Thrombin Generation Assay of human plasma (n=5). Upon activation of the extrinsic pathway by tissue factor, prothrombin (factor II) is converted to thrombin by factor Xa. A fluorogenic substrate is cleaved by thrombin, and the fluorescence output is proportional to the concentration of thrombin. The assay tracks thrombin generation from initiation (steep initial portion of curve), through fibrin formation (peak), and through inactivation (down slope post peak).

From the raw TGA curves, PEG-20K and RS-SBMA decrease the peak and shift the thrombin generation curve down to later time points. Figure 22 below shows the typical TGA metrics.

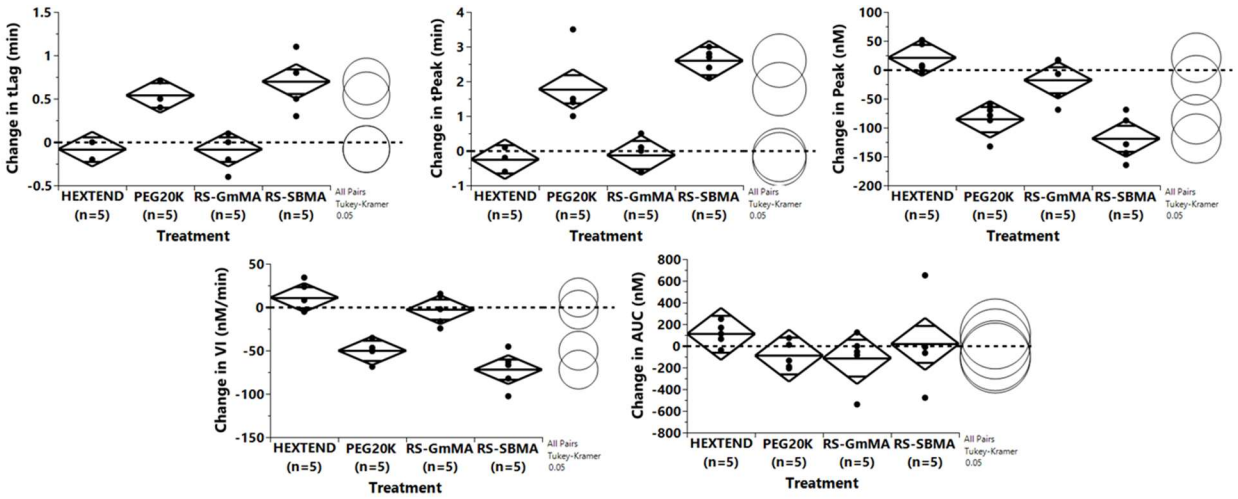

Figure 22. Thrombin Generation Assay metrics for n=5 human donors. The data displayed is the difference from a saline volume control run at the same time for each donor. A dotted line is placed at zero to represent no change from the saline control. Top left: Change in tLag measured in minutes, both PEG20K and RS-SBMA were statistically different from the saline control ($p = 0.0004$ and $p = <0.0001$, respectively). Top middle: Change in tPeak measured in minutes, both PEG20K, and RS-SBMA were all statistically different from the saline control ($p = 0.0002$ and $p = <0.0001$, respectively). Top right: Change in the peak thrombin concentration measured in nM, both PEG20K and RS-SBMA were statistically different from the saline control ($p = 0.0001$ and $p = <0.0001$, respectively). Bottom left: Change in VI or the slope of the initiation phase measured in nM/min, both PEG20K and RS-SBMA were statistically different from the saline control ($p = <0.0001$ and $p = <0.0001$, respectively). Bottom right: Change in the area under the curve maximum measured in nM, no treatment was statistically different from the saline control. A fit model for a repeated measure, one-way anova with tukey post-hoc analysis ($\alpha = 0.050$) with donor as a random source effect was used.

PEG20K and RS-SBMA affected thrombin generation similarly. They both increased the lag phase of the TGA curve and led to a slower rate of plasmin generation resulting in an overall lower peak thrombin concentration, and a prolonged inactivation phase. However, the total amount of thrombin generated, quantified from the AUC, stays the same across treatments meaning the same

amount of thrombin was generated. Since thrombin concentration affects fibrin fibril structure, it appears that PEG20K and RS-SBMA are delaying prothrombin to thrombin conversion, but not fully disrupting it, which could be leading to softer clots.[34] While Hextend is not affecting thrombin, but most likely directly acting on fibrin(ogen). As mentioned earlier, SEMs and turbidity assays could be run to investigate structural changes in fibrin further. To investigate their effect on primary hemostasis, we investigated the effect of the treatments on platelet aggregation (Figures 23 and 24 below). Note due to the time sensitivity of platelet aggregation tests, and only four channels available on the Chronolog, Hextend was not evaluated.

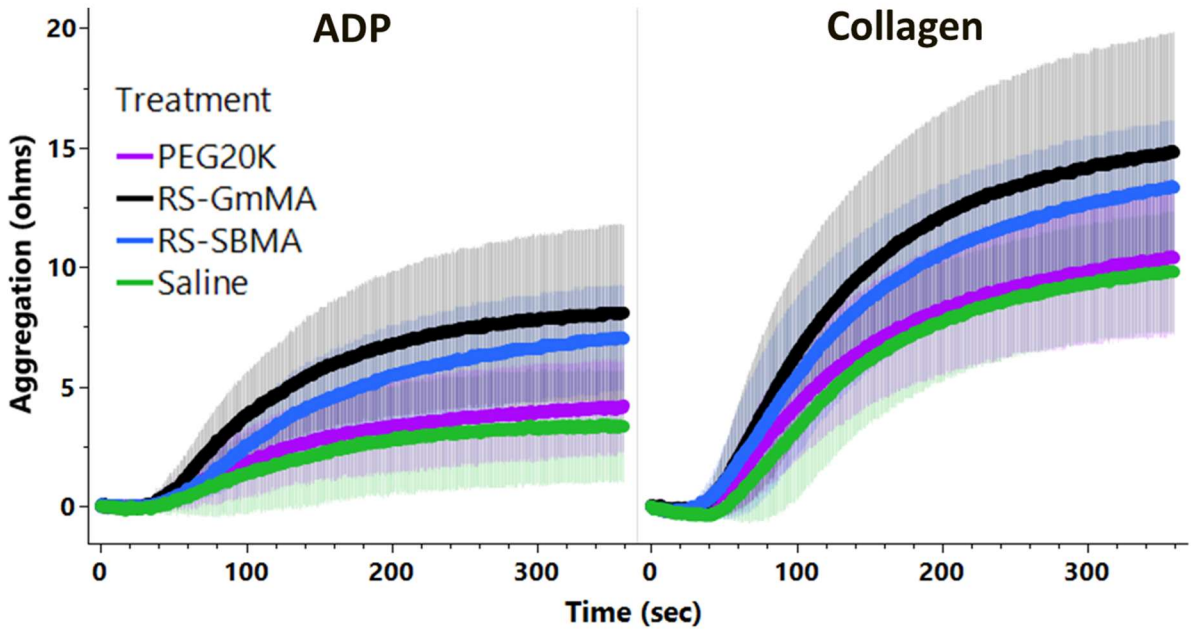

Figure 23. Aggregation curves from platelet aggregometry evaluation of treatments in human whole blood (n=4) using impedance. Both ADP (left) and Collagen (right) were used as agonists to evaluate the $P2Y_1$ and GPVI binding on the surface of platelets to trigger aggregation. The error bands represent one standard deviation from the mean.

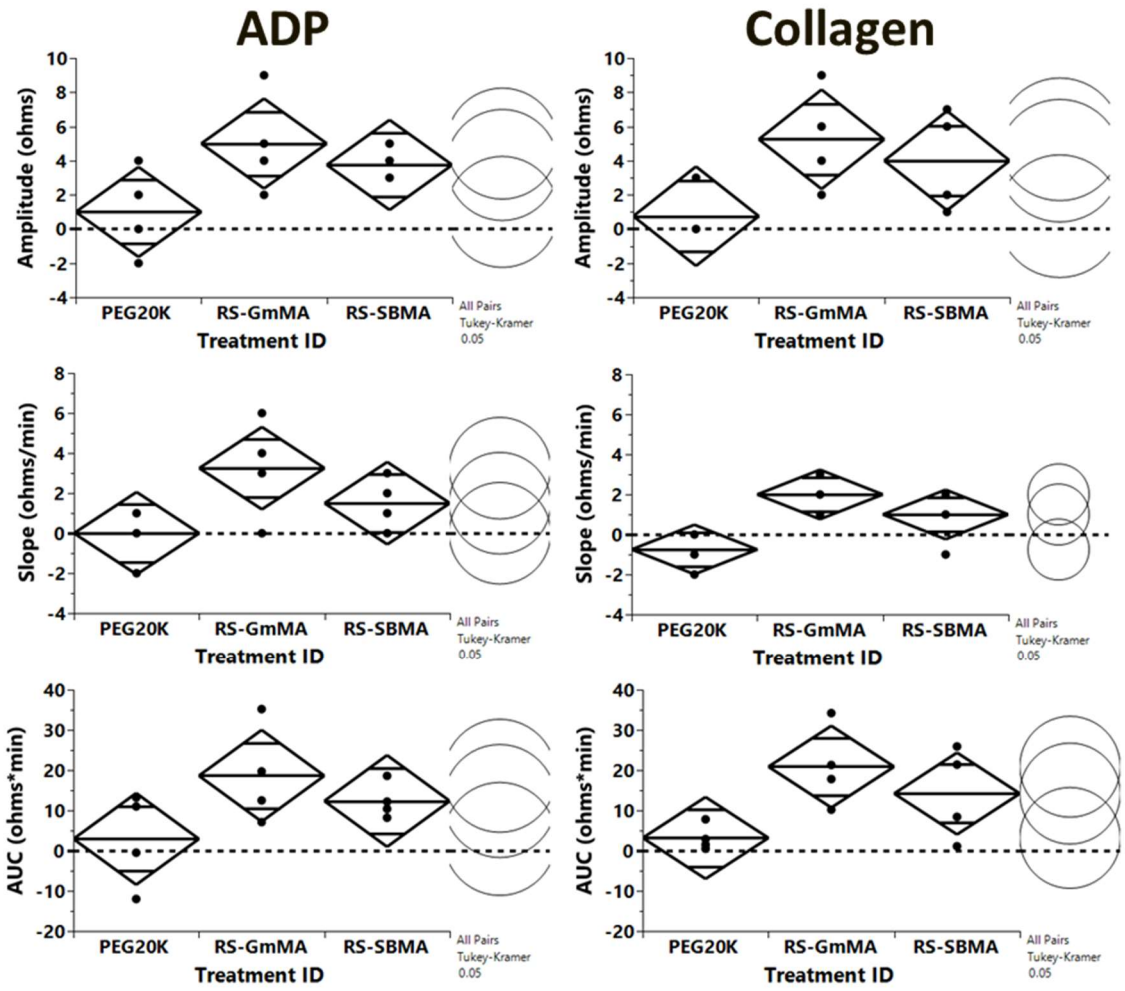

Figure 24. Typical reported metrics from impedance-based platelet aggregometry evaluation of treatments in human whole blood (n=4). Both ADP (left) and Collagen (right) were used as agonists to evaluate the $P2Y_1$ and GPVI binding, respectively, on the surface of platelets to trigger aggregation. The data displayed is the difference from a saline volume control run at the same time for each donor. A dotted line is placed at zero to represent no change from the saline control. Top left: Change in amplitude (agonist = ADP) measured in ohms, there was no significant change from the saline control. Top right: Change in amplitude (agonist = collagen) measured in ohms, there was no significant change from the saline control. Middle left: Change in slope (agonist = ADP) measured in ohms/min, there was no significant change from the saline control. Middle right: Change in slope (agonist = collagen) measured in ohms/min, there was no significant change from the saline control, however there was a statistically significant difference between PEG 20k and RS-GmMA ($p = <0.0153$, respectively). Bottom left: Change in area

under the curve (AUC) (agonist = ADP) measured in ohms*min, there was no significant change from the saline control. Bottom right: Change in area under the curve (AUC) (agonist = collagen) measured in ohms*min, there was no significant change from the saline control. A fit model for a repeated measure, one-way anova with tukey post-hoc analysis ($\alpha = 0.050$) with donor as a random source effect was used.

Interestingly, in the full aggregation curves for both agonists, the radiant stars lead to increased aggregation while PEG 20k shows similar aggregation to the saline volume control. It is good to see that the radiant stars do not interfere with the agonists ADP and collagen binding to $P2Y_1$ and GPVI, respectively, which would inhibit aggregation, and it is unknown whether the increase in aggregation would lead to any concerns with creating a prothrombotic response *in vivo*. Looking at the platelet aggregation parameters – amplitude, slope, and AUC, there is trend towards an increase in all parameters indicating that the radiant stars increase the maximum platelet aggregation, increase the rate of aggregation, an increase the overall total aggregation compared to the saline control. However, only a statistically significant difference in slope between PEG 20k and the pGmMA radiant star was found. Indicating that the RS-GmMA increases the rate of platelet aggregation compared to PEG 20k. From ROTEM, we can estimate the platelet contribution to the maximum clot firmness (SI Figure S5), by subtracting the MCF in plasma from the MCF measured in whole blood. We did not see a statistically significant effect on platelets for any of the treatments. To further investigate platelet effects, aggregometry tests, clot contraction using a rheometer, and platelet binding/activation using flow cytometry are additional evaluations that can be done to see if LVRs affect platelet function and if they non-specifically bind to surface of platelets.

Taken together these in vitro coagulation assays indicate that PEG20K and RS-SBMA, and to some extent Hextend can create a hypocoagulable state in human blood. It should be noted that all of these assays are static and designed to fully activate all the clotting factors present in blood. This is not representative of *in vivo* coagulation where clotting is occurring under flow and high shear rates. *In vitro* microfluidic assays and uncontrolled hemorrhage *in vivo* animal studies could be leveraged in the future to evaluate the risk of these LVRs creating significant coagulopathies.

5.3.5 *LVRs show similar ability to correct severe hemorrhagic shock in rats as PEG20K*

We proceeded to evaluate Hextend, PEG20K, RS-SBMA (DP400), and RS-GmMA (DP400) in a severe hemorrhagic shock rat model. Figure 25 below shows an overview of the model.

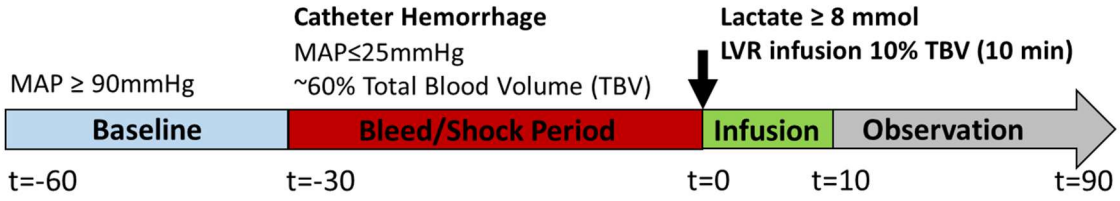

Figure 25. Overview of the severe hemorrhagic shock model.

All rats had similar average % of total blood volumes removed during the catheter hemorrhage period, ~58%, ~60%, ~57%, and ~59% for Hextend, PEG20K, RS-SBMA, and RS-GmMA, respectively. After achieving a lactate ≥ 8 mmol (typically 30-45 minutes of shock), the rats were given a single bolus infusion of treatment over ten minutes. All treatments were administered at an estimated 10% of total blood volume for the rat (prior to severe hemorrhage). PEG20K was administered as a 10% w/v solution, Hextend was given as commercially formulated (6% w/v HES), while the radiant stars were given as 20% w/v solutions. Figure 26 below shows the increase in MAP during infusion of the treatments.

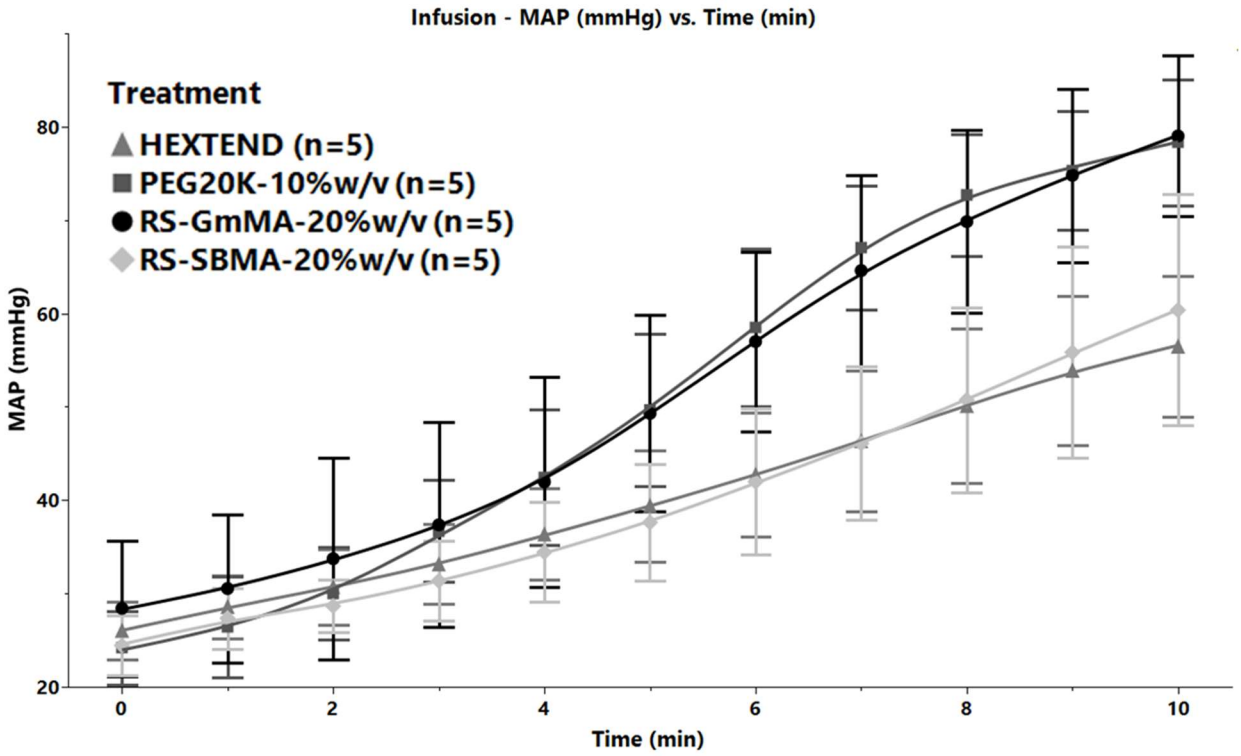

Figure 26. Blood pressure during infusion of treatment over 15 minutes. Hextend was statistically different from PEG20K and RS-GmMA at the following timepoints – T7, T8 ($p = 0.0042$ and $p = 0.0120$), T9, and T10 ($p = 0.0076$ and $p = 0.0060$). RS-SBMA was statistically different from PEG20K and RS-GmMA at the following timepoints – T7, T8 ($p = 0.0053$ and $p = 0.0151$), T9, and T10 ($p = 0.0297$ and $p = 0.0235$).

Interestingly, during the infusion the RS-SBMA showed similar rates of blood pressure increase as Hextend, whereas the RS-GmMA performed similar to PEG20K. This reflects the osmolarity measurements of RS-SBMA. At high concentrations during reconstitution at 20% w/v the RS-SBMA is probably self-assembled, then as it gets diluted in the bloodstream of the rat, it disassembles and as a result increases its osmolarity, leading to a greater oncotic response. Figure 27 below shows the blood pressure over the course of the entire study.

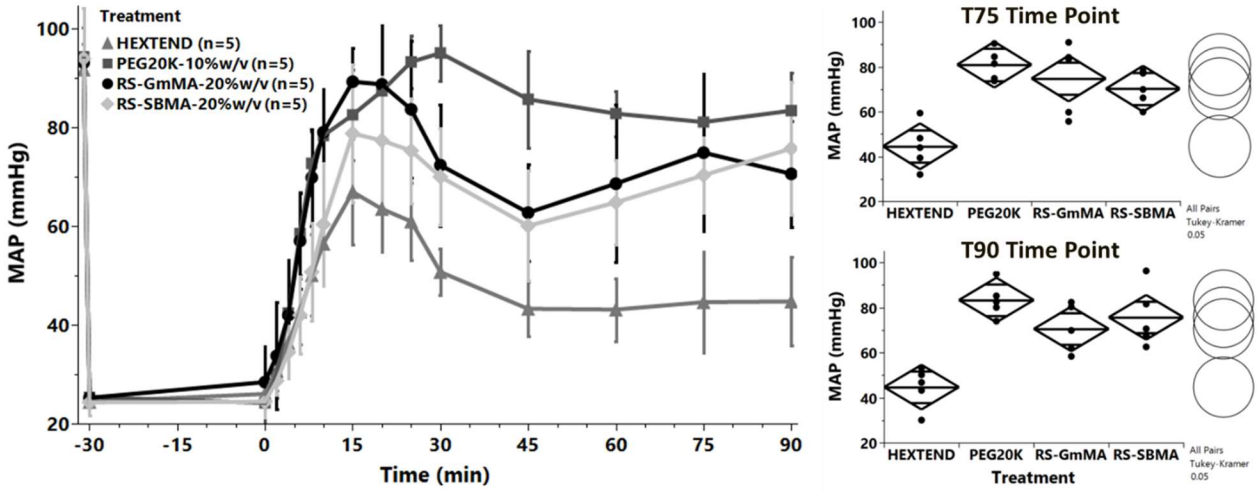

Figure 27. Blood pressure comparison of different LVRs during severe hemorrhagic shock rat model. Left: Right top: MAP for the T75 time point, there was no statistical difference between PEG20K, RS-SBMA, and RS-GmMA, however, Hextend was significantly different from the other treatments ($p = 0.0004$, $p = 0.0083$, and $p = 0.0021$, respectively). Bottom right: MAP for the T90 time point, there was no statistical difference between PEG20K, RS-SBMA, and RS-GmMA, however, Hextend was significantly different from the other treatments ($p = 0.0001$, $p = 0.0013$, and $p = 0.0061$, respectively). A fit model for a repeated measure, one-way anova with tukey post-hoc analysis ($\alpha = 0.050$) was used for statistical analysis.

All treatments show an initial peak of blood pressure between 15 and 30 minutes after administration, followed by a drop in blood pressure. At T75 and T90 there is no statistical difference between PEG20K, RS-GmMA, and RS-SBMA, while Hextend is significantly lower than the other three treatments. It is interesting that SBMA infused similarly to Hextend but over time increased MAP similar to RS-GmMA and PEG20K. It is well known in literature that SBMA displays self-assembly as a function of concentration.[35,36] Potentially, the 20% w/v solution results in self-assembly of RS-SBMA into larger particles that then slowly disassemble in the bloodstream when they are diluted. We observe this self-assembly when we remove counter ions and suspend the SBMA polymers in DI H2O. When salt is added, the polymer goes back into solution. The radiant star LVRs show promising results in correcting blood pressure, Figure 28 below shows blood gas results from the study to monitor how well the radiant stars correct the metabolic disfunction of hemorrhagic shock.

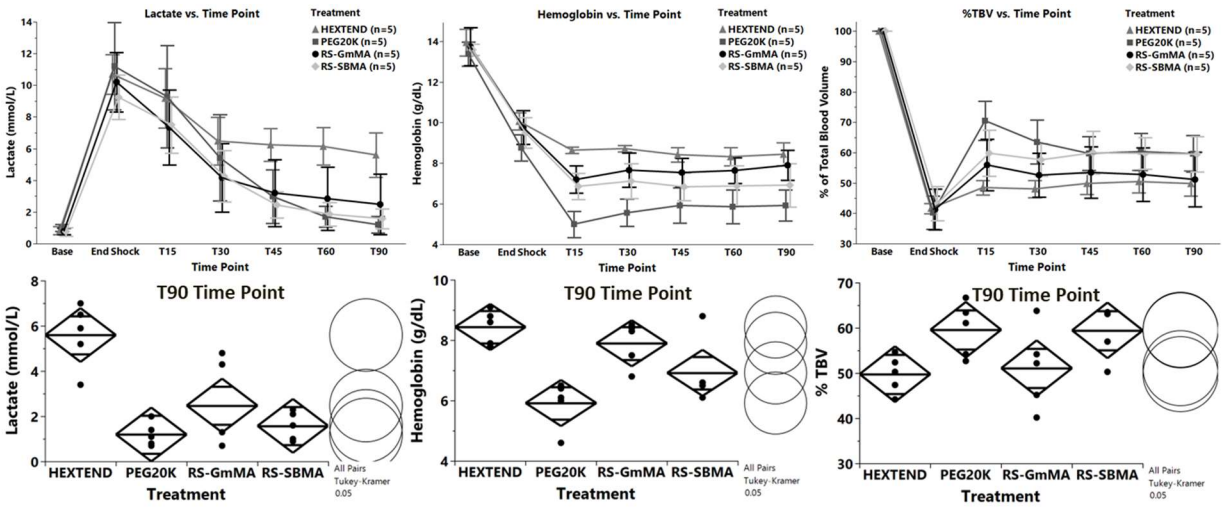

Figure 28. Blood gas and estimated total blood volume at different time points during hemorrhagic shock model. Left: Lactate concentration (mmol/L) at various time points during the study. At T90, rats given Hextend had statistically higher lactate levels compared to PEG20K, RS-GmMA, and RS-SBMA ($p = 0.0002$, $p = 0.0006$, and $p = 0.0059$, respectively). There was no statistical difference between the other three treatments. Middle: Hemoglobin (Hb) concentration (g/dL) at various time points during the study. At T90, rats given PEG20K had statistically lower concentrations of Hb compared to both Hextend and RS-GmMA ($p = 0.0008$ and $p = 0.0064$, respectively). While rats given RS-SBMA had statistically lower concentration of Hb compared to Hextend ($p = 0.0393$). Right: Percentage of total blood volume for rats during the study. The hemorrhage volumes and hemoglobin concentrations at different time points were used to calculate the percentage of the baseline total blood volume at various time points. At T90, there was no statistical difference between the treatments. A fit model for a repeated measure, one-way anova with tukey post-hoc analysis ($\alpha = 0.050$) was used for statistical analysis.

Both RS-GmMA and RS-SBMA were able to bring lactate levels down similar to PEG20K, while Hextend was not able to fully correct the metabolic deficit created by the severe hemorhagic shock. Although statistically not significant, RS-GmMA did not seem to bring lactate levels as far down as RS-SBMA. This was reflected in the hemoglobin levels. The more water that is pulled into the vascular space results in a greater hemodilution of the blood. RS-GmMA not having as high of a osmolarity compared to RS-SBMA, decreased the amount of water drawn into the bloodstream and as a result the hemoglobin levels stayed higher. The percentage of total blood volumes reflect

this as well, although once again not statistically significant, PEG20K and RS-SBMA show similar ability to refill the lost blood volume by pulling water into the bloodstream. Future studies using fluorescent dextran and fluorescently labeled LVRs could provide a more accurate measurement of total blood volume and LVR concentration in the blood.

Another interesting trend observed in the blood gas measurements of the rats were the potassium and sodium levels during the study and across the treatments (Figure 29 below).

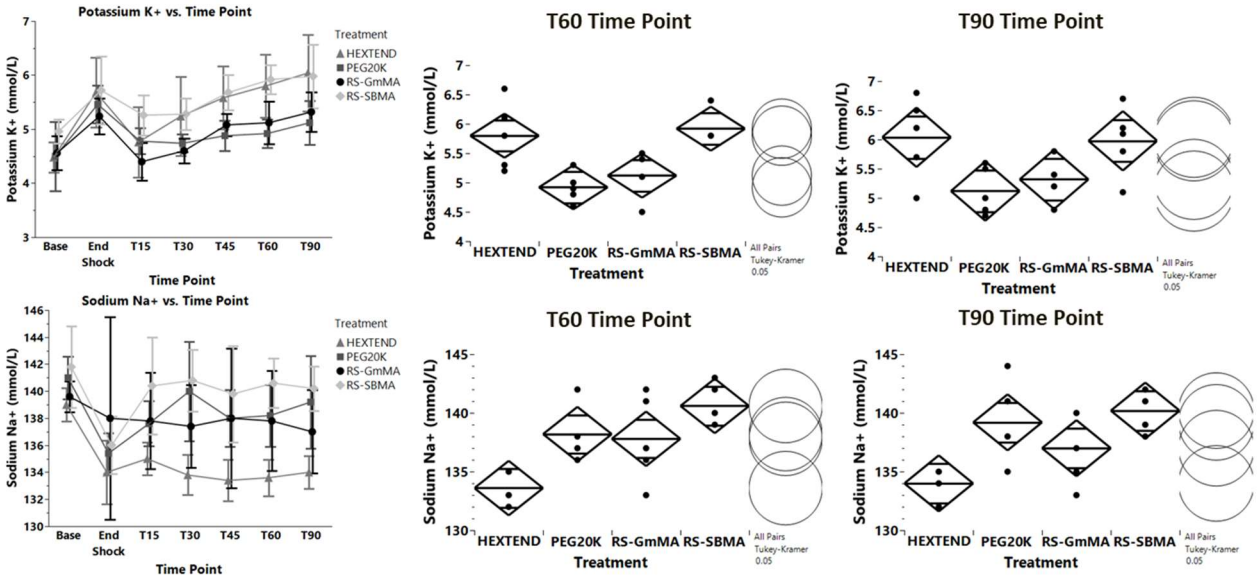

Figure 29. Potassium (top) and sodium (bottom) concentrations from blood gas measurements at different time points during hemorrhagic shock model. Top left: Potassium (K^+) concentration (mmol/L) at various time points during the study. Top middle: At T60, rats given Hextend had statistically higher potassium levels compared to PEG20K ($p = 0.0137$) and rats given RS-SBMA had statistically higher sodium levels compared to PEG20K ($p = 0.0052$) and RS-GmMA ($p = 0.0259$). Top right: At T90, There was no statistical difference in potassium levels between the treatments. Bottom left: Sodium (Na^+) concentration (mmol/L) at various time points during the study. Bottom middle: At T60, rats given Hextend had statistically lower sodium levels compared to RS-SBMA ($p = 0.0018$) and PEG20K ($p = 0.0406$). Bottom right: At T90, rats given Hextend had statistically lower sodium levels compared to RS-SBMA ($p = 0.0064$) and PEG20K ($p = 0.0228$). A fit model for a repeated measure, one-way anova with tukey post-hoc analysis ($\alpha = 0.050$) was used for statistical analysis.

As to be expected, the hemorrhagic shock led to the shutdown of cellular pumps,[3] which led to potassium ions flowing out of cells, and sodium ions flowing into cells, resulting in an increase in potassium concentration and a decrease sodium concentration in the blood. The inability of Hextend to fully refill the vascular space and correct hemorrhagic shock, led to the ion concentrations returning to the level measured at the end of shock. Both PEG20K, and RS-GmMA showed the ability to return ion concentrations back to levels similar to baseline. However, the RS-SBMA treated rats, even though they showed similar blood pressure, hemoglobin, and lactate levels to PEG20K, showed elevated levels of both potassium and sodium in the blood stream at T60 and T90. It is believed that this is the Gibbs-Donan effect in action, that RS-SBMA is coordinating counter ions and retaining them in the blood. If we assume a similar osmotic reflection coefficient for RS-SBMA as measured for PEG 20K by Parrish *et al*. meaning 70% of the dose stays in the vascular space, and we assume that we are refilling the blood volume back to baseline, so we are diluting the RS-SBMA to 20 mg/mL from our original 200 mg/mL dose, then we end up with ~0.12 mmol/L concentration of RS-SBMA in the blood. RS-SBMA is a DP400 polymer, therefore we have 400x the concentration of 3-sulfopropyl groups (~48 mmol/L) that can coordinate with cations in the blood. It is plausible that there is a high enough concentration of 3-sulfopropyl groups available to raise the concentration of potassium by ~1 mmol/L as observed in the rat study. Potassium is known to be especially dangerous for the heart and can lead to arrythmias, however even with the elevated potassium levels, there were no irregular traces observed in the blood pressure waveforms. Future work can monitor the rats by EKG to look for signs of arrythmias.

In summary, the *in vivo* blood pressure and hemoglobin levels indicate that PEG20K, RS-GmMA, and RS-SBMA show similar ability to refill the vascular space, while lactate levels support they show similar ability to correct the metabolic deficit created by hemorrhagic shock. The radiant stars were given as 20% w/v solutions while the PEG20K is given as a 10% w/v solution, and both were given at 10% of the estimated total blood volume for the rat. When accounting for the molecular weight of the treatments, for RS-GmMA we are infusing 1.75x less moles of polymer, and for RS-SBMA we are infusing 2.9x less moles of polymer compared to PEG20K. Similarly, in our scouting studies with L-GmMA (DP300) and L-SBMA (DP300), we were infusing the same number of moles as PEG20K, however their radiant star formats allowed us to infuse 1.75x and

2.9x less moles of polymer, supporting we are increasing the water-carrying capacity by moving to radiant stars.

5.4 Conclusions

In this study, methacrylates of various sizes, chemistries, and architecture were evaluated as low volume resuscitants. Future studies will evaluate the biodistribution of these methacrylate-based LVRs, conduct longer hemorrhagic shock studies to see how long they are able to correct the metabolic disfunction, and combine the shock model with an uncontrolled hemorrhage model to see if they lead to any bleeding disorders.

5.5 Acknowledgements

The authors acknowledge the use of facilities and instrumentation supported by the U.S. National Science Foundation through the Major Research Instrumentation (MRI) program (DMR-2116265) and the UW Molecular Engineering Materials Center (MEM-C), a Materials Research Science and Engineering Center (DMR-1719797). This work benefited from the use of the SasView application, originally developed under NSF Award DMR - 0520547. SasView also contains code developed with funding from the EU Horizon 2020 programme under the SINE2020 project Grant No 654000.

5.6 References

(1) Cannon, J. W. Hemorrhagic Shock. *N Engl J Med* **2018**, *378* (4), 370–379. https://doi.org/10.1056/NEJMra1705649.

(2) White, N. J.; Ward, K. R.; Pati, S.; Strandenes, G.; Cap, A. P. Hemorrhagic Blood Failure: Oxygen Debt, Coagulopathy, and Endothelial Damage. *Journal of Trauma and Acute Care Surgery* **2017**, *82*, S41–S49. https://doi.org/10.1097/TA.0000000000001436.

(3) Moore, E. E.; Moore, H. B.; Kornblith, L. Z.; Neal, M. D.; Hoffman, M.; Mutch, N. J.; Schöchl, H.; Hunt, B. J.; Sauaia, A. Trauma-Induced Coagulopathy. *Nat Rev Dis Primers* **2021**, *7* (1), 1–23. https://doi.org/10.1038/s41572-021-00264-3.

(4) Barbee, R. W.; Reynolds, P. S.; Ward, K. R. Assessing Shock Resuscitation Strategies by Oxygen Debt Repayment. *Shock* **2010**, *33* (2), 113–122. https://doi.org/10.1097/SHK.0b013e3181b8569d.

(5) Spinella, P. C.; Cap, A. P. Whole Blood: Back to the Future. *Curr Opin Hematol* **2016**, *23* (6), 536–542. https://doi.org/10.1097/MOH.0000000000000284.

(6) Muir, W. Effect of Intravenously Administered Crystalloid Solutions on Acid-Base Balance in Domestic Animals. *J Vet Intern Med* **2017**, *31* (5), 1371–1381. https://doi.org/10.1111/jvim.14803.

(7) Rudloff, E.; Hopper, K. Crystalloid and Colloid Compositions and Their Impact. *Frontiers in Veterinary Science* **2021**, *8*.

(8) Plant, V.; Parrish, D. W.; Limkemann, A.; Ferrada, P.; Aboutanos, M.; Mangino, M. J. Low-Volume Resuscitation for Hemorrhagic Shock: Understanding the Mechanism of PEG-20k. *J Pharmacol Exp Ther* **2017**, *361* (2), 334–340. https://doi.org/10.1124/jpet.116.239822.

(9) Khoraki, J.; Kang, H. S.; Wickramaratne, N.; Xu, H.; Li, R.; Mangino, M. J. Low-Volume Resuscitation with Polyethylene Glycol-20k for Post-Traumatic Hemorrhagic Shock in a Hybrid Model of Controlled and Uncontrolled Hemorrhage. *Journal of the American College of Surgeons* **2020**, *231* (4), S322. https://doi.org/10.1016/j.jamcollsurg.2020.07.663.

(10) Plant, V.; Limkemann, A.; Liebrecht, L.; Blocher, C.; Ferrada, P.; Aboutanos, M.; Mangino, M. J. Low Volume Resuscitation Using Polyethylene Glycol-20k in a Pre-Clinical Porcine Model of Hemorrhagic Shock. *J Trauma Acute Care Surg* **2016**, *81* (6), 1056–1062. https://doi.org/10.1097/TA.0000000000001155.

(11) Wickramaratne, N. A.; Khoraki, J.; Seth, A.; Hopkins, K. S.; Archambault, C.; Blocher, C.; Li, R.; Mangino, M. J. Low-Volume Resuscitation with Polyethylene Glycol-20k Confers Survival after Severe Hemorrhagic Shock. *Journal of the American College of Surgeons* **2019**, *229* (4), S301–S302. https://doi.org/10.1016/j.jamcollsurg.2019.08.660.

(12) Chan, L. W.; Wang, X.; Wei, H.; Pozzo, L. D.; White, N. J.; Pun, S. H. A Synthetic Fibrin Cross-Linking Polymer for Modulating Clot Properties and Inducing Hemostasis. *Science translational medicine* **2015**, *7* (277).

(13) Das, D.; Srinivasan, S.; Brown, F. D.; Su, F. Y.; Burrell, A. L.; Kollman, J. M.; Postma, A.; Ratner, D. M.; Stayton, P. S.; Convertine, A. J. Radiant Star Nanoparticle Prodrugs for

the Treatment of Intracellular Alveolar Infections. *Polym. Chem.* **2018**, *9* (16), 2134–2146. https://doi.org/10.1039/C8PY00202A.

(14) Arora, T. K.; Malhotra, A. K.; Ivatury, R.; Mangino, M. J. L-Arginine Infusion during Resuscitation for Hemorrhagic Shock: Impact and Mechanism. *J Trauma Acute Care Surg* **2012**, *72* (2), 397–402.

(15) Doucet, M.; Cho, J. H.; Alina, G.; Attala, Z.; Bakker, J.; Bouwman, W.; Butler, P.; Campbell, K.; Cooper-Benun, T.; Durniak, C.; Forster, L.; Gonzalez, M.; Heenan, R.; Jackson, A.; King, S.; Kienzle, P.; Krzywon, J.; Murphy, R.; Nielsen, T.; O'Driscoll, L.; Potrzebowski, W.; Prescott, S.; Ferraz Leal, R.; Rozyczko, P.; Snow, T.; Washington, A. SasView Version 5.0.4, 2021. https://doi.org/10.5281/zenodo.4467703.

(16) Debye, P. Molecular-Weight Determination by Light Scattering. *J. Phys. Chem.* **1947**, *51* (1), 18–32. https://doi.org/10.1021/j150451a002.

(17) Roe, R.-J. *Methods of X-Ray and Neutron Scattering in Polymer Science*; Topics in Polymer Science; Oxford University Press: Oxford, New York, 2000.

(18) Benoit, H. On the Effect of Branching and Polydispersity on the Angular Distribution of the Light Scattered by Gaussian Coils. *Journal of Polymer Science* **1953**, *11* (5), 507–510. https://doi.org/10.1002/pol.1953.120110512.

(19) *star_polymer — SasView 5.0.6 documentation*. https://www.sasview.org/docs/user/models/star_polymer.html (accessed 2023-08-16).

(20) *7.1: Segment Models*. Chemistry LibreTexts. https://chem.libretexts.org/Bookshelves/Biological_Chemistry/Concepts_in_Biophysical_Chemistry_(Tokmakoff)/02%3A_Macromolecules/07%3A_Statistical_Description_of_Macromolecular_Structure/7.01%3A_Segment_Models (accessed 2023-07-24).

(21) *Freely Jointed Chain*. https://polymerdatabase.com/polymer%20physics/Kuhn.html (accessed 2023-07-24).

(22) *Persistence Length*. https://polymerdatabase.com/polymer%20physics/lp%20Table.html (accessed 2023-07-24).

(23) *Characteristic Ratio*. https://polymerdatabase.com/polymer%20physics/C%20Table2%20.html (accessed 2023-07-24).

(24) Shiomoto, S.; Inoue, K.; Higuchi, H.; Nishimura, S.; Takaba, H.; Tanaka, M.; Kobayashi, M. Characterization of Hydration Water Bound to Choline Phosphate-Containing Polymers. *Biomacromolecules* **2022**, *23* (7), 2999–3008. https://doi.org/10.1021/acs.biomac.2c00484.

(25) Wen, J.; Weinhart, M.; Lai, B.; Kizhakkedathu, J.; Brooks, D. E. Reversible Hemostatic Properties of Sulfabetaine/Quaternary Ammonium Modified Hyperbranched Polyglycerol. *Biomaterials* **2016**, *86*, 42–55. https://doi.org/10.1016/j.biomaterials.2016.01.067.

(26) Yao, H.; D. Olsen, B. SANS Quantification of Bound Water in Water-Soluble Polymers across Multiple Concentration Regimes. *Soft Matter* **2021**, *17* (21), 5303–5318. https://doi.org/10.1039/D0SM01962C.

(27) Mani, S.; Khabaz, F.; Godbole, R. V.; Hedden, R. C.; Khare, R. Structure and Hydrogen Bonding of Water in Polyacrylate Gels: Effects of Polymer Hydrophilicity and Water Concentration. *J. Phys. Chem. B* **2015**, *119* (49), 15381–15393. https://doi.org/10.1021/acs.jpcb.5b08700.

(28) Liebrecht, L. K.; Newton, J.; Martin, E. J.; Wickramaratne, N.; Jayaraman, S.; Han, J.; Aboutanos, M.; Brophy, D. F.; Mangino, M. J. Thromboelastographic Analysis of Novel Polyethylene Glycol Based Low Volume Resuscitation Solutions. *PLOS ONE* **2018**, *13* (11), e0207147. https://doi.org/10.1371/journal.pone.0207147.

(29) Wickramaratne, N.; Kenning, K.; Reichstetter, H.; Blocher, C.; Li, R.; Aboutanos, M.; Mangino, M. J. Acute Resuscitation with Polyethylene Glycol-20k: A Thromboelastographic Analysis. *Journal of Trauma and Acute Care Surgery* **2019**, *87* (2), 322–330. https://doi.org/10.1097/TA.0000000000002332.

(30) Toffaletti, J. G.; Buckner, K. A. Using α-Angle and A10 ROTEM Parameters for Earlier Information on Clotting Status in Surgery, Postpartum Hemorrhage, and ICU Patients. *Point of Care* **2019**, *18* (2), 56. https://doi.org/10.1097/POC.0000000000000188.

(31) Chapanian, R.; Constantinescu, I.; Rossi, N. A. A.; Medvedev, N.; Brooks, D. E.; Scott, M. D.; Kizhakkedathu, J. N. Influence of Polymer Architecture on Antigens Camouflage, CD47 Protection and Complement Mediated Lysis of Surface Grafted Red Blood Cells. *Biomaterials* **2012**, *33* (31), 7871–7883. https://doi.org/10.1016/j.biomaterials.2012.07.015.

(32) Imran ul-haq, M.; Lai, B. F. L.; Chapanian, R.; Kizhakkedathu, J. N. Influence of Architecture of High Molecular Weight Linear and Branched Polyglycerols on Their

Biocompatibility and Biodistribution. *Biomaterials* **2012**, *33* (35), 9135–9147. https://doi.org/10.1016/j.biomaterials.2012.09.007.

(33) Jawanda, M.; Lai, B. F. L.; Kizhakkedathu, J. N.; Ishihara, K.; Narain, R. Linear and Hyperbranched Phosphorylcholine Based Homopolymers for Blood Biocompatibility. *Polym. Chem.* **2013**, *4* (10), 3140–3146. https://doi.org/10.1039/C3PY00248A.

(34) Wolberg, A. S.; Campbell, R. A. Thrombin Generation, Fibrin Clot Formation and Hemostasis. *Transfus Apher Sci* **2008**, *38* (1), 15–23. https://doi.org/10.1016/j.transci.2007.12.005.

(35) Seuring, J.; Agarwal, S. Polymers with Upper Critical Solution Temperature in Aqueous Solution: Unexpected Properties from Known Building Blocks. *ACS Macro Lett.* **2013**, *2* (7), 597–600. https://doi.org/10.1021/mz400227y.

(36) Wang, N.; Seymour, B. T.; Lewoczko, E. M.; Kent, E. W.; Chen, M.-L.; Wang, J.-H.; Zhao, B. Zwitterionic Poly(Sulfobetaine Methacrylate)s in Water: From Upper Critical Solution Temperature (UCST) to Lower Critical Solution Temperature (LCST) with Increasing Length of One Alkyl Substituent on the Nitrogen Atom. *Polym. Chem.* **2018**, *9* (43), 5257–5261. https://doi.org/10.1039/C8PY01211C.

5.7 SUPPLEMENTAL

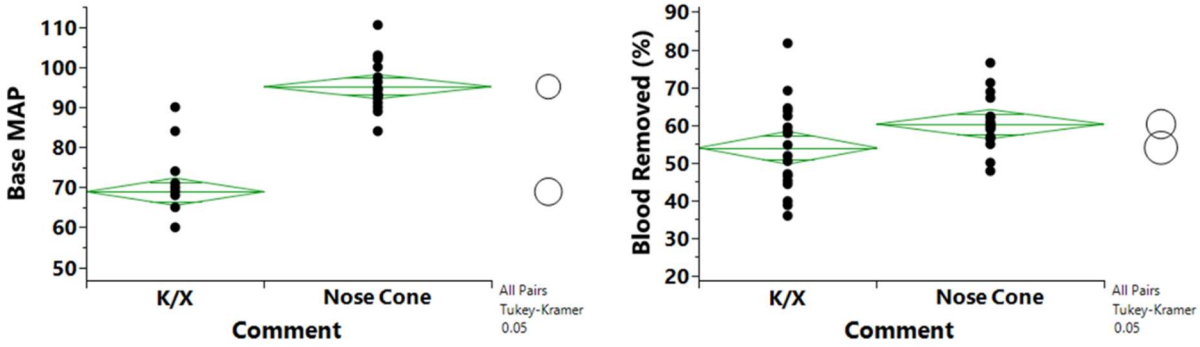

Figure S 1. Comparison of ketamine-xylazine injection vs. isofluorane only via nose cone for rats in severe hemorrhagic shock model. Moving from K/X injection to nosecone with isofluorane-only resulted in a higher base blood pressure and more consistent and higher hemorrhage volumes to reach necessary shock levels in rats.

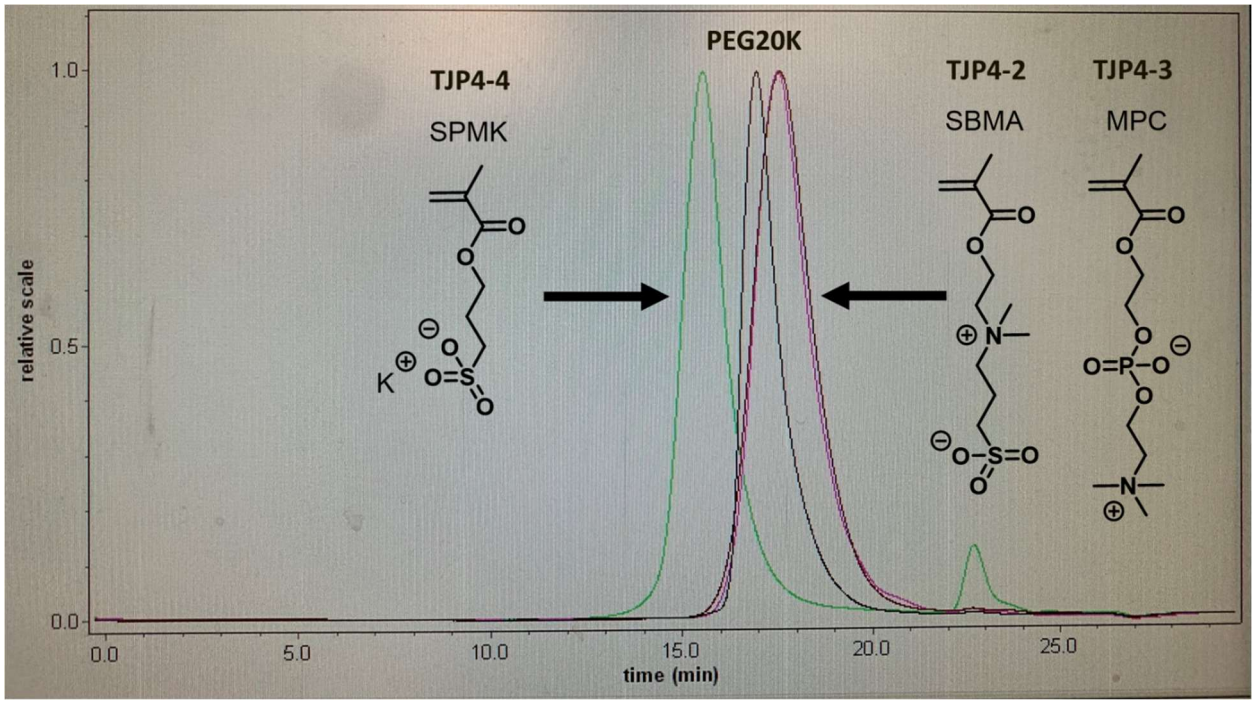

Figure S 2. GPC chromatogram of 20kDa SPMK linear polymer.

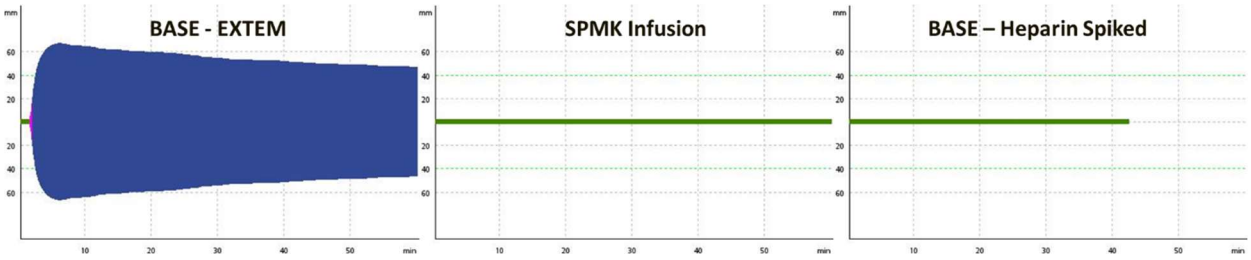

Figure S 3. ROTEM of blood taken from rat administered linear 20kDa SPMK. SPMK acts as syntheLeft: Baseline ROTEM of whole blood sample from rat. Middle: ROTEM of blood taken from rat after administration of SPMK. Right: Same baseline whole blood but spiked with heparin.

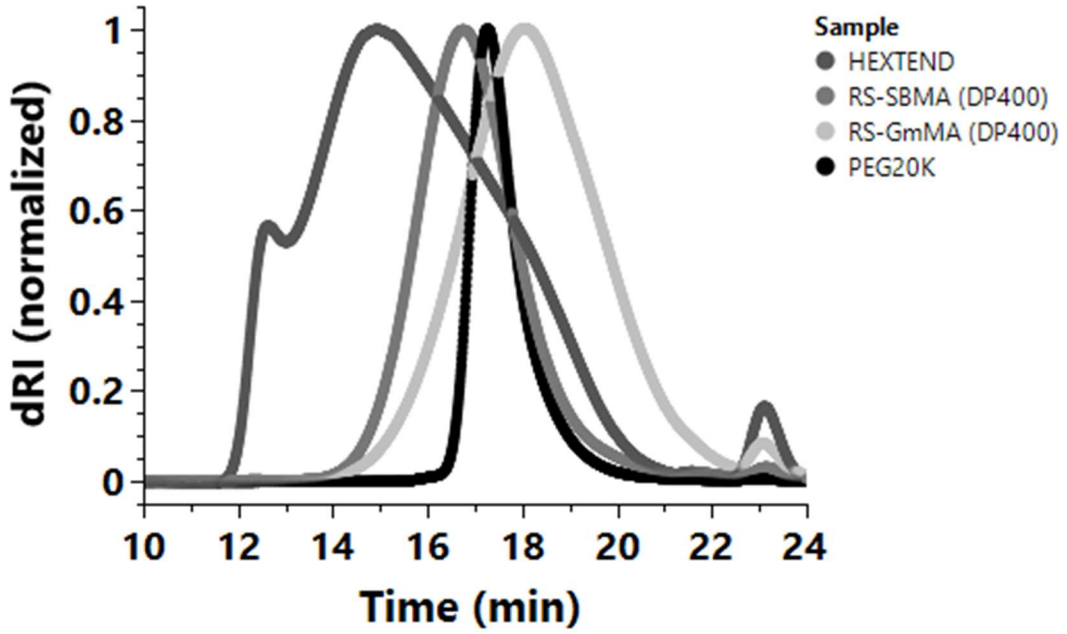

Figure S 4. GPC chromatograms of treatments evaluated in the in vivo rat study. To analyze the hydroxyethyl hetastarch (HES) from Hextend, it was dialyzed against DI water for three days then lyophilized to isolate just the HES. From commercial literature, Hextend has a reported average molecular weight of 670 kDa with a range of 450 kDa to 800 kDa, and at least 80% of the polymer units falling within the range of 20 kDa to 2.5 MDa. The HES is larger than the upper limit of the column used on the GPC and therefore was unable to be measured accurately.

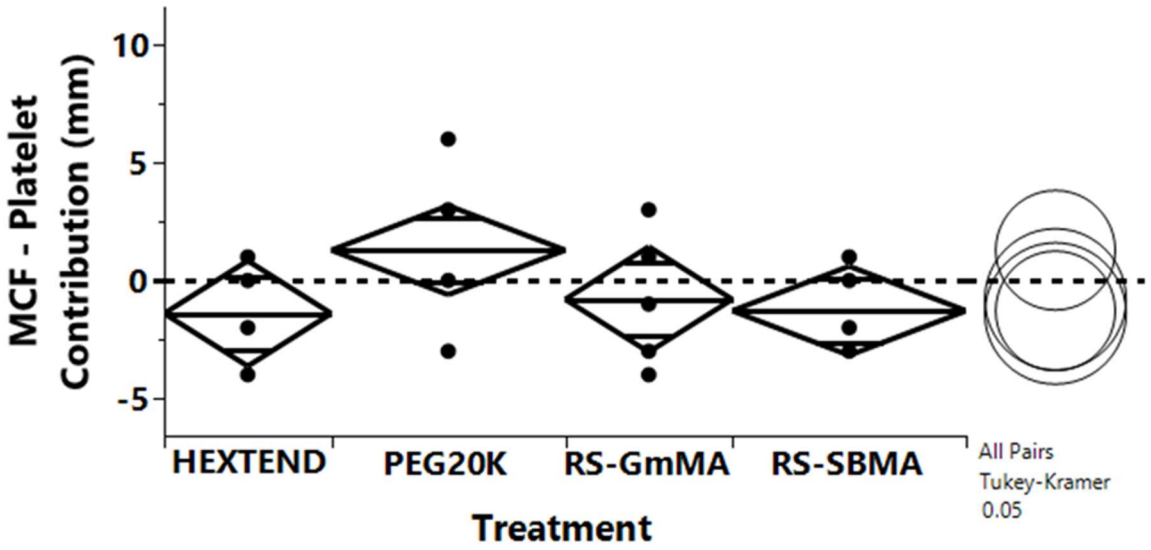

Figure S 5. Platelet contribution to maximum clot firmness measured in ROTEM (n = 5-7). Calculated by subtracting the plasma MCF from the whole blood MCF. The data displayed is the

difference from a saline volume control run at the same time for each donor. A dotted line is placed at zero to represent no change from the saline control. No statistical difference was observed for any of the treatments compared to the saline control.

Chapter 6. INTRATUMORAL ACTIVATION OF FLUORESCEIN-SPECIFIC CAR T CELLS FOLLOWING ADMINISTRATION OF A SYNTHETIC FIBRIN-HOMING POLYMER DISPLAYING FLUORESCEIN

Clinton M. Heinze[†], Trey J. Pichon[†], Michael Baldwin, James Matthaei, Meilyn Sylvestre, Joshua Gustafson, Nathan White, Michael C. Jensen & Suzie H. Pun

[†]Authors contributed equally to this work.

Abstract: CAR T cell therapies often lack specificity, leading to issues ranging from inadequate antigen targeting to off-tumor toxicities. To counter that lack of specificity, we expanded tumor targeting capabilities with a universal CAR and spatially defined CAR T cell engagement with targets through a combination of synthetic biology and biomaterial approaches. We developed a novel framework, called "In situ Mobilization: Polymer Activated Cell Therapies" (IMPACT) for polymer-mediated, anatomical control of IF-THEN gated CAR T cells. With IMPACT, a regulated payload such as a BiTE or tumor-targeting CAR will only be expressed after engineered cells engage a tumor-localizing polymer ("IF" condition). In this first demonstration of IMPACT, we engineered CAR T cells to respond to fluorescein that is displayed by an injectable polymer that binds to and is retained at fibrin deposits in tumor microenvironments. This interaction then drives selective and conditional expression of a protein within tumors ("THEN" condition). Here, we develop the polymer and CAR T cell infrastructure of IMPACT and demonstrate tumor-localized CAR T cell activation in a murine tumor model after intravenous administration of polymer and engineered T cells.

6.1 INTRODUCTION

Chimeric antigen receptor (CAR) T cell therapy has demonstrated unprecedented efficacy against hematological malignancies,[1] producing high remission rates and resulting in six FDA-approved therapies to date.[1–3] Despite this clinical success, currently available CARs employ a relatively simple design. All FDA-approved products contain a single monovalent CAR with unregulated function post-infusion into patients. The ramifications of this range from hypo-functional behavior to toxicity-inducing over-reactivity. Tumor heterogeneity, in the form of antigen diversity and tumor plasticity, and subsequent antigen loss are primary factors that lead to CAR T cell underperformance.[4] CARs specific for a single target are unable to handle tumors with diverse antigen profiles, resulting in an outgrowth of tumor cells unrecognizable to the CAR T cells. On the flip side, current CAR T cells lack specificity, driving systemic toxicity issues, such as cytokine release syndrome (CRS),[5] or site-specific damage due to on-target, off-tumor reactivity.[6,7] To deal with these deficiencies, next generation CAR T cell systems must have the ability for multivalent targeting, enhanced control over cell activity, and selective activation within tumors.

Universal CARs are a class of receptors that may offer a potential solution to both antigen escape and off-site toxicities.[8] T cells featuring universal CARs can engage tumors exclusively via synthetic bifunctional intermediate adaptor molecules, which present both CAR epitope and tumor targeting moieties. The dependency of the CAR on these bridging molecules for antigen recognition and immune synapse formation allows for highly regulated, multivalent CAR T cell effector function. For example, multiple tumor antigens can be simultaneously targeted with a single CAR T cell by creating a panel of intermediate adaptors with a constant CAR epitope but different tumor targeting moieties. The strength of the T cell response can then be modulated by adjusting the dose and frequency of intermediate adaptors given to the patient. The specificity of this response can be refined further by implementing an IF-THEN gate on effector function. IF-THEN gates enable conditional expression of a therapeutic agent or CAR via an inducible promoter. It is therefore possible to put a tumor-targeting CAR under the regulation of an inducible promoter and define an “IF” condition that creates a spatial distinction between tumors and surrounding tissue. One way to accomplish this is by taking advantage of irregular coagulation patterns within the vasculature of malignant tissue. Fibrin clots are hallmark components of

wounds and tissue regeneration that are rarely observed under normal conditions.[9] Since solid tumors are destructive to surrounding tissue and require continuously expanding vasculature to grow, they are often characterized by significant fibrin deposits.[10]

Here, we describe a novel framework for IF-THEN gating CAR T cell function called "***I****n situ* **M**obilization: **P**olymer **A**ctivated **C**ell **T**herapies" (IMPACT) (**Figure 1**). In this system, we adapted PolySTAT, a fibrin-binding polymer developed in our lab,[11,12] to bind within the tumor microenvironment (TME) and provide an "IF" condition to logic-gated CAR T cells. We modified PolySTAT to display multiple fluorescein (FL) tags along its backbone for recognition by a constitutively expressed anti-FL universal CAR ("cCAR") on our T cells.[13,14] Upon engagement with its epitope, FL CAR signaling activates inducible synthetic promoter (iSynPro), which, is a synthetic promoter responsive to TCR or CAR signaling.[15] iSynPro then drives expression of an mCherry:ffluc fusion protein ("iCherry") in an anatomically-restricted manner. These cCARiCherry T cells are a proof-of-concept platform to model future therapies with an iSynPro-restricted therapeutic payload, such as a BiTE[16] or another CAR that can target a TAA or an intermediate adaptor. Collectively, these data provide proof-of-concept validation of our IMPACT system.

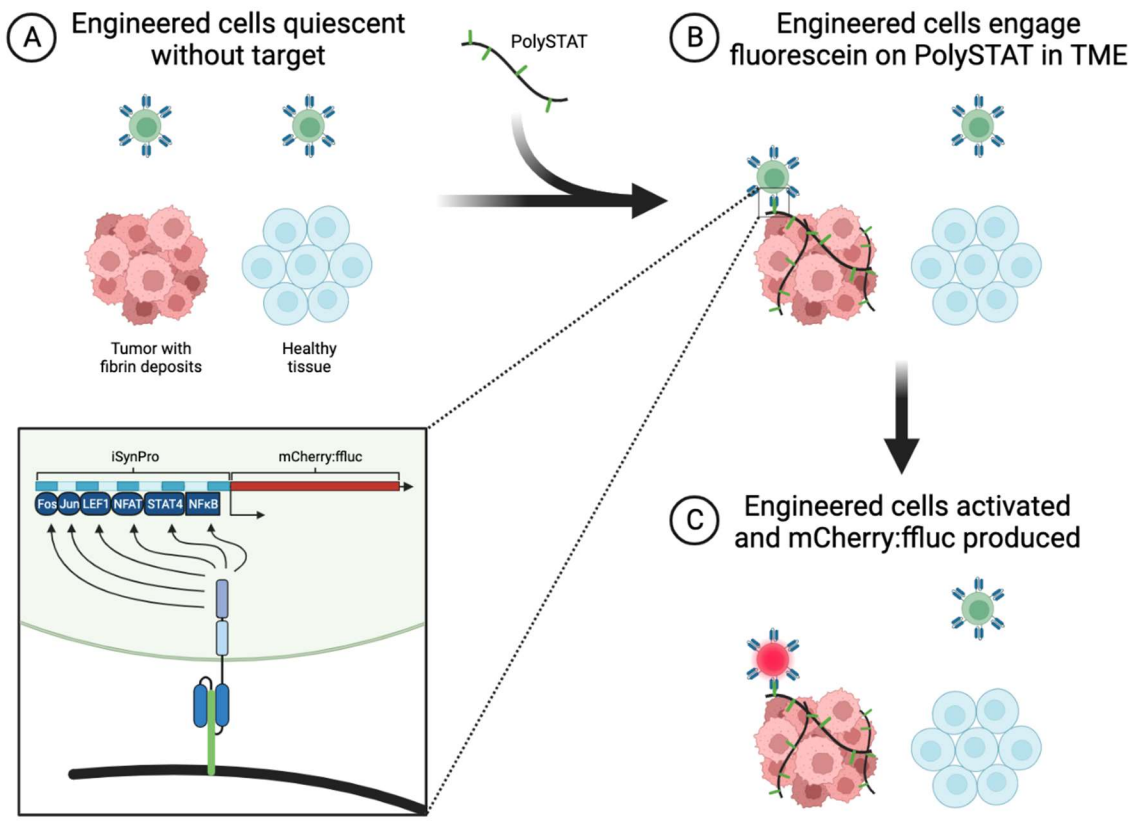

Figure 1. **In situ Mobilization: Polymer-Activated Cell Therapies (IMPACT) rely on PolySTAT to induce regulated transgene expression IMPACT therapy payload is only delivered after the engineered cells engage their ligand on the PolySTAT polymer. A** Cells remain in a quiescent state regardless of their local environment. **B** PolySTAT, once administered, binds to fibrin in tumor microenvironments and presents the cognate antigen to the engineered cells. **C** This interaction stimulates the cells and drives expression of an iSynPro-restricted transgene, such as an mCherry:ffluc reporter protein in this proof-of-concept demonstration.

6.2 RESULTS

6.2.1 *Design of a PiggyBac Nanoplasmid Vector For Constitutive Expression of a Fluorescein-Specific CAR and Activation-Dependent Transcription of a mCherry:ffLuc Reporter*

The first step in developing IMPACT was to design reporter IF-THEN-gated CAR T cells that recognize an antigen via a constitutively-expressed CAR and subsequently induce expression of a reporter mCherry:ffluc protein (cCARiCherry) when stimulated (**Figure 1**). To this end, a plasmid

was constructed that contains the inducible synthetic promoter, iSynPro, and the human eukaryotic translation elongation factor 1α (EF1α) promoter, which constitutively drives high transgene expression.[17] Inserted under EF1α control is an anti-FL(E2-mut2) CAR with CD19t expression marker and methotrexate (MTX)-resistant double mutant dihydrofolate reductase (DHFRdm) separated by 2A ribosomal skip sequences.[18] Inserted under iSynPro regulation is an mCherry:ffluc fusion protein (**Figure 2A**), which allows for *in vitro* validation of cell activation via mCherry and *in vivo* validation of cell activation via ffluc. The iSynPro promoter stringently restricts expression of the mCherry:ffluc fusion protein until the CAR (or TCR) engages its ligand. Once the CAR-ligand interaction is engaged, the cells transiently transcribe the mCherry:ffluc transgene (**Figure 2B**). These components were all cloned into a piggyBac transposon vector[19–22] for electroporation (EP) into $CD8^+$ primary human T cells. Following EP, CAR^+ populations were selected with administration of 50 nM methotrexate for 18 days. At the end of the initial 21-day cell production, cells underwent a rapid cell expansion protocol (REP) (**Supplementary Figure 1**). On the last day of REP, cell staining for CD19t revealed a 77.8% CAR^+ population of cells when compared to untransduced, donor-matched negative control (mock) cells (**Figure 2C**). Once CAR expression was validated, we needed to confirm that iSynPro was responsive to anti-FL CAR signaling. cCARiCherry T cells were incubated with the following at a 1:1 effector:target (E:T) ratio for 24 hours and then assessed for CD69 expression (an early T cell activation marker)[23] and mCherry expression: K562 OKT3 cells (positive control), which stimulate the T cells via endogenous TCRs, K562 parental (K562 P) cells (negative control), and K562 P cells labeled with FL-PLE (**Figure 2D**). T cells stimulated with both K562 OKT3 and K562 FL-PLE cells expressed mCherry and upregulated CD69; importantly, mCherry expression was dependent on CAR expression ($CD19t^+$ cells **Figures 2E-G**), further confirming IF-THEN controlled gene expression. These data confirmed that our dual promoter system was functional and ready to be tested with PolySTAT.

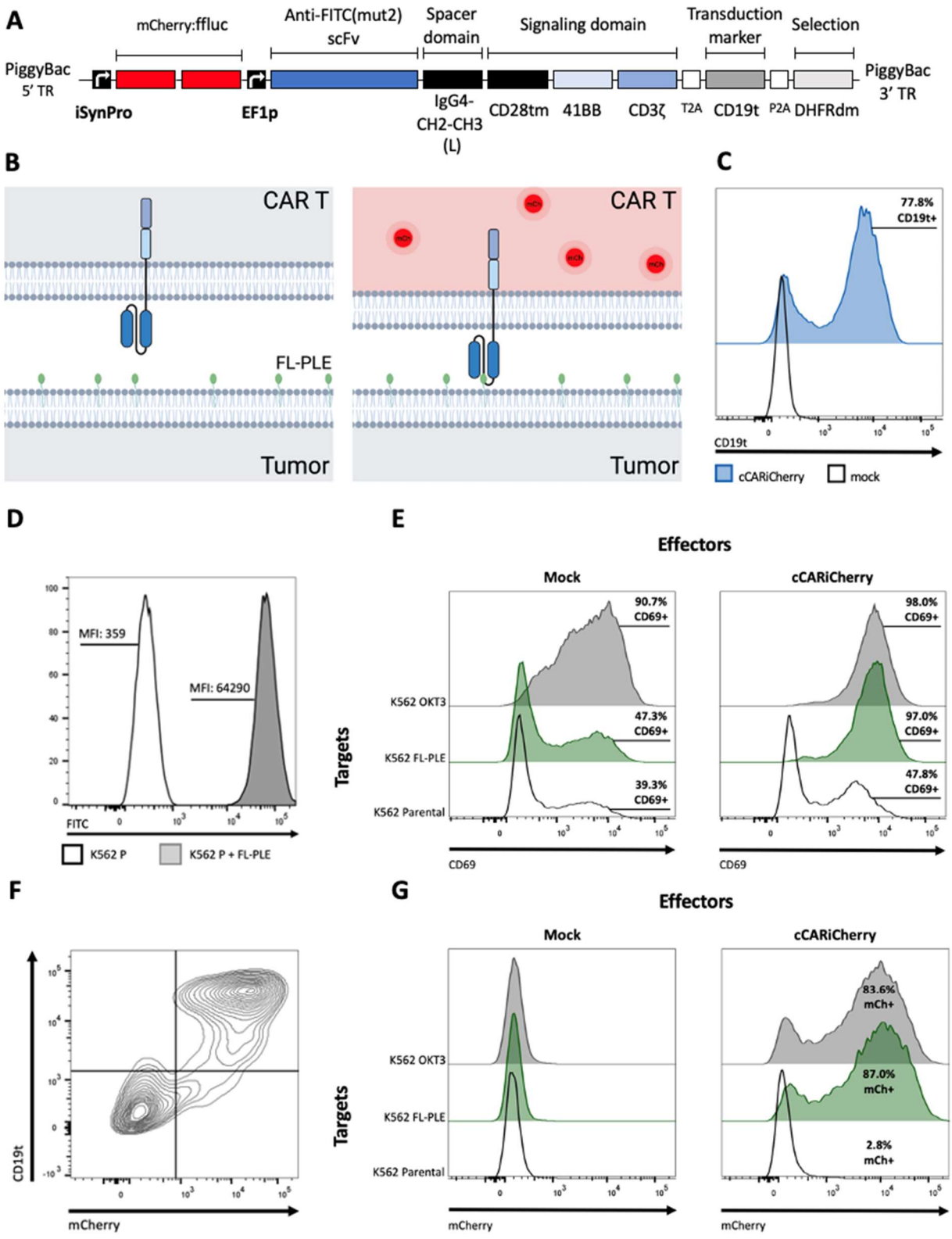

Figure 2. **cCARiCherry T cells demonstrate stringent activation-dependent transcription from the iSynPro promoter cCARiCherry T cells demonstrate restricted payload expression**

until their CARs or TCRs are engaged. All results are representative of 2 donors. **A** Design of the cCARiCherry Piggybac construct. The construct includes an iSynPro-driven mCherry:ffluc fusion protein and an EF1α promoter-driven anti-FITC(E2-mut2) CAR. **B** Diagram showing restricted payload expression until CAR engages ligand. **C** Purity of CAR+ T cells (CD19t expression marker) was determined by flow cytometry. **D** Flow cytometry shows that K562 P cells emit strong FL signal when labeled with FL-PLE. **E-G** cCARiCherry or mock T cells were stimulated with K562 P, FL-PLE-labeled K562 P, or K562 OKT3 cells for 24 hours. **E** CD69 expression was upregulated in mock and cCARiCherry T cells incubated with positive control K562 OKT3 cells. CD69 was comparably upregulated in cCARiCherry T cells, but not mock T cells, incubated with FL-PLE-labeled K562 P cells. **F** Expression of mCherry was upregulated in cCARiCherry T cells when stimulated with FL-PLE-labeled K562 cells and dependent on CAR expression. CAR-negative cells did not produce mCherry when stimulated. **G** Expression of mCherry was upregulated comparably in cCARiCherry T cells stimulated with K562 OKT3 cells and FL-PLE-labeled K562 cells.

6.2.2 *Fluorescein conjugation chemistry, polymer composition and polymer structure influence the efficiency of cCARiCherry T cell activation*

We next engineered our PolySTAT platform to enhance the presentation of fluorescein (FL) and recognition by cCARiCherry T cells. Commercially available, fluorescein O-methacrylate (FMA) was co-polymerized with 2-hydroxyethyl methacrylate (HEMA) and methacrylic acid N-hydroxysuccinimide ester (NHSMA) to create a 2% FL statistical copolymer backbone (**Supplementary Figure 2 and 3**), followed by conjugation of a fibrin-binding peptide (FBP) to generate FMA-PolySTAT (**Supplementary Figure 4A**). Fibrin gels containing escalating doses of FMA-PolySTAT or FMA-PolySCRM (a non-fibrin binding, scrambled peptide negative control for PolySTAT) were then constructed in 48-well tissue culture plates using previously-described materials and concentrations (**Supplementary Figure 4B)**.[24] cCARiCherry T cells or mock cells were then loaded onto the gels in cytokine-free media for 20 hours and analyzed via flow cytometry for activation markers and mCherry expression (**Supplementary Figure 4C**). We observed PolySTAT dose-dependent activation of cCARiCherry T cells, as evident by both mCherry production and CD69 expression (**Supplementary Figure 4D**). Lower levels of activation were

recorded from CAR T cells on FMA-PolySCRM-loaded gels and mock cells on any gel. Although PolySTAT was able to activate cCARiCherry T cells, the levels of activation were low by both metrics. As a result, a series of improvements were made to PolySTAT to enhance CAR binding and cell activation.

Our first step to improve PolySTAT was to enhance CAR binding by synthesizing a new FL monomer with better FL presentation and hydrolytic stability. The commercially available FMA monomer uses a phenyl ester linkage that prevents one of the phenols from being available for CAR binding and is a well-known hydrolysable linker used in drug delivery.[25] Therefore, we conjugated FL to a methacrylate monomer with a pendant primary amine via an isothiocyanate reaction (**Supplementary Figure 5A**) to form a more stable N,N'-disubstituted urea bond that is commonly used to conjugate FL to proteins. This new FL monomer, 2-propenoic acid, 2-methyl-2-[[[(3'6'-dihydroxy-3-oxospiro[i-sobenzofuran-1(3H),9'-[9H]xanthen]-5-yl)amino]thioxomethyl]amino]ethyl ester or "AEMA-FL" (**Figure 3A**) was confirmed by proton NMR spectroscopy (**Supplementary Figure 5B**). AEMA-FL-PolySTAT and AEMA-FL-PolySCRM with statistically incorporated 4% FL content were made using the same synthesis steps as FMA-PolySTAT above (**Supplementary Figures 6-9**). The % FL/number of FL attached to copolymers were measured by NMR (**Supplementary Figure 10**). The fibrin-binding ability of AEMA-FL-PolySTAT was then confirmed *in vitro* by rotational thromboelastometry (ROTEM) (**Supplementary Figure 11**).[11,26] AEMA-FL-PolySTAT binding to fibrin was also confirmed by confocal microscopy imaging of blood clots harvested from rats infused with AEMA-FL-PolySTAT or AEMA-FL-PolySCRM (**Supplementary Figure 12**).

We developed an ELISA assay for rapid evaluation of PolySTAT designs that we termed PolySTAT ELISA (PS-ELISA). In PS-ELISA, fibrin gels with FMA-PolySTAT or AEMA-FL-PolySTAT at various concentrations were made and exposed to a biotinylated anti-FL antibody. Antibody binding to PolySTAT-bound fibrin gels was then assessed using a streptavidin-conjugated horseradish peroxidase (HRP) in the presence of a fluorogenic peroxidase substrate. Relative fluorescence unit (RFU) outputs indicated peak antibody signal on 5 μM gels, so this PolySTAT concentration was used for subsequent studies (**Supplementary Figure 13**). The PS-ELISA was conducted with AEMA-FL PolySTAT, FMA-PolySTAT, and their respective negative

controls. We observed significantly higher antibody binding to AEMA-FL-PolySTAT over FMA-PolySTAT (P=0.0021) and negative controls (**Figure 3A**). Although specific antibody binding to FMA-PolySTAT was observed, the data suggest that the AEMA-FL monomer bound more robustly than the FMA monomer, and we therefore proceeded with AEMA-FL for future studies.

One of the issues with FMA-PolySTAT and AEMA-FL PolySTAT was limited water solubility due to the inclusion of hydrophobic fluorescein-containing monomers. To counter this, we replaced HEMA comonomers in the polymer backbone with glycerol monomethacrylate (GmMA) (**Figure 3B, Supplementary Figure 10, and Supplementary Table 1**). Recently, we reported that substituting HEMA monomers with GmMA monomers enhanced the water solubility of PolySTAT by incorporating more hydroxyl groups into the polymer.[11] We also hypothesized that the more hydrophilic GmMA would both increase the total polymer solubility and also reduce fluorescein π-π stacking with the tyrosines of FBP, resulting in better presentation of fluorescein for CAR T cell binding. In PS-ELISA we observed a statistically significant (p<0.0001) improvement in antibody binding to the GmMA version of AEMA-FL-PolySTAT compared with the HEMA version (**Figure 3B**). Therefore, all future AEMA-FL-PolySTATs were synthesized with a GmMA backbone.

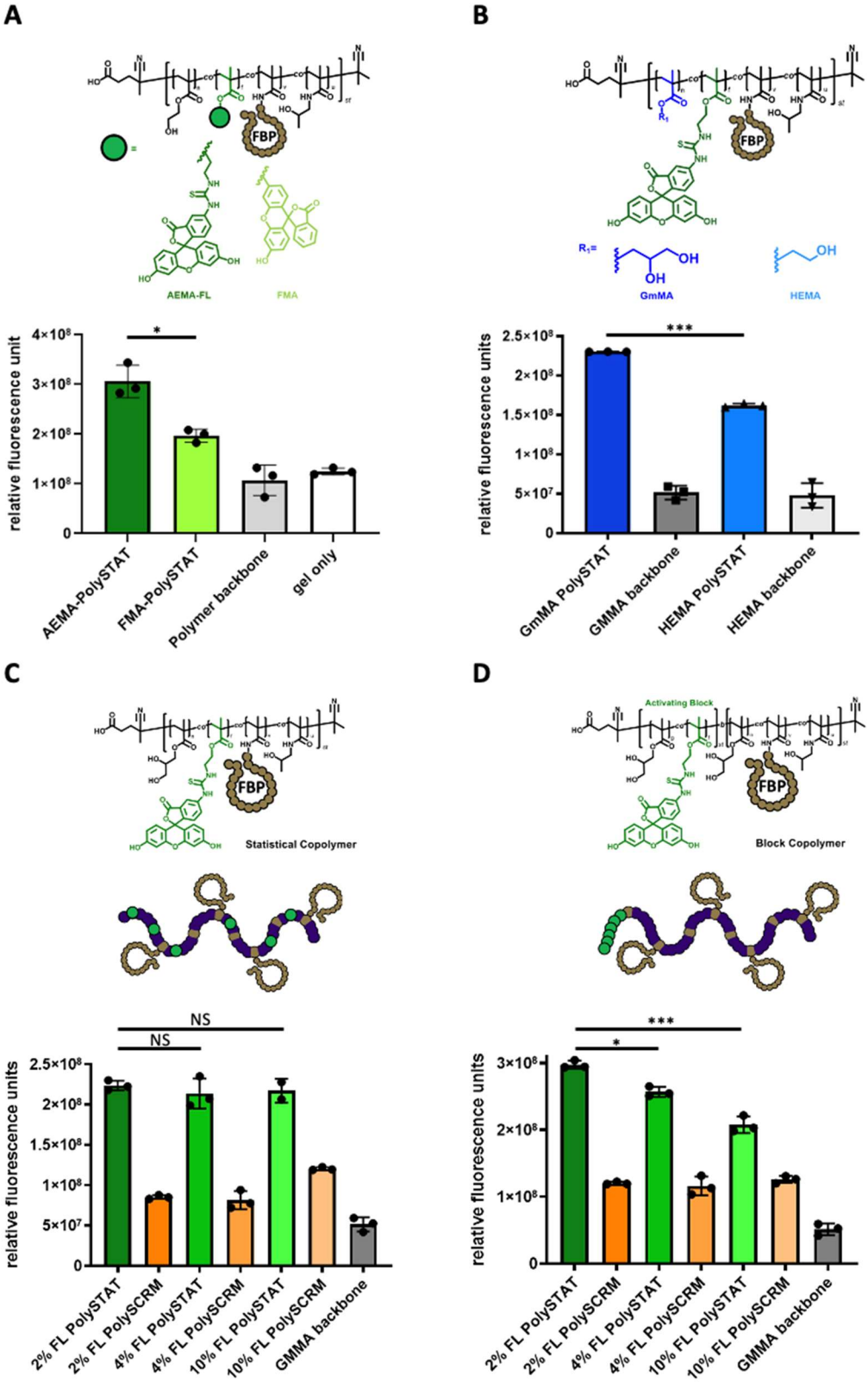
A
FBP
AEMA-FL
FMA
relative fluorescence unit
4×10⁸
3×10⁸
2×10⁸
1×10⁸
0
*
AEMA-PolySTAT
FMA-PolySTAT
Polymer backbone
gel only
B
FBP
R1=
OH
OH
GmMA
HEMA
relative fluorescence units
2.5×10⁸
2×10⁸
1.5×10⁸
1×10⁸
5×10⁷
0
***
GmMA PolySTAT
GMMA backbone
HEMA PolySTAT
HEMA backbone
C
FBP
Statistical Copolymer
NS
NS
relative fluorescence units
2.5×10⁸
2×10⁸
1.5×10⁸
1×10⁸
5×10⁷
0
2% FL PolySTAT
2% FL PolySCRM
4% FL PolySTAT
4% FL PolySCRM
10% FL PolySTAT
10% FL PolySCRM
GMMA backbone
D
Activating Block
FBP
Block Copolymer
***
*
relative fluorescence units
3×10⁸
2×10⁸
1×10⁸
0
2% FL PolySTAT
2% FL PolySCRM
4% FL PolySTAT
4% FL PolySCRM
10% FL PolySTAT
10% FL PolySCRM
GMMA backbone

Figure 3. **Fluorescein orientation and linker design impact anti-FL antibody binding to PolySTAT was modified to improve anti-fluorescein antibody binding. A** Polymer structures for PolySTATs containing our newly developed AEMA-FL monomer and fluorescein O-methacrylate (FMA). PS-ELISA outputs demonstrate that AEMA-FL PolySTAT provided a better platform for anti-FL antibody binding than FMA-PolySTAT in a PolySTAT-ELISA. **B** Polymer structures for AEMA-FL PolySTATs containing 2-hydroxylethyl methacrylate (HEMA) or glycerol monomethacrylate (GmMA) backbone monomers. Polymers with GmMA have enhanced anti-FL antibody binding compared with polymers with HEMA monomers. **C** PolySTATs and non-fibrin-binding PolySCRMs with 2% (original percentage), 4% and 10% AEMA-FL monomers in statistical polymer structure. PolySTAT-ELISA indicated that increasing FL content did not increase antibody binding signal. **D** Evaluation of PolySTATs and non-fibrin-binding PolySCRMs with 2%, 4%, and 10% AEMA-FL monomers in block copolymer structure. PolySTAT-ELISA suggest that increasing FL content had a negative effect on anti-FL antibody binding signal. For all bar graphs, n=3. Data presented are mean values +/- SD. *=p<0.01, **=p<0.001, ***=p<0.0001.

For our final design optimization of PolySTAT, we varied both AEMA-FL content and polymer structure. For AEMA-FL content, we hypothesized that increasing the number of FL molecules per polymer would increase the number of binding sites and improve avidity of binding to the antigen-binding domain. To this end, we synthesized a series of AEMA-FL-PolySTATs with a range of FL content (2%, 4%, and 10%). Proton NMR and UV-Vis measurements confirmed the FL content in each polymer (**Supplementary Figure 14, Supplementary Figure 15 A/B and Supplementary Table 2**). However, PS-ELISA results indicated no improvement in antibody binding with the incorporation of more FL monomer in PolySTAT (**Figure 3C**).

For polymer structure, we hypothesized that moving from a statistical-incorporation of FL throughout the PolySTAT backbone to a block-copolymer, where the AEMA-FL is concentrated in an "activating block" that is separate from the fibrin-binding domain of PolySTAT, would promote receptor clustering and enhance the CAR T cell response.[27] To this end, we synthesized a series of block copolymers with discrete segments of AEMA-FL monomers (**Figure 3D, Supplementary Figure 16**). For block polymers, macroCTAs or the "activating blocks" with

degrees of polymerization (DP) of 13-20 containing varying ratios of GmMA to AEMA-FL (80:20, 60:40, and 70:30) were synthesized via RAFT polymerization (**Supplementary Figure 17, Supplementary Figure 18, and Supplementary Table 3**). These macroCTAs were then chain extended with GmMA and NHSMA to create block copolymers of similar size and AEMA-FL content (2%, 4%, and 10%) as the previous statistical copolymers (**Supplementary Table 4, Supplementary Figure 19D**). Characterization by gel permeation chromatography (GPC) refractive index (RI) traces indicated successful chain extension of macroCTAs (**Supplementary Figure 19C and Supplementary Table 5**). Finally, the fibrin-binding peptides were conjugated via the NHS-handle. These polymers were tested by PS-ELISA and compared with their respective PolySCRM negative controls. Interestingly, the addition of more AEMA-FL monomer to the polymer decreased antibody binding (**Figure 3D**). With the block copolymers we observe during the synthesis of the activating block that the AEMA-FL preferentially copolymerizes with itself at higher loading of AEMA-FL (**Supplementary Table 6**). Due to the multiple protonation states of fluorescein,[28] the local pKa in the immediate area of the homopolymerized blocks of AEMA-FLs could be different from the bulk solution the block copolymers are in. Whereas in the statistical copolymers, AEMA-FL are much more spaced out, and unable to affect the protonation state of other AEMA-FLs. We hypothesize this could affect binding.

6.2.3 *Quantitative analysis of cCARiCherry T cells shows varied reactivity to different AEMA-FL PolySTAT variants.*

We next generated a large batch of cCARiCherry CAR T cells with high CAR expression efficiency (**Supplementary Figure 20**) for *in vitro* cell activation studies with our panel of AEMA-FL-PolySTAT polymers. For each PolySTAT and PolySCRM, 2%, 4%, and 10% FL in both statistical and block copolymer formats were assessed. cCARiCherry CAR T cells or mock cells were added onto the polymer-incubated gels in cytokine-free media, and images of the cells were taken every 2 hours in an IncuCyte cell imager for 20 hours. Red image mean analyses of the images revealed upregulated mCherry expression within four hours of being added to gels, with peak expression occurring around 8 hours after addition to gels, followed by a plateaued expression level for the remainder of the experiment (**Figure 4A**). As expected, mock cells produced no

mCherry signal under any conditions (**Supplementary Figure 21A**). The images also indicate the highest mCherry expression in cells stimulated with the 2% FL statistical polymer. This observation was corroborated by mCherry and CD69 expression in cells harvested at the end of the 20-hour incubation and analyzed with flow cytometry (**Figure 4B, 4C, Supplementary Figure 21B, C**). Each block polymer resulted in about 50% $mCherry^+$ and 75% $CD69^+$ cells, with lower FL content inducing slightly higher CD69 expression. For the statistical polymers, there was a clear inverse relationship between FL content and activation of the cells by both metrics. With about 60% $mCherry^+$ cells and CD69 expression over 80%, the 2% statistical AEMA-FL-PolySTAT elicited higher cell activation than the other polymers and comparable activation levels to positive controls. Mock or cCARiCherry T cells were then added onto plain or 2% statistical AEMA-FL-PolySTAT or PolySCRM-loaded gels for 24 hours and imaged by confocal microscopy. Imaging confirmed mCherry-expressing cells distributed across PolySTAT gels but not plain gels (**Figure 4D**). PolySCRM gels show some cells expressing mCherry, which is likely due to residual PolySCRM left on the gels after their fabrication and washes. Higher magnification (40X) imaging of PolySTAT gels show mCherry-expressing cCARiCherry T cells engaging the PolySTAT matrix (**Supplementary Figure 22**)

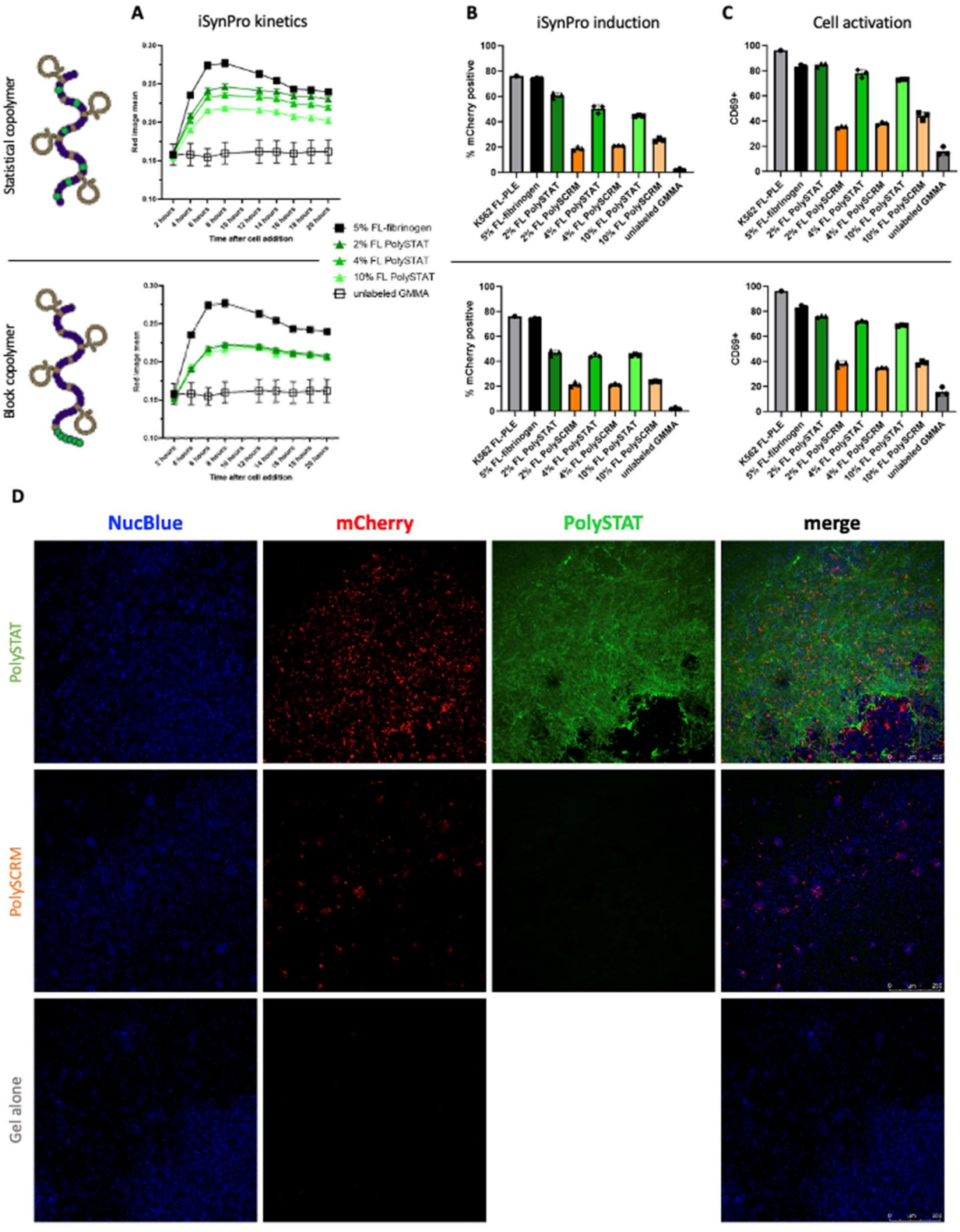

Figure 4. **cCARiCherry cells express mCherry when stimulated with various AEMA-FL PolySTAT variants cCARiCherry T cells are rapidly activated and drive payload expression**

in vitro **when incubated on PolySTAT-fibrin gel. A** Red image means of gels measured by an IncuCyte every 2 hours for 20 hours demonstrate mCherry:ffluc production from cCARiCherry T cells incubated on different AEMA-FL-PolySTAT/fibrinogen gels. **B, C** After a 20-hour incubation on AEMA-FL-PolySTAT gels, cCARiCherry T cells were harvested and mCherry (B) and CD69 (C) expression were analyzed by flow cytometry. **D** 10x Confocal microscope images of cCARiCherry T cells after a 24-hour incubation on 2% FL PolySTAT, 2% FL PolySCRM, or polymer-absent fibrin gels. Images show widespread mCherry production among cells on PolySTAT gels compared with cells incubated on PolySCRM and polymer-absent gels.

6.2.4 *AEMA-FL-PolySTAT binds to fibrin in the ECM of BT-20 tumors following intravenous injection*

With the evidence that PolySTAT drives robust cCARiCherry activation *in vitro*, we next confirmed that the polymer accumulates near tumor fibrin deposits after systemic administration and locally stimulates the cells in tumors. To this end, we engrafted five million BT-20 cells, a slow-growing human breast cancer cell line that forms tumors with documented fibrin structures in the tumor microenvironment,[29] subcutaneously in the left flank of NSG mice. After allowing the tumors to grow for 4 weeks, PBS, 2% AEMA-FL-PolySTAT, or the equivalent PolySCRM control were injected intravenously. Tumors were harvested 24 hours later and co-stained with anti-FL-AF488 (to enhance the FL signal from the polymer) and an anti-fibrinogen antibody. Immunofluorescence (IF) images show extensive FL signal in tumors from mice that received PolySTAT but no FL signal in tumors from mice that received PolySCRM (**Figure 5A**). AF647 (fibrinogen) and AF488 (PolySTAT) signals were analyzed in Image J (Fiji) using the JACoP plugin to quantify signal overlap from these two layers. Distance-based colocalization analyses from six images between two tumors provide an average PolySTAT on fibrinogen overlap of 92.7% with a standard deviation of 4.8%. Costes automatic threshold mask highlights where the two signals overlap (**Figure 5A**). The same tumors were also co-stained with anti-FL AF488 and anti-CD31 AF647 antibodies. Confocal images indicate that PolySTAT depositions are also found near vascularized sections of the tumors (**Figure 5B**). Collectively, these data indicate that PolySTAT will accumulate in well vascularized tumors with fibrin deposits.

6.2.5 *cCARiCherry T cells are activated and express mCherry:ffluc locally in BT-20 tumors following administration of AEMA-FL-PolySTAT*

Finally, we evaluated whether cCARiCherry T cells can interact with tumor bound PolySTAT and turn on iSynPro. To do this, five million BT-20 cells were engrafted subcutaneously on the left flank of NSG mice. After 4 weeks, 10^6 cCARiCherry or mock T cells were injected IV into the mice (n=4 per group). Two days (48 hours) later, PBS or 10mg/kg of 2% AEMA-FL-PolySTAT or PolySCRM were injected IV. Mice were imaged with a Xenogen IVIS imaging machine to monitor induction of iSynPro-regulated mCherry:ffluc production (**Figure 5C**). IVIS images over this period indicate transient ffluc expression primarily limited to the engrafted flank tumor, peaking within the first 24 hours, in mice that received PolySTAT and cCARiCherry T cells (**Figure 5D**). Minimal signal was observed in mice that received cCARiCherry T cells and PolySCRM (**Figure 5D**) or PBS (**Supplementary Figure 23**). Outside of the flank tumor, activated cells appear to have accumulated in the heads of most PolySTAT-treated mice. This is likely an indicator of brain metastases, a very common metastasis destination for BT-20 cells.[30] At each time point with significance by one-way ANOVA, (p<0.05), Tukey's HSD post-hoc analysis was performed between each group. Statistical significance was found between the cCARiCherry + PolySTAT group and the cCARiCherry + PBS at t=24 hours (p<0.0001), t=48 hours (p<0.0001), t=72 hours (p<0.0001), t=96 hours (p=0.0003), t=120 hours (p=0.0233), and t=144 hours (p=0.0150). Statistical significance was also found between the cCARiCherry + PolySTAT and mock + PolySTAT groups at t=24 hours (p<0.0001), t=48 hours (p<0.0001), t=72 hours (p<0.0001), t=96 hours (p=0.0034), t=120 hours (p=0.0106), and t=144 hours (p=0.0113), and t=168 hours (p=0.0219). These results demonstrate for the first time spatially restricted CAR T cell activation controlled by a polymer that accumulates in the tumor microenvironment.

Importantly, there was only significant difference between cCARiCherry|PolySCRM and cCARiCherry|PBS groups (p=0.0201) at the 24-hour time point, despite PolySCRM, identical to PolySTAT but with a scrambled FBP sequence, being injected after the T cells. Thus, circulating FL-conjugated polymers have limited impact on circulating T cell activation, reducing toxicity concerns associated with possible PolySTAT re-doses. This also suggests that the order of T cell or polymer injection does not matter. The later claim was supported with another animal

experiment. Five million BT-20 cells were engrafted subcutaneously on the left flank of NSG mice. After 4 weeks, 10mg/kg of 2% AEMA-FL-PolySTAT or PolySCRM were injected IV. One day (24 hours) later, 10^6 cCARiCherry or mock T cells were injected IV into the mice (n=3 per group). Mice were imaged with a Xenogen IVIS imaging machine to monitor induction of iSynPro-regulated mCherry:ffluc production 8 hours, 24 hours, and every subsequent 24 hours after T cell injections (**Supplementary Figure 24A**). All mice had high non-specific signal for the first 24-48 hours following T cell injections with concentrated flux in the lungs. This transient non-specific ffluc expression is characteristic of iSynPro function following cell injections and concentrating in the lungs is characteristic of CAR T cell migration following IV injections.[31] Flux from the tumors was quantified and unpaired one-way T tests with Welch's correction for unequal variance was conducted at each time point (**Supplementary Figure 24B**). Statistical significance was found between the cCARiCherry + PolySTAT and the cCARiCherry + PolySCRM groups at t=24 hours (p=0.0255), t=48 hours (p=0.0428), t=72 hours (p=0.0257), t=96 hours (p=0.0473), t=120 hours (p=0.0127), and t=144 hours (p=0.0389).

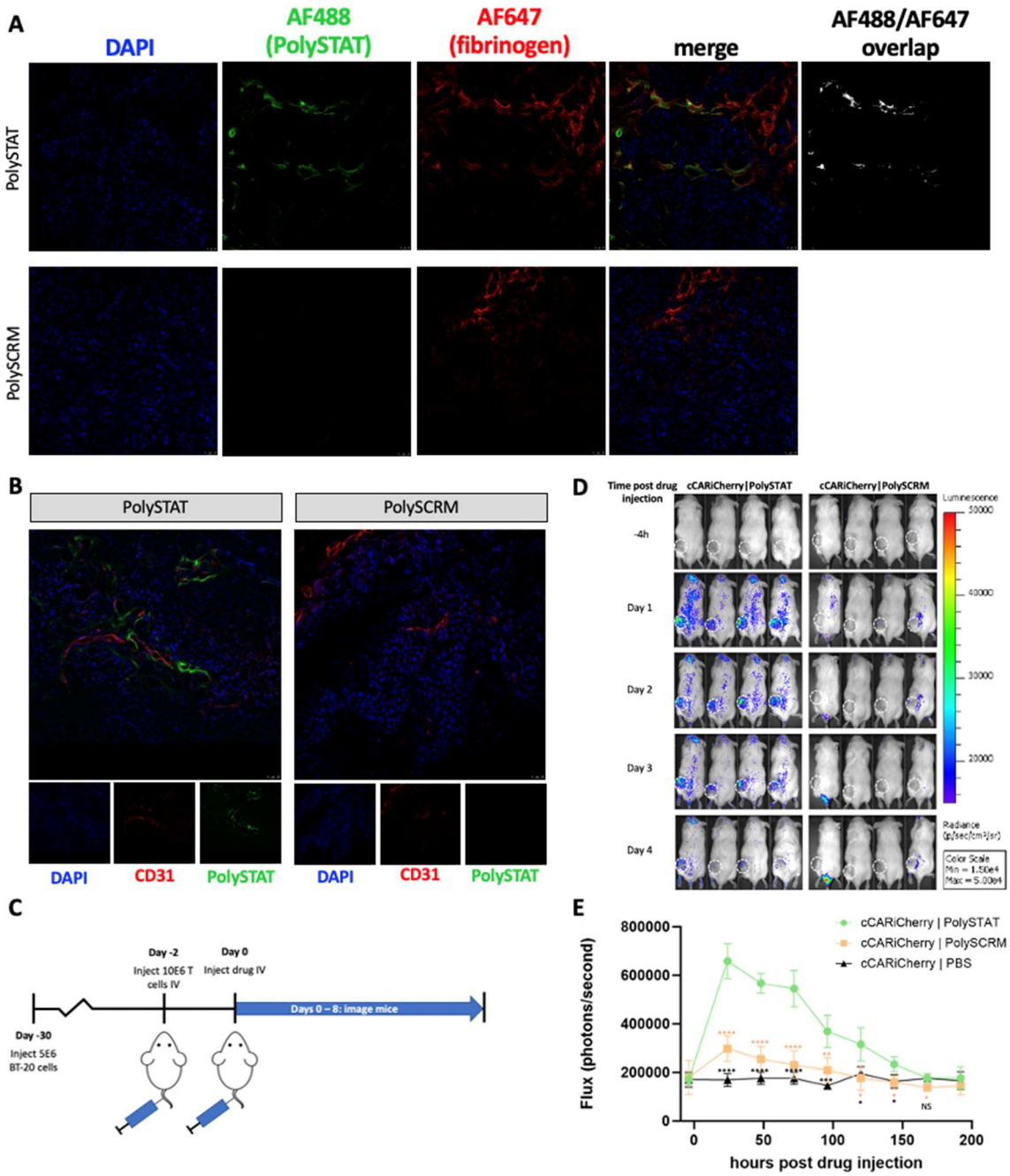

Figure 5. **AEMA-FL PolySTAT requires vasculature and fibrin deposits to accumulate in tumors *in vivo* FL-PolySTAT accumulates in perivasculature intratumoral fibrin deposits and locally activates FL-specific CAR T cells for iSynPro reporter expression. A** PolySTAT (top) and PolySCRM (bottom) accumulation in BT-20 breast cancer tumors 24 hours following IV injection. Strong co-localization of PolySTAT (green) but not PolySCRM with fibrinogen deposits (red) was observed via confocal microscopy. **B** PolySTAT and CD31 (red) co-stain demonstrating PolySTAT deposits near vascularized tissue regions. **C** Schematic diagram of

cCARiCherry T cell activation experiment. Mock or cCARiCherry T cells were injected IV into NSG mice. Two days later, PBS, or 10mg/kg of 2% AEMA-FL-PolySTAT or PolySCRM were injected IV. Mice were then imaged every 24 hours for 7 days to record induced ffluc signal. **D** Daily bioluminescence images of mice injected IV with cCARiCherry T cells and either PolySTAT or PolySCRM. Images of hour -4 and days 1-4 demonstrate transient activation of cells in mice that received PolySTAT but minimal activation in mice that received PolySCRM. **E** Quantification of bioluminescence flux (photons/second). Results show significantly higher flux from cCARiCherry T cells in mice injected with AEMA-FL-PolySTAT than either negative control. For **E**, a one-way ANOVA test was performed at each time point. Tukey's HSD post-hoc analysis was then performed between each group. *=p<0.05, **=p<0.01, ***=p<0.001, ****=p<0.0001. n=4 biologically independent replicates +/- SD.

6.3 DISCUSSION

IF-THEN gated systems can be used to guide the effector function of CAR T cell therapies by spatially differentiating tumors from healthy tissues. *In vivo* spatial control of CAR T cell response can alleviate CAR specificity issues, such as on-target, off-tumor toxicity. Because tumor-specific antigens are rare, CARs usually target tumor-associated antigens (TAAs). Although these antigens are highly expressed on the cancer cells, they may also be found on select healthy tissues, potentially rendering those tissues susceptible to CAR T cell-inflicted damage. While CAR T cell-related toxicities are currently managed by anti-inflammatory drugs such as corticosteroids or tocilizumab,[32] therapeutic CAR T cell strategies with more specificity are preferred. To this end, we created the IMPACT system, which utilizes a dual promoter construct with a constitutively expressed anti-FL CAR and inducible mCherry:ffluc fusion protein (cCARiCherry). The stringent, switch-like function of cCARiCherry T cells allows for conditional expression of mCherry:ffluc ("THEN" outcome) when provided a spatially-restricted "IF" condition. For this, we utilize fluorescein-modified PolySTAT to bind fibrin deposits in irregular tumor vasculature and provide an epitope for fluorescein-specific CARs. In this work, we altered the presentation and linker chemistry of FL tags on PolySTAT to maximize CAR binding and cCARiCherry T cell activation *in vitro* and *in vivo*.

Anti-fluorescein, or anti-FITC, CARs are a type of universal CAR with specificity for fluorescein-modified intermediate adapter molecules. Being one of the first universal CARs developed, a multitude of different adaptor molecules have effectively been used with anti-FL CARs, resulting in similar or superior performance when compared with benchmark CAR T cells.[13,33–35] This success has led to the opening of ENGLIGHTen-01, the first in-human clinical trial with a universal CAR therapy, which pairs an anti-FITC CAR with FITC-folate to target folate receptor^{+} (FOLR1^{+}) osteosarcoma.[36] The development of multiple targeting molecules has also translated into multiplexed targeting abilities with the anti-FL CAR, leading to enhanced reactivity against heterogenous tumors.[37] Recently, a pair of FL-conjugated intermediate adaptor molecules were developed that integrate into the cell membranes of target cells, opening up the opportunity for even broader tumor targeting capabilities using a single cell product.[38,39] Although adaptor molecules can be injected locally or have shown preferential retention in malignant cells,[40] this generalized targeting method creates a high risk for on-target, off-tumor toxicity. As CAR T cells

are used for more expansive cancer targeting applications, measures need to be taken for CAR T cells to spatially differentiate malignant and healthy tissues.

IF-THEN gating can be used to add a layer of specificity to differentiate malignant from healthy tissues. With CAR T cell therapies, this gate can be created with an inducible promoter that drives a therapeutic transgene when provided an "IF" condition. One inducible promoter platform, SynNotch, has been used to regulate the expression of different therapeutic transgenes, including a CAR,[41–43] but it requires orthogonal promoters and large sensor-transcription factor proteins, thereby rendering viral encoding cumbersome. Other inducible promoters consisting of repeated endogenous transcription response elements (TREs), such as repeated NFAT TREs, have been used to drive exogenous cytokine secretion following CAR or TCR stimulation.[44,45] However, such promoters are limited in their reactivity due to their reliance on a single transcription factor. To address this limitation, others have made more complex synthetic promoters by adding multiple different TRE's upstream from a minimal (core) promoter.[46] Here, we chose to use one of these more complex systems, inducible synthetic promoter (iSynPro), in our IF-THEN gating system due to its low genetic profile, stringent off-state, and strong induction following stimulation with antigen.

With the IMPACT platform, a spatial distinction is made between cancerous and healthy tissues by labeling irregular tumor ECM rather than a cell marker to provide the "IF" condition for iSynPro induction. We targeted a tumor characteristic rather than an antigen directly on cancerous cells to enable *in situ* cell activation with no possibility that the anti-FL CAR (cCAR) could engage tumors directly. Targeting abnormal tumor ECM characteristics also provides a degree of universality unavailable if we target a specific TAA, as this approach can be broadly applied across different tumors. Furthermore, PolySTAT needed to bind to a tumor attribute that is relatively static temporally and spatially to ensure adequate retention time in tumors. Therefore, targeting structural components of the ECM were preferential to soluble targets or cell receptors, which are subject to degradation, metabolization, and internalization. In this work, we use PolySTAT to target fibrin, as it is a well-documented component of solid tumor ECMs.[10] Fibrin matrices are able to form networks in the ECM of many tumors due to the high permeability of tumor

microvasculature,[47] which allows substantial fibrinogen to extravasate into the ECM where it is rapidly clotted.[10] As tumors expand, new fibrin matrices form at sites of growth and older fibrin matrices transform into vascularized and collagenous matrices, characteristic of mature tumor stroma.[48] This paradigm results in relatively constant fibrin distribution patterns throughout tumors, thereby making fibrin a viable marker of tumor ECM. This also indicates the possible utility of tailoring PolySTAT to target other solid tumor attributes, such as collagen. Like fibrin, collagen is abundant in a variety of tumors, having a critical role in their growth and ability to metastasize.[49,50] As a result, other groups have used collagen as a target for various cancer therapies.[51,52] By replacing our fibrin-binding peptide with one of the many collagen-binding peptides reported, PolySTAT can be re-directed as desired.[53,54] Similarly, the extra-domain B (EDB) splice variant of fibronectin is strongly associated with solid malignancies in adults[55] and has recently been used as a cancer drug-delivery target.[56] Further demonstrating the modularity of PolySTAT, EBD-fibronectin could be used as another target for PolySTAT in the IMPACT system.

There were several characteristics that were considered when designing PolySTAT for the IMPACT system. In addition to modifications made to improve FL presentation and hydrolytic stability, we also considered polymer structure and molecular weight, as they are main factors determining the circulation half-life of polymers. The polymers tested in this work were 43.8-47.5kDa (**Table 4**), which is a similar size to PolySTAT used in our hemostasis work. Biodistribution studies in rats with radiolabeled PolySTAT revealed initial distribution half-life of 20 min and elimination half-life of 14.4 hours, with >50% of PolySTAT cleared from the body within 1 hour through renal clearance.[12] Importantly, PolySTAT did not accumulate in the heart and lungs at any time.[12] While soluble PolySTAT is rapidly eliminated, PolySTAT extravasated and penetrated the tumor effectively, binding to fibrin throughout the tumor microenvironment (**Figure 5A, B**). The PolySTAT size used in these studies is well-suited for CAR T cell activation; smaller polymers would reduce fibrin-binding valency and shorten the therapy's half-life, but larger polymers would reduce the polymer's ability to extravasate and diffuse through the tumor.

The CAR epitope presented on PolySTAT can also be modulated to accommodate other universal CARs and further enhance tumor specificity. Namely, PolySTAT can be modified to replace the current CAR epitope, FL, with the cognate target of one of the many other reported universal CARs.[57–59] The CAR epitope can also be modified to have a "mask" that is removed upon exposure to the TME or an external stimulus. Tumor microenvironments are known to have upregulated MMP activity, reactive oxygen species, and acidic conditions, all of which can be taken advantage of when designing an antigen mask.[60] In the case of fluorescein, one could leverage self-immolative linkers such as difluorophenyl esters or p-aminobenzlyalcohol attached to an MMP-cleavable peptide, ROS-cleavable boronate fluorescent probe, or a caged fluorescein that requires UV light to unmask the phenols in the binding domain.[61–64] Similar modifications could feasibly be made for other universal CAR targets.

Additional safety interventions can be used to complement the IMPACT system. Once activated, iSynPro does not return to an off state for several days, and this timeline is extended if the cells continue to be stimulated. Furthermore, if the iSynPro-restricted transgene is another CAR, stimulation via that CAR can induce a feedback loop that self-perpetuates its own expression. If this phenomenon occurs outside the TME, toxicities can ensue. Fortunately, this loop can be broken with the inclusion of a suicide gene on our CARs, which degrade the receptor upon exogenous delivery of a suicide switch-inducing drug. A more interesting approach may be the use of dasatinib, a tyrosine kinase inhibitor, which has previously been used turn off CAR T cell function.[65] This can be applied to our system, as dasatinib blocks the intracellular signaling pathways responsible for iSynPro induction. We can therefore use dasatinib as a manual switch to block the "IF" condition if necessary.

While we demonstrated the functionality of IMPACT here, there are a few limitations to the system. First, IMPACT in its current iteration necessitates the presence of fibrin deposits near tumors, thereby excluding all liquid cancers, such as leukemias and lymphomas, from consideration for this therapeutic strategy. Another possible limitation to this iteration of IMPACT is that there are scenarios where tumors are not the only sites of fibrin deposits. Because CAR T cells will become activated in regions of high tissue regeneration due to PolySTAT, IMPACT may

not limit cell activation to tumors in patients who recently underwent a major surgery or have a condition associated with upregulated fibrin deposition, such progressed arthritis.[66] Although fibrin deposits will dissolve as wounds heal, it may not be in the patient's best interest to delay the commencement of treatment if the tumor is aggressive.

Collectively, our work builds the foundation for the IMPACT system to enhance the safety and specificity of universal CAR therapies. This strategy uses novel conditional requirements to anatomically control expression of a therapeutic payload. The IF-THEN gate imposed with IMPACT first employs a synthetic biomaterial to mark a specific anatomic region (tumors) for the CAR T cells to activate. The CAR T cells are then primed and able to a multitude of tumor targeting agents, such as a BiTE[16] or another CAR. Due to the synthetic and modular nature of IMPACT, various pieces of the system can be refined to accommodate the situational requirements of different patients. Although these data are proof-of-concept, this work demonstrates the framework of a robust system with a plethora of new avenues for future CAR T cell approaches. Moving forward, a therapeutic payload needs to be placed under iSynPro control and toxicity/therapeutic outcome needs to be compared with an equivalent treatment without the IMPACT system. Testing different payloads, and therefore different types of therapies, will be central to subsequent efforts to demonstrate the versatility of this system.

6.4 MATERIALS AND METHODS

6.4.1 *Material for Polymer synthesis*

Fluorescein O-methacrylate (FMA), fluorescein 5(6)-isothiocyanate (BioReagent, mix of isomers, ≥90% by HPLC), 2-aminoethyl methacrylate hydrochloride (AEMA), 2,2′-Azobis(2-methylpropionitrile) (AIBN), 4-((((2-carboxyethyl)thio)carbonothioyl)thio)-4-cyanopentanoic acid (CCC), 2-hydroxyethyl methacrylate (HEMA), and all other reagents were purchased from Sigma-Aldrich (Saint Louis, MO) unless noted otherwise. N-hydroxysuccinimide methacrylate (NHSMA) was purchased from TCI America (Portland, OR). Glycerol monomethacrylate (GmMA) was purchased from Polysciences, Inc. (Warrington, PA). The fibrin binding peptide (FBP; Sequence: Ac-Y(DGl)C(HPr)YGLCYIQGK),[67] developed by the Caravan group, as well as

the scrambled peptide (Ac-YICGQ(DGl)AC(HPr)LYGK) were both purchased from two suppliers, GL Biochem (Shanghai, China) and Elim Biopharm (Hayward, California), as custom orders. Human fibrinogen, thrombin, and plasmin were purchased from Enzyme Research Laboratories (South Bend, IN). Human Fibrinogen Purified FL Labeled (4-8 FL/fibrinogen) was purchased from Molecular Innovations (Novi, MI).

6.4.2 *Cloning of the PiggyBac construct*

All oligonucleotides used were synthesized by Integrated DNA Technologies. All DNA fragments were available in-house. Different sections of donor plasmids, including a piggyBac transposon vector (Aldevron), the anti-FL (E2-mut2) CAR, iSynPro promoter, and mCherry:ffluc fusion protein were digested using NheI, BlpI, NotI, SalI, NruI, and PacI restriction enzymes (NEB). Digested DNA fragments were gel purified with a ZymoClean Gel DNA Recovery Kit (Zymo Research) and PCR amplified with Q5® High-Fidelity DNA Polymerase master mix (NEB). PCR products were again gel purified with a ZymoClean Gel DNA Recovery Kit and ligated together via Gibson assembly using Takara's In-Fusion® Snap Assembly Master Mix. Stellar™ chemically competent *E. coli* (Takara) were transformed with the Gibson assembly products, and kanamycin-selected colonies were screened by PCR for correct insert lengths using SapphireAmp® Fast PCR Master Mix (Takara). Correct DNA sequences at ligation sites were verified by Sangar sequencing (Genewiz) of miniprep DNA (Qiagen). Final colonies were then selected and grown to prepare transfection-grade plasmid DNA via maxiprep (Macherey-Nagel).

6.4.3 *T cell isolations*

For all donor cells used in this study, Leukocyte Reduction System (LRS) cones were obtained from Bloodworks Northwest. CD4+ and CD8+ T cells were isolated with EasySep HLA CD4 and CD8 Chimerism Kits and a RoboSep™-S Automated Cell Separation Instrument (STEMCELL Technologies). PBMCs from negative fractions were then isolated using SepMate ™ PBMC Isolation Tubes (STEMCELL Technologies). Aliquots of $CD4^+$ and $CD8^+$ T cells were set aside and stained with anti-CD45RO APC (BioLegend), anti-CD62L PE (BioLegend), anti-CD4 FITC (BioLegend), and anti-CD8 BUV395 (BD Horizon). After the stain and subsequent washes, cells were fixed in 0.5% paraformaldehyde and kept in the dark at 4°C until running on a LSRII Fortessa

(BD Biosciences). Compensation was performed using tubes of UltraComp eBeads Compensation Beads (ThermoFisher Scientific) individually stained for each specific fluorophore used, and the compensation matrix was calculated using FlowJo Software (TreeStar). FlowJo software was also used for data analysis.

6.4.4 *T cell manufacturing (original protocol)*

Freshly isolated CD8+ T cells were cultured in RPMI (Gibco) with a final concentration of 10% heat-inactivated and gamma irradiated FBS (VWR) and 2mmol/L L-Glutamine (ThermoFisher Scientific) (Complete RPMI) plus 4.6ng/mL IL2 (STEMCELL Technologies) and 0.5ng/mL IL15 (Miltenyi). Cells were stimulated with 25µL /mL ImmunoCult™ Human CD3/CD28 T cell Activator for 72 hours. After 72 hours, cells were centrifuged and prepared for electroporation (EP) using a 4D-Nucleofector™ X Kit (Lonza). Each well, except mock cells, received 10nM DNA and 0.528µL of Piggybac transposon RNA. After EP, cells were immediately added to warm cytokine supplemented complete RPMI following electroporation and incubated for 3 days. Methotrexate (Medline) was then added to each CAR T cell well, and half medium changes were performed every 2-3 days. 21 days after EP, cells stained with anti-CD19 SB600 (ThermoFisher Scientific) to assess CAR positivity via flow cytometry.

6.4.5 *Cell line culturing*

K562s (an erythroleukemia cell line) were obtained from the European Collection of Cell Cultures through Sigma-Aldrich. K562 OKT3 cells were made by lentiviral transduction of an OKT3scFv-CD4tm-T2A-Her2tG_epHIV7.2 vector into the K562 parental cell line, thereby leading to expression of an anti-CD3 agonist OKT3scFv. K562 cell lines were cultured in RPMI (Gibco) with a final concentration of 10% heat-inactivated/gamma irradiated FBS (Seradigm) and 2mmol/L L-Glutamine (ThermoFisher Scientific) in 5% CO_2 at 37ºC. BT-20 cells were obtained from ATCC[68] and cultured in DMEM (Gibco) with final concentration of 10% heat-inactivated/gamma irradiated FBS (Seradigm) and 2mmol/L L-Glutamine (ThermoFisher Scientific) in 5% CO_2 at 37ºC. All lines were tested for mycoplasma contamination.

6.4.6 *Synthesis of 2-Propenoic acid, 2-methyl-, 2-[[[(3',6'-dihydroxy-3-oxospiro [isobenzofuran-1(3H),9'-[9H]xanthen]-5-yl)amino]thioxomethyl]amino]ethyl ester (AEMA-FL)*

Fluorescein 5(6)-isothiocyanate (1 g/2.58 mmol) and 1.1 equivalents of 2-aminoethyl methacrylate hydrochloride (470 mgs/2.84 mmol) were added to a round bottom flask with a stir bar. DMSO (25.8 mL/0.1 M) was added. Once the constituents were dissolved (pale yellow solution), 2.6 equivalents of DIPEA (1.29 mL) were added dropwise (turned to deep orange color). The mixture was stirred at RT overnight. The solution was precipitated one time in cold 6% HCl solution (10x volume of reaction) constantly swirled over ice. The orange precipitate was filtered off with a glass frit. The precipitate was collected into a glass vial then lyophilized overnight. The solid, orange monomer was stored at -20 °C. Yield was > 90%. The monomer was pure by ^{1}H nuclear magnetic resonance (NMR) spectroscopy on a Bruker AV 300 (**Figure S3.3**) and TLC (not shown).

6.4.7 *Synthesis of Statistical Copolymer Backbones*

pHEMA-co-FMA-co-NHSMA, pHEMA-co-AEMA-FL-co-NHSMA, and pGmMA-co-AEMA-FL-co-NHSMA were synthesized via reversible addition-fragmentation chain transfer (RAFT) polymerization as described previously.[12] Briefly, comonomers HEMA or GmMA were combined with the FL comonomer (FMA or AEMA-FL) and NHSMA at different ratios to achieve desired FL content. The comonomers were combined with CCC and AIBN at 200:1:0.333 ratio in dimethylacetamide at a monomer concentration of 0.6 M. This mixture reacted for 20 h at 70 °C. pHEMA copolymers were precipitated in diethyl ether, redissolved in dimethylacetamide, and precipitated again in diethyl ether. pGmMA copolymers were precipitated in diethyl ether followed by dissolution in dimethylsulfoxide and a second precipitation in 50-50 acetone/diethyl ether. Precipitated polymer was collected by centrifugation at 7197 x g. Dithiobenzoate groups were removed via an end-capping reaction with 20x molar excess AIBN at 70 °C for 12 hours. **Supplementary Information Table** 1 outlines all the statistical copolymer backbones synthesized.

6.4.8 *Synthesis of Block Copolymer Backbones*

First, macroCTAs (activating blocks) were synthesized via RAFT. A CTA:I ratio of 5:1, target DP of 30, and monomer concentration of 0.6M were used for all the reactions. The ratio of GmMA to AEMA-FL and polymerization time were changed to hit a desired number of FL molecules in the MacroCTA. **Supplementary Information Table 3** summarizes the different MacroCTAs. MacroCTAs were precipitated in diethyl ether followed by dissolution in dimethylsulfoxide and a second precipitation in 50-50 acetone/diethyl ether. Precipitated polymer was collected by centrifugation at 7197 x g. Dissolution in DMSO followed by precipitation in 50-50 actetone/diethyl ether was repeated 3-5 times to remove residual monomer (monitored by ^{1}H nuclear magnetic resonance spectroscopy). The macroCTAs were chain extended with GmMA and NHSMA at a GmMA:NHSMA:MacroCTA:AIBN ratio of 160:40:1:0.333 in dimethylacetamide with a monomer concentration of 0.6 M. This mixture reacted for 20 h at 70 °C. Copolymers were precipitated in diethyl ether followed by dissolution in dimethylsulfoxide and a second precipitation in 50-50 acetone/diethyl ether. Precipitated polymer was collected by centrifugation at 7197 x g. Dithiobenzoate groups were removed via an end-capping reaction with 20x molar excess AIBN at 70 °C for 12 hours. **Supplementary Information Table 5** outlines all the block copolymer backbones synthesized.

6.4.9 *Synthesis of PolySTAT via conjugation*

PolySTAT was synthesized via reversible addition-fragmentation chain transfer (RAFT) polymerization as described previously.[12,69] Backbone polymers synthesized as described above were conjugated to FBP via reaction of the C-terminal lysine in the peptide under organic basic conditions in DMSO at a varying ratios of peptide:NHS with N.N-diisopropylethylamine added at a 5:1 ratio base:peptide[70] for 24 h at 50 °C, after which unreacted NHSMA groups were capped with 10x molar ratio of 1-amino-2-propanol. Peptide-polymer conjugates were purified by extensive dialysis as follows. First, the product was dialyzed against phosphate-buffered saline (PBS) for 24 h (3 buffer changes, 4 L of buffer) during which a precipitate formed. Contents of the dialysis bag were collected and centrifuged at 4500 x g for 8 min to remove insoluble material; the supernatant was collected and moved to a fresh dialysis bag. Dialysis continued for 24 h (3 buffer changes), followed by ~pH 8 water (NaOH added) for 48 h (6 dialysate changes) to

remove PBS salts. To synthesize control polymers for UV-Vis characterization of FL content, the same exact procedure was followed, however no peptide was added for conjugation and all NHSMA groups were capped with 1-amino-2-propanol. Purification was identical. **Supplementary Table 4** outlines all the PolySTAT (FBP), PolySCRAM (SCRAM - scrambled peptide control), and control polymers (Control) synthesized.

6.4.10 *Polymer characterization*

Polymers were characterized via GPC in dimethylformamide with static light scattering and refractive index detectors (MiniDawn Treos and OptilabTRex, respectively, both from Wyatt Technology, Santa Barbara, CA) to determine molecular weight and dispersity index (PDI). ^{1}H nuclear magnetic resonance (NMR) spectroscopy on a Bruker AV 300 was utilized to determine conversion of the polymer prior to purification, and composition after purification. Conversion of the FL comonomers (FMA and AEMA-FL) were monitored during polymerization to estimate final FL content. Ultraviolet-visible spectroscopy (UV-Vis) was used to determine FL content in the final control polymers (**Supplementary Figure 14 and Supplementary Figure 15**). **Supplementary Table 2** shows the measured FL content for each control polymer.

6.4.11 *ROTEM Characterization of FL-PolySTATs from various synthesis strategies*

ROTEM whole blood hemostasis analyzer (ROTEM, Instrumentation Laboratory, Bedford, MA, USA) was used to confirm activity of different PolySTAT formulations as previously described.[11,26] Briefly, 300 µL of a clotting solution with final concentrations in the ROTEM were 1.5 mg/mL fibrinogen, 0.5-1 IU/mL thrombin, 2-4 µg/mL plasmin, 0.1 mmol/L CaCl2, and 5 µmol/L PolySTAT at pH 7.4. Measured parameters in ROTEM included: (i) the clotting time (CT), measured as the time between reagent addition to clot formation; (ii) α-angle, which reflects the rate of clot formation, (iii) the maximum clot firmness (MCF), the highest strength observed for the clot, (iv) the lysis index-30 minutes (LI-30), the percentage of MCF retained 30 minutes after initiation of clot formation, and (v) maximum lysis (ML), the percentage of clot strength lost compared to the MCF at the end of analysis. An example of active PolySTAT is shown in **Supplementary Figure 11.** Complete data for all formulations is not shown.

6.4.12 *PolySTAT gel manufacturing*

To make PolySTAT gels, we first made compounded HEPES buffer (44nM HEPES (Gibco), 2nM $CaCl_2$, and 140mM NaCl in PBS pH 7.4). Compounded HEPES buffer (145 µL) was then mixed with 10 µL of 20 mg/mL CaCl and 2.5 µL of 80IU/mL thrombin, thereby making the "activating mixture." The activating mixture was then mixed with 5 µL of PolySTAT in a 48-well plate (for 5uM PolySTAT gels, the PolySTAT stock would be at 200uM). Last, 40 µL of 10 mg/mL fibrinogen was carefully mixed in to avoid forming bubbles. Completed gels incubated at 37°C for 1 hour followed by a 5-minute incubation at -20 °C to bring the plate to room temperature.

6.4.13 *PolySTAT-ELISA protocol*

To analyze anti-FL antibody binding to PolySTAT, PolySTAT-loaded fibrin gels were washed with PBS and blocked with 5% BSA (ENZO life sciences) for 1 hour at room temperature. The BSA was then aspirated off the gels and 1µg/mL of biotinylated anti-Fluorescein antibody (abcam) was added onto the gels in 5% BSA PBS solution for 20 minutes. Gels were then washed five times with PBS + 0.05% Tween20. For each wash, gel plates were placed on a shaker at 700RPM for 2 minutes. After the washes, streptavidin-HRP in 200uL was added to each well and incubated for 20 minutes. Gels were then washed three times with PBS + 0.05% Tween20 and three times with PBS. A QuantaRed ™ Enhanced Chemifluorescent HRP Substrate Kit (ThermoFisher Scientific) was then used for the ADHP/HRP enzymatic reaction. After a 15-minute reaction, reactions were quenched with the provided reagent and plates were imaged on a plate reader.

6.4.14 *In vitro cell activation experiments: cells*

CD69 and mCherry expression were examined after stimulation of 500,000 mock or cCARiCherry CAR T cells with a 1:1 E:T co-incubation with K562 Parental, K562 OKT3, or FL-PLE-labeled K562 Parental cells. T cells and target cells were co-incubated in 200µL of cytokine-free compounded media at 37°C and 5% CO_2 for 24 hours. Cells were then harvested and stained with live/dead FVS780 (BD Horizon), anti-CD19 BV421 (BioLegend), and anti-CD69 APC (BioLegend). Cells were then fixed with 0.5% paraformaldehyde and kept in the dark at 4°C until running on a LSRII Fortessa (BD Biosciences). FlowJo software was used for data analysis.

Compensation was performed using UltraComp eBeads Compensation Beads (ThermoFisher Scientific) and FlowJo Software (TreeStar) to analyze data.

6.4.15 *In vitro cell activation experiments: gels*

CD69 and mCherry expression were examined after stimulation of cCARiCherry CAR T cells with different polymer-loaded gels. Statistical and block AEMA-FL-PolySTAT (5μM) and associated PolySCRM-loaded gels were manufactured as described above. One million mock or cCARiCherry CAR T cells were added to designated wells in 200μL of cytokine-absent compounded media. 5% FL-fibrinogen gels, 1:1 E:T FL-PLE-labeled K562 cells, and 100X Cell Stimulation Cocktail (ThermoFisher Scientific) were used as positive controls. Plates were then placed in an IncuCyte® Live-Cell Analysis System (Essen Bioscience) at 37ºC and 5% CO_2, and images were taken every 2 hours for 20 hours. After the incubation, samples were harvested and stained with live/dead FVS780 (BD Horizon), anti-CD19 BV421 (BioLegend), and anti-CD69 APC (BioLegend). Cells were then fixed and analyzed on a LSRII Fortessa as described.

6.4.16 *PolySTAT in vivo tumor localization study*

Five million BT-20 breast cancer cells (ATCC) were engrafted subcutaneously in six NSG mice. Tumors were allowed to grow for 4 weeks until tumors were ~80mm^3. At this point, PBS or 10 mg/kg 2% statistical AEMA-FL PolySTAT or AEMA-FL-PolySCRM were injected IV into 2 mice/group. After 24 hours, mice were euthanized and immediately sequentially perfused with PBS and a 10% formalin solution. Tumors were excised and frozen in OTC. Frozen tumors were then cut into 10 μm thick slices using a cryotome and placed on clean microscope slides. Tumor slices were stained with a primary anti-fibrinogen antibody (abcam) and secondary AF647 antibody (Abcam) and an anti-FITC AF488 antibody (Jackson ImmunoResearch). Slices were imaged using a confocal microscope (Nikon).

6.4.17 *In vivo cell activation study*

Five million BT-20 breast cancer cells (ATCC) were engrafted subcutaneously in six NSG mice. Tumors were allowed to grow for 4 weeks until tumors were ~80mm^3. At this point, 10 million mock or cCARiCherry T cells were intravenously administered. After 48 hours, PBS or 10 mg/kg

2% statistical AEMA-FL PolySTAT or AEMA-FL-PolySCRM were injected IV into 4 mice per condition. Mice were then administered 4.29mg of D-luciferin (Perkin Elmer) and imaged every 24 hours for 8 days with an IVIS imaging machine (Xenogen). Flux was quantified using Perkin Elmer's Living Image® software. A one-way ANOVA test with repeated measures between the cCARiCherry|PolySTAT, cCARiCherry|PolySCRM, and cCARiCherry|PBS groups was performed, followed by Tukey's HSD post-hoc analysis to compare each group with one another.

6.4.18 *ImageJ analyses*

Confocal images were imported into Fiji (ImageJ) and split into individual RGB images. Red (fibrinogen) and green (PolySTAT) sub images were then converted to masks to produce pixel binary images for each color (signal or no signal). Masked images were imported into the JACoP plugin in Fiji to conduct distance-based colocalization analyses and generate a color overlap image (**Figure 5A**). Each colocalization analysis produced an overlap percentage. Mean and standard deviation for overlap percentages were then calculated in Microsoft Excel.

6.4.19 *Statistical analyses*

Statistical significance for PS-ELISA was performed using GraphPad software. A one-way ANOVA was performed on the groups broadly. Once population-wide significance was determined, a Tukey's posttest was conducted to compare between groups. Data presented are mean values +/- SD. *p<0.01, **p<0.001, ***p<0.0001. Statistical significance for *in vivo* studies was calculated using GraphPad software. For the experiment in our main figure, we performed a one-way ANOVA with a Tukey's posttest to compare each group. Data presented are mean values +/- SD. **** = p<0.0001, *** = p<0.001, ** = p<0.01, * = p<0.05. For the experiment included in the supplemental work, we performed an unpaired one-tailed T test with a Welch's correction for unequal variance. Data presented are mean values +/- SD, * = p<0.05.

6.5 AUTHOR CONTRIBUTIONS

S.H.P. and M.C.J. provided experimental advice and funding support. J.M., M.S., and J.G. provided supporting input for the project. C.M.H., T.J.P., and S.H.P. conceived and interpreted the

experiments. T.J.P. designed and fabricated the polymers. C.M.H. produced and tested molecular and cellular products. C.M.H. and M.B. performed the *in vivo* experiments.

6.6 ACKNOWLEDGEMENTS

This work was supported in part by NIH 1R01HL139007. We are grateful to all Pun lab members and Seattle Children's Therapeutics for experimental support and advice. We would specifically like to thank Ginny Hoglund (Seattle Children's Hospital) for assisting with confocal imaging, and Kefan Song (University of Washington) for assisting with animal injections. C.M.H. and T.J.P. were supported by NSF Graduate Fellowships (DGE1762114).

6.7 COMPETING INTERESTS

The authors declare no competing interests.

6.8 REFERENCES

1. Maude, S. L. *et al.* Chimeric antigen receptor T cells for sustained remissions in leukemia. *N. Engl. J. Med.* **371**, 1507–1517 (2014).
2. Brentjens, R. J. *et al.* CD19-targeted T cells rapidly induce molecular remissions in adults with chemotherapy-refractory acute lymphoblastic leukemia. *Sci. Transl. Med.* **5**, 177ra38 (2013).
3. Lee, D. W. *et al.* T cells expressing CD19 chimeric antigen receptors for acute lymphoblastic leukaemia in children and young adults: a phase 1 dose-escalation trial. *Lancet* **385**, 517–528 (2015).
4. Majzner, R. G. & Mackall, C. L. Tumor antigen escape from CAR T-cell therapy. *Cancer Discov.* **8**, 1219–1226 (2018).
5. Bonifant, C. L., Jackson, H. J., Brentjens, R. J. & Curran, K. J. Toxicity and management in CAR T-cell therapy. *Mol. Ther. Oncolytics* **3**, 16011 (2016).

6. Morgan, R. A. *et al.* Case report of a serious adverse event following the administration of T cells transduced with a chimeric antigen receptor recognizing ERBB2. *Mol. Ther.* **18**, 843–851 (2010).
7. Parkhurst, M. R. *et al.* T cells targeting carcinoembryonic antigen can mediate regression of metastatic colorectal cancer but induce severe transient colitis. *Mol. Ther.* **19**, 620–626 (2011).
8. Minutolo, N. G., Hollander, E. E. & Powell, D. J., Jr. The emergence of universal immune receptor T cell therapy for cancer. *Front. Oncol.* **9**, 176 (2019).
9. Obonai, T. *et al.* Tumour imaging by the detection of fibrin clots in tumour stroma using an anti-fibrin Fab fragment. *Sci. Rep.* **6**, 23613 (2016).
10. Dvorak, H. F. Tumors: wounds that do not heal. Similarities between tumor stroma generation and wound healing. *N. Engl. J. Med.* **315**, 1650–1659 (1986).
11. Lamm, R. J. *et al.* Optimizing the polymer structure and synthesis method of PolySTAT, an injectable hemostat. *ACS Biomaterials Sci Eng* **6**, 7011–7020 (2020).
12. Chan, L. W. *et al.* A synthetic fibrin cross-linking polymer for modulating clot properties and inducing hemostasis. *Sci. Transl. Med.* **7**, 277ra29-277ra29 (2015).
13. Kim, M. S. *et al.* Redirection of genetically engineered CAR-T cells using bifunctional small molecules. *J. Am. Chem. Soc.* **137**, 2832–2835 (2015).
14. A Phase I Feasibility And Safety Study of Fluorescein-Specific (FITC-E2) CAR T Cells In Combination With Parenterally Administered Folate-Fluorescein (UB-TT170) For Osteogenic Sarcoma. *ClinicalTrials.gov* https://www.clinicaltrials.gov/ct2/show/NCT05312411 (2022).
15. Wei, J. & Jensen, M. C. Generating mammalian t cell activation inducible synthetic promoters (syn+pro) to improve t cell therapy. *US Patent* (2020).
16. Staerz, U. D., Kanagawa, O. & Bevan, M. J. Hybrid antibodies can target sites for attack by T cells. *Nature* **314**, 628–631 (1985).
17. Wang, X. *et al.* The EF-1α promoter maintains high-level transgene expression from episomal vectors in transfected CHO-K1 cells. *J. Cell. Mol. Med.* **21**, 3044–3054 (2017).
18. Jonnalagadda, M. *et al.* Efficient selection of genetically modified human T cells using methotrexate-resistant human dihydrofolate reductase. *Gene Ther.* **20**, 853–860 (2013).

19. Manuri, P. V. R. *et al.* piggyBac transposon/transposase system to generate CD19-specific T cells for the treatment of B-lineage malignancies. *Hum. Gene Ther.* **21**, 427–437 (2010).
20. Nakazawa, Y. *et al.* Optimization of the PiggyBac transposon system for the sustained genetic modification of human T lymphocytes. *J. Immunother.* **32**, 826–836 (2009).
21. Nakazawa, Y. *et al.* PiggyBac-mediated cancer immunotherapy using EBV-specific cytotoxic T-cells expressing HER2-specific chimeric antigen receptor. *Mol. Ther.* **19**, 2133–2143 (2011).
22. Bishop, D. C. *et al.* PiggyBac-engineered T cells expressing CD19-specific CARs that lack IgG1 fc spacers have potent activity against B-ALL xenografts. *Mol. Ther.* **26**, 1883–1895 (2018).
23. Arvå, E. & Andersson, B. Kinetics of cytokine release and expression of lymphocyte cell-surface activation markers after in vitro stimulation of human peripheral blood mononuclear cells with Streptococcus pneumoniae. *Scand. J. Immunol.* **49**, 237–243 (1999).
24. Murphy, K. C. & Leach, J. K. A reproducible, high throughput method for fabricating fibrin gels. *BMC Res. Notes* **5**, 423 (2012).
25. Das, D. *et al.* RAFT polymerization of ciprofloxacin prodrug monomers for the controlled intracellular delivery of antibiotics. *Polym. Chem.* **7**, 826–837 (2016).
26. Chan, L. W., White, N. J. & Pun, S. H. A fibrin cross-linking polymer enhances clot formation similar to factor concentrates and tranexamic acid in an in vitro model of coagulopathy. *ACS Biomater. Sci. Eng.* **2**, 403–408 (2016).
27. Wang, Y. *et al.* Chimeric antigen receptor clustering via cysteines enhances T-cell efficacy against tumor. *Cancer Immunol. Immunother.* **71**, 2801–2814 (2022).
28. Le Guern, F., Mussard, V., Gaucher, A., Rottman, M. & Prim, D. Fluorescein derivatives as fluorescent probes for pH monitoring along recent biological applications. *Int. J. Mol. Sci.* **21**, 9217 (2020).
29. Starmans, L. W. E. *et al.* Noninvasive visualization of tumoral fibrin deposition using a peptidic fibrin-binding single photon emission computed tomography tracer. *Mol. Pharm.* **12**, 1921–1928 (2015).
30. Jin, X. *et al.* A metastasis map of human cancer cell lines. *Nature* **588**, 331–336 (2020).

31. Skovgard, M. S. *et al.* Imaging CAR T-cell kinetics in solid tumors: Translational implications. *Mol. Ther. Oncolytics* **22**, 355–367 (2021).
32. Gardner, R. *et al.* Decreased rates of severe CRS seen with early intervention strategies for CD19 CAR-T cell toxicity management. *Blood* **128**, 586–586 (2016).
33. Ma, J. S. Y. *et al.* Versatile strategy for controlling the specificity and activity of engineered T cells. *Proc. Natl. Acad. Sci. U. S. A.* **113**, E450-8 (2016).
34. Tamada, K. *et al.* Redirecting gene-modified T cells toward various cancer types using tagged antibodies. *Clin. Cancer Res.* **18**, 6436–6445 (2012).
35. Cao, Y. J. *et al.* Switchable CAR-T cells outperformed traditional antibody-redirected therapeutics targeting breast cancers. *ACS Synth. Biol.* **10**, 1176–1183 (2021).
36. Albert, C. M. *et al.* ENLIGHten-01: A phase 1 study of fluorescein-specific (FITC-E2)-CAR T cells in combination with folate-fluorescein (UB-TT170) for osteosarcoma. *J. Clin. Oncol.* **41**, TPS11581–TPS11581 (2023).
37. Lee, Y. G. *et al.* Use of a single CAR T cell and several bispecific adapters facilitates eradication of multiple antigenically different solid tumors. *Cancer Res.* **79**, 387–396 (2019).
38. Jensen, M. C. & James, M. Phospholipid ether (PLE) CAR T cell tumor targeting (CTCT) agents. *WorldPatent* (2018).
39. Zhang, A. Q. *et al.* Universal redirection of CAR T cells against solid tumours via membrane-inserted ligands for the CAR. *Nat. Biomed. Eng.* (2023) doi:10.1038/s41551-023-01048-8.
40. Weichert, J. P. *et al.* Alkylphosphocholine analogs for broad-spectrum cancer imaging and therapy. *Sci. Transl. Med.* **6**, 240ra75 (2014).
41. Moghimi, B. *et al.* Preclinical assessment of the efficacy and specificity of GD2-B7H3 SynNotch CAR-T in metastatic neuroblastoma. *Nat. Commun.* **12**, 511 (2021).
42. Srivastava, S. *et al.* Logic-gated ROR1 chimeric antigen receptor expression rescues T cell-mediated toxicity to normal tissues and enables selective tumor targeting. *Cancer Cell* **35**, 489-503.e8 (2019).
43. Choe, J. H. *et al.* SynNotch-CAR T cells overcome challenges of specificity, heterogeneity, and persistence in treating glioblastoma. *Sci. Transl. Med.* **13**, (2021).

44. Hooijberg, E., Bakker, A. Q., Ruizendaal, J. J. & Spits, H. NFAT-controlled expression of GFP permits visualization and isolation of antigen-stimulated primary human T cells. *Blood* **96**, 459–466 (2000).
45. Zhang, L. *et al.* Improving adoptive T cell therapy by targeting and controlling IL-12 expression to the tumor environment. *Mol. Ther.* **19**, 751–759 (2011).
46. Blazeck, J. & Alper, H. S. Promoter engineering: recent advances in controlling transcription at the most fundamental level. *Biotechnol. J.* **8**, 46–58 (2013).
47. Dvorak, H. F., Harvey, V. S. & McDonagh, J. Quantitation of fibrinogen influx and fibrin deposition and turnover in line 1 and line 10 guinea pig carcinomas. *Cancer Res.* **44**, 3348–3354 (1984).
48. Folkman, J. Tumor angiogenesis. *Adv. Cancer Res.* **43**, 175–203 (1985).
49. Nerenberg, P. S., Salsas-Escat, R. & Stultz, C. M. Collagen--a necessary accomplice in the metastatic process. *Cancer Genomics Proteomics* **4**, 319–328 (2007).
50. Winkler, J., Abisoye-Ogunniyan, A., Metcalf, K. J. & Werb, Z. Concepts of extracellular matrix remodelling in tumour progression and metastasis. *Nat. Commun.* **11**, 5120 (2020).
51. Liang, H. *et al.* A collagen-binding EGFR antibody fragment targeting tumors with a collagen-rich extracellular matrix. *Sci. Rep.* **6**, 18205 (2016).
52. Baldari, S., Di Modugno, F., Nisticò, P. & Toietta, G. Strategies for efficient targeting of tumor collagen for cancer therapy. *Cancers (Basel)* **14**, 4706 (2022).
53. Anderson, C. F. *et al.* Collagen-binding peptide-enabled supramolecular hydrogel design for improved organ adhesion and sprayable therapeutic delivery. *Nano Lett.* **22**, 4182–4191 (2022).
54. Ezeani, M. *et al.* Collagen-targeted peptides for molecular imaging of diffuse cardiac fibrosis. *J. Am. Heart Assoc.* **10**, e022139 (2021).
55. Rick, J. W. *et al.* Fibronectin in malignancy: Cancer-specific alterations, protumoral effects, and therapeutic implications. *Semin. Oncol.* **46**, 284–290 (2019).
56. Kumra, H. & Reinhardt, D. P. Fibronectin-targeted drug delivery in cancer. *Adv. Drug Deliv. Rev.* **97**, 101–110 (2016).
57. Urbanska, K. *et al.* A universal strategy for adoptive immunotherapy of cancer through use of a novel T-cell antigen receptor. *Cancer Res.* **72**, 1844–1852 (2012).

58. Rodgers, D. T. *et al.* Switch-mediated activation and retargeting of CAR-T cells for B-cell malignancies. *Proc. Natl. Acad. Sci. U. S. A.* **113**, E459-68 (2016).
59. Minutolo, N. G. *et al.* Quantitative control of gene-engineered T-cell activity through the covalent attachment of targeting ligands to a universal immune receptor. *J. Am. Chem. Soc.* **142**, 6554–6568 (2020).
60. Yin, L., Wang, A., Shi, H. & Gao, M. Quantitatively visualizing the activity of MMP-2 enzyme in vivo using a ratiometric photoacoustic probe. *Methods Enzymol.* **657**, 59–87 (2021).
61. Huang, H.-Y. *et al.* Self-immolative difluorophenyl ester linker for affinity-based fluorescence turn-on protein detection. *Anal. Chem.* **92**, 15463–15471 (2020).
62. Richard, J.-A. *et al.* Latent fluorophores based on a self-immolative linker strategy and suitable for protease sensing. *Bioconjug. Chem.* **19**, 1707–1718 (2008).
63. Miller, E. W., Albers, A. E., Pralle, A., Isacoff, E. Y. & Chang, C. J. Boronate-based fluorescent probes for imaging cellular hydrogen peroxide. *J. Am. Chem. Soc.* **127**, 16652–16659 (2005).
64. Kobayashi, T. *et al.* Highly activatable and rapidly releasable caged fluorescein derivatives. *J. Am. Chem. Soc.* **129**, 6696–6697 (2007).
65. Mestermann, K. *et al.* The tyrosine kinase inhibitor dasatinib acts as a pharmacologic on/off switch for CAR T cells. *Sci. Transl. Med.* **11**, eaau5907 (2019).
66. Hügle, T. *et al.* Fibrin deposition associates with cartilage degeneration in arthritis. *EBioMedicine* **81**, 104081 (2022).
67. Kolodziej, A. F. *et al.* Fibrin specific peptides derived by phage display: characterization of peptides and conjugates for imaging. *Bioconjug. Chem.* **23**, 548–556 (2012).
68. BT-20. https://www.atcc.org/products/htb-19.
69. Lamm, R. J. *et al.* Peptide valency plays an important role in the activity of a synthetic fibrin-crosslinking polymer. *Biomaterials* **132**, 96–104 (2017).
70. Yanjarappa, M. J., Gujraty, K. V., Joshi, A., Saraph, A. & Kane, R. S. Synthesis of copolymers containing an active ester of methacrylic acid by RAFT: controlled molecular weight scaffolds for biofunctionalization. *Biomacromolecules* **7**, 1665–1670 (2006).

6.9 SUPPLEMENTARY INFORMATION

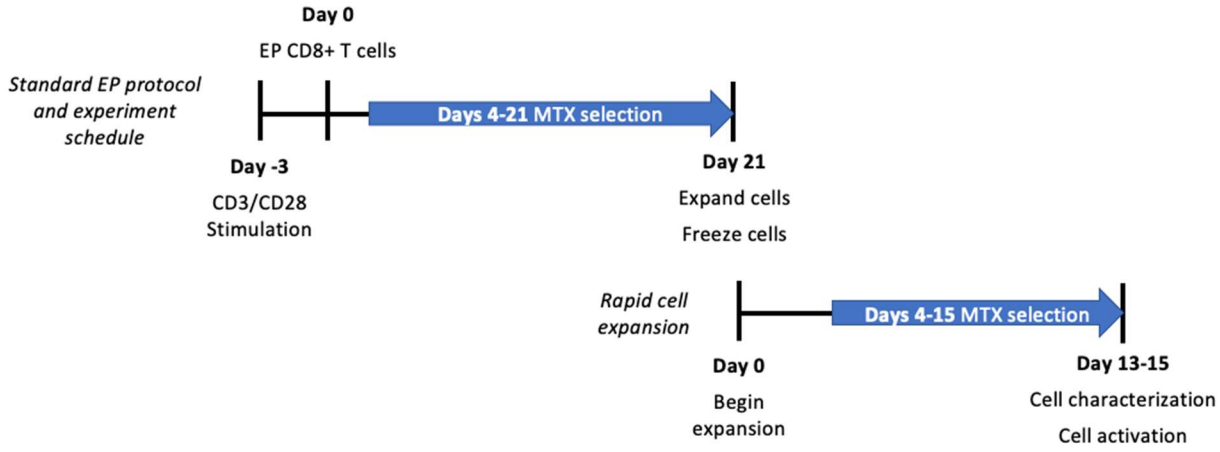

Figure S 1. Time course for original cell production and assays. CD8+ T cells were incubated with a soluble CD3/CD28 stimulation agent for 3 days prior to EP. Cells were then cultured for 21 days under MTX selection from days 4-21. 21 days after EP, cells were expanded using the rapid expansion protocol (REP). 13-15 days after the start of the REP, cells were characterized and run through cell activation assays.

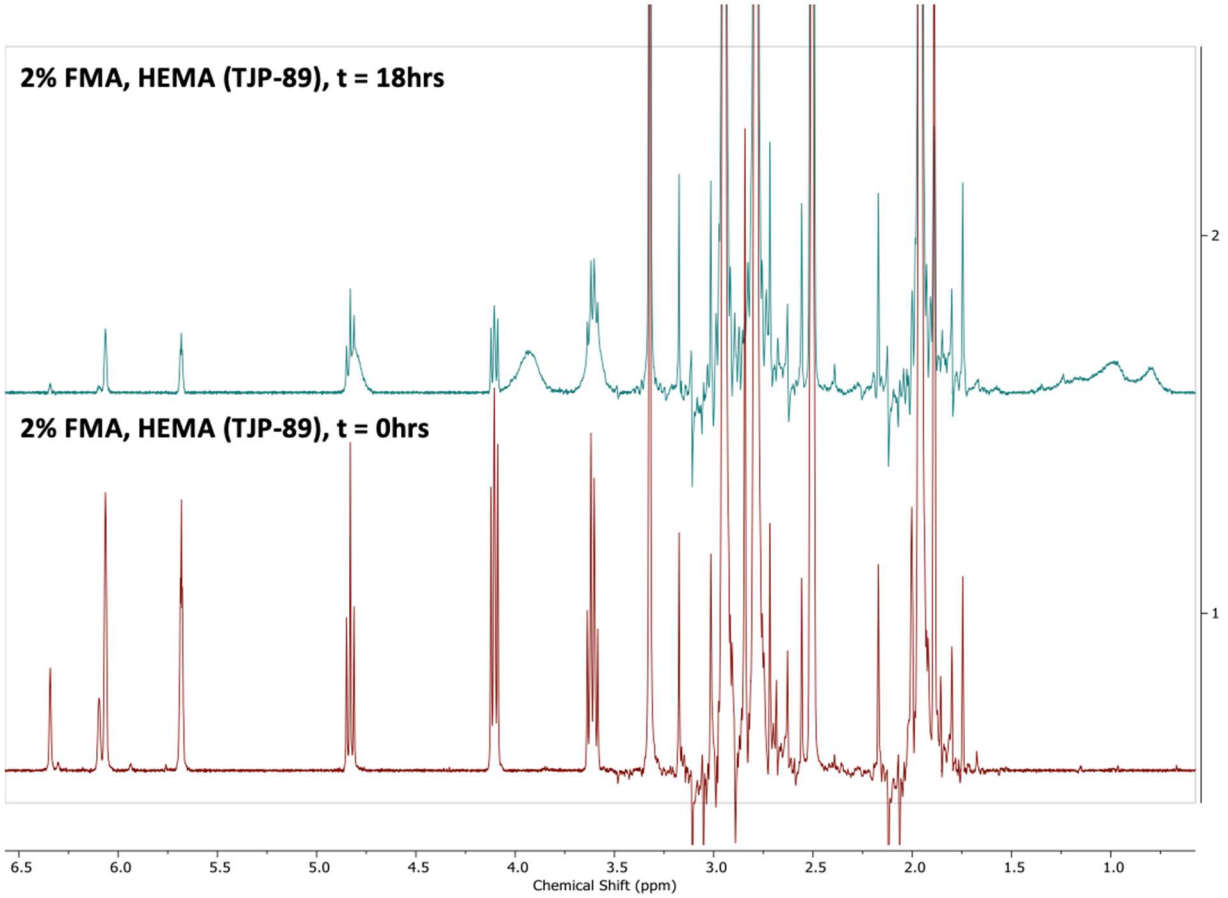

Figure S 2. Proton NMR spectroscopy of 2% FMA p(HEMA-co-FMA-co-NHSMA) backbone (TJP-89) in DMSO-d6 at both the time zero and time 18 hours. The ratio of the alkene peaks at 6.34 (NHSMA), 5.94 (FMA), and (5.68) to the HEMA hydroxyl peak at 4.83 were used to measure conversion of each monomer.

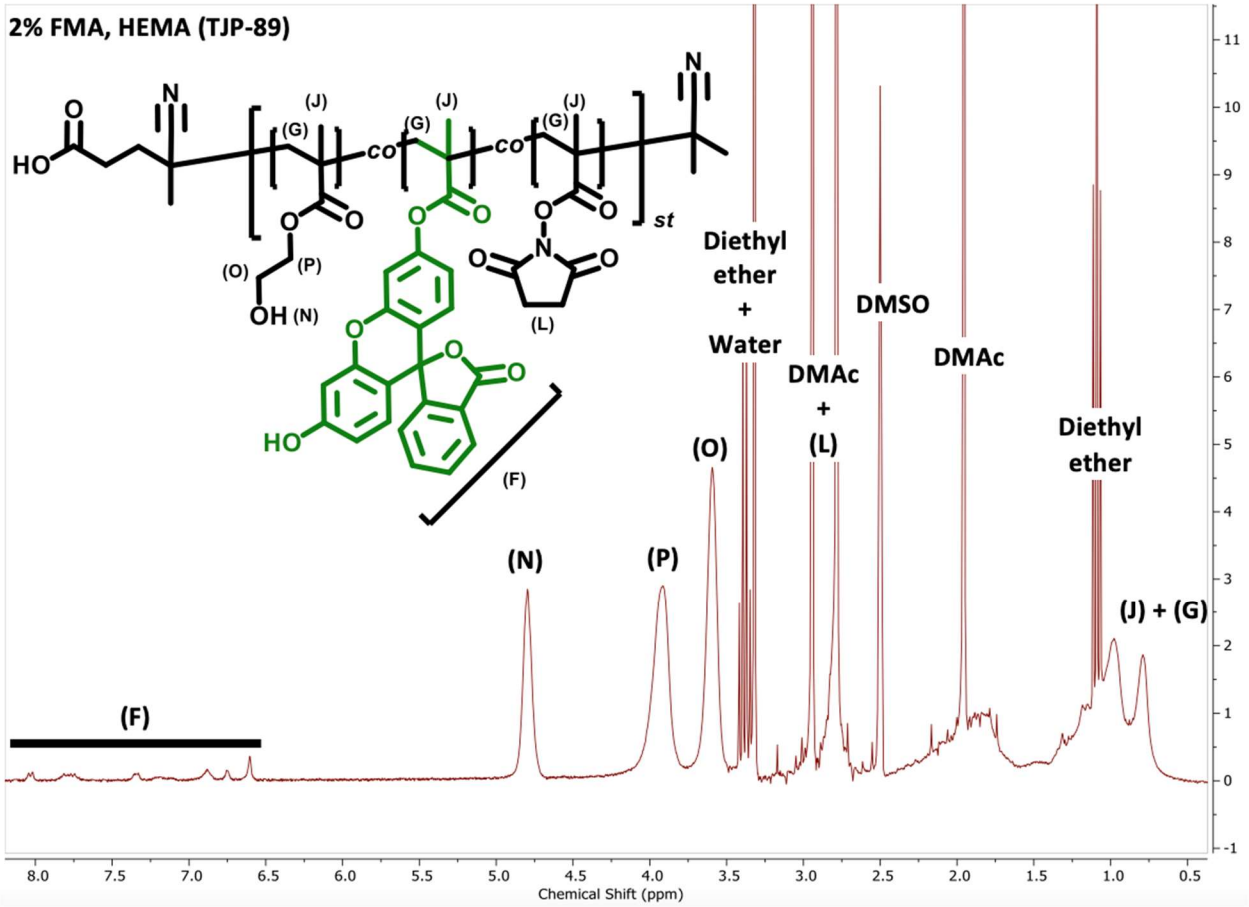

Figure S 3. Proton NMR spectroscopy of precipitated 2% FMA p(HEMA-co-FMA-co-NHSMA) backbone (TJP-89) in DMSO-d6. HEMA copolymers were precipitated 2x in diethyl ether.

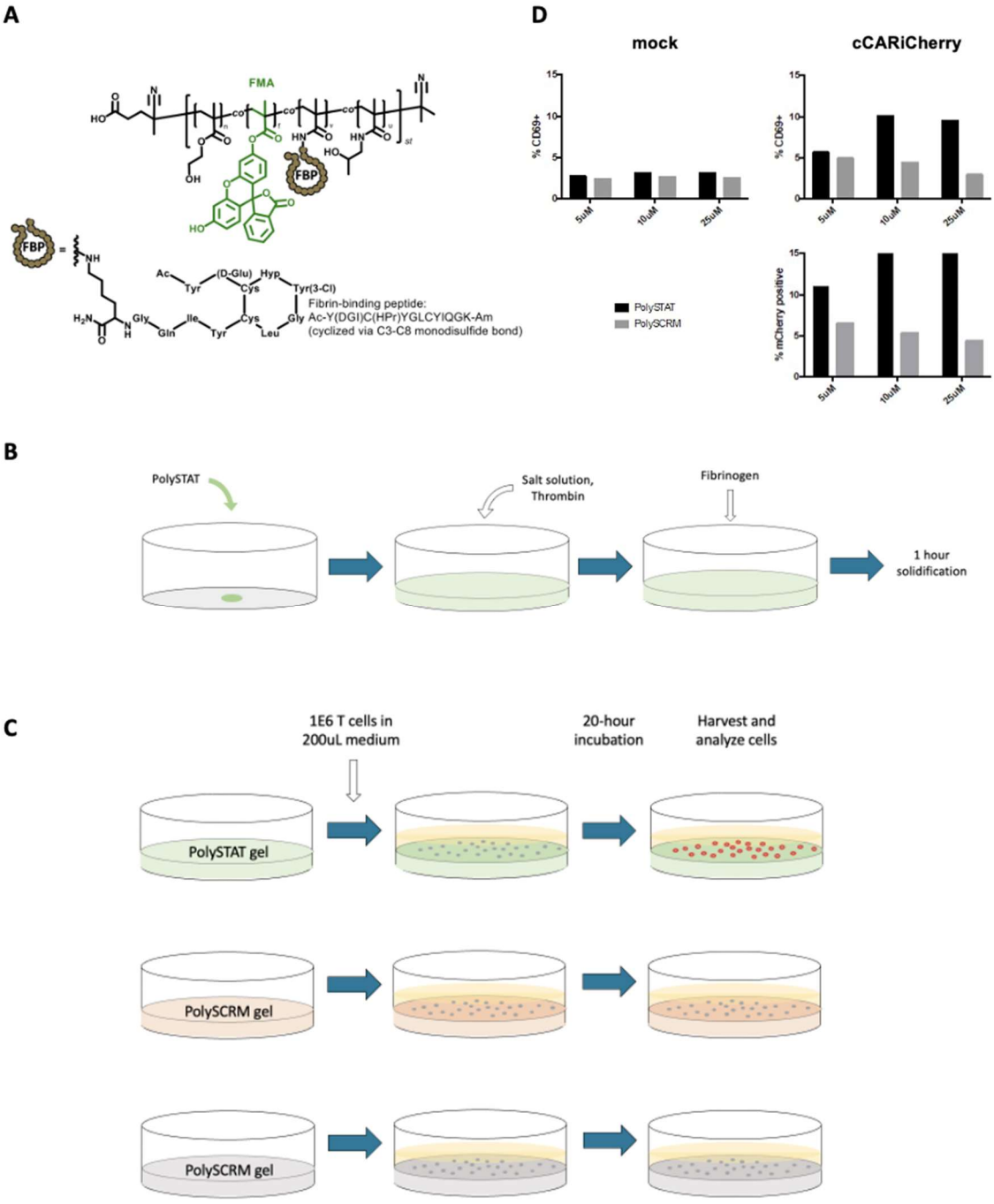

Figure S 4. FMA-PolySTAT can activate cCARiCherry T cells. (A) FMA-PolySTAT and fibrin binding protein chemical structures. (B) Diagram depicting the gel fabrication process. Thrombin and salt solution is mixed with PolySTAT. Fibrinogen is then added, and the gels are cured for one hour. (C) Diagram depicting the cell activation process. Cells are added onto solidified gels and incubated until harvested and analyzed. (D) CD69 expression and mCherry

production from mock or cCARiCherry T cells incubated on 5 µM, 10 µM, or 25 µM FMA-PolySTAT and FMA-PolySCRM gels for 20 hours. Results are for one donor.

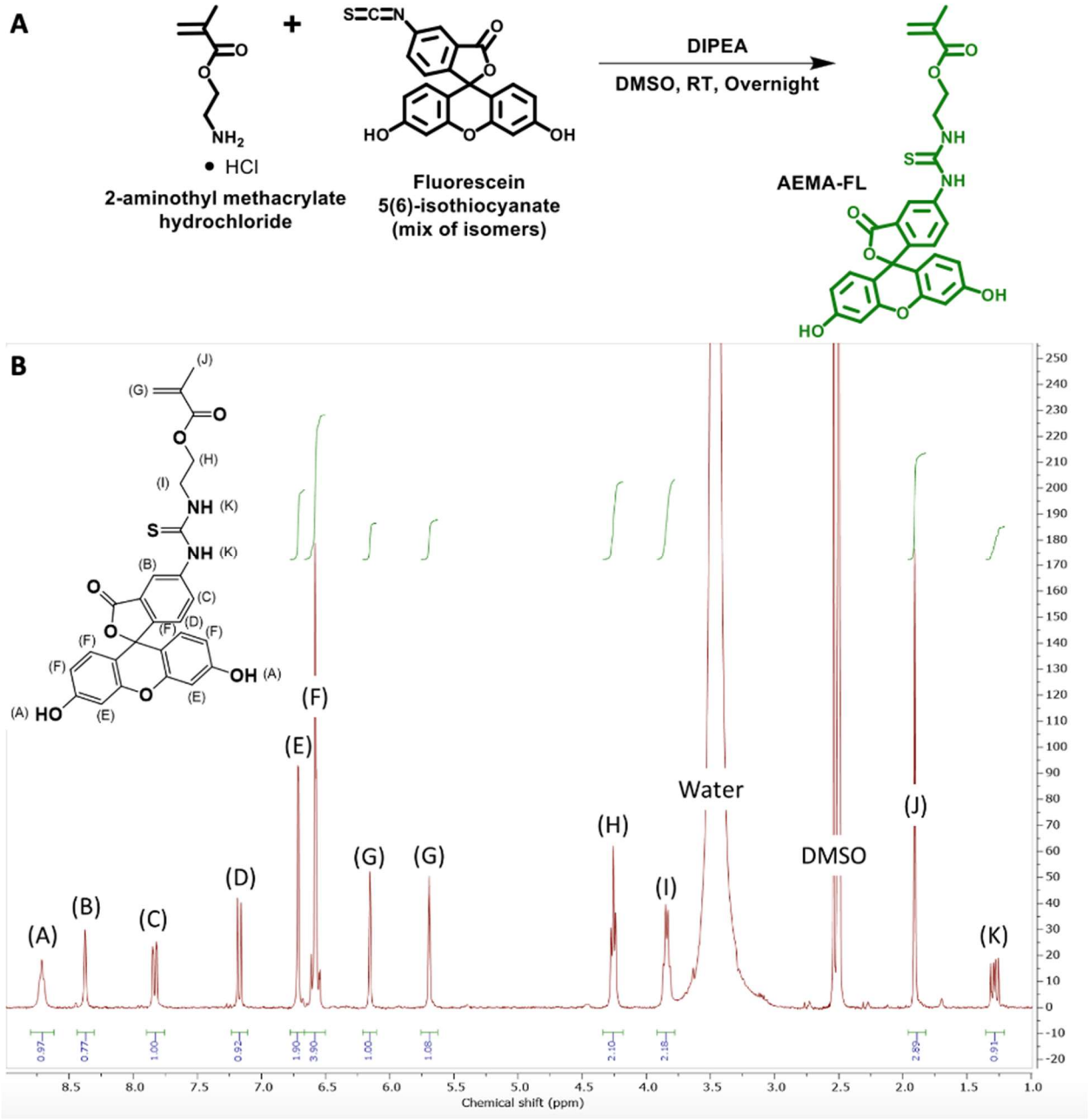

Figure S 5. Synthesis of AEMA-FL monomer. (A) 2-aminoethyl methacrylate hydrochloride was reacted with fluorescein isothiocyanate overnight at room temperature in DMSO with DIPEA. The monomer was then precipitated in 6% HCl solution, filtered, and lyophilized. (B) Proton NMR spectroscopy of AEMA-Fl in DMSO-d6.

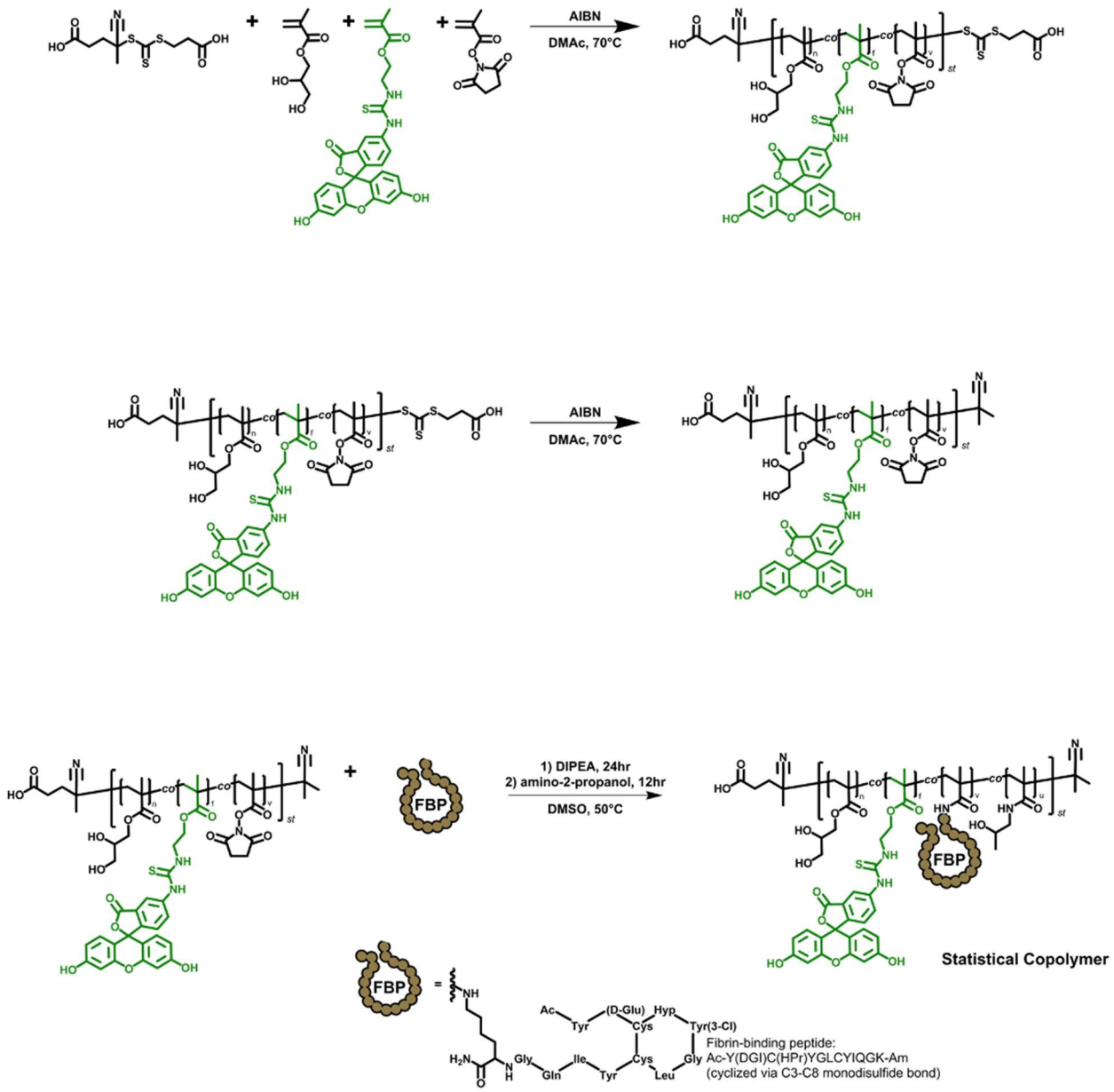

Figure S 6. Synthesis scheme for statistical AEMA-FL PolySTAT.

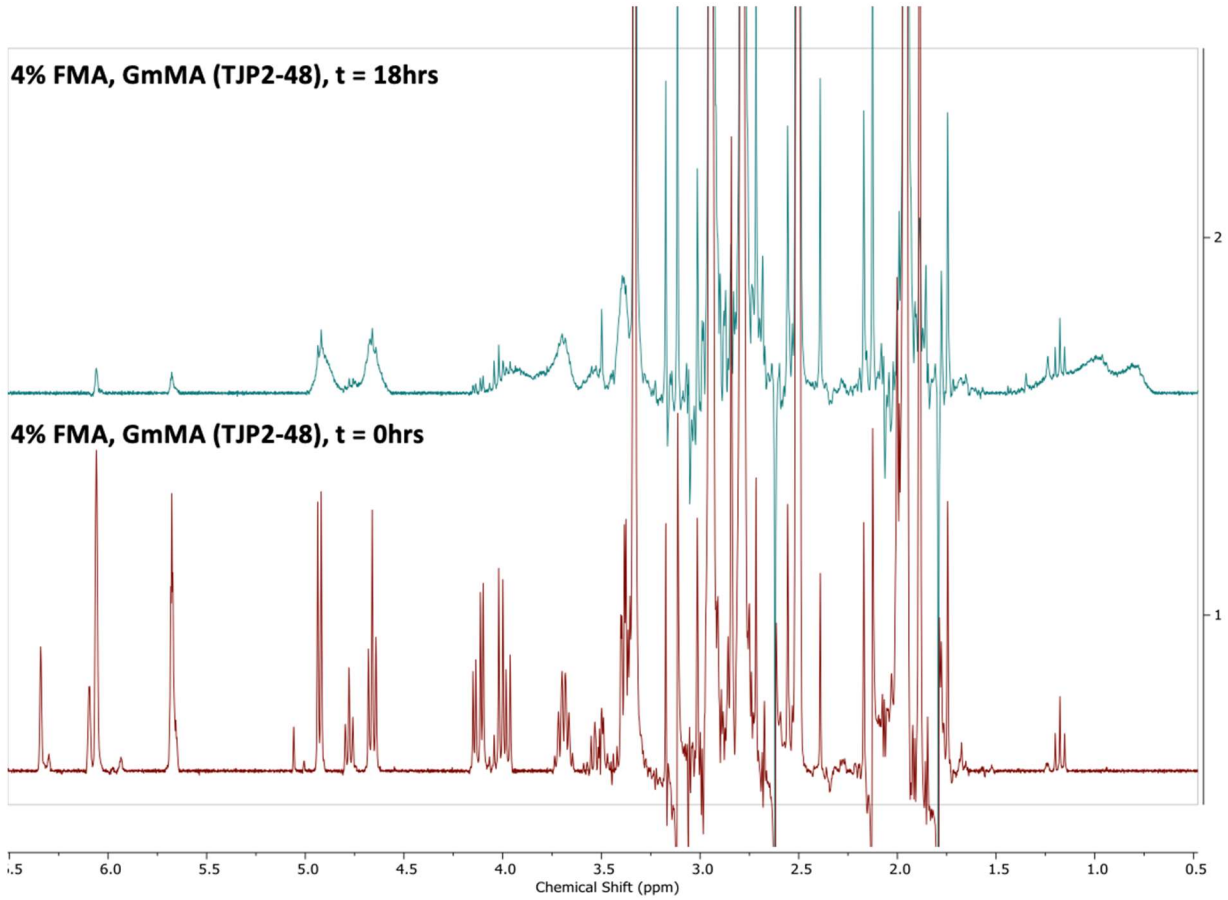

Figure S 7. Proton NMR spectroscopy of 4% FMA p(GmMA-co-FMA-co-NHSMA) backbone (TJP2-48) in DMSO-d6 at both the time zero and time 18 hours time points. The ratio of the alkene peaks at 6.34 (NHSMA), 5.94 (FMA), and (5.68) to the GmMA hydroxyl peaks at 4.92, 4.78, and 4.66 were used to measure conversion of each monomer.

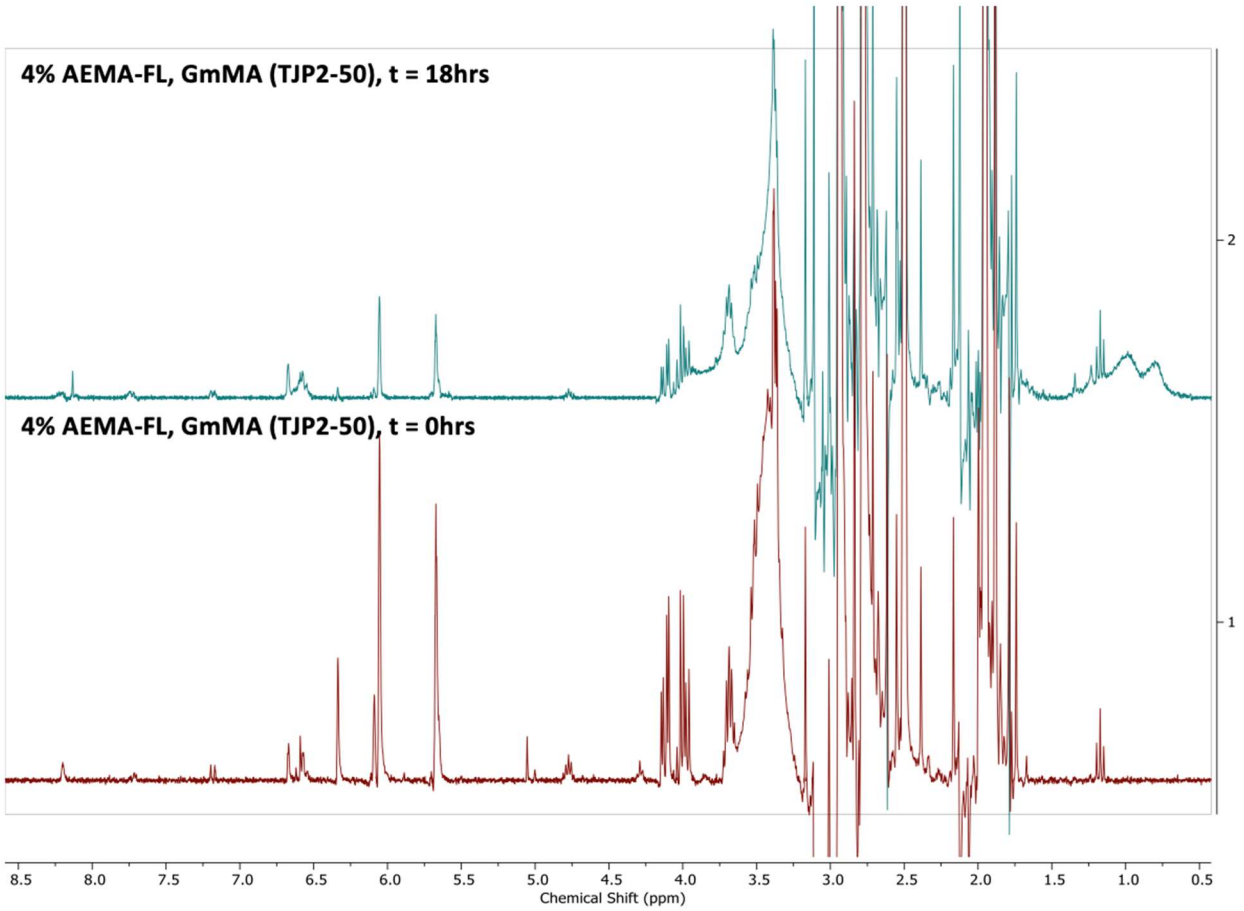

Figure S 8. Proton NMR spectroscopy of 4% AEMA-FL p(GmMA-co-AEMA-FL-co-NHSMA) backbone (TJP2-50) in DMSO-d6 at both the time zero and time 18 hours time points. The ratio of the alkene peaks at 6.34 (NHSMA) and 6.06 (GmMA) to the AEMA-FL peaks at 6.68 and 6.54 were used to measure conversion of each monomer. To calculate the AEMA-FL conversion, the difference in the 6.34 (NHSMA) and 6.10 (NHSMA + AEMA-FL) alkene peaks and the difference in the 6.06 (GmMA) and 5.68 (GmMA + AEMA-FL) were used.

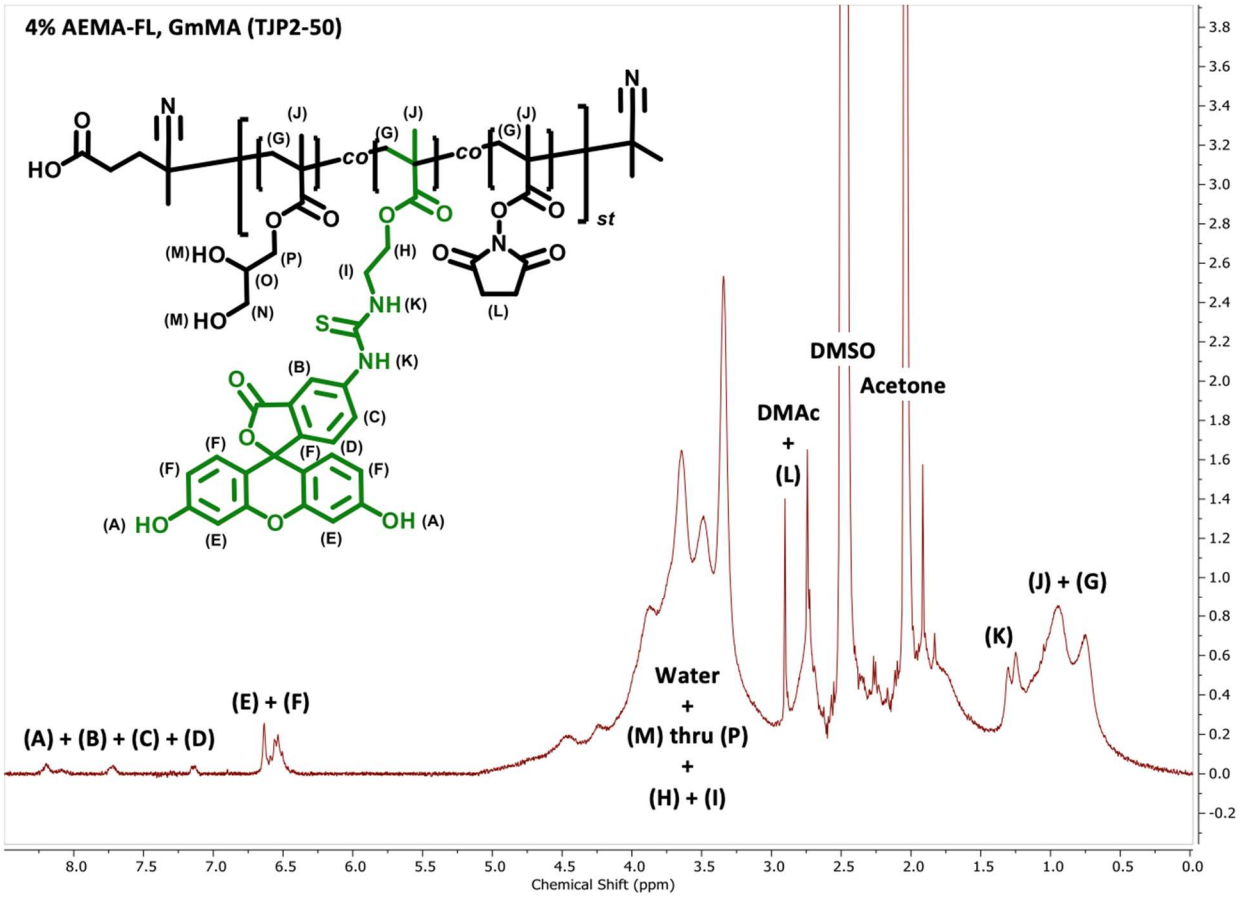

Figure S 9. Proton NMR spectroscopy of precipitated 4% AEMA-FL p(GmMA-co-AEMA-FL-co-NHSMA) backbone (TJP2-50) in DMSO-d6. GmMA copolymers were precipitated 1x in diethyl ether followed by redissolving in DMSO, then precipitating 1x in 50:50 diethyl ether:acetone.

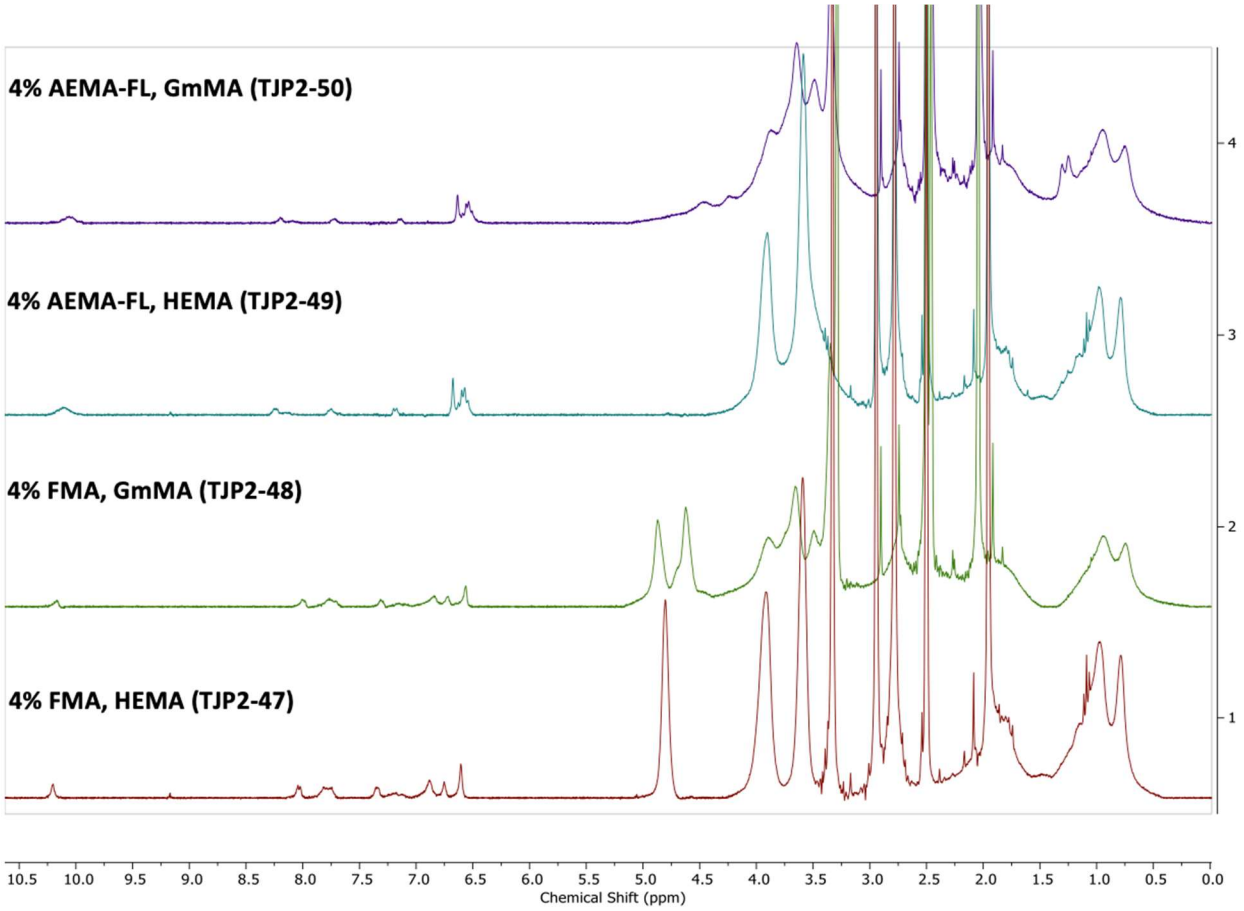

Figure S 10. Proton NMR spectroscopy (from bottom to top) of precipitated 4% FMA p(HEMA-co-FMA-co-NHSMA) backbone (TJP2-47), 4% FMA p(GmMA-co-FMA-co-NHSMA) backbone (TJP2-48), 4% AEMA-FL p(HEMA-co-AEMA-FL-co-NHSMA) backbone (TJP2-49), and 4% AEMA-FL p(GmMA-co-AEMA-FL-co-NHSMA) backbone (TJP2-50) in DMSO-d6. HEMA copolymers were precipitated 2x in diethyl ether, while GmMA copolymers were precipitated 1x in diethyl ether followed by redissolving in DMSO, then precipitating 1x in 50:50 diethyl ether:acetone.

Table S 1. Overview of the statistical copolymer backbones synthesized.

D	Comonomer	FMA or AEMA-FITC	% Comonomer	% FITC	% NHSMA	% Conversion (HEMA or GmMA)	% Conversion (FITC)	% Conversion (NHSMA)	PDI	MW (kDa)
TJP-89	HEMA	FMA	76	2	20	77	100	92	1.10	23.9
TJP2-47	HEMA	FMA	76	4	20	90	100	100	1.06	28.3
TJP2-49	HEMA	AEMA-FITC	76	4	20	76	100	90	1.18	24.8
TJP2-48	GmMA	FMA	76	4	20	90	100	100	1.11	32.4
TJP2-50	GmMA	AEMA-FITC	76	4	20	76	100	94	1.02	28.6
TJP2-97	GmMA	AEMA-FITC	78	2	20	83	100	95	1.17	28.2
TJP2-98	GmMA	AEMA-FITC	76	4	20	76	100	96	1.43	28.1
TJP2-99	GmMA	AEMA-FITC	72	8	20	73	89	90	1.58	29.6

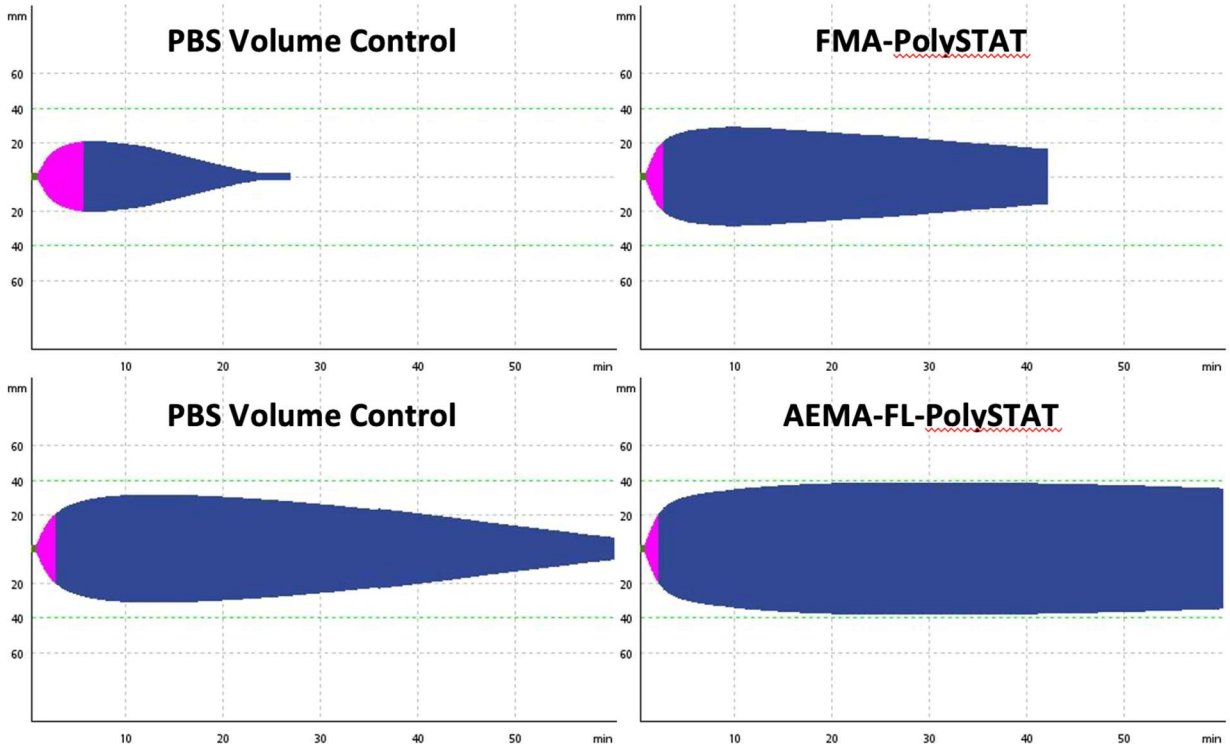

Figure S 11. Representative images of ROTEM QC of both FMA-PolySTAT and AEMA-FL PolySTAT. All PolySTATs synthesized for the study decreased lysis and increased clot firmness similar to traditional PolySTAT.

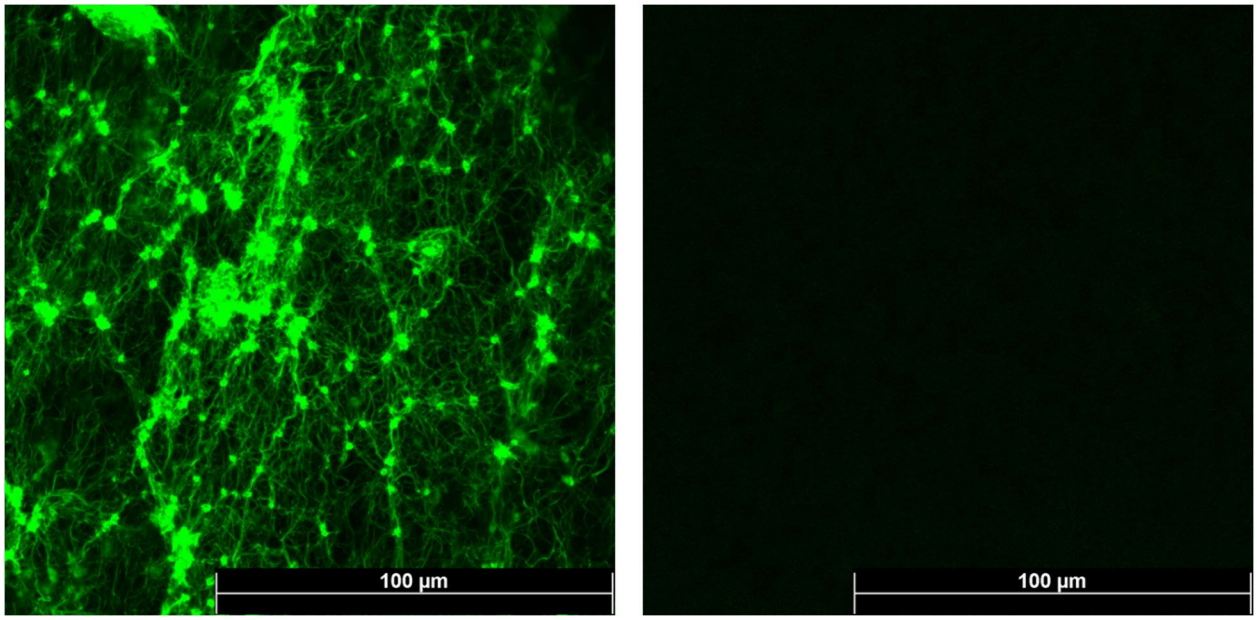

Figure S 12. Confocal microscopy of blood clot harvested from a rat infused with FL-PolySTAT. The PolySTAT used had 10% AEMA-FL incorporated into a statistical copolymer backbone. The PolySTAT was infused intravenously, and the blood clot was harvested from a wound on the femoral artery. Left image shows the FL-PolySTAT, while the image on the right is a PolySCRAM control clot. No FL was observed in the control clot.

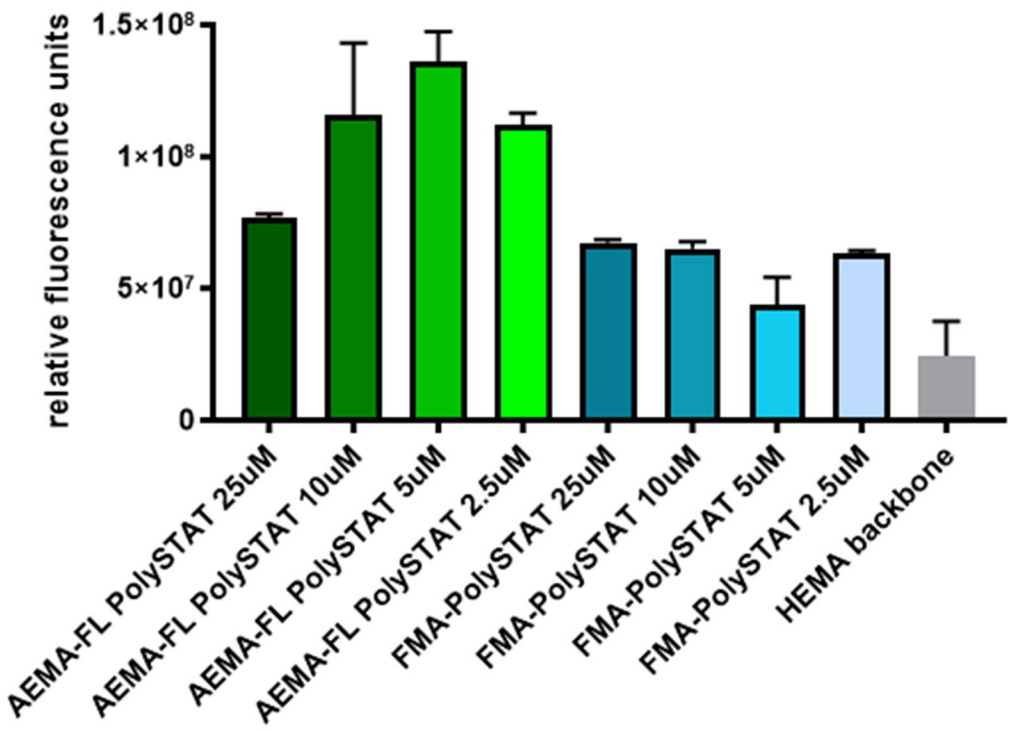

Figure S 13. Anti-fluorescein antibody binding to titrated doses of FMA-PolySTAT and AEMA-FL-PolySTAT in fibrin gels. The dose of FMA-PolySTAT did not impact antibody binding, but 5 μM AEMA-FL-PolySTATs are the ideal concentration for antibody binding. n = 3 technical replicates. Data shown are means +/- SD.

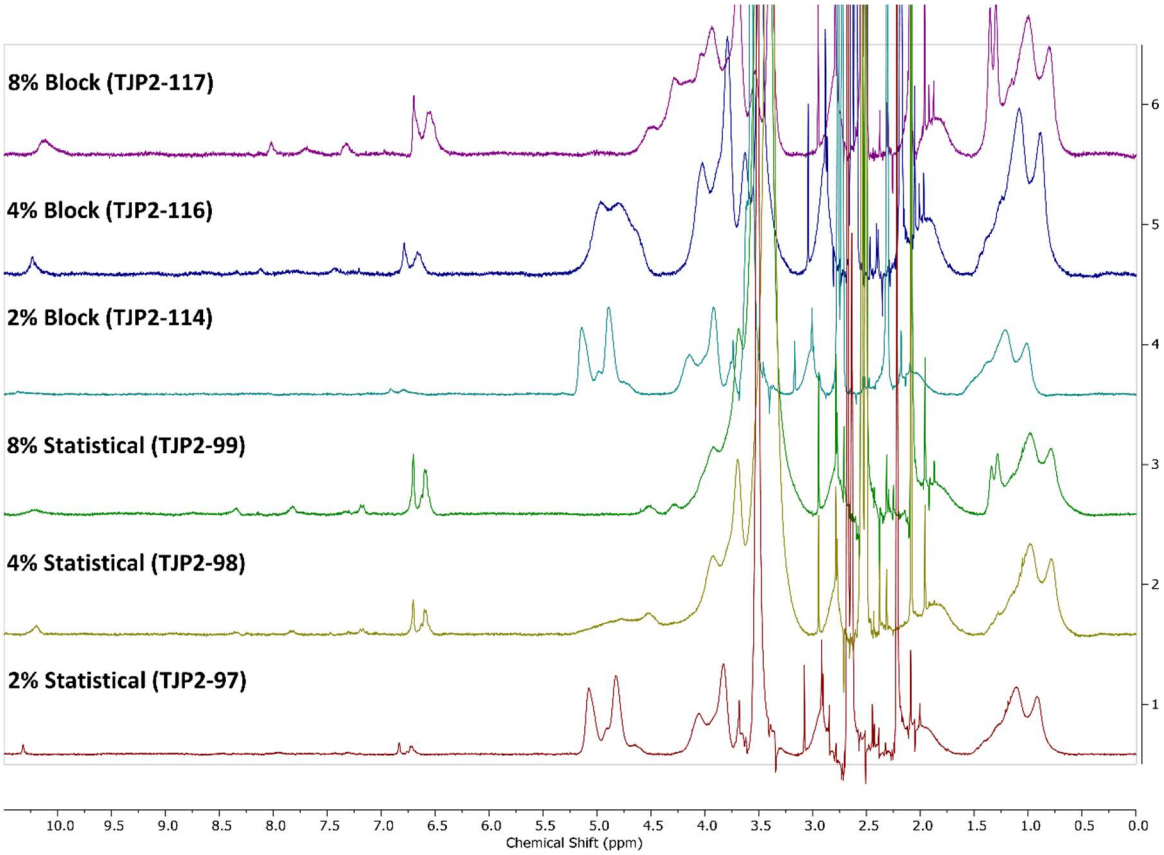

Figure S 14. Proton NMR spectroscopy (from bottom to top) of precipitated 2% Statistical p(GmMA-co-AEMA-FL-co-NHSMA) backbone (TJP2-97), 4% Statistical p(GmMA-co-AEMA-FL-co-NHSMA) backbone (TJP2-98), 8% Statistical p(GmMA-co-AEMA-FL-co-NHSMA) backbone (TJP2-99), 2% Block p([GmMA-co-AEMA-FL]-block-[GmMA-co-NHSMA]) backbone (TJP2-114), 4% Block p([GmMA-co-AEMA-FL]-block-[GmMA-co-NHSMA]) backbone (TJP2-114), and 8% Block p([GmMA-co-AEMA-FL]-block-[GmMA-co-NHSMA]) backbone (TJP2-114) in DMSO-d6.

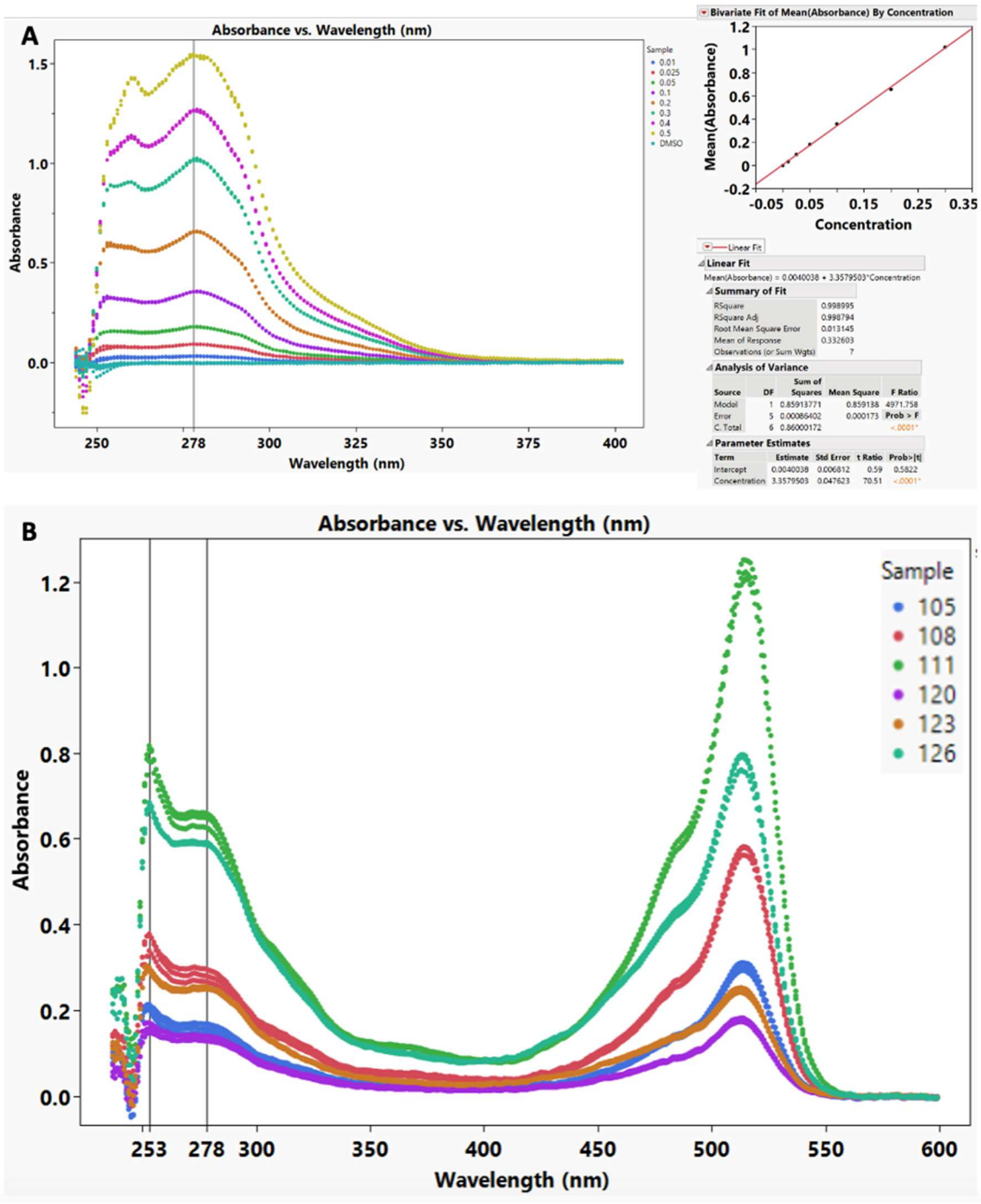

Figure S 15. UV-Vis Measurement of AEMA-FL concentration of control backbones for AEMA-FL PolySTAT (Statistical and Block). (A) Generation of standard curve at 278 nm using AEMA-FL monomer dissolved in DMSO with triethylamine (TEA) added to neutralize HCl and ensure all FITC was in the same protanation state. (B) Full UV-Vis spectrum of different control backbones. The control backbones went through the full synthesis process for PolySTAT;

however, no peptide was conjugated, only amino-2-propanol. The backbones were dissolved in DMSO, and TEA was added to make sure all FITC were in the same protonation state. Absorbance at 278 nm was used to measure FITC content.

Table S 2. Overview of the statistical copolymer backbones synthesized.

ID	Type	Backbone ID	MacroCTA	DP	MW (kDa)	PDI	% FITC Target	UV-Vis (full process)		NMR (polymerization)	
								% FITC	# FITC	% FITC	# FITC
TJP2-105	ST	TJP2-97	N/A	172	28.2	1.1	2	2.1	3.7	2.3	4.0
TJP2-108	ST	TJP2-98	N/A	162	28.1	1.1	4	4.8	7.8	4.9	8.0
TJP2-111	ST	TJP2-99	N/A	155	29.6	1.3	8	10.3	15.9	9.2	14.2
TJP2-120	B	TJP2-114	100	176	28.8	1.1	2	1.8	3.1	2.4	4.2
TJP2-123	B	TJP2-116	101	173	29.6	1.2	4	3.6	6.3	4.5	7.8
TJP2-126	B	TJP2-117	112	165	32	1.3	8	10.1	16.7	11.0	18.1

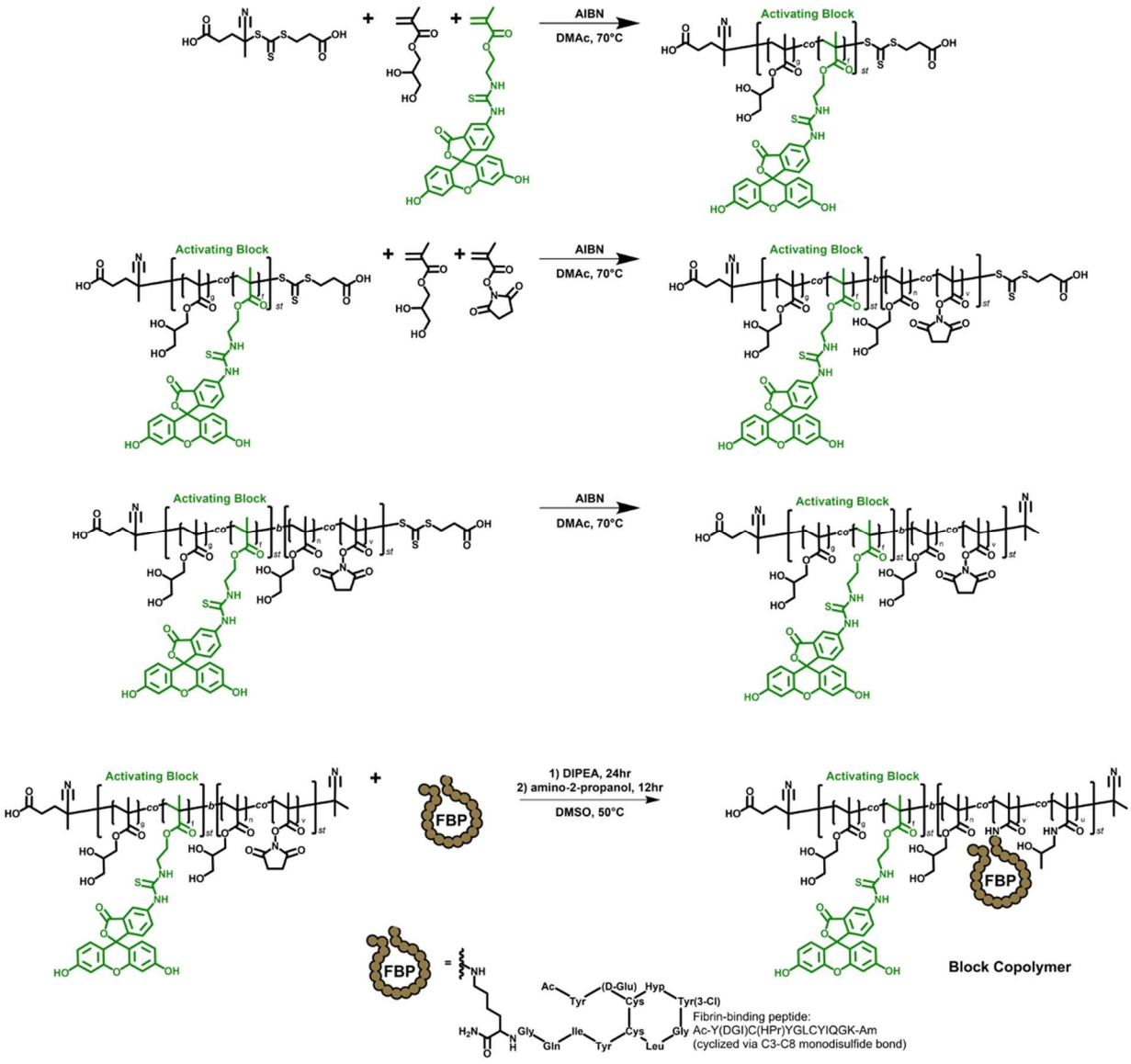

Figure S 16. Synthesis scheme for block copolymer AEMA-FL PolySTAT.

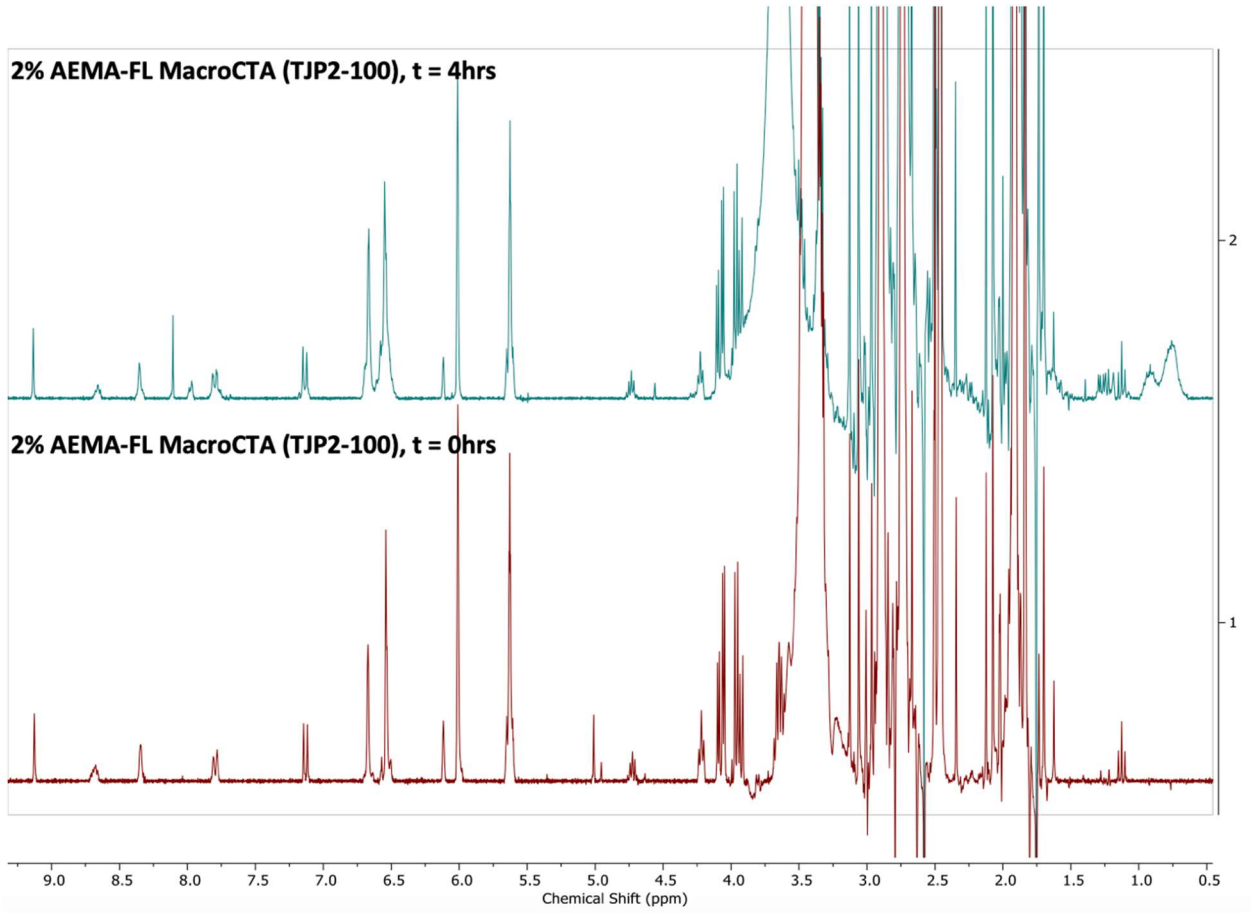

Figure S 17. Proton NMR spectroscopy of the macroCTA (TJP2-100) for 2% Block p([GmMA-co-AEMA-FL]-block-[GmMA-co-NHSMA]) backbone (TJP2-114) in DMSO-d6 at both the time zero and time 4 hours time points. The ratio of the alkene peaks at 6.10 (AEMA-FL) and 6.06 (GmMA) to the AEMA-FL peaks at 6.68 and 6.54 were used to measure conversion of each monomer.

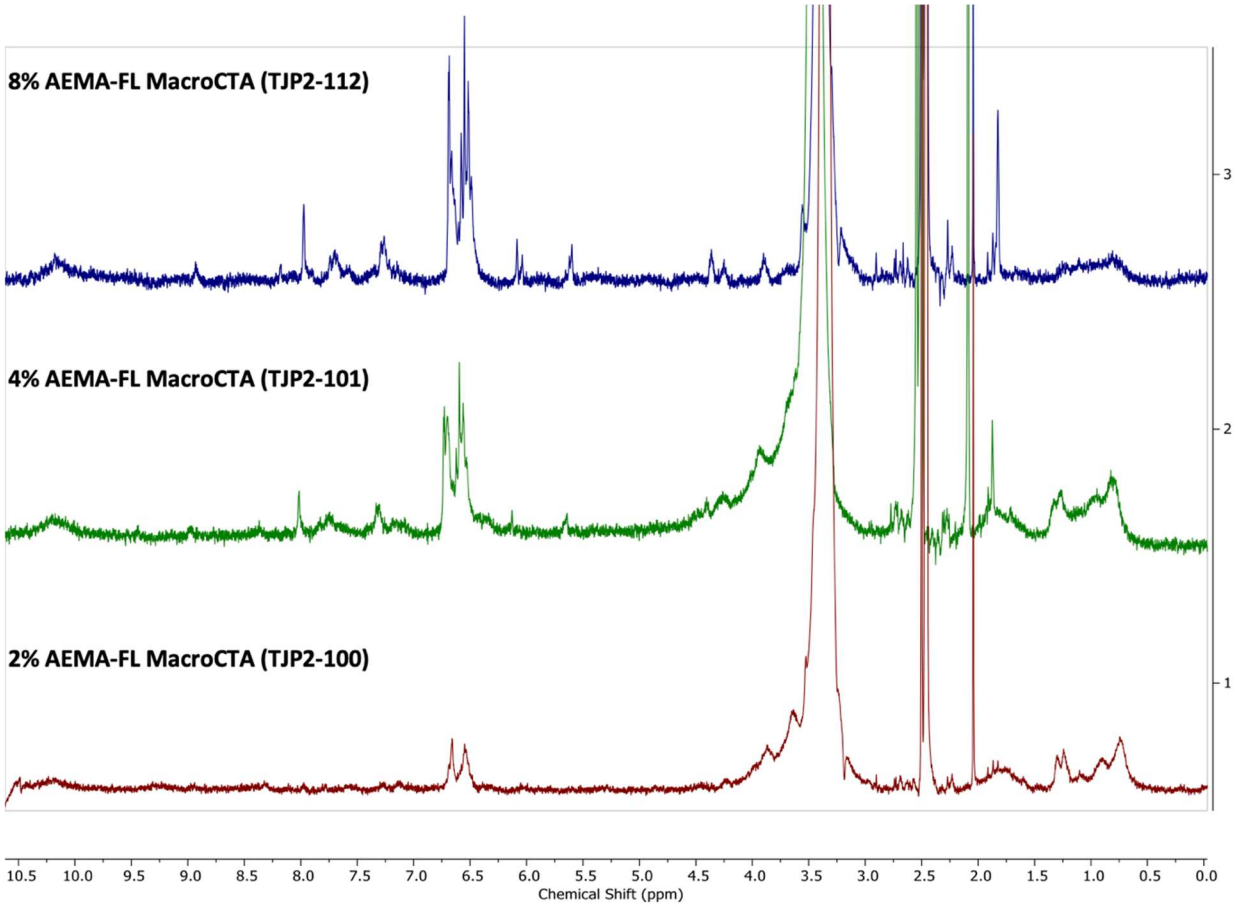

Figure S 18. Proton NMR spectroscopy in DMSO-d6 of the purified macroCTAs used to create the AEMA-FL block copolymers. The macroCTAs were precipitated 5x in 50:50 diethyl ether:acetone, redissolving in DMSO each time.

Table S 3. Overview of the macroCTAs synthesized for block copolymers.

ID	% AEMA-FITC	% GmMA	Time (hrs)	% Conversion (GmMA)	% Conversion (AEMA-FITC)	DP (GmMA)	DP (AEMA-FITC)	DP (Total)	PDI	MW (kDa)
TJP2-100	20	80	4	57	70	13.7	4.2	17.9	1.04	4.4
TJP2-101	40	60	12	43	65	7.7	7.8	15.5	1.03	5.3
TJP2-112	70	30	16.5	27	88	2.4	18.5	20.9	1.02	10

Table S 4. Overview of the all the PolySTAT, PolySCRAM, and Controls synthesized.

ID	Peptide	Pep/back (Theoretical)	Theoretical MW (kDa)	Backbone ID	Type	FITC Monomer	Comonomer	%FITC Target	%FITC (measured)	#FITC (measured)
TJP2-51	FBP	10	47.5	TJP2-48	STAT	FMA	GmMA	4	4.3	8.0
TJP2-52	SCRAM	10	46.2							
TJP2-53	Control	0	30.8							
TJP2-54	FBP	10	42.3	TJP2-50		AEMA-FITC			5.0	8.0
TJP2-55	SCRAM	10	41							
TJP2-56	Control	0	25.6							
TJP2-57	FBP	10	42.3	TJP2-47		FMA	HEMA		4.3	8.0
TJP2-58	SCRAM	10	41.1							
TJP2-59	Control	0	25.6							
TJP2-60	FBP	10	37.9	TJP2-49		AEMA-FITC			5.0	8.0
TJP2-61	SCRAM	10	36.6							
TJP2-62	Control	0	21.2							
TJP2-103	FBP	10	43.8	TJP2-97			GmMA	2	2.2	3.8
TJP2-104	SCRAM	10	42.5							
TJP2-105	Control	0	28.2							
TJP2-106	FBP	10	43.6	TJP2-98				4	4.9	7.9
TJP2-107	SCRAM	10	42.3							
TJP2-108	Control	0	28.1							
TJP2-109	FBP	10	45.1	TJP2-99				8	9.7	15.1
TJP2-110	SCRAM	10	43.8							
TJP2-111	Control	0	29.6							
TJP2-118	FBP	10	44.3	TJP2-114	BLOCK			2	2.1	3.7
TJP2-119	SCRAM	10	43.1							
TJP2-120	Control	0	28.8							
TJP2-121	FBP	10	45.1	TJP2-116				4	4.1	7.0
TJP2-122	SCRAM	10	43.8							
TJP2-123	Control	0	29.6							
TJP2-124	FBP	10	47.5	TJP2-117				8	10.5	17.4
TJP2-125	SCRAM	10	46.2							
TJP2-126	Control	0	32							

Table S 5. Overview of the block copolymer backbones synthesized.

ID	MacroCTA	Time (hrs)	% Conversion (GmMA)	% Conversion (NHSMA)	DP	% FITC	PDI	MW (kDa)
TJP2-114	TJP2-100	20	76	90	176	2.4	1.23	28.8
TJP2-116	TJP2-101	20	76	90	173	4.5	1.25	29.6
TJP2-117	TJP2-112	20	69	87	166	11.1	1.25	32

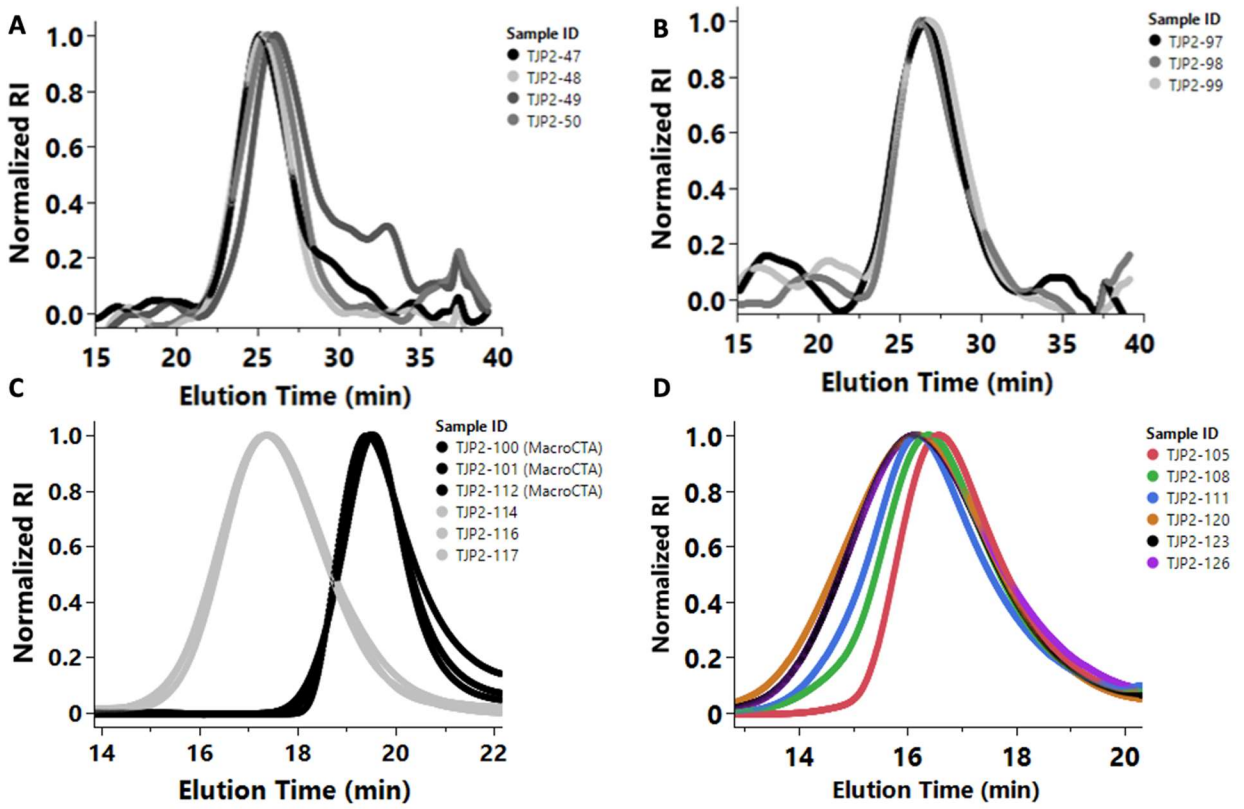

Figure S 19. Gel Permeation Chromatography (GPC) characterization of copolymers. (A) Statistical copolymers p(HEMA-co-FMA-co-NHSMA) with 4% FMA (TJP2-47), p(GmMA-co-FMA-co-NHSMA) with 4% FMA (TJP2-48), p(HEMA-co-AEMA-FL-co-NHSMA) with 4% AEMA-FL (TJP2-49), p(GmMA-co-AEMA-FL-co-NHSMA) with 4% AEMA-FL (TJP2-50). (B) Statistical copolymers p(GmMA-co-AEMA-FL-co-NHSMA) with 2% (TJP2-97), 4% (TJP2-98), and 8% (TJP2-99) AEMA-FL loading. (C) MacroCTAs (Black) and Block copolymers (Gray) with 2% (TJP2-114), 4% (TJP2-116), and 8% (TJP2-117) AEMA-FL loading showing shift to earlier elution times indicating successful chain extension of the MacroCTAs. (D) Control backbones (no peptide) that went through complete PolySTAT production process for both statistical copolymers with 2% (TJP2-105), 4% (TJP2-108), 8% (TJP2-111) AEMA-FL loading and block copolymers with 2% (TJP2-120), 4% (TJP2-123), 8% (TJP2-126) AEMA-FL loading. For (A), (B), and (C) the running solvent was DMF with 1g/L LiBr, while for (D) the running solvent was Acetate Buffer (0.1M, pH 5.0).

Table S 6. **Overview of the DPs of GmMA vs. AEMA-FL in macroCTAs.**

	% Conversion		DP	
Block	**GmMA**	**FITC**	**GmMA**	**FITC**
2%	57	70	13.7	4.2
4%	43	65	7.7	7.8
8%	27	88	2.4	18.5

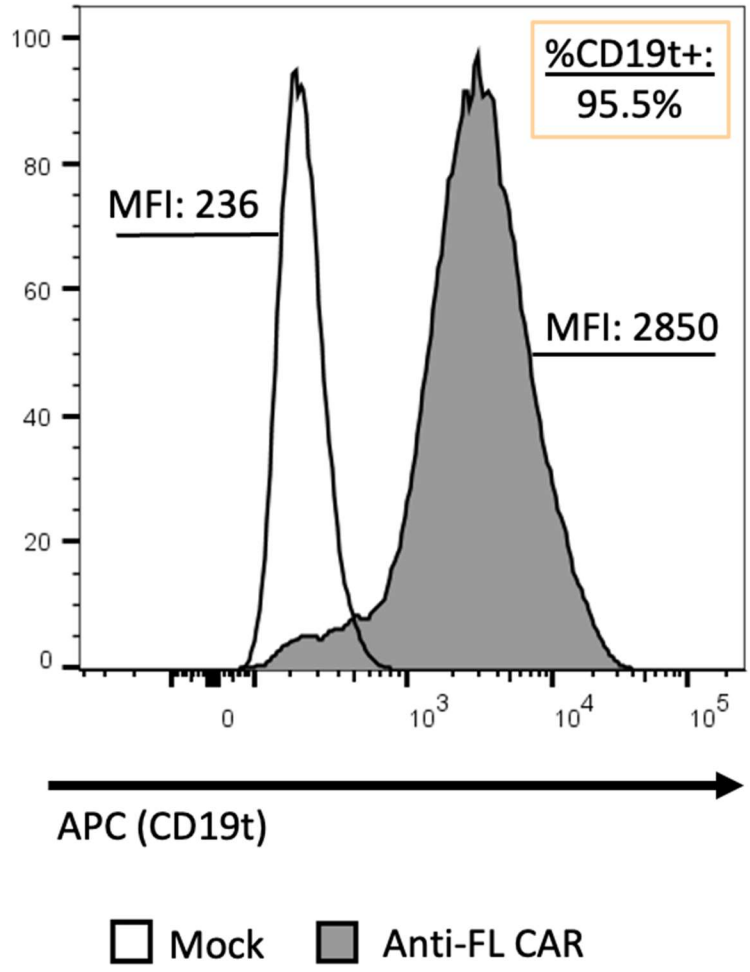

Figure S 20. **C**AR expression (CD19t expression marker) of cCARiCherry T cells made with the large-scale manufacturing protocol was confirmed by flow cytometry.

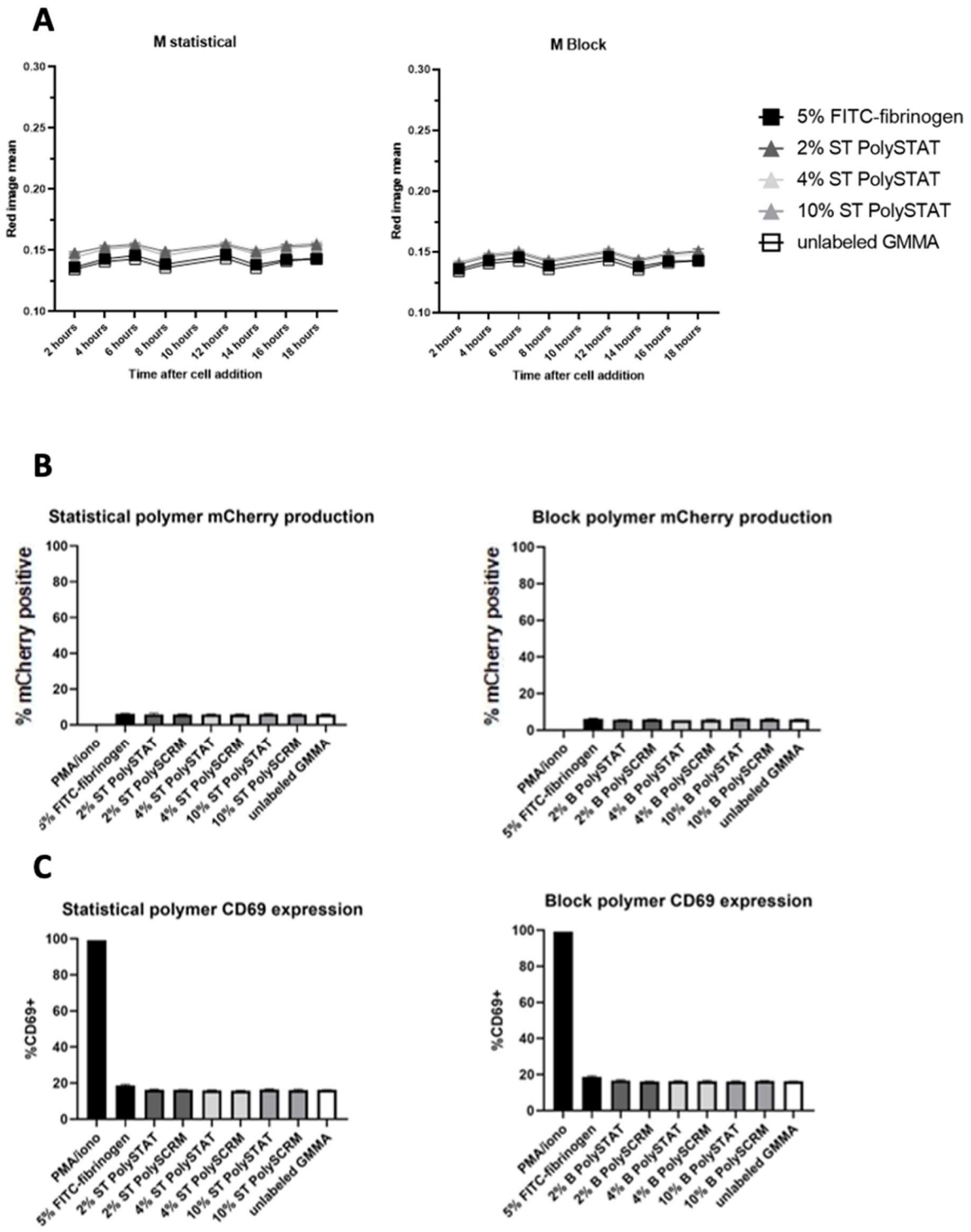

Figure S 21. **A** IncuCyte time courses of mock cells resting on AEMA-FL-PolySTAT gels over an 18-hour period. **B, C** Activation markers of mock cells resting on AEMA-FL-PolySTAT gels for 20 hours. Here, **B** mCherry and **C** CD69 expression were analyzed by flow cytometry to

determine cell activation. Since these are mock cells, these are baseline activation levels by each metric. n = 3 technical replicates. Data shown are means +/- SD.

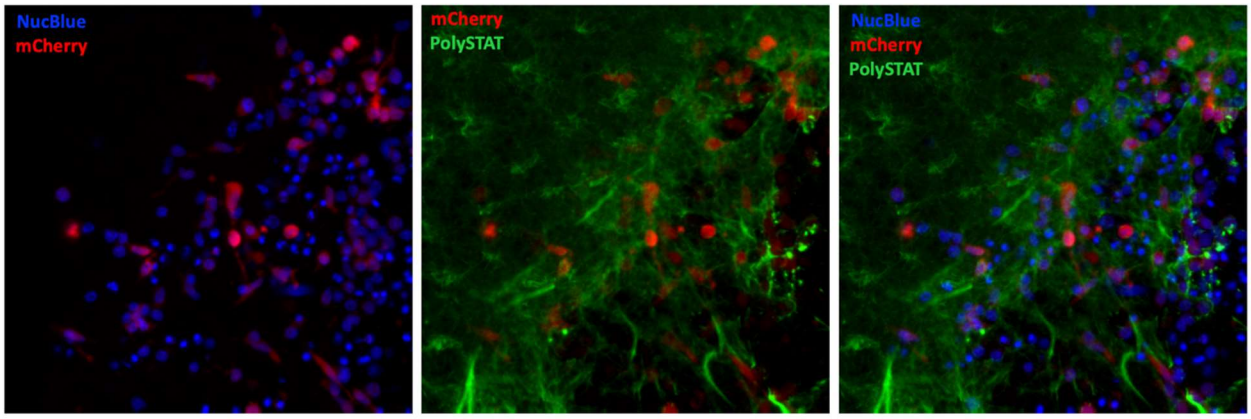

Figure S 22. 40X confocal images of cCARiCherry T cells with iSynPro-driven mCherry after being incubated on PolySTAT gels for 24 hours.

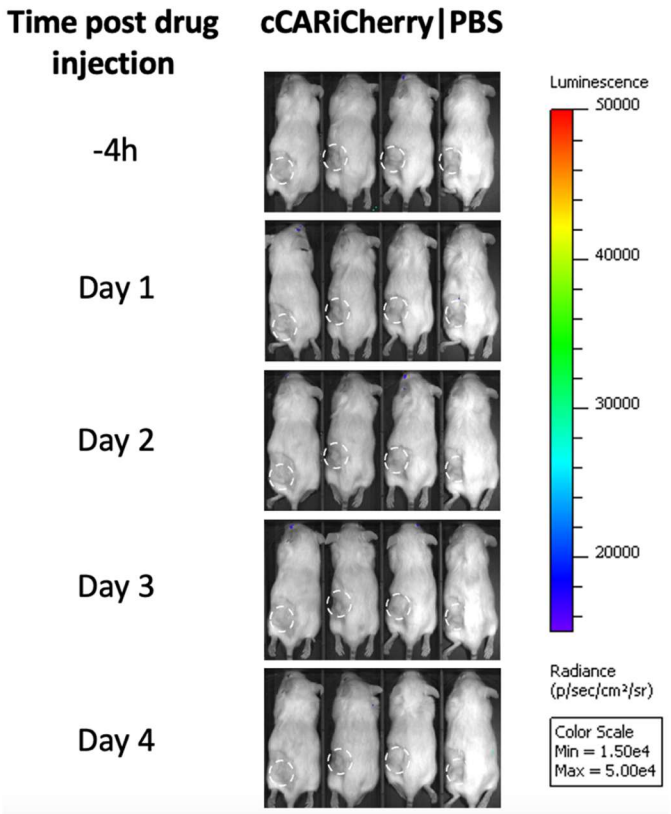

Figure S 23. Bioluminescence images of mice injected IP with PBS and cCARiCherry T cells and incubated for one week. Images of hour -4 and days 1-4 demonstrate no activation.

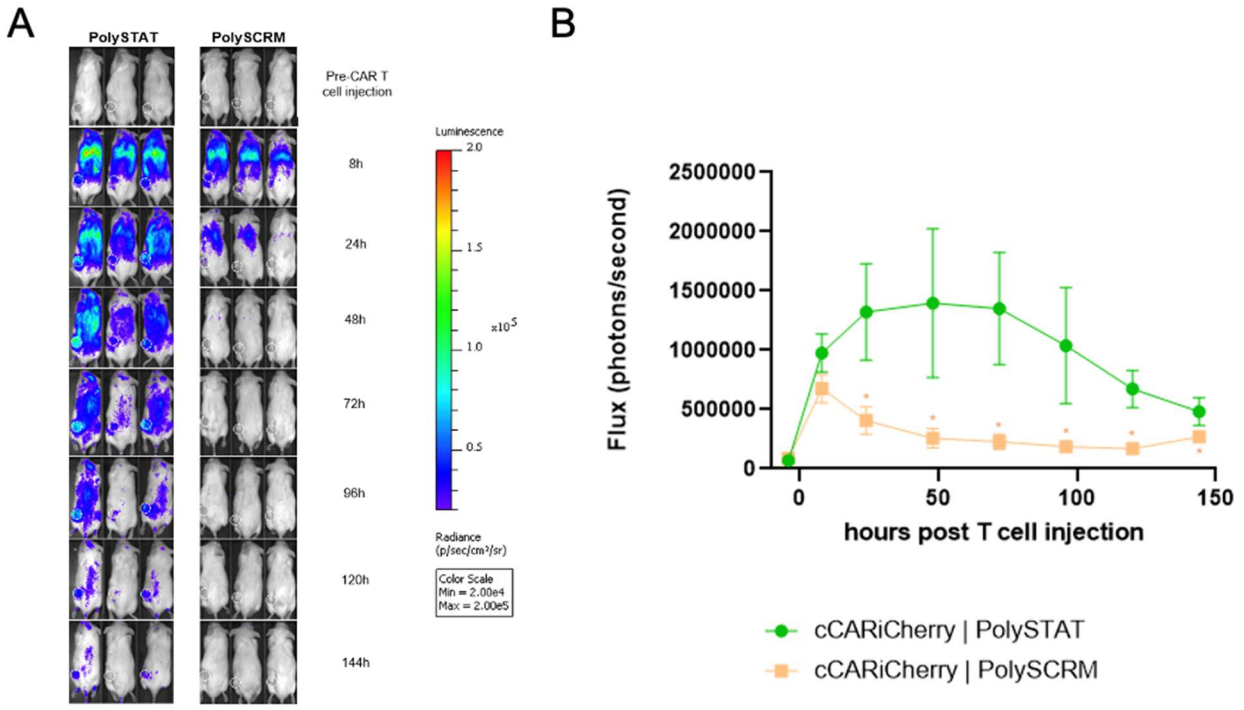

Figure S 24. Daily bioluminescence images of mice injected IV with either PolySTAT or PolySCRM followed by cCARiCherry T cells 24 hours later. Images of hour -4, hour 8, and days 1-6 demonstrate transient activation of cells in mice that received PolySTAT but minimal activation in mice that received PolySCRM. **E** Quantification of bioluminescence flux (photons/second). Results show significantly higher flux from cCARiCherry T cells in mice injected with AEMA-FL-PolySTAT than either negative control at numerous time points. For **E**, a one-way unpaired T test with Welch's correction was performed at each time point. *=p<0.05, n=3 biologically independent replicates +/- SD.

Chapter 7. PROPOSED FUTURE WORK

Trey J. Pichon, Nathan J. White, Suzie H. Pun

7.1 GENIPIN-FUNCTIONALIZED POLYSTAT AND LVRS

Fibrin provides binding sites for both plasminogen and t-PA, which provides the optimal conformation to upregulate activation of plasminogen to plasmin[1]. Binding of t-PA to fibrin is crucial to localizing and confining fibrinolysis to the wound site[2]. As fibrin is cleaved by plasmin, it creates new C-terminal lysine residues. This allows more t-PA and plasminogen to bind, resulting in a 3000-fold increase in catalytic efficiency of plasminogen activation compared to free t-PA[3]. To counter this, activated thrombin-activatable fibrinolysis inhibitor (TAFIa) will cleave lysine residues, and is able to decrease t-PA catalytic efficiency by 97% (Figure 1)[4,5].

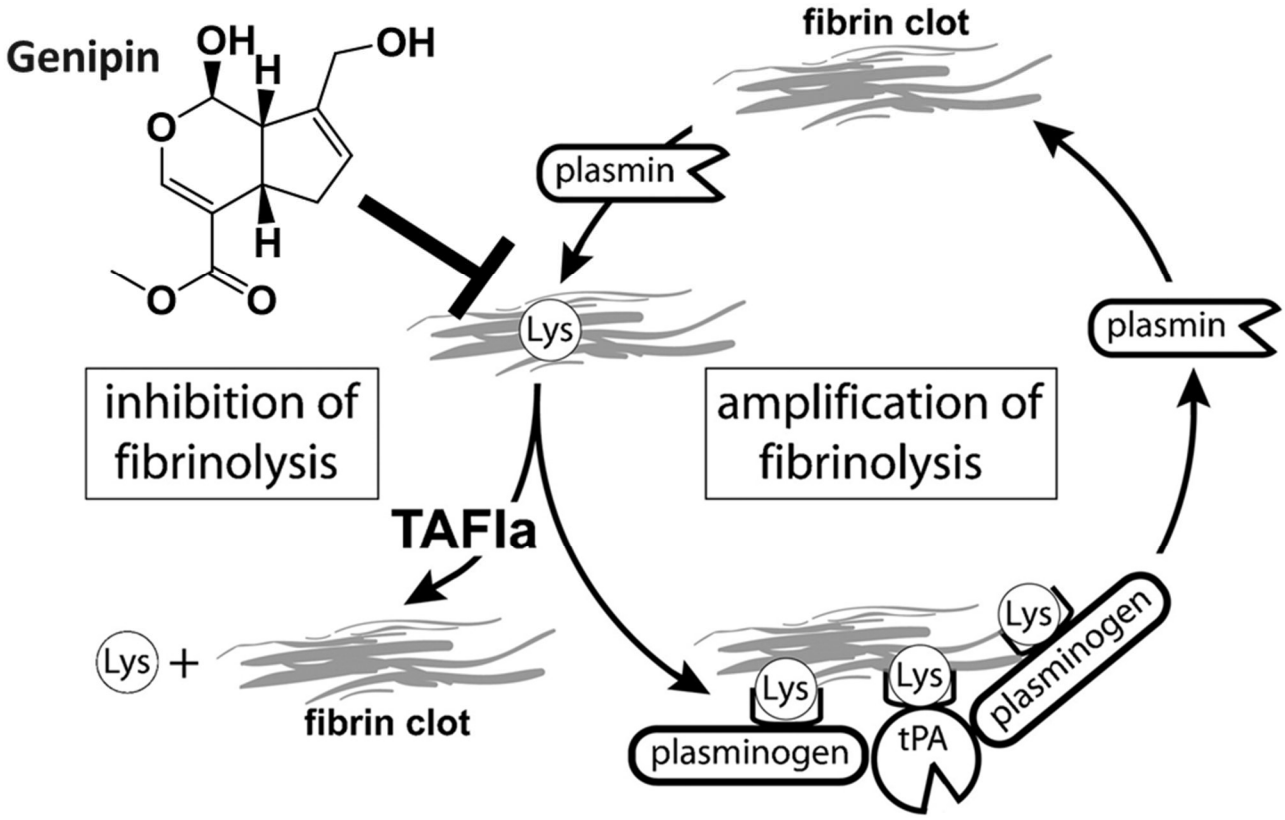

Figure 1. Illustration of Genipin capping of free lysines generated during fibrinolysis after the cleavage of fibrin by plasmin. The free lysines are sites for plasminogen and t-PA binding. This catalyzes the conversion of plasminogen to plasmin. Thrombin activatable fibrinolysis inhibitor or TAFI is responsible for cleaving lysines from fibrin to inhibit fibrinolysis. Figure was reused with permission from Taylor & Francis Online for [6] by Bonno N. Bouma and Laurent O. Mosnier.

Additionally, fibrin that has been carbonylated by arolein is highly-resistant to fibrinolysis and is found in aortic aneurysms.[7] If PolySTAT could be functionalized with a molecule that can "cap" free lysines, this might be able to confer additional anti-fibrinolytic properties. Additionally, PolySTAT would ensure that this therapy was targeted and not freely reacting with lysines throughout the body. Genipin is an aglycone extracted from gardenias that has been used extensively in Chinese medicine, and as an alternative to glutaraldehyde in the cross-linking of biomaterials due to its inherent lower-toxicity[8–11]. Currently, its cross-linking ability is being investigated as a treatment for glaucoma[12–14], and it has shown promise in treating vascular hyperpermeability during hemorrhagic shock due to its upregulation of autophagy[15,16]. Figure 2-4 below outline the mechanism by which Genipin reacts with free amines and becomes REDOX active.

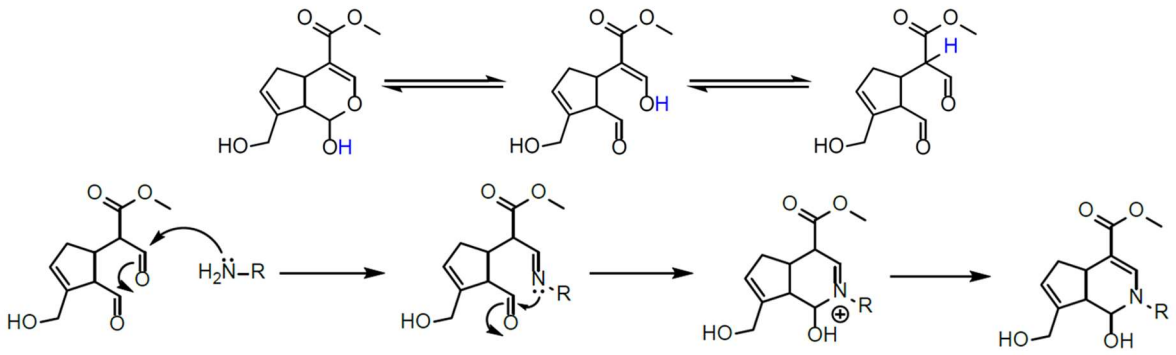

Figure 2. Ring-opening of the hemiacetal via intramolecular proton transfer in water to reveal two aldehydes (top) and subsequent SN2 nucleophilic attack by the primary amine to form an imine (Schiff base). This imine intramolecularly attacks the other aldehyde, and subsequent loss of water closes the ring back.[17]

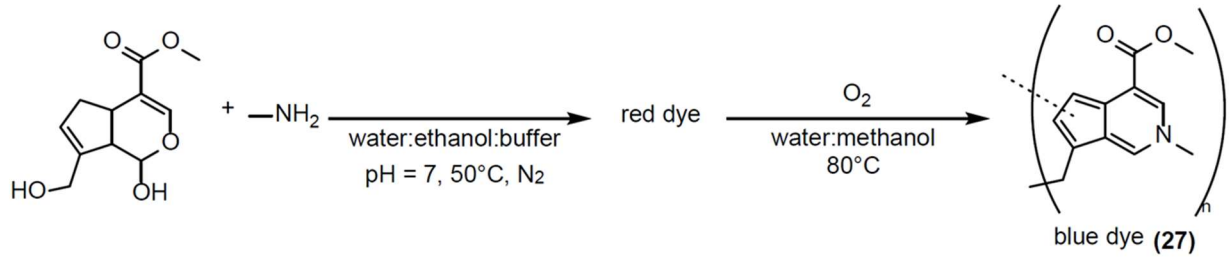

Figure 3. Color change associated with Genipin reactions. Upon reaction with free amines in the absence of oxygen, a red dye is formed, then after reaction with oxygen it turns blue and can self-polymerize to form dimers, trimers, and tetramers.[8]

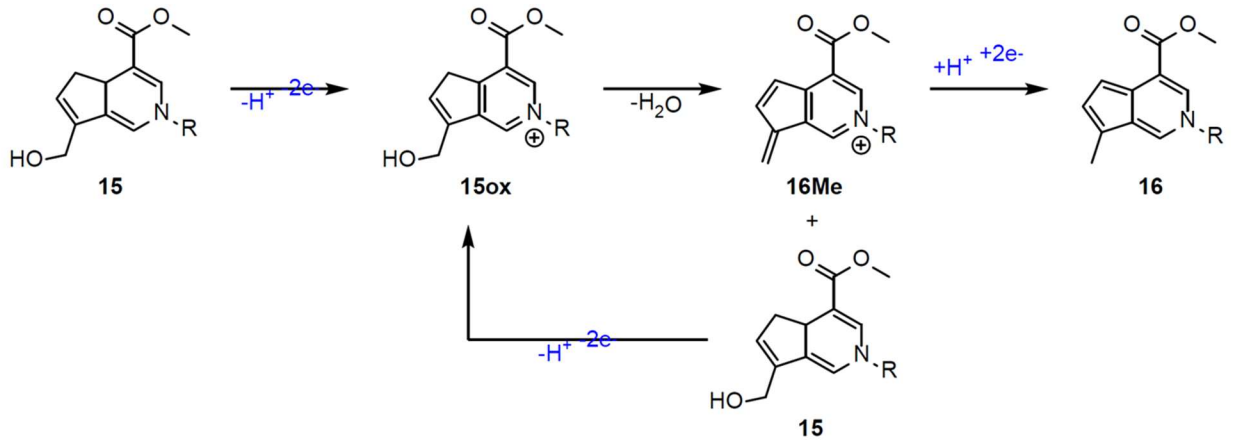

Figure 4. REDOX activity of Genipin. After reaction with amines, Genipin becomes REDOX active, and can undergo reversible color change from red to blue, which has been demonstrated via cyclic voltammetry.[8]

The unique structure of Genipin allows it to "hide" aldehydes and is a good candidate to achieve in vivo capping of free lysines. This work will seek to combine Genipin with PolySTAT to try and increase its antifibrinolytic properties. In addition, Genipin-PolySTAT could have the added benefit of increasing the adhesive properties of clots by crosslinking with the ECM in the extravascular space similar to the role of FXIIIa[18], upregulating autophagy to reverse hyperpermeability during shock, and provide a REDOX active molecule that can scavenge ROS species.

7.1.1 *Methods*

Synthesis of FBP-containing methacrylate monomer, FBP-methacrylate

NHS-activated mono-2-(methacryloyloxy)ethyl succinate (NHS-SMA) was synthesized as described previously.[19] FBP-methacrylate was synthesized via reaction of the C-terminal lysine in FBP with NHS-SMA under organic basic conditions in DMSO at a 1:2 ratio with base added at a 5:1 ratio base:peptide.[20] A common reaction contained 176 mg FBP (100 mg/mL) dissolved in DMSO, 67 mg NHS-SMA, 94 µL N,N-diisopropylethylamine. This was reacted for 24 h at 50° C and subsequently precipitated in diethyl ether to remove unreacted NHS-SMA. Reaction progress was monitored by the ninhydrin test[21] for unreacted amines.

Synthesis of Genipin-Methacrylate

Genipin (1 g, 4.42 mmol) was added to a round bottom flask with a stir bar then dissolved in DCM (44 mL, 0.1 M reaction concentration). Pyridine (525 µL, 6.63 mmol) was added to the mixture, the RBF was capped, and the mixture was sparged with argon for 15 min then cooled over ice. Methacryloyl chloride (508 µL, 4.86 mmol) was then added dropwise. The reaction was stirred overnight at room temperature. The mixture was washed 1:1 volume with a saturated ammonium chloride solution, followed by a saturated sodium chloride solution, and finally with a 5% copper (II) sulfate solution. The collected DCM was dried over sodium sulfate. Three spots were seen in TLC (50-50 EA/PE). The product was isolated (1st spot) by flash chromatography (20g silica, 10in tall column) with 25% EA/PE as the running solvent. The solvent was rotovapped off to obtain a light brown oil. Purity was confirmed by proton NMR and TLC. The genipin methacrylate was stored at -20C.

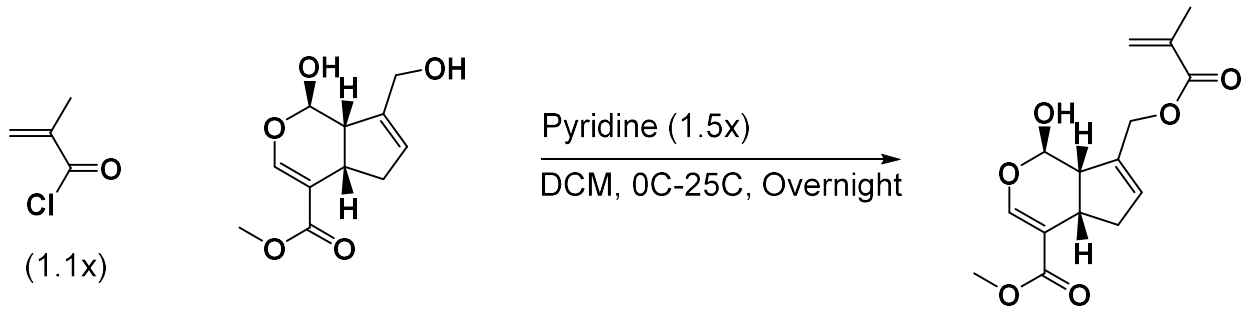

Figure 5. Reaction scheme for the synthesis of Genipin-methacrylate.

Synthesis of Genipin-PolySTAT via FBP-methacrylate

A composition of 5% FBP-methacrylate and 10% Genipin-methacrylate was targeted by combining FBP-methacrylate, Genipin-methacrylate, and GmMA at a ratio of 10:20:170:1:0.333 FBP-methacrylate:Genipin-methacrylate:GmMA:CTA:Initiator. Polymers were precipitated, end-capped, then dialyzed against DI H2O for two days, then lyophilized. FBP content was measured via UV-VIS. Genipin content was quantified via proton NMR spectroscopy. Figure 6 below shows the chemical structure of the statistical copolymer.

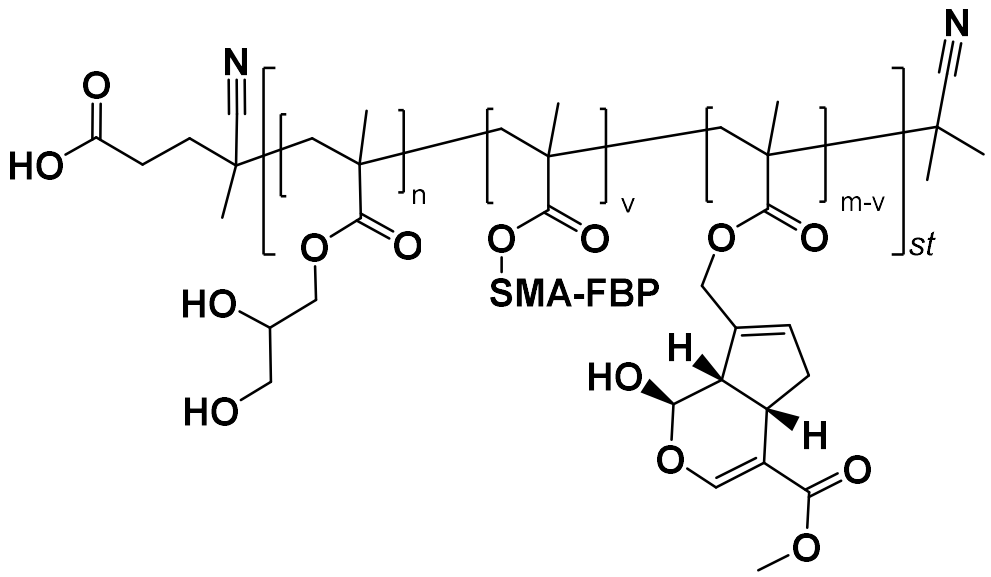

Figure 6. Chemical structure of Genipin-PolySTAT. For this work, the following monomer loadings were targeted; n = 170, v = 10, m = 20.

ROTEM Characterization of Genipin-PolySTAT

ROTEM experiments consisted of 300 µL of clotting solution in a standard ROTEM cup placed in a ROTEM whole blood hemostasis analyzer (ROTEM, Instrumentation Laboratory, Bedford, MA, USA). The clotting solution consisted of human fibrinogen, thrombin, and plasmin that were purified from human plasma. All clotting factors were purchased from Enzyme Research Laboratories (South Bend, IN). Final concentrations in the ROTEM were 1.5-2 mg/mL fibrinogen, 0.5-1 IU/mL thrombin, 2-4 µg/mL plasmin, 0.1 mmol/L CaCl2, and 5 µmol/L PolySTAT at pH 7.4. Measured parameters in ROTEM included: (i) the clotting time (CT), measured as the time between reagent addition to clot formation; (ii) α-angle, which reflects the rate of clot formation, (iii) the maximum clot firmness (MCF), the highest strength observed for the clot, (iv) the lysis index-30 minutes (LI-30), the percentage of MCF retained 30 minutes after initiation of clot formation, and (v) maximum lysis (ML), the percentage of clot strength lost compared to the MCF at the end of analysis.

TPA-Plasminogen ROTEM Characterization of Genipin-PolySTAT

ROTEM experiments will consist of 300 µL of clotting solution in a standard ROTEM cup placed in a ROTEM whole blood hemostasis analyzer (ROTEM, Instrumentation Laboratory, Bedford,

MA, USA). The clotting solution will consist of human fibrinogen, thrombin, plasminogen, and tissue plasminogen activator that were purified from human plasma. All clotting factors will be purchased from Enzyme Research Laboratories (South Bend, IN). Final concentrations in the ROTEM will be 1.5-2 mg/mL fibrinogen, 0.5-1 IU/mL thrombin, 200 μg/mL plasminogen, 10-80 ng/mL tissue plasminogen activator, 0.1 mmol/L CaCl2, and 5 μmol/L PolySTAT at pH 7.4. The same ROTEM parameters as above will be measured.

Monitoring Genipin cross-linking via UV-Vis, fluorescence, and ninhydrin assay

Monitoring of genipin crosslinking can be monitored with two different methods from Ninh *et al.*[22] The first is using the ninhydrin assay to monitor the number of free amines present in the fibrin gels over time. The structure of genipin can be monitored directly using two peaks seen in UV-Vis as it reacts there is a decrease in absorbance at 240 nm with a corresponding increase at 290 nm. The final method from Rivera-Delgado *et al.* measures genipin fluorescence as it reacts with free amines by excitation at 590 nm and emission at 630 nm.[23]

7.1.2 *Preliminary Results*

Synthesis of Genipin-Methacrylate

Genipin-methacrylate was successfully synthesized. Figure 7 below confirms its structure by proton NMR.

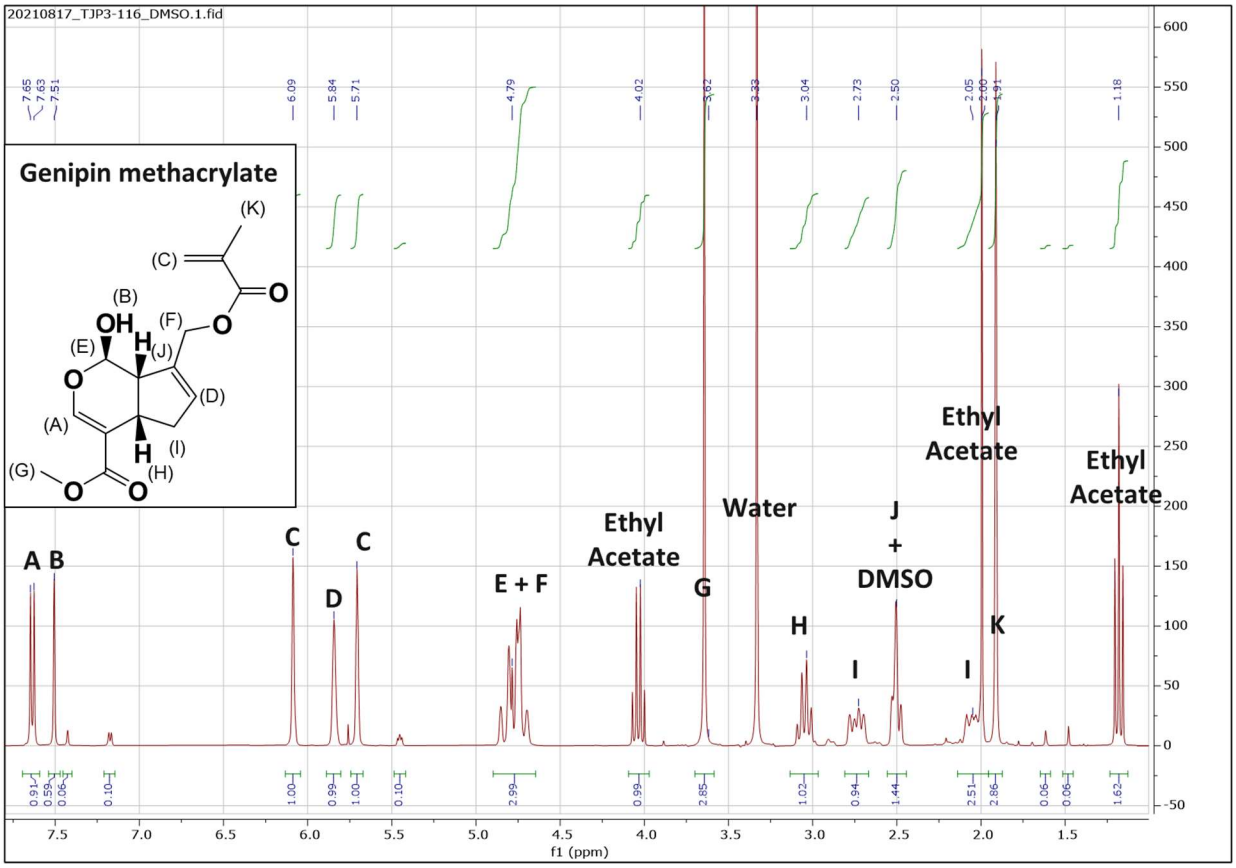

Figure 7. Proton NMR spectroscopy of Genipin-methacrylate in DMSO-d6.

The activity of the monomer was confirmed by reacting it with amino-2-propanol. Figure 8 below shows the proton NMR.

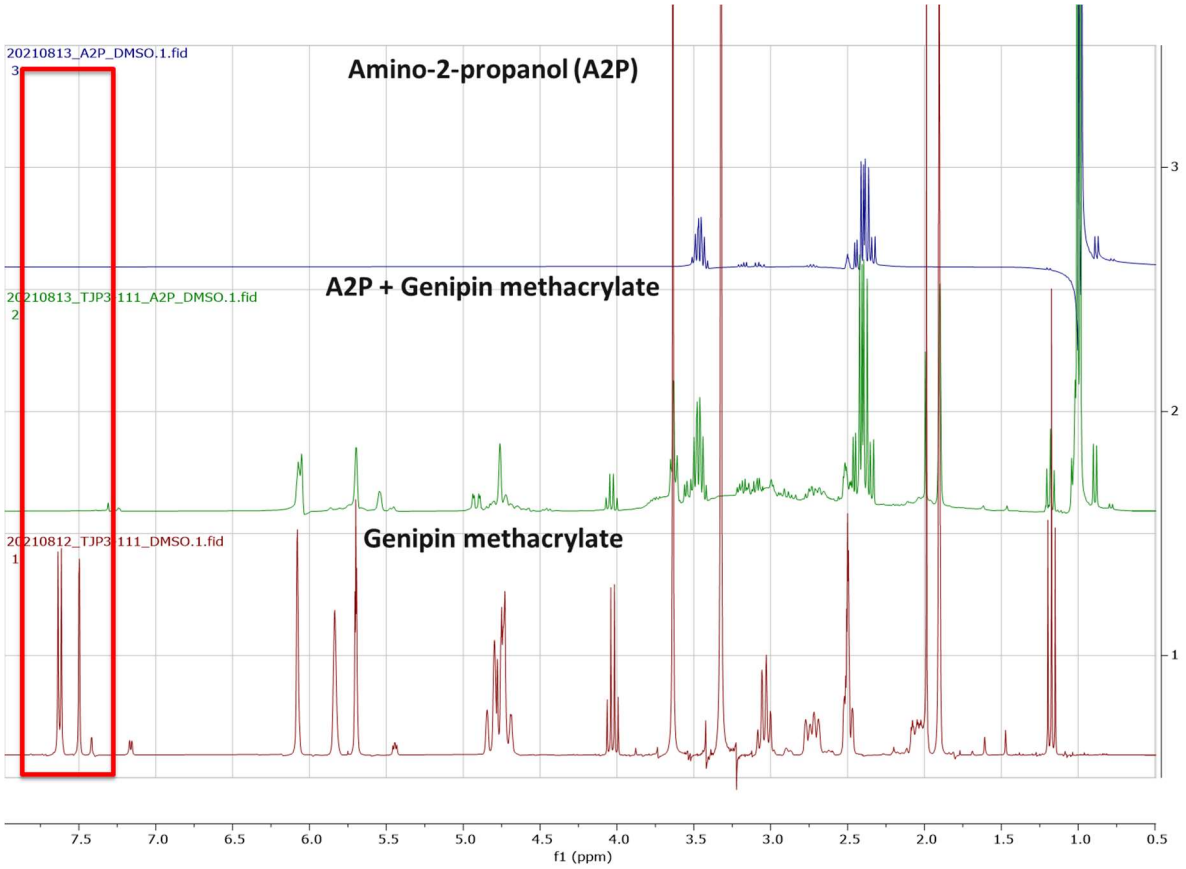

Figure 8. Proton NMR spectroscopy genipin-methacrylate reacting with amino-2-propanol in DMSO-d6.

Immediately after the addition of amino-2-propanol (A2P), a reddish-brown color was observed indicating a reaction between Genipin and A2P. The reaction slowly turned darker blue as oxygen reacted with the mixture (Figure 9 below).

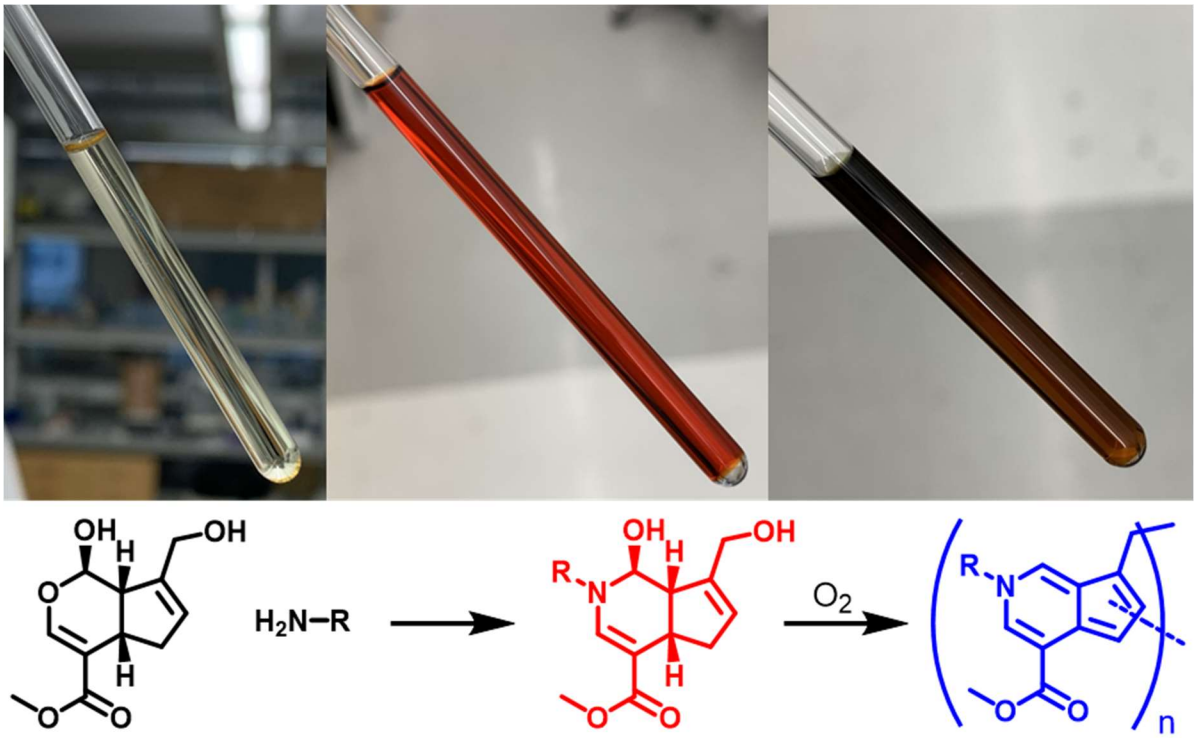

Figure 9. NMR tubes showing color change as genipin-methacrylate reacted with amino-2-propanol, (left) genipin-methacrylate in DMSO-d6, (middle) ~15 minutes after addition of amino-2-propanol, (right) ~2 days sitting at RT on benchtop after the addition of amino-2-propanol.

Synthesis of Genipin-PolySTAT via FBP-methacrylate

P(GmMA-co-Genipin) was successfully synthesized, however issues with solution gelling occurred when SMA-FBP was incorporated in attempts to make Genipin-PolySTAT. The same gelling phenomenon was observed without the inclusion of Genipin methacrylate, indicating the SMA-FBP is leading to the solution gelling. The GPC RI traces in Figure 10 below show that p(GmMA-co-SMA-FBP) is crosslinking during polymerization, while p(GmMA-co-Genipin) does not show any evidence of crosslinking.

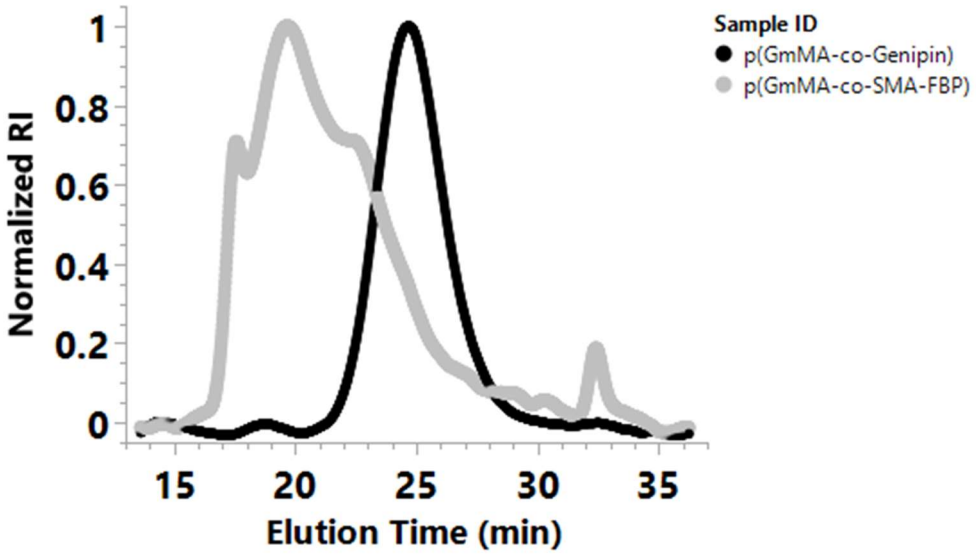

Figure 10. Normalized RI trace from GPC showing crosslinking of p(GmMA-co-SMA-FBP).

Outlined in Table 1 below are attempts at polymerizing PolySTAT using the SMA-FBP monomer.

Table 1. Overview of PolySTAT polymerizations using the FBP monomer SMA-FBP.

ID	CTA	Initiator	% FBP	CTA:I	Conc. (M)	Time (hrs)	Conversion
132	CCC	V70	5	1.5:1	0.6	24	40
133	CCC	V70	2.5	1.5:1	0.6	24	58
136	ECT	V70	2.5	1.5:1	0.6	24	75
144	ECT	AIBN	5	1.5:1	0.5	16	Gelled
145	ECT	AIBN	5	1.5:1	0.4	16	Gelled
149	ECT	AIBN	5	3:1	0.4	13	22
149	ECT	AIBN	5	3:1	0.4	36	62
150	ECT	AIBN	5	5:1	0.4	13	4
150	ECT	AIBN	5	5:1	0.4	36	17
152	ECT	AIBN	5	3:1	0.6	15	Gelled
153	ECT	AIBN	5	2:1	0.4	15	Gelled
154	ECT	AIBN	5	3:1	0.5	16	Gelled
155	ECT	AIBN	5	2:1	0.2	9	53
155	ECT	AIBN	5	2:1	0.2	16	75

There has not been a synthesis window where a PolySTAT of >4 FBP/polymer has been achieved. Therefore, a Genipin-PolySTAT was synthesized with < 4 FBP per polymer in hopes that it would still target to the clot and the genipin would crosslink into the fibrin gel. Figure 11 below shows the proton NMR spectroscopy of a Genipin PolySTAT with <4 FBP/polymer.

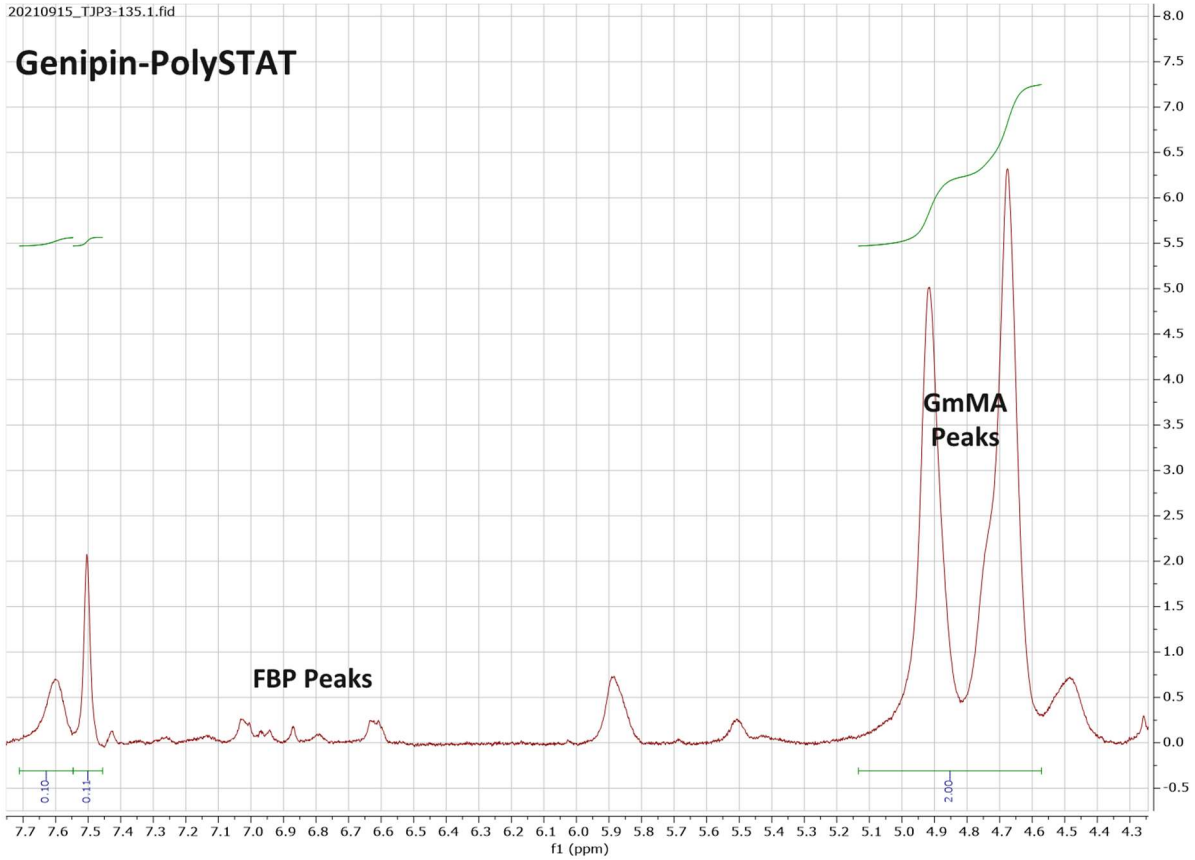

Figure 11. Proton NMR spectroscopy of p(GmMA-co-Genipin-co-SMA-FBP) or Genipin-PolySTAT in DMSO-d6. The functionality of genipin was retained by NMR and no color change was observed through the entire synthesis, purification, and lyophilization process.

The correct loading of Genipin was achieved, and it also confirmed the incorporation of SMA-FBP. Although this did not achieve the desired FBP loading, it was still evaluated in ROTEM to see if the incorporation of Genipin could decrease the valency of FBP necessary for PolySTAT activity.

ROTEM Evaluation of Genipin-PolySTAT with <4 FBP/Polymer

The typical ROTEM QC was run with the Genipin-PolySTAT with <4 FBP per polymer. Figure 12 shows the typical ROTEM traces for the experiment.

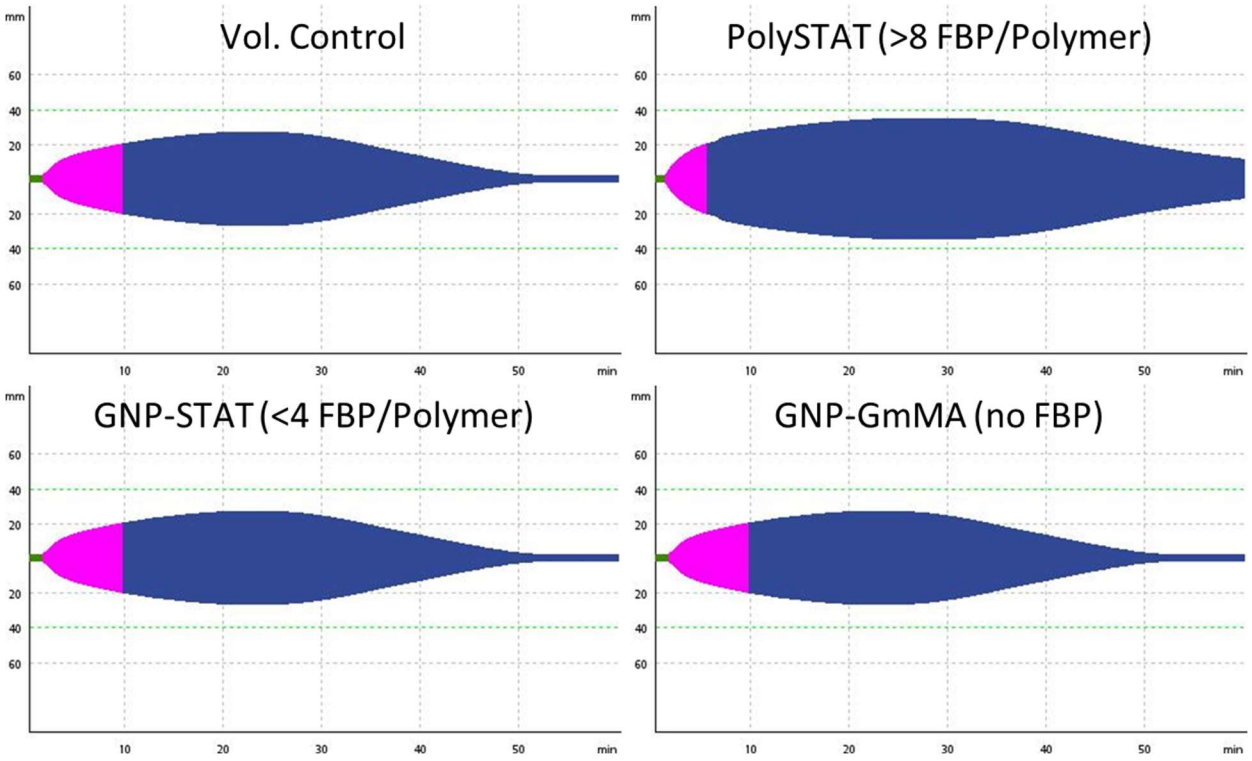

Figure 12. ROTEM evaluation of Genipin-PolySTAT in the typical purified clotting factors QC setup. No difference was observed between the volume control (top left), Genipin-PolySTAT (bottom left) with ~3 FBP/backbone, and p(GmMA-co-Genipin) with ~10% Genipin loading. PolySTAT showed the typical improvement in clot firmness, and decrease in lysis (top right).

No effect was observed with the Genipin-PolySTAT nor p(Genipin-co-GmMA). Figure 13 below shows plots of the results (n =3 for each condition).

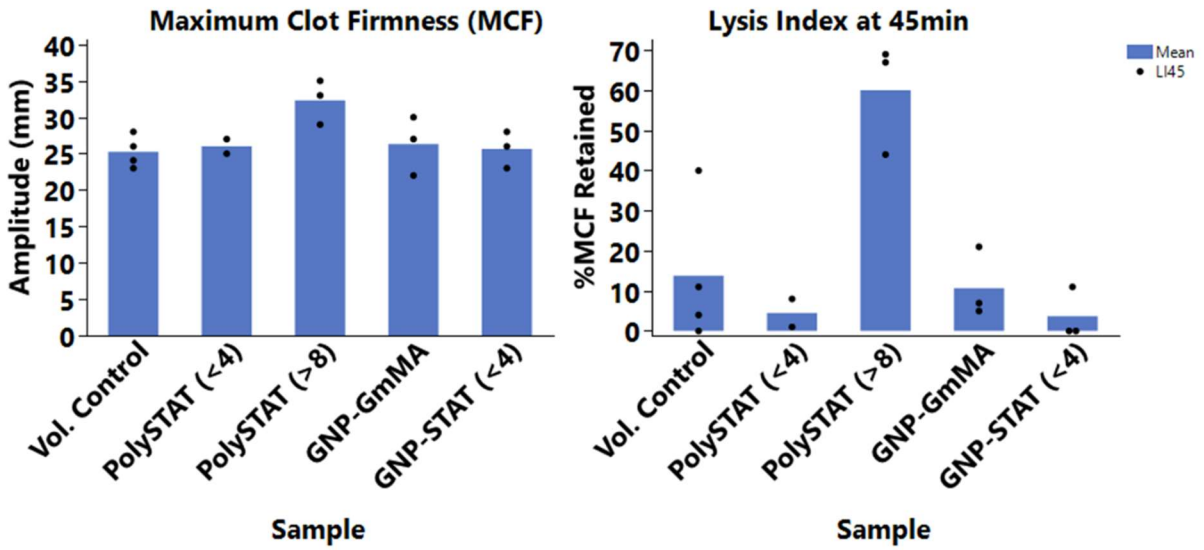

Figure 13. Average ROTEM results (n=3 per treatment) for MCF (left) and LI45 (right) comparing Genipin-PolySTAT (<4 FBP) to PolySTAT with both >8 FBP and <4 FBP. No difference was observed across treatments, except for PolySTAT with >8 FBP.

Interestingly, no effect was observed with the addition of genipin, and PolySTAT with <4 FBP/polymer performed similar to the volume control, genipin-PolySTAT, and p(GmMA-co-Genipin). As expected, the PolySTAT with >8 FBP/backbone showed increased MCF and increased LI45. Encouragingly, the incorporation of Genipin did not cause any off target effects such as cross-linking fibrinogen or deactivating thrombin. If this had occurred there would be a change in the clot formation. It should be noted that this assay uses plasmin not plasminogen. A new assay needed to be developed to evaluate the effect on t-PA and plasmin generation from plasminogen.

Development of t-PA/Plasminogen ROTEM Assay

Figure 14 below shows the ROTEM curves generated in the t-PA/Plasminogen ROTEM assay.

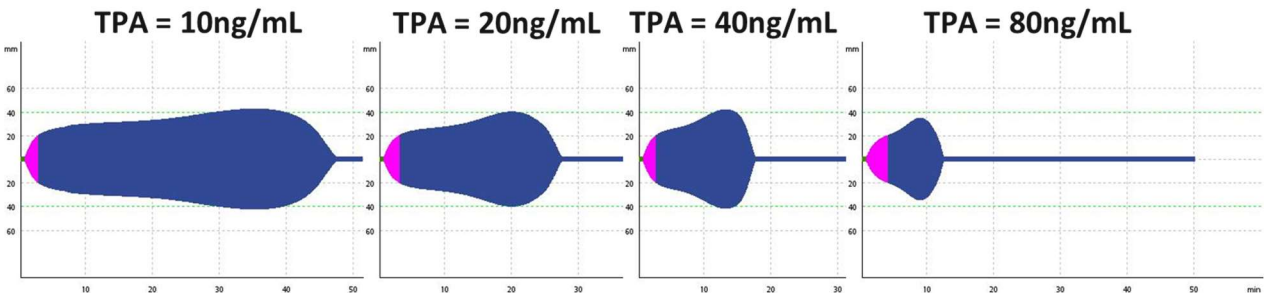

Figure 14. t-PA/Plasminogen ROTEM assay with 1.5 mg/mL fibrinogen, 0.5-1 IU/mL thrombin, 200 µg/mL plasminogen, and 0.1 mmol/L CaCl2. From left to right is increasing t-PA concentrations from 10 ng/mL to 80 ng/mL.

Unlike in the typical ROTEM assay using plasmin, these curves show normal clot forming kinetics. Plasmin can digest fibrinogen, leading to dysfunction in clot formation. In this assay the fibrin clot must form first before the t-PA can significantly catalyze the activation of plasminogen to plasmin. It is unknown what causes the rapid increase in clot firmness ("bump") prior to lysis. This assay will be important for investigating the effects of Genipin-PolySTAT.

7.1.3 *Conclusions and Future Work*

Genipin-PolySTAT has been successfully synthesized, however with too low of an FBP/polymer loading to confer activity in ROTEM (<4 FBP/polymer). Although it did not show activity in ROTEM, it is encouraging to see no immediate off-targeting issues with materials tested thus far. Future work will seek to increase FBP loading to at least 8, which is similar to the current formulation of PolySTAT. The current hypothesis for the issues with the synthesis is that the initiator radicals are leading to dityrosine formation (Figure 15 below) between FBPs, which could lead to the observed gelling.

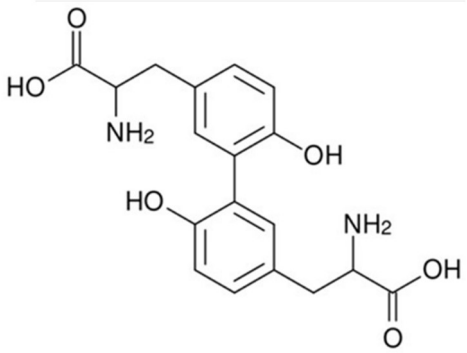

Figure 15. Structure of dityrosine.

Dityrosines are common in nature as both beneficial structural reinforcements for biopolymers, as well being common in diseased tissues that have experienced high oxidative stress, i.e. Alzheimer's and Parkinson's.[24–27] FBP contains three tyrosines (out of 13 amino acids), with one being a 3-chloro tyrosine. Previous peptide monomer synthesis with SMA-FBP used a loading of 2.5%, whereas we are doubling the FBP loading at 5%. Dityrosine formation can be easily monitored by fluorescence (excitation 315 nm/emission 420 nm)[27]. The next section 7.2 Pursuit of a Non-dityrosine coupling FBP-monomer outlines work to overcome this challenge.

In addition, Genipin-methacrylate has been easily copolymerized with GmMA with good control. Genipin could be easily incorporated into the arms of the radiant stars synthesized in Chapter 5 (LVRs). This could provide an active mechanism for upregulating autophagy and repairing the hyperpermeable vascular system during hemorrhagic shock,[15] and actively treat trauma-induced endotheliopathy.

7.2 Pursuit of a Non-dityrosine Coupling FBP-monomer

As observed in the Genipin PolySTAT work above, it was discovered that PolySTAT cannot be made with > 4 FBP per polymer in the FBP-monomer synthesis route. It is suspected that the tyrosines in FBP are leading to this, due to a few-documented examples of polyphenols requiring protection/deprotection for successful polymerization.[28,29] Creating an FBP-monomer that is compatible with RAFT polymerization would be immensely helpful in pursuing the proposed PolySTAT 2.0 work proposed in the next section. The fibrin-binding peptide (FBP) used in PolySTAT is based on the Tn6 peptide XArXCPY(G/D)LCArIX (Ar = aromatic) developed by the Caravan group.[30,31] Currently, the aromatic groups (Ar) in the sequence are tyrosines. The Caravan group showed Tn6 retained its high affinity when Tryptophans were used (Tn6-2b in Figure 16 below).

Tn6-1	K_i (μM)	Tn6-2b	K_i (μM)	Tn7-3	K_i (μM)	Tn10-4	K_i (μM)
WFHCPYDLCHIL	3.1	QWECPYGLCWIQ	2.3	LPCDYYGTCLD	2.8	NHGCYNSYGVPYCDYS	3.5
AFHCPYDLCHIL	8.0	**A**WECPYGLCWIQ	--	**A**LCDYYGTCLD	3.1	NHGCYDSYGVPYCDYS	>100
W**A**HCPYDLCHIL	3.9	Q**A**ECPYGLCWIQ	4.3	L**A**CDYYGTCLD	2.9	NHGCYNYYGVPYCDYS	5.9
WF**A**CPYDLCHIL	3.3	QW**A**CPYGLCWIQ	6.2	LPC**A**YYGTCLD	5.9	NHGCYNYYGTPYCDYS	>500
WFHC**A**YDLCHIL	62	QWEC**A**YGLCWIQ	32	LPCD**A**YGTCLD	4.5	NHGCYDYYGTPYCDYS	>500
WFHCP**A**DLCHIL	16	QWECP**A**GLCWIQ	42	LPCDY**A**GTCLD	>100		
WFHCPY**A**LCHIL	16	QWECPY**A**LCWIQ	7.7	LPCDYY**A**TCLD	12		
WFHCPYD**A**CHIL	97	QWECPYG**A**CWIQ	93	LPCDYYG**A**CLD	>100		
WFHCPYDLC**A**IL	28	QWECPYGLC**A**IQ	4.3	LPCDYYGTC**A**D	15		
WFHCPYDLCH**A**L	19	QWECPYGLCW**A**Q	17	LPCDYYGTCL**A**	7.3		
WFHCPYDLCHI**A**	2.6	QWECPYGLCWI**A**	--	LPCDYYG**V**CLD	28		

Figure 16. Alanine scanning of three different families of fibrin-binding peptides. Tn6 was the family used for FBP in PolySTAT. Reprinted with permission from Kolodziej *et al*. [30] Copyright 2012 American Chemical Society.

This would allow for the removal of 2 out of 3 of the tyrosines. Unfortunately, from the alanine scanning of Tn6-2b, it appears that substituting the tyrosine in the cyclized portion of the peptide with alanine resulted in ~18x lower affinity. However, it would be interesting to evaluate binding with tryptophan substituted instead, since the caravan group notes that aromatic groups seem to improve the affinity of the peptide towards fibrin. Polytryptophan polymers have been synthesized with good control using RAFT,[32] so we believe this tryptophan-FBP would be compatible with the FBP-monomer synthesis route.

7.3 Pursuit of a Truly Hyperfibrinolysis Model in Rats and Swine

As outlined in Chapter 3, hyperfibrinolysis in rats and pigs is extremely difficult to create. Native pig blood is very difficult to lyse due to extremely dense fibrin networks[33], low plasminogen concentration[34], high concentrations of PAI-1[35], and poor activation of plasminogen by t-PA[36], as a result it takes very large doses of thrombolytics to see an effect.[37] Figure 17 below highlights this difficulty with plasma from the aorta tear swine study.

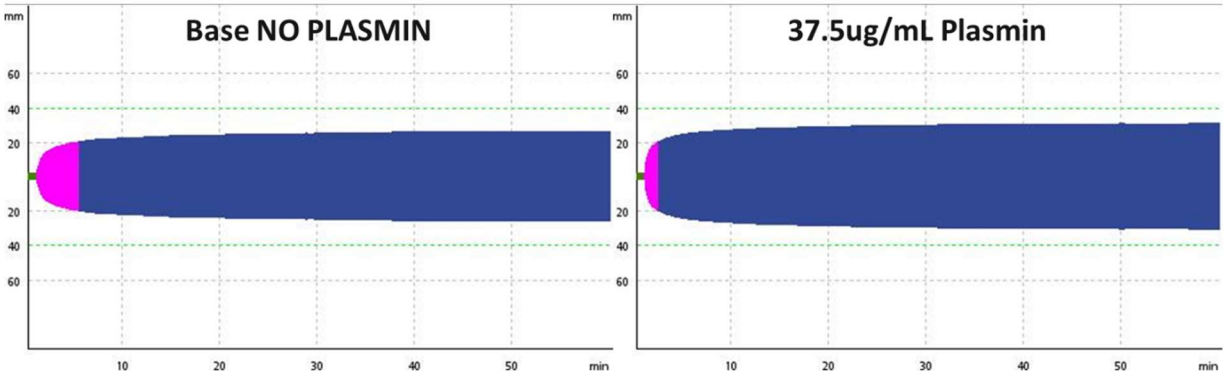

Figure 17. Swine baseline platelet poor plasma evaluated in EXTEM with no plasmin/volume control (left) and 37.5 µg/mL plasmin (right).

The typical plasmin dose used in ROTEM QC evaluations is 1 µg/mL. Even at this high dose, no lysis is observed. However, we observed with a 60% hemodilution of the plasma in combination with human fibrinogen concentrate does show evidence of lysis in ROTEM (Figure 18 below).

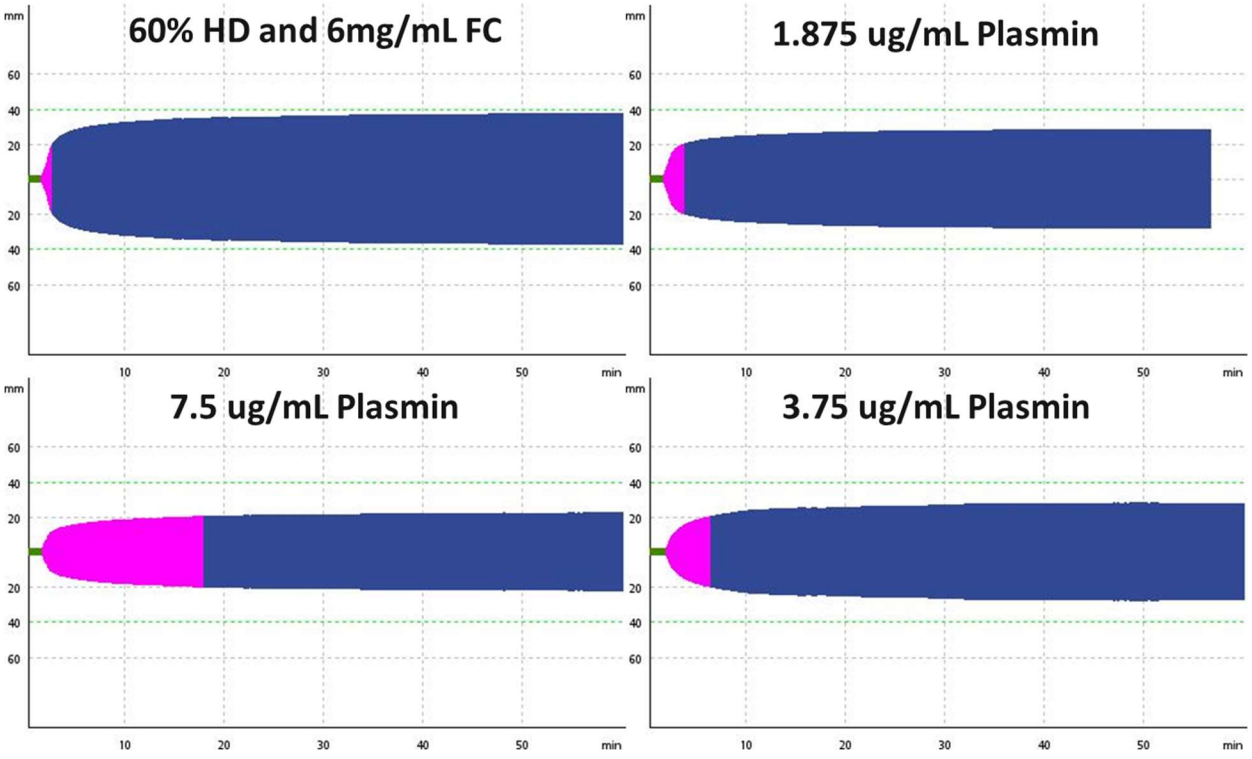

Figure 18. Plasma samples from simulated 60% hemodilution with 6 mg/mL FC added to rescue clotting. Top left, no plasmin/volume control, top right 1.875 µg/mL, bottom left 7.5 µg/mL, and bottom right 3.75 µg/mL of plasmin added. Increasing lysis is observed with increasing doses of plasmin, however total clot dissolution is not observed during the 1 hour test.

Plasmin can digest fibrinogen, therefore it is unknown if this lysis is due solely to fibrinogenolysis or some fibrinolysis. All the plasmin concentrations tested would normally fully lyse the clots. It is surprising that the pig fibrinogen or something else in the pig plasma can halt lysis as the clots form. To investigate this further, we propose the following:

First, moving to a tPA-plasminogen ROTEM *in vitro* assay as created above in the Genipin section to investigate if the lysis observed is due to fibrinogenolysis or fibrinolysis.

Second, purchasing pig-derived fibrinogen, and investigating different ratios of human and pig fibrinogen in the tPA-plasminogen and plasmin ROTEM *in vitro* assay to investigate what concentrations of swine fibrinogen are tolerable, and what concentrations of human fibrinogen are necessary to recapitulate clinically relevant hyperfibrinolysis curves. PolySTAT will be spiked into samples to see if it is able to correct the hyperfibrinolysis.

Third, once concentrations of swine and human fibrinogen levels are identified, these can be recapitulated in vivo using different levels of hemodilution and fibrinogen concentrate based on the work of Martini *et al*.[38,39] This can be evaluated with ROTEM post dilution.

Finally, a recent study by Tarandovskiy et al. used a plasmin generation assay to show that there is no plasmin generated in swine blood.[34] After the level of hemodilution and fibrinogen concentrate are selected, then a series of tPA, plasminogen, and plasmin infusions will need to be evaluated. Blood samples will be monitored in ROTEM to identify the necessary concentrations of thrombolytics needed to recapitulate hyperfibrinolysis.

Once the correct bleed profile is created in ROTEM, intravenous infusions of PolySTAT can be done to see if it corrects hyperfibrinolysis. If this work looks promising, then the model could be integrated into the swine aorta tear model or liver laceration model.

To make this more feasible from a cost perspective, the outline work above could be first attempted in rats to decrease the quantities of clotting factors needed. Additionally, the work with TUCA in

rats by Moore *et al*. highlighted the potential of PAI-1 in playing a role in preventing hyperfibrinolysis in rats.[40] There are small-molecule inhibitors of PAI-1 that have been developed,[41,42] and these could be evaluated in the shock-only rat model to see if they improve the potency of intravenously infused thrombolytics.

7.4 PolySTAT 2.0

Due to the difficulty of showing efficacy of PolySTAT in swine, it may be necessary to reformulate PolySTAT to improve its activity in coagulopathic blood that does not show hyperfibrinolysis. Currently in swine, we are unsure where the failure point of PolySTAT exists. Is the PolySTAT-fibrin gel showing adhesive or cohesive failure at the wound site? If it is adhesive failure this would lead us down the path of improving adhesion at the wound site through targeting other ECM proteins or targeting the surface of activated platelets. If it is cohesive failure, this would lead us down the path of improving the strength of the PolySTAT-fibrin network that forms by focusing on its strength, elasticity, and toughness to prevent rupture during clotting.

Adhesive Failure: Collagen Hybridizing Peptide (CHP), Platelet Targeting, and in vivo crosslinking

A recent study by Oshinowo et al. showed that pig platelet's preferentially bind to collogen over fibrinogen at an abnormally high rate compared to human, mouse, dog, and sheep platelets (Figure 19 below).[43]

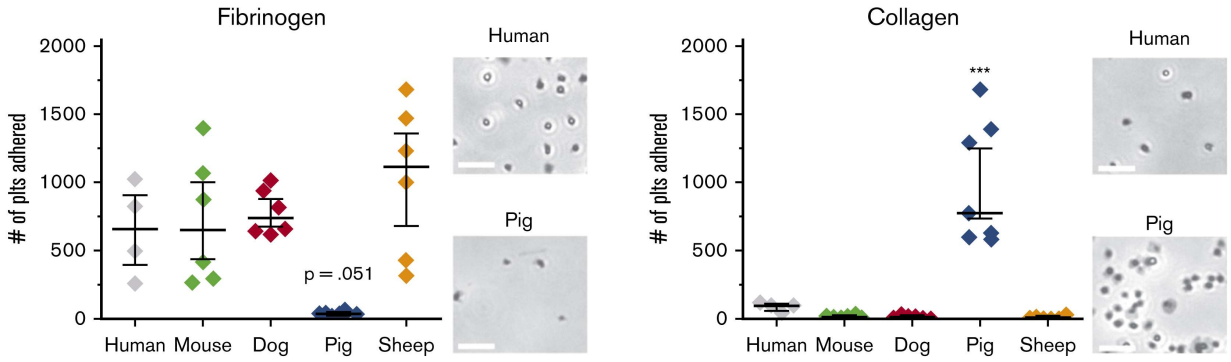

Figure 19. The number of platelets adhered to fibrinogen (left) for pigs is significantly lower compared to human, mouse, dog, and sheep platelets, while number of platelets adhered to

collagen (right) for pigs is significantly higher compared to the same species. Used with permission from Oshinowo *et al*. [43] under license 5612210725392 Copyright 2021 Elsevier.

This could indicate that PolySTAT might increase efficacy in swine by improving the fibrin network's adhesion through the direct binding to collagen. While a universal collagen binder might lead to systemic thrombosis concerns, Zitnay et al. evaluated a Collagen Hybridizing Peptide (CHP) that only binds mechanically damaged collagen that has an unfolded triple helix (Figure 20 below).[44]

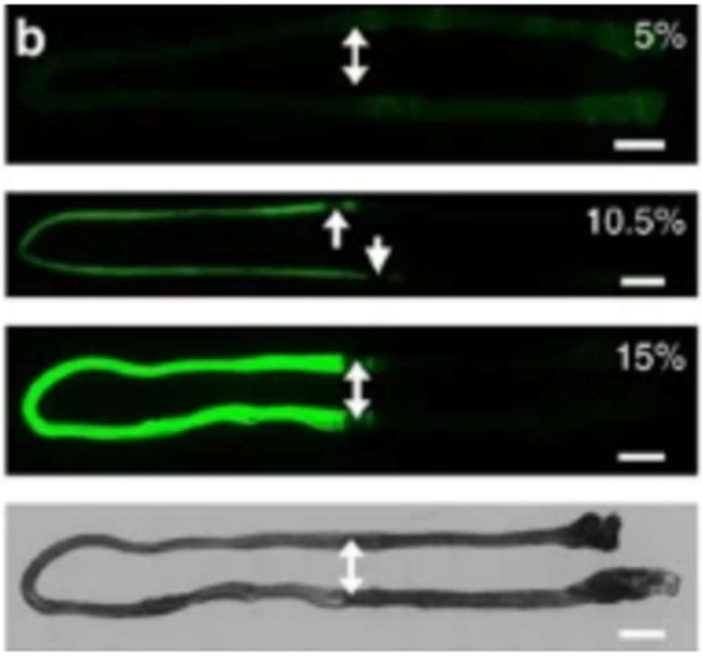

Figure 20. Increasing percent strain 5-15% of collogen leads to increased binding by a fluorescently labeled collagen hybridizing peptide (CHP). Used with permission from Zitnay et al. [44] under Creative Commons CC BY license Copyright 2017 Springer Nature.

This peptide consists of the following peptide sequence $(GPO)_9$ or nine glycine (G)-proline (P)-hydroxyproline (O) amino acids. A few approaches could be taken to incorporate CHP into PolySTAT. One approach is to make a z-group functionalized CTA using a CHP with a lysine-handle ($K(GPO)_9$), allowing us to use the normal synthesis procedure of PolySTAT. This would ensure each polymer has one single CHP. A second approach to achieve >1 CHPs attached to PolySTAT, would be to do the normal NHSMA-amine conjugation reaction with the same lysine-

handled CHP (K(GPO)$_9$). FBP and CHP could be mixed in different molar ratios or could be added sequentially to obtain different ratios of each peptide. A third approach would be to use a cysteine-handled CHP (C(GPO)$_9$) and connect it via the thiol-reactive pyridyl disulfide ethyl methacrylate (PDSEMA). This would make the conjugation of FBP and CHP orthogonal to each other and could make it easier to control the concentrations of each. To evaluate if CHP-functionalized PolySTAT results in higher adhesive forces between the ECM and the clot, adhesion should be evaluated both parallel (lap shear) and perpendicular (stud-pull) to the adhered surface. Two established lap shear tests exist in literature, one develop by the Kastrup group using a dynamic mechanical analyzer[18], and the other using a standard Instron tensile tester.[45] For stud-pull, we did some initial test method development using a Bose tensile tester at the UW Center for Research in Education and Simulation Technologies (CREST), and this method can be adapted to the DHR rheometer housed in the Emergency Medicine lab (Figure 21 below).

Figure 21. Images from stud-pull adhesion test developed on Bose tensile tester. The laser cut discs were coated in rat tail vein collagen, then blood was clotted in between the discs, followed by a uniaxial tensile test. This test could be adapted to the DHR-3 rheometer in the EM group.

Using these techniques, adhesion of blood clots with CHP-PolySTAT and current PolySTAT can be evaluated on surfaces coated with collagen and other ECM proteins. If the CHP peptide does not increase clot adhesion, another approach could be to target the surface of activated platelets directly through incorporating cyclic RGD peptides which would bind the integrin GPIIb-IIIa of activated platelets.[46]

Cohesive Failure: Self-Assembling Polymers, and modulating crosslink density

Another opportunity to improve the efficacy of PolySTAT is to shift our focus to improving the mechanical properties of the resulting fibrin-PolySTAT gel that forms. The PolySTAT polymer backbone has been optimized for increased water-solubility, and the minimum FBP needed to confer its anti-fibrinolytic activity, however it has never been optimized for its mechanical properties. Recent work has demonstrated that the side-chains of methacrylates and acrylamides can be engineered to increase the elasticity, strength, and toughness of hydrogels through reversible bonds (Figure 22 below).[47]

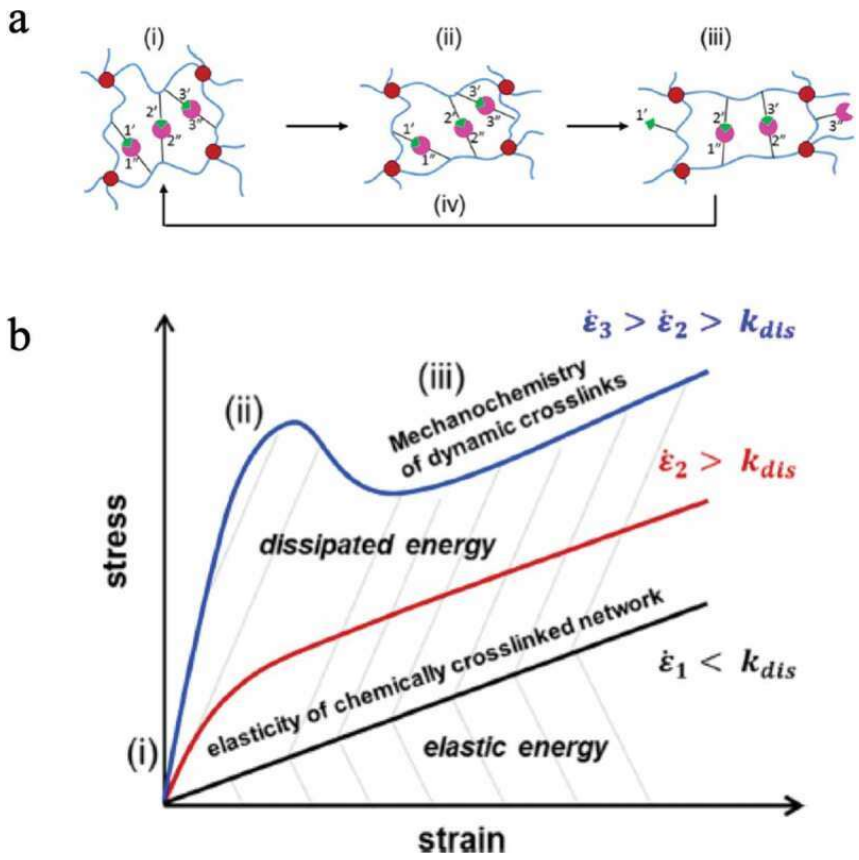

Figure 22.Stress-strain curve for a hydrogel that contains both covalent and dynamic/reversible crosslinks. The dynamic crosslinks can break during stretching to dissipate energy leading to a tougher hydrogel. Figure was reused with permission from Taylor & Francis Online for [47] by Takeoka *et al*.

The reversible bonds (ionic, hydrogen-bonded, metal chelation) help dissipate energy when mechanically stressed, which increases the toughness of hydrogels beyond the elastic energy of covalent cross links. SBMA is an example of a zwitterionic polymer that has been used to create tough hydrogels, and as was observed in Chapter 5 (LVRs), DP200 and DP300 pSBMA showed self-assembly due to ionic bonds. During infusion of PolySTAT, the concentration in the blood would be low enough to stay in a unimer state. However, when the PolySTAT starts accumulating at the site of bleeding, the increase of pSBMA would reach concentrations to self-assemble and the ionic side-chains will form dynamic bonds with each other (increasing cross link density). PolySTAT with a pSBMA backbone could be synthesized by synthesizing a DMAEMA-STAT followed by conversion of DMAEMA into SBMA using 1,3-propanesultone (Figure 23 below).[48]

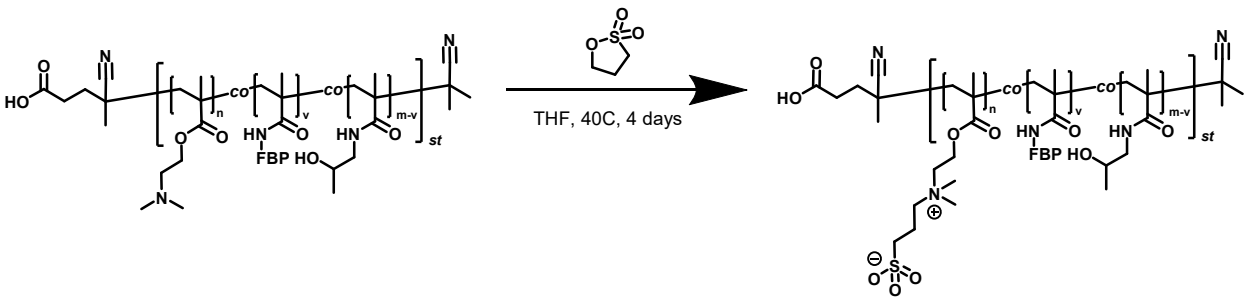

Figure 23. Synthesis approach to making PolySTAT with an SBMA zwitterionic backbone.

Another route, would be to incorporate strong hydrogen-bonding by creating a p(N-aryloyl glycinamide) (pNAGA) backbone which has also been used to create high strength hydrogels (Figure 24 below).[49]

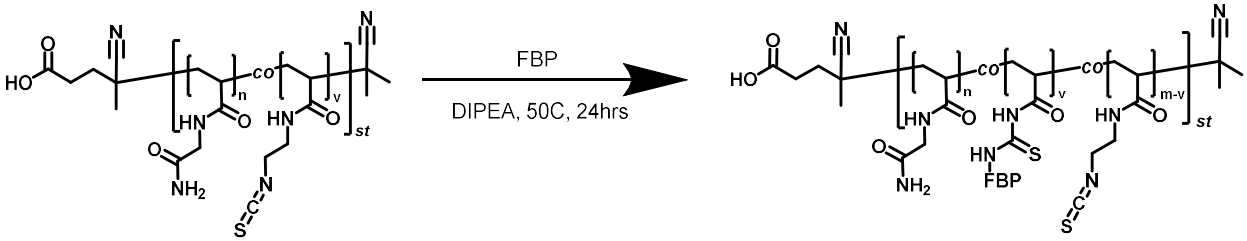

Figure 24.Synthesis approach to making PolySTAT with a pNAGA backbone.

However, this would require adapting PolySTAT to a synthesis route compatible with acrylamides, which would require a new conjugation handle. We would propose an isothiocyanate-amine conjugation strategy.

To investigate the mechanical impact of these new PolySTAT backbones, the following mechanical testing can be performed:

1. A rheometer can be used to measure elastic modulus, loss modulus, and yield stress.
2. An Instron tensile tester can be used to measure fracture mechanics with lap shear and a double cantilever test,[45] while toughness can be evaluated with a notch test.[50]

7.5 Pursuit of a Slow-Release LVR

One potential drawback of LVRs is the initial rapid increase in MAP during the infusion (Figure 25 below), which could exacerbate uncontrolled hemorrhage.

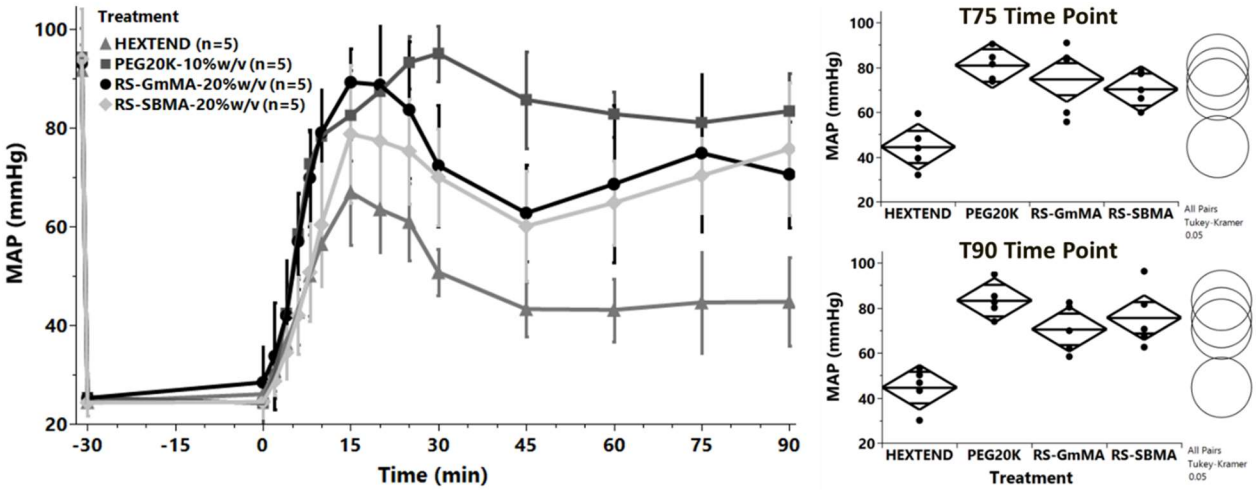

Figure 25. Blood pressure comparison of different LVRs during severe hemorrhagic shock rat model. Left: Right top: MAP for the T75 time point, there was no statistical difference between PEG20K, RS-SBMA, and RS-GmMA, however, Hextend was significantly different from the other treatments ($p = 0.0004$, $p = 0.0083$, and $p = 0.0021$, respectively). Bottom right: MAP for the T90 time point, there was no statistical difference between PEG20K, RS-SBMA, and RS-GmMA, however, Hextend was significantly different from the other treatments ($p = 0.0001$, $p = 0.0013$, and $p = 0.0061$, respectively). A fit model for a repeated measure, one-way anova with tukey post-hoc analysis ($\alpha = 0.050$) was used for statistical analysis.

To avoid this, the infusion could be given over a longer period to slow down the initial large increase in MAP. However, since these therapies are envisioned for military and austere environments, a slower infusion may not be feasible, and the priority is to get the patient stable and transported the hospital as quickly as possible. Therefore, an LVR with slow-release designed into the polymer would be desirable. From our work in Chapter 5, we saw some interesting aspects to the SBMA LVRs (Figures 26 and 27 below).

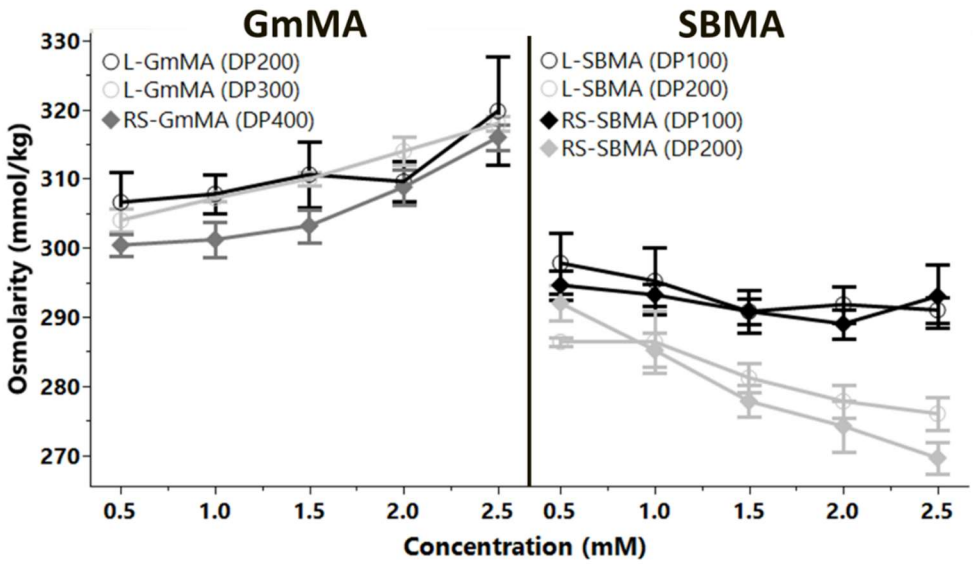

Figure 26. Vapor pressure osmometry measurements of pGmMA (left) and pSBMA (right). All measurements were done using a Vapro 5600 in triplicate. Error bars are 1 standard deviation from the mean.

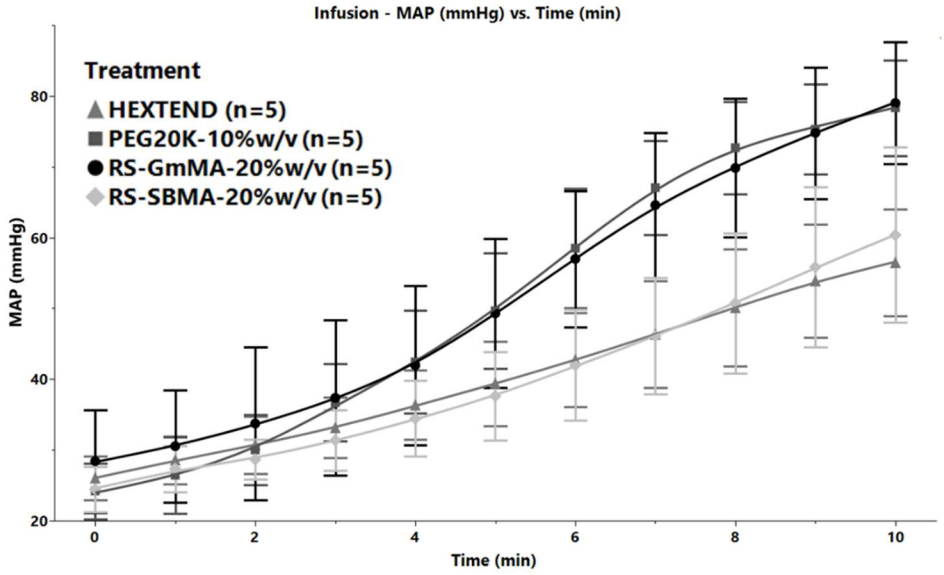

Figure 27. Blood pressure during infusion of treatment over 15 minutes. Hextend was statistically different from PEG20K and RS-GmMA at the following timepoints – T7, T8 ($p = 0.0042$ and $p = 0.0120$), T9, and T10 ($p = 0.0076$ and $p = 0.0060$). RS-SBMA was statistically different from PEG20K and RS-GmMA at the following timepoints – T7, T8 ($p = 0.0053$ and $p = 0.0151$), T9, and T10 ($p = 0.0297$ and $p = 0.0235$).

We believe the decrease in osmolarity and the slower rate of increase in blood pressure during infusion were due to pSBMA self-assembly. The SBMA was self-assembled into larger macromolecules, then upon dilution or infusion, the SBMA disassembled into unimers that increased the number of moles of solute in solution, resulting in an increase in osmolarity. Therefore, a potential LVR with slow-infusion properties could be created if we can harness this disassembly in a controlled manner upon infusion (Figure 28 below).

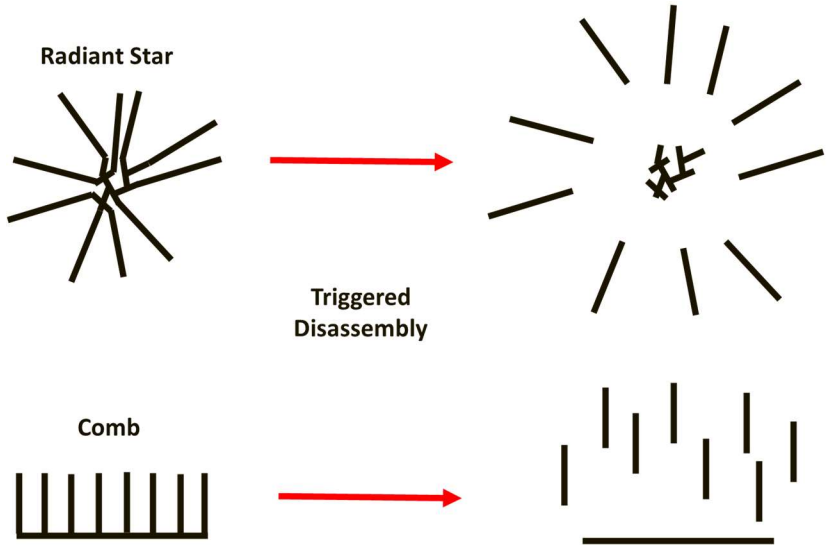

Figure 28. Triggered disassembly of radiant star and bottle brush/comb polymers to increase the number of moles of polymer in solution.

The current radiant stars with ~7 arms would allow for ~6-7x increase molar concentration, while a comb or bottle brush polymer could provide upwards of 100x increase in molar concentration.

Das *et al*. created radiant stars with a hydrolytically cleavable linker that allowed the arms to be nearly fully cleaved off over 30 days.[51] Although this degradation could be desirable to clear the therapy from a trauma patient and avoid edema, this degradation rate is too slow to be useful for resuscitation over 1-6 hours. Another linker to explore is the thioketal linker which is cleaved by reactive oxygen species (ROS).[52] A ROS-cleavable linker is desirable because our group has shown that leukocytes generate ROS-species during trauma, and this linker would also serve as a therapeutic by neutralizing ROS species. Of concern, this linker generates acetone as a byproduct, which the liver can breakdown in small amounts, but in a trauma patient this could lead to toxicity concerns. Also, this route is more synthetically challenging. Another option is boronic acids (Figure 29 below) which form dynamic covalent bonds with 1,2 and 1,3 diols.[53]

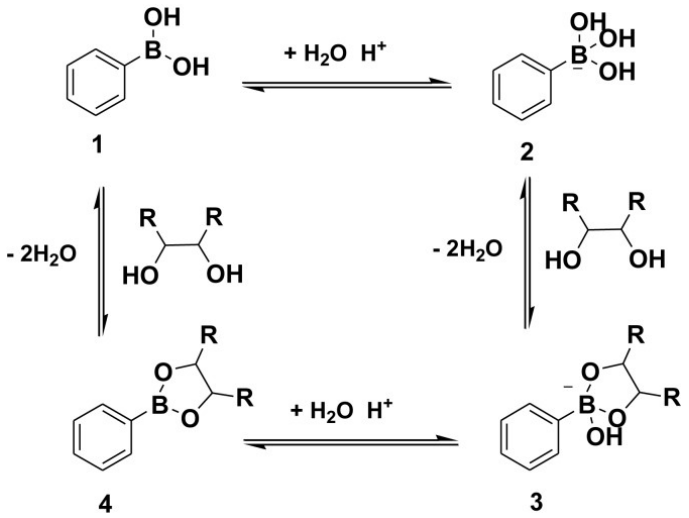

Figure 29. Mechanism of dynamic covalent bond between phenyl boronic acid and a diol. Reused with permission from Melavanki *et al.* [53] under the CC BY-NC-ND creative commons license Copyright 2020 Elsevier.

Boronic acids have been used to create polymer micelles with glucose-triggered disassembly.[54,55] Depending on the formulation, the disassembly occurred within minutes to an hour. Interestingly, during traumatic injury, the body undergoes a "fight or flight" response which results in a large increase in glucose levels.[56] Hyperglycemia in trauma patients correlates with higher mortality and morbidity.[57] This hyperglycemia was observed in the LVR rat study (Figure 30 below).

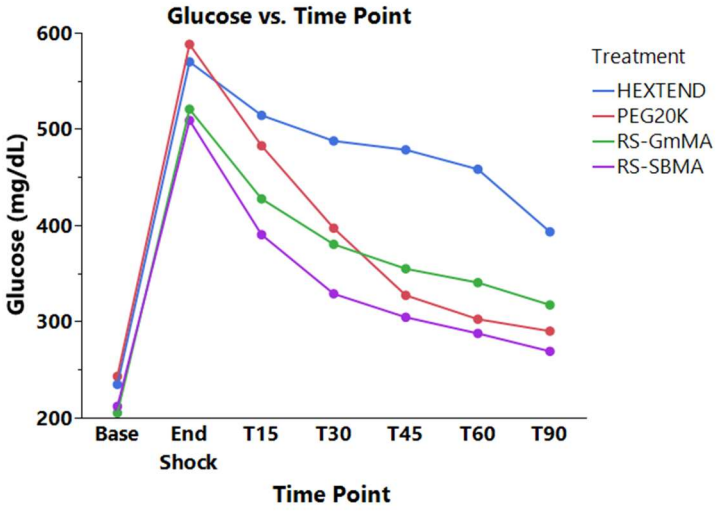

Figure 30. Glucose concentration over various time points during the severe hemorrhagic shock rat model evaluating different LVRs in Chapter 5.

Glucose levels increased by ~2-3x during the shock period and decreased as the rats were resuscitated. The rats reached concentrations of ~500-600 mg/dL, which corresponds to ~28-33 mmol/L of glucose in the bloodstream. In the LVR study, the radiant stars were estimated to reach concentrations of ~0.12 - 0.2 mmol/L, therefore with 100 arms, the glucose concentration would be > 10x higher than the concentration of boronic acid-diol complexes. Given the experience of the Pun lab with boronic acids, this is a very approachable pathway synthetically. Additionally, we would move away from polymer micelles which present stability concerns with lyophilization, and during injection.[58] To start, there are clear examples in literature where CTA agents with a z-group attached boronic acid or catechol have been used to click together two polymers (Figure 31 below).[59]

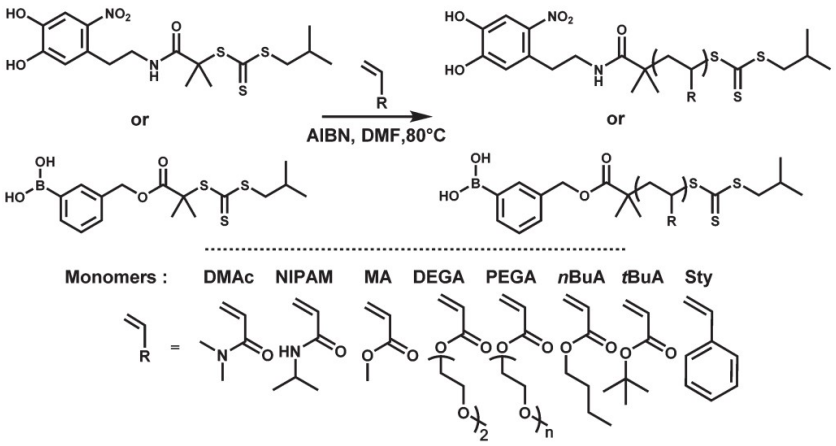

Figure 31. Examples from literature of phenyl boronic acid and catechol functionalized CTAs used to synthesize various polymers via RAFT. Used with permission from Coumes *et al.* [59] Copyright 2016 The Royal Society of Chemistry.

A similar approach would be used to create radiant stars or comb polymers with arms connected via boronic acid-diol dynamic bonds (Figure 32 below).

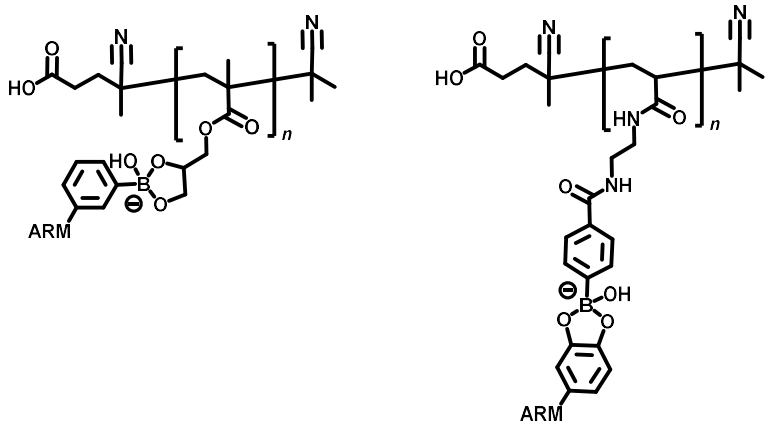

Figure 32. Two approaches to synthesize comb/bottle brush LVRs with arms connected via phenyl boronic acid-diol complexes. Left: A pGmMA backbone with pHPMA arms connected via the z-group of a phenyl boronic acid CTA. Right: A pPhenyl Boronic Acid backbone with pHPMA arms connected via the z-group of a catechol CTA.

The first approach would be to synthesize a pGmMA homopolymer to serve as the comb backbone. Next, pHPMA arms would be synthesized via RAFT with a boronic acid-functionalized CTA agent. The two polymers would then be mixed to form bottle brush polymers. Benefits of this approach are that the vicinal diol of GmMA most likely has a lower binding constant compared to a catechol and would be easier for glucose to competitively bind. Also, this is extremely easy synthetically. However, having the boronic acid present on the arm could cause issues after the arms are released, such as sticking to the glycocalyx or binding to glycosylated proteins on the surface of cells or in the interstitial space.

The second approach moves the boronic acid to the backbone, and the arm is synthesized with a catechol-functionalized CTA agent. This approach avoids the issue of the arms sticking to glycosylated proteins, however the bond between the catechol and boronic acid is stronger and would most likely result in a slower release *in vivo*. For both approaches, it is not known if the single hydroxyl on HPMA would lead to issues with binding the arms, if this occurs another water-soluble polymer could be used. Also, when the boronic acid-diol complexes form, the backbone of the bottle brush polymer becomes anionic. Anionic polymers preferentially accumulate in the kidneys and can interfere with coagulation; however, it is believed the neutral arms will be able to

shield these negative charges while in circulation, and the negative charge will be decreased over time as the arms fall off.

This solution is attractive for its simplicity in design, but also the strength of the boronic acid-diol complexation is easily tailored,[60] which can tune the release *in vivo*. Vapor pressure based osmometry can be used to quickly iterate on these designs. The polymers can be incubated in a glucose solution at pH 7.4, and the osmolarity of the solutions can be measured over time. This *in vitro* setup can be used to understand the dissociation kinetics as a function of glucose concentration. Similarly, the effect of these on coagulation can be evaluated by a similar time study in ROTEM. It will be important to see if the final concentration of unimers (fully disassembled) will lead to any issues in coagulation. Finally, the severe hemorrhagic shock model in rats can be used to evaluate the blood pressure response *in vivo*, and the glucose levels of the rats can be monitored via blood gas. The final design should be evaluated in an uncontrolled hemorrhage model in rats to see if the slow release is beneficial for survival.

7.6 REFERENCES

(1) Wilhelm, S. E.; Lounes, K. C.; Lord, S. T. Investigation of Residues in the Fibrin(Ogen) γ Chain Involved in Tissue Plasminogen Activator Binding and Plasminogen Activation. *Blood Coagulation & Fibrinolysis* **2004**, *15* (6), 451–461.

(2) Weisel, J. W.; Litvinov, R. I. Fibrin Formation, Structure and Properties. *Subcell Biochem* **2017**, *82*, 405–456. https://doi.org/10.1007/978-3-319-49674-0_13.

(3) Longstaff, C.; Thelwell, C.; Williams, S. C.; Silva, M. M. C. G.; Szabó, L.; Kolev, K. The Interplay between Tissue Plasminogen Activator Domains and Fibrin Structures in the Regulation of Fibrinolysis: Kinetic and Microscopic Studies. *Blood* **2011**, *117* (2), 661–668. https://doi.org/10.1182/blood-2010-06-290338.

(4) Suzuki, Y.; Sano, H.; Mochizuki, L.; Honkura, N.; Urano, T. Activated Platelet-Based Inhibition of Fibrinolysis via Thrombin-Activatable Fibrinolysis Inhibitor Activation System. *Blood Advances* **2020**, *4* (21), 5501–5511. https://doi.org/10.1182/bloodadvances.2020002923.

(5) Miljić, P.; Heylen, E.; Willemse, J.; Djordjević, V.; Radojković, D.; Colović, M.; Elezović, I.; Hendriks, D. Thrombin Activatable Fibrinolysis Inhibitor (TAFI): A Molecular Link

between Coagulation and Fibrinolysis. *Srp Arh Celok Lek* **2010**, *138 Suppl 1*, 74–78. https://doi.org/10.2298/sarh10s1074m.

(6) Bouma, B. N.; Mosnier, L. O. Thrombin Activatable Fibrinolysis Inhibitor (TAFI)—How Does Thrombin Regulate Fibrinolysis? *Annals of Medicine* **2006**, *38* (6), 378–388. https://doi.org/10.1080/07853890600852898.

(7) Suzuki, Y.; Tanaka, H.; Horinouchi, T.; Sano, H.; Honkura, N.; Unno, N.; Miwa, S.; Urano, T. Fibrinolysis-Resistant Carbonylated Fibrin Detected in Thrombi Attached to the Vascular Wall of Abdominal Aortic Aneurysms. *Sci Rep* **2020**, *10* (1), 20728. https://doi.org/10.1038/s41598-020-77582-1.

(8) Jeeva, F. Insights into Genipin Dye Mechanisms and Colour Origins. **2021**.

(9) Jeeva, F.; Caputo, C. Substituent Effects of Amines on Genipin Dye Formation – Insights into Dye Origin. 2021. https://doi.org/10.26434/chemrxiv.13604006.v1.

(10) Mallov, I.; Jeeva, F.; Caputo, C. B. An Edible Genipin-Based Sensor for Biogenic Amine Detection. *Journal of Chemical Technology & Biotechnology n/a* (n/a). https://doi.org/10.1002/jctb.6556.

(11) Mallov, I.; Jeeva, F.; Caputo, C. A Dual Sensor for Biogenic Amines and Oxygen Based on Genipin Immobilized in Edible Calcium Alginate Gel Beads. **2020**. https://doi.org/10.26434/chemrxiv.12252323.v1.

(12) Hannon, B. G.; Schwaner, S. A.; Boazak, E. M.; Gerberich, B. G.; Winger, E. J.; Prausnitz, M. R.; Ethier, C. R. Sustained Scleral Stiffening in Rats after a Single Genipin Treatment. *J. R. Soc. Interface.* **2019**, *16* (159), 20190427. https://doi.org/10.1098/rsif.2019.0427.

(13) Campbell, I. C.; Hannon, B. G.; Read, A. T.; Sherwood, J. M.; Schwaner, S. A.; Ethier, C. R. Quantification of the Efficacy of Collagen Cross-Linking Agents to Induce Stiffening of Rat Sclera. *J. R. Soc. Interface.* **2017**, *14* (129), 20170014. https://doi.org/10.1098/rsif.2017.0014.

(14) Liu, T.-X.; Wang, Z. Biomechanics of Sclera Crosslinked Using Genipin in Rabbit. *Int J Ophthalmol* **2017**, *10* (3), 355–360. https://doi.org/10.18240/ijo.2017.03.05.

(15) Shumin, C.; Wei, X.; Yunfeng, L.; Jiangshui, L.; Youguang, G.; Zhongqing, C.; Tao, L. Genipin Alleviates Vascular Hyperpermeability Following Hemorrhagic Shock by Up-

Regulation of SIRT3/Autophagy. *Cell Death Discovery* **2018**, *4* (1), 1–10. https://doi.org/10.1038/s41420-018-0057-2.

(16) Yang, Y.; Yang, Y.; Hou, J.; Ding, Y.; Zhang, T.; Zhang, Y.; Wang, J.; Shi, C.; Fu, W.; Cai, Z. The Hydroxyl at Position C1 of Genipin Is the Active Inhibitory Group That Affects Mitochondrial Uncoupling Protein 2 in Panc-1 Cells. *PLoS ONE* **2016**, *11* (1), e0147026. https://doi.org/10.1371/journal.pone.0147026.

(17) Jeeva, F. Insights into Genipin Dye Mechanisms and Colour Origins. **2021**.

(18) Chan, K. Y. T.; Yong, A. S. M.; Wang, X.; Ringgold, K. M.; John, A. E. S.; Baylis, J. R.; White, N. J.; Kastrup, C. J. The Adhesion of Clots in Wounds Contributes to Hemostasis and Can Be Enhanced by Coagulation Factor XIII. *Scientific Reports* **2020**, *10* (1), 20116. https://doi.org/10.1038/s41598-020-76782-z.

(19) Das, D.; Srinivasan, S.; Kelly, A. M.; Chiu, D. Y.; Daughtery, B. K.; Ratner, D. M.; Stayton, P. S.; Convertine, A. J. RAFT Polymerization of Ciprofloxacin Prodrug Monomers for the Controlled Intracellular Delivery of Antibiotics. *Polym. Chem* **2016**, *7*, 826–837. https://doi.org/10.1039/c5py01704a.

(20) Yanjarappa, M. J.; Gujraty, K. V; Joshi, A.; Saraph, A.; Kane, R. S. Synthesis of Copolymers Containing an Active Ester of Methacrylic Acid by RAFT : Controlled Molecular Weight Scaffolds for Biofunctionalization. *Biomacromolecules* **2006**, *7*, 1665–1670.

(21) Sun, S.-W.; Lin, Y.-C.; Weng, Y.-M.; Chen, M.-J. Efficiency Improvements on Ninhydrin Method for Amino Acid Quantification. *Journal of Food Composition and Analysis* **2006**, *19* (2–3), 112–117. https://doi.org/10.1016/j.jfca.2005.04.006.

(22) Ninh, C.; Iftikhar, A.; Cramer, M.; Bettinger, C. J. Diffusion–Reaction Models of Genipin Incorporation into Fibrin Networks. *J. Mater. Chem. B* **2015**, *3* (22), 4607–4615. https://doi.org/10.1039/C4TB02025A.

(23) Rivera-Delgado, E.; Learn, G. D.; Kizek, D. J.; Kashyap, T.; Lai, E. J.; von Recum, H. A. A Polymeric Delivery System Enables Controlled Release of Genipin for Spatially-Confined In Situ Crosslinking of Injured Connective Tissues. *Journal of Pharmaceutical Sciences* **2021**, *110* (2), 815–823. https://doi.org/10.1016/j.xphs.2020.09.044.

(24) Al-Hilaly, Y. K.; Williams, T. L.; Stewart-Parker, M.; Ford, L.; Skaria, E.; Cole, M.; Bucher, W. G.; Morris, K. L.; Sada, A. A.; Thorpe, J. R.; Serpell, L. C. A Central Role for

Dityrosine Crosslinking of Amyloid-β in Alzheimer's Disease. *Acta Neuropathol Commun* **2013**, *1*, 83. https://doi.org/10.1186/2051-5960-1-83.

(25) Al-Hilaly, Y. K.; Biasetti, L.; Blakeman, B. J. F.; Pollack, S. J.; Zibaee, S.; Abdul-Sada, A.; Thorpe, J. R.; Xue, W.-F.; Serpell, L. C. The Involvement of Dityrosine Crosslinking in α-Synuclein Assembly and Deposition in Lewy Bodies in Parkinson's Disease. *Sci Rep* **2016**, *6* (1), 39171. https://doi.org/10.1038/srep39171.

(26) Partlow, B. P.; Applegate, M. B.; Omenetto, F. G.; Kaplan, D. L. Dityrosine Cross-Linking in Designing Biomaterials. *ACS Biomater. Sci. Eng.* **2016**, *2* (12), 2108–2121. https://doi.org/10.1021/acsbiomaterials.6b00454.

(27) Mukherjee, S.; Kapp, E. A.; Lothian, A.; Roberts, A. M.; Vasil'ev, Y. V.; Boughton, B. A.; Barnham, K. J.; Kok, W. M.; Hutton, C. A.; Masters, C. L.; Bush, A. I.; Beckman, J. S.; Dey, S. G.; Roberts, B. R. Characterization and Identification of Dityrosine Cross-Linked Peptides Using Tandem Mass Spectrometry. *Anal. Chem.* **2017**, *89* (11), 6136–6145. https://doi.org/10.1021/acs.analchem.7b00941.

(28) Khalil, A.; Gerardin-Charbonnier, C.; Chapuis, H.; Ferji, K.; Six, J.-L. Original Bio-Based Antioxidant Poly(Meth)Acrylate from Gallic Acid-Based Monomers. *ACS Sustainable Chem. Eng.* **2021**, *9* (34), 11458–11468. https://doi.org/10.1021/acssuschemeng.1c03607.

(29) Lee, C.-U.; Roy, D.; Sumerlin, B. S.; Dadmun, M. D. Facile Synthesis of Thiol-Terminated Poly(Styrene-Ran-Vinyl Phenol) (PSVPh) Copolymers via Reversible Addition-Fragmentation Chain Transfer (RAFT) Polymerization and Their Use in the Synthesis of Gold Nanoparticles with Controllable Hydrophilicity. *Polymer* **2010**, *51* (6), 1244–1251. https://doi.org/10.1016/j.polymer.2010.01.033.

(30) Kolodziej, A. F.; Nair, S. A.; Graham, P.; McMurry, T. J.; Ladner, R. C.; Wescott, C.; Sexton, D. J.; Caravan, P. Fibrin Specific Peptides Derived by Phage Display: Characterization of Peptides and Conjugates for Imaging. *Bioconjugate Chem.* **2012**, *23* (3), 548–556. https://doi.org/10.1021/bc200613e.

(31) Oliveira, B. L.; Caravan, P. Peptide-Based Fibrin-Targeting Probes for Thrombus Imaging. *Dalton Trans.* **2017**, *46* (42), 14488–14508. https://doi.org/10.1039/C7DT02634J.

(32) Mori, H.; Takahashi, E.; Ishizuki, A.; Nakabayashi, K. Tryptophan-Containing Block Copolymers Prepared by RAFT Polymerization: Synthesis, Self-Assembly, and Chiroptical

and Sensing Properties. *Macromolecules* **2013**, *46* (16), 6451–6465. https://doi.org/10.1021/ma400596r.

(33) Landskroner, K.; Olson, N.; Jesmok, G. Cross-Species Pharmacologic Evaluation of Plasmin as a Direct-Acting Thrombolytic Agent: Ex Vivo Evaluation for Large Animal Model Development. *Journal of Vascular and Interventional Radiology* **2005**, *16* (3), 369–377. https://doi.org/10.1097/01.RVI.0000148828.40438.D3.

(34) Tarandovskiy, I. D.; Shin, H. K. H.; Baek, J. H.; Karnaukhova, E.; Buehler, P. W. Interspecies Comparison of Simultaneous Thrombin and Plasmin Generation. *Scientific Reports* **2020**, *10* (1), 3885. https://doi.org/10.1038/s41598-020-60436-1.

(35) Fay, W. P.; Murphy, J. G.; Owen, W. G. High Concentrations of Active Plasminogen Activator Inhibitor-1 in Porcine Coronary Artery Thrombi. *Arteriosclerosis, Thrombosis, and Vascular Biology* **1996**, *16* (10), 1277–1284. https://doi.org/10.1161/01.ATV.16.10.1277.

(36) Flight, S. M.; Masci, P. P.; Lavin, M. F.; Gaffney, P. J. Resistance of Porcine Blood Clots to Lysis Relates to Poor Activation of Porcine Plasminogen by Tissue Plasminogen Activator. *Blood Coagul Fibrinolysis* **2006**, *17* (5), 417–420. https://doi.org/10.1097/01.mbc.0000233374.79593.57.

(37) Neto-Neves, E. M.; Beam, D. M.; Kline, J. A. The Resistance of Swine Blood Clots to Alteplase-Induced Thrombolysis in Vitro Is Concentration-Dependent. *Thrombosis Update* **2021**, *2*, 100035. https://doi.org/10.1016/j.tru.2021.100035.

(38) Martini, J.; Maisch, S.; Pilshofer, L.; Streif, W.; Martini, W.; Fries, D. Fibrinogen Concentrate in Dilutional Coagulopathy: A Dose Study in Pigs. *Transfusion* **2014**, *54* (1), 149–157. https://doi.org/10.1111/trf.12241.

(39) Martini, W. Z.; Rodriguez, C. M.; Cap, A. P.; Dubick, M. A. Efficacy of Resuscitation with Fibrinogen Concentrate and Platelets in Traumatic Hemorrhage Swine Model. *J Trauma Acute Care Surg* **2020**, *89* (2S Suppl 2), S137–S145. https://doi.org/10.1097/TA.0000000000002736.

(40) Moore, H. B.; Moore, E. E.; Lawson, P. J.; Gonzalez, E.; Fragoso, M.; Morton, A. P.; Gamboni, F.; Chapman, M. P.; Sauaia, A.; Banerjee, A.; Silliman, C. C. Fibrinolysis Shutdown Phenotype Masks Changes in Rodent Coagulation in Tissue Injury versus

Hemorrhagic Shock. *Surgery* **2015**, *158* (2), 386–392. https://doi.org/10.1016/j.surg.2015.04.008.

(41) Pandya, V.; Jain, M.; Chakrabarti, G.; Soni, H.; Parmar, B.; Chaugule, B.; Patel, J.; Joshi, J.; Joshi, N.; Rath, A.; Raviya, M.; Shaikh, M.; Sairam, K. V. V. M.; Patel, H.; Patel, P. Discovery of Inhibitors of Plasminogen Activator Inhibitor-1: Structure-Activity Study of 5-Nitro-2-Phenoxybenzoic Acid Derivatives. *Bioorg Med Chem Lett* **2011**, *21* (19), 5701–5706. https://doi.org/10.1016/j.bmcl.2011.08.031.

(42) Rouch, A.; Vanucci-Bacqué, C.; Bedos-Belval, F.; Baltas, M. Small Molecules Inhibitors of Plasminogen Activator Inhibitor-1 – An Overview. *European Journal of Medicinal Chemistry* **2015**, *92*, 619–636. https://doi.org/10.1016/j.ejmech.2015.01.010.

(43) Oshinowo, O.; Copeland, R.; Sakurai, Y.; Fay, M. E.; Petrich, B. G.; Leong, T.; Brainard, B.; Lam, W. A. Significant Differences in Single-Platelet Biophysics Exist across Species but Attenuate during Clot Formation. *Blood Advances* **2021**, *5* (2), 432–437. https://doi.org/10.1182/bloodadvances.2020003755.

(44) Zitnay, J. L.; Li, Y.; Qin, Z.; San, B. H.; Depalle, B.; Reese, S. P.; Buehler, M. J.; Yu, S. M.; Weiss, J. A. Molecular Level Detection and Localization of Mechanical Damage in Collagen Enabled by Collagen Hybridizing Peptides. *Nat Commun* **2017**, *8* (1), 14913. https://doi.org/10.1038/ncomms14913.

(45) Liu, S.; Bao, G.; Ma, Z.; Kastrup, C. J.; Li, J. Fracture Mechanics of Human Blood Clots: Measurements of Toughness and Critical Length Scales. bioRxiv March 14, 2021, p 2021.03.13.435277. https://doi.org/10.1101/2021.03.13.435277.

(46) Srinivasan, R.; Marchant, R. E.; Gupta, A. S. In Vitro and In Vivo Platelet Targeting By Cyclic RGD-Modified Liposomes. *J Biomed Mater Res A* **2010**, *93* (3), 1004–1015. https://doi.org/10.1002/jbm.a.32549.

(47) Takeoka, Y.; Liu, S.; Asai, F. Improvement of Mechanical Properties of Elastic Materials by Chemical Methods. *Sci Technol Adv Mater 21* (1), 817–832. https://doi.org/10.1080/14686996.2020.1849931.

(48) Wang, N.; Seymour, B. T.; Lewoczko, E. M.; Kent, E. W.; Chen, M.-L.; Wang, J.-H.; Zhao, B. Zwitterionic Poly(Sulfobetaine Methacrylate)s in Water: From Upper Critical Solution Temperature (UCST) to Lower Critical Solution Temperature (LCST) with

Increasing Length of One Alkyl Substituent on the Nitrogen Atom. *Polym. Chem.* **2018**, *9* (43), 5257–5261. https://doi.org/10.1039/C8PY01211C.

(49) Xu, Z.; Liu, W. Poly(N-Acryloyl Glycinamide): A Fascinating Polymer That Exhibits a Range of Properties from UCST to High-Strength Hydrogels. *Chem. Commun.* **2018**, *54* (75), 10540–10553. https://doi.org/10.1039/C8CC04614J.

(50) Tutwiler, V.; Singh, J.; Litvinov, R. I.; Bassani, J. L.; Purohit, P. K.; Weisel, J. W. Rupture of Blood Clots: Mechanics and Pathophysiology. *Sci. Adv.* **2020**, *6* (35), eabc0496. https://doi.org/10.1126/sciadv.abc0496.

(51) Das, D.; Srinivasan, S.; Brown, F. D.; Su, F. Y.; Burrell, A. L.; Kollman, J. M.; Postma, A.; Ratner, D. M.; Stayton, P. S.; Convertine, A. J. Radiant Star Nanoparticle Prodrugs for the Treatment of Intracellular Alveolar Infections. *Polym. Chem.* **2018**, *9* (16), 2134–2146. https://doi.org/10.1039/C8PY00202A.

(52) Rinaldi, A.; Caraffi, R.; Grazioli, M. V.; Oddone, N.; Giardino, L.; Tosi, G.; Vandelli, M. A.; Calzà, L.; Ruozi, B.; Duskey, J. T. Applications of the ROS-Responsive Thioketal Linker for the Production of Smart Nanomedicines. *Polymers (Basel)* **2022**, *14* (4), 687. https://doi.org/10.3390/polym14040687.

(53) Melavanki, R.; Kusanur, R.; Sadasivuni, K. K.; Singh, D.; Patil, N. R. Investigation of Interaction between Boronic Acids and Sugar: Effect of Structural Change of Sugars on Binding Affinity Using Steady State and Time Resolved Fluorescence Spectroscopy and Molecular Docking. *Heliyon* **2020**, *6* (10), e05081. https://doi.org/10.1016/j.heliyon.2020.e05081.

(54) Roy, D.; Sumerlin, B. S. Glucose-Sensitivity of Boronic Acid Block Copolymers at Physiological PH. *ACS Macro Lett.* **2012**, *1* (5), 529–532. https://doi.org/10.1021/mz300047c.

(55) Gaballa, H.; Theato, P. Glucose-Responsive Polymeric Micelles via Boronic Acid–Diol Complexation for Insulin Delivery at Neutral PH. *Biomacromolecules* **2019**, *20* (2), 871–881. https://doi.org/10.1021/acs.biomac.8b01508.

(56) Eakins, J. Blood Glucose Control in the Trauma Patient. *J Diabetes Sci Technol* **2009**, *3* (6), 1373–1376.

(57) Laird, A. M.; Miller, P. R.; Kilgo, P. D.; Meredith, J. W.; Chang, M. C. Relationship of Early Hyperglycemia to Mortality in Trauma Patients. *Journal of Trauma and Acute Care Surgery* **2004**, *56* (5), 1058. https://doi.org/10.1097/01.TA.0000123267.39011.9F.

(58) Lu, Y.; Zhang, E.; Yang, J.; Cao, Z. Strategies to Improve Micelle Stability for Drug Delivery. *Nano Res* **2018**, *11* (10), 4985–4998. https://doi.org/10.1007/s12274-018-2152-3.

(59) Coumes, F.; Woisel, P.; Fournier, D. *Facile Access to Multistimuli-Responsive Self-Assembled Block Copolymers via a Catechol/Boronic Acid Ligation*. ACS Publications. https://doi.org/10.1021/acs.macromol.6b01889.

(60) Brooks, W. L. A.; Deng, C. C.; Sumerlin, B. S. Structure–Reactivity Relationships in Boronic Acid–Diol Complexation. *ACS Omega* **2018**, *3* (12), 17863–17870. https://doi.org/10.1021/acsomega.8b02999.